Characterization and Development of Algorithms for Array Processing Architectures of Adaptive Antennas in Wireless Communication

A Thesis submitted
for the award of the degree of
DOCTOR OF PHILOSOPHY

by

RAJESH KHANNA

Supervisor

Prof. (Dr.) RAJIV SAXENA
Professor & Head, Department of Electronics Engineering
Madhav Institute of Technology & Science, Gwalior-474005(M.P)
(Formerly: Professor & Head, Department of Electronics & Communication Engineering,
Thapar Institute of Engineering and Technology, Patiala)

Electronics and Communication Engineering Department
Thapar Institute of Engineering and Technology
(Deemed University)
Patiala-147004 (India)

Certificate

Certified that the thesis entitled **"Characterization and Development of Algorithms for Array Processing Architectures of Adaptive Antennas in Wireless Communication"** which is being submitted by **Mr. Rajesh Khanna** to **Department of Electronics & Communication Engineering, Thapar Institute of Engineering and Technology, Patiala** in fulfillment of the requirements for the award of degree of "Doctor of Philosophy" is a record of bonafide research work carried out by him under my guidance and supervision. The matter presented in this thesis does not incorporate without acknowledgment any material previously published or written by any other person except where due reference is made in the text.

(Dr. Rajiv Saxena)
Professor and Head,
Department of Electronics & Communication Engineering,
Madhav Institute of Technology and Science
Gwalior

Abstract

To set up an efficient wireless and mobile communication system, requires characterization of its environments and its components, in particular, its array processing architecture. This research work has been prompted by the current thrust in wireless and mobile communication technology to look for new approaches and technologies to improve performance of array processing architectures, thereby improving spectrum efficiency and to be able to support the projected capacity demands with the introduction of new personal communication services. The results presented in this thesis constituted four targets.

First, new side lobe control beamforming algorithms for array processing architectures of CDMA based wireless communication systems are developed for interference reduction. It is shown that conventional arrays based on nulling procedure are unlikely to be applicable in practical CDMA based wireless communication systems for large number of interferers. The role of FrFT in providing taper of varying side-lobe level and beamwidth is investigated. A procedure for tapering in FrFT domain is proposed, which can be used with optimal array processing also. The weights obtained by FrFT taper are found to be practically realizable weights. The one to one relationship between capacity and beampattern is established. A relationship between the side-lobe level and number of interferers is derived. A new algorithm capable of synthesizing Chebyshev-like low side-lobe beam patterns with adjustable beamwidth and steering invariance is developed. The proposed algorithm is shown to handle large angular spreads of interference effectively. The increase in information capacity and the performance improvement in various performance metrics viz; Signal-to-interference-plus-noise ratio (SINR), Normalized SINR (NSNIR), Array gain (AG) and Mean square error (MSE), of array processing architectures, by implementation of new beamforming algorithm, are investigated. It is shown through Monte Carlo simulations that for large number of interferers the proposed algorithm outperforms the adaptive algorithm.

The second target of this thesis has been the development and application of advanced array signal processing techniques to wireless and mobile communication systems that have a practical implementation complexity and achieve high performance levels. The second target is achieved by development of FrFT based beamforming

algorithms, in non stationary environments, towards improving the performance of array processing architectures of adaptive antenna from the point of view of reducing mean squared error. It is shown that the FrFT based optimal beamformer reduces the Mean Square Error to a greater extent for multipath fading signal over the additive white Gaussian channel. The proposed optimum FrFT beamformer is shown yielding small errors in case of accelerating source problems also which are common in wireless communication. The proposed FrFT based beamforming algorithm is investigated in different fading channels to demonstrate the merits of the algorithm. The superiority of the proposed beamforming technique over time and frequency domain beamforming is established in fading channels. The proposed FrFT based optimum beamformer outperforms the time domain and frequency domain optimum beamformer in terms of bit error rate in Rayleigh and Nakagami fading channels.

The use of FrFT based arrays for MIMO systems is proposed for decreasing channel estimation errors caused by Gaussian noise. A new optimum FrFT based MIMO receive beamformer is proposed. The performance of proposed beamformer is evaluated for spatial multiplexed systems in terms of bit error rate and block error rate. The use of proposed beamformer with rate one systems is also demonstrated. It is shown that BER of spatial multiplexed as well as rate one system can be decreased with use of proposed beamformer.

The use of adaptive antennas on handheld radios is a new area of research. All the research in the field of smart antennas at handset is in the area of diversity, capacity improvement, reduction of multi- path fading, suppression of interference signals, improvements of call reliability, mitigation against dead zones, increased data rates, spectral efficiency etc. The effectiveness of smart antenna in controlling radiation hazards at handset is explored in the light of establishing the advantages of smart antenna over a single antenna system at the handset. The adaptive antenna at the handset constantly forms a broad null towards the user head. The power absorbed and rise in temperature of various tissues of head is compared for omni directional as well as adaptive antenna. It is established that future mobile handset employing adaptive antenna, could also reduce the RF hazards.

Acknowledgements

First above all, I would like to thank my *Babaji* of *Radha Soami Satsang Beas, Beas* for his grace, love and for providing with an opportunity to pursue a doctoral degree and helping me see through to finishing this work. As I discover myself at the tail end of this work. I recollect many indispensable events that enabled smooth and proper completion of this work. I am undoubtly thankful to all people who were involved in the background for such events to materialize and I wish to recollect and acknowledge them all.

I feel proud to be a student of Dr. R.Saxena. With great pleasure and a deep sense of gratitude, I wish to thank him for his continuous and invaluable guidance as well as his timely advice that contributed greatly to the completion of this dissertation. His profound technical insight, entering effort and vision has helped to give the proper shape to this dissertation. Without his thought-provoking guidance and never-ending encouragement, this dissertation would not have been possible.

I would like to greatly acknowledge and thank the entire administration and management of Thapar Institute of Engineering and Technology, Patiala for enabling and supporting me for this work, I have great pleasure in recording grateful thanks to Director of Thapar Institute for his constant encouragement, timely advice and support throughout. I greatly acknowledge Dr. Sushil Mittal, Dean (Research and Sponsored Projects) for closely monitoring the work and providing discussions and continuous encouragements to complete this work. I also thank him for his constant encouragement and motivation in completion of this work. His watchful way of critically promoting and monitoring research activities helped me a lot to complete this work.

I would also like to thank doctoral committee members for sparing their time and interest in serving on my doctoral committee.

Special thanks are due to my colleagues in the Department of Electronics & Communication Engineering who provided help and advice throughout my entire PhD work. My special thanks to Ajay Batish for his continuous encouragement throughout thesis work. I am thankful to my students for patiently bearing with me when I used to busy with this work.

I also express my sincere gratitude to my in laws for their ceaseless love and firm support. My parents, Sh.Y.P.Khanna and Smt. Sheela Khanna, I find no words to convey how happy and contended I feel to acknowledge that it is only your hard work, untiring efforts and confidence in me which made me what I am today and for instilling in me a love of learning. The moral and ethical values which you have imbibed in me always showed me a path in hardships.

Last but not the least, I understand and value all the cooperation, help and the sacrifices my wife, Gagandeep, and my children Shefali and Rahul had to undergo. I would like to thank my wife, Gagandeep, for enduring a seemingly endless ordeal, for sacrificing some of her best years so that I could finally finish this research work. I wish to tell you something you know it is only now, I am able to complete my work because of your true love, support, patience and caring nature.

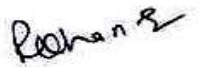

Rajesh Khanna

Contents

List of Figures

List of Tables

Acronyms and Abbreviations

1G	First Generation
2G	Second Generation
3G	Third Generation
3GPP	Third Generation Partnership Project
4G	Fourth Generation
AG	Array Gain
AMPS	Advanced Mobile Phone System
AOA	Angle of Arrival
ATIS	Alliance for Telecommunications Industry Solutions
AWGN	Additive White Gaussian Noise
BER	Bit Error Rate
BLER	Block Error Rate
BPSK	Binary Phase Shift Keying
BS	Base Station
CDMA	Code Division Multiple Access
CMA	Constant Modulus Algorithm
CSI	Channel State Information
CSIR	Channel state information at receiver
CSIT	Channel State information at Transmitter
DF	Direction-Finding
DMI	Direct Matrix Inversion
DOA	Direction of Arrival
DOP	Depth of Penetration
DS-CDMA	Direct Sequence Code Division Multiple Access
EMR	Electromagnetic Radiations
ESC	Extra Surface Cooling
ESR	Error to signal ratio
ETSI	European Telecommunications Standards Institute
FA	Finite Alphabet
FDD	Frequency Division Duplex Mode
FDMA	Frequency Division Multiple Access
FFT	Fast Fourier Transform
FIR	Finite Impulse Response
FrFT	Fractional Fourier Transform
FT	Fourier Transform
GBSBC	Geometrical Based Single Bounce Circular

GBSBE	Geometrical Based Single Bounce Elliptical
GSM	Global System For Mobile Communication
ITU	International Telecommunication Union
IMT-2000	International Mobile Telecommunication-Year -2000
JARIB	Japan's Association of Radio Industry And Business
LOS	Line of Sight
LS	Least Squares
LSC	Low Surface Cooling
LTV	Linear Time-Variant
MA	Multiple Access
MAI	Multiple Access Interference
MBC	Multiple Beam Constraint
Mbps	Mega bits per second
Mcps	Mega chips per second
MHz	Mega Hertz
MIMO	Multiple Input Multiple Output
ML	Maximum Likelihood
MMSE	Minimum Mean Squared Error
MRC	Maximal Ratio combiner
MSE	Mean Squared Error
MSLL	Maximum Side Lobe Level
MSNR	Maximum Signal to Noise Ratio
MV	Minimum Variance
MVDR	Minimum-Variance Distortion Less Response
NSC	Normal Surface Cooling
NSINR	Normalized SINR
O&M	Operation and Maintenance
OFMRB	Optimal FrFT based MIMO Receive Beamformer
OSNR	Output SNR
OSTBC	Orthogonal Space time block code.
OVSF	Orthogonal Variable Spreading Factor
PDC	Pacific Digital Cellular
pdf	Probability Density Function
PSTN	Public Switched Telephone Network
PTR	Power Transferred Ratio
QPSK	Quadrature Phase Shift Keying
RF	Radio Frequency
RX	Receive Antennas

RV	Random Variable
SAR	Specific Absorption Rate
SBA	Switching Beam Array
SEP	Symbol Error Probability
SER	Symbol Error Rate
SDMA	Space Division Multiple Access
SINR	Signal-To-Interference-Plus-Noise Ratio
$SINR_{ele}$ or $SINR_{input}$	Elemental Level Signal-to-Interference-Plus-Noise Ratio
$SINR_{opt}$	Optimal SINR
$SINR_{out}$	Output Signal-to-Interference-Plus-Noise Ratio
SIR	Signal to Interference Ratio
SMG	Special Mobile Group
SNR	Signal to Noise Ratio
SNR_{ele}	Elemental Level SNR
SNR_{array}	SNR at the output of array
SM	Spatial Multiplexing
ST	Space time
STBC	Space time block code
STTC	Space time trellis coding
STD	Simple transmit diversity
TBA	Tracking Beam Array
TCP	Telephone Communication Power
TDD	Time Division Duplex Mode
TDMA	Time Division Multiple Access
TIA	Telecommunications Industry Association
tr	Trace of Matrix
TX	Transmit Antennas
ULA	Uniform Linear Array
UMTS	Universal Mobile Telecommunication System
USDC	United States Digital Cellular
UTRA	UMTS Terrestrial Radio Access
WARC	World Administrative Radio Conference
WCDMA	Wideband Code Division Multiple Access
WHT	Wireless Handheld Terminal
WWRF	Wireless World Research Forum

Glossary of Symbols

ε	Electrical Permittivity
μ_p	Magnetic Permeability
σ	Electrical Conductivity
α	Attenuation Constant
β	Phase Constant
τ	Fraction of Energy Transmitted in the Tissue
γ_t, γ_b	Density of Tissue and blood
α	Phase Difference
$\Gamma(.)$	Gamma Function
ε_0	Permittivity of Vacuum
μ_0	Magnetic Permeability of Vacuum
σ_0	Electrical Conductivity of Vacuum
$\sigma 0.1$	Electrical Conductivity at 0.1 GHz
γ_b	Density of Blood in Gm/Cm3
ε_s^m	Extrapolated Microwave Permittivity
σ_s^m	Extrapolated Conductivity
'a'	ath Order of Fractional Fourier Transform
A	Cross Section Area of Tissue
a_m, b_m	Semi major and Semi minor Axis
c_t, c_b	Specific Heat of Tissue and blood Cal/Gm-^{0}C
d	Distance Between Two Elements
E,H	Electric and Magnetic Field Intensity
e	Error Output
f	Frequency in GHz
f_D	Doppler Frequency
J	Mechanical Equivalent of Heat
m	Volumetric Flow Rate of Blood Per Unit of the Mass of Tissue
P_i	Incident Power Density
R	Reflection Coefficient
T	Transmission Coefficient
tan δ	Loss Tangent
T_c	Temperature Outside Tissue Plane
T_i	Initial Temperature of Tissue
w_b	Mass Flow Rate of Blood Through Unit Volume
$\boldsymbol{w}_{opt}$	Optimal Wiener Filter Weight
Z_{peak}	Location of Peak Temperature Within Tissue

G_t, G_r	Gains of the Transmit and Receive One-Element Antennas
β	Random Phase
ρ	Normalized SINR
AF	Adaptive Filter
ξ	Ratio of maximum weight to minimum weight.
C	Capacity
F^a	a^{th} Order Fractional Fourier Operator
T_{one}	Operator Representing the Overall Filtering Configuration
P_r, P_t	Received and Transmitted Powers Respectively
H_t, H_r	Effective Heights of Transmit and Receive Antennas Respectively
K	Size of Cell Cluster
R_{x_a}	Covariance of the a^{th} Order FrFT of The Signals Arriving at Sensors
$r_{x_a d}$	Cross-Covariance Between a^{th} Order FrFT of the Desired Signal and FrFT of the Signal Arriving at the Sensor
M_R, M_T	Number of receive and transmit antennas
H	Channel Matrix
E_s	Energy/symbol period
C_{det}, C_{cu}, C_{WF}	Capacity of deterministic, unknown and water filling channel
W	Bandwidth of channel
λ_i	Eigen values
r	Rank of channel
γ_i^{opt}	Optimal energy allocation
T_{code}	Code word Length
Δ	Coherence interval of channel
$C_{out,q}$	Outage capacity
Prob.	Probability
r_t	Temporal code rate
r_s	Spatial code rate
ZMCSCG	Zero mean circularly symmetric complex Gaussian
N_0	Noise variance
h	Channel vector
$\boldsymbol{H}_{eff}$	Effective channel vector
U_{MRC}, U_{STD}	Decision RV for MRC and STD scheme
P_e	Probability of error
$c(\theta)$	Beamformer response
$C[\theta]$	Information Capacity

Chapter 1

1.1 INTRODUCTION

The goal for the next generation of wireless communication systems is to seamlessly provide a wide variety of communication services to anybody, anywhere, anytime. Radio communication has been mobile since the early work of Marconi, transmitting Morse signals wirelessly across the Atlantic Ocean in 1901. Technical advances in this field have promptly been adopted by the public. Cellular radios can be regarded as the earliest form of "Wireless Personal Communications" [85]. In the last twenty years, mobile radio communication has become a consumer product. In some areas the cellular phones are even more common than phones connected to the fixed net. The first generation (1G) of wireless networks, commonly referred to as analog systems, was primarily concerned with the provision of voice services, allowing user's transition from conventional fixed telephony to mobile telephony. The Advanced Mobile Phone System (AMPS) is the most notable of the 1G systems developed by the Bell Telephone System. Due to limited spectrum and high capacity demand, Bell Tell Labs proposed the frequency reuse concept.

In the system proposed by Bell-Tell Labs, a mobile entity is linked to a base station (BS). BS's are connected to a radio network controller, which uses additional interfaces that cater for the access to the public switched telephone network (PSTN). As the signals on the air–interface experience a distance dependent attenuation and transmit powers are limited, the coverage area of a BS is limited. The area which is covered by a BS is referred to as a cell. When modeling cellular systems, cells are approximated by hexagons as they can be used to cover a plane without overlap and represent a good approximation of circles [167]. Since the total available radio resource is limited, the spatial dimension is used to allow wide area coverage. This is achieved by splitting the radio resource into groups. These groups are then assigned to different contiguous cells. This pattern is repeated, as often as necessary, until the entire area is covered. A single pattern is equivalent to a cluster. Therefore, a radio resource which is

split into K groups directly corresponds to a cell cluster of size K. In this way, it is ensured that the same radio resource is only used in cells that are separated by a defined minimum distance. When mobile moves from one base station to another, a handover takes place.

1.2 EVOLUTION OF MOBILE COMMUNICATION

As the wireless communication systems evolved, service quality and capacity were of primary importance. To develop such spectrum efficient systems a suitable air interface is required. For this four multiple access (MA) techniques are used. MA technique is the approach to accommodate a large number of users simultaneously and at the same time separate their signals, so that they do not cause interference to each other called multiple access interference (MAI). An ideal MA technique supports the time variant request of radio capacity because this means that, at any given time, only those resources are allocated which are actually required [156]. The four MA principles are:-

- Frequency Division Multiple Access(FDMA)
- Time Division Multiple Access (TDMA)
- Code Division Multiple Access (CDMA)
- Space Division Multiple Access (SDMA)

In FDMA, the total available bandwidth is divided into a number of non overlapping frequency bands. In FDMA, the user signal is separated in frequency domain and at the receiver band pass filter is used for signal separation. In TDMA, the user signal is separated in time domain by dividing time axis into non overlapping time frames consisting of non overlapping time slots. With in these time frames one or more time slots are allocated to each user. In CDMA, a reuse factor of unity can be realized [128]. Here the user signals are transmitted simultaneously and are separated by a unique orthogonal PN sequence code. The technique is also called “spread spectrum”. Spread spectrum technique was first invented in the beginning of 1950 and since then it has mostly been used for military purposes. The spread spectrum was especially used in anti jamming (strong intentional interference) techniques. Now, after almost 50 years, the CDMA technique is highly in focus again, this time for advanced digital radio communication. Of all the variants of CDMA, the Direct Sequence Code Division Multiple Access (DS-CDMA) technique is used in the next generation of mobile

communication systems [92]. The space dimension (SDMA) is of particular significance as it allows the use of the same radio resource at the same time, frequency and with the same code at another physical location, which is spatially separated in distance or angle. The magnitude of spatial separation depends on the required level of interference protection.

The rapid growth in the number of subscribers and the proliferation of many incompatible first generation systems were the main reason behind the evolution of the second generation cellular systems. Second generation (2G) systems take the advantage of compression and coding techniques associated with digital technology. All the second generation systems employ digital modulation schemes. Multiple access techniques, like TDMA and CDMA are used along with FDMA in the second generation systems. 2G cellular systems include: United States Digital Cellular (USDC) standards IS-54 and IS-136[158], Global System for Mobile communications (GSM) [109], Pacific Digital Cellular (PDC) and cdmaOne. These systems have transitioned the voice services supported by analog networks into a digital environment, thus increasing the supported capacity and allowing for additional services, such as text messaging and limited access to data services. GSM, IS54 and PDC systems use a combination of FDMA and TDMA [85, 109], while the IS 95 system uses a combination of CDMA and FDMA [13]. Second generation networks, currently in use, are very near to their maximum capacity but they still lack in two aspects:-

- Unable to meet increase demand for capacity [45]
- Incompatible standards in 2G systems [2,68]

Merrill Lynch had already forecasted per diem traffic of 7000 Gigabytes to be carried by 1 million base stations in 2003 and by 2005; 1 billion subscribers are predicted [131]. In order to accommodate the growth in capacity and bandwidth needs, the World Administrative Radio Conference (WARC) of the International Telecommunications Union (ITU) [68] has identified extended spectrum for third generation (3G) systems, around the 2GHz band. Additionally, the 3G technology proposals, known as International Mobile Telecommunications for the year 2000 (IMT-2000), use improved and more sophisticated modulation schemes, so as to maximize the new spectrum allocation. 3G systems offer enhanced features, adding video and images to the voice services and allowing improved access to data networks and to the Internet. Unlike the transition from first to second generation, the migration from 2G to

3G is occurring smoothly. Existing 2G networks evolved to 3G, with transitional solutions known as 2.5G, bridging the gap between them. The increasing demand for capacity in the already saturated 2G networks, as well as for enhanced data and Internet services, have made 2.5G solutions very appealing and important. These solutions relied on technology improvements to existing networks and allowed for an extension of their "lifespan", until the 3G proposals were finalized and validated. The introduction of multimedia services in 3G networks implies an increase in the bandwidth requirements. 3G cellular systems are being designed to support wideband services like high speed Internet access, video and high quality image transmission with the same quality as the fixed networks. The primary requirements of the 3G systems are [68]:-

- Voice quality comparable to Public Switched Telephone Network.
- Support of both packet-switched and circuit-switched data services.
- More efficient usage of the available radio spectrum.
- Backward Compatibility with pre-existing networks and flexible introduction of new services and technology.
- An adaptive radio interface suited to the highly asymmetric nature of most Internet communications.
- A much greater bandwidth for the downlink than the uplink.
- Support of high data rate.

The table 1.1 shows the data rate requirement of the 3G systems

Table-1.1: 3G Data Rate

S. No	Type of traffic	Data rate
1.	Vehicular	144kbps
2.	Outdoor & Pedestrian	384kbps
3.	Indoor	2Mbps

The CDMA technology is the base of 3G wireless personal communication systems [128-129, 94]. There are two proposed wideband CDMA systems as the 3G standards, which meet the IMT-2000 requirements. The first standard is the Wideband CDMA (WCDMA) system, often called Third Generation Partnership Project (3GPP) [2] that were proposed by Europe and Japan. The 3GPP system was designed to be backward compatible with the GSM system, which is a second generation TDMA

standard deployed in Europe. The second standard is the cdma2000 system [69, 158] proposed by Telecommunications Industry Association (TIA). The cdma2000 system is evolved from IS-95, which is a second generation CDMA standard deployed in the North America and Korea. For the 3GPP system, there are two modes for the radio access technologies: a Time Division Duplex (TDD) mode and a Frequency Division Duplex (FDD) mode. The 3GPP system with the FDD mode is a CDMA system, but the 3GPP system with the TDD mode is a combined system of CDMA and TDMA. In this thesis CDMA based wireless communication system, which is backward compatible to GSM, is considered[1]. The WCDMA standard is discussed next in brief.

1.3 WIDEBAND CODE DIVISION MULTIPLE ACCESS

Several proposals supporting WCDMA were submitted to the ITU and IMT-2000 for taking initiative for 3G. Among several organizations trying to merge their various WCDMA proposals were:-

- Japan's Association of Radio Industry and Business (JARIB)
- Alliance for Telecommunications Industry Solutions (ATIS)
- European Telecommunications Standards Institute (ETSI) through its Special Mobile Group (SMG)

All these schemes try to take advantage of the WCDMA radio techniques without ignoring the numerous advantages of the already existing GSM networks. Thus the most promising feature of 3G is to combine a WCDMA air interface with the fixed network of GSM. The standard that has emerged is based on ETSI's Universal Mobile Telecommunication System (UMTS) and is commonly known as UMTS Terrestrial Radio Access (UTRA) [41-42,157]. The access scheme for UTRA is DS-CDMA. The information is spread over a band of approximately 5 MHz. This wide bandwidth has given rise to the name Wideband CDMA or WCDMA. WCDMA can operate in FDD or TDD mode.

1.3.1 Main WCDMA Technical Features

The chip rate of the WCDMA system is 3.84 Mcps. The frame length is 10 ms and each frame is divided into 15 slots (2560 chip/slot at the chip rate 3.84 Mcps). Spreading factors range from 256 to 4 in the uplink and from 512 to 4 in the downlink. Thus, the respective modulation symbol rates vary from 960ksymbols/s to15 symbols/s

1. [P3] "3G Evolution towards Broadband", Telecommunications: The Indian Journal of Telecommunications, (Special issue on broadband services) pp.41-47, May-June 2005.

(7.5 k symbols/s) for FDD uplink. For separating channels from the same source, orthogonal variable spreading factor (OVSF) channelization codes are used. In the downlink, Gold codes with a 10-ms period (38400 chips at 3.84 Mcps) are used to separate different cells, with the actual code itself length 2^{18}-1 chips. In the uplink, Gold codes with a 10 ms period, or alternatively short codes with a 256-chip period, are used to separate the different users. For the channel coding three options are supported: Convolutional coding, Turbo coding, or no channel coding. Channel coding selection is indicated by upper layers. Bit interleaving is used to randomize transmission errors. The modulation scheme is QPSK. The carrier spacing has a raster of 200 kHz and can vary from 4.2 to 5.4 MHz. The different carrier spacing can be used to obtain suitable adjacent channel protections depending on the interference scenario. The table 1.2 shows the main technical features of the WCDMA radio interface:-

Table-1.2: Main WCDMA Technical Specifications

Channel bandwidth	5 MHz
Duplex mode	FDD and TDD
Downlink RF channel structure	Direct spread
Chip rate	3.84 Mcps
Frame length	10 ms
Spreading modulation Balanced	QPSK (downlink) Dual-channel QPSK(uplink) Complex spreading circuit
Data modulation	QPSK (downlink) BPSK (uplink)
Channel coding	Convolutional and turbo codes
Coherent detection	User dedicated time multiplexed pilot (downlink and uplink), common pilot in the downlink
Channel multiplexing in downlink	Data and control channels time multiplexed
Channel multiplexing in uplink	Control and pilot channel time multiplexed I&Q multiplexing for data and control channel
Multirate	Variable spreading and multi code
Spreading factors	4–256 (uplink), 4–512 (uplink)

Power control	Open and fast closed loop (1.6 kHz)
Spreading (downlink)	OVSF sequences for channel separation Gold sequences $2^{18}-1$ for cell and user separation (truncated cycle 10 ms)
Handover	Soft handover Inter frequency handover

1.4 MOBILE WIRELESS COMMUNICATIONS BEYOND 3G SOME OPEN QUESTIONS

As the deployment of 3G wireless systems begins, research on the enhancement of 3G systems and new fourth generation (4G) systems accelerates to pave the way for the future and there are still some open questions which need to be answered before putting next generation systems into use.

Question 1: 3G is expected to support more multimedia services, at improved quality and higher data rates, compared to 2G and 2.5G. However, increasing data rates and supporting multirate services in 3G systems is difficult because of excessive interference and the shortcomings of air interface in CDMA based systems. 3G performance does not seem to be sufficient to meet needs of future applications like multimedia, full motion video, and wireless teleconferencing. Can, 3G capacity be increased for new high performance applications?

Question 2: The challenge for the fourth generation of mobile radio systems is no longer to transmit a conversation between two parties, but rather to transmit large quantities of data. The public has become used to fast Internet access and the aim is to provide that service for mobile users too. The radio frequencies used by mobile radio systems have become a scarce resource. To satisfy a growing number of users with increasing demands on the data rates, the need is to come up with mobile communication systems that send more bits faster within a given bandwidth. This means that the quest is for higher spectral efficiency. In order to meet the demands of multirate multimedia communications, next-generation wireless systems must employ advanced algorithms and signal processing techniques that enable the system to guarantee the quality of service desired by the various media classes. Is it possible to develop such advanced signal processing techniques, which can guarantee a desired quality of service required?

Question 3: A core issue in 4G communication systems involves putting the necessary hooks in the standards such that smart antenna technology can be used effectively. In second generation cellular systems, ANSI-136 and IS-95, implementing smart antennas had problems because the standards did not consider their use. In particular, ANSI-136 required a continuous downlink signal to all three users in a frequency channel, which precludes the use of different beams for each of these three users. In IS-95, there is a common downlink pilot, which also precludes the use of different beams for each user, as all users need to see the pilot. For 3G systems, smart antennas were taken into account in WCDMA, where downlink pilots are dedicated to each user and therefore smart antennas can be effectively used on the downlink. Thus, further research is needed to ensure that smart antennas can be effectively used in WCDMA system. For 4G systems, therefore, smart antennas must be taken into account in standard development. Specifically, any packet or multimedia access to all users, as well as pilots, must be transmitted or done in such a way so as to not preclude the use of smart antennas, if this technology is to be used to its full benefit. Since these standards are international, research in this area needs being done globally. In CDMA systems the adaptive array will realize the beam steering rather than null steering because many interference sources surround the array. Will low side-lobe techniques instead of nulling techniques; improve the capacity in wireless communication systems?

Question 4: Digital communication using (Multiple-Input Multiple-Output) MIMO, sometimes called a “volume-to-volume” wireless link, has recently emerged as one of the most significant technical breakthrough in modern communications. The technology figures prominently on the list of recent technical advances with a chance of resolving the bottleneck of traffic capacity in future Internet-intensive wireless networks [35]. The communication techniques in MIMO systems depend on the degree of channel state information (CSI) available at the transmitter and at the receiver. The more channel information, the better the performance of the system [6, 9]. A number of papers have appeared in the literature studying the effect of channel estimation error at receiver and transmitter on various transmission techniques in MIMO [36, 47, 161]. Reducing channel estimation error would require complex signal processing techniques. Is it possible to develop such advanced signal processing technique which can reduce channel estimation error and improve the performance of MIMO system?

Question 5: Although during the last decade, advanced signal processing techniques and the rapid evolution of cheap and fast electronics, have attracted an increased interest in the use of multiple antennas at both the base stations and hand held terminals of wireless communication networks, but the problem faced by a receiver for MIMO system is the presence of multistream interference (MSI), since the signals launched from the different transmit antennas interfere with each other. There are three types of receivers which are used for linear processing or receive beamforming viz. linear decorrelator, matched filter receiver and MMSE receiver. A tradeoff between completely eliminating inter-stream interference and preserving as much energy content of the stream of interest as possible is observed. The decorrelator and the matched filter operate at two extreme ends of this tradeoff [37]. The MMSE receive beamformer is found to be the best amongst three receivers. Can the performance of MMSE receive beamformer be improved further in MIMO systems?

Question 6: It is pointed out by Wireless World Research Forum (WWRF) that requirements such as data rate, link quality, spectral efficiency and mobility in next generation systems cannot be met with conventional beamforming at handsets. Hence WWRF has suggested the use of beamforming and space-time processing at the handset in next generation systems for interference suppression thereby, increasing the capacity of wireless communication systems [168]. With on going advancements in semiconductor technology the possibility of smart antenna on handset seems possible and there is no doubt that the smart antenna will become an integral part of handset in next generation systems. But the exposure to the radio waves still remains a matter of public concern and research is still in progress concerning exposure aspects of WCDMA based systems [70]. Will it be possible to reduce the biological hazards by using smart antenna at handset?

1.5 MOTIVATION FOR THESIS

1.5.1 Development of low side-lobe control antenna beamforming algorithms for array processing architectures of WCDMA systems

In CDMA wireless access scheme, all users share the entire available frequency spectrum and the same bandwidth is used in all the cells, with the most efficient frequency reuse [42, 154]. As all users communicate simultaneously in the same frequency band, multiple access interference is the major cause of transmission

impairment. The system capacity is limited, unlike FDMA/TDMA systems, by the existing intracell and intercell interference level only. Therefore, each solution aimed at reducing the interference level, is directly transformed in capacity increase [4, 38]. Hence considerable research and effort is being devoted to developing systems that either tolerate a higher level of interference (i.e. by using advanced modulation and coding schemes) or try to reduce the intercell and intracell interference by efficient cell planning, dynamic channel assignment or transmission power control. Besides these methods the use of beamforming and array processing has also been proposed for interference suppression. With the CDMA technique, since all users share the same band, the number of potential interfering units is very high; certainly higher than the number of antennas in the array, i.e. the number of degrees of freedom of the adaptive system. As a consequence, the behaviour of the radiation pattern adaptation system is no longer of the null steering type but instead, an antenna pattern with reduced response towards undesirable interferences is desired. In this thesis, the first phase of research focuses on development of new side-lobe control beamforming algorithms for array processing architectures of WCDMA systems for interference suppression. In next phase of research, the increase in information capacity and the performance improvement in various performance metrics of array processing architectures, by implementation of new beamforming algorithms, are investigated. The role of Fractional Fourier transform (FrFT) in providing a flexible taper is also investigated.

1.5.2 Fractional Fourier Transform (FrFT) Based Beamforming

For next generation systems, smart antennas have been taken into account in standard development [14, 16-17, 80, 101, 107, 110]. By equipping the base station of wireless networks with antenna arrays, it is possible to fully exploit the spatial dimension of wireless communication systems. The signals that arrive at the array input can be regarded as random. The transmitted signal undergoes a delay and frequency shift in the narrowband case and a delay and scale offset in the wideband case. The received signal is usually modified in amplitude and phase by the multipath, which by themselves might be changing with time and spatial position. In all of these cases, the signals that arrive at the array are regarded as random, and at times the physical phenomena responsible for the randomness in the signal makes them non-stationary random processes [142]. Since the natural causes responsible for the signal and noise

are often unrelated, it is customary to assume that the signal and noise are uncorrelated with each other [23]. These uncertainties, combined with the non-stationary nature of the signal and noise processes, make FrFT a potentially powerful tool in designing the optimal beamformer in the array environment. The second phase of research involves development and application of FrFT based advanced signal processing techniques, for array processing architectures of mobile and wireless communication systems, which have a practical implementation complexity and achieve high performance levels in complex environments. The bit error rate (BER) performance of FrFT based beamformer in Single-Input Multiple-Output (SIMO) systems is considered as a part of this phase of research.

1.5.3 FrFT based Receive Beamforming in MIMO systems

The subscriber units (SU) in mobile communication are gradually evolving to become sophisticated wireless Internet access devices rather than just pocket telephones, the stringent size and complexity constraints are becoming somewhat more relaxed. This makes multiple antenna elements transceivers a possibility at both sides of the link, even though pushing much of the processing and cost to the network's side still makes engineering sense. A particular and important attraction of the use of antenna arrays at both ends of the communication link is in high data rate wireless communication, such as transmission of high quality video information. A primary solution to this high data rate requirement may be the increase in bandwidth (BW) or the transmit power. However, these solutions are neither cost efficient nor satisfactory in practice. It has been shown that data rate of 3.75 Mbps is achievable with single transmit antenna and receive technology but needs 10^5 times higher signal to noise ratio (SNR) or transmit power compared with a four transmit and four receive antenna configuration [9]. Thus MIMO systems will help future wireless communication systems to operate at considerably higher data rates with higher reliability than what we have today. MIMO systems are revolutionizing the way we transmit and receive data and have key applications in the future high-speed high-spectrum efficiency wireless networks (3G and beyond). There are various research issues in MIMO systems which are still being looked into [9, 10, 35]. Two research issues have been taken up in this thesis as third phase of research, one is the improved channel estimation and the other is improved receive beamforming. Spatial diversity in systems with multiple antennas at the transmitter requires the signal to be preprocessed or pre-coded prior to

transmission. The set of schemes aimed at realizing encoding of multiple transmit antennas are called Space Time Coding (STC) techniques [143]. The first smart antenna simple technique called 'Simple Transmit-Diversity' (STD) based on a code proposed by Alamouti is adopted for 3G WCDMA standard. These techniques assume perfect knowledge of channel at the receiver. It has been shown that with noisy channel estimation, STD has a poorer performance than maximal ratio combining (MRC). STD suffers 3dB degradation in BER relative to MRC when channel estimation error is dominant [36]. The first issue taken up in this chapter is the reduction of channel estimation error caused by Gaussian noise. In MIMO systems the meaning of the term beamforming, initially used for smart antennas applications, is referred to a linear processing scheme along an arbitrary dimension (not necessarily the spatial dimension), thus becoming virtual beamforming [34]. In a communication system, the optimal receiver is given by the Maximum Likelihood (ML) detector, also known as Maximum Likelihood Sequence Estimation (MLSE) [37]. The ML detector is a nonlinear signal processing method and has an exponential complexity in the number of channel dimensions or transmitted symbols [37]. A more pragmatic solution is the utilization of linear signal processing techniques such as Minimum Mean Square Error (MMSE) filtering or beamforming which has low complexity [34]. Second issue taken up in this chapter is the improved linear processing at receiver in MIMO system using FrFT.

1.5.4 Use of Adaptive antenna at Handset in controlling RF Hazards

In next generation systems, smart antennas will not only be used at the base station side but shall be implemented at handset also [1]. The use of adaptive antennas on handheld radios is a new area of research. All the research, in the field of smart antennas at handset, has been in the area of diversity, capacity improvement, reduction of multi-path fading, suppression of interference signals, improvements of call reliability, mitigation against dead zones, increased data rates, spectral efficiency [21,131,152-153]. The recent developments in mobile communication has also drawn attention towards the biological effects of the electromagnetic fields on vital organs of human body like brain, kidney, heart and liver. With smart antenna being deployed at handsets also, the fourth part of research focuses on the use of smart antenna in controlling the radiation hazards. The effectiveness of smart antenna, in controlling radiation hazards is explored in the light of establishing the advantages of smart antenna over conventional single antenna system at the handset.

1.6 THESIS ORGANIZATION

This thesis has four main objectives:

- To develop a new technique of tapering using FrFT. To develop new antenna beamforming algorithms with controllable side-lobes for array processing architectures of CDMA based wireless communication systems and to quantify the advantages of proposed algorithms to the existing algorithms in wireless communication.
- To develop new FrFT based optimal beamforming technique for array processing architecture which achieves high performance levels in non stationary environments of mobile and wireless communication systems. To find the performance of FrFT based optimal beamformer in various mobile fading channels in terms of BER in a SIMO system.
- To reduce channel estimation error caused by Gaussian noise and to improve the linear processing at the receiver in MIMO systems by FrFT based receive beamformer.
- To find effectiveness of smart antenna in controlling radiation hazards. To analyze the advantage of adaptive antenna, over a single antenna in reducing radiation hazards.

To start with, in the **second chapter**, a detailed description of various algorithms of array processing architectures is presented. The role of FrFT based beamforming, in non stationary environment, is discussed. The application of multiple antennas in mobile wireless is discussed. The research in the area of the use of smart antenna at handset is presented.

In **third chapter,** the various low side-lobe beamforming algorithms, to suppress the amount of interference in CDMA systems are discussed. The use of various taper functions in forming low side-lobe is reviewed. The role of the FrFT, in providing taper of varying side-lobe level and beamwidth is discussed. It is shown that by varying a single parameter ‘a’ the FrFT can provide a taper of varying side-lobe level and beamwidth. An algorithm for tapering in FrFT domain is proposed. This method provides practically realizable weights. The use of FrFT taper with optimum beamformer is proposed. The one to one relationship between information capacity and beampattern is established. A new technique capable of synthesizing Chebyshev-like

low side-lobe beam patterns with adjustable beamwidth and steering-invariance is developed. The technique is based on uniform and Taylor current distribution and gives practically realizable weights. The convergence of Taylor based algorithm is found to be fast as compared to uniform distribution based algorithm. Lastly the various performance metrics of array processing architectures of wireless communication are discussed and the improvement in various performance metrics by use of proposed algorithm is established. The validity is shown by comparing three beamforming algorithms viz: Chebyshev, Sample Matrix Inversion (SMI) and proposed algorithm using Monte Carlo simulations.

In the **fourth chapter** optimal beamforming for various multipath fading channels in wireless and mobile communication using the FrFT, is considered. The conventional MMSE beamforming in the frequency domain or time domain becomes a special case of optimal beamforming with FrFT. The method is especially useful in moving and accelerating source problems, where Doppler Effect produces frequency shift when the source is moving as in mobile communication and a chirped type signal is produced when the source is accelerating as in wireless communication. It is demonstrated that the proposed method yields improved results i.e. a smaller Mean Squared Error (MSE), in a moving source scenario, which is common in mobile communication. The MSE, in case of an accelerating source is also shown to be less as compared to moving source. The optimum FrFT beamformer is evaluated in Rayleigh, Ricean and Nakagami fading channels. The same results are also found in microcellular and macro cellular environments using Geometrically Based Single Bounce Elliptical (GBSBE) and Geometrically Based Single Bounce Circular (GBSBC) channel models. It is shown that existing beamforming algorithms are not very effective in rapidly time-varying channels, while the FrFT based algorithm maintains a strong superiority over the existing algorithms in time varying channels. The advantage of the proposed optimum FrFT domain beamformer is the practical consideration that the synthesis or analysis of the FrFT can be implemented with the same complexity as the conventional Fast Fourier Transform (FFT). The BER performance of the proposed optimal FrFT beamformer is found in Rayleigh and Nakagami mobile fading channels.

In the **fifth chapter,** an overview of recent progress in the area of MIMO wireless technology covering space-time wireless communication, capacity, signaling, spatial diversity and beamforming is presented. The Alamouti transmit diversity

scheme is discussed in the presence of channel estimation errors. It is shown that by using FrFT based channel estimation technique the Gaussian noise errors can be reduced thereby improving the performance of STD scheme. MIMO beamforming with emphasis on linear receive beamforming has been discussed. The performance of optimal FrFT based MMSE receive beamformer has been studied for spatial multiplexed systems in terms of BER and BLER. It is proposed that FrFT based beamformer can be used with rate one MIMO systems also.

In the **sixth chapter** the use of smart antenna in controlling the radiation hazards is discussed. The smart antenna at the handset constantly forms a broad null towards the user head. The effect of R.F on human brain is analyzed by taking a simple model of the head. The power absorbed and the rise in temperature of various tissues of the head is compared for omni directional as well as adaptive antenna. In determining the temperature rise the effect of blood flow and transfer of heat from tissue into the space is taken into account.

The **last chapter** concludes with a critical discussion of the results of the investigations carried out. Important observations are made and useful conclusions are drawn. New contributions are proposed which will increase the performance of current state of art. The thesis **concludes** with a list of reference books and the research publications found useful during the course of investigations.

1.7 SUMMARY OF THE CHAPTER

This chapter is a capsule of the motivation of the thesis. An introduction to the evolution of the third generation (3G) WCDMA based wireless communication system is presented, highlighting the requirements that are still to be investigated. New algorithm for tapering in FrFT domain, New antenna beamforming algorithms with controllable side-lobes, FrFT based optimal beamforming technique for array processing architectures in mobile wireless, BER performance of FrFT based optimal beamformer, FrFT based arrays for MIMO systems and the effectiveness of smart antenna in controlling the radiation hazards, are identified as the goal of the thesis. In the next chapter an exhaustive literature survey is presented that has helped the author during the course of investigations.

Chapter 2

SMART ANTENNAS IN WIRELESS COMMUNICATIONS

2.1 INTRODUCTION

Today's mobile and wireless communication systems are primarily designed to provide cost efficient wide area coverage for a limited number of users with moderate bandwidth (voice + low rate data).The future telecommunication will provide the same services in a wireless fashion as provided by fixed network these days, hence requiring large bandwidths [110]. Future telecommunication users will neither be willing to sacrifice functionality for the added value of mobility nor to pay more for it [101]. The 3G and 2G systems will only partially address these requirements. 3G mobile systems proposals such as UMTS and IMT-2000 interpret these requirements as only providing mobile internet services, with up to 2 Mbps. In order to enable the use of truly new wireless services, such as voice, data, facsimile, electronic mail and the future high-performance applications like new innovative multimedia, full motion video, and wireless teleconferencing, one can expect that not only higher bandwidths need to be provided, but also that the cost should be comparable or even lower than in 2G and 3G systems. Current 2G and 3G, CDMA based systems operate with a constant chip rate which defines a certain transmission bandwidth. The 3G wireless systems support online services and offer information on demand for location-based and interactive services. But the 3G standards will not be able to support broadband services since they limit the maximum data rate to 2 Mbps in indoor communications and less than 1 Mbps in outdoor communications. Thus, the future mobile and wireless applications will require significantly higher data rates and significantly reduced costs per transmitted bit as compared to 3G and 2G systems. Both network capacity and transmission capacity per user in 3G systems need to be increased substantially in order to allow video applications to become widely used.

As data rates supported by 4G systems should reach 100 Mbps, price per bit should drop by at least a factor of 100. The 4G is not one of solely higher data rates but has the focus of public service. The 4th Generation Wireless Infrastructures project has been started with the vision "Mobile multimedia to all at today's prices for fixed telephony" and is expected to support more multimedia services at improved quality and higher data rates compared to 3G, 2.5G and 2G [26, 110, 112, 122]. Providing these services, at these high transmission rates, over the harsh and hostile wireless channels with a limited spectrum, however, creates many difficult and challenging problems. The three major factors driving more spectrally efficient high data rate technologies[1] are:-

- Continued growth in wireless subscribers and in the voice and data demand forecasts
- Financial pressure to lower the cost of providing service to the end customer at the same time, improving the wireless customers overall wireless experience
- Government regulations that place a premium on Spectrum, restrict land use and cell site locations, plus a push by regulators on licensees to adopt more spectrally efficient technology

There are various approaches suggested to achieve the above objectives and the WWRF has identified the following related research items [168]:-

- Beamforming and space-time processing at the transmitter as well as the receiver;
- Realistic channel models and interference scenarios to evaluate the performance of smart antennas;
- Multiple input and Multiple output (MIMO) transmission systems;
- Incorporation of MIMO techniques into multi-technology radio networks;
- Re-configurable and robust signal processing techniques;
- Multi-user detection and interference cancellation techniques.

One thing is sure that these requirements on data rate, link quality, spectral efficiency and mobility cannot be met with conventional beamforming.

---

1. [P18] "Smart Antennas for Wireless Communication Systems", Proceedings of IE(E) on Challenges ahead with IT, SLIET, Longowal,pp.130-134, Jan 19-20, 2002

Therefore new beamforming techniques are essential to increase the spectral efficiency of wireless communication systems. To achieve the required system performance and spectrum efficiency, the International Telecommunication Union, under document number M.1036 vide item no.6 and Para (a), has also recommended that methods should be employed to ensure efficient use of the spectrum, such as Radio transceiver technology and access protocols including access technology, modulation and coding, adaptive interference management, diversity techniques and smart antennas [68]. Smart antennas offer a broad range of ways to improve wireless system performance. Smart antennas have potential to provide enhanced range and reduced infrastructure costs in early deployments, enhanced link performance as the system is built out and increased long term capacity [80]. Thus smart antennas are essential to next generation of wireless communication systems. The basic structure of smart or adaptive antenna system is discussed next.

2.2 ADAPTIVE BEAMFORMING SYSTEM

An adaptive antenna array system consists of an array of spatially distributed antennas and an adaptive signal processor that generates a weight vector for combining the array output [87]. The sensor array consists of N sensors designed to receive (and transmit) signals. The output of each of the N sensor elements is fed into the pattern forming network, where the outputs are processed by linear time-variant (LTV) filters. These filters determine the directional pattern of the 'smart' antenna. Fig. 2.1 shows a block diagram of an adaptive array system. The exact structure of the signal processor is dependent on the amount of information that is available or can be estimated at the base station. This information includes the type of modulation and signaling format, the number of resolvable signal paths that are received at the base station, the direction of arrival and time delay of each path signal, availability of reference or training signals, and the complexity of the propagation environment. The outputs of the LTV filters are then summed to form the overall output y(t). The complex weights of the LTV filters are determined by the adaptive signal processor. There are many possible equipment configurations that can be used to perform the digital processing. Since the beam forming instructions are driven by software routines, there is wide ranging flexibility in the types of beams that can be produced including scanned beams, multiple beams, shaped beams & beams with steered nulls [17].

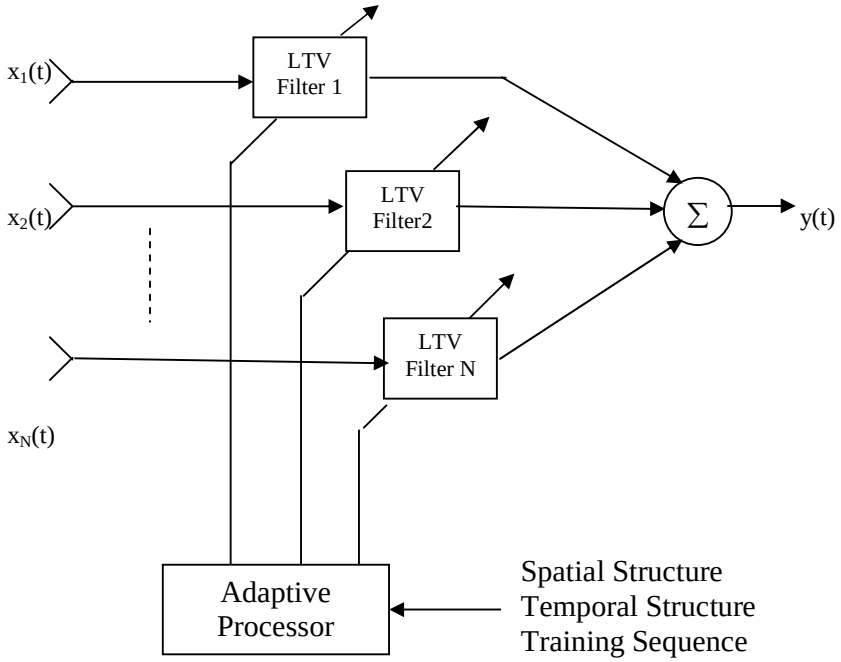

Figure 2.1-A typical array processing architecture

Adaptive beam forming technology is also referred to as smart antenna technology in some literature. Smart antenna generally refers to switched beam systems as well as steered beam systems. On the fundamental principle, smart antenna is similar to the adaptive antenna but the electromagnetic environment, in which they are operated, is different. That is, for the adaptive array, the beam pattern changes as the desired user and the interferers move and for the smart antenna the beam is steered or switched as the desired user moves. The adaptive antennas are designed to restrain a small number of strong interferers, while the smart antenna is designed to suppress a large number of strong interferers. The only way for smart antenna to suppress large number of interferers is, by depressing the side lobes, while adaptive antenna forms a null at the incident angles of the interferences [97, 151]. Thus switched beam or steered beam antenna tries to place maximum gain towards desired user. The performance of adaptive array is much better as compared to switched beam or steered beam systems for less number of interferers [151]. In general the relative performance of smart antenna systems versus fully adaptive systems depends upon the propagation environment and multiple access schemes (TDMA, FDMA or CDMA). In this thesis

beamforming algorithms are developed for CDMA based systems, for smart as well as adaptive antenna array systems. A brief review of historical development of smart or adaptive antenna systems in wireless communication is given next.

2.3 ADAPTIVE ANTENNAS FOR ARRAY PROCESSING ARCHITECTURES OF MOBILE WIRELESS COMMUNICATION SYSTEMS

The investigations into use of adaptive arrays in communication began with the objective to develop a system for receiving signals in the presence of interfering signals especially in Military communications. The concept of using antenna array is not new to radar and aerospace technology also. Adaptive antennas have been developed for receiving TDMA satellite communication signals and spread spectrum communication signals. In 1980, G.Turin, introduced the use of spread spectrum for development of anti multipath techniques and found its application to urban digital radio [56]. Yeh & Reudink discussed the use of antenna arrays in mobile radio systems to combat cochannel interference in 1982 [171]. They showed that with a large number of antenna elements, it is possible to carry out frequency reuse to achieve high frequency spectrum efficiency. Bogachev and Keselev suggested a similar concept around the same time [159]. They derived the expression for the probability of signal to interference ratio in the presence of Rayleigh fading. In 1983, Marcus suggested that, by using SDMA multiple users in the same cell can be accommodated on the same frequency and time slot [99]. Numerous approaches have been suggested in order to exploit spatial domain for example by optimally combining antenna outputs, adaptive antennas also can reduce the multipath fading and permit the use of the spatial dimension to suppress co-channel interference [76-77,115,126,138]. The operation of optimally combining the array output is called beamforming or spatial filtering. In 1990, Swales et al. demonstrated that by employing adaptive antenna array, the co channel interference from neighboring cells can be reduced [139]. G.K.Chan studied the effect of sectorization on spectrum efficiency of cellular radio systems in 1992 [49]. In 1996, A. F. Naguib et al. investigated the capacity improvement with base station antenna arrays in CDMA systems [4]. Gradually the capability and potential of adaptive arrays, to increase the spectrum efficiency in mobile communication, was recognized by the wireless industry. In 1997, Y.Li et al. experimentally evaluated the performance of

multi-beam antenna array relative to dual diversity three sector antennas [169]. The results indicated that 5 dB of gain enhancement can be achieved with 24 beam base station antenna, compared to traditional sector configuration. Tadashi et al., theoretically analyzed the probability of incorrect beam selection with a switched beam antenna system under power limited and interference limited mobile communication environments [103]. In the same year, S.Choi and D.Yun designed an adaptive array for tracking the source of maximum power in CDMA mobile communications [141]. They assumed that the desired signal is large enough compared to each of the interfering signals. The increase in capacity and trunking efficiency of switched beam antenna, for cellular radio systems, was investigated by Ming Jo Ho et al. in 1998 [113]. They found that reverse link performance was a limiting factor in switched beam antenna. Paul Petrus et al. found that adaptive antennas can significantly increase the cell capacity, improve signal quality and reduce transmitter power requirements in AMPS [117]. They considered two types of beamformers, an ideal one and flat top for calculating outage probability and capacity increase. An ideal beamformer was having a flat main lobe and no side lobes, while a flat top beam former has flat main and side lobes. In 1999, Yueh Karen Lee et al., described a beamformer and equalizer system capable of separating and demodulating several co-channel GSM signals [172]. J.H.Winters compared the increase in range of multiple antenna base stations using adaptive array combining with that of phased array combining [82]. Both combining methods increased the range but with adaptive method the range increase was 5.5 fold as compared to 2.8 fold achieved with phased combining. S.Choi et al., in 1999 compared two different types of smart antenna systems viz.; tracking beam array (TBA) and switching beam array (SBA) in terms of performance and hardware complexity for CDMA systems [149]. In the year 2000, Josef Johannes Blanz et al. exploited the use of smart antenna diversity to increase spectral efficiency by proposing a scheme for combined DOA (Direction of arrival) and joint channel estimation for time slotted CDMA mobile radio systems [89]. In 2001, Jonathan et al., investigated the performance of adaptive antenna arrays in conjunction with fixed channel and dynamic channel allocation schemes [88]. Faisal et al. introduced the concept of dynamic slot allocation in packet switched systems using smart antennas [46]. S.Durrani and M.E.Bailowaski have simulated reverse link of CDMA system using smart antenna under perfect adaptation [151]. They have simulated the bit error rate

(BER) performance for different number of active users and varying number of elements of adaptive array. The performance of digital mobile radio communication systems is limited by signal fading and interference from other co-channel users. Both these effects can be reduced by the use of antenna arrays at the base station with the appropriate signal processing and combining of the received signals. Thus adaptive beamforming for array processing architecture is important for mobile wireless communication as it can reduce the co-channel interference, multipath fading and background noise more as compared to conventional antenna systems [136]. The potential benefits also include improved coverage area, extended range, increased capacity, reduced interference and improved quality of service (QOS).

The main Advantages of Smart Antennas Technology for operators and users are:

Operator	: Network capacity, coverage, filling "dead spots", less amount of BS, QoS, and new services.
Operation and Maintenance (O&M)	: New more advanced BSS equipment, more flexible radio network control...
User	: Higher QoS, more reliable, secure communication, longer battery life...

In general the performance enhancement attainable with antenna array depends heavily upon array geometry. The array geometry should be matched to the spatial characteristics of radio environment. For rural environments the angular spread is low and received signals tend to have well defined directions of arrival. For indoor and microcellular scenarios the angular spread is high and signals may not have well defined directions of arrival. The choice of array topography as well as their control algorithm should also reflect these differences in the signal environments. Next a brief review of some of these algorithms is given.

2.4 ADAPTIVE ALGORITHMS FOR BEAMFORMING

In adaptive beamforming the optimum complex valued weights are derived according to some algorithm. The output of the beamformer shown in Fig. 2.1 can be written as

$$y(t) = \boldsymbol{w}^{*}\ \boldsymbol{x}(t)\,, \tag{2.1}$$

where, $\boldsymbol{w}$ are weights of adaptive array, $\boldsymbol{x}(t)$ in input signal vector and y(t) is the output signal. $(.)^*$ indicates complex conjugate operation. Several adaptive beamforming algorithms have been proposed in the literature. A general view of the most important algorithms is given in Fig. 2.2

2.4.1 Spatial Reference Based Beamforming

The spatial reference or direction-finding (DF) based beamforming techniques are based on number of high resolution techniques such as Multiple signal classification (MUSIC) and Estimation of signal parameters via rotational invariance techniques (ESPRIT),which can be used to estimate the DOA [4, 8, 22]. Spatial reference beamforming techniques are considered to be suitable for large cell systems.

2.4.2 Temporal Reference Based Beamforming

The temporal reference signal based technique offers computationally inexpensive estimates of the signal waveforms, without requiring a preceding DOA estimation step [4]. The advantage of this method is that knowledge of the DOA or the array manifold is not necessary. Moreover, this technique does not make any assumption about the multipath angle spread and it does not place any structural constraints on the antenna array itself. The weight vector estimate can be calculated by a number of different techniques such as Least Mean Square (LMS) or Direct Matrix Inversion (DMI) [23, 24]. The technique of training-signals based beamforming was studied for use with the digital mobile radio system IS-54 in [77].

2.4.3 Signal-Structure-Based Beamforming

In signal-structure based beamforming techniques, the base station adaptive processor exploits the temporal and/or spectral structure and properties of the received signal to construct the beamformer. The signal property is damaged by the presence of interference and the adaptive beamformer attempts to restore the signal property at its output and thus automatically reduces interference [4]. Examples of property restoral beamforming techniques include the constant modulus algorithm (CMA), finite alphabet (FA) and spectral self-coherence [20, 124,146,154,155].

A reasonable strategy in all of these algorithms is to find the best weight vector to optimally combine the array outputs under some suitable optimization criterion. On the basis of the optimization criterion these algorithms generally fall into two main categories viz.

(i) Maximum Signal to Interference plus Noise Ratio (SINR) beamforming;

(ii) Maximum Signal to Noise Ratio (SNR) beamforming.

Both these techniques have been widely used in mobile and wireless communication [4, 81, 89,140,141,149,150].

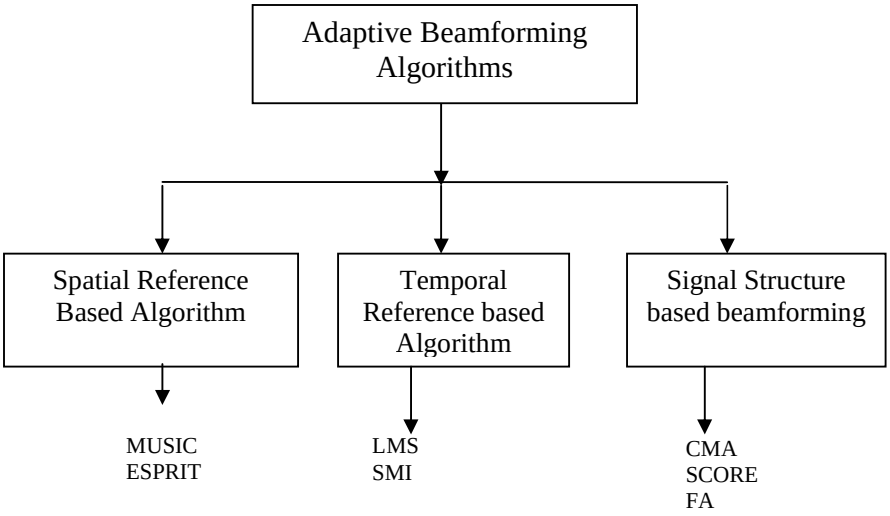

Figure 2.2-Adaptive beamforming algorithms

2.5 BEAMFORMING FOR CDMA BASED SYSTEMS

The various beamforming techniques described above are not suited for CDMA based wireless systems as the numbers of interferers are quite high in these systems. The spatial reference based beamforming techniques are analytically more tractable and they suffer from several drawbacks that may limit their applicability in a wireless setting. First, all spatial reference based beamforming techniques start with a DOA estimation step that involves an eigen-decomposition and one or more multidimensional, non-linear optimizations, which may be a difficult and time consuming task. Also, the DOA step requires knowledge of the array manifold and is very sensitive to errors in this knowledge. The presence of multipath in urban or suburban environments, where the condition of zero or relatively small angle spread does not hold, makes knowledge of the array manifold unreliable. Moreover, a key assumption in all DOA estimation techniques is that the number of signal wave fronts including cochannel interference signals must be less than the number of antennas in

the array, a fact that restricts their applicability in a CDMA wireless setting. All users in a CDMA wireless system are cochannel and their number may easily exceed the number of antennas. Moreover, due to multipath propagation and the fact that each transmission path may contain direct, reflected and diffracted paths at different time delays, the array manifold may be poorly defined. Therefore spatial reference based beamforming techniques are not applicable. Moreover spatial methods provide low carrier to interference enhancement when compared with temporal methods [80].

The use of temporal reference based signal requires prior carrier and symbol recovery, which is made difficult by the presence of co-channel interference. In addition, sending a training signal along with the information signal reduces the payload efficiency of the system. Also, training-signals based beamforming techniques are not applicable in systems where training or synchronization signals are not available such as in the IS-95 CDMA standard [5]. Therefore, reference-signal based techniques cannot be used. The signal-structure based beamforming techniques are very robust against different propagation conditions. No knowledge of the array manifold or DOA is required. However, a drawback that limits the applicability of signal structure-based beamforming methods for wireless applications is that the convergence and capture characteristics are still not well understood.

Temporal reference based antenna control methods can theoretically approach optimum performance for any given array deployment and thus offer much better performance than spatial reference and signal-structure based algorithms. However in order to use these algorithms in CDMA based systems a proper temporal reference is required for necessary signal correlation [80]. As discussed in chapter 1, in 3G communication systems, the necessary provisions in standards have been made such that smart antenna technology can be effectively used. In second generation cellular systems, ANSI-136 and IS-95, implementing smart antennas had problems because the standards did not consider their use. For 3G systems, smart antennas were taken into account in WCDMA, where downlink pilots are dedicated to each user, and therefore smart antennas can be effectively used on the downlink. Specifically, any packet or multimedia access to all users, as well as pilots, must be transmitted or done in such a way as to not preclude the use of smart antennas, if this technology is to be used to its full benefit. Hence for 4G systems smart antennas are taken into account in standard development. Thus the use of temporal reference based algorithms is possible in 3G

and 4G systems. In this thesis, in chapter 4, advanced array processing techniques are developed for mobile communication systems in which the temporal reference signal is assumed to be known at the beamformer.

One of the major issues in beamforming in a CDMA cellular system, all users shares the entire available frequency spectrum and the same bandwidth is used in all the cells, with the most efficient frequency reuse. Each user within a cell modulates the information signal with a wideband semi-orthogonal coding sequence. Although all users use the same frequency band at the same time, the base station can separate each of the received signals by separately decoding each spreading sequence. However, since the codes are semi-orthogonal, the users within a cell interfere with each other (intracell interference) and with other users in other cells (intercell interference) [121]. Adaptive antennas can decrease the system interference and thus cause better link and speech quality. This interference decrease is used to increase the system capacity and the spectral efficiency.

It is obvious that in CDMA based systems the numbers of potential interferers are higher than the number of antenna elements i.e. the number of degrees of freedom of the adaptive system. Interfering units can also be considered uniformly distributed around the base station. So, in such systems, the antenna array shall realize the beam steering rather than null steering. Therefore in 3G & 4G systems the research should focus on antenna algorithms which can point main beam in the direction of desired user and low side-lobes towards interferers because many interference sources surround the array. In [80-81, 110, 151] it is also pointed that for increasing the capacity of 3G & 4G systems, smart antenna arrays should reduce intercell and intracell interference by pointing the main beam towards the direction of the desired user and by minimizing the sidelobe towards other users. It is also discussed in [97,117,150] that for CDMA based systems the only way, for smart antenna to improve SIR, is by depressing the side lobes, while adaptive antenna forms a null at the incident angles of the interferences. Thus new beamforming algorithms for controlling side lobes are required for reduction of interference and the enhancement of capacity.

Most of the beamforming techniques which have been proposed for wireless communications perform spatial filtering by forming sharp nulls in the direction of the interfering mobiles. There are cases when angular spread of the rays, impinging on the array, is large and a sharp null can not provide efficient interference suppression. The

beamformer should be able to form broad nulls. However there is very less work in the literature concerning broad nulls in wireless communication regardless of the considerable advantages they have in cases of cochannel interferences with large angular spread or when motion is involved. Thus the beamforming algorithms have to be developed, that are able to provide broad steer able low side lobes in certain directions.

2.6 NEW OPTIMUM ARRAY SIGNAL PROCESSING TECHNIQUES FOR BEAMFORMING IN WIRELESS COMMUNICATION SYSTEMS

Adaptive antennas are a promising technique, which can increase system capacity. Today adaptive antennas and algorithms to control them are vital to high capacity system development. In optimal beamforming techniques the weights of an array of sensors are selected according to optimization criteria, which minimize a cost function. Typically the cost function is inversely associated with the quality of signal at the array output, so when cost function is minimized the quality of signal is maximized. Two most popular techniques, which have been applied extensively to communication systems are the MMSE and Least Squares (LS) criteria [80]. In both these techniques the square of the difference between the array output and a locally generated estimate of the desired signal is minimized by finding an appropriate weight vector. MMSE solutions are posed in terms of ensemble averages and produce a single weight vector, which is optimal over ensemble of possible realizations [87]. This is the approach used in Wiener Filter Theory [142]. The Wiener filter is optimal in the sense of minimizing the MSE of the output.

A study in 1987 has shown that the adaptive antenna based on MMSE criterion can suppress the multipaths signals with large delay differences and can be employed for high speed mobile communications [170]. As mentioned by WWRF any robust signal processing technique, which can result in lesser MSE, will definitely improve the performance of wireless communication systems [168]. One such tool which is recognized is Fractional Fourier Transform (FrFT). The ordinary Fourier transform (FT) is suited best for analysis and processing of time invariant signals and systems. When dealing with time varying signals and systems, filtering in Fractional Fourier Domains might allow us to estimate signals with smaller minimum mean squared error.

The class of Fractional Fourier domain filters is a subclass of the class of linear filters [104]. The optimal filter found in this Fractional Fourier domain is not most optimal among all filters. However the class of Fractional Fourier domain filters is much broader class than the class of ordinary domain filters, so that in general the optimal filter found in FrFT domain result in much smaller errors as compared to ordinary time or Fourier domain filters. This reduction in error comes at no additional cost, because FrFT can be implemented with the same cost as ordinary FT [59].

The continuum of fractional Fourier domains corresponds to oblique axes in the time frequency plane, with the ordinary time or frequency domains as special cases as shown in Fig. 2.3. In wireless communication received signal is generally degraded by distortion, fading and noise and the signal can be considered as non stationary or time varying signal.

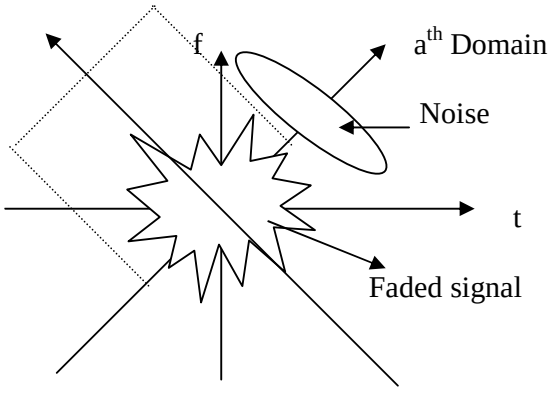

Figure 2.3-Filtering in fractional Fourier domain

Although there is very less work which has been reported in literature for applying the FrFT to mobile wireless communication except [64, 111]. In [111] a wireless communication system, based on FrFT, has been proposed. In this work, the author has introduced the idea that frequency varying basis functions are more suitable for multi-carrier transmission over rapidly time-varying channels with respect to traditional frequency-invariant carriers. The basic concept is based on a chirp-like harmonic decomposition for the RF propagation channel that matches the essential time-varying characteristics of the system. The proposed methodology is an approximation to the optimum nonstationary approach which, in channels characterized by large Doppler spread, remarkably outperforms the classical (Fast Fourier Transform) FFT-based scheme. In the proposed scheme, at no extra computational cost, it is

possible to obtain a significant performance improvement in rapidly fading channels. In [64], I.S.Yetik has introduced the concept of FrFT beamforming in Additive White Gaussian Noise (AWGN) channels. In this paper the central concept in beamforming, in a single time domain or in a single frequency domain, has been generalized to beamforming in a single fractional Fourier domain. In this thesis the work of [64] is extended to consider FrFT based beamforming for multipath fading signals over AWGN channel for reducing MSE at no extra computational cost. The BER performance of optimum FrFT beamformer is evaluated in mobile environment.

2.7 APPLICATION OF ANTENNA ARRAYS IN MOBILE WIRELESS SYSTEMS

Application of antenna arrays in mobile and wireless communication has been of special interest. It has been shown by many studies that when an array is appropriately employed in a communication system, it helps in improving the system performance by increasing channel capacity and spectrum efficiency, extending range coverage, tailoring beam shape, steering multiple beams to track many subscribers, compensating antenna aperture distortion electronically, reducing multipath fading, cochannel interference (CCI) and BER [9]. Table 2.1 details the three main areas of study in the field of radio antennas and antenna arrays.

Table-2.1: Performance goals for antennas in wireless communication [9]

Antenna design	AOA estimation	Performance criteria
Gain	Error variance	Coverage
Bandwidth	Bias	Quality
Radiation pattern	Resolution	Interference rejection
Size		Spectral Efficiency
Sidelobe level		Low power requirements

The research in the third area of mobile wireless communication has been of special interest, particularly in the last two decades. The growth of third area of antenna applications in wireless communications is shown in Fig.2.4. The use of multiple antennas at the transmitter and/or receiver has opened up a new dimension space [9].

Paulraj and Kailath in 1994 proposed a technique for increasing the capacity of wireless link using multiple antennas both at transmitters and receivers [11]. Their idea along with fundamental research done at Bell Labs began a new revolution in

information and communication theory in mid 1990s. This theory states that the antenna array may be used together with other methods such as channel coding, adaptive equalization and interference canceling to enhance the system performance.

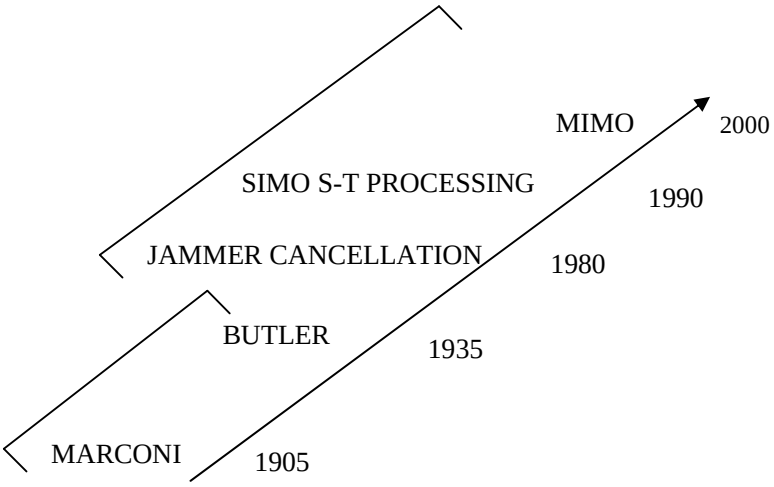

Goals: quality, capacity, coverage, spectral efficiency

Fig 2.4: Link Performance Enhancement-Evolution [9]

The idea behind MIMO is that the signals on the transmit (TX) antennas at one end and the receive (RX) antennas at the other end are "combined" in such a way that the quality (or BER) or the data rate (bits/sec) of the communication for each MIMO user will be improved. Such an advantage can be used to increase both the network's quality of service and the operator's revenues significantly [35]. The prospect of many orders of magnitude improvement in mobile wireless communication performance at no cost of extra spectrum (only hardware and complexity are added) is largely responsible for the success of MIMO as a topic for new research. This has prompted progress in areas as diverse as channel modeling, information theory and coding, channel estimation error, linear receive signal processing, antenna design and multiantenna aware cellular design, fixed or mobile [35].

Multiple antenna structures can be divided into four groups: use of single antenna at transmitter and receiver (SISO), use of antenna (M_R) array only at receiver, known as single-input multiple-outputs (SIMO) system; use of antenna (M_T) array only at transmitter, known as multiple-inputs single-output (MISO) system; and use of antenna arrays at both transmitter (M_T) and receiver (M_R), known as multiple-inputs multiple-outputs (MIMO) systems. A key feature of MIMO systems is the ability to

turn multipath propagation, traditionally a pitfall of wireless transmission, into a benefit for the user. MIMO effectively takes advantage of random fading [50, 51, 71] and when available, multipath delay spread [35] for multiplying transfers rates. MIMO systems have a number of advantages over traditional SISO systems such as the beamforming (or array) gain, the diversity gain and the multiplexing gain. The beamforming and diversity gains are no exclusive of MIMO systems and also exist in SIMO and MISO systems. The multiplexing gain, however, is a unique characteristic of MIMO systems. An overview of the gains of MIMO systems is given in [57]. A brief discussion about these gains and their mutual comparison is given in chapter 5.

The underlying mathematical nature of MIMO, where data is transmitted over a *matrix* rather than a vector channel, creates new and enormous opportunities beyond just the added diversity or array gain benefits. In a MIMO link, the benefits of conventional smart antennas are retained since the optimization of the multiantenna signals is carried out in a larger space, thus providing additional degrees of freedom. In particular, MIMO systems can provide a joint transmit-receive diversity gain, as well as an array gain upon coherent combining of the antenna elements (assuming prior channel estimation). The more general and appealing case of simultaneous transmit and receive diversity (*i.e.*, MIMO systems) is being extensively addressed since recent studies on wireless multi-antenna MIMO channels showed a linear increase of capacity with the number of antennas [50, 71].

In fact, the advantages of MIMO are far more fundamental. This was shown in [50], where the author shows how one may under certain conditions transmit min (M, N) independent data streams simultaneously over the *eigenmodes* of a matrix channel created by TX and RX antennas. A little known yet earlier version of this ground breaking result was also released in [11] for application to broadcast digital TV. Information theory can be used to demonstrate these gains rigorously.

MIMO system also use Spatial Multiplexing (SM), in which a high-rate bit stream is decomposed into M_T independent rate bit sequences which are then transmitted simultaneously using M_T multiple antennas. A simple example of such a SM technique is V-BLAST [52, 53]. In SM the signals are launched and naturally mix together in the wireless channel as they use the same frequency spectrum. At the receiver, after having identified the mixing channel matrix through training symbols, the individual bit streams are separated and estimated. This occurs in the same way as

M unknowns are resolved from a linear system of M equations. This assumes that each pair of transmit receive antennas yields a single scalar channel coefficient, hence flat fading conditions under perfect knowledge of the channel.

As mentioned above communication techniques in MIMO systems depend on the degree of channel state information (CSI) available at the transmitter and at the receiver [6]. Clearly the more channel information, the better the performance of the system. CSI at the receiver (CSIR) is traditionally acquired via the transmission of a training sequence (pilot symbols) that allows the estimation of the channel [30]. It is also possible to use blind methods that do not require any training symbols but exploit knowledge of the structure of the transmitted signal or of the channel.

CSI at the transmitter (CSIT) cannot be directly obtained as happened with CSIR. One possible way to achieve CSIT is to have a feedback channel from the receiver to the transmitter to send back the channel state as side information. Another traditional way to acquire CSIT is to infer knowledge about the transmit channel from previous receive measurements [98]. When perfect CSIT is available it is called closed loop diversity and with no CSIT, open loop diversity[2]. For transmit diversity adopted for WCDMA standards both open loop and closed loop diversity are specified [173]. For the case of no CSIT, the transmit diversity can be exploited either indirectly or directly. Indirect transmit diversity schemes convert spatial diversity into time or frequency diversity which can then be readily exploited by the receiver [78]. In direct transmit diversity, Space-time coding (STC) techniques independent of the channel realization can be readily used [49, 143, 145, 160]. With perfect CSIT, the transmission can be adapted to each channel realization using signal processing techniques [54-55]. In [134], the combination of beamforming and space-time codes in a system with multiple antennas at both sides of the link was considered aiming at maximizing the average SNR for scenarios with partial CSIT.

It is generally assumed that perfect CSI is available at the receiver. Nevertheless, the case of no CSI at any side of the link has also been considered using the so-called unitary and differential STC [166]. The communication techniques in MIMO systems assume perfect channel estimation at the receiver and transmitter. The effect of imperfect channel estimates on the receiver performance of MIMO systems has been widely studied [36, 47,161].

2. [P23] Invited Talk on "Transmit Diversity Schemes-A Review" in Conference on Information and Communication Technologies, JMIT Radur, 9-11 February, 2006.

In this thesis the reduction in channel estimation error using FrFT has been taken as the one area of research. The second issue which has been taken up in this study is the optimal linear receive beamforming in MIMO systems. The proposed optimal receive beamforming can be extended to joint optimal transmit-receive beamforming.

2.8 SMART ANTENNAS AT HANDSET

The use of smart antennas on handheld radios is a new area of research. Smart antenna technology at the cellular mobile base station has been a subject of interest for many years and finds applications in base stations for their potential in improving signal-to-noise ratio (SNR), link quality and reliability, and providing position location capability to user terminals. Smart antenna systems are traditionally designed for base station applications, since the base station has space and enough processing power to support array processing. As wireless communication systems evolve, service quality and capacity are of primary importance. With ongoing advancements in the performance of semiconductor technology, chipsets that are both smaller and more powerful are now available for handheld mobiles. The trend is not expected to slow down in near future and thus the possibility of incorporating smart antenna technology at the handset seems possible. The factor driving research interest in this direction is that if beamforming can be performed in the downlink at a base station, then the need for an antenna array at the mobile unit is obviated, thus reducing complexity and power consumption. Papers, investigations and research have been emerging concerning adaptive antennas on handsets dating from since 1997. In 1988, Vaughn [123] concluded that with then-current technology, adaptive beamforming would work for units moving at pedestrian speeds but would be difficult for high-speed mobile units. In 1999, Braun, et al. [25] reported experiments in which data was recorded using a two-element handheld antenna array and processed using diversity and optimum beamforming techniques. Use of smart antenna at the handset and performance improvement has been reported in [119]. Recently there have been reports of commercial prototypes of using two-element smart antenna systems for user terminals [1, 18]. Antenna arrays at the handset can improve reliability and capacity in two ways. First, diversity combining or adaptive beamforming techniques can combine the signals from multiple antennas in a way that mitigates multipath fading. Second, adaptive

beamforming using antenna arrays can provide capacity improvement through interference reduction. The adaptive antennas at the handset offer the following improvements: -

- Reduction of multi- path fading;
- Suppression of interference signals;
- Improvements of call reliability;
- Lowering the specific absorption rate (SAR);
- Mitigation against dead zones;
- Increased data rates;
- Increased spectral efficiency.

The major research in smart antenna, at the handheld terminal, is going on in various universities and companies as listed below:

Table-2.2: Universities researching Adaptive Antennas on Handsets

Name of Company /University	Area of Research	Results produced
Allgon Mobile Communications, Sweden with Department of Signals, Sensors and Systems, Royal Institute of Technology, Sweden and Hong Kong University of Science and Technology, Hong Kong	Adaptive antenna for handset for SIR improvement [25]	Investigated two branch antenna at handset for interference reduction
Virginia Polytechnic Institute and State University	Smart antenna at handset for diversity [46,127]	Handset diversity is measured for various propagation environments
University of Surrey center for Communications System Research	Beamforming and diversity at handset [144]	Developed a Quadrifilar antenna and studied various combining techniques.
Antenova Limited	New generation antennas [18]	Development of Small size, higher efficiency antenna
Bradley Department of Electrical	Reduced power	Gains in the link budget of 7-

and Computer Engineering & Virginia Polytechnic Institute and State University Blacksburg, Virginia	consumption, improved capacity and better link reliability [106]	9dB at the 99% reliability level and single interfering signal can be reduced by 25-40dB using adaptive beamforming algorithms
Virginia Tech VLSI for Telecommunications Laboratory Department of Electrical and Computer Engg Virginia Tech, Blacksburg, Virginia	Performance gain of smart dual antennas with adaptive combining Dual smart antenna system for 3GPP WCDMA handsets [48,152-153]	Reduction in FER by adaptive combining over a single antenna system. A dual smart antenna system with diversity combining at handsets is developed for the 3GPP WCDMA system
Adaptive Antennas at the Mobile and Base Stations in an OFDM/TDMA System Institute of Electrical and Electronics Engineers, USA	Use of adaptive antennas at the base station and mobile station operating jointly in combination with OFDM[93]	Reduction in average error probability for frequency selective fading channels, as compared to OFDM without antenna diversity.
Mobile Portable Radio Group (MPRG) Virginia Polytechnic Institute and State University, Virginia	Transmit diversity to counter fading and improve signal quality [127]	Narrowband channel measurements for a two-element transmitter antenna array and a single antenna receiver in an indoor environment.
Virginia Technical Antenna Group Electrical and Computer Engineering Department , Virginia	Adaptive Beamforming [29]	SINR improvement in various environments reported

All the research described above has been in the direction of Diversity, Capacity improvement, Reduction of multi- path fading, Suppression of interference signals, Improvements of call reliability, Mitigation against dead zones, Increased data rates, Spectral efficiency. The recent developments in mobile communication has drawn attention towards the biological effects of the electromagnetic fields on vital organs of human body like brain, kidney, heart and liver [66-67,73,100]. But no research has been done in the direction of controlling the radiation hazards using adaptive antenna at the handset. Health aspects due to the use of mobile phones have been a public concern globally, especially following the large market penetration of the digital GSM phones and 3rd generation W-CDMA terminals [72]. There is a need for the assessment of the exposure of the user and the public in general from these terminals. With the implementation of smart antenna being suggested at handset also the use of smart antenna in controlling radiation hazards is considered as a research problem.

2.9 SUMMARY OF THE CHAPTER

At the start of 21st century, the wireless and mobile markets are witnessing unprecedented growth fueled by an information explosion and a technology revolution. While a great effort in second-generation wireless communication systems, has been focused on the development of modulation, coding, protocols etc. The antenna related technology has received relatively less attention up to now. Also the fragmented nature of the International Mobile Communication market (illustrated by growing numbers of standards) was a hurdle for the researchers to develop equipment to support a wide range of air interfaces. During the next generation mobile communication systems, the network operators may not achieve full network capacity, without use of antenna array technologies. Future mobile communication aims to support multiple air interface standards, which will require beam-forming architectures. This chapter gives a brief overview of antenna arrays, their use in future generation CDMA based wireless systems, a FrFT based optimal signal processing technique for mobile wireless, FrFT based processing for MIMO systems and research in use of smart antenna at handset. In the next chapter, low side lobe algorithms for array processing architectures of smart antennas, is taken up as a first research problem.

Chapter 3

LOW SIDE LOBE ALGORITHMS FOR ARRAY PROCESSING ARCHITECTURES OF WCDMA BASED SYSTEMS

3.1 INTRODUCTION

Wideband direct sequence code division multiple access is accepted as a wireless access scheme for 3G systems [1]. One of the key features in a 3G wireless system is high data rate. For a high data rate, a lower BER and a smaller spreading factor are required. In the uplink of the 3G systems, each user signal is transmitted asynchronously and traverses different paths from the mobile station to the base station. Furthermore both distance dependent path loss and shadowing exist, producing the well known near/far problem. Thus, the main source of interference is coming from other users' signals within the same cell known as intra-cell interference. However, in the downlink of the 3G systems, the signal transmitted from the base station is the superposition of all active users' signals and common control signals. The desired user signal and multiple access interference signals traverse the same paths, but they are inherently orthogonal with each other. Therefore it does not pose a serious problem at handsets. Another source of interference is coming from adjacent cells called inter-cell interference, which can have a substantial impact on the performance [33]. Thus, in CDMA systems multiple access interference (MAI) is the major cause of transmission impairment. A promising technique to reduce this MAI is adaptive antenna array and there has been great deal of interest in reducing MAI through use of beamforming to improve the capacity and performance of CDMA based systems [154]. As discussed in chapter 2, beamforming techniques which have been proposed for wireless communications perform spatial filtering by forming sharp nulls in the direction of the interferers. Will null beamforming help in reducing MAI in CDMA based wireless communication systems?

3.2 NULL vs. LOW SIDE LOBE BEAMFORMING

A null in an antenna pattern denotes a zero response. One may shape the antenna pattern in such way that it cancels interferers and produces a strong beam towards the wanted signal. This is done by placing the nulls in the pattern in the corresponding known directions of these interferers and simultaneously steering the main beam in the direction of the desired signal. This method of beam forming is known as Null Beam Forming [33]. Adaptive arrays, often referred as “Smart antennas”, were suggested in the early 1960’s and proved to be useful to cancel directional interfering signals, improving the performance of wireless communications systems [126]. An adaptive array with optimum weight vector can be used for null beamforming. The flexibility of array weighting to get the desired array pattern can be exploited to cancel directional sources operating even at the same frequency as that of the desired source, provided these are not in the same direction of the desired source. In adaptive antenna theory, the basic concept of nulling is based on number of antenna elements. An array with M number of antenna elements can null out M-1 interferers only. If the number of interferers is more than M-1, then the array becomes overloaded and its performance starts degrading. One thing is sure that the adaptive antennas are designed to restrain a small number of strong interferers in wireless communication.

With the CDMA technique, all users communicate simultaneously in the same frequency band. Thus the number of interferers in CDMA signal environment is at least of the order of tens and it is never realistic to have that many antenna elements in the cell site of a given wireless communication system for nulling these interferers. This means the behaviour of the radiation pattern adaptation system is no longer of the null steering type but instead, an antenna pattern with reduced response toward undesirable interferences is desired [38]. This technique also helps to reduce co-channel interference due to less energy being transmitted in unwanted directions. The main beam is simply pointed in the direction of the desired mobile unit. In this way, the reduction in interference level will be only partial, however it is no longer necessary to put nulls in the direction of the interfering units with critical precision, the adaptation system actually requires less complexity.

In wireless communications there are cases where the angular spread of the rays impinging on the array is so large that a sharp null can not provide efficient interference

suppression [151]. Such cases, which arise when the mobile station is located close to the base station or when the direction of arrival changes quickly due to the motion of the mobile, can significantly degrade the performance of the system. Because in such case one has to form a broad null towards the complete angular spread. The large angular spread can also be handled if a broad low side lobe is formed towards the direction of the largely spread interference. There has been considerable interest in the recent years in beamformers which are able to synthesize controlled broad low side lobe in the mobile radio networks.

From the above discussion it is obvious that in the next generation wireless systems the side lobe control will play a major part in reducing interference and improving capacity. The conventional arrays based on nulling procedure are unlikely to be applicable in practical CDMA wireless communication even if their beamforming procedure is valid for coherent interferers [97, 117, 150]. In next generations systems the side lobe topography will play an important role in controlling interference and antenna arrays shall be able to reduce interference by pointing the main beam towards the direction of the desired user and by minimizing the sidelobes towards other interferering users. This ability of the array system shall lead to increased system capacity. The side lobe control can be achieved by use of, both, tapered beamformers non-adaptively and by shaping the antenna pattern adaptively. The array mathematical model used in thesis is derived next.

3.3 ARRAY MATHEMATICAL SIGNAL MODEL

To derive array mathematical signal model consider an M-element uniformly spaced linear array (ULA), as shown in Fig.3.1 [21]. The model considered here is for single signal, which can be extended to multiple signals. In Fig.3.1, the array elements are equally spaced by a distance d, and a plane wave arrives at the array from a direction θ off the array broadside. The angle θ is called the direction-of-arrival (DOA) or angle-of-arrival (AOA) of the received signal. Assume a single carrier modulated signal is arriving from angle θ_s that is received by the 1st sensor given by

$$x_1(t) = u(t)\cos(2\pi f_c t + \gamma(t) + \beta), \tag{3.1}$$

where, f_c is the carrier frequency of the modulated signal, $\gamma(t)$ is the information carrying component, u(t) is the amplitude of the signal, and β is a random phase.

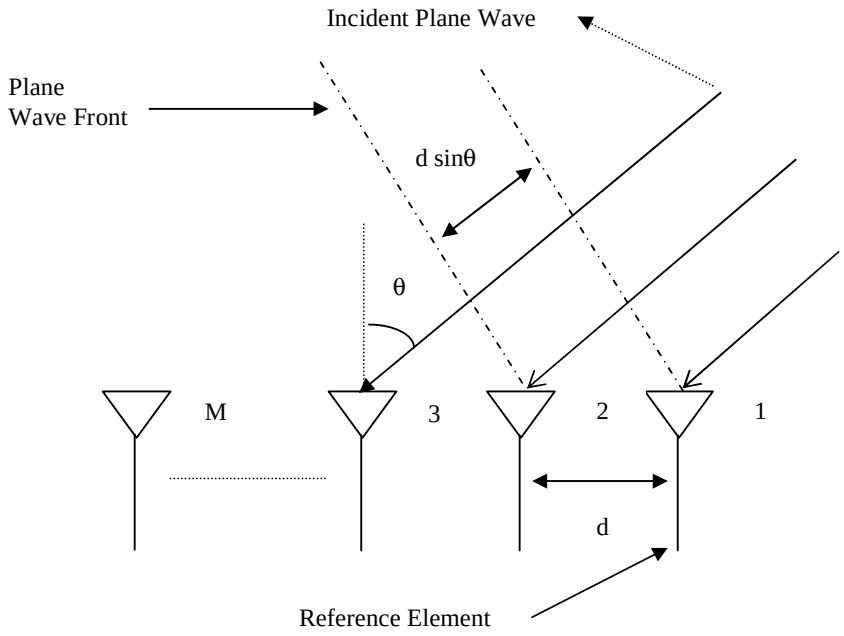

Figure 3.1-An 'M' Element Uniformly Spaced Linear Array

The complex envelope $\tilde{x}_1(t)$ of $x_1(t)$ is given by

$$\tilde{x}_1(t) = u(t)\exp[j(\gamma(t)+\beta)]. \tag{3.2}$$

Thus the received signal at the first element $x_1(t)$ and its complex envelope $\tilde{x}_1(t)$ may be related by

$$\tilde{x}_1(t) = \mathrm{Re}[x_1(t)\exp(j2\pi f_c t)] \ , \tag{3.3}$$

where, Re [.] stands for the real part of [.]. Upon reception of signal $x(t)$ the signal is demodulated to recover the signal $\tilde{x}(t)$ back as shown in Fig.3.2.

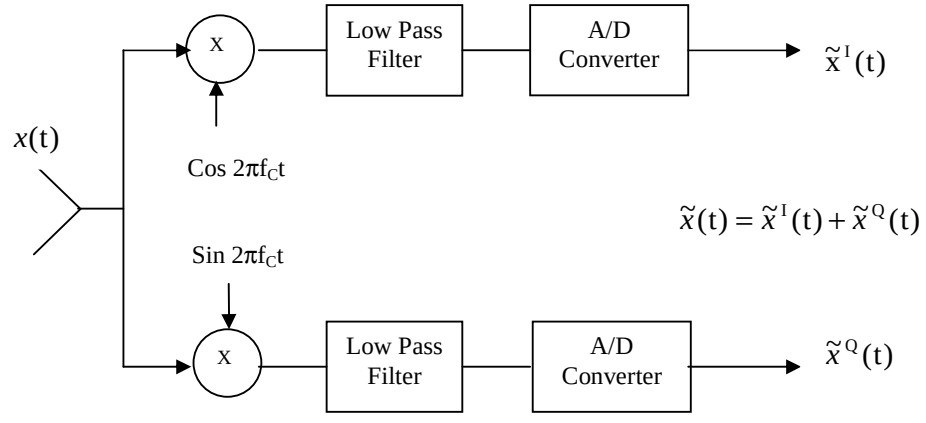

Figure 3.2- Block Diagram of Sensor with Receiver

In Fig.3.1 taking the first element in the array as the reference point, assuming medium to be non dispersive, the time delay up to second element due to additional propagation distance'd sinθ' is given by

$$\tau = \frac{d \sin\theta}{c}. \tag{3.4}$$

The received signal of the second element may be expressed as

$$x_2(t) = x_1(t-\tau) = u(t-\tau)\cos(2\pi f_c(t-\tau) + \gamma(t-\tau) + \beta). \tag{3.5}$$

If the carrier frequency f_c is large compared to the bandwidth of the impinging signal, then the modulating signal may be treated as quasi-static during time intervals of order τ and in that case (3.5) reduces to

$$x_2(t) = u(t)\cos(2\pi f_c t - 2\pi f_c \tau + \gamma(t) + \beta). \tag{3.6}$$

The complex envelope $\tilde{x}_2(t)$ of $x_2(t)$ is therefore given by

$$\tilde{x}_2(t) = u(t)\exp[j(-2\pi f_c \tau + \gamma(t) + \beta)] \quad = \quad \tilde{x}_1(t)\exp[-j(2\pi f_c \tau)]. \tag{3.7}$$

The effect of the time delay on the signal can now be represented by a phase shift term exp {-j ($2\pi f_c \tau$)}. Substituting (3.4) into (3.7),

$$\tilde{x}_2(t) = \tilde{x}_1(t)\exp[-j(2\pi f_c \frac{d\sin\theta}{c})] \qquad = \tilde{x}_1(t)\exp[-j\frac{2\pi}{\lambda} d\sin\theta)], \tag{3.8}$$

where, λ is the wavelength of the carrier. Similarly, for i^{th} element the complex envelope of the received signal may be expressed as

$$\tilde{x}_i(t) = \tilde{x}_1(t)\exp[-j(\frac{2\pi}{\lambda}(i-1)d\sin\theta)]. \tag{3.9}$$

Denoting the received signal vector by

$$\boldsymbol{x}(t) = [\tilde{x}_1(t) \quad \tilde{x}_2(t) \quad \tilde{x}_3(t). \ . \ . \ \tilde{x}_M(t)]^T, \tag{3.10}$$

where, $(.)^T$ denotes conventional transpose then $\boldsymbol{x}(t)$ may be expressed in vector form as

$$\boldsymbol{x}(t) = \boldsymbol{a}(\theta)\tilde{x}_1(t), \tag{3.11}$$

where,

$$\boldsymbol{a}(\theta) = \begin{bmatrix} 1 \\ \exp(-j\frac{2\pi}{\lambda} d\sin\theta) \\ . \\ . \\ . \\ \exp[-j\frac{2\pi}{\lambda}(M-1)d\sin\theta] \end{bmatrix}. \tag{3.12}$$

The vector $\boldsymbol{x}(t)$ is often referred to as the array input data vector and $\boldsymbol{a}(\theta)$ is called the steering vector. The collection of steering vectors for all angles and frequencies is referred to as the array manifold. In the above discussion, the bandwidth of the impinging signal expressed in (3.1) is assumed to be much smaller than the reciprocal of the propagation time across the array. Any signal satisfying this condition is referred to as narrowband; otherwise it is referred to as wideband. In most of the discussion that follows, the signal is assumed to be narrowband unless specified otherwise. The discrete time signals from a ULA in (3.10) can be written as:

$$\boldsymbol{x}(n) = [\tilde{x}_1(n) \quad \tilde{x}_2(n) \quad \tilde{x}_3(t) \quad \tilde{x}_M(n)]^T . \tag{3.13}$$

The above simple case can be extended to a more general case. Suppose there are k narrowband signals, all centered around a known frequency, say f_c, impinging on the array with DOA θ_i, i = 1, 2,……, k. Let $s_1(t)$, ……., $s_k(t)$ be the complex envelopes of these signals at first sensor. These signals may be uncorrelated, as for the signals coming from different users, or can be fully correlated as happens in multipath propagation, where each path is a scaled and time-delayed version of the original transmitted signal or can be partially correlated due to the noise corruption (How noise corruption leads to partial correlation of signals? The proof of this statement is given in Appendix A). The received signal at the array is a superposition of all the impinging signals and noise. Therefore, the input data vector may be expressed as

$$\boldsymbol{x}(t) = \sum_{i=1}^{k} \boldsymbol{a}(\theta_i)\, s_i(t) + \mathbf{n}(t), \tag{3.14}$$

where, $\mathbf{n}(t)$ denotes the $M \times 1$ vector of the noise at the array elements. $\boldsymbol{a}(\theta_i)$ is given by

$$\boldsymbol{a}(\theta_i) = \begin{bmatrix} 1 \\ \exp(-j\frac{2\pi}{\lambda} d \sin\theta_i) \\ . \\ . \\ \exp[-j\frac{2\pi}{\lambda}(M-1) d \sin\theta_i] \end{bmatrix} . \tag{3.15}$$

In matrix notation, (3.14) can be written as

$$\boldsymbol{x}(t) = \boldsymbol{A}(\Theta)\, \boldsymbol{s}(t) + \mathbf{n}(t), \tag{3.16}$$

where, $\boldsymbol{A}(\Theta)$ is the $M \times k$ matrix of the steering vectors given by

$$\boldsymbol{A}(\Theta) = [\boldsymbol{a}(\theta_1)\,\boldsymbol{a}(\theta_2)\,.....\boldsymbol{a}(\theta_k)]\,, \tag{3.17}$$

$$\boldsymbol{s}(t) = [s_1(t)\,s_2(t)\,.....s_k(t)]^T\,. \tag{3.18}$$

(3.16) represents the most commonly used narrowband input data model. Based on the array model described above beamforming fundamentals are discussed next.

3.4 FUNDAMENTALS OF BEAMFORMING

Beamforming is the name given to a wide variety of array processing algorithms that focus array capabilities in a particular direction. A beamforming algorithm points the array spatial filter towards the desired direction algorithmically rather than physically. Beamforming algorithms perform operations on the array output regardless of the sources or the character of noise present in the wave field so as to accept the signal from a particular direction while suppressing signals from undesired directions. Beamforming is also referred to as "electronic" steering since the weights are applied using electronic circuitry following the reception of the signal for the purpose of steering the array in a particular direction. This can be contrasted with mechanical steering, in which the antenna is physically pointed in the direction of interest. Conventional beamforming algorithms also use modern digital processing algorithms to linearly combine the signals from all the sensors in a manner, that is, with a certain weighting, so as to examine signals arriving from a specific angle. The beamforming operation is shown in Fig. 3.3.

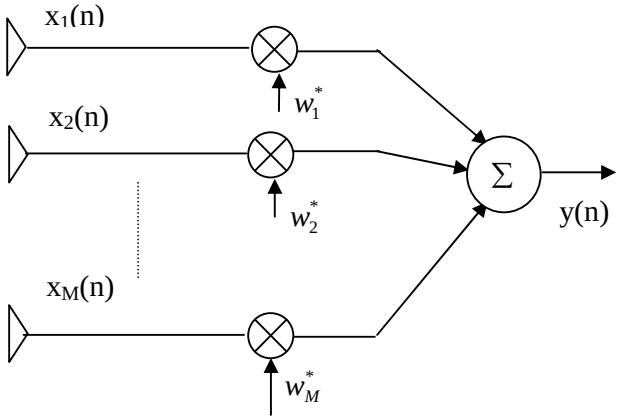

Figure 3.3-Beamforming Operation

As shown in Fig. 3.3, a beamformer produces its output by forming a weighted combination of signals from the M elements of the sensor array, that is,

$$y(n) = \sum_{i=1}^{M} w_i^* x_i(n) = \boldsymbol{w}^{\boldsymbol{H}} \boldsymbol{x}(n), \tag{3.19}$$

where, w_i^* is the weight applied to the i^{th} sensor. $\boldsymbol{w}$ is the M×1 column vector of complex antenna weights given and $(.)^H$ denotes conjugate transpose. $\boldsymbol{w}$ is commonly referred as beamforming vector given by

$$\boldsymbol{w} = [w_1 \ldots\ldots\ldots\ldots\ldots w_M]^T . \tag{3.20}$$

Typically, beamforming process as seen from (3.19) is filtering a signal from a specific location and attenuating signals from other locations. Thus a beamformer linearly combines the spatially sampled time series from each sensor to obtain a scalar output time series in the same manner that a Finite Impulse Response (FIR) filter linearly combines temporally sampled data. Implementing a temporal filter requires processing of data collected over a temporal aperture. Similarly, implementing a spatial filter requires processing of data collected over a spatial aperture. The beampattern and element spacing of an antenna array may be viewed as the equivalent to magnitude response of a FIR filter and the sampling period of a discrete time signal in the time domain, respectively [32]. To illustrate this point, consider a signal $x(t)$ composed of k complex sinusoids with unknown parameters embedded in additive noise:

$$x(t) = \sum_{i=1}^{k} a_i \exp[j(2\pi f_i t + \phi_i)] + n(t), \tag{3.21}$$

where, f_i, a_i, and ϕ_i are the frequency, amplitude, and phase, respectively, of the i^{th} sinusoid. Suppose that the sampling period of signal is T_s unrelated to the frequency of the unknown sinusoid, and let $x(l)$ denote the signal at time instant lT's, then

$$x(l) = \sum_{i=1}^{k} a_i \exp[j(2\pi f_i (lT_s) + \phi_i)] + n(lT_s). \tag{3.22}$$

Suppose the sampled signal is fed into an FIR filter with M -1 delay units, which is shown in Fig.3.4, to perform filtering. At time instant lT_s, the filter input and the (M –1) outputs of the delay units may be expressed as

$$\boldsymbol{x}(l) = \sum_{i=1}^{k} \boldsymbol{a}(f_i) s_i(l) + \boldsymbol{n}(l), \tag{3.23}$$

where,

$$\boldsymbol{x}(l) = [x(l) \ldots\ldots\ldots\ldots\ldots x(l - M + 1)]^T, \tag{3.24}$$

$$\boldsymbol{n}(l) = [n(l) \ldots\ldots\ldots\ldots\ldots n(l - M + 1)]^T, \tag{3.25}$$

$$\mathbf{a}(f_i) = \begin{bmatrix} 1 \\ \exp(-j2\pi T_s \mathrm{f}_i) \\ . \\ . \\ . \\ \exp(-j2\pi(M-1)T_s \mathrm{f}_i) \end{bmatrix}, \tag{3.26}$$

and $$s_i(l) = a_i \exp[\, j(2\pi f_i (lT_s) + \phi_i \,]. \tag{3.27}$$

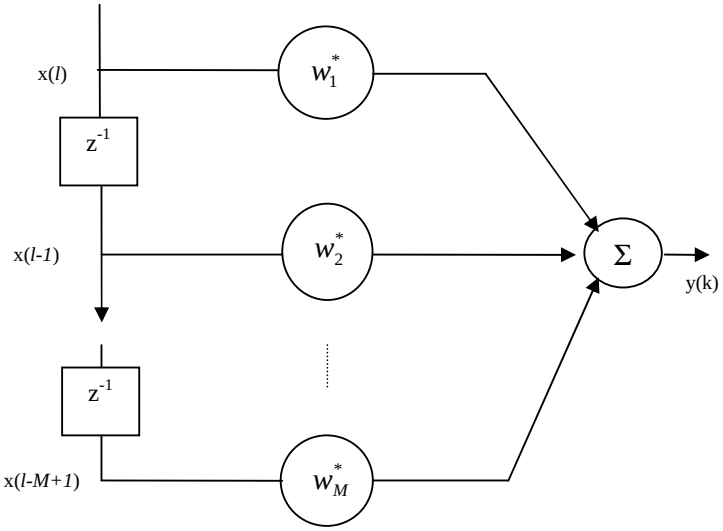

Figure 3.4-Filtering in time domain using FIR filter

Comparing (3.23) with (3.14), it can be seen that for a narrowband ULA, there is a correspondence between the normalized element spacing, d/λ, and the sampling period, T_s, in the FIR filter. The sine of the DOA θ_i, $\sin\theta_i$, corresponds to the temporal frequency f_i of the FIR filter input [32]. So there is a mapping between the ULA and the FIR filter, a theorem applied to the FIR filter in the time domain may also be applied to the uniform linear array in space domain. In time domain, the Nyquist sampling theorem states that a band limited signal with highest frequency f, is uniquely determined by its discrete time samples if the sampling rate is equal to or greater than 2f. If the sampling rate is less than 2f, aliaising will occur. In the space domain, the sampling rate corresponds to the inverse of the normalized element spacing, and the highest frequency is corresponding to 1 (since sin θ_i is always less than or equal to 1). From the Nyquist sampling theorem, to avoid spatial aliasing,

$$\frac{1}{\frac{d}{\lambda}} \geq 2 \qquad \text{or} \qquad d \leq \frac{\lambda}{2} \quad . \tag{3.28}$$

Therefore, the element spacing of an array should always be less than or equal to half of the carrier wavelength. The frequency response of an FIR filter with tap weights w^*_i, i = 1……. M and a sampling period T_s is given by

$$H(e^{j2\pi f}) = \sum_{i=1}^{M} w_i^* \exp[-j2\pi f T_s (i-1)], \tag{3.29}$$

where, $H(e^{j2\pi f})$ represents the response of the filter to a complex sinusoid of frequency f. For the harmonic retrieval problem, in order to extract the signal with frequency f_i, a set of complex weights are needed such that the frequency response of the filter has a higher gain at f_i and lower gains (or ideally, nulls) at other frequencies. For the beamforming problem, f and T_s are corresponding to sinθ and d/λ respectively. Hence replacing f and T_s in equation (3.29) with sinθ and d/λ respectively, yields the beamformer response,

$$c(\theta) = \sum_{i=1}^{M} w_i^* \exp[-j\frac{2\pi}{\lambda}(i-1)d\sin\theta], \tag{3.30}$$

where, c(θ) represents the response of the array to a signal with DOA equal to θ. So if there are several signals coming from different directions, and in order to extract the signal with direction θ_i, a set of weights are required to be found such that the array response has a higher gain at direction θ_i and lower gains (or ideally, nulls) at other directions. The array response c(θ) may also be expressed in vector form as

$$c(\theta) = \boldsymbol{w}^H \mathbf{a}(\theta), \tag{3.31}$$

where, $\boldsymbol{w}$ and $\boldsymbol{a(\theta)}$ is defined in (3.20) and (3.15) respectively.

3.4.1 Types of Beamformers

There are two types of beamformers, narrowband and wideband beamformer. A narrowband beamformer is shown in Fig.3.1. In Fig.3.1 the output at time k, y (k), is given by a linear combination of the data at the M sensors at time k:

$$y(k) = \boldsymbol{w}^H \boldsymbol{x}(k) \; . \tag{3.32}$$

A wideband beamformer samples the propagating wave field in both space and time and is often used when signals of significant frequency extent (broadband) are of interest [21]. A wideband beamformer is shown in Fig.3.5. It samples signal both in

space and time. The output in this case may be expressed as

$$y(k) = \sum_{i=1}^{M} \sum_{l=0}^{K-1} w_{i,l}^{*} x_i(k-l), \tag{3.33}$$

where, (K – 1) is the number of delays in each of the M sensor channels. The criterion for the choice of K is given in Appendix-B.

Let $$\boldsymbol{w} = [w_{1,0}, \ldots\ldots\ldots\ldots w_{1,K-1}, \ldots\ldots\ldots, w_{M,0}, \ldots\ldots\ldots, w_{M,K-1}]^T \tag{3.34}$$

and $$\boldsymbol{x}(k) = [x_1(k), \ldots\ldots x_1(k-K+1), \ldots\ldots\ldots x_M(k), \ldots\ldots\ldots\ldots x_M(k-K+1)]^T, \tag{3.35}$$

then (3.33) may also be expressed in vector form as in (3.31). In this case, both $\boldsymbol{w}$ and $\boldsymbol{x}(k)$ are $MK \times 1$ column vectors.

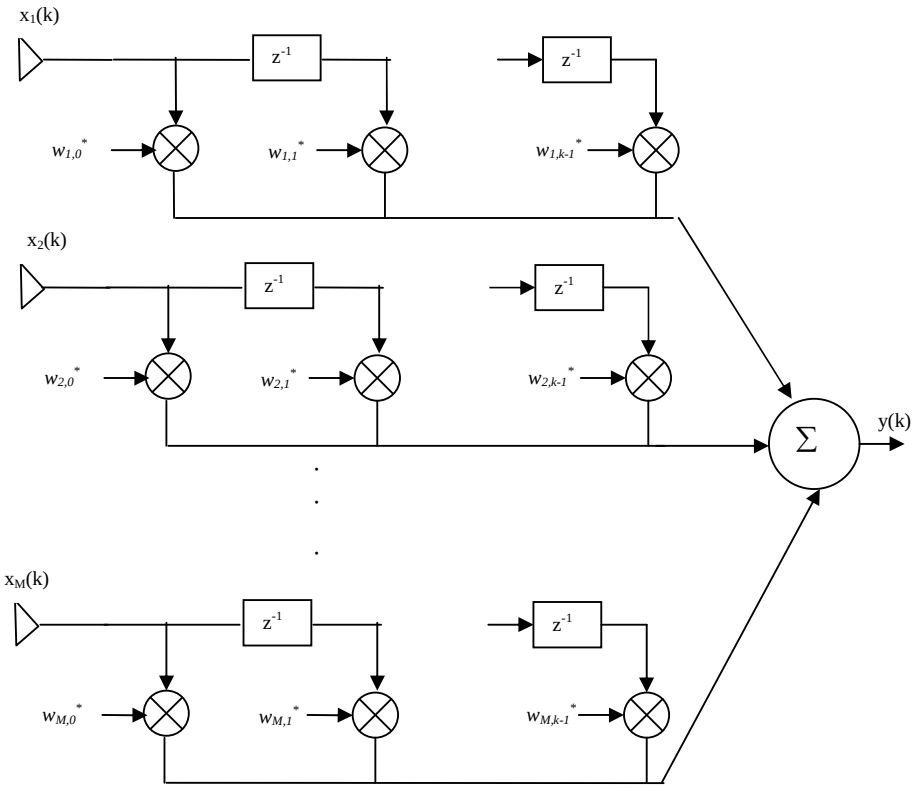

Figure 3.5-Wideband beamformer

3.4.2 Beam Response

A standard tool for analyzing the performance of a beamformer is the response for a given weight vector of $\boldsymbol{w}$ as a function of angle θ, known as the beam response. This angular response is computed by applying the beamformer $\boldsymbol{w}$ to a set of array response vectors from all possible angles, that is, $-90° \le \theta < 90°$, and given by

$$c(\theta) = \boldsymbol{w}^{H} \mathbf{a}(\theta). \tag{3.36}$$

$|c(\theta)|^2$ is known as the beampattern. Using $c(\theta)$,the normalized beamformer response may be defined as,

$$c_n(\theta) = \frac{c(\theta)}{\max(|c(\theta)|)}. \quad (3.37)$$

A sample normalized beampattern, expressed in dB, is shown for a 12-element uniform linear array in Fig. 3.6.

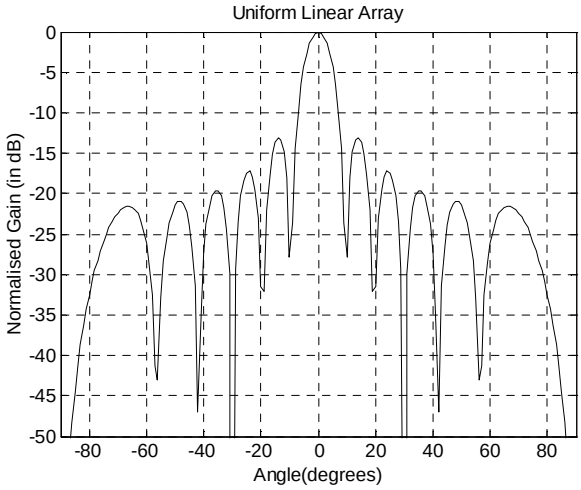

Figure 3.6-Beampattern of ULA for M=12, θ=0^0, d=0.5λ

In Fig.3.6, the large mainlobe is centered at $\theta = 0°$ and the beamformer response corresponding to $w_i = 1 \; \forall i$, is given by

$$c(\theta) = \sum_{i=1}^{M} \exp[-j\frac{2\pi}{\lambda}(i-1)d\sin\theta] = \frac{\sin(\pi\frac{Md}{\lambda}\sin\theta)}{\sin(\pi\frac{d}{\lambda}\sin\theta)}\exp[-j\pi\frac{(M-1)d}{\lambda}\sin\theta]. \quad (3.38)$$

3.4.3 Beamforming Gain

The signal to noise ratio (SNR) of the beamformer output determines the improvement in SNR with respect to each element, known as the beamforming gain. To derive the improvement in SNR in wireless environment, consider the signal model for a ULA from (3.16), which consists of a signal of interest arriving from an angle θ_s and thermal sensor noise w(n). The input to beamformer is array signal of single source from direction θ_s given by

$$\boldsymbol{x}(n) = \sqrt{M}\,\boldsymbol{v}(\theta_s)\,s(n) + \mathbf{w}(n), \quad (3.39)$$

where, $$\boldsymbol{v}(\theta_s) = \frac{[\boldsymbol{a}(\theta_s)]}{\sqrt{M}}\ , \tag{3.40}$$

and $s(n)$ is the signal of interest within a single sensor including the sensor response. The output of the beamformer is given by

$$y(n) = \boldsymbol{w}^{H}\boldsymbol{x}(n) = \sqrt{M}\boldsymbol{v}(\theta_s)\boldsymbol{w}^{H}s(n) + \overline{\mathbf{w}}(n)\,. \tag{3.41}$$

$\overline{\mathbf{w}} = \boldsymbol{w}^{H}\mathbf{w}(n)$ is the noise at the beamformer output and is also temporally uncorrelated. The beamformer output power is

$$P_y = E\left\{\left|y(n)\right|^2\right\} = \boldsymbol{w}^{H}\boldsymbol{R}_x\boldsymbol{w}, \tag{3.42}$$

where, $\boldsymbol{R}_x = E\left\{\boldsymbol{x}(n)\boldsymbol{x}^{H}(n)\right\}$ is the correlation matrix of the array signal $\boldsymbol{x}(n)$. The SNR in each element is given by $$SNR_{elm} = \frac{\sigma_s^2}{\sigma_w^2}\ , \tag{3.43}$$

where, $\sigma_s^2 = E\left\{\left|s(n)\right|^2\right\}$ is element level signal power and $\sigma_w^2 = E\left\{\left|w(n)\right|^2\right\}$ is the element level noise power. This SNR_{elm} is commonly referred to as the element level SNR. The signal and noise powers P_s& P_n at the output of the beamformer are

$$P_s = E\{|\sqrt{M}\ [\boldsymbol{w}^{H}\boldsymbol{v}(\theta_s)]s(n)|^2\} = M\sigma_s^2\,|\,\boldsymbol{w}^{H}\boldsymbol{v}(\theta_s)\,|^2\ , \tag{3.44}$$

$$P_n = E\{|\boldsymbol{w}^{H}\mathbf{w}(n)|^2\} = \boldsymbol{w}^{H}\mathbf{R}_n\boldsymbol{w} = \|\boldsymbol{w}\|^2\sigma_w^2\,, \tag{3.45}$$

where, $\mathbf{R}_n = \sigma_w^2\boldsymbol{I}$. Therefore, the resulting SNR at the beamformer output known as the array SNR, is given by $$SNR_{array} = \frac{P_s}{P_n} = \frac{M\left|\boldsymbol{w}^{H}\boldsymbol{v}(\theta_s)\right|^2}{\left\|\boldsymbol{w}\right\|^2}\frac{\sigma_s^2}{\sigma_w^2}\,. \tag{3.46}$$

(3.46) is simply the product of the beamforming gain and the element level SNR. Thus, the beamforming gain is given by

$$G_{bf} \overset{\Delta}{=} \frac{SNR_{array}}{SNR_{elm}} = \frac{\left|\boldsymbol{w}^{H}\boldsymbol{v}(\theta_s)\right|^2}{\left|\boldsymbol{w}\right|^2}M\,. \tag{3.47}$$

The beamforming gain is strictly a function of the angle of arrival θ_s of the desired signal, the beamforming weight vector $\boldsymbol{w}$, and the number of sensors M.

3.4.4 Estimation of Direction of Arrival

The dependence of beamforming gain on angle of arrival θ_s of the desired signal is given by (3.47). Thus during the beamforming operation as shown above in Fig.3.2, the DOA, θ_s of the signal incident upon the antenna array must be estimated. There are

two main types of algorithms for performing this DOA estimation. The first class of algorithms is the Spectral-based methods in which, a spatial spectrum is generated which gives array output power versus direction information. Spectral based methods can themselves be divided into two categories, beamforming techniques and subspace-based techniques. The beamforming DOA algorithms essentially electronically "steer" the antenna array in a direction at a time and "measure" the output power to determine the spatial spectrum. This is a purely mathematical operation that makes use of the steering vectors of the array along with the spatial covariance matrix. Subspace-based techniques use more complex decompositions of the spatial covariance matrix for generating the spatial spectrum. The second, more accurate classes, of DOA algorithms are the parametric methods which are also generally far more abstract and computationally intensive than the Spectral based methods. These methods also require a simultaneous, high dimension search for all signal parameters of interest. The DOA estimation is shown in Fig.3.7. Since the primary focus of the research in this thesis was not to study DOA algorithm performance, there was not much emphasis placed on using highly sophisticated DOA estimation techniques. Further in this thesis it is assumed that DOA of the desired and interferers is available at the beamformer so that the low side lobe control techniques can be used effectively.

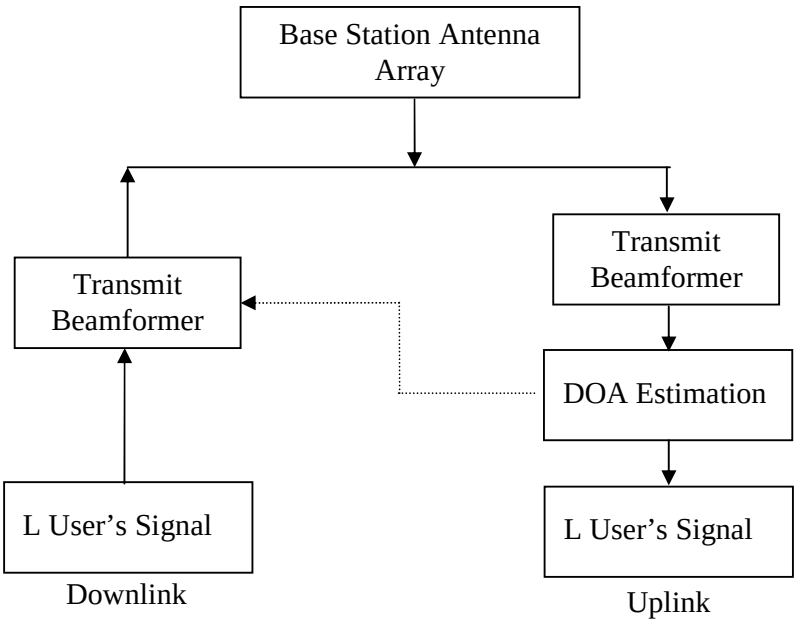

Figure 3.7-Beamforming in uplink and down link of Wireless Communication

3.5 LOW SIDE LOBE CONTROL TECHNIQUES

As discussed in section 3.2 any beamformer that can depress the large number of interferers will improve the capacity and performance of CDMA systems. Such beamformers called smart antennas improve signal to interference ratio (SIR) of the communication system efficiently by forming narrow beam towards desired user and low side towards undesired users. A brief review of narrow beam low side-lobe algorithms is given next.

3.5.1 Narrow-Beam Low-Sidelobe Designs

The problem of designing arrays having narrow beams with low sidelobes is equivalent to the digital signal processing problem of spectral analysis of windowed sinusoids. Consider the design of an infinitely narrow beam toward some look direction $\theta=\theta_0$. In ψ-plane, the array factor should be infinitely thin spectral line

$$A(\psi) = 2\pi\delta(\psi - \psi_0), \tag{3.48}$$

where, ψ = kd cosθ and ψ_0 = kd Cosθ_0, k is the wave number and d is inter element spacing. The term array factor for an array of antennas is given by the net field produced by the array of sources. The net effect of array factor is to modify the single-antenna radiation vector, of an array of identical antennas. Array factor incorporates all the translational phase shifts and relative weighting coefficients of the array elements.

Taking the inverse Fourier transform of (3.48), gives the double-sided infinitely-long array, for $-\infty < m < \infty$:

$$a(m) = \frac{1}{2\pi}\int_{-\pi}^{\pi} A(\psi)e^{-jm\psi}d\psi = \frac{1}{2\pi}\int_{-\pi}^{\pi} 2\pi\delta(\psi - \psi_0)e^{-jm\psi}d\psi = e^{-jm\psi_0}. \tag{3.49}$$

This is the spatial analog of an infinite sinusoid $a(n) = e^{j\omega_0 n}$ whose spectrum is the sharp spectral line $A(\omega) = 2\pi\delta(\omega - \omega_0)$. A finite-duration sinusoid is obtained by windowing it, with a length-N time window $b(n)$ resulting in $a(n) = b(n)e^{j\omega_0 n}$. In the frequency domain, the effect of windowing is to replace the spectral line $\delta(\omega-\omega_0)$ by its smeared version $W(\omega-\omega_0)$, where $W(\omega)$ is the Fourier transform of the window $b(n)$. The spectrum $W(\omega-\omega_0)$ exhibits a main lobe at $\omega = \omega_0$ and sidelobes. The main lobe gets narrower with increasing N.

Consider an array of N elements at locations x_m along the x-axis with element spacing d. If N is odd, say N = 2M + 1, the element locations x_m can be

defined symmetrically as:

$$x_m = md, \qquad m = 0,\pm1,\pm2, \ldots ,\pm M . \tag{3.50}$$

The array factor can be written then as a discrete-space Fourier transform or as a spatial z-transform:

$$\begin{aligned} A(\psi) &= \sum_{m=-M}^{M} a_m e^{jm\psi} = a_0 + \sum_{m=1}^{M}[a_m e^{jm\psi} + a_{-m} e^{-jm\psi}] \\ &= \sum_{m=-M}^{M} a_m z^m = a_0 + \sum_{m=1}^{M}[a_m z^m + a_{-m} z^{-m}]. \end{aligned} \tag{3.51}$$

On the other hand, if N is even, say N = 2M, in order to have symmetry with respect to the origin, the elements are placed at the half-integer locations

$$x_{\pm m} = \pm(md - \frac{d}{2}) = \pm(m - \frac{1}{2})d, \qquad m = 1,2,.....M. \tag{3.52}$$

The array factor is given by:

$$\begin{aligned} A(\psi) &= \sum_{m=1}^{M}\left[a_m e^{j(m-1/2)\psi} + a_{-m} e^{-j(m-1/2)\psi}\right] \\ &= \sum_{m=1}^{M}\left[a_m z^{(m-1)/2} + a_{-m} z^{-(m-1/2)}\right]. \end{aligned} \tag{3.53}$$

Thus a finite N-element array with a narrow beam and low side lobes, and steered towards an angle θ_0, can be obtained by windowing the infinite narrow-beam array with an appropriate length-N spatial window *b*(m). For odd N = 2M+ 1 and even N = 2M, the resulting window is defined respectively:

$$\begin{aligned} &a(m) = e^{-jm\psi_0} b(m) \qquad m = 0,\pm1,.....\pm M, \\ &a(\pm m) = e^{\pm j(m-1/2)\psi_0} b(\pm m) \qquad m = 1,2,.....M. \end{aligned} \tag{3.54}$$

For both cases of (3.54) the array factor of (3.51) & (3.53) becomes

$$A(\psi) = W(\psi - \psi_0), \qquad \text{(narrow beam array factor)} \tag{3.55}$$

where, W(ψ) is the DFT of the window, defined for odd or even N as:

$$\begin{aligned} W(\psi) &= b(0) + \sum_{m=1}^{M}[b(m)e^{jm\psi} + b(-m)e^{-jm\psi}], \\ W(\psi) &= \sum_{m=1}^{M}[b(m)e^{j(m-1/2)\psi} + b(-m)e^{-j(m-1/2)\psi}] \quad . \end{aligned} \tag{3.56}$$

Assuming a symmetric window, *b* (-m) = *b* (m), W(ψ) can be written as:

$$\begin{aligned} W(\psi) &= b(0) + 2\sum_{m=1}^{M} b(m)\cos(m\psi) \qquad \text{for} \quad N = 2M+1, \\ W(\psi) &= 2\sum_{m=1}^{M} b(m)\cos((m-1/2)\psi) \qquad \text{for} \quad N = 2M. \end{aligned} \tag{3.57}$$

At broadside, $\psi_0 = 0$, $\theta_0 = 90^o$, (3.54) reduces to *a*(m)= b(m) and the array factor becomes A(ψ)= *W(ψ)*. Thus, the weights of a broadside narrow beam array are

the window samples $a(m) = b(m)$. The weights of narrow beam array can be steered easily. The primary issue in choosing a window function $b(m)$ is the tradeoff between frequency resolution and frequency leakage, that is, between main-lobe width and side lobe level. Ideally, one would like to meet, as best as possible, the two conflicting requirements of having a very narrow mainlobe and very small sidelobes. Figs.3.8 & 3.9 show four narrow-beam design examples illustrating this tradeoff. All designs are with 7-element arrays with half-wavelength spacing, $d = \lambda/2$, and steered towards 90^o. The Dolph-Chebyshev and Taylor-Kaiser arrays were designed with side lobe level of 30 dB. For comparison the 3dB beamwidth of various windows is shown in table 3.1. The expressions of various taper functions used in Figs.3.8-3.9 are given in appendix-F.

Table-3.1: Beam width (3 dB) of various tapers

Taper	3 dB Beamwidth(N=7)	3 dB Beamwidth (N=16)
Uniform	14.5^0	6.34^0
Binomial	24.5^0	15.6^0
Dolph Chebyshev	18.6^0	7.97^0
Taylor Kaiser	23.5^0	10.1^0

From Figs.3.8-3.9, it is clear that the uniform array has the narrowest mainlobe but also the highest sidelobes. The Dolph-Chebyshev is optimum in the sense that, for the given sidelobe level of 30 dB, it has the narrowest width. The Taylor-Kaiser is somewhat wider than the Dolph-Chebyshev, but it exhibits better sidelobe behavior. The binomial array has the widest mainlobe but no sidelobes at all. The above results are also shown for number of elements N=16, $d=0.5\lambda$ in Fig.3.10 & 3.11. The 3 dB beamwidth for above cases is given in table 3.1. From the above discussion it is obvious that one way of creating low side lobes is to use windows functions. The array weights of a beamformer can be windowed with the array coefficients of a suitable window function to obtain a desired side lobe level. This process is known as tapered beamforming, resultant beamformer is called tapered beamformer, and window function is called taper. The tapered beamformers may be thought of as the truncated or windowed versions of the corresponding beamformer. Taper can be applied to any beamformer. To illustrate this, an example is given in which a matched filter beamformer output is tapered. The matched filter beamformer is also known as conventional beamformer.

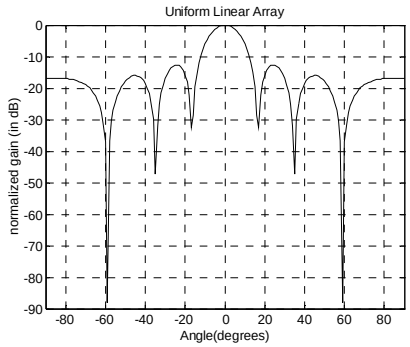

(a) Beampattern for uniform Linear array

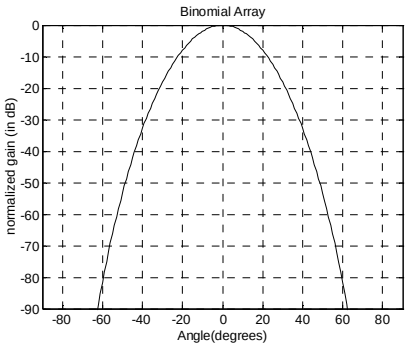

(b) Beampattern for Binomial array

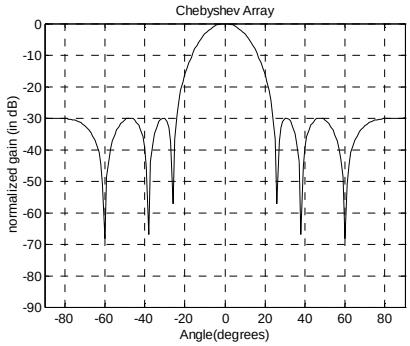

(c) Beampattern for Dolph Chebyshev array

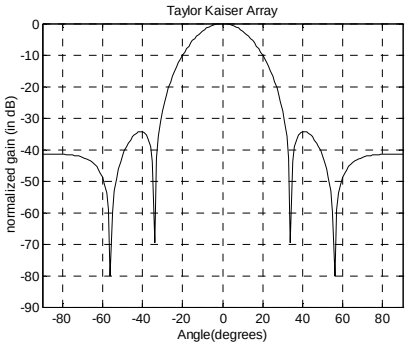

(d) Beampattern for Taylor Kaiser array

Figure 3.8-Beampattern for various window functions for N=7, d=0.5λ

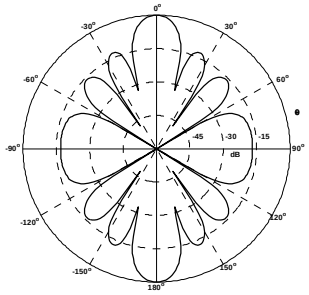

(a) Polar plot for uniform Linear array

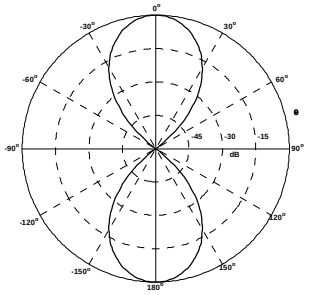

(b) Polar plot for Binomial array

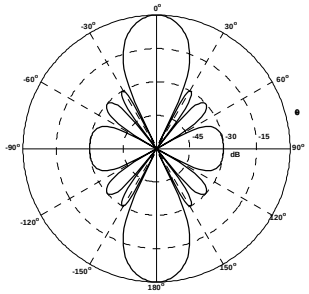

(c) Polar plot for Dolph Chebyshev array

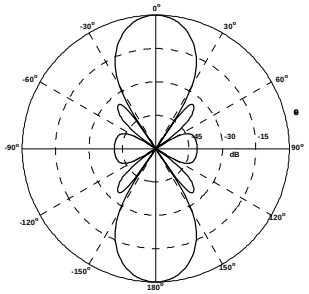

(d) Polar plot for Taylor Kaiser array

Figure 3.9- Polar Plot for various window functions for N=7, d=0.5λ

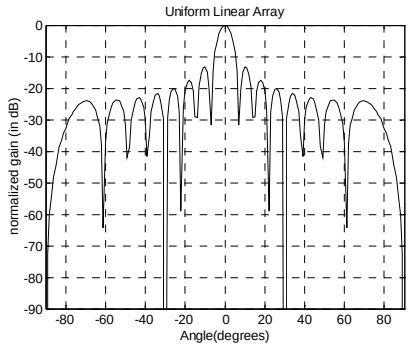

(a)Beampattern for uniform Linear array

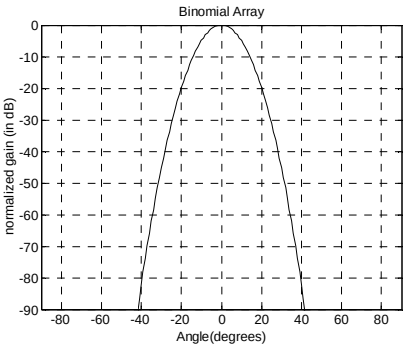

(b) Beampattern for Binomial array

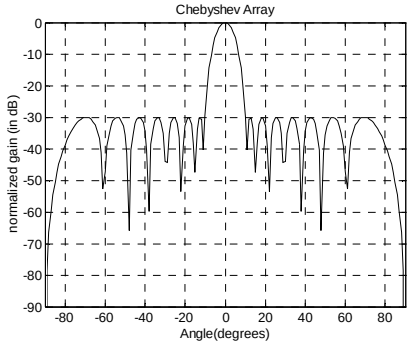

(c)Beampattern for Dolph Chebyshev array

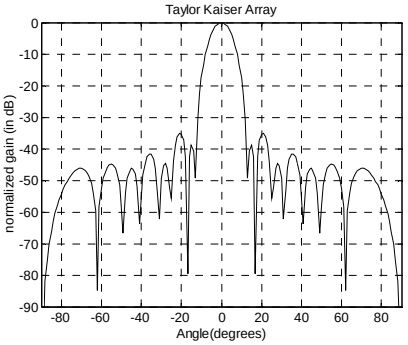

(d) Beampattern for Taylor Kaiser array

Figure 3.10-Beampattern for various window functions for N=16, d=0.5λ

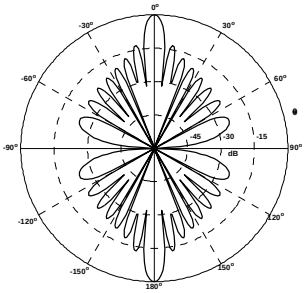

(a)Polar plot for uniform Linear array

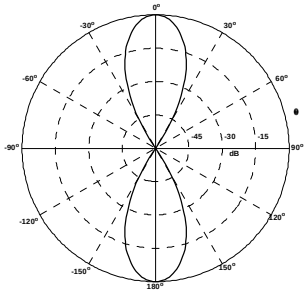

(b)Polar plot for Binomial array

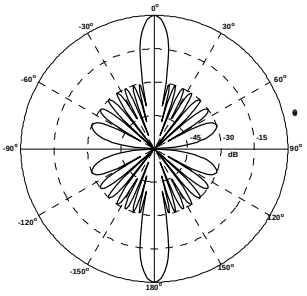

(c)Polar plot for Dolph Chebyshev array

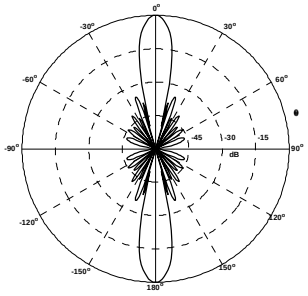

(d) Polar plot for Taylor Kaiser array

Figure 3.11-Polar plot for various window functions for N=16, d=0.5λ

3.5.2 Matched Filter Tapered Beamformer

Consider the single signal ULA model from (3.39), but now including an interference signal i(n) made up of P interference sources as in mobile environment

$$\boldsymbol{x}(n) = \sqrt{M}\boldsymbol{v}(\theta_s)s(n) + \sqrt{M}\sum_{p=1}^{P}\boldsymbol{v}(\theta_p)i_p(n) + \mathbf{w}(\mathrm{n}), \tag{3.58}$$

where, $\boldsymbol{v}(\theta_p)$ and $i_p(\mathrm{n})$ are the array response vector and signal due to the p^{th} interferer respectively. The components of noise vector are uncorrelated and have power σ_w^2 i.e. $E[\mathbf{w}(n)\mathbf{w}^H(n)] = \sigma_w^2\mathbf{I}$. The output of the beamformer is given by

$$\mathrm{y(n)} = \boldsymbol{w}^{\mathrm{H}}\boldsymbol{x}(\mathrm{n}). \tag{3.59}$$

The weight vector $\boldsymbol{w}$ which will result in exact replica of sensor signals is

$$\boldsymbol{w} = \boldsymbol{c}_{mf}^{H} = \boldsymbol{v}^{\mathrm{H}}(\theta_s). \tag{3.60}$$

The output of the beamformer can be expressed as

$$y(n) = \boldsymbol{c}_{mf}^{H}\boldsymbol{x}(n) = \boldsymbol{v}^{\mathrm{H}}(\theta_s)\,\boldsymbol{x}(\mathrm{n}). \tag{3.61}$$

$\mathbf{c}_{\mathrm{mf}}$ is called matched filter beamformer. In case of ULA with λ/2 element spacing, the beampattern of the spatial matched filter is shown in Fig.3.6. It has sidelobes that are high enough to pass interferers through the beamformer with enough gain to prevent the detection of the desired signal. For this array, if an interfering source is present at $\theta = 20^0$ with a power of 40dB, the power of the interference at the output of the spatial matched filter would be 20dB because the sidelobe level at θ=20° is only -20 dB. If the weaker signal is received from $\theta=0^0$ the array would be unable to extract it because of the side lobe leakage from the interferer. The spatial matched filter has all weights with equal magnitude of $\frac{1}{\sqrt{M}}$. The sidelobe levels can be further reduced by tapering the magnitudes of the spatial matched filter. A tapering vector $\boldsymbol{t}$ is applied to the spatial matched filter to realize a low sidelobe level beamformer

$$\boldsymbol{c}_{\mathrm{tbf}}(\theta_s) = \boldsymbol{t}\,\Theta\boldsymbol{c}_{\mathrm{mf}}(\theta_s), \tag{3.62}$$

where, Θ represents the Hadamard product, which is the element-by-element multiplication of the two vectors. The determination of a taper can be thought of as the design of the desired beamformer where $\boldsymbol{c}_{mf}$ simply determines the desired angle. The weight vector of the spatial matched filter from (3.60) has unit norm; that is, $\boldsymbol{c}_{\mathrm{mf}}^{\mathrm{H}}\boldsymbol{c}_{\mathrm{mf}} = 1$. Similarly, the tapered beamformer $\boldsymbol{c}_{\mathrm{tbf}}$ is normalized so that

$$\boldsymbol{c}_{\mathrm{tbf}}^{\mathrm{H}}(\theta_s)\boldsymbol{c}_{\mathrm{tbf}}(\theta_s)=1\ . \tag{3.63}$$

The tapered response of the matched filter beamformer is shown in Fig.3.12. The Dolph Chebyshev taper is used for illustration. The side lobe level of the taper is chosen to be -50dB. The same 40 dB interferer is now reduced to -10 dB. However, the use of tapers does not come without a cost. The main lobes of the beam patterns in Fig.3.12 are much broader for the tapered beamformers. The consequence is a less resolution that becomes more pronounced as the tapering is increased to achieve lower side lobe levels. Fig. 3.13 shows beamformer with -50dB and -70dB Dolph-Chebyshev tapers.

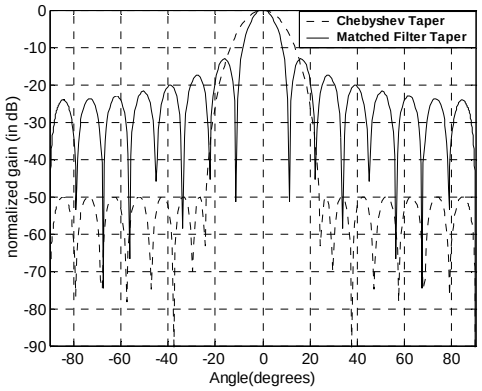

Figure 3.12-Beampattern for 16 element matched filter beamformer with no taper and -50dB taper

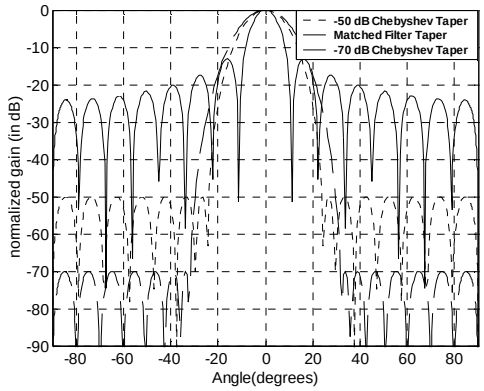

Figure 3.13-Beampattern for 16 element matched filter beamformer with no taper, -50dB taper and -70 dB taper.

From above discussion it is found that the role of window function is quite impressive and economical from the point of view of computational complexity and ease associated with its application in controlling side lobes. The patterns of these window functions are basically Fourier transform of the various windows function, which can be described mathematically by various distributions. There are many differing functional forms, which comprise a subset of classical windows known to most engineers. A complete review of many window functions and their properties was presented by Harris [44]. All windowing functions are designed to reduce the side lobes of the spectral output of FFT routines. However, in every area where Fourier Transform and frequency domain concepts are used, there exists the potential for generalization and implementation by using Fractional Fourier Transform (FrFT). Properties and applications of the ordinary Fourier Transform are special cases of those of the FrFT. The FrFT is being used in almost all applications where Fourier transforms were used.

In the next section the fractional Fourier transform of various window functions has been carried out, to provide taper of varying beamwidth and side-lobe level.

3.6 BEAMFORMING IN FRACTIONAL FOURIER DOMAIN

Before discussing beamforming in fractional Fourier domain, a brief overview of FrFT is given first.

3.6.1 Fractional Fourier Transform

The FrFT belongs to the class of time–frequency representations that have been extensively used by the signal processing community. In all the time–frequency representations, a plane with two orthogonal axes corresponding to time and frequency is used. If a signal $x(t)$ is represented along the time axis and its ordinary Fourier transform X(f) is represented along the frequency axis, then the Fourier transform operator (denoted by F) can be visualized as a change in representation of the signal corresponding to a counterclockwise rotation of the signal by an angle $\pi/2$.This is consistent with some of the observed properties of the Fourier transform. For example, two successive rotations of the signal through $\pi/2$ will result in an inversion of the time axis. Moreover, four successive rotations will leave the signal unaltered since a rotation through 2π of the signal should leave the signal unaltered. The FrFT is a linear operator that corresponds to the rotation of the signal through an angle, which is not a multiple of $\pi/2$, i.e. it is the representation of the signal along the axis u making an angle α with the time axis. The detailed development of the FrFT is established in [60, 96].

Definition:

The FrFT is defined with the help of the transformation kernel K_α as

$$K_\alpha(t,u)=\begin{cases}\delta(t-u) & \text{if } \alpha \text{ is a multiple of } 2\pi \\ \delta(t+u) & \text{if } \alpha+\pi \text{ is a multiple of } 2\pi \\ \sqrt{\dfrac{1-j\cot\alpha}{2\pi}}\,e^{(j(u^2+t^2)/2)\cot\alpha - jut\,\mathrm{cosec}\,\alpha} & \text{if } \alpha \text{ is not a multiple of } \pi\end{cases}. \tag{3.64}$$

The definition is discussed in detail in [15]. The FrFT is defined using this kernel as (FrFT of order α of $x(t)$ is denoted by $X_\alpha(u)$)

$$X_\alpha(u)=\int_{-\infty}^{\infty} x(t)K_\alpha(t,u)dt\,. \tag{3.65}$$

$$X_\alpha(u)=\begin{cases} x(t) & \text{if } \alpha \text{ is a multiple of } 2\pi \\ x(-t) & \text{if } \alpha+\pi \text{ is a multiple of } 2\pi \\ \sqrt{\dfrac{1-j\cot\alpha}{2\pi}}\, e^{j(u^2\cot\alpha/2)} \displaystyle\int_{-\infty}^{\infty} x(t)e^{jt^2\cot\alpha/2-jut\operatorname{cosec}\alpha}dt & \text{if } \alpha \text{ is not a multiple of } \pi \end{cases}. \quad (3.66)$$

The FrFT of a signal *x*(t) as given by (3.66) can be computed by the following steps:

1) Multiplying the function with a chirp,
2) Taking its Fourier transform,
3) Again multiplying with a chirp, and
4) Then multiplication with an amplitude factor.

The problem of the existence of the FrFT has been widely studied in [60] and it is found that the FrFT of a signal *x*(t) exists under the same conditions in which its Fourier transform exists. Some important properties of FrFT are discussed next.

3.6.2 Properties of Fractional Fourier Transform

Let F_α denote the operator corresponding to the FrFT of angle α or of order 'a' where $a=2\alpha/\pi$. Under this notation, some of the important properties of the FrFT operator are listed below. These properties are discussed in detail in [60].

a) **Identity operator**

F_0 is the identity operator. The FrFT of order $\alpha= 0$ is the input signal itself. The FrFT of order $\alpha= 2\pi$ corresponds to the successive application of the ordinary Fourier transform 4 times and therefore also acts as the identity operator,

$$\text{i.e. } F_0 = F_{2\pi} = I.$$

b) **Fourier transform operator**

The FrFT of order $\alpha= \pi/2$ gives the Fourier transform of the input signal.

c) **Successive applications of FrFT**

Successive applications of FrFT are equivalent to a single transform whose order is equal to the sum of the individual orders, i.e. $F_\alpha F_\beta=F_{\alpha+\beta}$.

d) **Inverse**

The FrFT of order $-\alpha$ is the inverse of the FrFT of order α since

$$F_{-\alpha}(F_\alpha) =F_{\alpha-\alpha}=F_0=I .$$

Property (a) follows from the direct definition of the kernel for $\alpha= 0$. Property (b) can be proved by expanding the Kernel for the special case when $\alpha=\pi/2$. Property

(c) can be proved using the convolution property of the kernel. Property (d) is a consequence of properties (b), (c) and the fact that four consecutive applications of the Fourier transform correspond to the Identity operator. Property (d) can also be proved using property (c). One important conclusion that can be drawn from these properties is that the signal x(t) and its FrFT (of order a) $X_\alpha(u)$ form a transform pair and are related to each other by the following equations:

$$X_\alpha(u) = \int_{-\infty}^{\infty} x(t) K_\alpha(u,t)\,dt\,, \tag{3.67}$$

$$x(t) = \int_{-\infty}^{\infty} X_\alpha(u) K_{-\alpha}(u,t)\,du\,. \tag{3.68}$$

Hence by varying angle α from 0 to 2π, the values of 'a' can be varied from 0 to 4. It can be shown that the transform kernel is periodic with a period of 4. The Fractional Fourier transform definition is also based upon the time frequency or space frequency distributions such as Wigner distribution [15]. Time frequency distributions have been applied in non stationary signal processing such as speech signal processing. Several transforms such as Short time Fourier transforms, Wavelet transforms, Wigner Ville transforms, Spectrogram and Choi-Williams etc are distinguished by their properties and kernels [60, 62].

The effect of FrFT on a signal can be seen easily in a time-frequency plane. It is well known that Wigner distribution of the Fourier transform of the function f(u) is obtained by rotating the Wigner distribution of f(u) by $\pi/2$ in the time frequency plane in clockwise direction. The Wigner distribution of the a^{th} order fractional Fourier transform of f(u) is obtained by rotating the Wigner distribution of f(u) by $a\pi/2$ [60]. The Wigner distribution function of a signal x can be defined in terms of time domain representation of x(u) as:

$$W(u,v) = \int_{-\infty}^{\infty} x(u+\frac{u'}{2}) x(u-\frac{u'}{2}) e^{2i\pi u'v}\,du'\ . \tag{3.69}$$

3.6.3 Parseval's Theorem in FrFT Domain

The well-known Parseval's theorem for Fourier transform can be easily extended to the FrFT as well. Parseval's theorem is the energy preservation property as given below. This property can be obtained by the application of Parseval's theorem in FrFT domain as follows

$$\int_{-\infty}^{\infty} |x(t)|^2 \, dt = \int_{-\infty}^{\infty} |X_\alpha(u)|^2 \, du \,. \tag{3.70}$$

The energy preservation property of the FrFT is expected because the FrFT is based on the decomposition of the signal on the orthonormal basis set of the chirp functions. Due to the energy preserving property of the Fourier transform, the squared magnitude of the Fourier transform of a signal is often called the energy spectrum of the signal and is interpreted as the distribution of the signal energy among the different frequencies. Similarly the squared magnitude of the FrFT of a signal is called as the fractional energy spectrum of the signal and is interpreted as the distribution of the signal energy between the different chirp basis functions.

3.6.4 Fractional Fourier Transform of Related Signals

The FrFT of signals related to x (t) are listed in Table 3.2.

Table-3.2: Fractional Fourier Transform of related signals [60]

Operation	Signal x(t)	Fractional Fourier Transform $X_\alpha(u)$
Time shift	x(t-τ)	$e^{j\frac{\tau^2}{2}(\sin\alpha\cos\alpha)-ju\tau\sin\alpha)} X_\alpha(u-\tau\cos\alpha)$
Modulation	$x(t)e^{jvt}$	$e^{-jv^2(\sin\alpha\cos\alpha)/2+juv\cos\alpha} X_\alpha(u-v\sin\alpha)$
Multiplication with chirp	t.x(t)	$u\cos\alpha X_\alpha(u) + j\sin\alpha X'_\alpha(u)$
Inversion of time axis	x(-t)	$X_\alpha(-t)$
Differentiation	$x'(t)$	$X'_\alpha(u)\cos\alpha + ju\sin\alpha X_\alpha(u)$
Integration	$\int_a^t x(t')dt'$	$\sec\alpha e^{-j(u^2/2)\tan\alpha} \int_a^u X_\alpha(z)e^{-j(z^2/2)\tan\alpha}dz$
Division by ramp	$x(t)/t$	$-j\sec\alpha e^{j(u^2/2)\cot\alpha} \int_{-\infty}^u x(z)e^{-j(z^2/2)\cot\alpha}dz$
Scaling of time axis	x(ct)	$\sqrt{\frac{1-j\cot\alpha}{c^2-j\cot\alpha}}e^{j(u^2/2)\cot\alpha(1-(\cos^2\beta/\cos^2\alpha)} X_\beta(\frac{u\sin\beta}{c\sin\alpha})$ *where* $\cot\beta = \frac{\cot\alpha}{c^2}$

The expressions for discrete versions of FrFT are given in Appendix-G.

3.6.5 Fractional Fourier Transform of Various Taper Functions

To find the effectiveness of various window functions in Fractional Fourier domains in terms of interference suppression, the FrFT of various taper functions has been carried out for different values of parameterα[1,2]. By varying parameter 'α' side lobe level and main lobe width can be varied. The results of some window functions are shown in Figs. 3.14-3.16. All taper functions are taken of 11 elements with inter element spacing d of 0.5λ, where λ is wavelength of operation. The Results of various window functions are summarized in tables 3.3 & 3.4.

3.6.6 Procedure for Tapering in FrFT Domain

To use these tapers in suppressing interference in FrFT domains two definitions are given below to find out resultant array weights:

Definition 1: The first definition includes performing an FrFT of order 'a' (denoted by F^a) over both window functions, multiplying the results, and then performing an additional FrFT with a fractional order of '–a'. This definition is asymmetric.

Definition 2 The second definition is more general definition according to which perform first an FrFT of the order 'a' over both functions, multiply them, and then perform an FrFT with a fractional order of '–q'. As a special case of this general definition is for q = 'a'. In this case the definition is symmetric. The steps for tapering in FrFT domain for two functions x(t) and y(t), are defined below:

(i) First perform FrFT of order 'a' over both taper functions

i.e. $F^a[x(t)]$ and $F^a[y(t)]$,

(ii) Take product of these functions and form function $z_a(t)$ i.e.

$$z_a(t)= F^a[x(t)] * F^a[y(t)].$$

(iii) Take inverse FrFT of order 'q' i.e. $W(t) =F^q[z_a(t)]$. Here 'q' = 'a' is a special case.

(iv) Form the array with weight function W(t) obtained from above procedure.

To derive the output weight function W(t), the most general case is investigated. Let us assume $a=P_1$ be the fractional operator before multiplication in step (ii) and $q=P_2$ be the fractional Fourier transform after the multiplication in step (iii).

---

1. [P19] "Rectangular & Bartlett windows in Fractional Fourier domain", Proceedings of National Conference of Mathematical & Computer *Applications in Science and Engineering* ,TIET, Patiala, Jan-2003
2. [P20] "Fractional Fourier domain analysis of Generalized Cosine windows", Proceedings of *IETE and CSI on Services through IT enabled systems, SITES-2003*, Gwalior, pp.144-151, 19-20 April, 2003

Let the resultant array weights be denoted by $W_{P_1,P_2}(u)$ and is given by

$$W_{P_1,P_2}(u) = \int_{-\infty}^{\infty}\int_{-\infty}^{\infty}\int_{-\infty}^{\infty} x(t)y(\pm t')\exp[j\pi\Psi_1(u,t,t',v)]\exp[-j2\pi\Psi_2(u,t,t',v)]dtdt'dv,$$

where,
$$\Psi_1(u,t,t',v) = \frac{u^2+v^2}{T_2} + \frac{t^2+v^2}{T_1} \mp \frac{t'^2+v^2}{T_1},$$

$$\Psi_2(u,t,t',v) = v\left(\frac{t \mp t'}{S_1} + \frac{t}{S_2}\right),$$

$$\begin{aligned} T_1 &= 2\pi\tan(\alpha_1), & T_2 &= 2\pi\tan(\alpha_2), \\ S_1 &= 2\pi\sin(\alpha_1), & S_2 &= 2\pi\sin(\alpha_2), \\ \alpha_1 &= P_1(\pi/2), & \alpha_2 &= P_2(\pi/2). \end{aligned} \qquad (3.70a)$$

Regarding the $\pm$ and $\mp$ symbols, the upper symbols are used if FrFT of y(t) is used and lower symbols are used if FrFT of y(-t) is used. For symmetric case using saddle point integration method $\int$.....dv can be estimated and (3.70a) becomes

$$W_{P_1,P_2}(u) = \int_{-\infty}^{\infty}\int_{-\infty}^{\infty} x(t)y(\pm t')\frac{\exp[-j\pi/4]}{\left(\left|\frac{1}{T_2}+\frac{1\mp 1}{T_1}\right|\right)^{1/2}}\exp\left[j\pi\left[\left(\frac{u^2}{T_2}+\frac{t^2\mp t'^2}{T_1}\right)+\frac{\left(\frac{t\mp t'}{S_1}+\frac{u}{S_2}\right)^2}{\frac{1}{T_2}+\frac{1\mp 1}{T_1}}\right]\right]dtdt'. \qquad (3.70b)$$

For the symmetric case of $P_2 = -P_1$, the value of $T_2 = -T_1$ and $S_2 = -S_1$, then from (3.70b)

$$W_{P_1,P_2}(u) = \int_{-\infty}^{\infty}\int_{-\infty}^{\infty} x(t)y(t')\frac{\exp[-j\pi/4]}{\left(\left|\frac{1}{T_1}\right|\right)^{1/2}}\exp\left[j\pi\left[\left(\frac{-u^2+t^2\mp t'^2}{T_1}\right)\mp T_1\left(\frac{t\mp t'-u}{S_1}\right)^2\right]\right]dtdt'. \qquad (3.70c)$$

Computer Simulation of FrFT domain tapering

The results of FrFT domain tapering of two taper function viz. uniform and Chebyshev are shown in Fig. 3.17.(A)-(C). Both taper functions are taken of 11 elements. The Chebyshev taper is taken with side lobe level of -30 dB. In Fig.3.17.(A) two taper functions are multiplied in a=0 domain. Here multiplying means element by element multiplication. The various gain patterns and beam patterns obtained by forming the array with the weights obtained by taking inverse FrFT of the resultant $z_0(t)$ in various a^{th} domains is shown in Fig.3.17.(A).The spacing between elements is assumed to be 0.5λ, where λ is wavelength of operation. The frequency is assumed to

be 100MHz. Fig.3.17.(A)a verifies the result of tapering in a=0 domain where the beam is formed by using the weights obtained by taking inverse FrFT of $z_0(t)$ in a=0 domain. In Figs.3.17.(A)c-h the beam patterns and gain patterns are obtained by forming the array with the weight function W(t) obtained by taking inverse FrFT of $z_0(t)$ in a=0.1, a=0.2 and a=0.7 domains.

In Fig.3.17.(B) the two taper functions are multiplied in a=0.1 domain. The beam pattern and gain pattern are obtained by forming the array with the weights W(t) obtained by taking inverse FrFT of $z_{0.1}(t)$ in a=0,a=0.1,a=0.2 and a=0.7 domains.

In Fig.3.17.(C) the two taper functions are multiplied in a=0.7 domain. The beam pattern and gain pattern are obtained by forming the array with the weights W(t) obtained by taking inverse FrFT of $z_{0.7}(t)$ in a=-0.1,a=-0.2,a=-0.3 and a=-0.5 domains.

Chebyshev Taper in FrFT domain

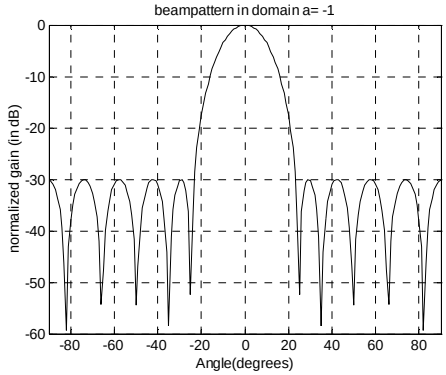

(a) Gain Pattern in domain a=1

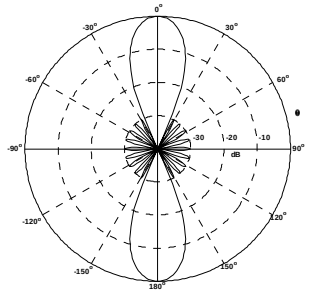

(b) Beam Pattern in domain a=1

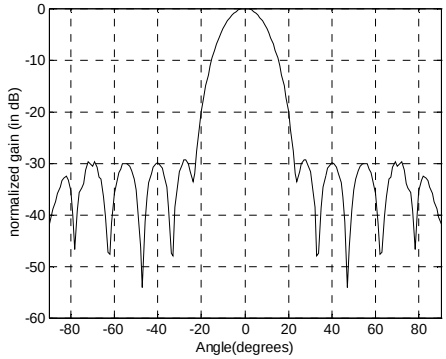

(c) Gain Pattern in domain a=0.8

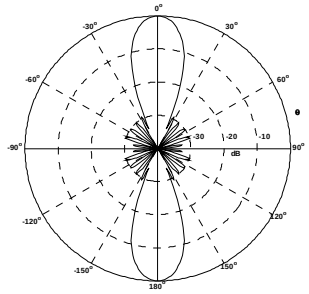

(d) Beam Pattern in domain a=0.8

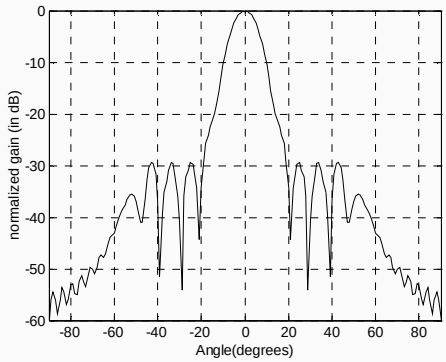

(e) Gain Pattern in domain a=0.4

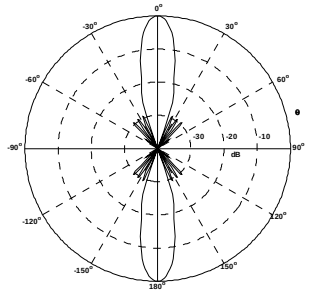

(f) Beam Pattern in domain a=0.4

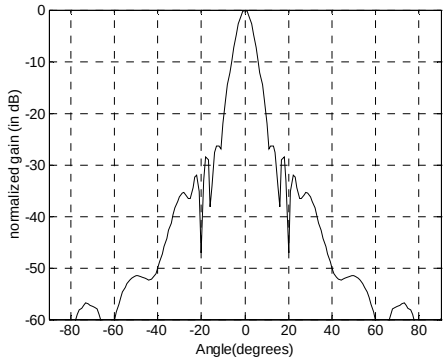

(g) Gain Pattern in domain a=0.2

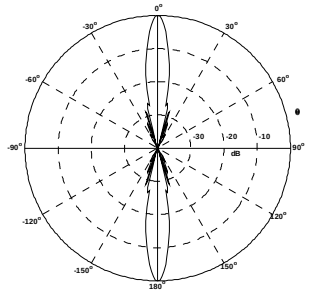

(h) Beam Pattern in domain a=0.2

Figure 3.14- Gain Pattern and Beampattern of Chebyshev taper in various FrFT domains

Taylor-Kaiser Taper in FrFT domain

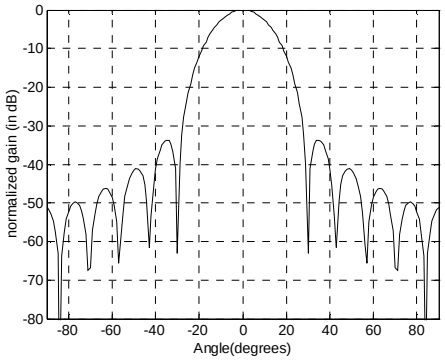

(a) Gain Pattern in domain a=1

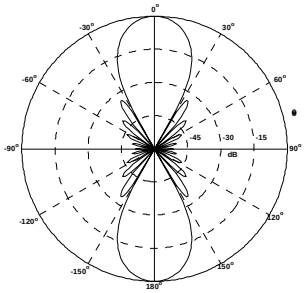

(b) Beam Pattern in domain a=1

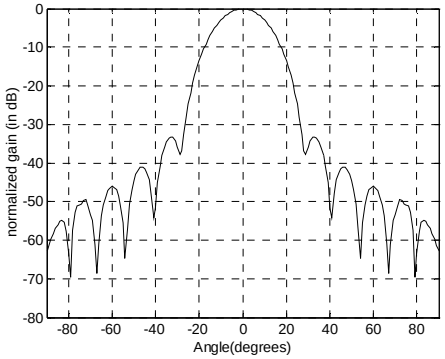

(c) Gain Pattern in domain a=0.8

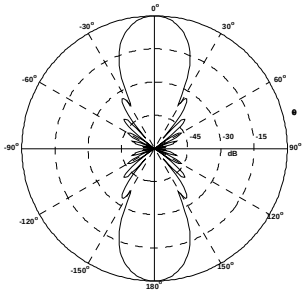

(d) Beam Pattern in domain a=0.8

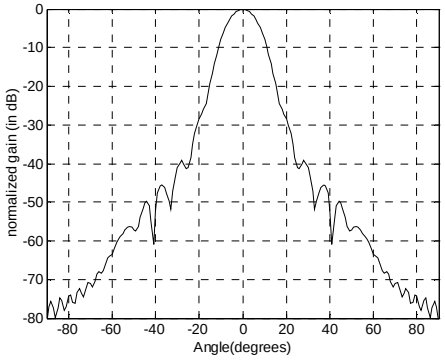

(e) Gain Pattern in domain a=0.4

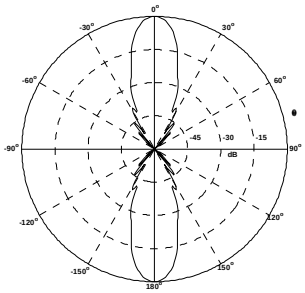

(f) Beam Pattern in domain a=0.4

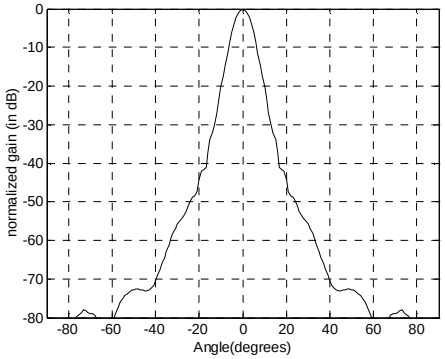

(g) Gain Pattern in domain a=0.2

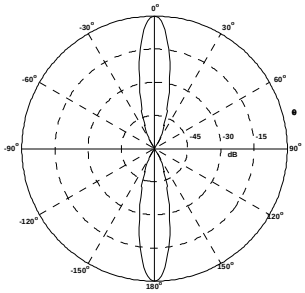

(h) Beam Pattern in domain a=0.2

Figure 3.15- Gain Pattern and Beampattern of Taylor Kaiser Taper in various FrFT domains

Uniform Taper in FrFT domain

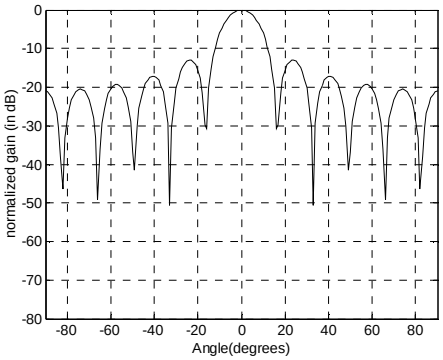

(a) Gain Pattern in domain a=1

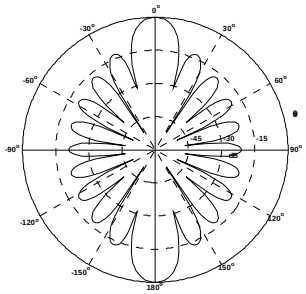

(b) Beam Pattern in domain a=1

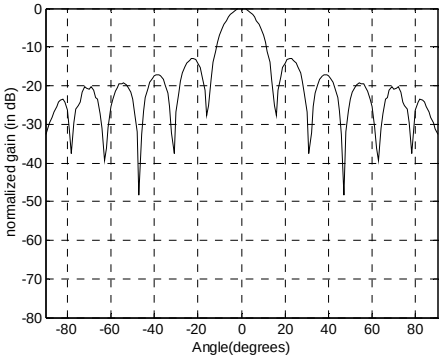

(c) Gain Pattern in domain a=0.8

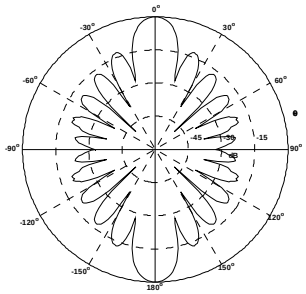

(d) Beam Pattern in domain a=0.8

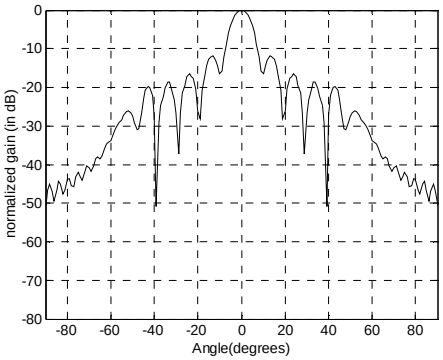

(e) Gain Pattern in domain a=0.4

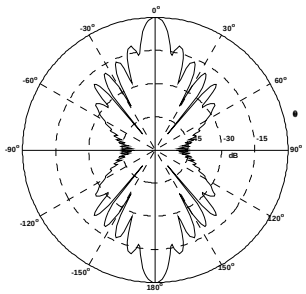

(f) Beam Pattern in domain a=0.4

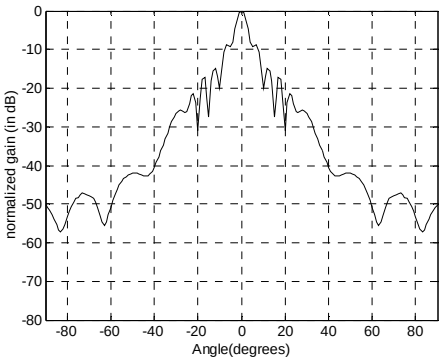

(g) Gain Pattern in domain a=0.2

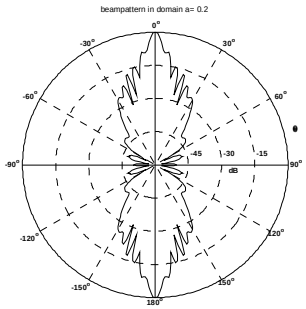

(h) Beam Pattern in domain a=0.2

Figure 3.16- Gain Pattern and Beampattern of Uniform Taper in various FrFT domains

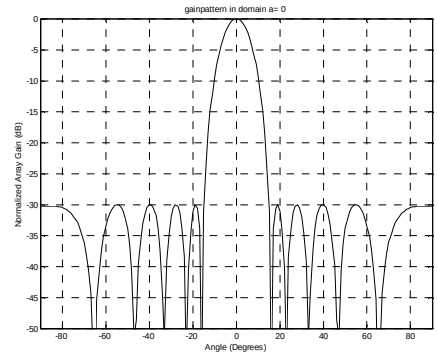

(a) Gain Pattern in domain a=0

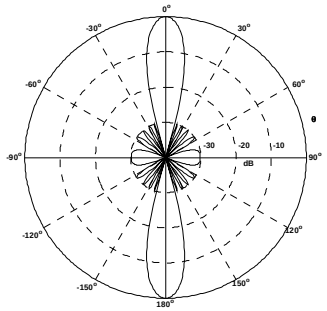

(b) Beam Pattern in domain a=0

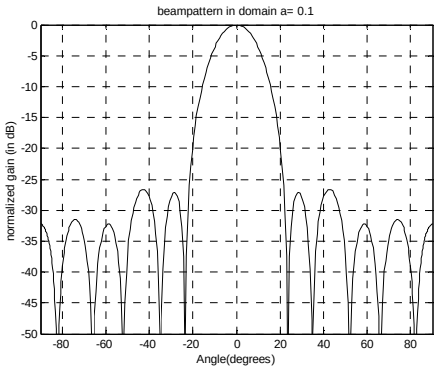

(c) Gain Pattern in domain a=0.1

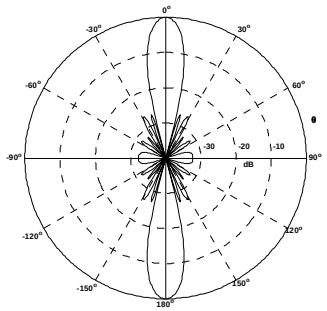

(d) Beam Pattern in domain a=0.1

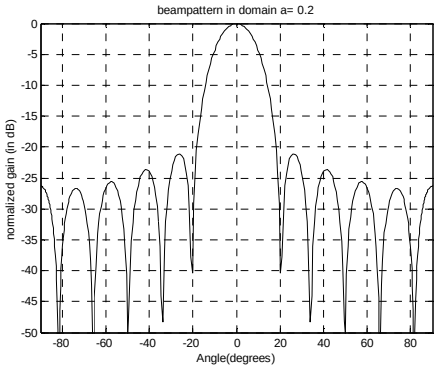

(e) Gain Pattern in domain a=0.2

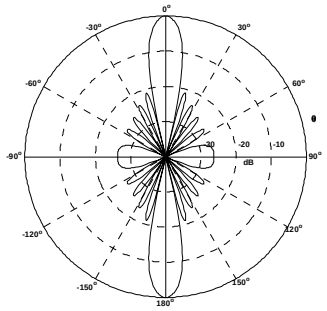

(f) Beam Pattern in domain a=0.2

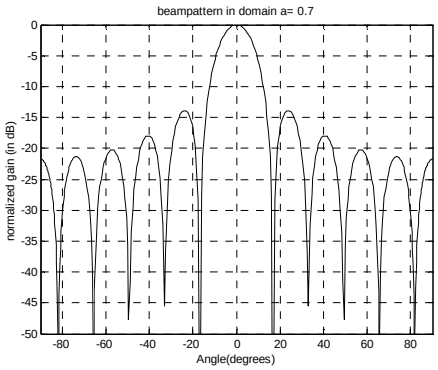

(g) Gain Pattern in domain a=0.7

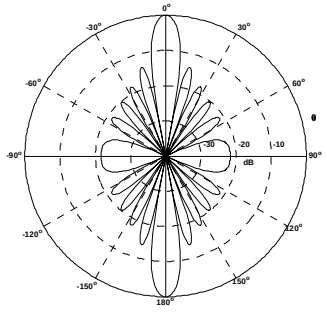

(h) Beam Pattern in domain a=0.7

Figure 3.17.(A)- Gain Pattern and Beampattern of a taper(Generated by multiplying a uniform and Chebyshev taper in 'a'=0 domain) in various FrFT domains

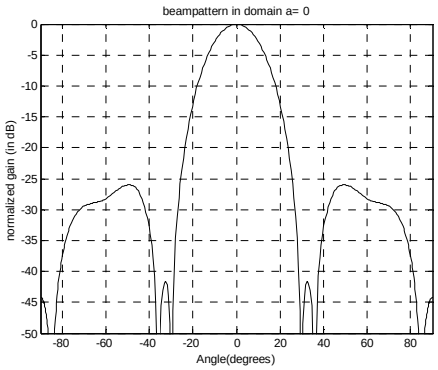

(a) Gain Pattern in domain a=0

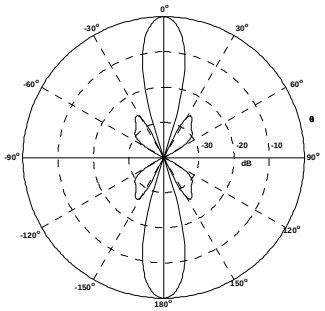

(b) Beam Pattern in domain a=0

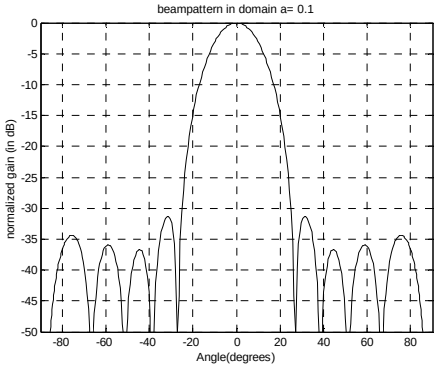

(c) Gain Pattern in domain a=0.1

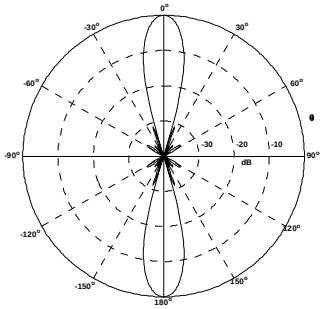

(d) Beam Pattern in domain a=0.1

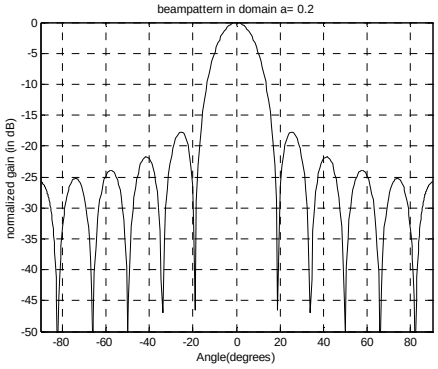

(e) Gain Pattern in domain a=0.2

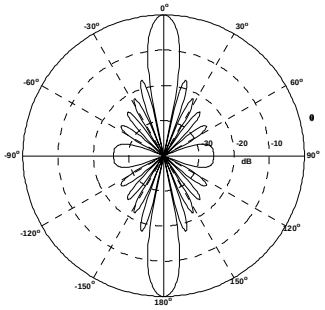

(f) Beam Pattern in domain a=0.2

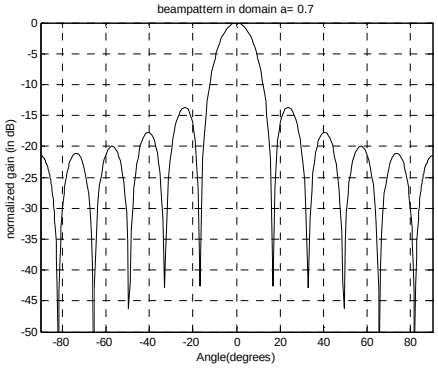

(g) Gain Pattern in domain a=0.7

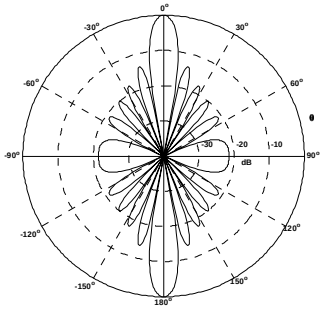

(h) Beam Pattern in domain a=0.7

Figure 3.17.(B) - Gain Pattern and Beampattern of a taper(Generated by multiplying a uniform and Chebyshev taper in 'a'=0.1 domain) in various FrFT domains

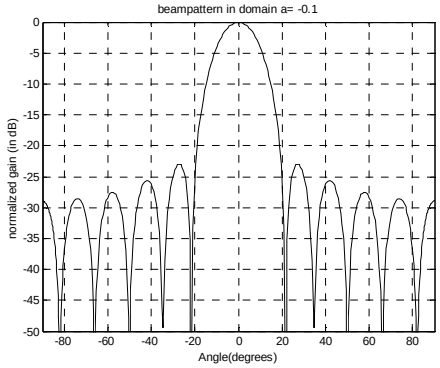

(a) Gain Pattern in domain a=-0.1

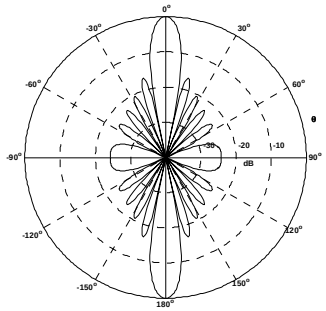

(b) Beam Pattern in domain a=-0.1

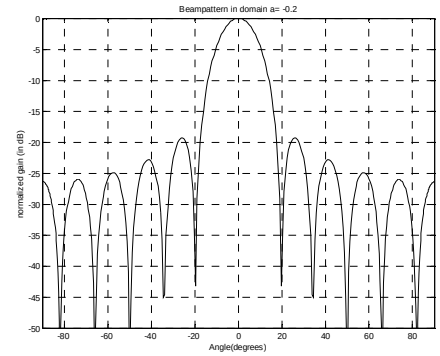

(c) Gain Pattern in domain a=-0.2

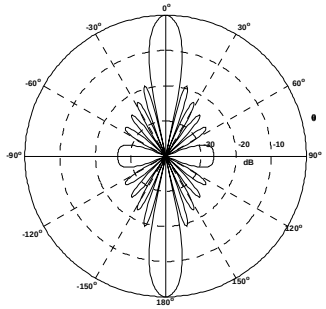

(d) Beam Pattern in domain a=-0.2

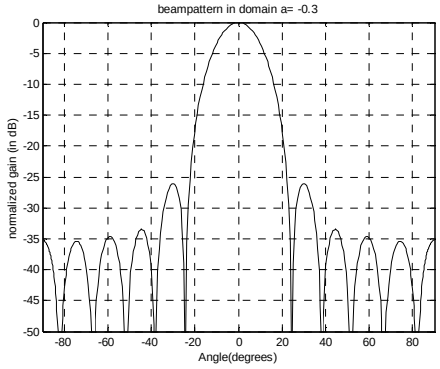

(e) Gain Pattern in domain a=-0.3

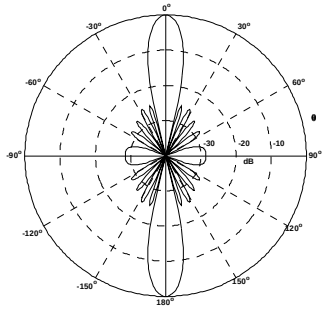

(f) Beam Pattern in domain a=-0.3

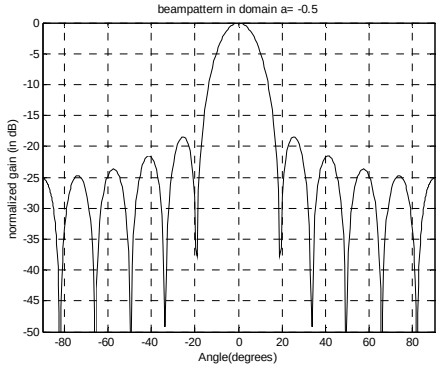

(g) Gain Pattern in domain a=-0.5

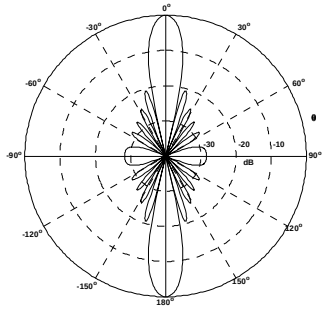

(h) Beam Pattern in domain a=-0.5

Figure 3.17.(C) - Gain Pattern and Beampattern of a taper(Generated by multiplying a uniform and Chebyshev taper in 'a'=0.7 domain) in various FrFT domains

3.6.7 Results and Discussions

The main conclusion form above analysis can be drawn as follows

1. The squared magnitude of the FrFT of a signal called fractional energy spectrum of the signal depends on parameter 'α'. Hence the same signal can have different distributions of energy in different domains[3,4].
2. By varying 'α' one can get different patterns of distribution of energy in space.
3. By change of parameter 'α' the chirp basis function changes but by Parseval's theorem the total energy content of the signal remains same in any domain.
4. For all tapering functions the minimum beamwidth occurs in a=0.1 domain and the beamwidth increases as value of 'a' increases, the maximum beamwidth occurs in a=1 domain. This means as the chirp frequency goes on increasing the energy spread is decreased and energy confines to a narrow beam.
5. The value of Maximum side lobe level (MSLL) is smallest for a=0.1 domain and increases as the value of 'a' increases (In certain tapering functions the value of MSLL was not readable as side lobe was too down).
6. The results of the taper in fraction Fourier domain are tabulated in tables 3.4 & 3.5. The array for comparison is taken to be a linear array with d=λ/2 spacing and with 11 elements.
7. A new procedure for tapering in FrFT domain is defined in section 3.6.6.
8. Simulation results of Fig.3.18 (a) and Fig.3.18 (b) using the procedure defined in 3.6.6 clearly show that the tapering in FrFT domain offers more flexibility as compared to tapering in time domain only. One can generate beampattern with different side lobe topography by varying only a single parameter 'a'.
9. The ratios of maximum to minimum weight (ξ) of W(t) obtained in various FrFT domains are given in table 3.3
10. Table 3.3 shows that the weights W(t) obtained in various FrFT domains are practically realizable weights. The maximum side lobe level in any domain never exceeds that of uniform taper.

---

3. [P8] "Analysis of rectangular and Bartlett windows in fractional Fourier domain using Mathematica 4.1", accepted at *5th* ***International Mathematica Symposium*** held at Imperial college London from 7-11, July 2003

4. [P13] "Rectangular and Triangular line source Amplitude distribution in Fractional Fourier Domain" Proceedings of ***International Radar Symposium, IRSI-2003, Bangalore,*** India, pp.308-314, Dec. 03-05, 2003.

Thus beamforming in FrFT domain provides an efficient way of side lobe control with single parameter ‘a’.

11. It is possible to improve performance of taper by use of the FrFT since the fractional Fourier transform can be computed in about the same time as the ordinary transform and the performance improvements come at no additional cost.
12. The flowchart for tapering in FrFT domain is shown below in Fig.3.18 in wireless environment.

Table: 3.3 Ratio of maximum to minimum weight (ξ)

ξ of W(t) in Domain	Multiplying Rectangular and Chebyshev taper Functions in			
	a = 0 Domain	a=0.1 Domain	a=0.5 Domain	a=0.7 Domain
a=-1	1.1019	1.0819	1.1270	1.2981
a=-0.9	1.1045	1.0858	1.1531	1.4081
a=-0.8	1.1132	1.0945	1.1993	1.5859
a=-0.7	1.1299	1.1112	1.2862	1.7938
a=-0.6	1.1597	1.1405	1.4671	2.0494
a=-0.5	1.2145	1.1913	1.8463	2.5538
a=-0.4	1.3212	1.3132	2.4750	3.2227
a=-0.3	1.5786	1.5990	4.8883	2.9294
a=-0.2	2.3110	2.3309	5.0576	2.0791
a=-0.1	3.8878	2.4168	2.8312	1.5857
a=0	3.9082	10.2631	1.6741	1.3759
a=0.1	3.8878	6.3919	1.3624	1.2739
a=0.2	2.3110	1.8303	1.2271	1.2184
a=0.3	1.5786	1.3626	1.1658	1.1871
a=0.4	1.3212	1.2123	1.1341	1.1701
a=0.5	1.2145	1.1538	1.1198	1.1624
a=0.6	1.1597	1.1147	1.1066	1.1648
a=0.7	1.1299	1.0982	1.1031	1.1752
a=0.8	1.1132	1.0890	1.1048	1.1965
a=0.9	1.1045	1.0829	1.1123	1.2341
a=1.0	1.1019	1.0819	1.1270	1.2981

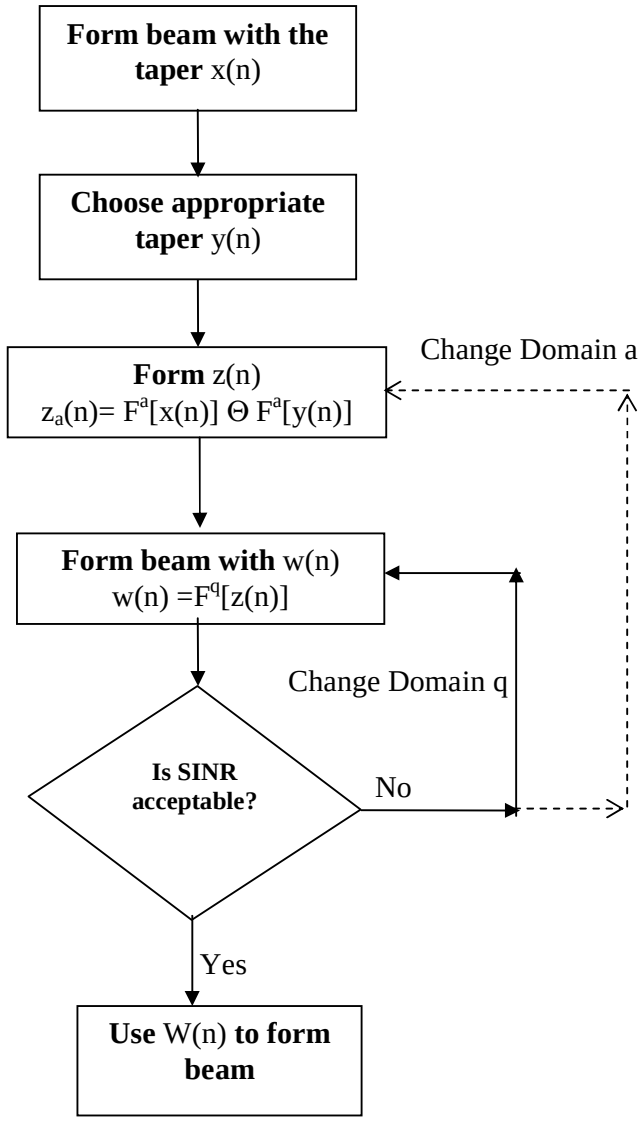

Figure: 3.18 Flow Chart of Beamforming in FrFT Domain

(Dotted line shows that in case the acceptable SINR is not achieved with varying ‘ q’ then vary ‘a’ in $z_a(n)= F^a[x(n)] \Theta F^a[y(n)]$ repeat it for all values of ‘q’)

Table3.4: Comparison of 10 dB down Beam widths of various taper in Fractional Fourier Domains

S. No	FrFT Domain	10dB down Beamwidth(Degrees)													
		Nutall Taper	Chebyshev Taper	Blackman Taper	Blackman Harris Taper	Bohman Taper	Hamming Taper	Taylor-Kaiser Taper	Binomial Taper	Uniform Taper	Gaussian Taper	Hanning Taper	Tukey Taper	Barlett Taper	Triangular Taper
1.	a=0.1	10.34^0	9.12^0	9.48^0	10.42^0	9.46^0	8.86^0	8.92^0	9.68^0	13.00^0	8.92^0	8.08^0	10.00^0	9.18^0	9.20^0
2.	a=0.2	19.14^0	12.00^0	17.00^0	19.40^0	17.32^0	13.90^0	12.90^0	17.32^0	15.40^0	13.82^0	14.70^0	11.20^0	13.62^0	12.60^0
3.	a=0.3	27.14^0	15.60^0	24.30^0	28.20^0	25.04^0	19.22^0	15.52^0	24.94^0	11.76^0	19.04^0	21.00^0	16.16^0	19.00^0	16.440
4.	a=0.4	36.00^0	20.00^0	31.20^0	36.64^0	32.24^0	24.36^0	22.26^0	32.10^0	14.70^0	24.12^0	26.94^0	20.70^0	24.38^0	20.58^0
5.	a=0.5	43.00^0	23.10^0	37.40^0	43.64^0	40.00^0	29.00^0	26.50^0	38.48^0	17.42^0	28.70^0	32.20^0	24.80^0	29.10^0	24.40^0
6.	a=0.6	49.20^0	26.24^0	42.80^0	50.80^0	44.00^0	33.00^0	30.00^0	44.00^0	19.80^0	32.64^0	36.80^0	28.32^0	33.40^0	29.90^0
7.	a=0.7	54.14^0	28.74^0	47.00^0	55.00^0	49.20^0	36.26^0	33.10^0	48.40^0	21.74^0	35.88^0	40.00^0	31.00^0	36.60^0	30.40^0
8.	a=0.8	57.76^0	30.60^0	50.00^0	60.00^0	52.00^0	38.60^0	35.30^0	51.60^0	23.12^0	38.20^0	42.12^0	33.20^0	39.00^0	32.30^0
9.	a=0.9	60.00^0	31.76^0	52.00^0	60.82^0	53.88^0	40.00^0	36.62^0	53.56^0	24.04^0	40.00^0	44.88^0	34.50^0	40.00^0	33.40^0
10.	a=1.0	60.70^0	32.16^0	52.18^0	61.58^0	54.54^0	40.60^0	39.00^0	54.24^0	24.30^0	40.12^0	45.40^0	34.92^0	41.00^0	34.00^0

Table3.5: Comparison of Maximum Side Lobe Level of various taper in Fractional Fourier Domains

S. No	FrFT Domain	Maximum side Lobe Level (dB)													
		Nutall Taper	Chebyshev Taper	Blackman Taper	Blackman Harris Taper	Bohman Taper	Hamming Taper	Taylor-Kaiser Taper	Binomial Taper	Uniform Taper	Gaussian Taper	Hanning Taper	Tukey Taper	Barlett Taper	Triangular Taper
1.	a=0.1	-111.00	-31.26	-	-	-136.59	-41.14	-80.85	-	-	-58.77	-	-66.23	-24.43	-22.70
2.	a=0.2	-102.06	-26.33	-	-	-45.27	-39.16	-72.70	-	-	-57.35	-	-13.48	-24.74	-26.71
3.	a=0.3	-86.85	-28.72	-66.67	-	-45.14	-36.95	-37.36	-	-11.22	-56.27	-40.53	-14.41	-24.66	-25.79
4.	a=0.4	-86.85	-29.33	-61.18	-	-44.97	-35.91	-39.26	-	-11.85	-54.67	-41.63	-14.74	-24.54	-25.33
5.	a=0.5	-86.36	-28.85	-61.78	-	-44.96	-35.63	-40.18	-	-12.45	-53.90	-30.45	-14.94	-24.11	-25.10
6.	a=0.6	-85.71	-26.87	-61.82	-89.73	-44.91	-36.39	-31.49	-	-12.73	-53.77	-31.00	-14.97	-23.91	-25.00
7.	a=0.7	-83.81	-28.49	-61.79	-89.14	-44.91	-36.18	-32.65	-	-12.87	-54.86	-31.33	-15.04	-23.99	-24.92
8.	a=0.8	-82.65	-29.42	-61.68	-88.83	-44.88	-36.23	-33.28	-	-12.98	-54.16	-31.55	-15.06	-24.07	-24.90
9.	a=0.9	-81.69	-29.88	-61.67	-88.72	-44.88	-36.67	-33.61	-	-13.02	-54.76	-31.61	-15.08	-24.08	-24.85
10	a=1.0	-81.28	-30.00	-61.63	-88.96	-44.87	-36.66	-33.72	-	-13.04	-54.72	-31.65	-15.09	-24.09	-24.86

- Indicates that the value is not readable as side lobe is too low.

3.7 TAPERED BEAMFORMING WITH OPTIMUM ARRAY PROCESSING

The beamformers considered above are data independent beamformers as their weights are determined without input data. If the actual beamforming weights are calculated on the basis of the array data, then the result is an adaptive array and the operation is known as adaptive beamforming. Ideally, the beamforming weights are adapted in such a way as to optimize the spatial response of the resulting beamformer based on a certain criterion. The criterion is chosen to enhance the desired signal while rejecting other, unwanted signals. Optimum array processing methods make use of the a priori known statistics of the data to derive the beamforming weights.

3.7.1 Array Signal Model for Optimum Array

Consider the array signal model of (3.39) that contains interference in addition to the desired signal and noise. To derive the optimum beamformer, the optimality criterion is the maximization of the theoretical SINR. Consider an array signal that consists of the desired signal s(n), an interference signal *i*(n), along with noise w(n), that is,

$$\boldsymbol{x}(\mathrm{n}) = \boldsymbol{x}'(\mathrm{n}) + \boldsymbol{i}(\mathrm{n}) + \mathbf{w}(\mathrm{n}) = \sqrt{\mathrm{M}}\boldsymbol{v}(\theta_{\mathrm{s}})\mathrm{s}(\mathrm{n}) + \boldsymbol{i}(\mathrm{n}) + \mathbf{w}(\mathrm{n}) . \quad (3.71)$$

Signal, s(n) is with deterministic amplitude σ_{s} and uniformly distributed random phase. The interference-plus-noise components of the array signal are modeled as zero-mean stochastic processes. The total noise and interference is given by

$$\boldsymbol{x}_{\mathrm{i+n}}(\mathrm{n}) = \boldsymbol{i}(\mathrm{n}) + \mathbf{w}(\mathrm{n}) . \quad (3.72)$$

The interference has spatial correlation according to the angles of the contributing interferers, while the noise is spatially uncorrelated. The interference component of the signal may consist of several sources, as modeled in (3.58). The noise is assumed to be uncorrelated with power σ_{w}^2. The assumption is made that all of these three components are mutually uncorrelated. As a result, the array correlation matrix is

$$\boldsymbol{R}_{\mathrm{x}} = \mathrm{E}[\boldsymbol{x}(\mathrm{n})\boldsymbol{x}^{\mathrm{H}}(\mathrm{n})] = \mathrm{M}\sigma_{\mathrm{s}}^2\boldsymbol{v}(\theta_{\mathrm{s}})\boldsymbol{v}^{\mathrm{H}}(\theta_{\mathrm{s}}) + \boldsymbol{R}_{\mathrm{i}} + \boldsymbol{R}_{\mathrm{n}} , \quad (3.73)$$

where, σ_{s}^2 is the power of the signal of interest and $\boldsymbol{R}_{\mathrm{i}}$ and $\boldsymbol{R}_{\mathrm{n}}$ are the interference and noise correlation matrices, respectively. The interference-plus-noise correlation matrix is the sum of these latter two matrices

$$\boldsymbol{R}_{\mathrm{i+n}} = \boldsymbol{R}_{\mathrm{i}} + \boldsymbol{R}_{\mathrm{n}} = \boldsymbol{R}_{\mathrm{i}} + \sigma_{\mathrm{w}}^2 \boldsymbol{I} \,. \tag{3.74}$$

3.7.2 Optimum Beamforming

The optimization criterion for adaptive beamformer is to maximize SINR. At the input of the array, that is, in each individual sensor, the SINR is given by

$$SINR_{ele} = \frac{\sigma_s^2}{\sigma_i^2 + \sigma_w^2}, \tag{3.75}$$

where, $\sigma_s^2, \sigma_i^2 \,\&\, \sigma_w^2$ are the signal, interference, and noise powers in each of the individual element. The SINR at the beamformer output, following the application of the beamforming weight vector $\boldsymbol{w}$ is

$$\mathrm{SINR}_{\mathrm{out}} = \frac{[\boldsymbol{w}^{\mathrm{H}} \boldsymbol{x}'(\mathrm{n})]^2}{\mathrm{E}\left\{\left|\boldsymbol{w}^{\mathrm{H}} \boldsymbol{x}_{\boldsymbol{i+n}}(\mathrm{n})\right|^2\right\}} = \frac{\mathrm{M}\sigma_{\mathrm{s}}^2 \left|\boldsymbol{w}^{\mathrm{H}} \boldsymbol{v}(\theta_{\mathrm{s}})\right|^2}{\boldsymbol{w}^{\mathrm{H}} \boldsymbol{R}_{\boldsymbol{i+n}}\, \boldsymbol{w}}. \tag{3.76}$$

In order to maximize array output SINR, the interference-plus-noise correlation matrix is factored as

$$\boldsymbol{R}_{\mathrm{i+n}} = \boldsymbol{L}_{\boldsymbol{i+n}} \boldsymbol{L}_{\mathrm{i+n}}^{\mathrm{H}}, \tag{3.77}$$

where, $\boldsymbol{L}_{i+n}$ is the Cholesky factor of the correlation matrix

$$\bar{\boldsymbol{w}} = \boldsymbol{L}_{\mathrm{i+n}}^{\mathrm{H}} \boldsymbol{w} \qquad \bar{\boldsymbol{v}}(\theta_{\mathrm{s}}) = \boldsymbol{L}_{\mathrm{i+n}}^{-1} \boldsymbol{v}(\theta_{\mathrm{s}}). \tag{3.78}$$

$$\mathrm{SINR}_{\mathrm{out}} = \frac{\mathrm{M}\sigma_{\mathrm{s}}^2 \left|\bar{\boldsymbol{w}}^{\mathrm{H}} \bar{\boldsymbol{v}}(\theta_{\mathrm{s}})\right|^2}{\bar{\boldsymbol{w}}^{\mathrm{H}} \bar{\boldsymbol{w}}}. \tag{3.79}$$

Using the Schwartz inequality

$$\bar{\boldsymbol{w}}^{\mathrm{H}} \bar{\boldsymbol{v}}(\theta_{\mathrm{s}}) \le \left\|\bar{\boldsymbol{w}}\right\| \left\|\bar{\boldsymbol{v}}(\theta_{\mathrm{s}})\right\|, \tag{3.80}$$

$$\mathrm{SINR}_{\mathrm{out}} \le \mathrm{M}\sigma_{\mathrm{s}}^2 \frac{\left\|\bar{\boldsymbol{w}}\right\|^2 \left\|\bar{\boldsymbol{v}}(\theta_{\mathrm{s}})\right\|^2}{\left\|\bar{\boldsymbol{w}}\right\|^2} = \mathrm{M}\sigma_{\mathrm{s}}^2 \left\|\bar{\boldsymbol{v}}(\theta_{\mathrm{s}})\right\|^2. \tag{3.81}$$

Thus, the maximum SINR is found by satisfying the upper bound for (3.81), which yields

$$\mathrm{SINR}_{\mathrm{out}}^{\max} = \mathrm{M}\sigma_{\mathrm{s}}^2 [\bar{\boldsymbol{v}}(\theta_{\mathrm{s}}) \boldsymbol{R}_{\mathrm{i+n}}^{-1} \boldsymbol{v}(\theta_{\mathrm{s}})]. \tag{3.82}$$

The maximum SINR is obtained if $\bar{\boldsymbol{w}} = \alpha\, \bar{\boldsymbol{v}}(\theta_{\mathrm{s}})$, where '$\alpha$' is an arbitrary constant. In other words, the SINR is maximized when these two vectors are parallel to each other and α can be chosen to satisfy other requirements. Therefore using (3.78), optimum weight vector can be found [32]

$$\boldsymbol{w}_0 = \alpha \boldsymbol{L}_{\mathrm{i+n}}^{-\mathrm{H}} \bar{\boldsymbol{v}}(\theta_{\mathrm{s}}) = \alpha \boldsymbol{R}_{\mathrm{i+n}}^{-1} \boldsymbol{v}(\theta_{\mathrm{s}}). \tag{3.83}$$

Thus, the optimum beamforming weights are proportional to $\boldsymbol{R}_{\mathrm{i+n}}^{-1}\boldsymbol{v}(\theta_s)$. The optimum beamformer is normalized to have unity gain in the look direction, i.e. $\boldsymbol{w}_0^{\mathrm{H}}\boldsymbol{v}(\theta_s)=1$.Therefore,

$$\boldsymbol{w}_0^{\mathrm{H}}\boldsymbol{v}(\theta_s)=\alpha[\boldsymbol{R}_{\mathrm{i+n}}^{-1}\boldsymbol{v}(\theta_s)]^{\mathrm{H}}\boldsymbol{v}(\theta_s)=1, \tag{3.84}$$

and the resulting optimum beamformer is given by

$$\boldsymbol{w}_0=\frac{\boldsymbol{R}_{\mathrm{i+n}}^{-1}\boldsymbol{v}(\theta_s)}{\boldsymbol{v}^{\mathrm{H}}(\theta_s)\boldsymbol{R}_{\mathrm{i+n}}^{-1}\boldsymbol{v}(\theta_s)}. \tag{3.85}$$

Alternately, the optimum beamformer can be derived by solving the following constrained optimization problem: Minimize the total power at the beamformer output

$$\mathrm{P}=\mathrm{E}\left\{\left|\boldsymbol{w}^{\mathrm{H}}\boldsymbol{x}(\mathrm{n})\right|^2\right\}=\boldsymbol{w}^{\mathrm{H}}\boldsymbol{R}_{\mathrm{x}}\boldsymbol{w}\ , \tag{3.86}$$

subject to a look-direction distortion less response constraint, i.e.

$$\min \mathrm{P} \qquad \text{subject to } \boldsymbol{w}^{\mathrm{H}}\boldsymbol{v}(\theta_s)=1.$$

The solution of this constrained optimization problem is found by using Lagrange multipliers and results in the same weight vector as (3.85), with $\boldsymbol{R}_{\mathrm{i+n}}$ being replaced by $\boldsymbol{R}_x$, as the available data is $\boldsymbol{x}$(n). Thus the resulting optimum weight vector is given by

$$\hat{\boldsymbol{w}}_0=\frac{\boldsymbol{R}_{\mathrm{x}}^{-1}\boldsymbol{v}(\theta_s)}{\boldsymbol{v}^{\mathrm{H}}(\theta_s)\boldsymbol{R}_{\mathrm{x}}^{-1}\boldsymbol{v}(\theta_s)}\ . \tag{3.87}$$

The optimum weight vectors found by using $\boldsymbol{R}_x$ and $\boldsymbol{R}_{i+n}$ are identical i.e. $\boldsymbol{w}_0=\hat{\boldsymbol{w}}_0$. The proof of $\boldsymbol{w}_0=\hat{\boldsymbol{w}}_0$ is given in Appendix C.

The optimum beamformer passes signals impinging on the array from angle θ_s while rejecting interference from all other angles. This beamformer can be thought of as an optimum spatial matched filter since it provides maximum interference rejection, while matching the response of signals impinging on the array from a direction θ_s. This advantage is best illustrated by using the beampattern of an optimum beamformer with an interferer at $\theta_1=20^0$ in Fig.3.19.

The side-lobes of the beamformer are still at the same levels as the spatial matched filter (non-adaptive beamformer) from (3.60), although with a different structure. Thus a desired signal at any angle θ_1 may be easily found by using an adaptive beamformer directed to angle $\theta_s=\theta_1$ assuming the signal strength after beamforming is significantly larger than the noise.

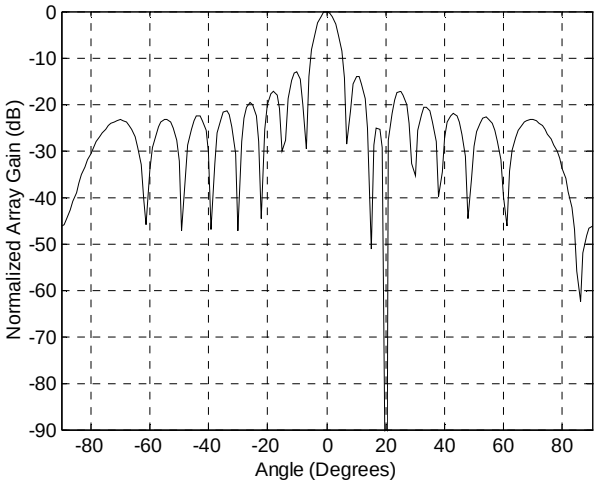

Figure 3.19-Optimum beamformer (no taper)

3.7.3 Tapered Optimum Beamforming

In the above example, if another interferering signal is present at $\theta_2 = -20^0$ that was not part of the interference (not accounted for in the interference correlation matrix), the gain of the optimum beamformer at $\theta_2 = -20^0$ is approximately –20 dB. If the strength of this signal is significantly greater than 20 dB, the optimum beamformer steered to $\theta_s = 0^0$ will pass this sidelobe signal with sufficient strength and it may be erroneously concluded that a signal is present at $\theta_s = 0^0$. The sidelobe signal problem described above can be cured, at least partially, by reducing the sidelobe levels of the beamformer to levels that sufficiently reject these side lobe signals. As described earlier, the application of a taper to a spatial matched filter resulted in a low sidelobe beampattern. The same principle is applied to the optimum beamformer. A tapered array response vector at an angle θ_s is defined as

$$\boldsymbol{v}_t(\theta_s) = \mathbf{c}_{tbf}(\theta_s) = \boldsymbol{t}\,\Theta\mathbf{c}_{mf}(\theta_s), \tag{3.88}$$

where, $\boldsymbol{t}$ is the tapering vector. The tapering vector is normalized such that $\mathbf{c}_{tbf}^{H}(\theta_s)\mathbf{c}_{tbf}(\theta_s) = 1$ as in (3.63). The resulting low sidelobe adaptive beamformer is given by substituting in $\boldsymbol{v}_t(\theta_s)$ for $\boldsymbol{v}(\theta_s)$ in (3.87)

$$\mathbf{c}_{to} = \frac{\boldsymbol{R}_x^{-1}\boldsymbol{v}_t(\theta_s)}{\boldsymbol{v}_t(\theta_s)\boldsymbol{R}_x^{-1}\boldsymbol{v}_t(\theta_s)}. \tag{3.89}$$

The Dolph-Chebyshev taper is again used because this choice of taper provides a uniform sidelobe level. Consider the optimum beamformer with an interferer at $\theta_2 = 20^0$ from Fig.3.19 with a potential signal leaking through the sidelobe at $\theta_1 = -20^0$. If

a tapered optimum beamformer from (3.89) with a -30dB sidelobe taper is used, a potential signal at $\theta_1 = -20^0$ receives a -30dB level of attenuation. Fig.3.20 shows the beampattern of this tapered optimum beamformer. The sidelobe levels are significantly reduced while the null on the interferer at $\theta=20^0$ has been maintained. The adaptive beamformer given by (3.89) is no longer optimal in any sense, unless the desired signal to be spatially matched to $\boldsymbol{v}_t(\theta_s)$. However, the resulting adaptive beamformer still provides rejection of unwanted interferers via spatial nulling through the use of $\boldsymbol{R}_x^{-1}$ in (3.89). In addition, the low sidelobe levels of the beampattern reject signals not contained in the interference that are present at angles other than the angle of look θ_s.

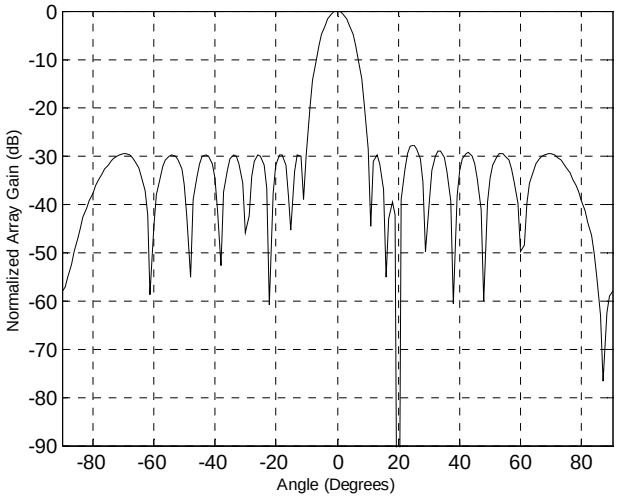

Figure 3.20-Beam pattern of tapered optimum beamformer

The penalty to be paid for the robustness provided by these low sidelobes is a small tapering loss in the direction of the look θ_s, given by (3.90) and a widening of the main lobe beamwidth, as can be seen in the beampattern in Fig.3.21. This tapering loss indicates a mismatch between the true signal and the constraint in the optimum beamformer and is given by

$$L_{taper} = \left|\boldsymbol{c}_{to}^H \boldsymbol{v}(\theta_s)\right|^2 = \left|\frac{\boldsymbol{v}_t^H(\theta_s)\boldsymbol{R}_x^{-1}\boldsymbol{v}(\theta_s)}{\boldsymbol{v}_t^H(\theta_s)\boldsymbol{R}_x^{-1}\boldsymbol{v}_t(\theta_s)}\right|^2 = \frac{\left|\boldsymbol{v}^H(\theta_s)\boldsymbol{R}_x^{-1}\boldsymbol{v}_t(\theta_s)\right|^2}{\boldsymbol{v}_t^H(\theta_s)\boldsymbol{R}_x^{-2}\boldsymbol{v}_t(\theta_s)} \quad . \tag{3.90}$$

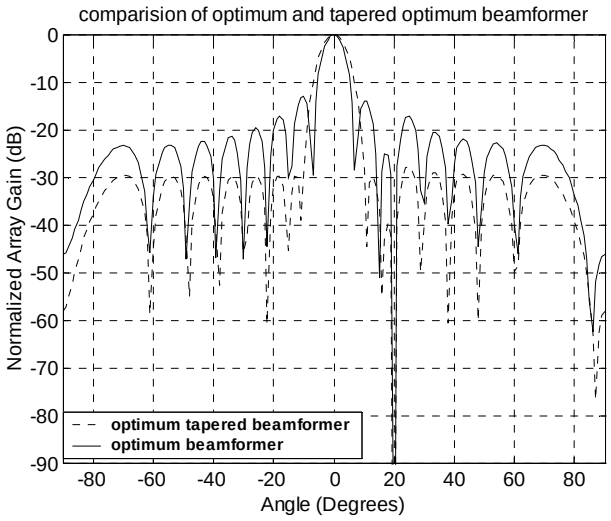

Figure 3.21-Beamppatern of an optimum and a tapered beamformer. Solid line is the optimum beamformer and dashed line is for tapered optimum beamformer.

3.7.4 FrFT based Tapered Optimum Beamforming

The optimum tapered beamformer can be obtained by using FrFT taper also. By replacing $\boldsymbol{t}$ by $\boldsymbol{t}_a$ (taper obtained in FrFT domain as described in section 3.6.6) in (3.88) the optimum tapering can be done in FrFT domain also. (3.88) can be written as $\boldsymbol{v}_{\text{ta}}(\theta_{\text{s}}) = c^{a}{}_{\text{tbf}}(\theta_{\text{s}}) = \boldsymbol{t}_{a} \Theta c_{\text{mf}}(\theta_{\text{s}})$. The FrFT based tapering vector is normalized such that $(c^{\text{a}}_{\text{tbf}})^{\text{H}}(\theta_{\text{s}}) c^{\text{a}}_{\text{tbf}}(\theta_{\text{s}}) = 1$ as in (3.63). The resulting low sidelobe adaptive beamformer is given by substituting in $\boldsymbol{v}_{\text{ta}}(\theta_{\text{s}})$ for $\boldsymbol{v}_{t}(\theta_{\text{s}})$ in (3.89) $c^{a}_{to} = \dfrac{\boldsymbol{R}_{\text{x}}^{-1}\boldsymbol{v}_{\text{ta}}(\theta_{\text{s}})}{\boldsymbol{v}_{\text{ta}}(\theta_{\text{s}})\boldsymbol{R}_{\text{x}}^{-1}\boldsymbol{v}_{\text{ta}}(\theta_{\text{s}})}$. The results of using FrFT taper with optimum array processing (generated by multiplying a uniform and Chebyshev taper in a=0.7 domain) are shown in Fig.3.21.(A). The number of elements in array is taken as 11. From figure 3.21(A) it is observed that FrFT taper provides more flexibility in tapering with optimum array processing also. The null in all cases is maintained at 20^0, while side lobe level is changing in each domain, thus the interferer at -20^0 shall receive attenuation depending upon FrFT taper chosen in a^{th} domain. From above examples, one issue is clear that in CDMA based wireless communication systems the tapered beamformers can control the large amount of interference. Moreover the FrFT taper, which is a more flexible taper as compared to fixed taper and can be applied to both adaptive as well as non adaptive beamformer, gives more flexibility to antenna designer. The increase in information capacity by use of tapered beamformer is found next.

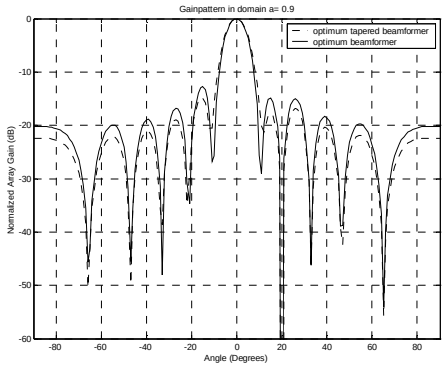

(a) Gain Pattern in domain a=0.9

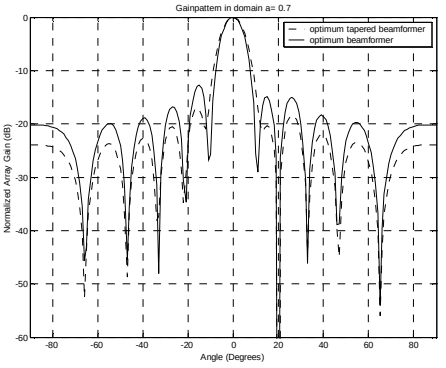

(b) Gain Pattern in domain a=0.7

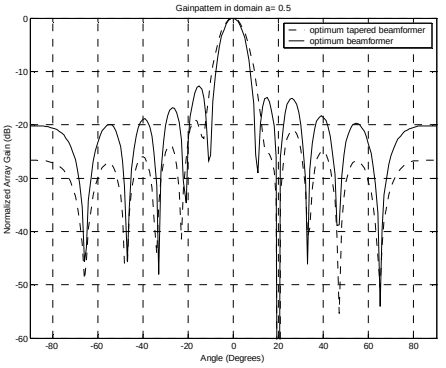

(c) Gain Pattern in domain a=0.5

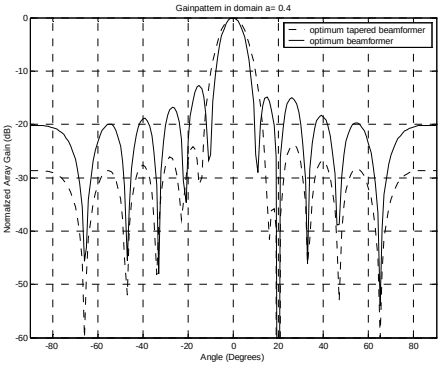

(g) Gain Pattern in domain a=0.4

Figure 3.21.(A) - Gain Pattern of FrFT taper with optimum array processing (Generated by multiplying a uniform and Chebyshev taper in 'a'=0.7 domain) in various FrFT domains

3.8 INFORMATION CAPACITY IMPROVEMENT USING TAPERED BEAMFORMING

Future wireless communications system will support a high level of user traffic along with a wide range of high quality services that not only include high quality voice but also data, facsimile, still pictures and video. The increase in information capacity required for such use is around three to four orders of magnitude. The spatial filtering using antenna arrays can increase information capacity. Various papers have been published reporting capacity improvements via spatial filtering techniques [4, 49, 117, 139, 169]. Some of the results of these studies are based on practical systems. The information capacity of CDMA systems depends upon the amount of interference rejection. The low side-lobe formation is suggested as a solution for rejection of large number of interferers present in the system. The advantage of the proposed technique in improving information capacity has to be investigated further. In this thesis an analytical approach is used to derive a relationship between information capacity and the array beam pattern.

Consider the uniformly spaced array of sensors as shown in Fig.3.2. Let the array have an even number of 2M sensors, each a distance, d, from its neighbours. The beamformer response is given by (3.30)

$$c(\theta) = \sum_{i=1}^{2M} w_i^* \exp[-j\frac{2\pi}{\lambda}(i-1)d\sin\theta]. \tag{3.91}$$

The beampattern or power gain is given by

$$\left|c(\theta)\right|^2 = \left|\sum_{i=1}^{2M} w_i^* \exp[-j\frac{2\pi}{\lambda}(i-1)d\sin\theta]\right|^2. \tag{3.92}$$

The gain function can also be written as

$$\left|c(u)\right|^2 = \left|\sum_{i=1}^{2M} w_i^* \exp[-j(i-1)u]\right|^2, \tag{3.93}$$

where, $u = \frac{2\pi}{\lambda} d\sin\theta$.

A typical array power gain function over the range of angles from -90^0 to 90^0 for uniform linear array with $w_i = 1 \; \forall i$ is shown in Fig.3.6. The beam pattern function for uniform linear array is given by,

$$|c(u)|^2 = \left|\frac{\sin(2Mu)}{\sin(u)}\right|^2 . \tag{3.94}$$

3.8.1 Information Capacity for One User

The power gain can be characterized as a function of the angle of arrival,θ, of a signal. Let the angle, θ_{max}, of the apex of the sensor array's main beam be set to be coincident with the direction of arrival of the desired user's signal and the power gain of signals arriving from this direction be $P_{\theta max}$. Consider the case of one interfering user with received interfering signal power identical to that of the desired user as in the case of CDMA. Let the interfering user's signal be arriving from a direction θ. The information capacity of the desired user given by well known Shannon formula is,

$$C[\theta] = B\log_2(1+\frac{P_{\theta\max}}{P(\theta)+\sigma^2}) \text{ bits/sec}, \tag{3.95}$$

where, σ^2 is the noise power. Fig. 3.22 shows the variation of capacity, $C[\theta]$ with the direction of arrival,θ, of the interfering user's signal. To obtain this graph, because it is the relative values rather than the absolute values that are of interest here, the bandwidth, B, is set to unity and the power gain function is normalized such that the maximum power gain, $P_{\theta max}$, is also 1. The signal-to-noise power ratio (SNR = $P_{\theta max}$ /σ^2) is set to 100 and the number of array sensors used is 16. Fig. 3.22 shows the inverse relationship between capacity and beampattern.

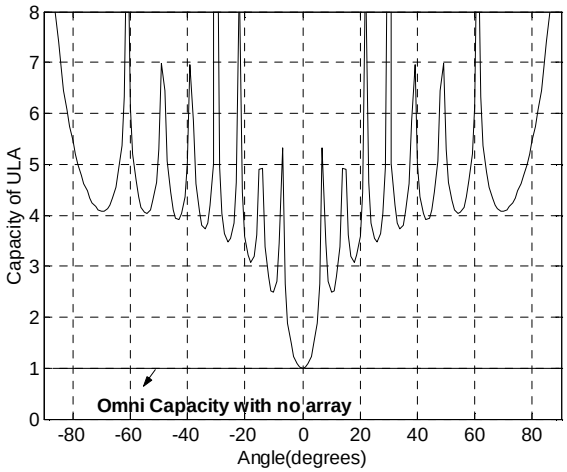

Figure 3.22-Capacity function plot with one interfering user.

3.8.2 Analysis of Information Capacity with One Interfering User

To analyze the information capacity two cases are considered. In first case the angle of arrival of the interfering user's signal is coincident with a *null* (zero power gain) in the beam pattern. That is, the effective power of the interfering user's signal is zero. Let the capacity in this case be $C_{\theta null}$ given by,

$$C_{\theta null} = B\log_2(1+\frac{P_{\theta \max}}{\sigma^2}) = B\log_2(1+SNR)\,. \tag{3.96}$$

This is equivalent to the case where there is no interfering user. Fig. 3.22 shows the level of the capacity when there is no interfering user. The second special case is when the angle of arrival of the interfering user coincides with that of the desired user. That is, the power gain of the interfering user's signal is also $P_{\theta max}$. The capacity in this case is given by,

$$C_{\theta \max} = B\log_2(1+\frac{P_{\theta \max}}{P_{\theta \max}+\sigma^2}) = B\log_2(1+\frac{1}{1+\frac{1}{SNR}})\,. \tag{3.97}$$

The capacity is independent of angle of arrival θ. This is equivalent to the case when there is only one sensor (no array) as shown in Fig.3.22 by a straight line. It can be seen that it coincides with the capacity function in only one place and is, in fact, the minimum value achieved by the capacity function, in the presence of one interferer. To find exactly where maximum and minimum capacity points occur:

$$\frac{dC}{d\theta} = \frac{dC}{dP}\cdot\frac{dP}{d\theta}\,. \tag{3.98}$$

Now, from (3.95) it can be seen that the capacity is a monotonically decreasing function of P(θ). Thus, dC/dP is always negative and never 0. Thus, from (3.95), the capacity can only have maxima and minima at the same angles as the power gain function or beam pattern. Because dC/dP is always negative, (3.95) also indicates that the maxima in the capacity function coincide with the minima in the beam pattern and the minima in the capacity function coincide with the maxima in the beam pattern. Let the gain in all directions except desired direction is higher than noise power but less than maximum gain, then the power function can be expressed in decibels (dB) via (3.99). The maximum power gain, $P_{\theta max}$ is taken as 1. Fig 3.23 shows plots of the capacity function and the approximation, given by (3.98).

$$C[\theta] \approx \frac{B}{\log 2} \log_{10}\left[\frac{1}{P(\theta)}\right]. \tag{3.99}$$

In Fig.3.23 it can be seen that the approximation fits very well at the first sidelobe and for most of the largest lobe of the capacity function. The smaller negative pointing lobes in the capacity function have the same widths as the sidelobes in the beam pattern.

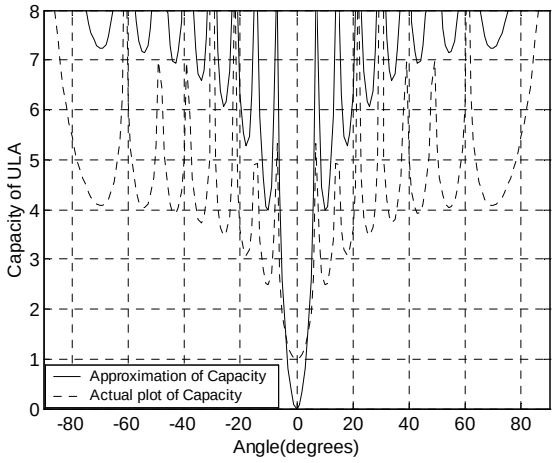

Figure 3.23-Approximate Capacity in Presence of One Interferer for ULA

Equation (3.99) shows that the magnitude of the capacity function is inversely proportional to the magnitude of the beam pattern. The smaller negative pointing lobes of the capacity function indicate the effect on capacity as the direction of arrival of the interfering user's signal moves through the sidelobes of the beam pattern. To have a minimum drop in capacity as the interfering user moves through the sidelobes, the maximum sidelobe level should be as low as possible. As noted earlier that the extrema of the capacity and power functions are coincident, but opposite. It is relatively straightforward to conclude that the large negative pointing lobe in the capacity function corresponds to the main lobe in the beam pattern. Thus, the large negative pointing lobe in the capacity function is identical in width to the main beam of the beam pattern. The large negative pointing lobe indicates the drastic drop in capacity which occurs when the direction of arrival of the interfering user's signal approaches the direction of arrival of the desired user's signal within the main beam of the beam.

3.8.3 Capacity with Multiple Interfering Users in Case of CDMA

Let the number of interfering users be K with directions of arrival of the signals of all of the interfering users coinciding with nulls in the beam pattern. The capacity in

this case is given by, (3.96) independent of the number of interfering users. If the directions of arrival of the signals of all of the interfering users coincide with the main beam of the beam pattern, i.e., $P(\theta_k) = P_{\theta max}$ {k = 1…….K}. The capacity in this case is given by,

$$C_{K\theta max} = B\log_2(1+\frac{P_{\theta max}}{KP_{\theta max}+\sigma^2}). \quad (3.100)$$

It is evident from (3.96) & (3.100) that the capacity in CDMA systems will be maximum, when all interfering users coincide with nulls in beampattern which is not possible due to large number of uniformly distributed users in CDMA systems. Hence as suggested earlier in section 3.2 in CDMA system the interference can be reduced by depressing side lobes and thereby increasing capacity of the CDMA systems.

3.8.4 Significance of the Main Beam to Maximum Side lobe Ratio

Let the angles of arrival of the signals of all of the interfering users coincide with one of the maximum level sidelobe. Let the power gain at these points be $P_{\theta SL}$. And let $\tau = P_{\theta max}/P_{\theta SL}$ be the ratio of the main beam to the maximum sidelobe level. The capacity in this case is given by,

$$C_{K\theta SL} = B\log_2(1+\frac{P_{\theta max}}{KP_{\theta SL}+\sigma^2}) = B\log_2(1+\frac{1}{K\frac{P_{\theta SL}}{P_{\theta max}}+\frac{\sigma^2}{P_{\theta max}}}) = B\log_2(1+\frac{1}{\frac{K}{\tau}+\frac{1}{SNR}}), \quad (3.101)$$

where, $$\frac{1}{\tau} = \frac{P_{\theta SL}}{P_{\theta max}} = SideLobeLevel \ . \quad (3.102)$$

Comparing (3.101) and (3.95), shows that the capacity will be maximum when K=τ, and τ is given by the maximum number of interfering users in the system. Hence in case of multiple interfering users the side lobe level is defined by the number of interfering users. Specifically (3.101) indicates that the level of degradation of the capacity in the presence of multiple interferers is directly related to the ratios of the sidelobes levels to the main beam, when interferers are outside of the main beam. (3.102) is a useful design tool in choosing a beamforming algorithm for CDMA systems. Thus any beam forming algorithm that can reduce the maximum side lobe level will directly translate into an increase in capacity.

An array with Chebyshev weights is known to give the lowest maximum sidelobe level for a given main beam width, such an array can control interference in CDMA systems [28]. Figs. 3.24 and 3.25 illustrate comparisons between the power gain and capacity functions, respectively, achieved using Chebyshev and Uniform sensor weights. With identical main beam widths, the Chebyshev weights afford a lower maximum sidelobe level than the uniform weights. This translates to a higher minimum capacity level in the presence of multiple interfering users.

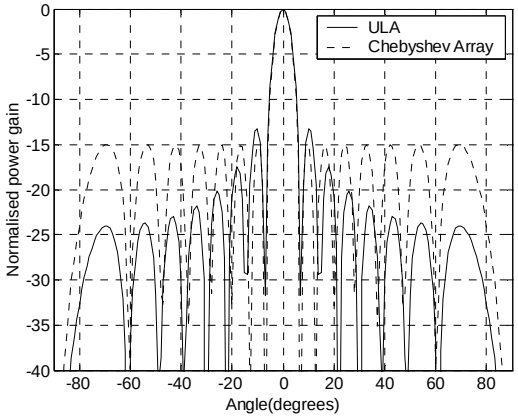

Figure 3.24-Normalized power pattern for ULA & Chebyshev array

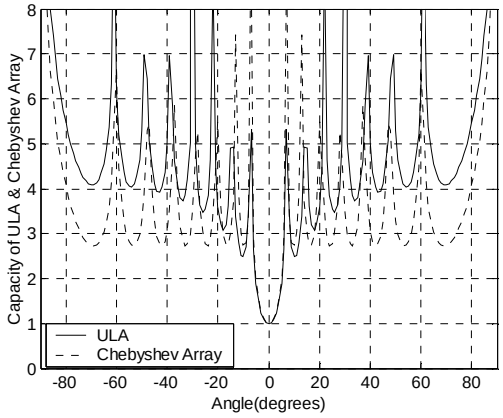

Figure 3.25-Capacity comparison of ULA and Chebyshev array

3.8.5 Results and Discussions

Based on above discussion the following points can be considered in CDMA systems

1. The capacity function has a one-to-one relationship with the beam pattern and its salient features are directly related to those in the beam pattern.
2. The maximum possible capacity occurs when there are no interfering users. This is equivalent to the case when the angles of arrival of all interfering users coincide with nulls in the beam pattern, assuming perfect nulls.
3. The minimum capacity occurs when there is no array, i.e. the sensor is omni directional. This is equivalent to the case when the angles of arrival of all interfering users coincide with the apex of the main beam in the beam pattern.
4. To have a minimum drop in capacity as the angles of arrival of any interfering users move through the sidelobes, the maximum sidelobe level must be as low as possible[5].

---

5. [P21] "Interference rejection in WCDMA systems using tapered beamformers", Proceedings of IE(E) on CDMA Technology: Advanced wireless services for today and tomorrow, N.Delhi,pp.85-90, April 2-3, 2004

5. Any array processing algorithm which can decrease the maximum side lobe level equivalent to Chebyshev will definitely improve the capacity of CDMA system, where number of interferes are quite large. The tapering can also increase the information capacity of CDMA based system.
6. Any such algorithm should have adjustable low side-lobe level and beamwidth with steerable main-lobe. It should be capable of forming broad low side-lobe level towards interferering sources having large angular spreads.

A new beamforming algorithm capable of obtaining a Chebyshev pattern with minimum equal side lobe level for a given main lobe beam-width and vice versa is presented next.

3.9 NEW ARRAY PROCESSING ALGORITHM FOR SYNTHESIZING CHEBYSHEV-LIKE LOW SIDE LOBE BEAM PATTERNS WITH ADJUSTABLE BEAMWIDTH AND STEERING-INVARIANCE

This beamforming algorithm based on linear arrays is formulated as the problem of "finding an array weight vector such that the array output power in the side lobe is minimized subject to Multiple Beam Constraint (MBC)". By constructing a steering matrix with each column vector corresponding to the steering vector of a selected sidelobe and a constraint vector with each entry equal to the gain of a selected lobe, an array beamformer can be designed with multiple-beam constraints. Based on multiple constraints, the optimum weight vector is calculated till corresponding side lobe level is achieved. This is a flexible and computationally efficient algorithm that can provide any desired antenna patterns. This pattern synthesis procedure can even be applied to antenna arrays with non-isotropic elements with arbitrary spacing and any initial current distribution. The major advantage of this algorithm is its simplicity and robustness in adapting to the need. To derive this algorithm consider 2N+1 isotropic element linear array with a uniform spacing, non-uniform amplitude and progressive phase excitation. According to Schelkunoff [40], the field due to this antenna array could be represented in a polynomial form as

$$f(u)= \sum_{n=-N}^{N} w_n^* e^{jnu} , \qquad (3.103)$$

where, u = kdsinθ**,** where θ denotes the angle from broadside, *d* is the element spacing, k is the wave number and w_n is the complex excitation of the n^{th} element. In this algorithm the attention is paid to the case where f(u) is a real function so that weights are real and $w_{-n} = w_n^*$, with the asterisk denoting complex conjugate. The problem is to find *2N* + 1 excitation perturbations w_n, such that the perturbed pattern f(u) has desired low side-lobe levels at the prescribed directions $u=u_m$,m=1,2,…….M. Let $\boldsymbol{w}_m$ be the complex weight vector required for antenna to look in the m^{th} direction and

$$\Omega_m = e^{ju_m} \quad \& \quad u_m = (\frac{2\pi}{\lambda}).d.\sin(\theta_m) . \tag{3.104}$$

In the vector notation (3.103) can be represented as

$$f(\Omega_m) = \boldsymbol{w}_m^T.(\Omega_m)^n \qquad -N \le n \le N, 1 \le m \le M . \tag{3.105}$$

This array factor gives the field due to the antenna array with complex coefficients fed at each antenna element in m^{th} direction. If 'M' directions on the angular space in the range $[0, \pi]$ are considered, then the above equation can be written in matrix form as

$$\begin{bmatrix} \Omega_1^{-N} & \Omega_1^{-(N-1)} ..... & \Omega_1^0 ..... & \Omega_1^N \\ \Omega_2^{-N} & \Omega_2^{-(N-1)} ..... & \Omega_2^0 ..... & \Omega_2^N \\ & . & & \\ & . & & \\ \Omega_M^{-N} & \Omega_M^{-(N-1)} ..... & \Omega_M^0 ..... & \Omega_M^N \end{bmatrix} \begin{bmatrix} w_{-N} \\ w_{-(N-1)} \\ . \\ . \\ . \\ w_N \end{bmatrix} = \begin{bmatrix} f(\Omega_1) \\ f(\Omega_2) \\ . \\ . \\ . \\ f(\Omega_M) \end{bmatrix} . \tag{3.106}$$

(3.106) can be written as

$$\boldsymbol{F}_{Mx1} = \boldsymbol{\Omega}_{Mx(2N+1)} \cdot \boldsymbol{w}^T_{(2N+1)x1} , \tag{3.107}$$

where, $\boldsymbol{F}$ is the field vector giving desired lobe level required in 'M' directions, $\boldsymbol{\Omega}$ is the steering matrix and $\boldsymbol{w}$ is (2N+1) weight vector. If symmetric excitement is considered i.e. the reference point is the center of the array, summation of phases with weights would yield real steering vectors and a weight vector $\boldsymbol{w}$ of dimension N. To obtain specific power pattern weight vector $\boldsymbol{w}$ need to be calculated for particular $\boldsymbol{F}$. Thus, if the corresponding field points are provided in the angular space, the desired beam can obtained with specified side lobe levels. In the far field, the $\boldsymbol{F}$ will be real vector denoting the magnitude of the field strength. This lead to the

$$Re[\boldsymbol{F}_{Mx1}] = Re[\boldsymbol{\Omega}_{MxN}].\boldsymbol{w}^T_{Nx1} . \tag{3.108}$$

The solution to this set of M[th] order linear equations would be a set of real weight vector, given as

$$\boldsymbol{w} = \boldsymbol{\Omega}^{-1}\boldsymbol{F} \ . \tag{3.109}$$

Thus, using real weights at the antenna elements the desired beam can be formed, i.e. the appropriate levels of the main lobe and side lobes can be obtained. In CDMA system the vector $\boldsymbol{F}$ can be chosen in such a way that equal side lobes or depressed side lobes are formed in the direction of interferers. The low side lobe synthesis problem thus has only the dimensionality *M,* rather than the dimensionality *2N+1* of element space. This represents a significant simplification of the problem.

For inverse of $\boldsymbol{\Omega}$, matrix should be a square. In general for an N element array, there are N-2 distinct side lobes. To make lesser computation, instead of using singular value decomposition, the matrix is made square. This could be done in two different ways depending on the number of antenna elements.

1. If the number of antenna elements is even, a null in the end fire direction could be impressed at $\theta = 0$ or $\theta = \pi$ for broadside array and a null at $\theta = \pi/2$ for end fire array, to make the matrix square and vector $\boldsymbol{F}$ of length N. This is because even number of elements tends to have null in the endfire direction for broadside arrays and null at the broadside for the endfire arrays as shown in Fig. 3.26.

2. If the number of antenna elements is odd, repeat a side lobe at the endfire direction for $\theta = 0$ and $\theta = \pi$. This is because odd number of elements tends to have side lobes in the endfire direction in ULA as shown in Fig. 3.27.

Algorithm used:

The method for low sidelobe or depressed side lobe pattern synthesis starts from a given original pattern $f_o(u)$, with desired main beam and side lobe envelope, corresponding to given original element coefficients ($\boldsymbol{w}^0$). These coefficients are then perturbed such that the perturbed pattern has required side lobe levels in the desired directions. The algorithm described below is for the uniform linear array. Let $\boldsymbol{F}^0$ is the initial field vector containing values of field for main beam as well as side lobes for 2N+1 element ULA. $\boldsymbol{F}^0$ is given by

$$\boldsymbol{F}^{0} = \boldsymbol{\Omega}^{0}.(\boldsymbol{w}^{0})^{\mathrm{T}}, \tag{3.110}$$

with $\mathbf{w}^0$=1 for all elements. $\boldsymbol{\Omega}^{(0)}$ is the initial steering matrix with given main beam direction and the direction of the side lobes of ULA.

The basic property of beamforming is embedded in ULA, which is exploited in knowing the side lobe directions as an initial step. Once the side lobe directions are known, depending on the relative magnitude required for the side lobes, forcing vector $\boldsymbol{F}$ is formulated. The first set of weight vectors is calculated using (3.109). The steps required for the algorithm could be stated as follows:

1. Formulate ULA with equispaced elements with $d \leq \lambda/2$.
2. Find the positions of the side lobes by simple peak finding (change in slope routine).
3. Formulate the matrix $\boldsymbol{\Omega}^0$ and vector $\boldsymbol{F}^0$.
4. Formulate vector $\boldsymbol{F}$ with the desired sidelobe levels (Don't change it during subsequent iterations).
5. Find the new weight vector, $\boldsymbol{w} = (\boldsymbol{\Omega}^0)^{-1}\boldsymbol{F}$
6. Obtain the pattern with this weight vector $\boldsymbol{w}$ and find the magnitude of the side lobes and form the vector $\boldsymbol{F}^1$.
7. Find the error between the desired $\boldsymbol{F}$ and new side lobe peaks, $\boldsymbol{F}^1$.
8. If $|\boldsymbol{F} - \boldsymbol{F}^1| \leq \varepsilon$ where ε is the acceptable error, then stop, else repeat from step 2.

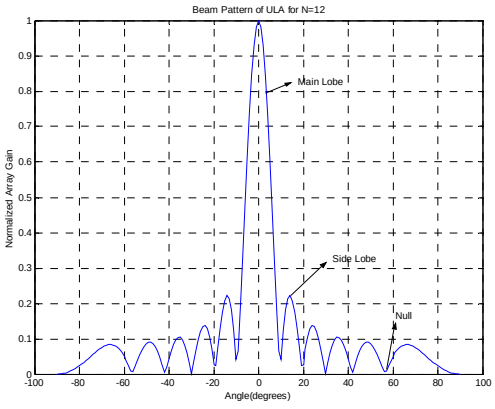

Figure 3.26-Normalized field pattern for ULA with N=12, d=λ/2, $\alpha = 0$

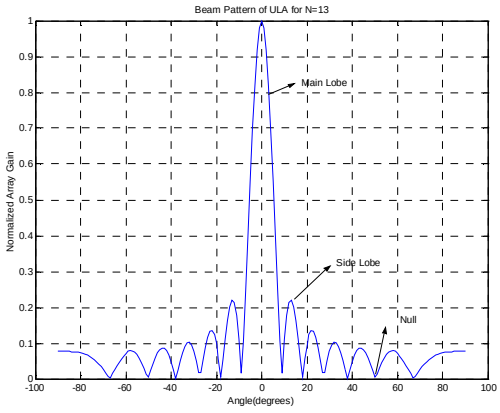

Figure 3.27-Normalized field pattern for ULA with N=11,d=λ/2, $\alpha = 0$

Although the algorithm has been discussed considering the array with uniform current distribution but it has been observed with simulation results that it is possible to get the equal side lobe pattern using Taylor current distribution also. For both current distributions, the resultant array approaches the Chebyshev pattern thereby lowering the side lobe level presented to all interferers and hence increasing the capacity of the

system. By application of above algorithm the beampatterns obtained form uniform and Taylor current distributions are shown in Figs. 3.28-3.32. In Figs.3.28 & 3.31, the beampatterns after each iteration are shown. Figs. 3.29 & 3.32, show the polar plot obtained after each iteration. It is also shown in Fig. 3.30 that beam can be steered in any direction. Figs. 3.33 to 3.34 show a low side lobe adjustment based on above algorithm[6]. The algorithm places a low side lobe level at any position in the pattern depending upon direction arrival of the interferers. The convergence of algorithm with Taylor and Uniform current distribution is shown in Figs. 3.35 & 3.36 respectively. A comparison of normalized array gain of Chebyshev and MBC algorithm is shown in Fig.3.37. The same plot shows the comparison of capacity function also.

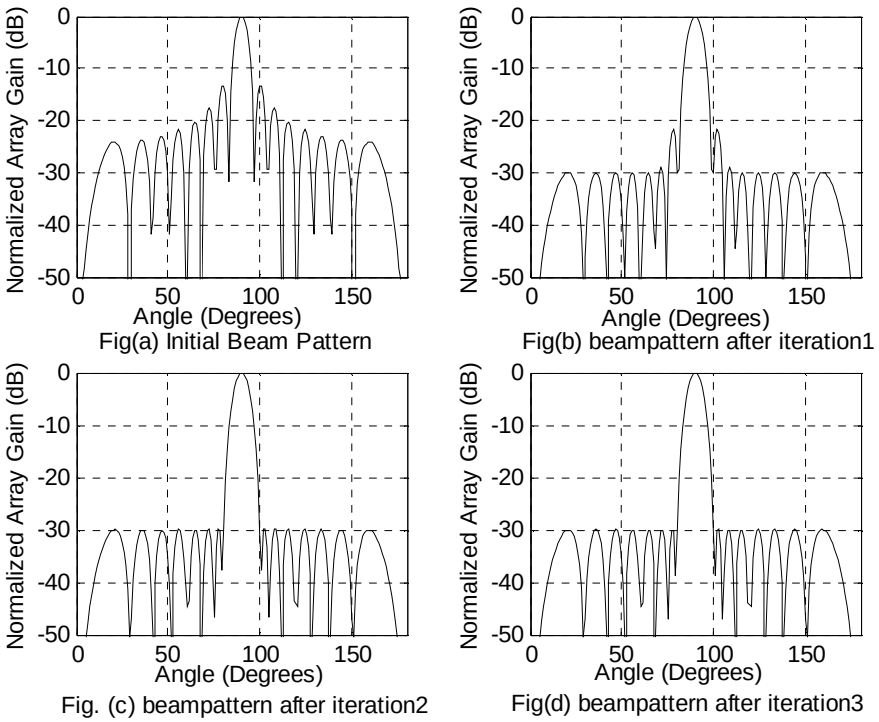

Figure 3.28-Chebyshev Patterns obtained using ULA with uniform current distribution

---

6. [P16] "Independent angular steering of each zero of a directional pattern of a linear array", Proceedings of International conf. on challenges in networking and Future comm.(CNFE-05)APIIT,Panipat,India,pp.91-95,April 9-10,2005.

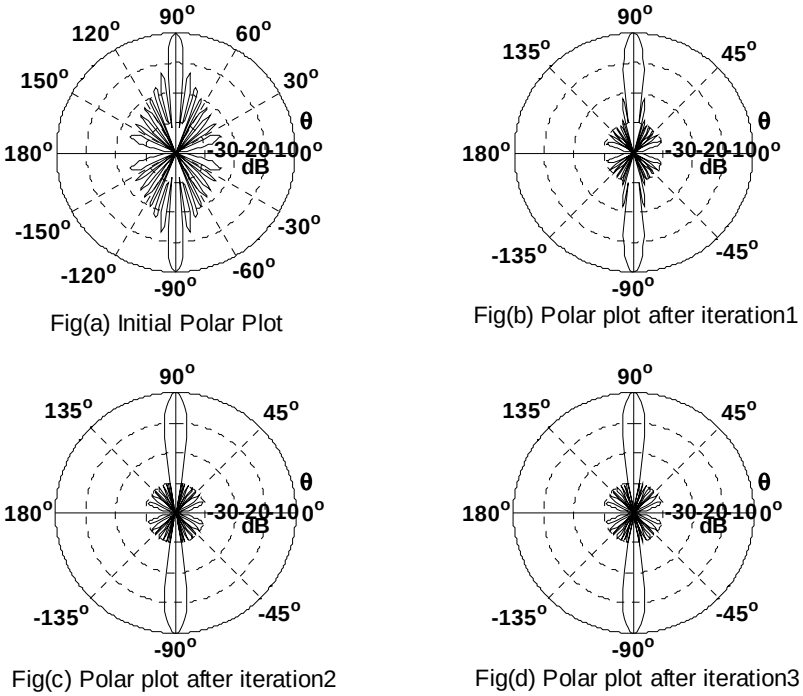

Fig(a) Initial Polar Plot

Fig(b) Polar plot after iteration1

Fig(c) Polar plot after iteration2

Fig(d) Polar plot after iteration3

Figure 3.29-Polar Plots obtained after each iteration

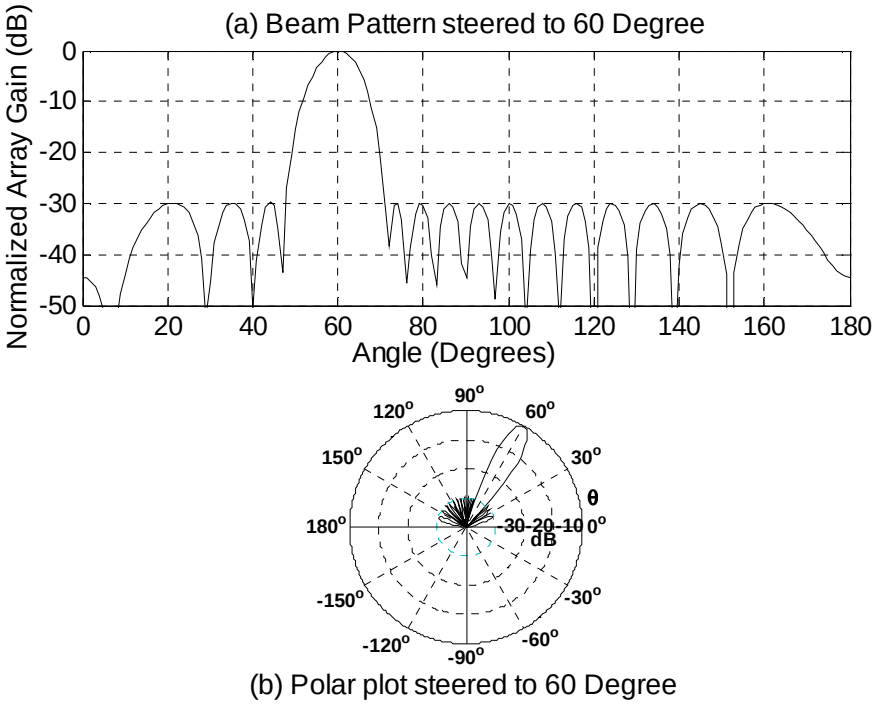

(b) Polar plot steered to 60 Degree

Figure 3.30-Beam Pattern & Polar Plot steered to 60^0

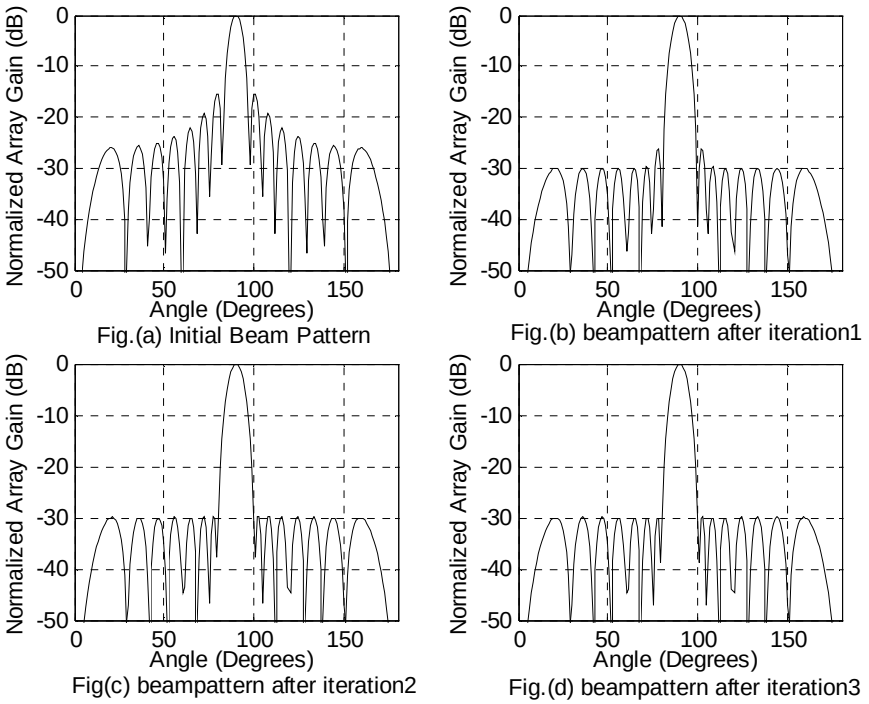

Fig.(a) Initial Beam Pattern

Fig.(b) beampattern after iteration1

Fig(c) beampattern after iteration2

Fig.(d) beampattern after iteration3

Figure 3.31-Chebyshev Patterns obtained using ULA with Taylor current distribution

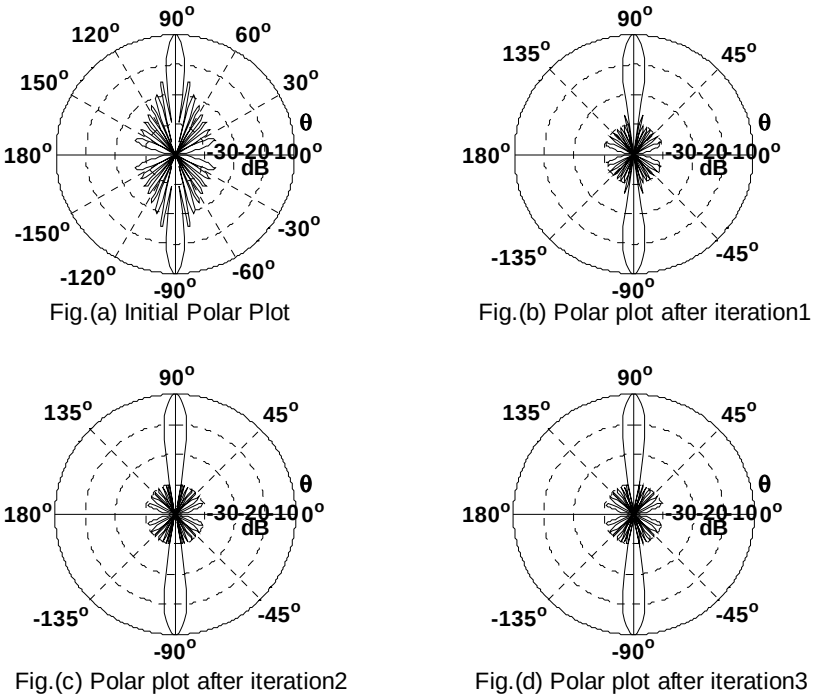

Fig.(a) Initial Polar Plot

Fig.(b) Polar plot after iteration1

Fig.(c) Polar plot after iteration2

Fig.(d) Polar plot after iteration3

Figure 3.32-Polar Plots obtained after each iteration

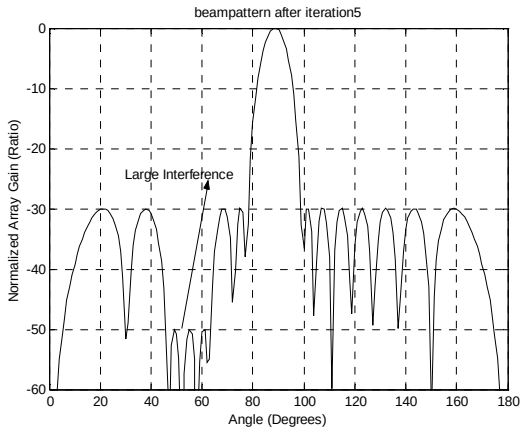

(a) A low side lobe at 3rd to 6th side lobe positions with uniform current distribution

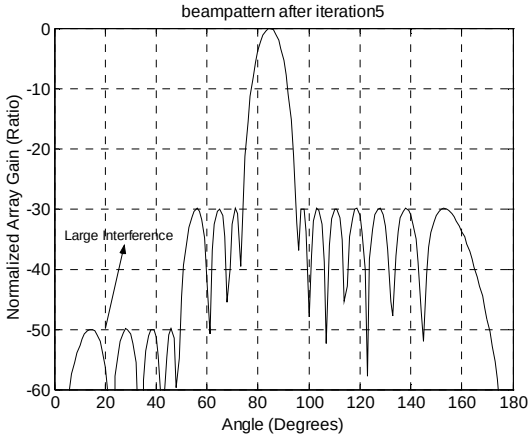

(b) A low side lobe at last four side lobe positions with Uniform current distribution

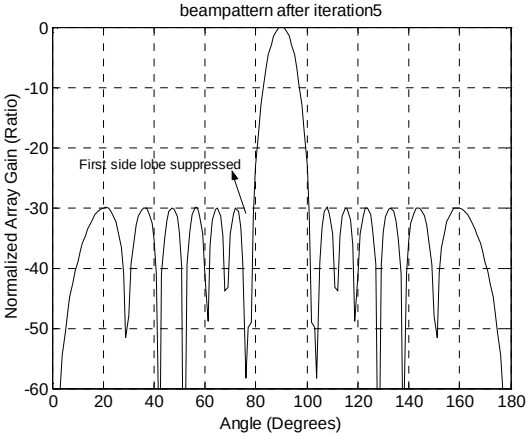

(c)A low side lobe at first side lobe position with Uniform current distribution

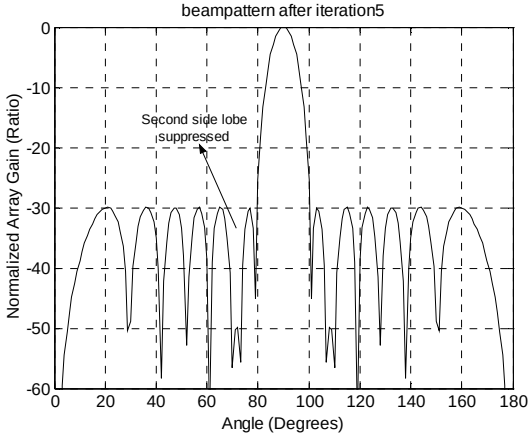

(d) A low side lobe at second side lobe position with Uniform current distribution

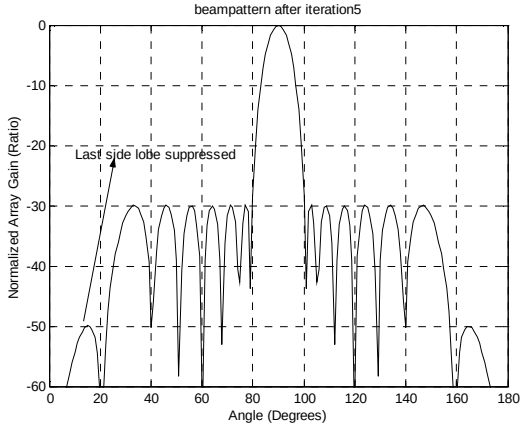

(e) A low side lobe at last side lobe positions with Uniform current distribution

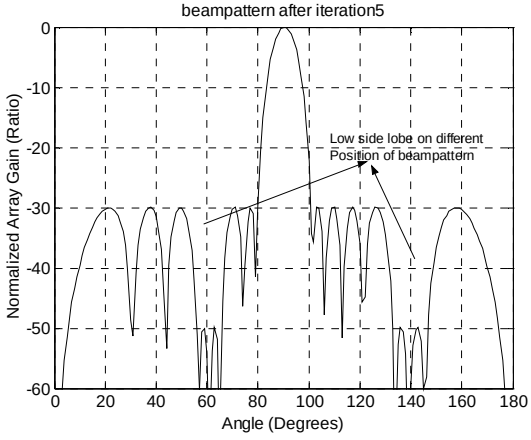

(f) A low side lobe at different positions with Uniform current distribution

Figure 3.33-Side Lobe adjustment with Uniform current distribution

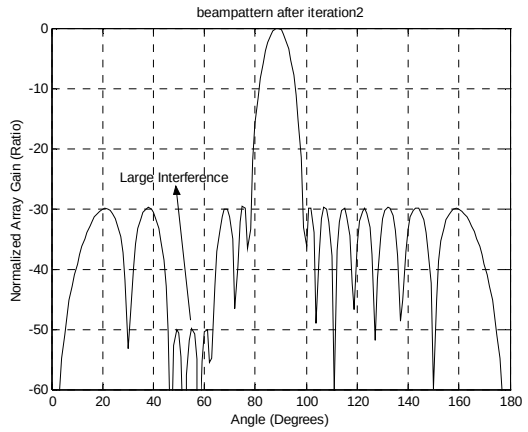

(a) A low side lobe at 3rd to 6th side lobe positions with Taylor current distribution

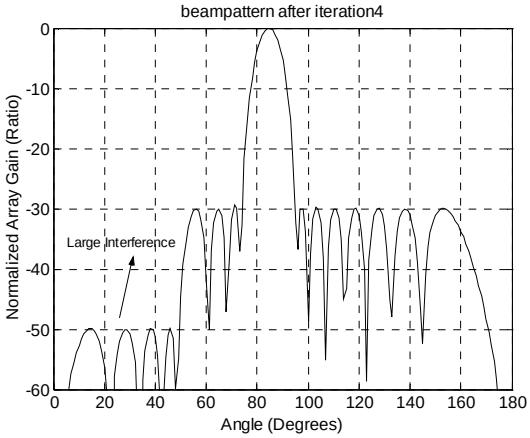

(b) A low side lobe at last four side lobe positions with Taylor current distribution

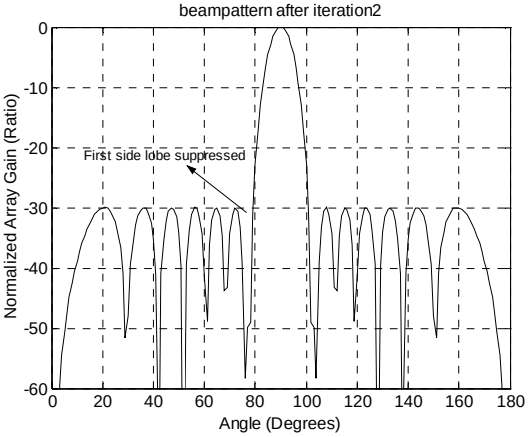

(c)A low side lobe at first side lobe position with Taylor current distribution

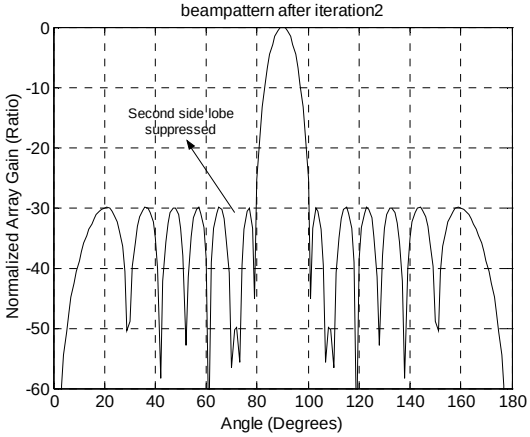

(d)A low side lobe at second side lobe position with Taylor current distribution

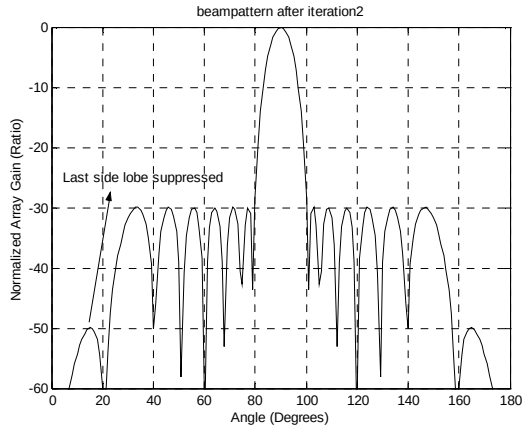

(e) A low side lobe at last side lobe positions with Taylor current distribution

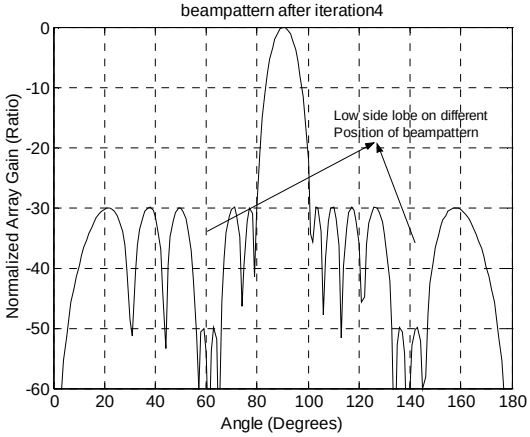

(f)A low side lobe at different positions with Taylor current distribution

Figure 3.34-Side Lobe adjustment with Taylor current distribution

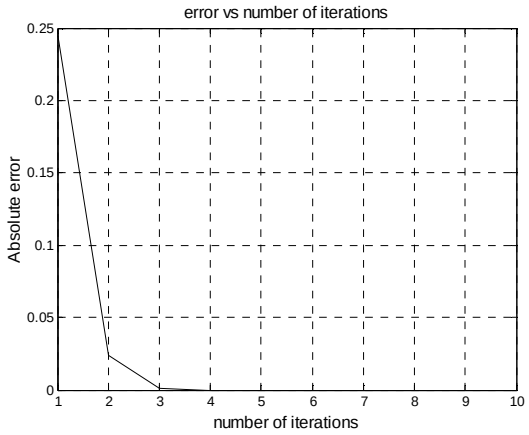

(a) Convergence with Taylor distribution

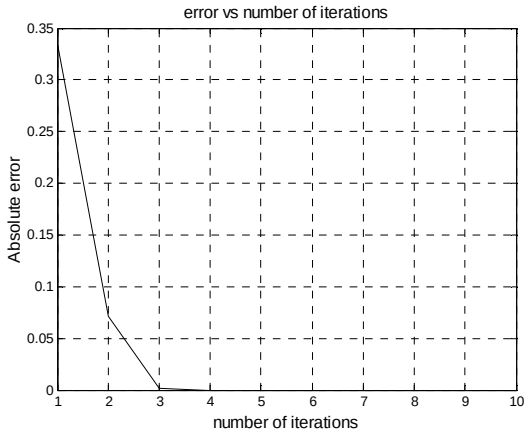

(b) Convergence with Uniform Distribution

Figure 3.35-Convergence with Taylor Distribution and Uniform Distribution (Without adjustable side lobe topography)

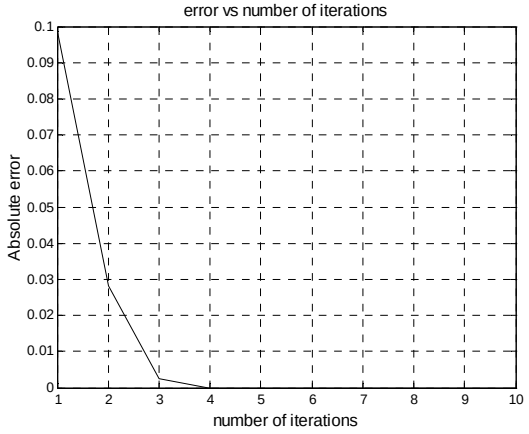

(a) Convergence with Taylor Distribution

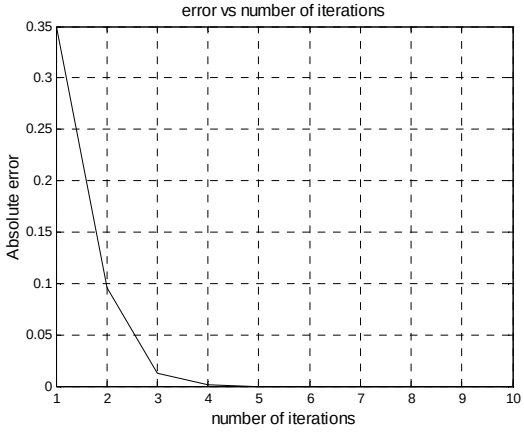

(b) Convergence with Uniform Distribution

Figure 3.36-Convergence with Taylor Distribution and Uniform Distribution (with adjustable side lobe topography)

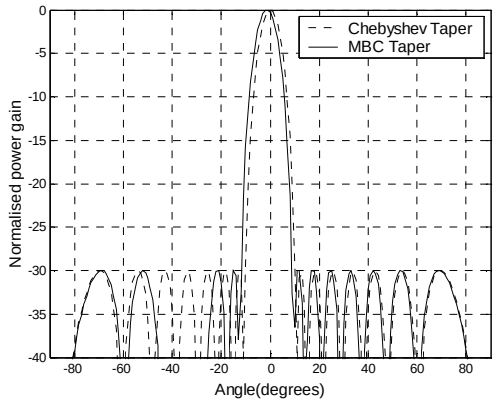

(a) Array gain of Chebyshev Taper and MBC Taper with depressed 3rd to 6th lobe

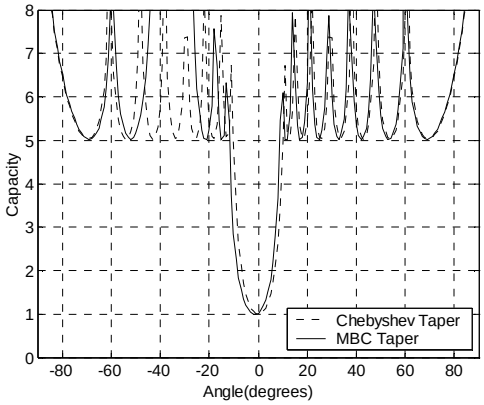

(b) Capacity Function of Chebyshev Taper and MBC Taper with depressed 3rd to 6th lobe

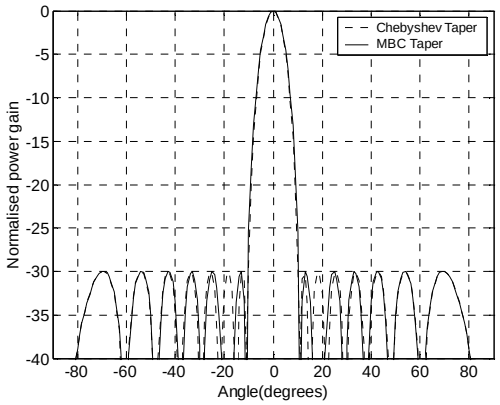

(c)Array gain of Chebyshev Taper and MBC Taper with depressed 2nd lobe

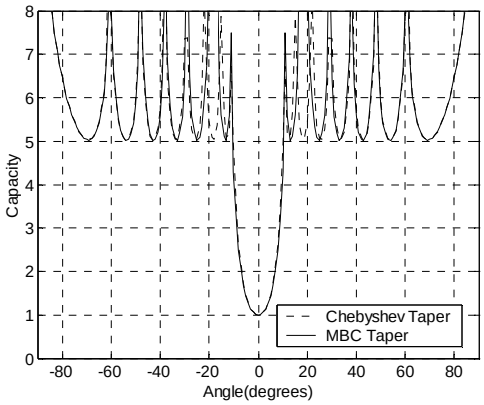

(d) Capacity Function of Chebyshev Taper and MBC Taper with depressed 2nd lobe

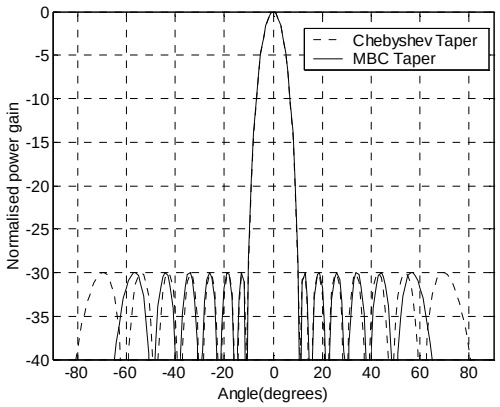

(e) Array gain of Chebyshev Taper and MBC Taper with last 2 lobes depressed

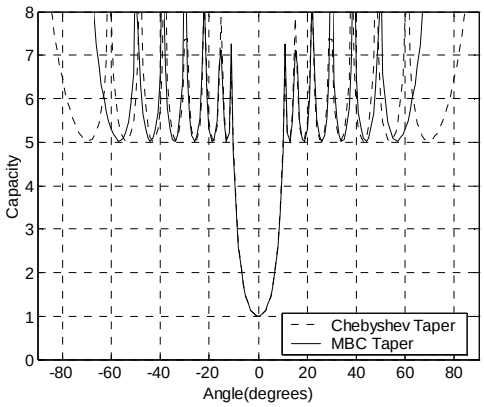

(f) Capacity Function of Chebyshev Taper and MBC Taper with last 2 lobes depressed

Figure 3.37-Comparison of Normalized array gain and capacity function of Chebyshev Taper and MBC Taper with different side lobe topology

3.9.1 Results and Discussion

1. The convergence of Taylor distribution based algorithm is faster as compared to uniform array. The convergence of each array is shown in Figs. 3.35 & 3.36 for both the cases of adjustable side lobe topography and without adjustable side lobe topography.
2. It is important to note that proposed method a suboptimal weight vector that does not null out interferers. Beampattern simply maximizes the gain in the direction of the desired signal source and minimizes the gain in the direction of interferers.
3. As discussed earlier in cases of large angular spread, a sharp null can not provide efficient interference suppression. These cases can however be handled if a broad low side lobe is formed towards the direction of the interference. With the proposed algorithm a controlled broad low side lobe can be easily synthesized.
4. As proved earlier to have a minimum drop in capacity as the interfering user moves through the sidelobes, the maximum sidelobe level should be as low as possible. The algorithm provides a low side lobe level to all users in case they are uniformly distributed in the side lobe region. Also if the interferers are concentrated over a broad angle still the algorithm places a low side level in the direction of interferes. Moreover the algorithm convergence is faster as compared to other adaptive algorithms. The capacity improvement obtained by use of above algorithm is shown in Fig. 3.37.

It is important to analyze the performance of proposed MBC beamforming algorithm, when it is used in array processing architectures. Four performance metrics are commonly used in array processing architectures viz.:

- Signal-to-interference-plus-noise ratio (SINR),
- Normalized SINR (α),
- Array gain (AG) and
- Mean square error (MSE).

These quantities are computed at the output of the array beamformer in the presence of interferers in wireless communication. The proposed MBC algorithm, Chebyshev algorithm and one adaptive algorithm (SMI) are simulated to illustrate the behavior of these metrics in a more complex environment. The mathematical formulation of these metrics is done next.

3.10 PERFORMANCE METRICS OF AN ARRAY PROCESSING ARCHITECTURE & THEIR DERIVATION

3.10.1 Signal-to-interference-plus-noise ratio (SINR)

SINR is a generalization of SNR (signal-to-noise ratio) that explicitly takes into account the impact of interference, i.e., jamming. Maximizing SINR is the optimal criterion for most detection and estimation problems [32]. SINR is computed either at the input to the array (i.e., element level) or at the output of the array. In this work SINR at the output of the array is of concern, therefore SINR means output SINR. Input SINR, or element-level SINR, is ratio of the signal power to the interference plus noise power at the individual element

$$SINR_{input} = \frac{\sigma_s^2}{\sigma_i^2 + \sigma_n^2}, \tag{3.111}$$

where, $\sigma_s^2, \sigma_i^2, \sigma_n^2$ are the desired signal, interference, and noise powers at the individual element level. Output SINR is the ratio of the signal power to the interference-plus-noise power at the output of the array as given by (3.76)

$$\mathrm{SINR}_{\mathrm{out}} = \frac{[\boldsymbol{w}^{\mathrm{H}} \boldsymbol{x}'(\mathrm{n})]^2}{\mathrm{E}\left\{\left|\boldsymbol{w}^{\mathrm{H}} \boldsymbol{x}_{\mathrm{i+n}}(\mathrm{n})\right|^2\right\}} = \frac{\sigma_{\mathrm{s}}^2 \left|\boldsymbol{w}^{\mathrm{H}} \boldsymbol{a}(\theta)\right|^2}{\boldsymbol{w}^{\mathrm{H}} \boldsymbol{R}_{\mathrm{i+n}} \boldsymbol{w}}, \tag{3.112}$$

where, $[\boldsymbol{a}(\theta)]^2$ is the array manifold vector defined in (3.12). For the distortion less constraint with no steering vector mismatch, i.e., the steering vector used to compute $\boldsymbol{w}$ is identical to the steering vector used to evaluate the SINR, (3.112) can be simplified as

$$\mathrm{SINR}_{\mathrm{out}} = \frac{\sigma_{\mathrm{s}}^2 \mathrm{M}}{\boldsymbol{w}^{\mathrm{H}} \boldsymbol{R}_{\mathrm{i+n}} \boldsymbol{w}}. \tag{3.113}$$

Now, mean square error (MSE) is defined as a measure of an array's ability to cancel noise. MSE is defined as

$$\mathrm{MSE} = \mathrm{E}[\left|\boldsymbol{w}^{\mathrm{H}} \boldsymbol{x}_{\mathrm{i+n}}\right|^2] = \boldsymbol{w}^{\mathrm{H}} \boldsymbol{R}_{\mathrm{i+n}} \boldsymbol{w}. \tag{3.114}$$

Substituting (3.113) into (3.114) yields the final expression for the output SINR

$$SINR_{output} = \frac{M\sigma_s^2}{MSE}. \tag{3.115}$$

(3.115) shows that output SINR is inversely proportional to MSE

3.10.2 Normalized SINR (ρ)

Normalized SINR is the ratio of the SINR for a given weight vector to the SINR for the optimal weight vector. Normalized SINR is an important metric because there are classic theoretical results that have been derived using this metric. The normalized SINR is defined as follows

$$\rho = \frac{SINR}{SINR_{opt}}, \tag{3.116}$$

where SINR is the output SINR for a given weight vector (e.g., computed using an estimated covariance matrix), and $SINR_{opt}$ is the optimal output SINR (i.e., computed using the true covariance matrix). Substituting (3.115) into (3.116) yields

$$\rho = \frac{MSE_{opt}}{MSE} = \frac{MMSE}{MSE}, \tag{3.117}$$

where, the optimal MSE is more commonly referred to as the minimum MSE (MMSE). It can be noted that MMSE will be a fixed quantity for a given scenario while the MSE will vary for each weight vector being evaluated. Therefore (3.117) shows the inverse relationship of normalized SINR with MSE.

3.10.3 Array Gain

Array gain (AG) is the third metric of interest. Array gain is the ratio of the SINR at the output of the array to the SINR at the input of the array. It is a measure of the productivity of the array and also directly impacts system detection performance. Some authors use array gain also called improvement factor, as their primary metric [63]. It is important to note, however, that array gain is quite different from power gain, used in the radar range equation, or even directive gain. It is shown in simulation that the value of array gain can grow quite large as it reflects not only the coherent gain from the number of elements but also the impact of depressing interferers. Array gain is defined as follows

$$\mathrm{AG} = \frac{\mathrm{SINR}_{\mathrm{out}}}{\mathrm{SINR}_{\mathrm{input}}}. \tag{3.118}$$

Substituting (3.111) and (3.115) into (3.117) gives

$$\mathrm{AG} = \frac{\mathrm{M}\sigma_{\mathrm{i,n}}^2}{\mathrm{MSE}}, \tag{3.119}$$

where, $\sigma_{\mathrm{i,n}}^2 = \sigma_{\mathrm{n}}^2 + \sigma_{\mathrm{i}}^2$. (3.119) again shows the inverse relationship of array gain with MSE.

3.10.4 Minimum Mean Squared Error

The last metric of interest is minimum mean square error (MMSE). MMSE is a measure of an adaptive beamformer ability to give the desired output. MMSE is the most fundamental of the four metrics. Each of the other three metrics is proportional to MMSE under the conditions cited at the beginning of this section. MMSE will be used widely throughout next chapter to evaluate algorithms. The derivation of MMSE is based on Wiener's solution discussed in next chapter. The various performance metrics are summarized in table 3.6

Table-3.6: Various Performance Metrics and Their Expressions

Performance Metric	Expression
Minimum Mean squared Error	$\boldsymbol{w^H R w}$
SINR (output)	$\frac{M\sigma_s^2}{MSE}$
Normalized SINR,ρ	$\frac{MMSE}{MSE}$
Array Gain	$\frac{M\sigma_{i,n}^2}{MSE}$

Based on above metrics the performance of a beamformer, with three different algorithms mentioned below, is evaluated,

1. Chebyshev weighting with -40 dB sidelobes,
2. Sample Matrix Inverse.
3. MBC with -40dB side lobe level a low side lobe level of -80dB from 38^0 to 48^0.

In each beamformer a 16 element uniform linear array processing architecture shown in Fig.3.1 with interferers at different DOAs is assumed. The interference power of each interferer is varied from 0 to 60dB. All individual interfering powers are the same during a given trial. The element level SNR is taken as 0dB, and thermal noise power is normalized to unity. Each realization consists of random draw of training data. Each realization is run for 10000 Monte Carlo trials. Figs. 3.39-3.47 show the variation of the performance metrics of a beamformer, with three different algorithms, under different interfering environments. The simulations are done by varying total number of interferers in each simulation. Fig.3.38(a & b) shows the beampattern and polar plot of MBC taper used in simulations. In Figs.3.39 – 3.47, part 'a' shows the variation of array gain, part 'b' shows the variation of output SNR, part 'c' shows the variation of normalized SINR and part 'c' shows variation of MSE with total interference power.

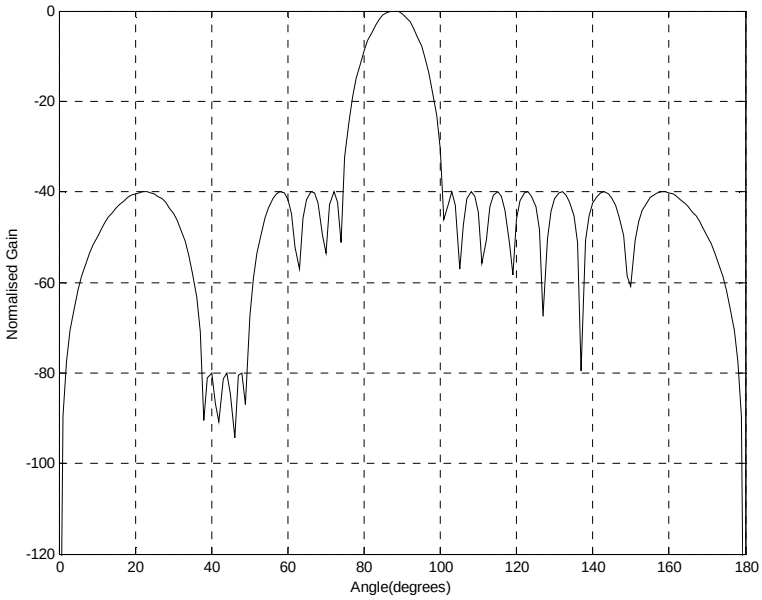

(a) Beampattern of MBC Taper with side lobe level of -80db from 38^0 to 48^0

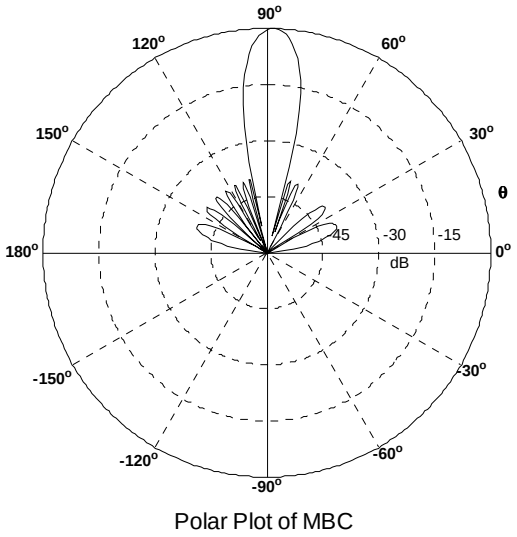

(b) Polar plot of MBC Taper with side lobe level of -80db from 38^0 to 48^0

Figure 3.38-Pattern of MBC beamformer used for comparison

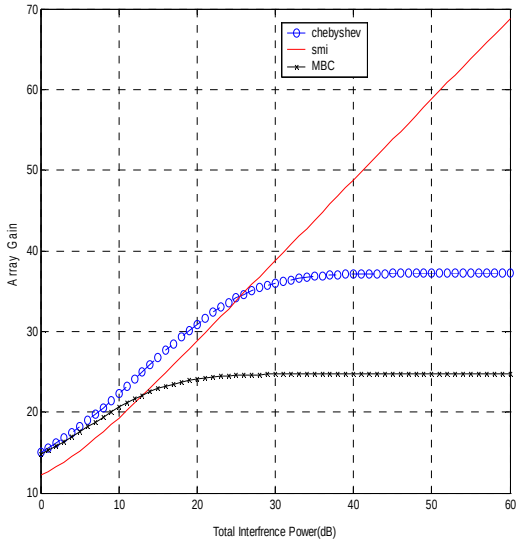

(a) Array Gain variation with Interference power of 5 interferers

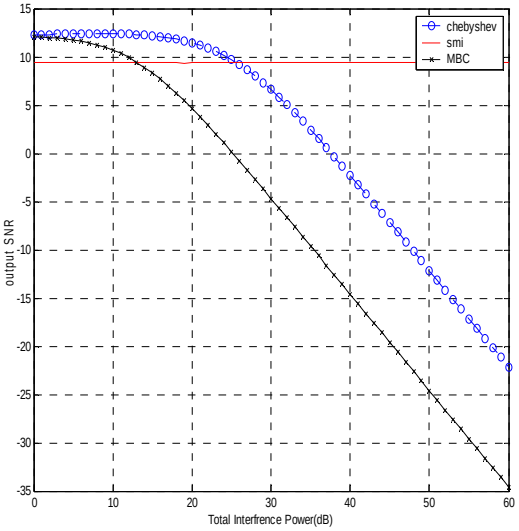

(b) Output SNR variation with Interference power of 5 interferers

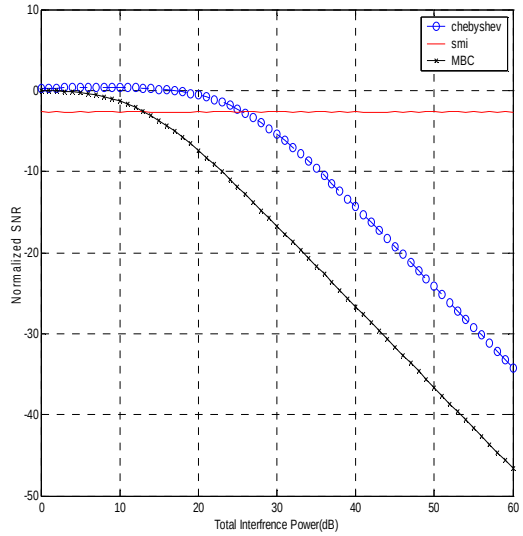

(c) Normalized SNR variation with Interference power of 5 interferers

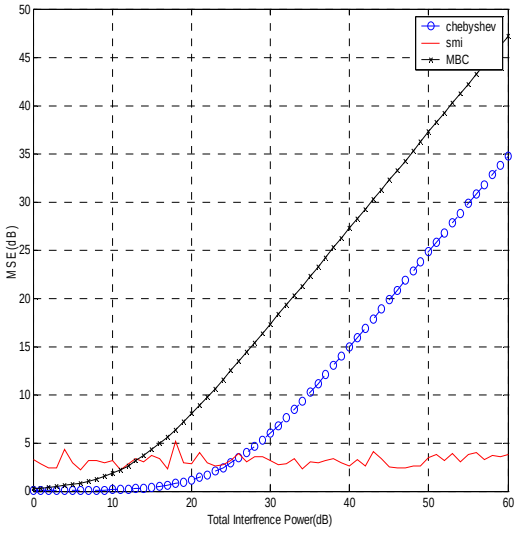

(d) MSE variation with Interference power of 5 interferers

Figure 3.39-Variation of different Performance Metrics of three beamformers for five interferers. The interferers are not lying in low side lobe region of MBC

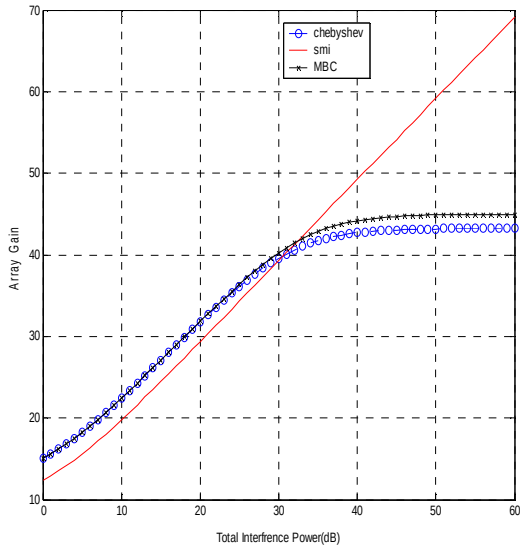

(a) Array Gain variation with Interference power for 5 Interferers

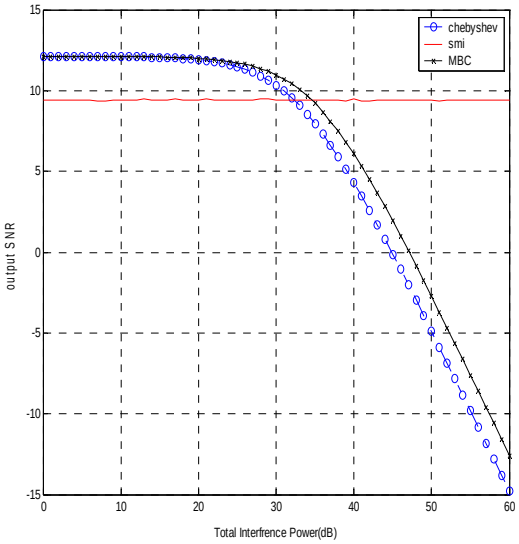

(b) Output SNR variation with Interference power for 5 Interferers

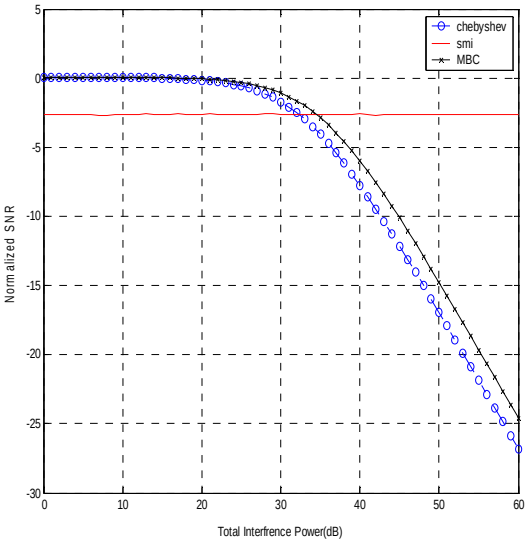

(c) Normalized SNR variation with Interference power for 5 Interferers

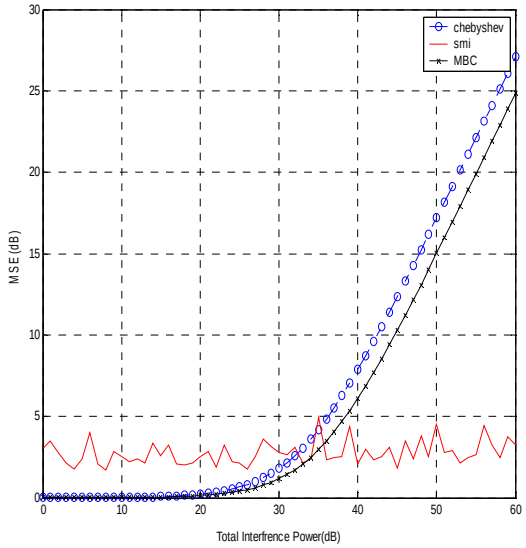

(d) MSE variation with Interference power for 5 Interferers

Figure 3.40- Variation of different Performance Metrics of three beamformers for five interferers. Few interferers are lying in low side lobe region of MBC

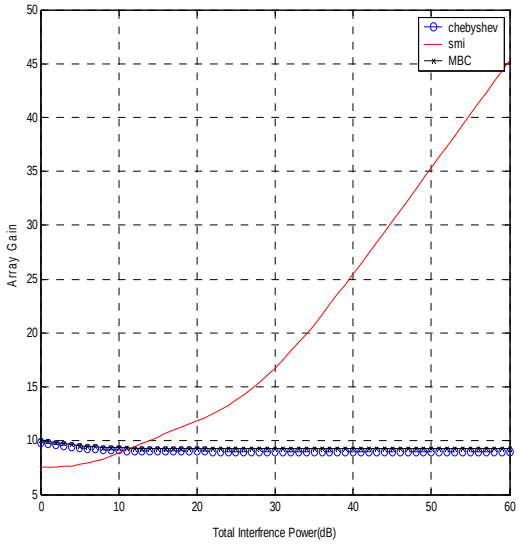

(a) Array Gain variation with Interference power for 9 Interferers

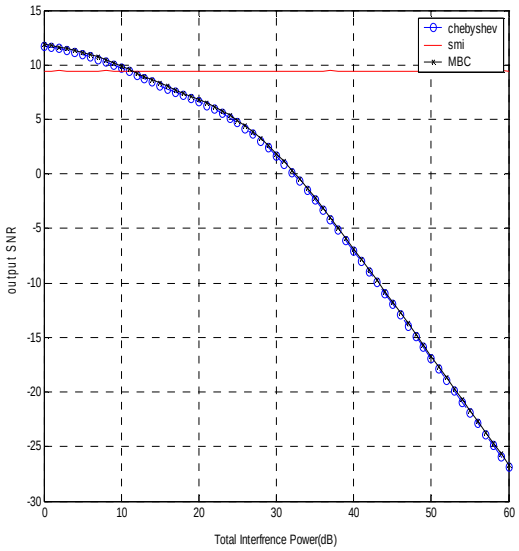

(b) Output SNR variation with Interference power for 9 Interferers

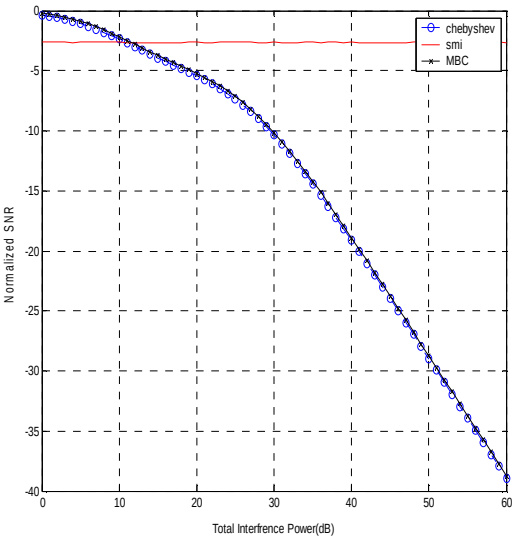

(c) Normalized SNR variation with Interference power for 9 Interferers

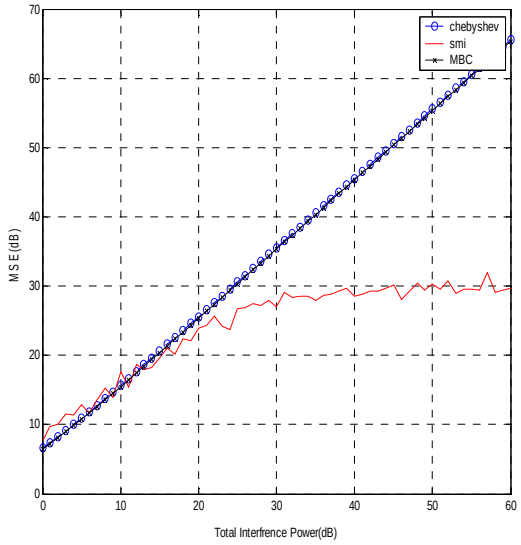

(d) MSE variation with Interference power for 9 Interferers

Figure 3.41- Variation of different Performance Metrics of three beamformers for nine interferers. No interferer is lying in low side lobe region of MBC

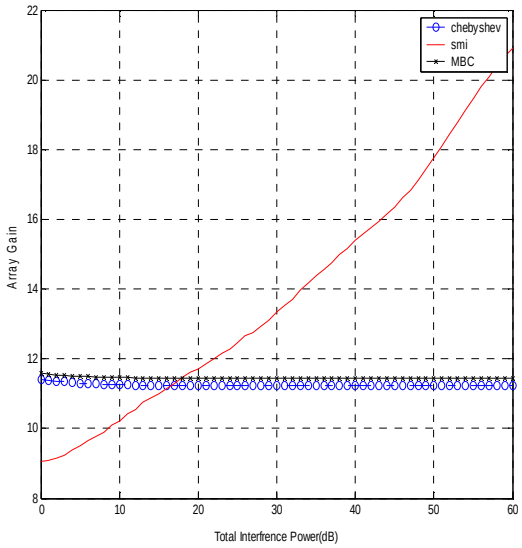

(a) Array Gain variation with Interference power for 15 Interferers

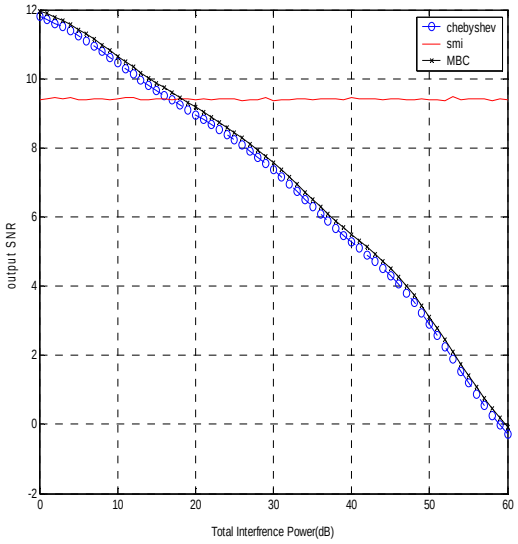

(b) Output SNR variation with Interference power for 15 Interferers

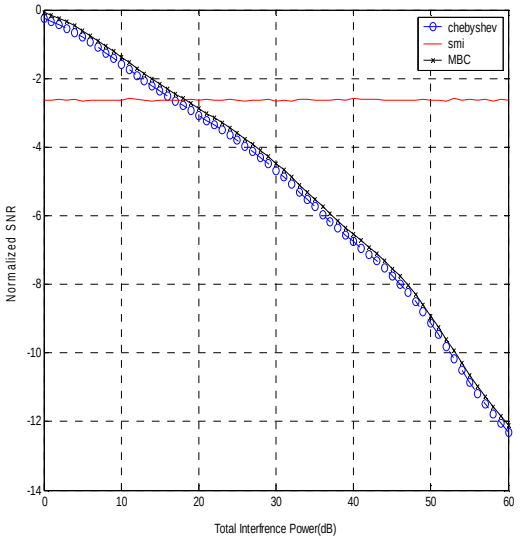

(c) Normalized SNR variation with Interference power for 15 Interferers

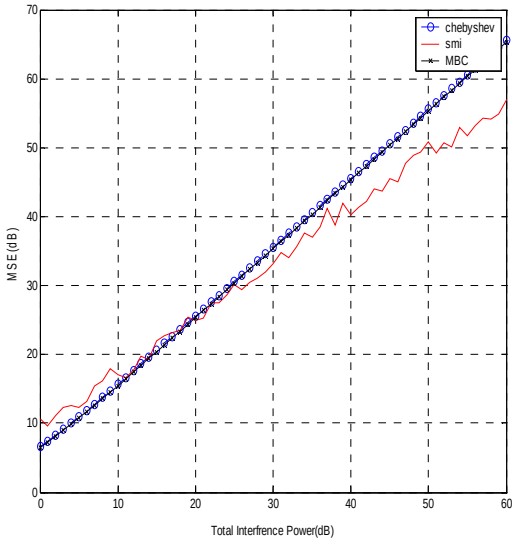

(d) MSE variation with Interference power for 15 Interferers

Figure 3.42- Variation of different Performance Metrics of three beamformers for fifteen interferers. One interferer is lying in low side lobe region of MBC

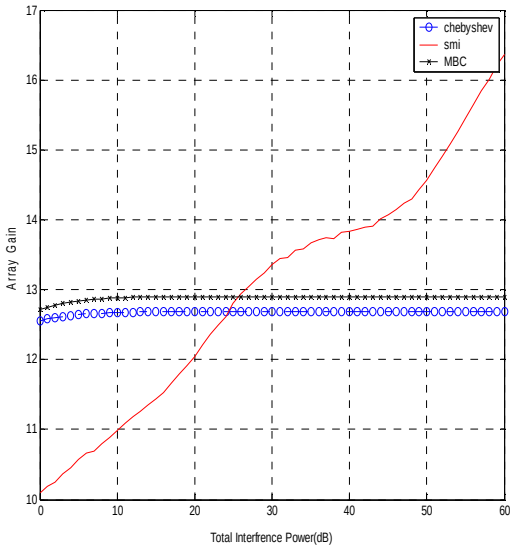

(a) Array Gain variation with Interference power for 21 Interferers

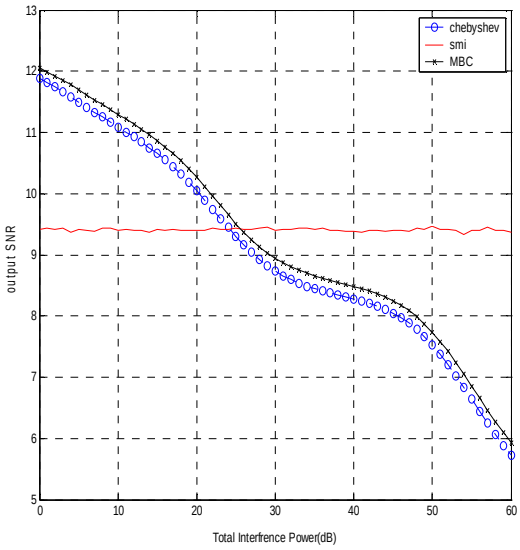

(b) Output SNR variation with Interference power for 21 Interferers

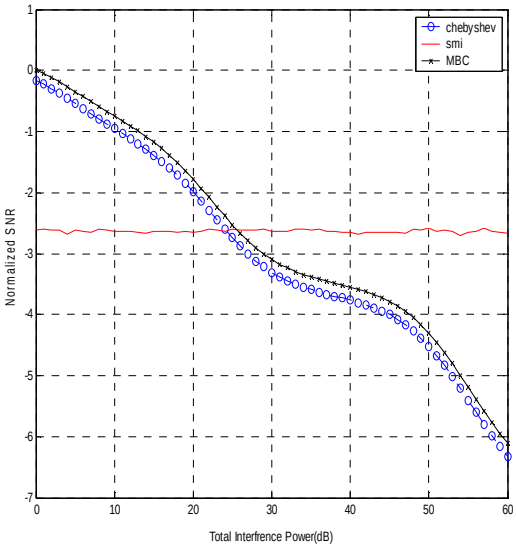

(c) Normalized SNR variation with Interference power for 21 Interferers

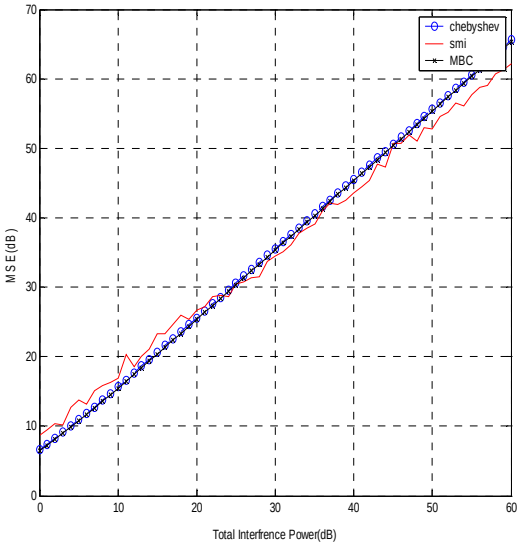

(d) MSE variation with Interference power for 21 Interferers

Figure 3.43- Variation of different Performance Metrics of three beamformers for 21 interferers. Few interferers are lying in low side lobe region.

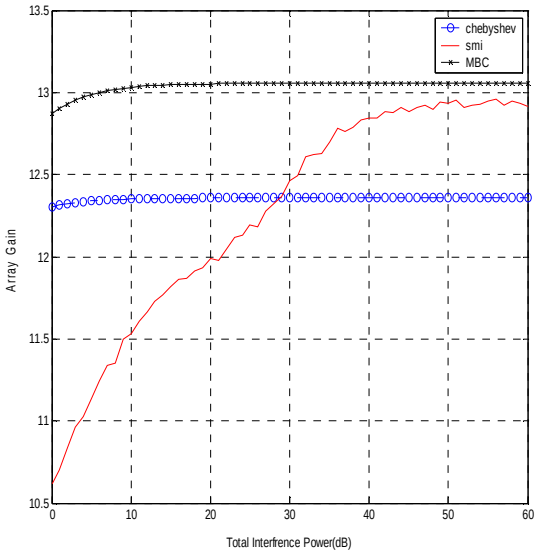

(a) Array Gain variation with Interference power for 25 Interferers

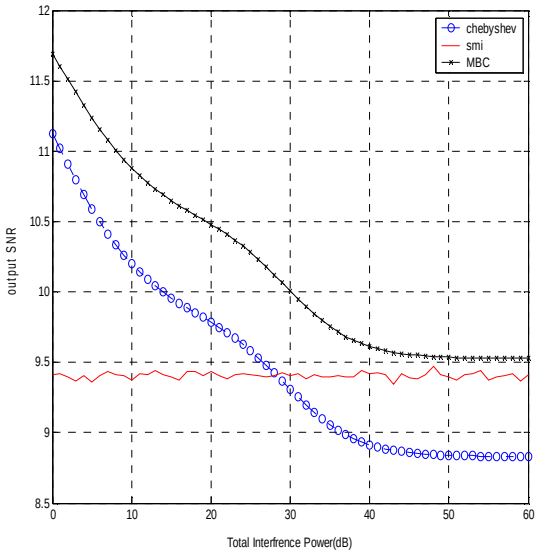

(b) Output SNR variation with Interference power for 25 Interferers

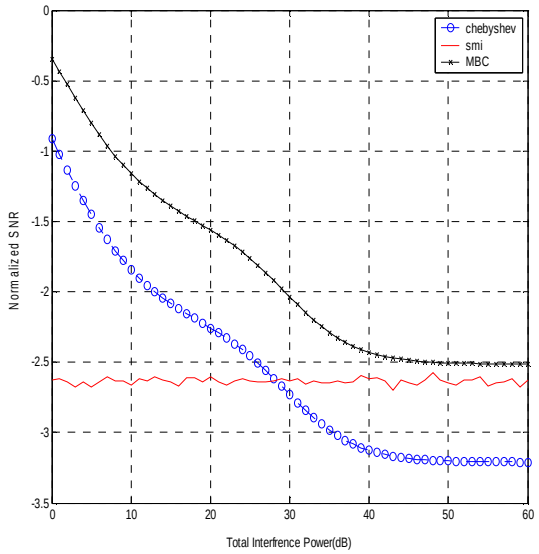

(c) Normalized SNR variation with Interference power for 25 Interferers

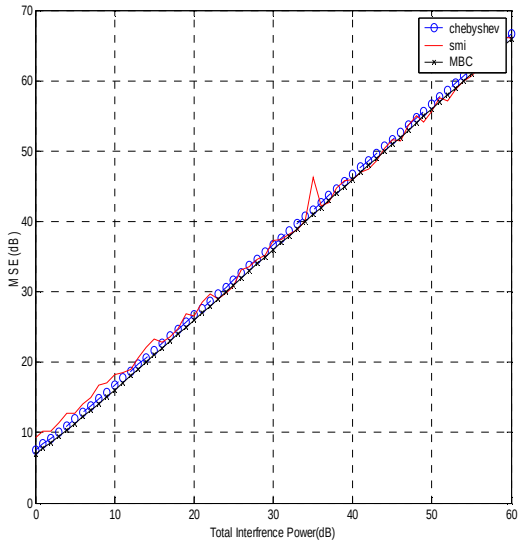

(d) MSE variation with Interference power for 25 Interferers

Figure 3.44- Variation of different Performance Metrics of three beamformers for 25 interferers. Few interferers are lying in low side lobe region of MBC

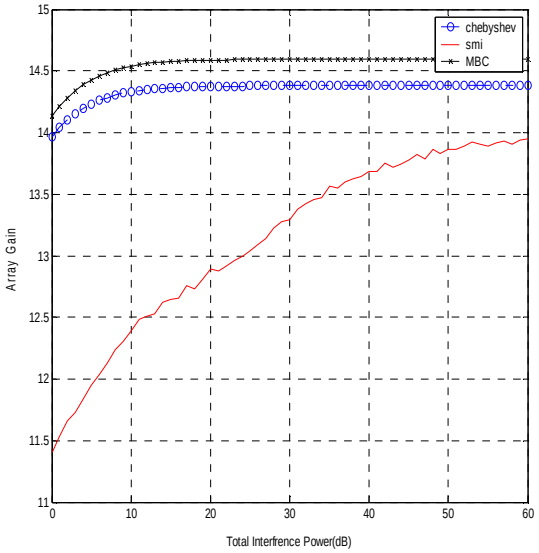

(a) Array Gain variation with Interference power for31 Interferers

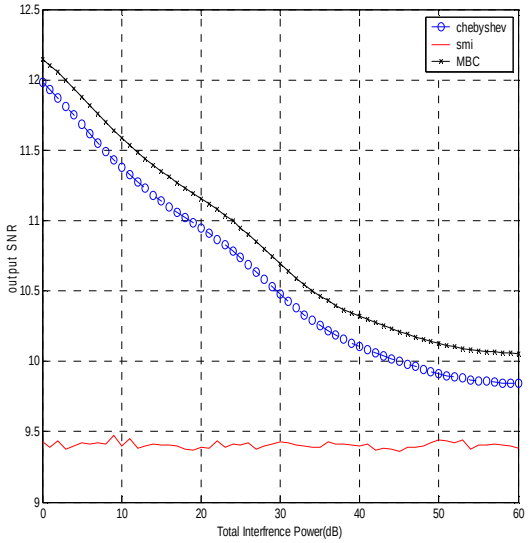

(b) Output SNR variation with Interference power for 31 Interferers

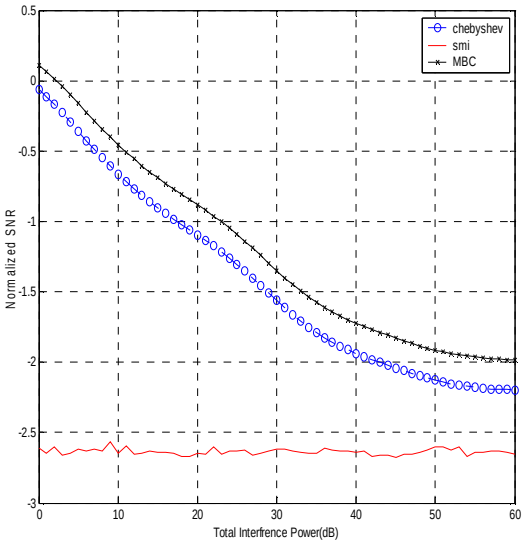

(c) Normalized SNR variation with Interference power for 31 Interferers

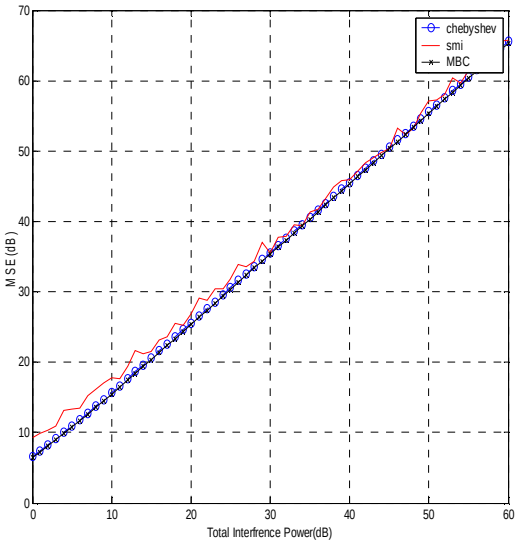

(d) MSE variation with Interference power for 31 Interferers

Figure 3.45- Variation of different Performance Metrics of three beamformers for 31 interferers. Few interferers are lying in low side lobe region of MBC

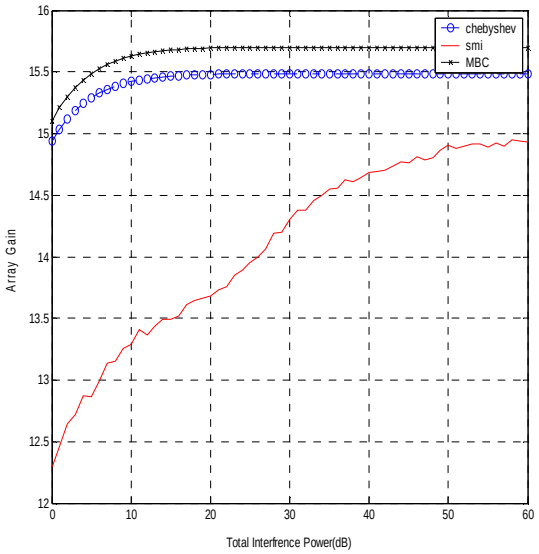

(a) Array Gain variation with Interference power for40 Interferers

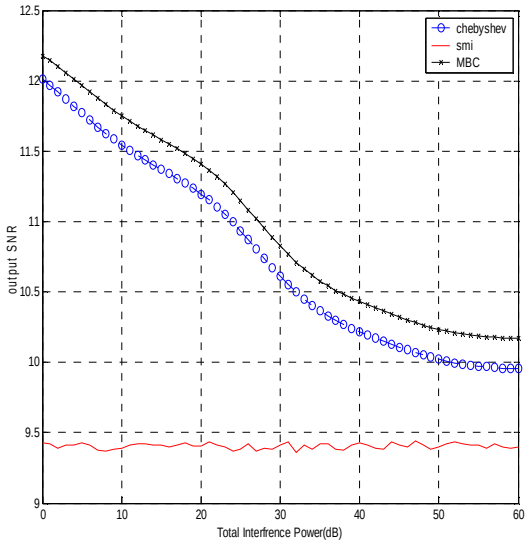

(b) Output SNR variation with Interference power for 40 Interferers

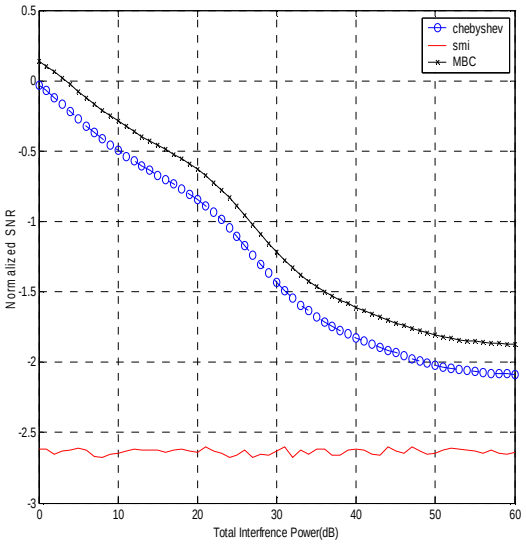

(c) Normalized SNR variation with Interference power for 40 Interferers

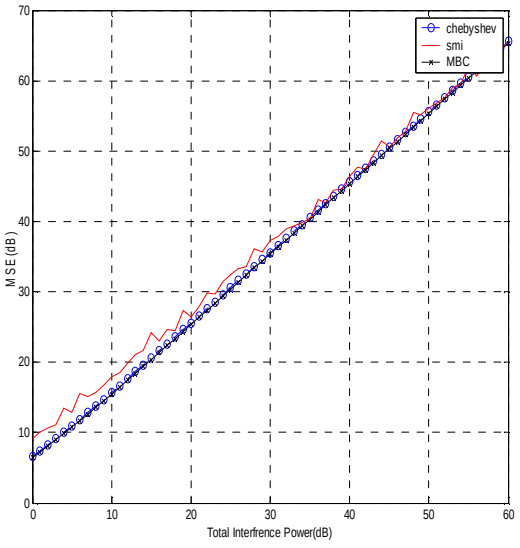

(d) MSE variation with Interference power for 40 Interferers

Figure 3.46- Variation of different Performance Metrics of three beamformers for 40 interferers. Few interferers are lying in low side lobe region of MBC

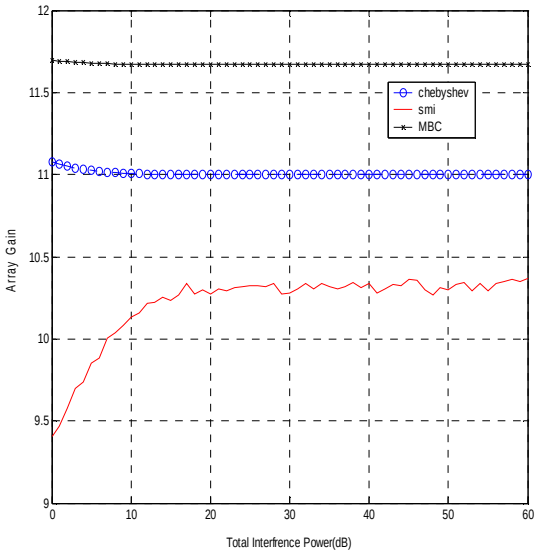

(a) Array Gain variation with Interference power for 54 Interferers

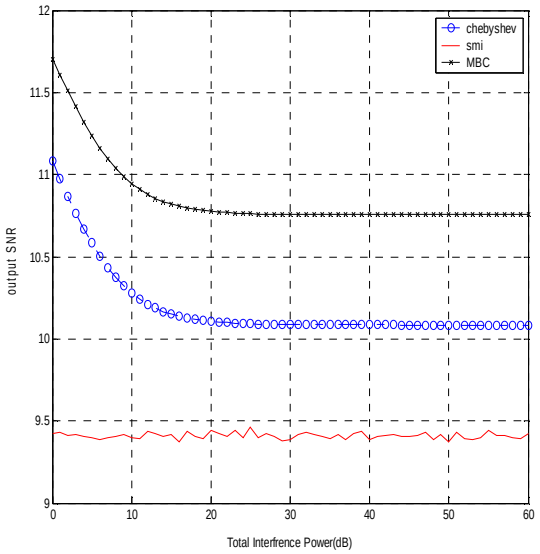

(b) Output SNR variation with Interference power for 54 Interferers

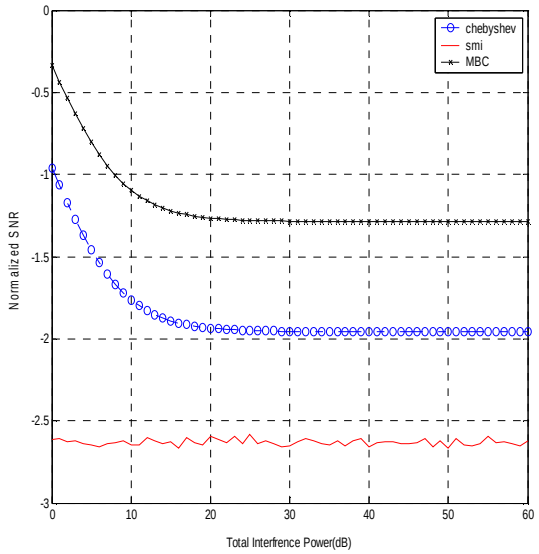

(c) Normalized SNR variation with Interference power for 54 Interferers

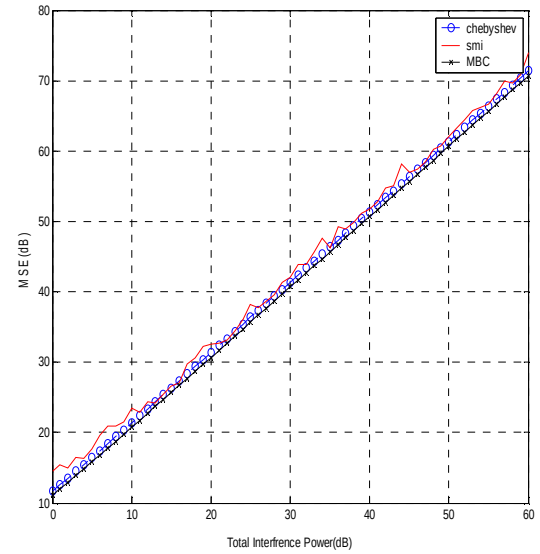

(d) MSE variation with Interference power for 54 Interferers

Figure 3.47- Variation of different Performance Metrics of three beamformers for 54 interferers. Few interferers are lying in low side lobe region of MBC

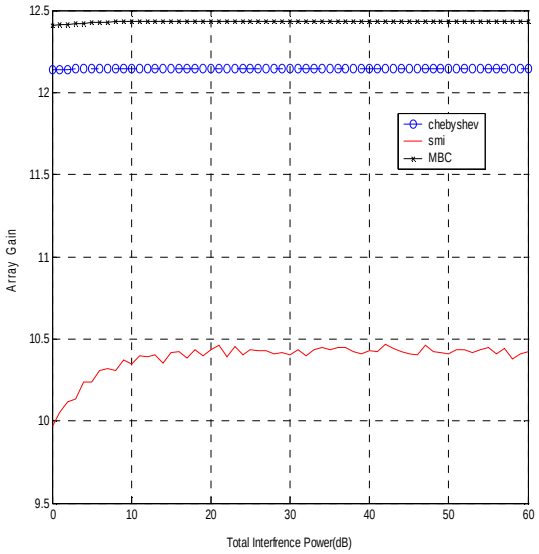

(a) Array Gain variation with Interference power for 65 Interferers

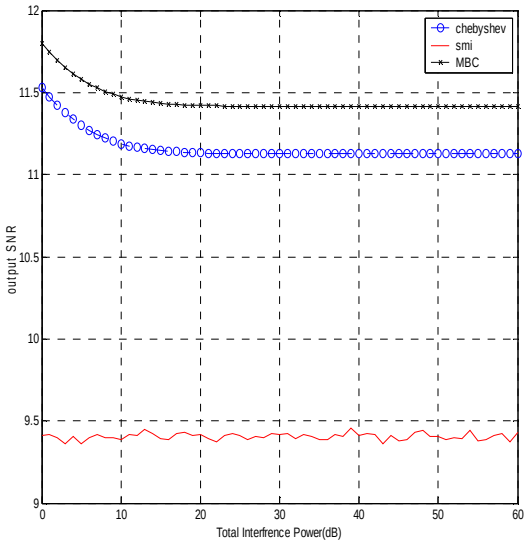

(b) Output SNR variation with Interference power for 65 Interferers

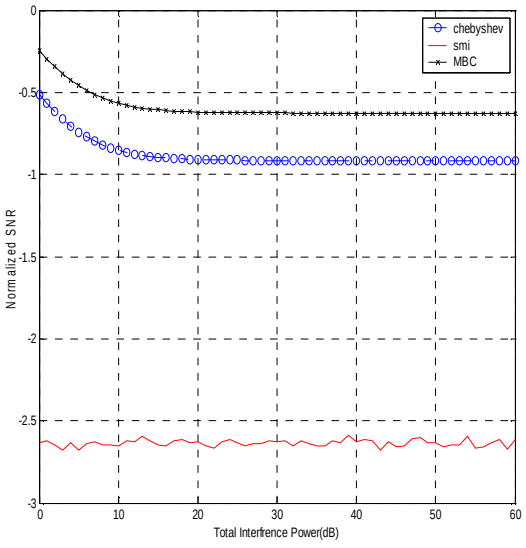

(c) Normalized SNR variation with Interference power for 65 Interferers

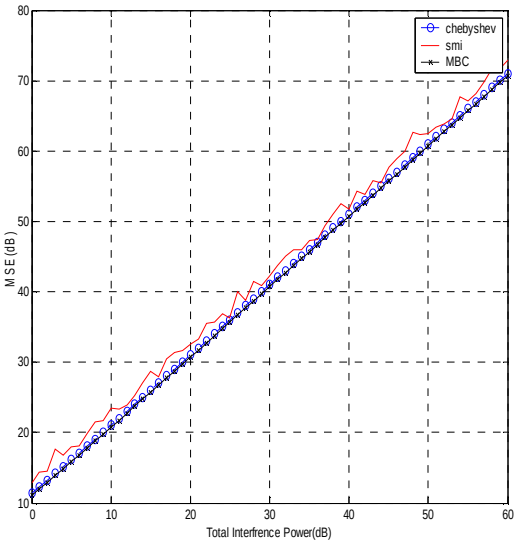

(d) MSE variation with Interference power for 65 Interferers

Figure 3.48- Variation of different Performance Metrics of three beamformers for 65 interferers. Few interferers are lying in low side lobe region of MBC

3.10.5 RESULTS AND DISCUSSIONS

1. Figs.3.39 and 3.40 show the performance metrics of three beamformers for five interferers. The difference between two figures is that in Fig.3.39 the interferers are not in the low side lobe region of MBC while in Fig.3.40 these interferers fall in the low side lobe region of MBC, resulting in improved performance of this beamformer.
2. For less number of interferers and for low level of jamming the array gain of Chebyshev beamformer is best amongst the three beamformers, the MBC's array gain is in between Chebyshev and SMI as shown in Fig.3.39 (a). For low level of jamming the Chebyshev & MBC beamformers array gain is better than the SMI weighted beamformer due to their much lower (-40 dB) sidelobe levels as shown in Fig.3.39 (a).
3. The array gain of Chebyshev and MBC, however, begins to degrade when the jamming level increases above about 28 dB. The reason that the degradation occurs around 28 dB as opposed to around 40 dB is because jamming, unlike noise, adds coherently across the array. There are 16 elements which provide 12 dB of coherent gain for the interferers. The SMI beamformer adaptively nulls each of the interferers, and thus provides performance that is independent of the jamming power. Overall the performance of SMI beamformer is quite good in terms of array gain for less number of interferers over high jamming powers.
4. For the case of largely spread interferers lying in deep low side level (-80dB) of MBC and for low level of jamming power, the MBC array gain is better than Chebyshev as sidelobe levels in MBC are better behaved than those of the Chebyshev beamformer as shown in Fig. 3.40(a).
5. The array gain is about 12 dB ($10 \log_{10} M$) for each of the three beamformers when the jamming level is small as shown in Figs.3.39 (a) and 3.40(a). As the jamming level increases the array gain values for each of the beamformers increase in recognition of the fact that the interferers are being suppressed. For the Chebyshev & MBC beamformers there is a limit to the amount of array gain is dictated by the level of the beampattern sidelobes. The adaptive beamformer, SMI is able to null the interferers all of the way down to the noise floor. Thus, they achieve an array gain that is equal to the total jamming power plus the coherent gain from M elements. For example, with M = 16 elements (12 dB) and a jamming power of 60

dB, a total array gain of ≈72 dB is possible. The SMI beamformer approaches this level of array gain. This shows the benefit of adaptive interferer nulling as opposed to deterministic side-lobe beamformer for small number of interferers even with large jamming powers[7].

6. In case of output SINR as shown in Fig.3.39 (b), for low jamming levels the beamformer results are clustered around 12 dB. The element-level SNR is 0 dB in this example and there are 16 elements. Thus 12 dB is the value of output SINR that would be expected. As the interferering level increases the Chebyshev and MBC beamformers each reach a threshold beyond which OSINR performance begins to degrade. The SMI algorithm however provides interferer nulling throughout jamming level and thus is able to maintain the peak level of OSINR[8].
7. The performance metric normalized SINR, being a normalized version of output SINR, the only difference between figures of the Output SINR and Normalized SINR is the y-axis scaling.
8. The performance metric MSE gives mean squared error variation with jamming level.
9. As the number of interferers is increased to 9 the array gain for MBC and Chebyshev remain constant around 10dB with increase in jamming power. The array gain for SMI, for 60 dB jamming power, has fallen from 72 dB to 45 dB as shown in Fig. 3.41(a). The MSE has also increased as compared to the case of 5 interferers. But the OSNIR of SMI remains constant and while that of Chebyshev and MBC falls, with increase in interfering power. In this case, the angles of arrival of interferers are not in the low side-lobe region of MBC.
10. When the number of interferes are increased to 15 as shown in Fig.3.42(a), the array gain for SMI has decreased to 21 db while the AG for Chebyshev and MBC increases to 11.2dB and 11.5 dB respectively. In this case, only one interferer is assumed to be lying in low side lobe region. The OSNIR of SMI starts falling and while that of MBC and Chebyshev starts improving for higher value of jamming power as shown in Figure 3.42(b). The MSE for SMI also increases with increase in jamming power as shown in figure 3.42(d).

---

7. [P4] "Output SNR Improvement in Array Processing Architectures of WCDMA Systems by Low Side Lobe Beamforming", ***accepted for publication in International Journal of Springer on Wireless Personal Communications.***
8. [P15] "Performance Improvement in Array Processing Architectures of WCDMA Systems by Low Side Lobe Beamforming", Proceedings of ***IEEE 9th International conf. on Personal Wireless Communications***,pp.324-328, 24-26th January, 2005, N.Delhi.
9. [P22] "Output SNR Improvement in Array Processing Architectures of WCDMA Systems by Low Side Lobe Beamforming", Proceedings of ***National Conference of Communications (NCC-2005) IIT, Kharagpur*** pp.167-171, 28-29th January, 2005

11. With increase in number of interferers to 21 and more interferers lying in low side lobe region of MBC, it is seen that the various performance metrics of SMI start falling, while that of Chebyshev and MBC start improving. But there is more improvement in case of MBC as compared to Chebyshev as shown in Fig. 3.43(a-d).The same improvement is observed for MBC beamformer in case of 25 interferers as shown in Fig.3.44(a-d)
12. In case the number of interferers are increased to 31 the various performance metrics of SMI falls below that of Chebyshev and MBC as shown in Figure 3.45(a-d). This clearly shows that in case of large number of interferers the adaptive nulling SMI algorithm is not able to give desired performance characteristics. It means the conventional arrays based on nulling procedure are unlikely to be applicable in practical CDMA based wireless communication even if their beamforming procedure is valid for coherent interferers[9]. The performance metrics for large number of interferers 40, 54 and 65 are shown in Figs. 3.46, 3.47and 3.48 respectively. The variation of various performance metrics with the increasing number of interferers and jamming power is given in tables 3.7 & 3.8.

3.11 SUMMARY OF THE CHAPTER

In a CDMA system all transmitted signals turn out to be disturbing factors to all other users in the system in the form of interference. Therefore the system capacity strongly depends on the interference level in the system. It is shown in this chapter that antenna arrays with steer able low side lobes can reduce interference in CDMA based wireless communication systems and can increase array performance. The various performance metrics of array processing architectures were found to be inversely proportional to MSE. Any signal processing technique by which MSE can be decreased, shall further improve the performance of array processing architectures. So in the next chapter new array processing algorithm based on Fractional Fourier Transform is developed, which can decrease the MSE in the a^{th} domain as compared to frequency or space domain. In chapter 6, an application of low side lobe beamforming is presented in which it is shown that by forming low side lobes towards the direction of head the radiation hazards can be reduced.

---

10. [P26] "Performance improvements in various performance metrics of array processing architectures of CDMA based systems by use of low side lobe beamforming" under review in *IETE Journal of research*.

Table-3.7: NSINR & OSNR of beamformers for increasing interfering powers and with increased number of interferers

NORMALIZED SIGNAL TO NOISE RATIO* (dB)

Total Interference power (dB)	Number of Interferers : 5			Number of Interferers : 9			Number of Interferers : 15			Number of Interferers : 21			Number of Interferers : 25			Number of Interferers : 31			Number of Interferers : 40			Number of Interferers : 54			Number of Interferers : 65		
	SMI	CHEB	MBC	SMI	CHEB	MBC	SMI	CHEB	MBC	SMI	CHEB	MBC	SMI	CHEB	MBC	SMI	CHEB	MBC	SMI	CHEB	MBC	SMI	CHEB	MBC	SMI	CHEB	MBC
0	2.65	0.02	0.02	2.60	0.34	0.18	2.64	0.24	0.08	2.63	0.15	0.01	2.65	0.91	0.34	2.68	0.06	0.10	2.63	0.02	0.13	2.63	0.95	0.33	2.63	0.51	0.24
10	2.64	0.01	0.02	2.63	2.37	2.17	2.63	1.62	1.41	2.63	0.95	0.74	2.62	1.84	1.16	2.65	0.66	0.45	2.61	0.49	0.29	2.61	1.76	1.09	2.64	0.85	0.56
20	2.60	0.22	0.12	2.63	5.44	5.22	2.63	3.13	2.92	2.61	1.99	1.78	2.59	2.25	1.56	2.61	1.09	0.88	2.61	0.84	0.63	2.62	1.93	1.26	2.68	0.91	0.62
30	2.61	2.32	1.66	2.62	10.3	10.1	2.59	4.71	4.50	2.66	3.30	3.09	2.60	2.73	2.03	2.66	1.56	1.34	2.60	1.43	1.22	2.64	1.95	1.28	2.60	0.91	0.62
40	2.64	9.17	7.68	2.65	19.1	18.8	2.63	6.77	6.56	2.62	3.76	3.55	2.65	3.12	2.42	2.62	1.93	1.72	2.65	1.82	1.61	2.61	1.95	1.28	2.60	0.91	0.62
50	2.63	18.6	16.9	2.61	28.9	28.7	2.59	9.14	8.93	2.64	4.51	4.30	2.60	3.20	2.50	2.63	2.12	1.91	2.61	2.02	1.81	2.61	1.95	1.28	2.66	0.91	0.62
60	2.62	28.5	26.8	2.64	38.9	38.7	2.60	12.3	12.1	2.64	6.32	6.10	2.65	3.20	2.51	2.60	2.19	1.98	2.63	2.09	1.87	2.61	1.95	1.28	2.63	0.91	0.62

*All values are -dB

OUTPUT SIGNAL TO NOISE RATIO (dB)

Total Interference power (dB)	Number of Interferers : 5			Number of Interferers : 9			Number of Interferers : 15			Number of Interferers : 21			Number of Interferers : 25			Number of Interferers : 31			Number of Interferers : 40			Number of Interferers : 54			Number of Interferers : 65		
	SMI	CHEB	MBC	SMI	CHEB	MBC	SMI	CHEB	MBC	SMI	CHEB	MBC	SMI	CHEB	MBC	SMI	CHEB	MBC	SMI	CHEB	MBC	SMI	CHEB	MBC	SMI	CHEB	MBC
0	9.38	12.0	12.0	9.43	11.6	11.8	9.39	11.7	11.9	9.40	11.8	12.0	9.38	11.1	11.6	9.35	12.0	12.1	9.40	12.0	12.2	9.40	11.1	11.7	9.41	11.5	11.8
10	9.39	12.0	12.0	9.40	9.66	9.86	9.40	10.4	10.6	9.40	11.1	11.2	941	10.2	10.8	9.38	11.4	11.5	9.43	11.5	11.8	9.42	10.3	11.0	9.39	11.1	11.5
20	9.43	11.8	11.9	9.41	6.60	6.81	9.40	8.90	9.11	9.42	10.0	10.2	9.44	9.78	10.4	9.42	11.0	11.1	9.43	11.2	11.4	9.41	10.1	10.8	9.35	11.1	11.4
30	9.43	10.3	10.3	9.42	1.66	1.87	9.44	7.32	7.53	9.37	8.73	8.94	9.43	9.31	10.0	9.37	10.5	107	9.43	10.6	10.8	9.40	10.1	10.7	9.43	11.1	11.4
40	9.39	-2.9	-4.3	9.38	-7.1	-6.8	9.40	5.26	5.47	9.41	8.27	8.48	9.38	8.91	9.61	9.41	10.1	10.3	9.38	10.2	10.4	9.42	10.1	10.7	9.43	11.1	11.4
50	9.40	-6.6	-4.9	9.42	-17	-16	9.44	2.89	3.10	9.39	7.52	7.73	9.43	8.83	9.53	9.40	9.91	10.1	9.42	10.0	10.2	9.42	10.1	10.7	9.38	11.1	11.4
60	9.42	-17	-15	9.39	-27	-26	9.43	-0.3	-0.1	9.39	5.72	5.93	9.38	8.83	9.52	9.43	9.84	10.0	9.40	9.95	10.2	9.42	10.1	10.7	9.40	11.1	11.4

Table-3.8: AG & MSE of beamformers for increasing total interfering powers and with increased number of interferers

ARRAY GAIN

Total Interference power (dB)	Number of Interferers : 5			Number of Interferers : 9			Number of Interferers : 15			Number of Interferers : 21			Number of Interferers : 25			Number of Interferers : 31			Number of Interferers : 40			Number of Interferers : 54			Number of Interferers : 65		
	SMI	CHEB	MBC	SMI	CHEB	MBC	SMI	CHEB	MBC	SMI	CHEB	MBC	SMI	CHEB	MBC	SMI	CHEB	MBC	SMI	CHEB	MBC	SMI	CHEB	MBC	SMI	CHEB	MBC
0	12.3	15.0	15.0	7.6	9.9	10.0	9.0	11.4	11.6	10.1	12.6	12.7	10.6	12.2	12.8	11.4	13.9	14.1	12.3	14.9	15.1	9.4	11.1	11.7	9.9	12.1	12.4
10	19.7	24.4	22.4	8.9	9.1	9.3	10.2	11.2	11.5	11.0	12.7	12.9	11.5	12.3	13.0	12.3	14.3	14.5	13.3	15.4	15.7	10.2	11.0	11.7	10.3	12.1	12.4
20	29.4	31.7	31.8	11.8	9.0	9.2	11.7	11.3	11.5	12.1	12.7	12.9	11.9	12.3	13.0	12.9	14.4	14.5	13.7	15.5	15.7	10.3	11.0	11.7	10.4	12.1	12.4
30	39.3	39.6	40.2	16.8	9.0	9.2	13.3	11.2	11.5	13.3	12.7	12.9	12.4	12.3	13.0	13.3	14.4	14.5	14.3	15.5	15.7	10.3	11.0	11.7	10.4	12.1	12.4
40	49.2	42.7	44.2	25.5	9.0	9.2	15.4	11.3	11.5	13.8	12.7	12.9	12.8	12.3	13.0	13.7	14.4	14.5	14.7	15.5	15.7	10.3	11.0	11.7	10.5	12.1	12.4
50	59.2	43.2	44.9	35.3	9.0	9.2	17.8	11.3	11.5	14.6	12.7	12.9	12.9	12.3	13.0	13.9	14.4	14.5	14.9	15.5	15.7	10.3	11.0	11.7	10.4	12.1	12.4
60	69.2	43.2	44.9	45.3	9.0	9.2	20.9	11.2	11.5	16.4	12.7	12.9	12.9	12.3	13.0	13.0	14.4	14.5	14.9	15.5	15.7	10.3	11.0	11.7	10.4	12.1	12.4

MEAN SQUARED ERROR

Total Interference power (dB)	Number of Interferers : 5			Number of Interferers : 9			Number of Interferers : 15			Number of Interferers : 21			Number of Interferers : 25			Number of Interferers : 31			Number of Interferers : 40			Number of Interferers : 54			Number of Interferers : 65		
	SMI	CHEB	MBC	SMI	CHEB	MBC	SMI	CHEB	MBC	SMI	CHEB	MBC	SMI	CHEB	MBC	SMI	CHEB	MBC	SMI	CHEB	MBC	SMI	CHEB	MBC	SMI	CHEB	MBC
0	2.48	.003	.002	9.31	6.63	6.46	9.95	6.6	6.4	10.7	6.63	6.46	9.0	7.51	6.94	9.20	6.63	6.5	9.69	6.6	6.4	13.7	11.7	11.0	14.6	11.4	11.1
10	2.57	0.03	0.02	16.2	15.7	15.4	17.7	15.6	15.4	18.2	15.6	15.4	17.0	16.7	16.0	17.4	15.6	15.5	18.7	15.6	15.5	21.7	21.4	20.7	23.9	21.0	20.8
20	2.68	0.32	0.22	23.2	25.6	25.3	25.4	25.5	25.3	26.7	25.5	25.3	27.0	26.5	26.0	26.7	25.6	25.4	28.4	25.5	25.3	32.7	31.3	30.6	33.2	31.0	30.7
30	1.94	2.44	1.78	27.1	35.7	35.3	34.3	35.5	35.3	35.1	35.5	35.3	36.7	36.6	36.0	36.1	35.6	35.4	37.0	35.5	35.3	42.1	41.4	40.6	42.8	41.0	40.7
40	4.02	9.33	7.84	28.4	45.7	45.3	41.5	45.5	45.3	43.7	45.5	45.3	46.8	46.6	46.0	46.1	45.6	45.4	48.0	45.5	45.3	51.8	51.4	50.6	53.1	51.0	50.7
50	2.44	18.8	17.2	30.2	55.7	55.3	48.2	55.5	55.3	3.0	55.5	55.3	55.1	56.6	56.0	56.4	55.6	55.4	56.1	55.5	55.3	61.8	61.4	60.6	63.9	61.0	60.7
60	4.15	28.8	27.0	27.9	65.7	65.3	55.7	65.5	65.3	63.0	65.5	65.3	66.4	66.6	66.0	66.7	65.6	65.4	66.5	65.5	65.3	72.2	71.4	70.6	71.5	71.0	70.7

Chapter 4

OPTIMUM ARRAY PROCESSING USING FRACTIONAL FOURIER TRANSFORM

4.1 INTRODUCTION

The subject of array processing is concerned with the extraction of information from signals collected using array of sensors. The information of interest may be the signal itself (communications) or the location of the source or reflection that produces the signal (radar and sonar). In communication the signal is transmitted by the wireless mobile or fixed transmitter. In all of these cases, the signal that arrives at the array can be regarded as a non-stationary random process [142]. In active sensing situations such as radar and sonar, a known waveform is generated which in turn propagates through a medium and is reflected by some target back to the array. In this chapter the multipath faded signal received at the array is processed to get the optimum weights using FrFT. As discussed in chapter 3 all performance metrics of array processing architecture are inversely proportional to mean square error (MSE), and if it is possible to reduce the MSE the performance of array processing architecture will definitely improve. Hence in this chapter the array processing algorithm using FrFT is proposed, by which the MSE of the beamformer can be reduced to a greater extent. This chapter deals with linear, discrete-time; FrFT based adaptive finite impulse response filtering for reducing MSE. The beamformer considered here is based on Wiener filtering discussed next.

4.2 WIENER FILTERING

The Wiener filter is a fundamental building block for linear adaptive filtering [142] as shown in Fig. 4.1. The Wiener filter is optimal in the sense of minimizing the MSE of the output [23]. The solution of the classical Wiener filter is given by

$$\boldsymbol{w}_{\text{opt}} = \boldsymbol{R}_{\text{x}_0}^{-1}\boldsymbol{r}_{\text{x}_0\text{d}_0} . \tag{4.1}$$

$\boldsymbol{R}_{x_0}$ is the correlation matrix of the input data vector $\boldsymbol{x}_0(k)$, and $\boldsymbol{r}_{x_0 d_0}$ is the cross-correlation vector between the input data vector $\boldsymbol{x}_0(k)$ and the desired signal $d_0(k)$

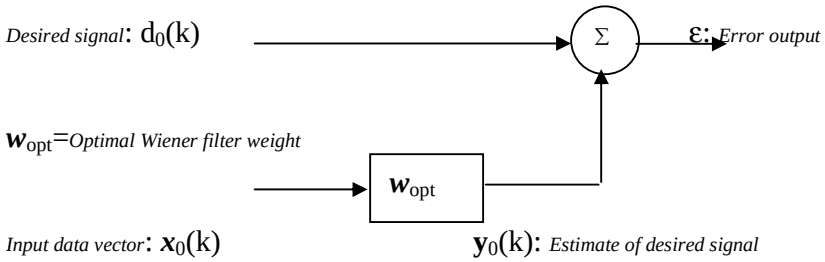

Figure 4.1-The Classical Wiener Filter

When the statistics associated with $\boldsymbol{R}_{x_0}$ and $\boldsymbol{r}_{x_0 d_0}$ are known exactly then the MMSE estimate of $d_0(k)$ is obtained and filter is referred as "optimal". In general, of course, the statistics are not known but rather are estimated from the data. This filtering solution is referred as "adaptive". The Wiener filter can be applied to a wide variety of adaptive signal processing problems. Four fundamental classes of problems are shown in Fig. 4.2. These are equalization, prediction, system identification, and interference cancellation. These problems represent different architectural arrangements of the plant, adaptive filter, and delay elements [23, 32,142].

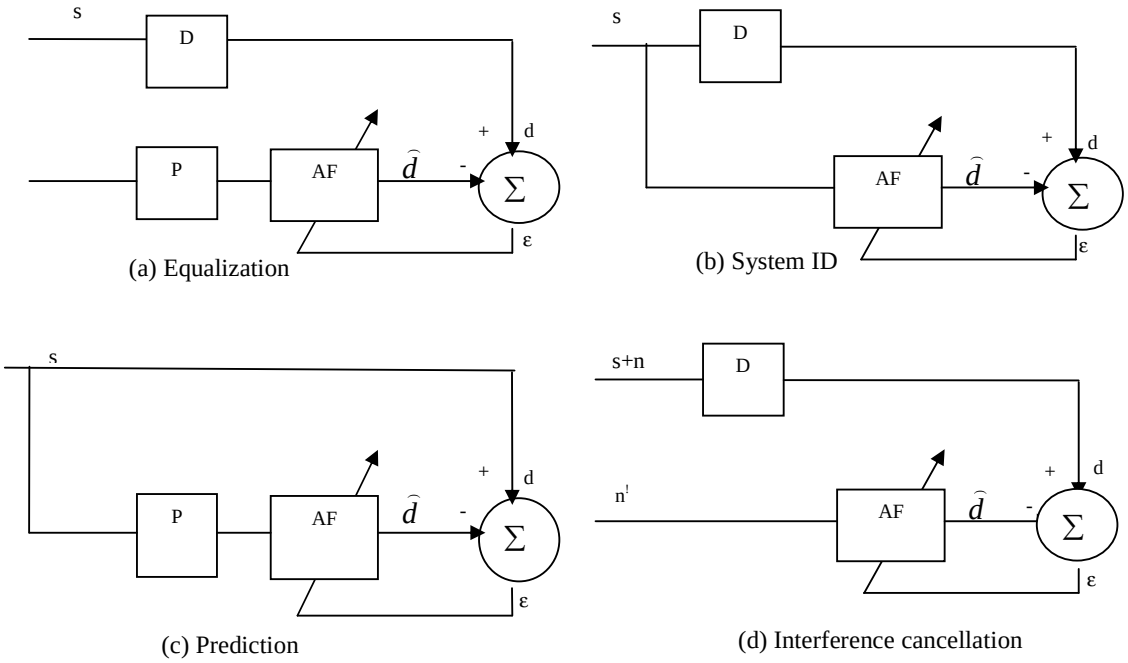

Figure 4.2-Different Classes of Problems for Adaptive Signal Processing: P=Plant, D=Delay, AF=Adaptive Filter, s=signal, n=noise, d=desired signal, ε=error signal

The applications of adaptive filter are listed in table 4.1

Table-4.1: Applications of adaptive filter

Class of adaptive filtering	Application	Purpose
Identification [23]	System identification	In exploration seismology
Inverse Modeling	Equalization	Channel equalization in communication
Prediction	Predictive coding, spectrum analysis	Power spectrum of signal of interest in coding of prediction error
Interference cancellation [31, 95]	Noise cancellation, beamforming	Echo cancellation, cancellation of interfering signals

From many of the system applications cited above, the work in this chapter is concerned with array processing for mobile communication and wireless communication. The block diagram of an adaptive array is shown in Fig.4.3. This array contains an individual receiver at each element and thus there are M simultaneous measurements, at the input to the adaptive array processor.

$$\boldsymbol{x} = [x_1\ x_2\ x_3\ \_\ \_\ \_\ x_M]^T , \tag{4.2}$$

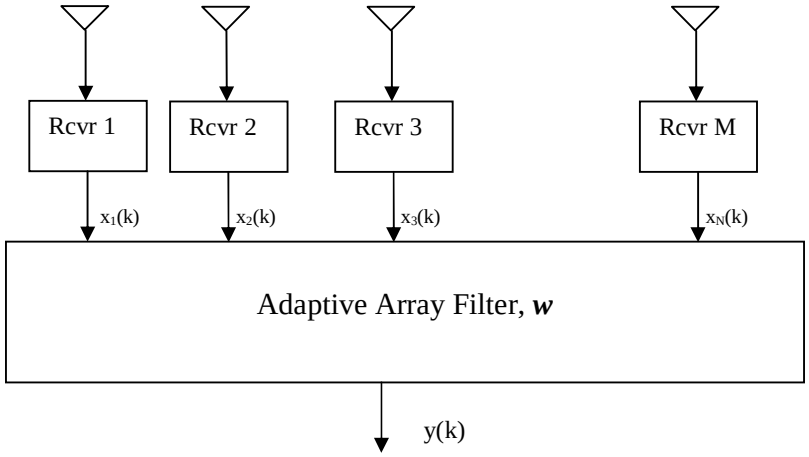

Figure 4.3-Block Diagram of an Adaptive Array: Each element has its own receiver.

The main aim of this chapter is to find array processing algorithm using FrFT with

1) Reduced Mean squared error in wireless as well as mobile communication.
2) Application to beamforming in Wireless and mobile communication with improved performance in different multipath environments.

Further the proposed algorithm shall be used to

1) Find the MSE at the output of a beamformer in time, frequency and FrFT domain for a moving source with fixed input SNR and to study the variation of MSE with varying input SNR, in case of a moving source.
2) Find the MSE at the output of a beamformer in time, frequency and FrFT domain beamforming for an accelerating source with fixed input SNR and to study the variation of MSE with varying input SNR in case of an accelerating source.
3) BER of proposed algorithm in a mobile environment in SIMO system.

A brief overview of adaptive array processing and Fractional Fourier Transform is given in chapter 3. The antenna array model used in this chapter for deriving optimal beamformer is discussed first.

4.3 ANTENNA ARRAY MODEL

In this chapter the antenna array model described in section 3.5.2 is used. The received signal, $\boldsymbol{x}$, is assumed to be the sum of three components [32]

$$x(t) = x_m(t) + x_i(t) + x_n(t), \tag{4.3}$$

where, $x_m(t)$ is the received multipath signal, $x_n(t)$ is the noise signal and $x_i(t)$ is the interference signal. The multipath signal is given by

$$x_m(t) = \sum_{i=1}^{L} a_i \cos(\omega_c t + \phi_i), \tag{4.4}$$

where, a_i is the unknown amplitude, L is the number of paths. The phase ϕ_i depends on the varying path lengths, changing by 2π when the path length changes by a wavelength. Therefore, the phases are uniformly distributed over $[0, 2\pi]$. The noise is modeled as zero-mean Gaussian random processes. Since each element of the adaptive array contains its own receiver, the noise is uncorrelated from channel to channel and the noise covariance matrix has the following structure

$$\boldsymbol{R}_n = \sigma_w^2 \boldsymbol{I}. \tag{4.5}$$

The desired signal is a nonrandom signal of known amplitude and phase, i.e.,

$$x_d(t) = \cos(\omega_c t + \phi). \tag{4.6}$$

It is assumed that the signal is narrowband and satisfies the plane-wave assumption. The plane wave approximation is true in the far field of an electromagnetic source [32]. In general, the output of the receiving antenna array at time k, $y(k)$, is a linear combination of inputs of the antennas in the array as shown in Fig.4.3, that is

$$y(k) = \boldsymbol{w}^{H}\boldsymbol{x}(k), \tag{4.7}$$

where, $\boldsymbol{x}$ is the received signal column vector, and $\boldsymbol{w}$ is the beamforming weight vector of same size. The objective is to recover the desired signal free from noise from the measured signal at the array output. The objective can be achieved by optimizing weights $\boldsymbol{w}$ based upon a criterion of optimization. The main criteria of optimization are Minimum Mean Squared Error (MMSE), Maximum Signal to Noise Ratio (MSNR) and Minimum Variance (MV). Each criterion has its own advantages and disadvantages. The MMSE requires the reference signal and there is no requirement of the information about DOA of the signal. The MSNR requires direction of arrival of both desired and interfering signals. In this the weights are chosen so that the SNR at the output of the beamformer is maximised. The MV method does not require knowledge of the angle of arrival of interferences but it requires the angle of arrival of desired signal. In this the output power is minimized to ensure that the effect of noise is minimized. The beamformer based on optimal weights is known as optimal beamformer. The method used in this work can be viewed as the generalization of MSE, which minimizes error between its output and the desired signal based upon Wiener solution.

4.4 WIENER SOLUTION

Most of the adaptive algorithms try to minimize the mean-squared error between the desired signal d(t) and the array output y(t). Let $y(k)$ and $d(k)$ denote the sampled signal of y(t) and d(t) at time instant t_k , respectively. Then the error signal is given by

$$e(k) = d(k) - y(k). \tag{4.8}$$

The estimation error $e(k)$ is the sample value of a random variable. To optimize filter design, the mean square value of $e(k)$ is minimized. The cost function of mean square error is defined as

$$J = E[|e(k)|^2], \tag{4.9}$$

where, E denotes the expectation operator.

$$J = E\,[\,|d(k) - y(k)|^2] \tag{4.10}$$

$$= E[|d(k)|^2] - \boldsymbol{p}^{H}\boldsymbol{w} - \boldsymbol{w}^{H}\boldsymbol{p} + \boldsymbol{w}^{H}\boldsymbol{R}\boldsymbol{w}, \tag{4.11}$$

where, $$\boldsymbol{R} = E[\boldsymbol{x}(k)\boldsymbol{x}^{H}(k)] \tag{4.12a}$$

and $$\boldsymbol{p} = E[\boldsymbol{x}(k)\boldsymbol{d}^{*}(k)]. \tag{4.12b}$$

$\boldsymbol{R}$ is the $M \times M$ correlation matrix of the input data vector $\boldsymbol{x}$(k), and $\boldsymbol{p}$ is the $M \times 1$ cross-correlation vector between the input data vector and the desired signal d(k). The requirement is to find the operating conditions under which $\boldsymbol{J}$ attains the minimum value. The gradient vector of $\boldsymbol{J}$, $\nabla \boldsymbol{J}$, is defined by

$$\nabla \boldsymbol{J} = 2\frac{\partial \boldsymbol{J}}{\partial \boldsymbol{w}^*}, \tag{4.13}$$

where, $\frac{\partial}{\partial \boldsymbol{w}^*}$, denotes the conjugate derivative with respect to the complex vector $\boldsymbol{w}$. When the mean-squared error $\boldsymbol{J}$ is minimized, the gradient vector will be equal to $\mathrm{M} \times 1$ null vector.

$$\nabla \boldsymbol{J} \Big|_{\boldsymbol{w}_{\mathrm{opt}}} = \boldsymbol{0}. \tag{4.14}$$

Substituting (4.11) into (4.14), gives

$$\boldsymbol{R}\boldsymbol{w}_{opt} = \boldsymbol{p}, \tag{4.15}$$

where, $\boldsymbol{w}_{opt}$ denotes the $\mathrm{M} \times 1$ optimum weight vector of the filter (optimum in mean square error sense) i.e.

$$\boldsymbol{w}_{opt} = [w_{o1}, w_{o1}, \ldots\ldots\ldots\ldots\ldots\ldots w_{oM}]. \tag{4.16}$$

Equivalently (4.15) can be written as

$$\boldsymbol{w}_{opt} = \boldsymbol{R}^{-1}\boldsymbol{p}. \tag{4.17}$$

The optimum weight vector $\boldsymbol{w}_{opt}$ in (4.17) is called the Wiener solution. From (4.17), it can be seen that computation of the optimum weight vector $\boldsymbol{w}_{opt}$ requires knowledge of two quantities:

(i) Correlation Matrix $\boldsymbol{R}$ of the input vector $\boldsymbol{x}$(k) of beamformer

(ii) Cross Correlation vector $\boldsymbol{p}$ between input vector $\boldsymbol{x}$(k) and desired response d(k).

(4.17) can also be written as $\boldsymbol{w}_{opt} = \boldsymbol{R}_x^{-1}\boldsymbol{r}_{xd}$, (4.18)

where, $\boldsymbol{R}_{\mathrm{x}}$ is the covariance matrix of the measurements at the sensor and $\boldsymbol{r}_{xd}$ is the cross covariance between the measurements at the sensors and the desired signal defined by (4.12a) and (4.12b).

4.5 WIENER FILTERING IN FRACTIONAL FOURIER DOMAIN

The FrFT and its properties have been explained in section 3.6.1.The FrFT, being just an extension of the classical Fourier transform (FT), can be used effectively

in all situations where the FT is presently being used [140]. The ordinary Fourier transform is suited for analysis and processing of time invariant signals and systems [114]. When dealing with time variant signals and systems the FrFT allows estimating signals with smaller MSE. Some gains can be expected in most of these applications because of the additional degree of freedom (angle of rotation) that the FrFT provides. The continuum of fractional Fourier domains corresponds to oblique axes in the time frequency plane, with the ordinary time or frequency domains as special cases as shown in Fig.4.4. The central concept in beamforming in time or frequency domain and the FrFT leads to generalization of these domains [64].

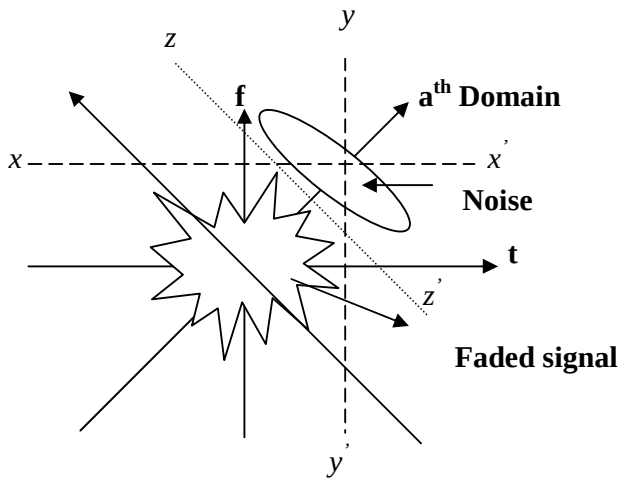

Figure 4.4-Filtering in Fractional Fourier Domain

In mobile communication and wireless communication the received signal is generally degraded by multiplicative fading and additive noise and the problem is to eliminate these degradations. The FrFT can remove these degradations effectively in Fractional Fourier domains as shown in Fig.4.4. This depends upon the observation model and the objectives as well as prior knowledge available about the desired signal, degradation process and noise. To find the advantage of filtering in fractional Fourier domains consider Fig. 4.4 [65] where the Wigner distribution of a desired signal and undesired noise are superimposed. The noise can not be separated completely in time or frequency domains. In case the noise is removed in time domain then filter will remove noise only after line yy′ so the filtered signal will be associated with some noise. Similarly in frequency domain, the filter will remove noise after line xx′ and the filtered signal will be having some noise. But, in case the filtering is done in a^{th} order fractional

Fourier domain then the noise will be completely removed, as it can be observed that the signal and noise are overlapping both in time and frequency domains but they don't overlap in a^{th} domain. So the signal can be separated from noise by cutting along line zz′. Thus the signal can be separated from noise easily in fractional Fourier domain.

The antenna array model described in section 4.3 is used for finding the optimum weights in FrFT domain. The weights of the array are chosen to minimize the MSE between the array output and reference signal. When the channel is time invariant and the input and noise processes are stationary the optimal filter is given by (4.18). The optimal Wiener filter thus formed is also time invariant and thus can be expressed as convolution and can be implemented using Fast Fourier Transform algorithm and can be expressed as a multiplicative filter in time or frequency domain as shown in Figs. 4.5a & 4.5b.

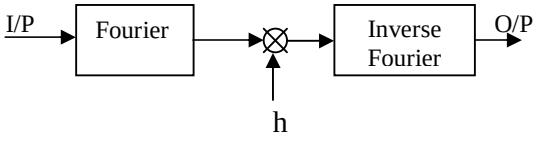

Figure 4.5(a)-Filtering in frequency domain

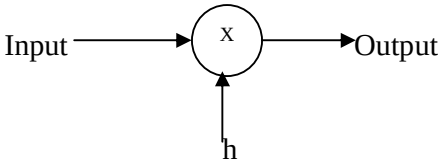

Figure 4.5(b)-Filtering in time domain

However for time variant or non stationary processes the optimal filter will not be time invariant and can not be expressed as shown in Fig.4.5. The wiener filter in ordinary time or frequency domain can be generalized to filtering in the a^{th} order Fractional Fourier domain as shown in Fig.4.6.

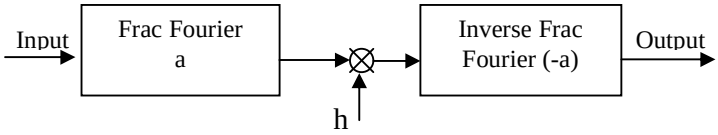

Figure 4.6-Filtering in a^{th} order fractional Fourier Domain

For a=1 it reduces to ordinary frequency domain multiplicative filter (Fig 4.5a) and for a=0 it reduces to time domain multiplicative filter (Fig 4.5b) [148]. The noise can be easily eliminated in fractional Fourier domain by using an amplitude mask in the a^{th} domain. Hence the process of obtaining the output of filter is defined as follows: First take a^{th} order fractional Fourier transform of the incoming signal x(n) then multiply the transformed signal with the filter function h(n) and finally take inverse a^{th} order fractional Fourier transform. The resulting estimate $f_{one}(n)$ is given by

$$f_{one}(n) = [F^{-a} \Lambda_h F^a]\boldsymbol{x}(n) = T_{one}\boldsymbol{x}(n) \quad , \tag{4.19}$$

where, F^a denotes the a^{th} order fractional Fourier operator and Λ_h denotes the operator corresponding to the multiplication by the filter function h(n) and T_{one} is the operator representing the overall filtering configuration. The FrFT has an efficient implementation at the same cost as Fourier domain filtering [104]. The problem remains only to find the optimum filter function. Once the optimal filter function is found it is possible to find the MSE for different values of 'a' and the value of 'a' resulting in lowest value of MSE can be determined. Fourier domain filtering is special case for a=1. In some cases the value of a=1 results in smallest error but in general it is found that the value of 'a' is different from a=1.

4.5.1 Derivation of the optimal filter function in fractional Fourier domain

To derive the optimal filter function let the observed signal *y* be related to transmitted signal *x* by

$$y(t) = \int_{-\infty}^{\infty} h(t,t')x(t')dt' + n(t), \tag{4.20}$$

where, $h(t,t')$ is the kernel of the degradation model and n(t) is the additive noise term. It is assumed that as a prior knowledge, the correlation functions of the input signal *x* (desired signal) and the noise are known

$$\begin{aligned} \boldsymbol{R}_{xx}(t,t') &= E[x(t)x^*(t')] \\ \boldsymbol{R}_{nn}(t,t') &= E[n(t)n^*(t')] \end{aligned} . \tag{4.21}$$

Further it is assumed that the noise is independent of the input and it is zero mean for all time, i.e. E[n(t)]=0 $\forall$t. Under these assumptions, the cross correlation function of the process *x* and *y* can also be found

$$\boldsymbol{R}_{xy}(t,t') = E[x(t)y^*(t)]. \tag{4.22}$$

First, consider the most general linear estimate of the form

$$\hat{x}(t) = \int_{-\infty}^{\infty} g(t,t')y(t')dt' . \tag{4.23}$$

Setting the objective is minimizing MSE defined as

$$\sigma_e^2 = E[\|x - \hat{x}\|^2], \tag{4.24}$$

where, E[.] denotes the expectation operator and $\|.\|$ denotes the L_2 norm given by

$$\|x\|^2 = \int_{-\infty}^{\infty} x(t)x^*(t)dt . \tag{4.25}$$

This definition (4.24) of the MSE is appropriate for nonstationary signals whose functional representations are square integrable (that are of finite energy). (For stationary processes, the MSE may be defined as the expected value of the magnitude squared of the difference term [142].) The recovery operator kernel is the solution to the minimization problem

$$g_{opt}(t,t') = \arg\min_{g} \sigma_e^2 , \tag{4.26}$$

that is, it is the function that minimizes the MSE. The solution to this problem, with the linear estimate defined in (4.23), is known. It is the solution of the following equation:

$$R_{xy}(t,t') = \int_{-\infty}^{\infty} g_{opt}(t,t'')\boldsymbol{R}_{yy}(t'',t')dt'' \qquad \forall t,t'. \tag{4.27}$$

The above equation can be solved numerically to obtain the kernel of the optimal linear recovery operator. However, application of this estimation operator on a given distorted and noisy signal would require O [N^2] time, where N is the time-bandwidth product of the signals. In this work, the estimate is restricted so that it corresponds to a multiplication with a filter function in the a^{th} fractional Fourier domain. This estimate can be written in operator notation as

$$\hat{x} = F^{-a}(g.F^{a}(y)), \tag{4.28}$$

where, F^a is the a^{th} order fractional Fourier transformation operator and g is the multiplicative filter. For a=1, this estimate corresponds to filtering in the conventional Fourier domain. With this form of estimation operator, the minimization problem considered can be defined as

$$g_{opt} = \arg\min_{g} \sigma_e^2 , \tag{4.29}$$

where, σ_e^2 is as defined in (4.24), and $\hat{x}$ is given by (4.28). The cost function J is defined to be equal to (4.24) with the estimate given by (4.28). Since fractional Fourier transform is unitary and it preserves norms, J is also equal to the MSE in the a^{th} domain

$$J = \sigma_e^2 = E[\|x - \hat{x}\|^2] = E[\|x_a - \hat{x}_a\|^2] . \tag{4.30}$$

From (4.28) $$\hat{x}_a = gy_a . \tag{4.31}$$

J varies with the choice of g since $\hat{x}_a$ varies. This function J is to be minimized with respect to g. Let $g=g_0+\alpha\delta g_0$, where α is a complex scalar parameter, g_0 is the optimum

filter, δg_0 is arbitrary perturbation term. Since α is a complex parameter, it can be expressed as $\alpha=\alpha_{re}+j\alpha_{im}$ Now, $\hat{x}_a$ and J varies with α for each fixed δg_0

$$\hat{x}_a(t_a,\alpha) = (g_0(t_a) + (\alpha_{re} + j\alpha_{im})\delta g_0(t_a))y(t_a)\,. \tag{4.32}$$

$$J(\alpha) = E\left[\int_{-\infty}^{\infty}(x_a(t_a) - \hat{x}_a(t_a,\alpha)).(x_a(t_a) - \hat{x}_a(t_a,\alpha))^* dt_a\right]. \tag{4.33}$$

The optimum value of J will be obtained from the conditions

$$\left.\frac{\partial J(\alpha)}{\partial \alpha_{re}}\right|_{\alpha=0} = 0 \qquad \left.\frac{\partial J(\alpha)}{\partial \alpha_{im}}\right|_{\alpha=0} = 0\,. \tag{4.34}$$

The partial derivatives of $J(\alpha)$ are given by

$$\frac{\partial J(\alpha)}{\partial \alpha_{re}} = -2E\left[\int_{-\infty}^{\infty}\mathrm{Re}(\kappa^*(t_a,\alpha)\tilde{\kappa}(t_a,\alpha)dt_a\right], \tag{4.35}$$

$$\frac{\partial J(\alpha)}{\partial \alpha_{im}} = -2E\left[\int_{-\infty}^{\infty}\mathrm{Im}(\kappa^*(t_a,\alpha)\tilde{\kappa}(t_a,\alpha)dt_a\right]. \tag{4.36}$$

where, $\kappa(t_a,\alpha) = x(t_a) - \hat{x}_a(t_{a,}\alpha),$ $\tilde{\kappa}(t_a,\alpha) = \dfrac{\partial \hat{x}_a(t_a,\alpha)}{\partial \alpha_{re}}\,.$ (4.37)

The condition of optimality as given in (4.34) imply

$$E\left[\int_{-\infty}^{\infty}\mathrm{Re}(\kappa^*(t_a,\alpha)\tilde{\kappa}(t_a,\alpha)dt_a\right]_{\alpha=0} = 0\,. \tag{4.38}$$

Evaluating at $\alpha=0$ gives $E\left[\int_{-\infty}^{\infty}(x_a(t_a) - \hat{x}_a(t_a,0))^*\delta g_0(t_a)y_a(t_a)dt_a\right] = 0\,.$ (4.39)

Since $\delta g_0(t_a)$ is an *arbitrary* term and (4.39) is true for all $\delta g_0(t_a)$, it can be inferred that

$$E\left[(x_a(t_a) - \hat{x}_a(t_a,0))^* y_a(t_a)\right] = 0\,. \tag{4.40}$$

(4.40) can be solved for the optimum filter function $g_0(.)$ by using the definition of $\hat{x}_a^*(t_a,0)$ and by taking the complex conjugate of both sides of the above equation

$$\boldsymbol{g}_0(\mathrm{t_a}) = \frac{\boldsymbol{R}_{\mathrm{x_a y_a}}(\mathrm{t_a},\mathrm{t_a})}{\boldsymbol{R}_{\mathrm{y_a y_a}}(\mathrm{t_a},\mathrm{t_a})}\quad, \tag{4.41}$$

where, the above correlation functions can be obtained from the correlation functions $\boldsymbol{R}_{\mathrm{xy}}$ and $\boldsymbol{R}_{\mathrm{yy}}$ by

$$\boldsymbol{R}_{\mathrm{x_a y_a}}(\mathrm{t_a},\mathrm{t_a}) = \int_{-\infty}^{\infty}\int_{-\infty}^{\infty}\mathrm{K_a}(\mathrm{t_a},\mathrm{t})\mathrm{K_{-a}}(\mathrm{t_a},\mathrm{t}).\boldsymbol{R}_{\mathrm{xy}}(\mathrm{t},\mathrm{t}')\mathrm{dt}'\mathrm{dt}\,, \tag{4.42}$$

$$\boldsymbol{R}_{y_a y_a}(t_a, t_a) = \int_{-\infty}^{\infty}\int_{-\infty}^{\infty} K_a(t_a, t) K_{-a}(t_a, t).\boldsymbol{R}_{yy}(t, t')dt'dt. \qquad (4.43)$$

The transformation kernel K_a is given by (3.64) with $\alpha = a\pi/2$. The (4.41) provides the optimal multiplicative filter function in the a^{th} fractional domain. To find the optimal value of 'a', that is, the domain in which the smallest error is obtained, substitute the optimum filter function into the MSE expression and then choose 'a' as the minimizer of $\sigma_{e,o}^2$ in the range [-1, 1] from (4.44).

$$\begin{aligned}\sigma_{e,o}^2 &= E\left[\int_{-\infty}^{\infty}(x_a(t_a) - \hat{x}_{a,o}(t_a))(x_a(t_a) - \hat{x}_{a,o}(t_a))^* dt_a\right], \\ &= \int_{-\infty}^{\infty}(\boldsymbol{R}_{x_a x_a}(t_a, t_a) - 2\,\mathrm{Re}(g_0^*(t_a)\boldsymbol{R}_{x_a y_a}(t_a, t_a)) + g_0(t_a) g_0^*(t_a)\boldsymbol{R}_{y_a y_a}(t_a, t_a)dt_a\end{aligned} \qquad (4.44)$$

This minimizer can be found analytically in certain cases but not in general. It can also be found by simply calculating the MSE for sufficiently closely spaced discrete values of 'a' (for example, by step size of 0.1) and choosing the one that minimizes the MSE. If greater accuracy is needed, this process can be refined around the neighborhood of the initially obtained value of 'a'. The key point is that given the noise and signal statistics, the optimum value of 'a' is calculated only once. After this, the filtering process can be implemented in time for arbitrary many realizations of that statistics.

Overall, the procedure can be outlined as follows: Given the autocorrelation functions of the input (x) and noise (n) processes and the degradation (h), the cross correlation function between the input and output(y) processes then the autocorrelation function of the output process can be found. Then, using these, the optimal filter function in the a^{th} domain can be found by using (4.41). The optimal value of 'a' is then chosen as that which minimizes (4.44).

4.5.2 Optimal Spatial Filtering

The optimal filtering in fractional Fourier domain can be extended to spatial filtering of signals arriving at antenna array also. The filter structure used for beamforming is shown in Fig. 4.7. In the Fig. 4.7 the output $y(n)$ is given by

$$y(n) = F^{-a}\boldsymbol{w}^H F^a \boldsymbol{x}(n). \qquad (4.45)$$

According to (4.45) the a^{th} order fractional Fourier transform of the observed signal $\boldsymbol{x}(n)$ is taken first, then it is multiplied with weights $\boldsymbol{w}$'s and finally the inverse a^{th} order transform is taken. For a=1 this procedure corresponds to ordinary frequency domain

beamforming [45, 84]. Substituting y(n) in (4.30) as estimate of x(n) with d(n) as desired signal

$$J(\boldsymbol{w}) = E\{\left\| d(n) - F^{-a}\boldsymbol{w}^{H}F^{a}\boldsymbol{x}(n)\right\|^{2}\} \tag{4.46}$$

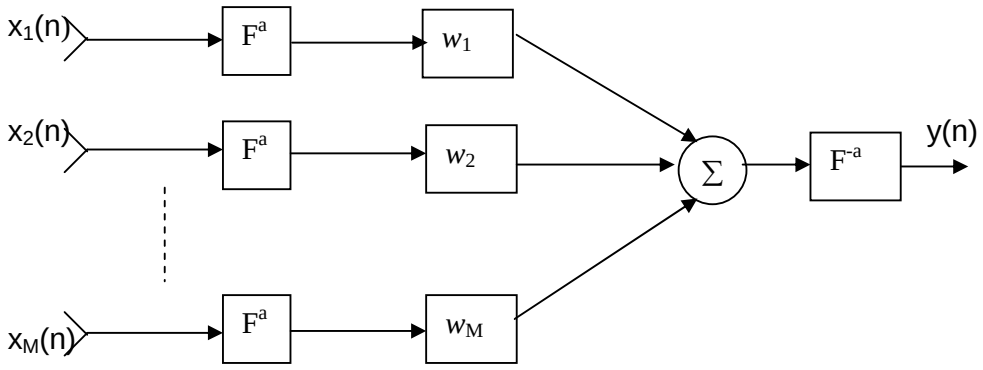

'a' denotes order of the FrFT

Figure 4.7-Block diagram of optimum FRFT domain beamformer

On minimizing the cost function (4.46) as described in section 4.3, the optimum weights are given by

$$\boldsymbol{w}_{opt} = \boldsymbol{R}_{x_a}^{-1} r_{x_a d} \ , \tag{4.47}$$

where, $\boldsymbol{R}_{x_a}$ is the covariance of the a[th] order FrFT of the signals arriving at sensors and $\boldsymbol{r}_{x_a d}$ is the cross-covariance between a[th] order FrFT of the desired signal and FrFT of the signal arriving at the sensor. The $\boldsymbol{R}_{x_a}$ and $\boldsymbol{r}_{x_a d}$ can be computed using the covariance as follows:

$$\boldsymbol{R}_{x_a} = \boldsymbol{R}_{x_a}(n,n') = \int_{-\infty}^{\infty}\int_{-\infty}^{\infty} K_a(n,n'')K_{-a}(n',n''')\boldsymbol{R}_x(n'',n''')dn''dn'''. \tag{4.48}$$

$$\boldsymbol{r}_{x_a d} = \boldsymbol{r}_{x_a d}(n,n') = \int_{-\infty}^{\infty}\int_{-\infty}^{\infty} K_a(n,n'')K_{-a}(n',n''')\boldsymbol{r}_{xd}(n'',n''')dn''dn'''. \tag{4.49}$$

The transformation kernel K_α is given by (3.64). The minimum error can be found by substituting the value of $\boldsymbol{w}_{opt}$ in (4.46). The value of minimum error is given by [61,148]

$$J_{\min}(\boldsymbol{w}_{opt}) = E\{\left\| d(n) - F^{-a}\boldsymbol{w}_{opt}^{H}F^{a}\boldsymbol{x}(n)\right\|^{2}\}. \tag{4.50}$$

This minimum error cannot be found analytically. It can be found by simply calculating (4.50) for different values of 'a' and choosing that value that result in minimum error as discussed in section 4.5.1.

Now, the performance of any antenna array system is highly dependent upon the characteristics of wireless channel. Channel modeling is an important issue for design

and analysis of mobile communication systems and spatial properties of the channel have enormous effect on the performance of the antenna array system. Channel models also help in motivating appropriate signal processing algorithms. Given a description of channel, an efficient array processing technique can be devised. To obtain realistic estimates of the performance of FrFT based antenna array architecture, accurate channel models for mobile wireless are needed [16, 135]. Channel models are discussed in next section.

4.6 CHANNEL MODELS FOR ANTENNA ARRAYS

Channel models capture radio propagation effects and are useful for simulation studies and performance prediction. The effects of radio propagation on the transmitted signal can be broadly categorized into two main classes, fading and spreading [16, 164]. Fading refers to the propagation losses experienced by the radio signal (on both the forward and reverse links). Channel spreading refers to the spreading of the information-carrying signal energy in space, and on the time or frequency axis [16].

4.6.1 Channel Fading

When changes take place in the propagation environment e.g. the user is a mobile, reflector and scatterers are moving or the medium itself is changing, then the channel response will also change as a function of time, the radio path is fading [130].

4.6.1.1 Mean path loss

The mean path loss describes the attenuation of a radio signal in a free space propagation situation, due to isotropic power spreading, and is given by the famous inverse square law [156]:

$$P_r = P_t\left(\frac{\lambda}{4\pi d}\right)^2 G_t G_r \ , \tag{4.51}$$

where, P_r and P_t are the received and transmitted powers, λ is the radio wavelength, d is the range, and G_t, G_r are the gains of transmit and receive one-element antennas respectively. In mobile environments, the main path is often accompanied by a surface reflected path which may destructively interfere with the primary path. Specific models have been developed that consider this effect. The path loss model becomes [162].

$$P_r = P_t\left(\frac{h_t h_r}{d^2}\right)^2 G_t G_r , \tag{4.52}$$

where, h_t & h_r are the effective heights of transmit and receive antennas respectively. Note that this particular path loss model follows an inverse fourth power law. In fact, depending on the environment, the path loss exponent may vary from 2.5 to 5.

4.6.1.2 Slow fading

Slow fading is caused by long-term shadowing effects of buildings or natural features in the terrain. It can also be described as the local mean of a fast fading signal. The statistical distribution of the local mean has been studied experimentally and was shown to be influenced by the antenna height, the operating frequency and the type of environment.

4.6.1.3 Fast fading

The multipath propagation of the radio signal causes path signals to add up with random phases, constructively or destructively at the receiver. These phases are determined by the path length and the carrier frequency, and can vary extremely rapidly with the receiver location. This gives rise to the so-called fast-fading phenomenon that describes the both rapid and large fluctuations of the received signal level in space.

4.6.2 Channel Spreading

Propagation to or from a mobile user, in a multipath channel, causes the received signal energy to spread in the frequency, time and space dimensions. The characteristics of the spreading (that is to say, the particular dimension(s) in which the signal is spread) affects the design of the beamformer. The realistic models for wireless communication systems should be modeled both in frequency and time domains. In traditional communication theory the Doppler spread in frequency domain and delay spread in time domain characterize these two effects [135].

4.6.2.1 Doppler spread

When the mobile is in motion, the radio signal at the receiver experiences a shift in the frequency domain (also called Doppler shift), the amplitude of which depends on the direction of arrival. In the presence of surrounding scatterers with multiple directions, a pure tone is spread over a finite spectral bandwidth. In this case, the Doppler power spectrum is defined as the Fourier transform of the time autocorrelation of the received signal and the Doppler spread is the support of the Doppler power spectrum. Assuming scatterers uniformly distributed in angle, the Doppler power spectrum is given by the so-called classical spectrum:

$$S(f) = \frac{3\sigma_s^2}{2\pi f_m}\left[1 - \left\{\frac{f - f_c}{f_m}\right\}^2\right]^{-\frac{1}{2}}, \quad f_c - f_m \langle f \langle f_c + f_m, \tag{4.53}$$

where, f_m = v/λ is the maximum Doppler shift, v is the mobile velocity, f_c is the carrier frequency and σ_s^2 is the signal variance. When there is a dominant source of energy coming from a particular direction (as in line-of-sight situations), the expression for the spectrum needs to be corrected according to the Doppler shift of the dominant path $f_{D,}$ and is given by $S(f) + B\delta(f - f_c - f_D)$. Here, B denotes the ratio of direct to scattered path energy. The Doppler spread causes the channel characteristics to change rapidly in time, giving rise to the so-called time selectivity. The coherence time, during which the fading channel can be considered as constant, is inversely proportional to the Doppler spread. A typical value of the Doppler spread in a macro-cell environment is about 200 Hz at 65 Mph, in the 1900 MHz band.

4.6.2.2 Delay spread

Multipath propagation is often characterized by several versions of the transmitted signal arriving at the receiver with different attenuation factors and delays. The spreading in the time domain is called delay spread and is responsible for the selectivity of the channel in the frequency domain (different spectral components of the signal carry different powers). The coherence bandwidth, which is the maximum range of frequencies over which the channel response can be viewed as constant, is inversely proportional to the delay spread. Significant delay spread may cause strong inter-symbol interference which makes necessary the use of a channel equalizer. In this work the coherence bandwidth is assumed to be smaller than the signal bandwidth.

4.6.2.3 Angle spread

Angle spread at the receiver refers to the spread of directions of arrival of the incoming paths. Likewise, angle spread at the transmitter refers to the spread of departure angle of the multipath. A large angle spread will cause the paths to add up in a random manner at the receiver as a function of the location of the receive antenna, hence it will be source of space selective fading. The range of space for which the fading remains constant is called the coherence distance and is inversely related to the angle spread. As a result, two antennas separated by more than the coherence distance tend to experience uncorrelated fading. When the angle spread is large, which is usually

the case in dense urban environments; a significant gain can be obtained from space diversity.

4.7 Mathematical modeling of fading channels

A precise mathematical description of fading phenomenon is either unknown or too complex for tractable communication systems analysis. However, considerable efforts have been devoted to the statistical modeling and characterization of these different fading effects. The result is a range of relatively simple and accurate statistical models for fading channels, which depend on the particular propagation environment and the underlying communication scenario [130]. A significant advantage of statistical models is their flexibility, which means by changing the statistical parameters; the same model can be used to simulate the channel under different conditions. The statistical model for the fading of the received signal level is based on the physical propagation environment consisting of a large number of isolated scatterers with unknown locations and reflection properties. Let the transmitted signal be

$$s(t) = \mathrm{Re}[\{u(t).e^{j(2\pi f_C t+\phi_0)}\}], \tag{4.54}$$

where, u(t) is the complex envelope of the signal with bandwidth B, f_c is the carrier frequency, ϕ_o is an arbitrary initial phase and Re(.) stands for real part of the signal. Let the signal be transmitted through a fading channel. The received signal is then expressed as a sum of line of sight (LOS) and N multipath components. The received signal can is given by

$$x(t) = \mathrm{Re}\left\{\sum_{n=0}^{N(t)} \alpha_n(t)u(t-\tau_n(t))e^{j(2\pi f_C(t-\tau_n(t))+\phi_{Dn})}\right\}, \tag{4.55}$$

where, n=0: LOS path,

N(t): Total number of Non LOS paths,

$\tau_n(t)$: Delay of LOS path and other multipath components,

$r_n(t)$: Path length corresponding to delay $\tau_n(t)=r_n(t)/v_0$,

v_0: Velocity of light,

$\alpha_n(t)$: Amplitude of the received multipath,

$\phi_{Dn}(t)$: Doppler phase shift depending upon Doppler frequency.

Since $\alpha_n(t)$, $\tau_n(t)$ and $\phi_{Dn}(t)$ associated with each component undergo a change with time hence they are characterized as random processes assumed to be stationary and erogodic. Let

$$\phi_n(t)=2\pi f_c\tau_n(t)- \phi_{Dn}, \tag{4.56}$$

then the received signal can be written as

$$x(t) = \mathrm{Re}\left\{ \left[\sum_{n=0}^{N(t)} \alpha_n(t) e^{-j\phi_n(t)} u(t-\tau_n(t)) \right] e^{j2\pi f_C t} \right\}. \tag{4.57}$$

As $\alpha_n(t)$ is function of path loss and shadowing while $\phi_n(t)$ depends upon delay and Doppler shift, it is assumed that these two processes are independent. Received signal can also be obtained by convolving baseband input signal u(t) with equivalent low pass time varying channel impulse response $c(\tau,t)$ and then up converting to the carrier frequency

$$x(t) = \mathrm{Re}\left\{ \left(\int_{-\infty}^{\infty} c(\tau,t) u(t-\tau) \right) e^{j2\pi f_c t} \right\}. \tag{4.58}$$

$c(\tau,t)$ has two parameters, t is the time when response of multipath channel is observed at the receiver for a transmission launched τ seconds earlier into the channel. From (4.57) and (4.58)

$$c(\tau,t) = \mathrm{Re}\left\{ \left[\sum_{n=0}^{N(t)} \alpha_n(t) e^{-j\phi_n(t)} \delta(t-\tau_n(t)) \right] \right\}. \tag{4.59}$$

If the channel is time invariant then time varying parameters of channel become constant, and $c(\tau,t) = c(\tau)$ is just a function of τ as given by

$$c(\tau,t)=c(\tau)= \sum_{n=0}^{N(t)} \alpha_n(t) e^{-j\phi_n} \delta(\tau-\tau_n). \tag{4.60}$$

Assume channel is slowly varying channel i.e. the delay spread T_m associated with the channel is small relative to inverse bandwidth of the transmitted signal

$$T_m << B^{-1}.$$

Under above condition $\tau_i \le T_m \ \forall\ i$ so that $u(t-\tau_i) = u(t) \ \forall\ i$ and (4.57) can be written as

$$x(t) = \mathrm{Re}\left\{ \left[\sum_{n=0}^{N(t)} \alpha_n(t) e^{-j\phi_n(t)} \right] u(t) e^{j2\pi f_C t} \right\}. \tag{4.61}$$

(4.61) differs from original transmitted signal s(t) by a complex factor written in parentheses. This multiplicative scale factor is independent of the transmitted signal s(t) or, equivalently, the baseband signal u(t), as long as the narrowband assumption $T_m << 1/B$ is satisfied. In order to characterize the random scale factor caused by multipath components let s(t) be unmodulated carrier without LOS component present in the multipath and given by

$$s(t) = \mathrm{Re}[\{e^{j(2\pi f_C t+\phi_0)}\}] = \cos(2\pi f_c t + \phi_0). \tag{4.62}$$

With this assumption the received signal becomes

$$x(t) = \mathrm{Re}\left\{\left[\sum_{n=1}^{N(t)} \alpha_n(t) e^{-j\phi_n(t)}\right] e^{j2\pi f_C t}\right\} = r_I(t)\cos(2\pi f_c t) + r_Q(t)\sin(2\pi f_c t). \quad (4.63)$$

where, in phase $r_I(t)$ and quadrature $r_Q(t)$ components are given by

$$r_I(t) = \sum_{n=1}^{N(t)} \alpha_n(t)\cos(\phi_n(t)) \qquad r_Q(t) = \sum_{n=1}^{N(t)} \alpha_n(t)\sin(\phi_n(t)), \quad (4.64)$$

where, the phase term $\phi_n(t) = 2\pi f_c \tau_n(t) - \phi_{Dn} = \varphi_n(t) - \phi_{Dn}$. (4.64a)

Thus the transmitted signal in multipath environment is modified by a multiplicative distortion and additive noise as given by (4.65)

$$x(t) = g(t).s(t) + n(t), \quad (4.65)$$

where, $g(t) = \mathrm{Re}\left\{\left[\sum_{n=1}^{N(t)} \alpha_n(t) e^{-j\phi_n(t)}\right]\right\}$ is the envelope of the s(t) and n(t) is AWGN. (4.65) is equivalently represented in Fig.4.8.

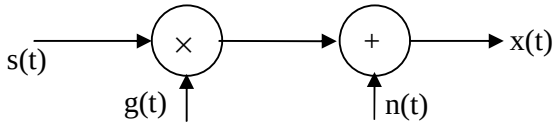

Figure 4.8: Model of mobile channel

4.7.1 Envelope modeling of received signal

In (4.64) if N(t) is large, then the application of Central Limit Theorem and the fact that $\alpha_n(t)$ and $\phi_n(t)$ are stationary and erogodic processes imply that $r_I(t)$ and $r_Q(t)$ are jointly Gaussian random processes. It is also assumed that amplitude $\alpha_n(t)$, multipath delay $\tau_n(t)$ and Doppler frequency $f_{Dn}(t)$ [$f_{Dn}(t) = v \cos \theta_n(t)/\lambda$ for $\theta_n(t)$ its angle of arrival] are changing slowly enough such that they are constant over the time interval of interest.

$$\alpha_n(t) = \alpha_n, \quad \tau_n(t) = \tau_n \text{ and } f_{D(n)}(t) = f_{Dn} = \frac{v\cos\theta}{\lambda}. \quad (4.66)$$

This assumption is true when each multipath is associated with a single reflector [68]. The n^{th} multipath component $2\pi f_c \tau_n$ in the term $\phi_n(t)$ in (4.64(a)) changes rapidly relative to other terms, hence the term $2\pi f_c \tau_n$ can undergo 360° rotation for a small change in multipath delay. (This is possible as f_c is large). Under this assumption $\phi_n(t)$ is uniformly distributed $[-\pi, \pi]$, therefore

$$E[r_I(t)] = \left[\sum_n \alpha_n \cos\phi_n(t)\right] = \left[\sum_n E[\alpha_n]E[\phi_n(t)]\right] = 0, \quad (4.67)$$

as α_n and ϕ_n are independent. Similarly $E[r_Q(t)] = 0$. Thus received signal is zero mean Gaussian process. Consider now the autocorrelation of the in-phase and quadrature components. Using the independence of α_n and ϕ_n, the independence of ϕ_n and ϕ_m, $n \neq m$, and the uniform distribution of ϕ_n it can be shown that

$$E[r_I(t)r_Q(t)] = E\left[\sum_n \alpha_n \cos\phi_n(t)\sum_m \alpha_m \mathrm{Sin}\phi_m(t)\right] = \sum_n\sum_m E[\alpha_n\alpha_m]E[\cos\phi_n(t)\sin\phi_m(t)],$$

$$= \sum_n E[\alpha_n^2]E[\cos\phi_n(t)\sin\phi_n(t)] = 0. \quad (4.68)$$

Thus $r_I(t)$ and $r_Q(t)$ are uncorrelated. Since they are Gaussian hence they are independent.

For any two Gaussian random variables *X* and *Y*, both with mean zero and equal variance σ^2, it can be shown that *G* = $\sqrt{X^2 + Y^2}$ is Rayleigh-distributed and G^2 is exponentially distributed [39]. As shown above that for $\phi_n(t)$ uniformly distributed, r_I and r_Q are both zero-mean Gaussian random variables. If a variance of σ^2 for both, in-phase and quadrature components, is assumed then the signal envelope is given by

$$g(t) = |x(t)| = \sqrt{r_I(t)^2 + r_Q(t)^2}. \quad (4.69)$$

Using above model the received signal at m^{th} element is given by

$$x_m(t) = g_m(t)\, s(t) + n_m(t), \quad (4.70)$$

where, the term $g_m(t)$ at the m^{th} element includes signal power fading. s(t) is the transmitted signal assumed to be unmodulated carrier, $n_m(t)$ denotes the noise at m^{th} element. The noise is assumed to be uncorrelated with signal.

4.7.2 Rayleigh Faded environment

In Rayleigh faded channel $g_m(t)$ has Rayleigh distribution. The probability density function (pdf), f (g), of the received signal amplitude (envelope) is given by [74]

$$f_G(g) = \frac{g}{\sigma^2}\exp\left\{-\frac{g^2}{2\sigma^2}\right\} \qquad g \geq 0, \quad (4.71)$$

where, σ^2 = variance of $r_I(t)$ and $r_Q(t)$ and let $P_r = \sum_n E[\alpha_n^2] = 2\sigma^2$ = Average received power of signal. For filtering in FrFT domain one needs to know the correlation R_{xx} of the x(t), and cross-correlation r_{xd} between the input x(t) and the desired signal d(t).

Knowing R_{xx} and r_{xd} the R_{x_a} and $r_{x_a d}$ in a^{th} domain can be computed using (4.48) and (4.49).

Correlation of received signal at m^{th} element

$$R_{x_m x_m} = E\left[x_m(t)x_m^*(t)\right] = E\left[(g_m s(t) + n_m(t))((g_m^* s^*(t) + n_m^*(t))\right],$$
$$= E\left[g_m g_m^* s(t)s^*(t) + g_m s(t)n_m^*(t) + n_m(t)g_m^* s^*(t) + n_m(t)n_m^*(t)\right],$$
$$= E\left[|g_m|^2\right]\left[s(t)s^*(t) + E[g_m]s(t)E[n_m^*(t)] + E[n_m(t)]E[g_m^*]s(t) + E[n_m(t)n_m^*(t)]\right]. \quad (4.72)$$

As $g_m(t)$ and $n(t)$ are uncorrelated, therefore

$$R_{x_m x_m} = E\left[|g_m|^2\right]s(t)s^*(t) + R_{nn}, \quad (4.73)$$

where, R_{nn} is the correlation of the input noise at the m^{th} element. pdf of $|g_m|^2$ is derived using transformation $Z = |g_m|^2$, thus received signal power is exponentially distributed

$$p_Z(z) = \frac{1}{P_r} e^{-\frac{z}{Pr}} = \frac{1}{2\sigma^2} e^{-\frac{z}{(2\sigma^2)}}, \; z \geq 0. \quad (4.74)$$

Cross-correlation of the received and desired signal at m^{th} element

$$r_{x_m d} = E\left[x_m(t)d(t)\right] = E[(g_m s(t) + n_m(t))d^*(t)]. \quad (4.75)$$

Two cases are considered here

(i) The desired signal be equal to the transmitted signal, d(t) = s(t)

$$r_{x_m d} = E[(g_m s(t) + n_m(t))s^*(t)] = E\left[g_m\right]s(t)s^*(t) + E[n_m(t)]\,s^*(t) = E\left[g_m\right]s(t)s^*(t). \quad (4.76)$$

(ii) The desired signal is estimated at the receiver and given by $d(t) = g_m(t)\, s(t)$

$$r_{x_m d} = E[(g_m s(t) + n_m(t))\, g_m s^*(t)] = E[|g_m|^2]\, s(t)s^*(t) + E[n_m(t)g_m]\, s^*(t),$$
$$= E[|g_m|^2]\, s(t)s^*(t). \quad (4.77)$$

The above mathematical model is valid for a constant velocity source as in the case of mobile wireless environment and also in wireless communication. The optimal spatial filtering problem is also useful for applications involving chirp signals such as signal enhancement problems with accelerating sinusoidal sources where the Doppler effect generates chirp signals and a frequency shift for example in radars. The model for such wireless communication is also developed.

Accelerating source in wireless communication

Assume that the source is moving with constant acceleration. Let v_i be the initial velocity of the source and ϖ be the acceleration of the source. The received

signal frequency differs from transmitted frequency f_c by virtue of the Doppler shift produced by the accelerating source. The Doppler frequency produced by accelerating source is

$$f_a = \frac{2\varpi}{\lambda} t . \tag{4.78}$$

Hence received signal is given by

$$x(t) = \mathrm{Re}\left[\left\{ \sum_n \alpha_n(t) e^{-j\phi_n(t)} \right\} e^{j2\pi f_c(t)} e^{-j2\pi f_a(t)} \right] = \mathrm{Re}\left[\left\{ \sum_n \alpha_n(t) e^{-j\phi_n(t)} \right\} e^{j2\pi (f_c - f_a)t} \right], \tag{4.79}$$

Hence the received signal at m^{th} antenna element is given by

$$x_m(t) = g_m(t)\, s'(t) + n_m(t), \tag{4.80}$$

where, $s'(t) = e^{j2\pi(f_c - f_a)t}$.

Correlation of signal

$$R_{x_m x_m} = E[x_m(t) x_m^*(t)] = E[|g_m|^2]\, s'(t) s'^*(t) + R_{nn} . \tag{4.81}$$

Cross - Correlation of received signal

Case (i) $d(t) = s(t)$,

$$r_{x_m d} = E[x_m(t) d(t)] = E[(x_m(t) s^*(t)] = E[(g_m s'(t) + n(t)) s^*(t)],$$

$$= E[g_m] s'(t) s^*(t) + E[n_m(t)] s^*(t),$$

$$= E[g_m] e^{j2\pi(f_c - f_a)t} e^{-j2\pi(f_c)t} = E[g_m] e^{-j2\pi(f_a)t} . \tag{4.82a}$$

Case (ii) $d(t) = g_m(t)\, s(t)$,

$$r_{x_m d} = E[|g_m|^2]\, e^{-j2\pi(f_a)t} . \tag{4.82b}$$

4.7.3 Ricean Faded Environment

The Ricean distribution is observed when, in addition to the multipath components, there exist a direct path between the transmitter and the receiver. In the Ricean case, the mean values of $r_I(t)$ and $r_Q(t)$ will not be zero because of the presence of the direct component. The pdf of Ricean distributed random variable is given by

$$p_G(g) = \frac{g}{\sigma^2} \exp\left[-\frac{g^2 + s^2}{2\sigma^2} \right] I_0\left(\frac{gs}{\sigma^2} \right), \tag{4.83}$$

where, $I_0(.)$ is the zeroth order modified Bessel function of the first kind. The Ricean distribution is often described in terms of a parameter k_r called Ricean factor. k_r is defined as the ratio between the deterministic signal power and the variance of the multipath and is given by $k_r = \frac{s^2}{2\sigma^2}$, where,

$s^2 =$ Power in LOS component and

$P_r = 2\sigma^2 =$ power in non LOS component

$$p_G(g) = \frac{2g(k_r+1)}{P_r}\exp\left[-k_r - \frac{(k_r+1)g^2}{P_r}\right] I_0\left(2g\sqrt{\frac{k_r(k_r+1)}{P_r}}\right), \qquad g \geq 0. \tag{4.84}$$

The n^{th} moment of Ricean faded RV is given by

$$\mu_n = E[g^n] = (\sigma^2)^{\frac{n}{2}}\sqrt{\frac{n}{2}+1}\exp(-k_r)\,{}_1F_1\left(\frac{n}{2}+1;1;k_r\right), \tag{4.85}$$

where, ${}_1F_1(.;.;.)$ is the confluent hyper geometric function and Γ is the gamma function.

For n=2 $$\mu_2 = E[g^2] = (\sigma^2)\Gamma 2\exp(-k_r)\,{}_1F_1(2;1;k_r). \tag{4.86}$$

For n=1 $$\mu_1 = E[g^1] = (\sigma^2)^{\frac{1}{2}}\sqrt{\frac{3}{2}}\exp(-k_r)\,{}_1F_1\left(\frac{3}{2};1;k_r\right). \tag{4.87}$$

In case of Ricean environment the signal received at the m^{th} antenna is given by

$$x_m(t) = g_m(t)s(t) + n_m(t),$$

where, g_m is Ricean distributed random variable.

Correlation of the signal in mobile and wireless environment

$$R_{x_m x_m} = E[x_m(t)x_m^*(t)]$$

$$= E[|g_m|^2]s'(t)s'^*(t) + R_{nn} = [\Gamma 2(\sigma^2)\exp(-k_r)\,{}_1F_1(2;1;k_r)]s'(t)s'^*(t) + R_{nn}. \tag{4.88}$$

Cross-correlation of the signal in mobile and wireless environment

Case (i) $d(t) = s(t)$,

$$r_{x_m d} = E[x_m(t)d(t)] = E[g_m]s(t)s^*(t) + E[n_m(t)]s^*(t),$$

$$= E[g_m]s(t)s^*(t) = \sqrt{\frac{3}{2}}(\sigma)\exp(-k_r)\,{}_1F_1\left(\frac{3}{2};1;k_r\right)s(t)s^*(t). \tag{4.89a}$$

Case (ii) $d(t) = g_m(t)\,s(t)$,

$$r_{x_m d} = E[|g_m|^2]s(t)s^*(t). \tag{4.89b}$$

Accelerating Source in wireless environment

$$R_{x_m x_m} = E[x_m(t)x_m^*(t)] = E[|g_m|^2]s'(t)s'^*(t) + R_{nn}. \tag{4.90}$$

Case (i) $d(t) = s(t)$,

$$r_{x_m d} = E[g_m]e^{-j2\pi f_a t}. \tag{4.91a}$$

Case (ii) $d(t) = g_m(t)\, s(t)$,

$$r_{x_m d} = E[|g_m|^2]\, e^{-j2\pi(f_a)t}. \tag{4.91b}$$

4.7.4 Nakagami Faded Environment

A more general distribution for the fading amplitude is given by the Nakagami distribution [74]

$$p_G(g) = \frac{2m^m g^{2m-1}}{\Gamma(m) P_r^m} \exp\left[-\frac{mg^2}{P_r}\right], \qquad m \geq 0.5, \tag{4.92}$$

where, $\sigma^2 = E\{g^2\}$ and $m = \sigma^4 / E\{(g^2 - \sigma^2)^2\}$. The Nakagami distribution is often used to model multipath fading as it can model fading conditions that are either more or less severe than Rayleigh fading. When m=1, Nakagami distribution becomes the Rayleigh distribution, when m=1/2 it becomes a one-sided Gaussian distribution and when $m \to \infty$ the distribution becomes an impulse (no fading). For $m > 1$, the fluctuations of the signal strength reduce compared to Rayleigh fading, and Nakagami tends to Ricean. The n^{th} moment of Nakagami random variable is given by

$$\mu_k = E\left[g_m^n\right] = \frac{\Gamma\left(m + \frac{n}{2}\right)}{\Gamma(m)} \left(\frac{P_r}{m}\right)^{\frac{n}{2}}. \tag{4.93}$$

n=2
$$\mu_2 = E\left[g_m^2\right] = \frac{\Gamma(m+1)}{\Gamma(m)} \left(\frac{P_r}{m}\right) = P_r. \tag{4.94}$$

In case of Nakagami environment the signal received at the m^{th} antenna is given by

$$x_m(t) = g_m(t) s(t) + n_m(t),$$

where, g_m is Nakagami distributed random variable

Correlation of the signal in mobile and wireless environment

The correlation function of the signal received at m^{th} antenna is given by

$$R_{x_m x_m} = E[|g_m|^2]\, s(t) s^*(t) + R_{nn}. \tag{4.95}$$

The expected value of g_m^2 is derived from transformation $Z = |g_m|^2$

$$E[Z] = E|g_m|^2.$$

pdf of Z is given by $p_Z(z) = \left(\frac{m}{P_r}\right)^m \frac{x^{m-1}}{\Gamma(m)} \exp\left(-\frac{mz}{P_r}\right)$. (4.96)

Cross-correlation of the signal in mobile and wireless environment

Case (i) $d(t) = s(t)$,

The cross-correlation function of the signal received at m^{th} antenna is given by

$$r_{x_m d} = E[x_m(t)d(t)] = E[g_m]s(t)s^*(t) = \frac{\sqrt{m+\frac{1}{2}}}{\sqrt{m}}\left(\frac{P_r}{m}\right)^{\frac{1}{2}} s(t)s^*(t), \quad (4.97)$$

where $$E[g_m] = \frac{\sqrt{m+\frac{1}{2}}}{\sqrt{m}}\left(\frac{P_r}{m}\right)^{\frac{1}{2}} . \quad (4.98a)$$

Case (ii) $d(t) = g_m(t)\, s(t)$,

$$r_{x_m d} = E[|g_m|^2]e^{-j2\pi(f_a)t} \quad (4.98b)$$

Accelerating Source in wireless environment

$$R_{x_m x_m} = E[|g_m|^2]s'(t)s'^*(t) + R_{nn} . \quad (4.99)$$

Case (i) $d(t) = s(t)$,

$$r_{x_m d} = E[g_m]e^{-j2\pi f_a t} . \quad (4.100a)$$

Case (ii) $d(t) = g_m(t)\, s(t)$,

$$r_{x_m d} = E[|g_m|^2]\, e^{-j2\pi(f_a)t} . \quad (4.100b)$$

4.7.5 Generation of various fading environments

In all these simulations the noise is taken as Zero Mean Circularly Symmetric Complex Gaussian (ZMCSCG) noise with variance 1.

(a) Rayleigh faded channel: For a given time instant, the received signal in the case of a stationary receiver was generated using equation (4.63) with $\phi_{Dn}(t)=0$. In simulation the total number of paths are taken as N=10. Generating the signal using equations (4.63), (4.64a) and (4.66) allow us to incorporate Doppler Effect by introducing motion. The path amplitudes α_n are taken to be Weibull distributed so as to allow flexibility in varying its parameters. The phases ϕ_n were taken to be uniform in $[0,2\pi]$. The Weibull random numbers were generated using the function *weibrnd* from the Statistics Toolbox, and the uniform phases were generated using the function *unifrnd*. The received signal was then demodulated to get the inphase and quadrature components,

using the command *demod* from the Signal Processing Toolbox. Subsequently, the envelope was calculated using equation (4.69).

(a) Ricean Faded channel- To simulate the presence of a direct component, the received signal was modeled by equation (4.38) but with additional LOS component. In the presence of such a path, the transmitted signal can be written as

$$x(t) = \mathrm{Re}\left\{ \left[\sum_{n=1}^{N(t)} \alpha_n(t) e^{-j\phi_n(t)} \right] e^{j2\pi f_C t} + k_r\, e^{j2\pi(f_C + f_d)t} \right\}. \qquad (4.101)$$

The rest of the simulation was carried out as in *part (a)*. The value of k_r was taken to be equal to 5.

(b) Nakagami Faded channel – Since Nakagami distribution encompasses both Rayleigh and Rician, the Nakagami distribution seems to be a good fit for Rayleigh fading with an average value of the parameter $m = 1$. It also seemed to fit the Rician distribution between $1 < m < 2$. The value of m was taken as 0.9 in simulations.

The fading envelopes for Rayleigh, Ricean and Nakagami environments were generated for mobile velocity varying from 0 and 100 m/s. In case of accelerating source the signal was generated using equation (4.79). The acceleration was varied from 0-6 m/sec^2.

4.8 Macro-cellular and Micro-cellular Propagation Environments

4.8.1 Macro-cells

A macro-cell is characterized by a large cell radius (up to a few tens of kilometers) and a base station located above the roof top. In macro-cell environment, the signal energy received at the base station comes from three main scattering sources: scatterers local to the mobile, remote dominant scatterers and scatterers local to the base [16] as shown in Fig.4.9.

The scatterers local to the mobile give rise to paths that reach the base station with small delay spread and small angle spread [16]. Of the paths emerging from the local-to-mobile scatterers, some reach remote dominant scatterers, like hills or high rise buildings, before eventually traveling to the base station. These paths will typically reach the base with medium to large angle and delay spreads. Once these multiple wave fronts reach the vicinity of the base station, they usually are further scattered by local structures such as buildings or other structures that are close to the base. These scatterers local to the base can cause large angle spread, therefore they can cause severe space-selective fading.

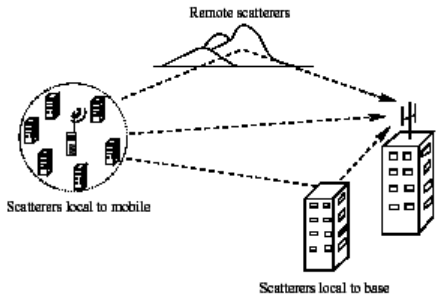

Figure 4.9-Different Scatterers surrounding the mobile in Micro and Macro Cellular Environment [16]

4.8.2 Micro-cells

Micro-cells are characterized by highly dense built-in areas, and by the user's terminal and base being relatively close (a few hundred meters). The base antenna has a low elevation and is typically below the roof top, causing significant scattering in the vicinity of the base. Micro-cell situations make the propagation difficult to analyze and the macro cell model described earlier does not necessarily hold anymore. Very high angle spreads along with small delay spreads are likely to occur in this situation. Doppler spread can be as high as in macro-cells, although the mobility of the user is expected to be limited, due to the presence of mobile scatterers.

For proper and efficient implementation of future systems, emerging wireless systems must be able to exploit processing of spatial information [132]. The design of these systems depends heavily on information about the typical channel response and requires signal information such as the amplitude, phase and AOA of multipath delay spreads. The models describing channels based on these parameters are known as parametric channel models. All these models provide multipath parameters including the AOA information essential to simulate an antenna array system. Some of these models are suited to the micro cells typically set up in urban areas, while others are more applicable for the macro cells found in the rural and suburban areas. There are also channel models based on propagation statistics in the indoor environment [3, 118].

In these models, it is assumed that the signals are arriving uniformly along the azimuthal direction. However in more realistic scenarios, the AOA of the multipaths depends on a number of factors, such as the distance between the transmitter and receiver, location of scatterers, size of the receiving antenna etc. as shown in Fig.4.10. Hence in order to test the performance of antenna arrays, an accurate description of the

spatio-temporal channel model is required, which requires real world data of above parameters. These models are known as Spatio Temporal Channel Models.

4.9 Spatio-Temporal Channel Models

In spatio-temporal models the multipath reflections are created by random placement of scatterers inside a region defined by a specific geometry. From the position of the scatterers, multipath delays, AOA and power levels are determined. Thus these models provide a statistical description of the wideband spatio-temporal radio channel, which is useful in simulating a space-time processing system. Fig. 4.10 depicts a general example of this multipath environment.

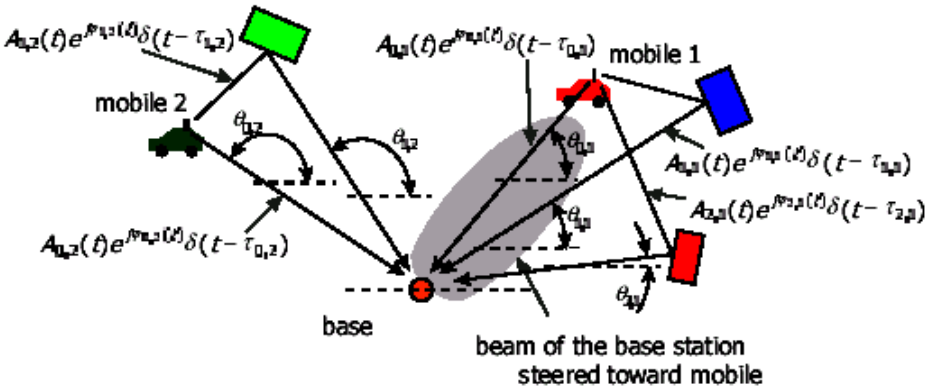

Figure 4.10-The Multipath Environment

In Fig.4.10, each signal component propagates through a different path, determining the amplitude $A_{l,k,}$ carrier phase shift $\varphi_{l,k,}$ time delay $\tau_{l,k,}$ angle of arrival $\theta_{l,k,}$ and Doppler shift f_d of the lth signal component of the k^{th} mobile. Accordingly, each of these signal parameters will be time-varying [116]. The vector channel impulse response characterizing Fig.4.10 is expressed in (4.102), where $a(\theta_l(t))$ is the array response vector.

$$\overrightarrow{h_1}(t,\tau) = \sum_{l=0}^{N(t)-1} A_{l,1}(t) e^{j\phi_l(t)} a(\theta_l(t)) \delta(t-\tau_l(t)) \; . \qquad (4.102)$$

The spatial channel impulse response for the first mobile user given by (4.102) is made up of the summation of several multipath components, each having its own amplitude, phase and angle-of-arrival. N(t) is the number of multipath components. When antenna arrays are employed, the array response vector is a function of the antenna array geometry and the AOA. This vector normally is described as in (4.103),

$$\boldsymbol{a}(\theta_l(t)) = \begin{bmatrix} \exp(-j\psi_{l,1}) \\ \exp(-j\psi_{l,2}) \\ .... \\ \exp(-j\psi_{l,m}) \end{bmatrix}, \qquad (4.103)$$

where, $\psi_{l,i}(t) = [x_i \cos(\theta_l(t)) + y_i \sin(\theta_l(t))]k$, and

$k = 2\pi/\lambda$ is the wave number. The variable, *m*, defines the number of elements and (x_i, y_i), is the coordinate of the ith element. The distribution of these parameters given in (4.103) is dependent upon the type of environment. Two statistical channel models known as Geometrically Based Single Bounce (GBSB) elliptical and GBSB circular are described next for micro and macro-cellular environments [116].

4.9.1 Geometrically Based Single Bounce Elliptical (GBSBE) Model

This GBSBE channel model is chosen to describe a typical urban multipath propagation scenario. In a typical urban environment, dense scattering coupled with abundance of reflection results in a rich multipath scenario. In this situation, the micro cellular concept where the base station has a relatively low antenna height is more appropriate. This implies that the multipath scatterers are located near the base station as well as near the mobile as shown in Fig.4.9. A channel model, which uses an elliptical scattering region surrounding the base station and the mobile, has been proposed for the micro cell environment. The following assumptions are made in developing the elliptical channel model [135].

1. The signals arriving at the base station are plane waves propagating along the horizon. As a consequence the AOA is calculated only in the azimuthal coordinates.
2. The scatterers are omni-directional re-radiating elements having identical scattering coefficients.
3. All scatterers are uncoupled. In other words, the signals reflected from each scatterer are not affected by the presence of the other scatterers.
4. The received multipath signals are subjected to distance-dependent path loss characterized by a path loss exponent.

4.9.1.1 Geometry and notation

In the GBSBE channel model the scatterers are assumed to be uniformly distributed in an elliptical region. The base station and the mobile form the foci of the ellipse as shown in Fig. 4.11

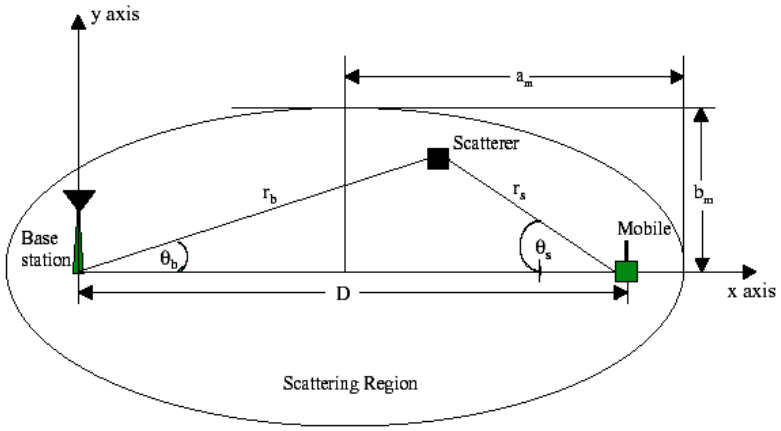

Figure 4.11-Geometry of the GBSB elliptical channel model

In Fig. 4.11, a distance D separates the base station and the mobile, with the base station at the origin. All scatterers lie in a plane that includes the base station and the mobile, implying that the reflected multipath waves will appear to have the same elevation angle. The elliptical region is completely described by its semimajor axis, a_m and its semiminor axis, b_m. The choice of these parameters is determined by the maximum delay, τ_{max} of the multipaths. Larger values of τ_{max} imply greater path loss for the multipaths and, consequently, lower relative power compared to those with shorter delays. Hence, this model has a nice physical interpretation in that, changing the geometry of the ellipse can automatically adjust the various channel parameters, such as multipath amplitudes, delay spread and angle spread.

4.9.1.2 Mathematical formulation

The semimajor axis, a_m and the semiminor axis, b_m are related to the maximum specified delay τ_{max} as below

$$a_m = \frac{c\tau_{max}}{2}, \qquad b_m = \frac{1}{2}\sqrt{c^2\tau_{max}^2 - D^2}\ , \tag{4.104}$$

where, D is the separation distance between the transmitter and the receiver and c is the speed of propagation. The equation of an ellipse in Cartesian coordinates

$$\frac{\left(x - D/2\right)^2}{\left(\frac{c\tau_{\max}}{2}\right)^2} + \frac{y^2}{\left(\frac{\sqrt{c^2\tau_{\max}^2 - D^2}}{2}\right)^2} = 1 \ . \qquad (4.105)$$

Substituting, $x = r_b \cos(\theta_b)$ and $y = r_b \cos(\theta_b)$, the equation of the ellipse in Polar coordinates

$$\frac{\left(r_b \cos\theta_b - D/2\right)^2}{\left(\frac{c\tau_{\max}}{2}\right)^2} + \frac{\left(r_b \sin\theta_b\right)^2}{\left(\frac{c^2\tau_{\max}^2 - D^2}{2}\right)^2} = 1 \ , \qquad (4.106)$$

where, r_b is the distance from the base station to a scatterer located at the boundary of the ellipse and θ_b is the AOA at the base station. Any scatterers inside the ellipse can be viewed as an equivalent one located at the boundary of a smaller concentric ellipse. (4.106) can then be solved for r_b for different values of the multipath propagation delay, $\tau \in [\tau_{min}, \tau_{max}]$. However an easier way is to utilize the coordinate location of the scatterer. Referring to Fig.4.11, the total propagation distance of a multipath ray from the mobile to the base-station

$$d = r_b + r_s = r_b + \sqrt{\left(D - r_b \cos(\theta_b)\right)^2 + \left(r_b \cos(\theta_b)\right)^2} \ . \qquad (4.107)$$

Substituting $d = \tau c$ in (4.107) and solving for r_b yields

$$r_b = \frac{D^2 - \tau^2 c^2}{2\left(D\cos(\theta_b) - \tau c\right)}; \qquad \frac{D}{c} \le \tau \le \tau_m \ . \qquad (4.108)$$

Due to the symmetric nature of the scattering region, similar expressions can be derived with respect to the mobile. The generation of samples of GBSBE channel model is described in section 4.9.3.

4.9.2 Geometrically Based Single Bounce Circular Model

A typical rural or suburban environment is characterized by local scatterers surrounding the mobile and number of large reflectors away from the vicinity of the mobile is visible at the base station. In such environments, macro cellular concept where the base station antenna height is considered to be above the local clutter is a more appropriate selection. Thus, the multipath channel parameters in the propagation model for rural or suburban environment are essentially determined by the distribution of the scatterers around the mobile. The model known as Geometrically Based Single Bounce (GBSB) circular model is specially suited for macro-cell environments and is

sufficient to represent a rural or suburban multipath propagation model. A Geometrically Based Single Bounce circular model presupposes the following underlying assumptions [7, 116].

- The signals received at the base station are plane waves propagating along the horizon. Thus only the azimuthal coordinates are required to represent the corresponding AOA. This is due to the fact that the separation distance between transmitter and receiver is large compared to the respective antenna heights.
- The scatterers are considered to be omni-directional re-radiating elements with identical scattering coefficients.
- Each multipath component at the base station has interacted with only a single scatterer and thus is not influenced by the other scatterers in the channel.

4.9.2.1 Geometry and notation

The Geometrically Based Single Bounce (GBSB) circular model assumes that the scatterers are uniformly distributed within a circle of radius, R around the mobile. The geometry of the circular model is shown in Fig. 4.12

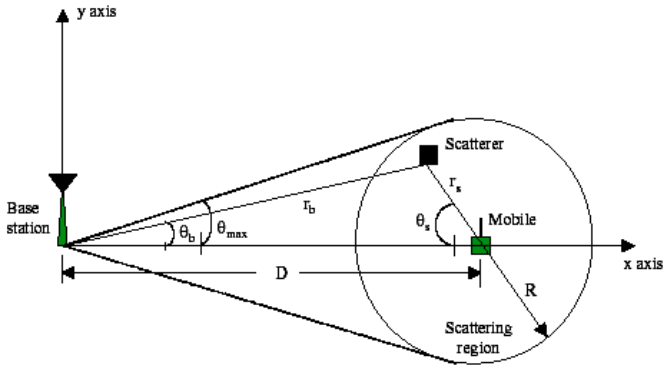

Figure 4.12-Geometry of the Circular Scattering Channel Model

In Fig.4.12, the base station and the mobile are separated by a distance *D*, with the base station at the origin of the coordinate system and the mobile is on the x-axis. The scatterers are uniformly placed in a circle of radius *R* with the mobile at the center. Typically, $R < D$, so that there are no scatterers local to the base station as is the case in a macro-cell region. For simplicity, the plane of the scatterer can be viewed as horizontal, which also includes the mobile and the base station. This will ensure that the angles of arrival of the received signal contain only azimuthal components. The AOA of the multipath components at the base station is denoted by θ_b and depends on two parameters: the angle of departure from the mobile and the position of the scatterer.

The location of the scatterer is specified by its distance from the base station, r_b, and from the mobile, r_s, respectively. Since the scatterers are confined in a circle around the mobile, the AOA at the base station, θ_b, is limited by a maximum value denoted by, θ_{max}. Similarly, the angle at the mobile, θ_s depends on the angle of departure from the base station and the scatterer location. In this case, as the mobile is located inside the scattering region, θ_s can be any value in the interval $[0,2\pi]$. The radius of the circular scattering region, *R*, is usually determined by equating the angle spread as predicted by the model with the measured angle spread. Typical values of angle spread in a macro cell environment ranges between one to six degrees for a transmitter to receiver separation distance of $D \approx 1$ km. Using the fact that the angle spread is inversely proportional to *D*, the measurement results suggest a radius of scatterer ranging from 30 to 200 m.

4.9.2.2 Mathematical formulation

The region of scatterer in the Cartesian coordinates is given by

$$(x - D)^2 + y^2 \leq R^2 \ . \tag{4.109}$$

Substituting, $x = r_b \cos(\theta_b)$ and $y = r_b \cos(\theta_b)$ in (4.109) and expanding, the scattering region in Polar coordinates

$$r_b^2 - 2r_b D\cos(\theta_b) + D^2 \leq R^2 \ . \tag{4.110}$$

Referring to Fig. 4.12, the total multipath propagation distance, *d* is given by

$$d = r_b + r_s = r_b + \sqrt{(D - r_b\cos(\theta_b))^2 + (r_b \sin(\theta_b))^2} \ . \tag{4.111}$$

Substituting $d = \tau c$, where τ is the multipath propagation delay, the distance of the scatterer from the base station, r_b, can be expressed as

$$r_b = \frac{D^2 - \tau^2 c^2}{2(D\cos(\theta_b) - \tau c)}. \tag{4.112}$$

As in the GBSB elliptical channel model, the symmetric nature of the scattering region allows similar expressions to be derived with respect to the mobile. The generation of samples of GBSBC channel model is described in section 4.9.4.

4.9.3 Generation of Samples of the Elliptical Channel Model

The elliptical model described in 4.9.1 can be used to generate various multipath signal parameters such as multipath delay τ_i, AOA θ_i, and power P_i of the i^{th}

multipath component. The idea is first to define an ellipse corresponding to the maximum multipath delay, τ_m and uniformly place the scatterers inside the ellipse. The relevant signal parameters can then be calculated from the coordinates of the scatterers. It is assumed that the number of multipath (scatterers), *N* and the transmitter to receiver separation distance, *D* is known. The procedure is outlined below

- A value of the maximum multipath propagation delay, τ_m is chosen
- Samples of two uniformly distributed random variables, x_l and y_l, l=1,2…*N* are generated over the interval [-1,1].
- Isolate the points that lie on and within a circle of unit radius centered at the origin. Translate them from the Cartesian coordinates (x_l, y_l) to the polar coordinates (r_l,θ_l) according to the following relationships

$$r_l = \sqrt{x_l^2 + y_l^2}, \quad \phi_l = \tan^{-1}\left(\frac{y_l}{x_l}\right); \qquad l = 1,2...N. \tag{4.113}$$

- Thus, *N* samples of a random variable described by the polar coordinates (r_l,θ_l) are obtained that are uniformly distributed in a circle of unit radius. These samples are translated so that they are uniformly distributed in an ellipse, the following two transformations are performed

$$x_l = a_m r_l \cos(\theta_l) + \frac{D}{2}, \quad y_l = b_m r_l \sin(\theta_l); \qquad l = 1,2...N, \tag{4.114}$$

where, a_m and b_m are the semimajor and the semiminor axes of the ellipse respectively corresponding to the specified τ_m and are given by (4.104). The multipath propagation distance, d_l; l=1,2…*N* can be calculated as

$$d_l = \sqrt{x_l^2 + y_l^2} + \sqrt{(D - x_l)^2 + y_l^2}; \quad l = 1,2...N. \tag{4.115}$$

- The propagation delays of the multipaths, τ_l; l=1,2…*N* will be

$$\tau_l = \frac{d_l}{c}; \quad l = 1,2...N; \quad c = 3\times 10^8 \, m/s. \tag{4.116}$$

- Following that the base station is located at the origin of the coordinate system, the angle of arrivals (AOA) of the multipaths at the base station are given by

$$\theta_{b,l} = tan^{-1}\left(\frac{y_l}{x_l}\right); \qquad l = 1,2...N. \tag{4.117}$$

- The power of the direct path component (LOS) can be calculated as below

$$P_0(dBm) = P_{ref}(dBm) - 10n\log\left(\frac{D/C}{d_{ref}}\right) + G_t(\theta_d) + G_r(\theta_a), \quad (4.118)$$

where, P_{ref} is the reference power measured at a distance d_{ref} from the transmitter using omni-directional antennas at the transmitter and the receiver. P_{ref} can be calculated using Friis' free space propagation model given by

$$P_{ref}(dBm) = P_T(dBm) - 20\log\left(\frac{4\pi d_{ref}}{\lambda}\right), \quad (4.119)$$

where, P_T is the transmitted power and $\lambda = c/f$ is the wavelength for a particular carrier frequency, *f*. The path loss exponent, *n* typically ranges from *3* to *4* in a micro cell environment. $G_t(\theta_d)$ and $G_r(\theta_a)$ are the gains of the transmit and the receive antennas as functions of the angle of departure, θ_d and the angle of arrival, θ_a respectively. For the LOS component, θ_d and θ_a are both zero. The power of each of the multipath component can be calculated as below

$$P_l(dB) = P_o(dB) - 10n\log(d_l) - L_r + G_t(\theta_{d,l}) - G_t(0) + G_r(\theta_{a,l}) - G_r(0). \quad (4.120)$$

where, L_r is the path loss in dB

- Assuming the phase of the multipath components, γ_l; l=1,2…N are uniformly distributed over the interval $(0,2\pi)$, the complex amplitudes of the multipath components are calculated as below

$$\alpha_l = 10^{(P_l - P_0)/20} e^{j\gamma_l}; \qquad l = 1,2...N. \quad (4.121)$$

4.9.4 Generation of Samples of the Circular Channel Model

As in the elliptical channel model, the same method is used to generate the multipath channel parameters using the circular channel model. Again, the basic idea is to define a uniform circular scattering surrounding the mobile with the radius corresponds to the maximum multipath delay, τm. The relevant signal parameters can then be calculated from the geometry of the scattering region. As in the case of elliptical model, it will be assumed that number of multipaths, *N* and the transmitter to receiver separation distance, D is known. The procedure is described below.

- A value of the maximum multipath propagation delay, τ_m, is chosen
- The radius of the scattering region is calculated according to the following relationship

$$R_m = \frac{(c\tau_m - D)}{2}, \tag{4.122}$$

where, c is the speed of propagation.

- Samples of two uniformly distributed random variables, x_l and y_l, l=1,2…N are generated over the interval [$-R_m$, R_m] and the points that lie on and inside a circle of radius R_m are isolated. The coordinates of these points to an origin at a distance D from the center of the circle is

$$x_c = x_l + D, \qquad y_c = y_l; \qquad l = 1,2...N. \tag{4.123}$$

The multipath propagation distance, d_l; l=1,2…N can be calculated as

$$d = \sqrt{x_c^2 + y_c^2} + \sqrt{(D - x_c)^2 + y_c^2}. \tag{4.124}$$

The propagation delays of the multipaths, τ_l and AOA at the base station (origin) l=1,2…N are

$$\tau_l = \frac{d_l}{c}, \qquad \theta_{b,l} = tan^{-1}\left(\frac{y_c}{x_c}\right); \qquad l = 1,2...N. \tag{4.125}$$

- The power of each of the multipath component can be calculated as below

$$P_l(dB) = P_o(dB) - 10n\log(d_l) - L_r + G_t(\theta_{d,l}) - G_t(0) + G_r(\theta_{a,l}) - G_r(0). \tag{4.126}$$

where L_r is the path loss in dB

- Assuming the phase of the multipath components, γ_l; l=1,2…N are uniformly distributed over the interval (0,2π), the complex amplitudes of the multipath components are calculated as below

$$\alpha_l = 10^{(P_l - P_0)/20} e^{j\gamma_l}; \qquad l = 1,2...N. \tag{4.127}$$

In both GBSBE and GBSBE channel the received signal at the m[th] antenna is given by

$$x_m(t) = \sum_{l=0}^{N} \alpha_l e^{j2\pi(f_c - f_d)t}, \tag{4.128}$$

where, α_l are generated as described above. f_d is the Doppler shift produced by a moving vehicle can be found using $f_d = v/\lambda$. In case of accelerating source f_d is replaced by f_a as given by (4.78). The maximum multipath propagation delay, τ_m is taken as 8 microseconds. The gain of each antenna is taken as 10 dB. The transmitted power is taken as 100 dBm In simulation of received signal at m[th] antenna through GBSBE and GBSBC channel models two paths (N=2) were assumed. The Doppler shift in both paths was assumed to be equal for moving as well as accelerating source.

4.10 A CASE STUDY

In this chapter the fractional Fourier domain beamforming is implemented using the beamformer shown in Fig. 4.7. The input signal is taken as a harmonic with frequency 100 MHz, which is falling at the beamformer along with AWGN. The source is assumed to be moving in a direction of the array. The input signal is also assumed to fade to take into account the multipath propagation scenario. The source is considered as a

a) Stationary source
b) Source moving with constant velocity
c) An accelerating source with initial velocity

The fading on the source is also considered to be

i) Rayleigh fading
ii) Ricean Fading
iii) Nakagami fading.

The beamformer's performance is also evaluated in microcellular and macro cellular environments using GBSBE and GBSBC models. In all these cases the noise is assumed to AWGN. The MSE in each case has been calculated using fractional Fourier domain beamforming, time and frequency domain beamforming. The input SNR to the array is also varied to show the robustness of the FrFT beamformer. The results are shown in the Figs. 4.13-4.48

4.11 Experimental Details

In the experiment a 5 element uniform linear array is taken. The spacing between elements is taken as $d=\lambda/2$. The harmonic source is in far field emitting frequency 100 MHz. The first element of beamformer is taken as reference element. The source is considered as stationary as well as moving with a constant velocity of 10 to 100m/sec.The acceleration of the source is varied from 2 to 6m/sec^2. Total 21 samples of the signal are taken as the value of 'a' is varied from -1 to 1 with a step of 0.1. For finding the variation of MSE with 'a', for each value of 'a', 500 independent realizations of the signal plus noise are considered. The average of these 500 squared estimation errors values gives an estimate of MSE. This procedure is repeated for each value of a, for a fixed SNR. The value of 'a', that minimizes the MSE for a given SNR is the optimum value of 'a' for that SNR. For finding the variation in MSE with SNR,

for each value of SNR, 200 independent realizations are taken. For obtaining plots MSE vs SNR the optimal value of 'a' is used for each value of SNR. The average of these 200 independent realizations gives MSE for that value of SNR.

4.12 Improvement in output SNR and Array Gain of the FrFT beamformer

The improvement in the output SNR and array gain of the FrFT beamformer are investigated next to find the superiority of the proposed beamforming technique over time and frequency domain beamforming. For AWGN case the output SNR and array gain is derived in section 3.10. The output SNR of FrFT beamformer is simulated in AWGN environment without fading. The array gain defined as the ratio of output SNR to input SNR is plotted for the AWGN case in Fig.4.49.The results of output SNR for AWGN environment are also shown in Fig.4.50a and Fig.4.50b. For a faded signal case the SNR is derived below. The input and output SNR in fading channels are defined next.

Input SNR

Using the model described in 4.7.1 the received signal at the m^{th} antenna in multipath environment is modified by a multiplicative distortion and additive noise and is given by

$$x_m(t) = g_m\, s(t) + n_m(t), \tag{4.129}$$

where, s(t) is transmitted signal or desired signal, n(t) is AWGN and where, g is a random variable and depends upon the fading distribution. The received power of signal is given by

$$P_r = \frac{1}{2}\frac{1}{T_s}\int_0^{Ts}\left|g_m\right|^2\left|s(t)\right|^2 dt = \left|g_m\right|^2\frac{1}{2T_s}\int_0^{Ts}\left|s(t)\right|^2 dt = \frac{\left|(g_m)\right|^2}{2}. \tag{4.130}$$

It is assumed that s(t) is normalized s.t. $\frac{1}{T_s}\int_0^{Ts}\left|s(t)\right|^2 dt = 1$. Factor $\frac{1}{2}$ is due to rms value of amplitude. As slow fading is assumed so the $\left|g_m\right|$ remains constant over a symbol period and can be brought out of integral. Thus SNR_{ele} at the m^{th} element is given by

$$SNR_{ele} = \gamma_m = \frac{\left|g_m\right|^2}{2\sigma_w^2}, \tag{4.131}$$

where, σ_w^2 is the noise power. Let us assume Rayleigh fading environment so that $\left|g_m\right|$ has Rayleigh pdf and $SNR_{ele}=\left|g_m\right|^2$ has exponential pdf given by

$$|g_m| \approx \frac{g_m}{P_r} e^{-\frac{|g_m|^2}{2P_r}}, \tag{4.132}$$

$$SNR_{ele} \approx \frac{1}{\Gamma} e^{-\frac{\gamma_m}{\Gamma}}. \tag{4.133}$$

$$\Gamma = E[SNR_{ele}] = \frac{E\{|g_m|^2\}}{\sigma_w^2} = \frac{P_r}{\sigma_w^2}. \tag{4.134}$$

It is noted that the SNR_{ele} at each element is an exponentially distributed random variable. Γ represents the average SNR at each element.

Output SNR

The received signals at the array elements are in a vector $\boldsymbol{x}(t)$ given by

$$\boldsymbol{x}(t) = \boldsymbol{g}s(t) + \boldsymbol{n}(t), \tag{4.135}$$

where, $$\mathbf{g} = [g_0\ g_1\ \ldots\ldots g_{M-1}]^T, \tag{4.136}$$

and $$\mathbf{n} = [n_0,\ n_1\ \ldots\ldots n_{M-1}]^T. \tag{4.137}$$

The output of the beamformer is given by

$$y(t) = \boldsymbol{w}^H \boldsymbol{x}(t) = \boldsymbol{w}^H \boldsymbol{g}\, s(t) + \boldsymbol{w}^H \boldsymbol{n}. \tag{4.138}$$

where, $\boldsymbol{w}$ is the optimum weight vector. SNR at the beamformer output known as the array SNR, is given by

$$SNR_{out} = \frac{E|\boldsymbol{w}^H \boldsymbol{g}|^2}{E|\boldsymbol{w}^H \boldsymbol{n}|^2}. \tag{4.139}$$

The denominator of (4.139) is given by

$$E\left\{|\boldsymbol{w}^H \boldsymbol{n}|^2\right\} = E\left\{|\boldsymbol{w}^H \boldsymbol{n}\boldsymbol{n}^H \boldsymbol{w}|\right\} = \boldsymbol{w}^H E[\boldsymbol{n}\boldsymbol{n}^H]\boldsymbol{w} = \sigma_w^2 \boldsymbol{w}^H \boldsymbol{I}_N \boldsymbol{w} = \sigma_w^2 \boldsymbol{w}^H \boldsymbol{w} = \sigma_w^2 \|\boldsymbol{w}\|^2, \tag{4.140}$$

where, $\boldsymbol{I}_N = M \times M$ = Identity matrix. The output SNR is therefore given by

$$SNR_{out} = \gamma = \frac{1}{\sigma_w^2} \frac{E|\boldsymbol{w}^H \boldsymbol{g}|^2}{\|\boldsymbol{w}\|^2}. \tag{4.141}$$

For Maximal ratio beamformer with $\boldsymbol{w}=\boldsymbol{g}$. The output SNR is given by

$$SNR_{out} = \sum_{m=0}^{M-1} \frac{|g_m|^2}{2\sigma_w^2} = \sum_{m=0}^{M-1} \gamma_m. \tag{4.142}$$

The output SNR is, therefore, the sum of the SNR at each element. The expected value of the output SNR is therefore M times the average SNR at each element, i.e. $E[\gamma]=M\Gamma$, which indicates that on average, the SNR improves by a factor of M.

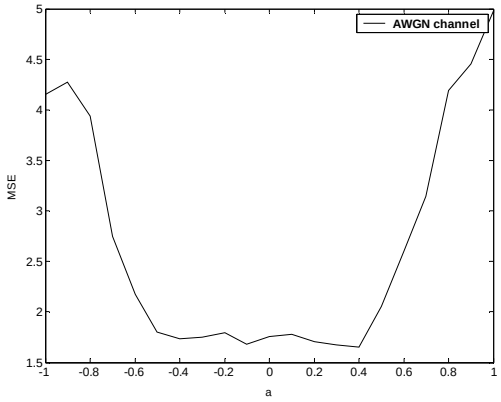

(a) A stationary source

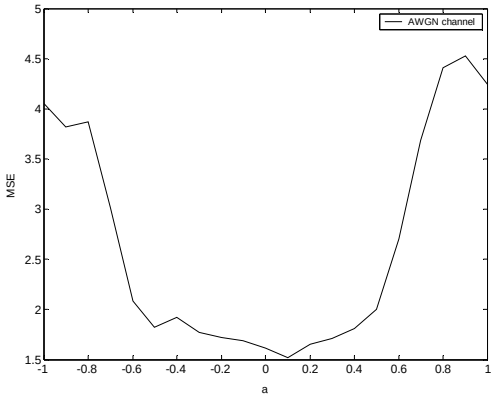

(b) A source with velocity of 20m/sec

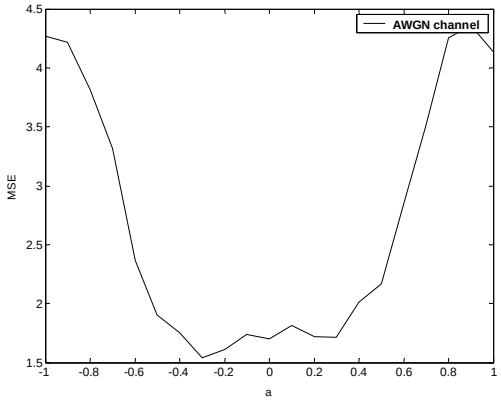

(c) A source with velocity of 40m/sec

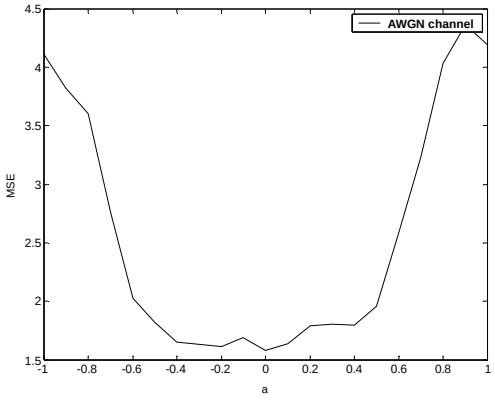

(d) A source with velocity of 60m/sec

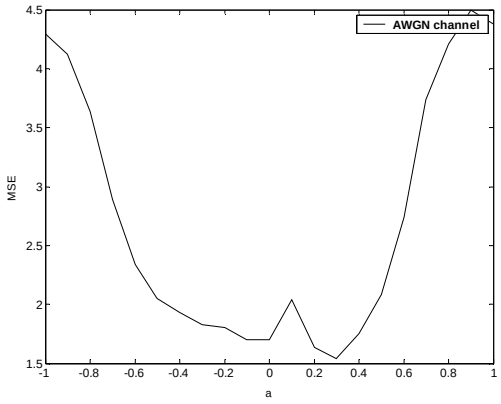

(e) A source with velocity of 80m/sec

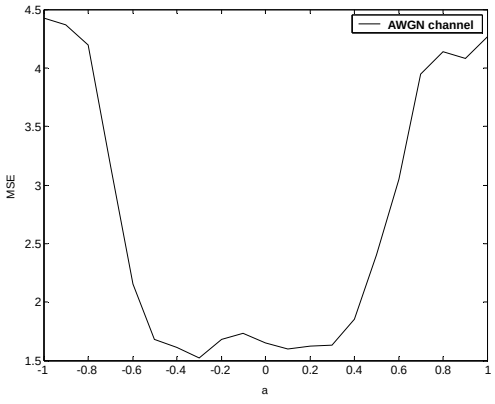

(f) A source with velocity of 100m/sec

Figure 4.13- MSE Vs 'a' for a source moving in AWGN channel

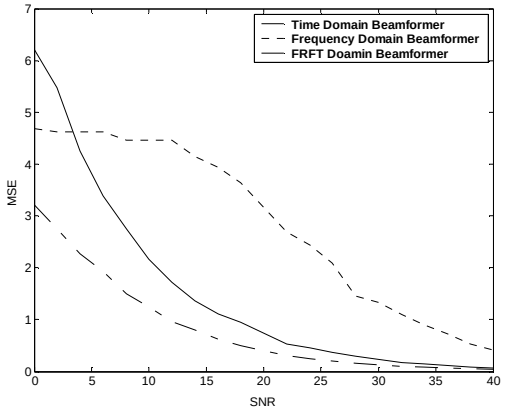

(a) A Stationary Source

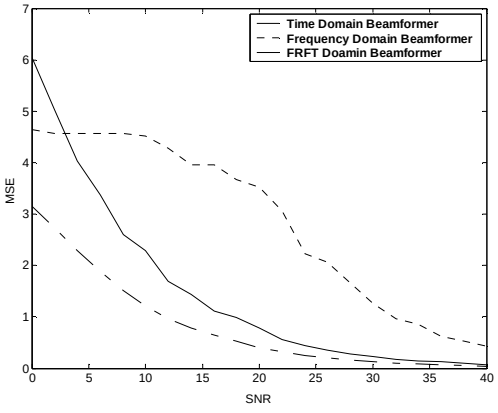

(b) A source with velocity of 20m/sec

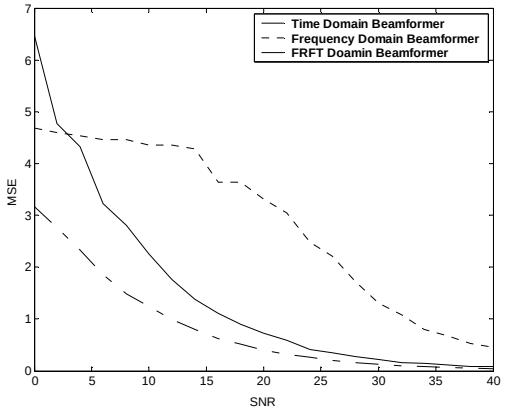

(c) A source with velocity of 40m/sec

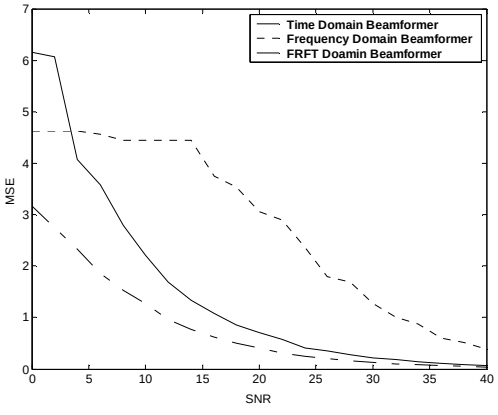

(d) A source with velocity of 60m/sec

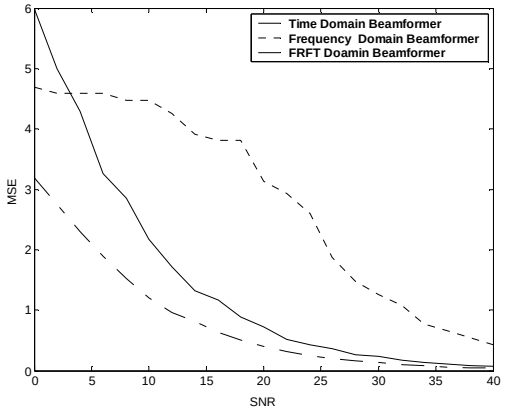

(e) A source with velocity of 80m/sec

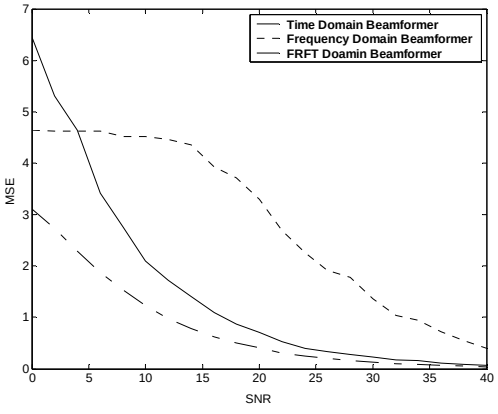

(f) A source with velocity of 100m/sec

Figure 4.14- MSE Vs 'SNR' for a source moving in AWGN channel

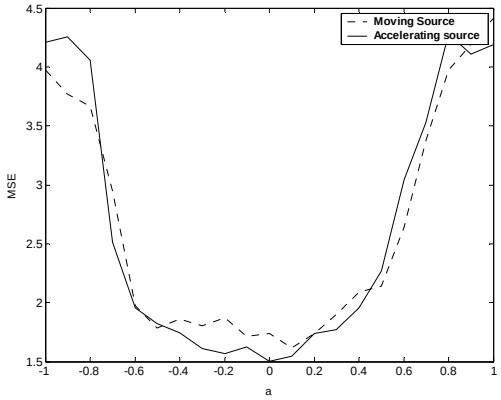

(a) A source with velocity 10m/sec and other source with acceleration 2m/sec^2

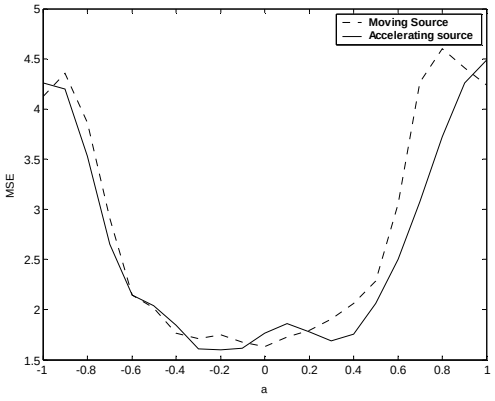

(b) A source with velocity 20m/sec and other source with acceleration 6m/sec^2

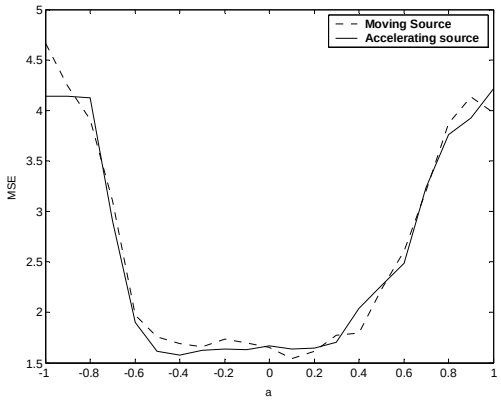

(c) A source with velocity 40m/sec and other source with acceleration 2m/sec^2

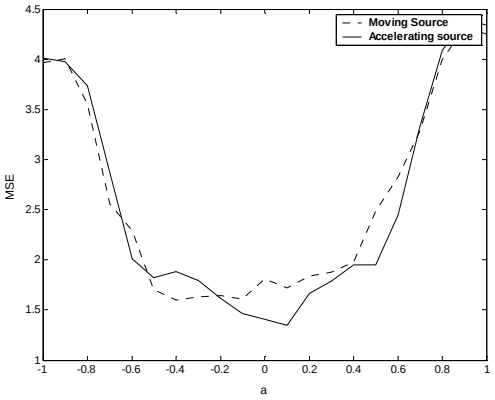

(d) A source with velocity 60m/sec and other source with acceleration 6m/sec^2

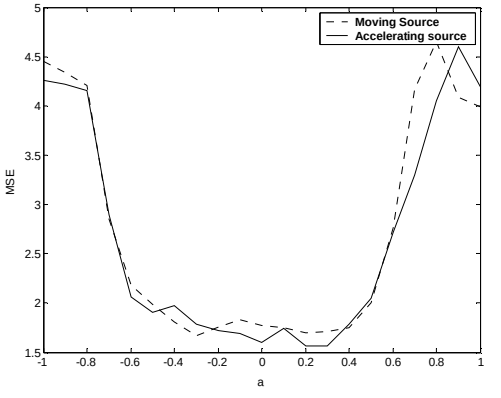

(e) A source with velocity 80m/sec and other source with acceleration 2m/sec^2

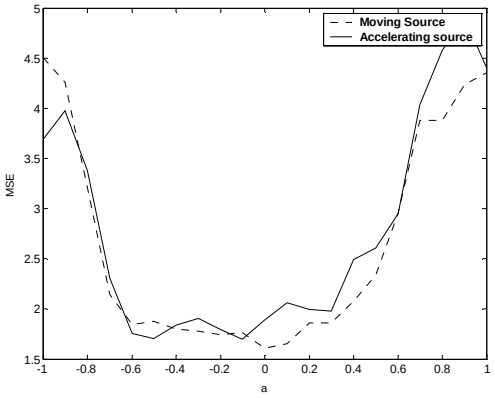

(f) A source with velocity 100m/sec and other source with acceleration 6m/sec^2

Figure 4.15-Comparison of the variation of the MSE with 'a' of two sources, one moving with constant velocity and an other accelerating source, moving with zero initial velocity, in AWGN channel

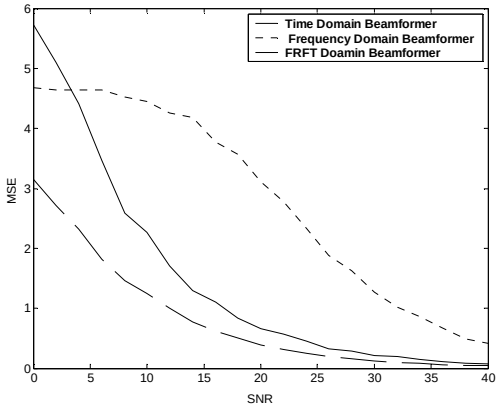

(a) Stationary Source with acceleration 2m/sce^2

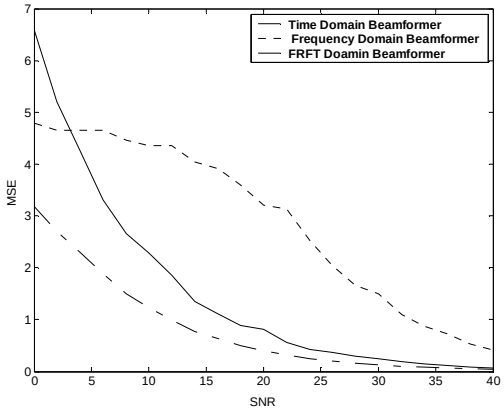

(b) Source with initial velocity 10m/sec and acceleration 2m/sce^2

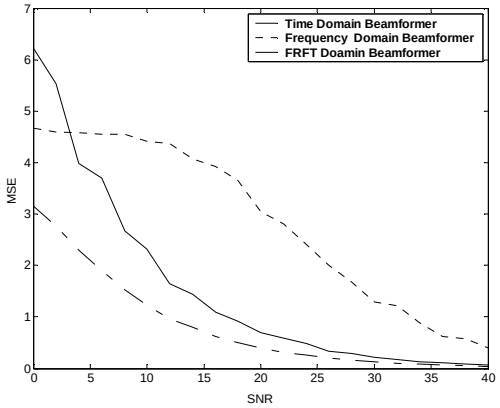

(c) Source with initial velocity 20m/sec and acceleration 6m/sce^2

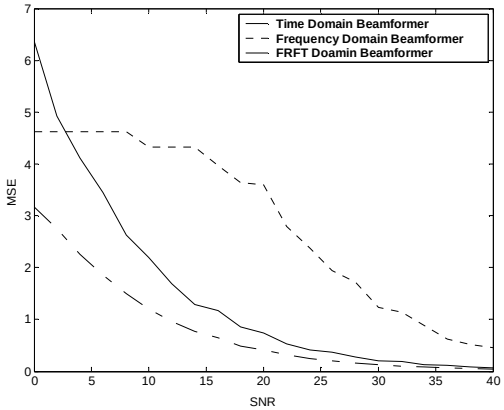

(d) Source with initial velocity 40m/sec and acceleration 2m/sce^2

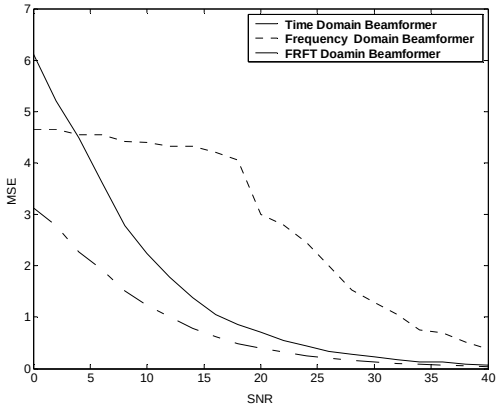

(e) Source with initial velocity 60m/sec and acceleration 6m/sce^2

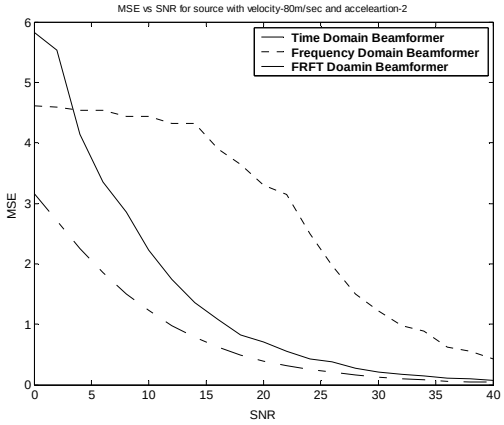

(f) Source with initial velocity 80m/sec and acceleration 2m/sce^2

Figure 4.16- MSE Vs 'SNR' of an accelerating source in AWGN channel

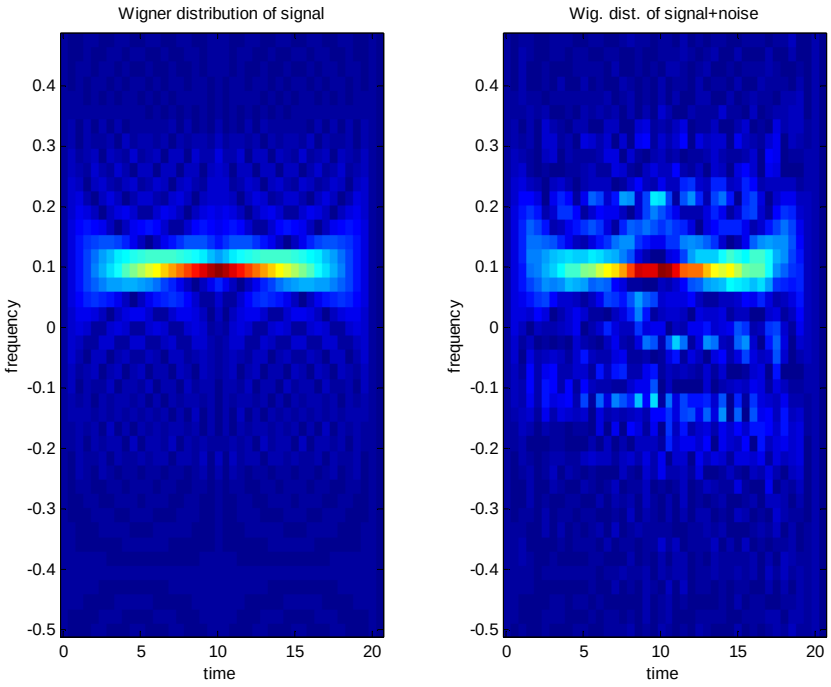

Figure 4.17- Wigner Distribution of signal (b) Wigner distribution of received signal in AWGN channel

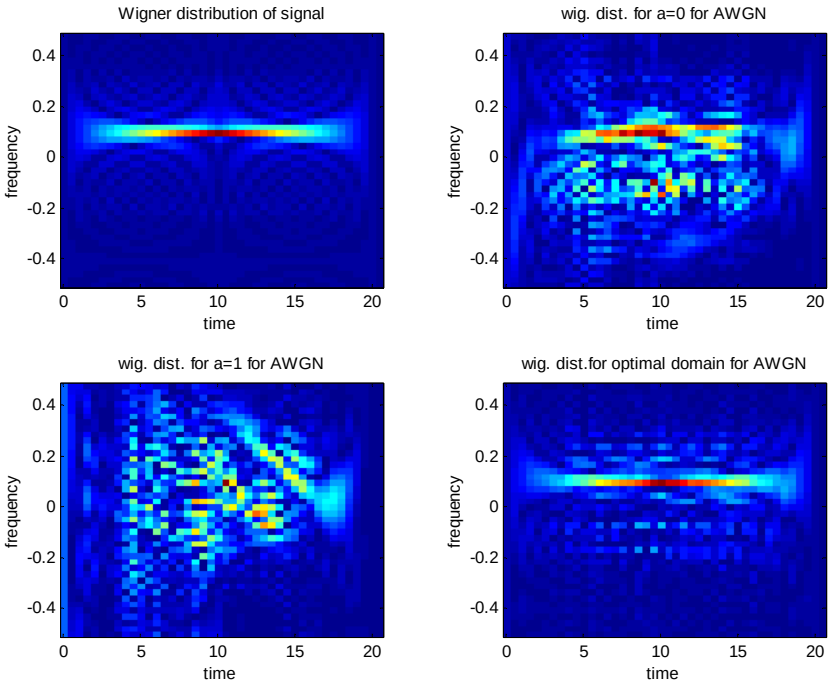

Figure 4.18 - (a) Wigner Distribution of signal (b-d) Wigner Distribution of estimated signal in (b)Time domain, (c)Frequency domain and (d)Optimal FrFT domain (AWGN channel)

Table-4.2: Performance of Optimum FrFT Domain Beamformer compared with Frequency (a=1) and Time Domain (a=0) beamformer in AWGN channel for a moving source

S. No	Velocity of Source (m/sec)	Optimal Domain	Beamformer's MSE for SNR=20 dB			Reduction in MSE in %	
			Time Domain a=0	Frequency Domain a=1	Optimum Domain a=aopt	Optimum Vs Time Domain	Optimum Vs Freq. Domain
1	0	0.4	0.7355	3.1663	0.3965	46.4%	87.0%
2	10	0.2	0.6320	3.3279	0.3867	43.1%	88.1%
3	20	0.1	0.7770	3.5208	0.3955	49.2%	88.7%
4	30	-0.1	0.6567	3.3659	0.3969	39.5%	88.3%
5	40	-0.3	0.7268	3.3126	0.4010	42.6%	87.8%
6	50	0.1	0.6809	3.4439	0.3905	42.6%	88.6%
7	60	0	0.7054	3.0649	0.4037	42.7%	86.8%
8	70	0.2	0.7215	3.6742	0.4036	44.0%	89.0%
9	80	0.3	0.7229	3.1394	0.4007	44.2%	87.2%
10	90	-0.2	0.6613	3.2051	0.3936	40.3%	87.7%
11	100	-0.3	0.7072	3.3050	0.4028	43.0%	87.8%

Table-4.3: MSE of moving and accelerating source for Optimum Domain Beamformer in AWGN channel

S. No	Velocity of Source (m/sec)	Acc. of Source (m/sec^2)	Optimum domain for moving source	Optimum domain for Acc. source	MSE in case of moving source	MSE in case of Acc. Source
1	10	2	0.1	0.0	1.61	1.50
2	10	6	-0.1	-0.4	1.55	1.51
3	20	2	-0.3	0.0	1.68	1.54
4	20	6	0	-0.2	1.62	1.59
5	40	2	0.1	-0.4	1.54	1.57
6	40	6	-0.3	0.3	1.58	1.58
7	60	2	-0.3	0.2	1.70	1.56
8	60	6	-0.4	0.1	1.60	1.34
9	80	2	-0.3	0.3	1.66	1.56
10	80	6	0.3	0.2	1.64	1.51
11	100	2	0.3	0.1	1.71	1.59
12.	100	6	0.1	0.1	1.65	1.69

Table-4.4: Performance of Optimum FrFT Domain Beamformer compared with Frequency (a=1) and Time Domain (a=0) beamformer in AWGN channel for an accelerating source

S. No	Velocity of Source (m/sec)	Acc. of Source (m/sec^2)	Beamformer's MSE for SNR=20 dB			Reduction in MSE in %	
			Time Domain a=0	Frequency Domain a=1	Optimum Domain a=aopt	Optimum Vs Time Domain	Optimum Vs Freq. Domain
1	10	2	0.7247	3.4150	0.4029	44.0%	88.3%
2	10	6	0.6159	3.1510	0.3863	37.2%	88.3%
3	20	2	0.7592	3.150	0.4203	44.6%	86.6%
4	20	6	0.6979	2.9496	0.3912	43.9%	86.7%
5	40	2	0.7357	3.5960	0.4107	44.2%	88.6%
6	40	6	0.7049	3.0804	0.3919	44.2%	87.2%
7	60	2	0.7244	3.2892	0.4033	44.3%	87.7%
8	60	6	0.7011	3.0065	0.4003	42.9%	86.6%
9	80	2	0.7077	3.2997	0.3890	45.0%	88.2%
10	80	6	0.6826	3.2459	0.3979	47.7%	87.7%
11	100	2	0.6958	3.2512	0.3861	44.5%	88.1%
12	100	6	0.7512	3.3663	0.4084	45.6%	87.6%

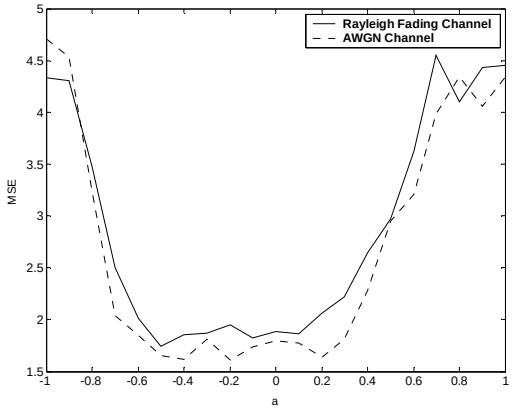

(a) A stationary source

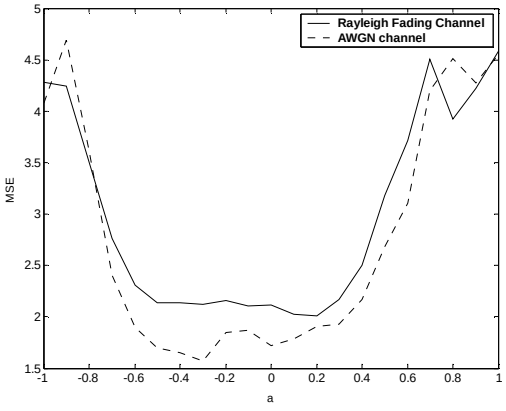

(b) A source with velocity of 20m/sec

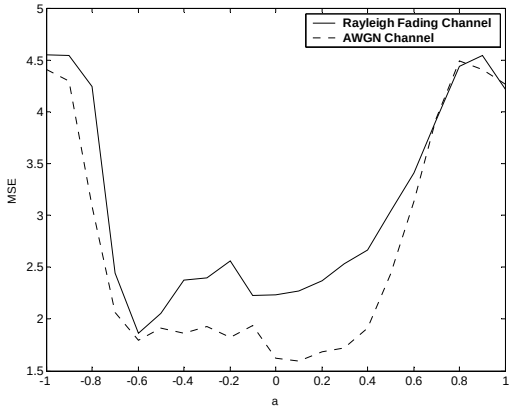

(c) A source with velocity of 40m/sec

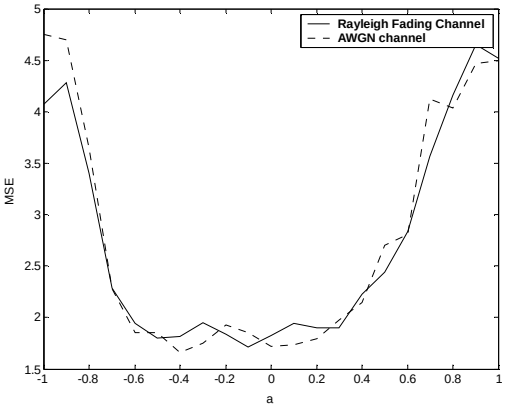

(d) A source with velocity of 60m/sec

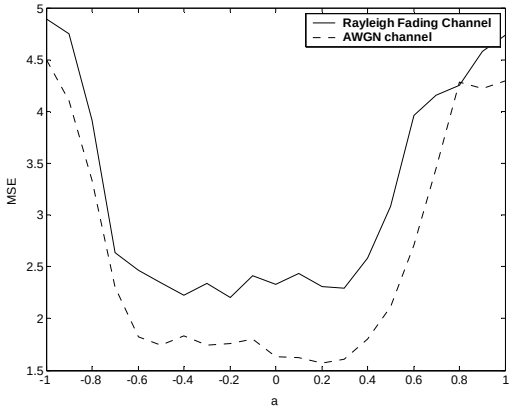

(e) A source with velocity of 80m/sec

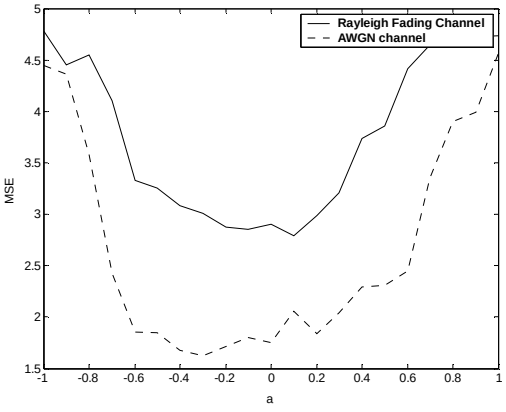

(f) A source with velocity of 100m/sec

Figure 4.19- MSE Vs 'a' of a source moving in Rayleigh faded channel

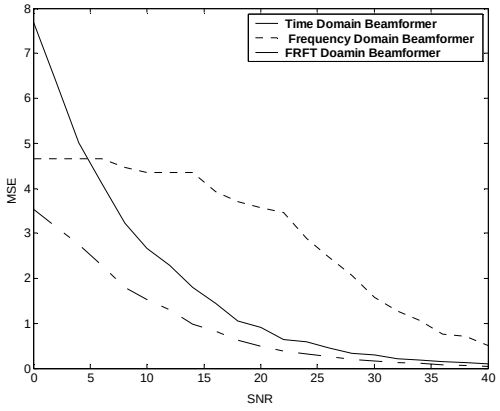

(a) A Stationary Source

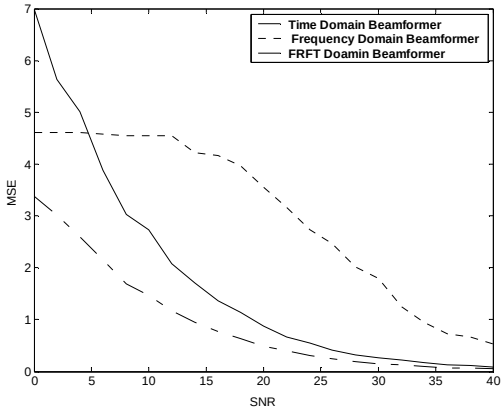

(b) A source with velocity of 20m/sec

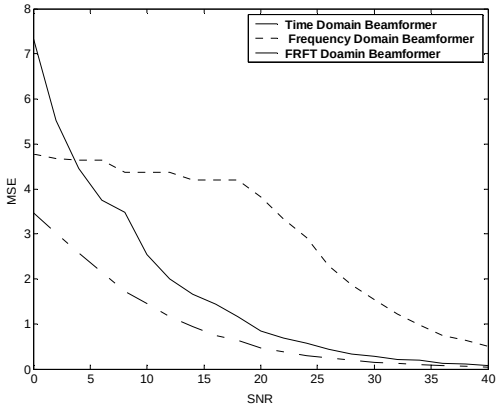

(c) A source with velocity of 40m/sec

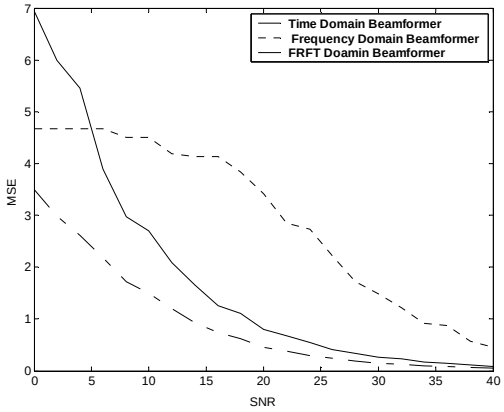

(d) A source with velocity of 60m/sec

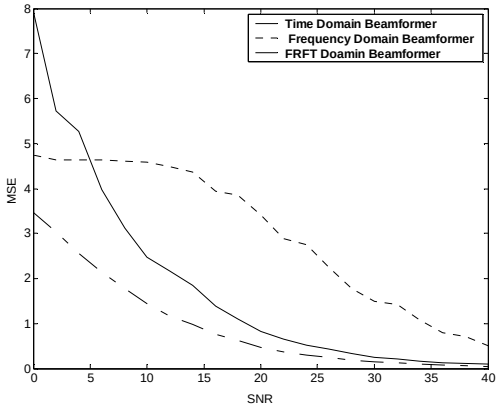

(e) A source with velocity of 80m/sec

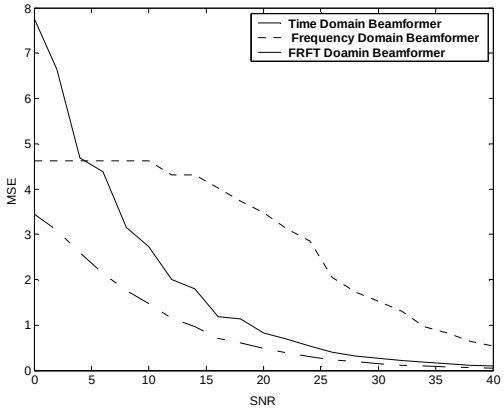

(f) A source with velocity of 100m/sec

Figure 4.20- MSE Vs 'SNR' of a source moving in Rayleigh faded channel

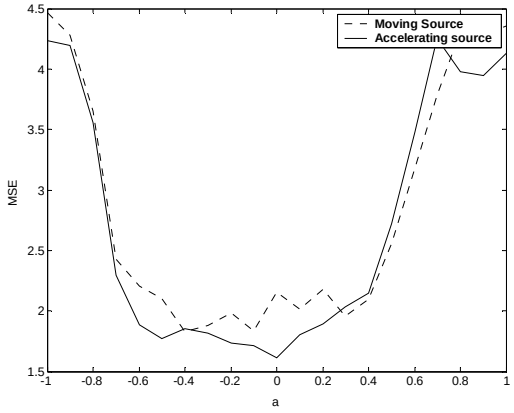

(a) A source with velocity 10m/sec and other source with acceleration 2m/sec^2

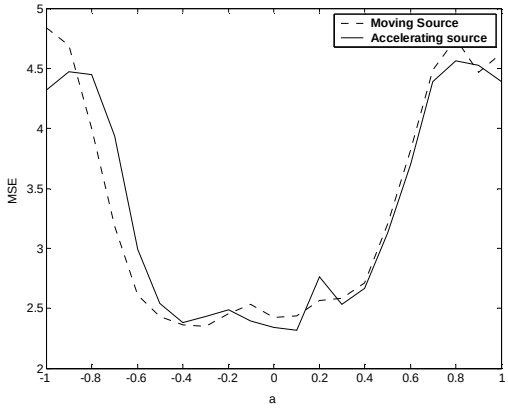

(b) A source with velocity 20m/sec and other source with acceleration 6m/sec^2

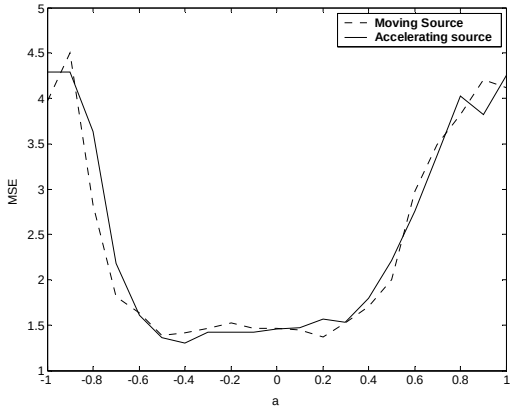

(c) A source with velocity 40m/sec and other source with acceleration 2m/sec^2

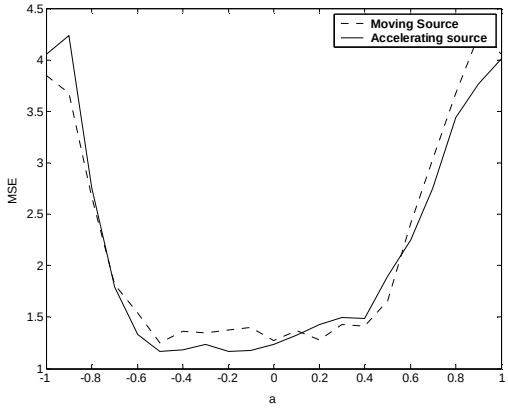

(d) A source with velocity 60m/sec and other source with acceleration 6m/sec^2

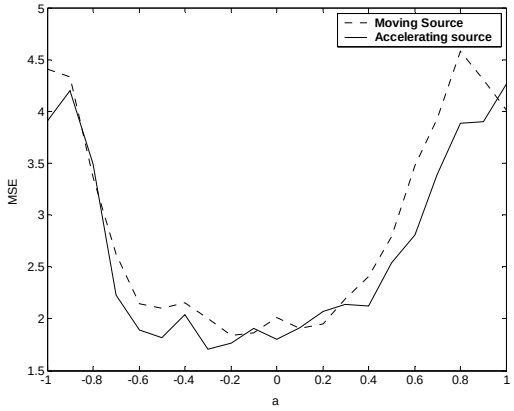

(e) A source with velocity 80m/sec and other source with acceleration 2m/sec^2

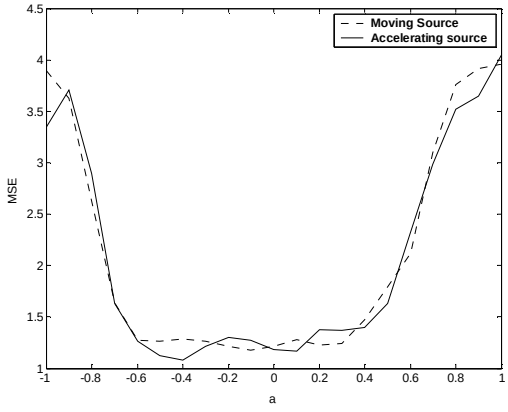

(f) A source with velocity 100m/sec and other source with acceleration 6m/sec^2

Figure 4.21- Comparison of the variation of the MSE with 'a' of two sources, one moving with constant velocity and an other accelerating source moving with zero initial velocity, in Rayleigh faded channel

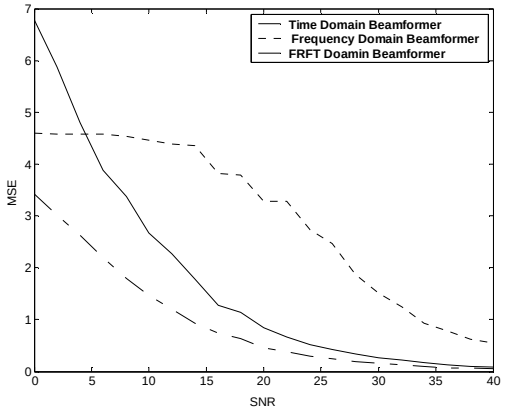

(a) Stationary Source with acceleration 2m/sce^2

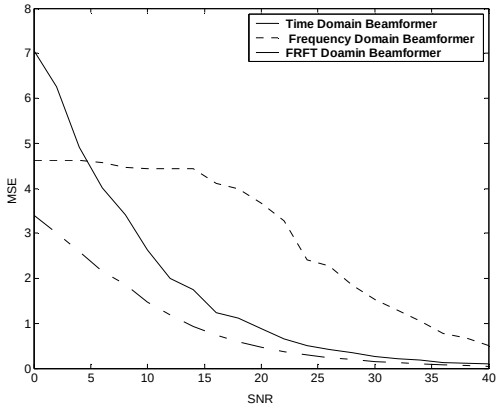

(b) Source with initial velocity 10m/sec and acceleration 2m/sce^2

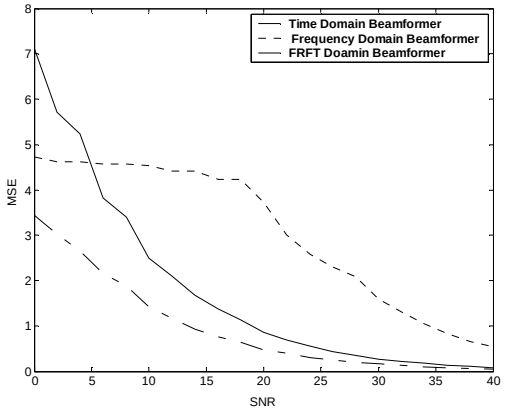

(c) Source with initial velocity 20m/sec and acceleration 6m/sce^2

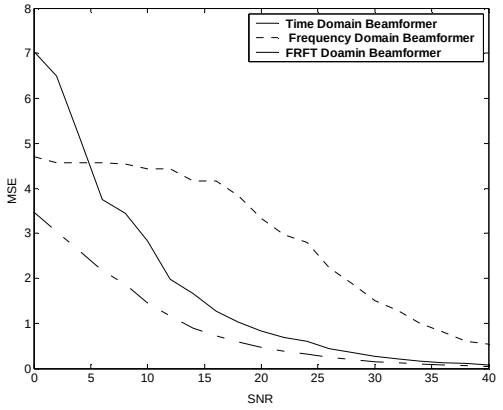

(d) Source with initial velocity 40m/sec and acceleration 2m/sce^2

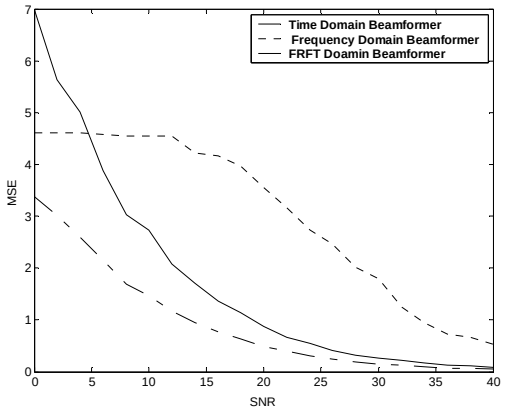

(e) Source with initial velocity 60m/sec and acceleration 6m/sce^2

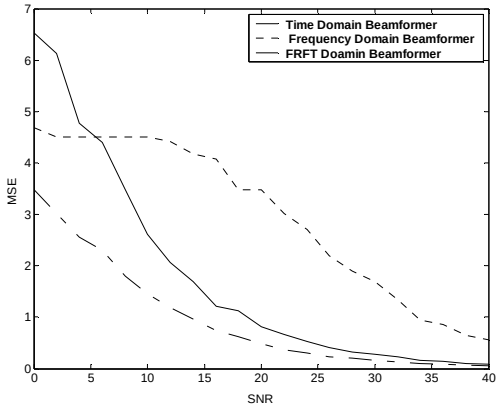

(f) Source with initial velocity 80m/sec and acceleration 2m/sce^2

Figure 4.22- MSE Vs 'SNR' of an accelerating source in Rayleigh faded channel

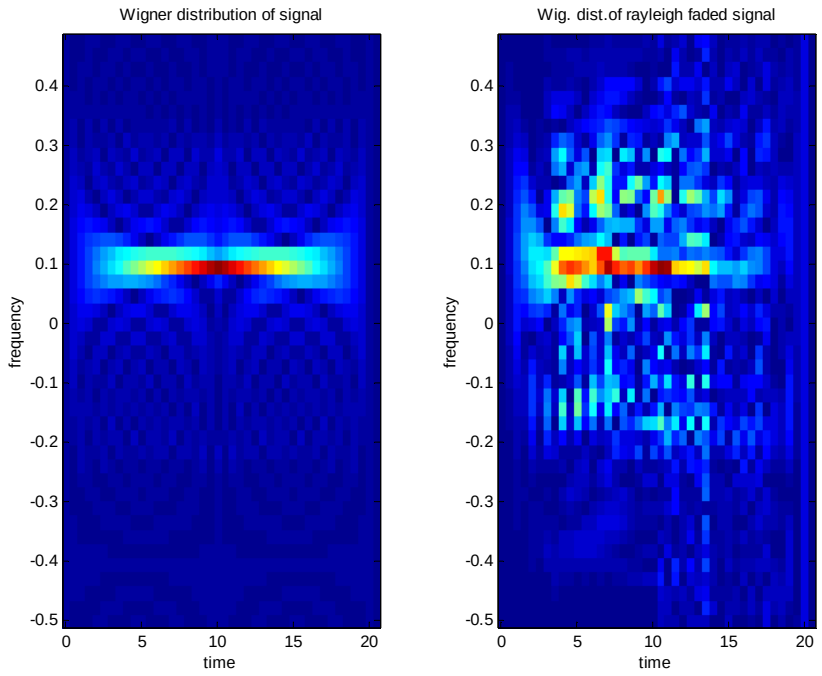

Figure 4.23-(a) Wigner Distribution of signal (b) Wigner distribution of received Rayleigh faded signal (Initial Velocity =10m/sec and acceleration 2m/sec^2)

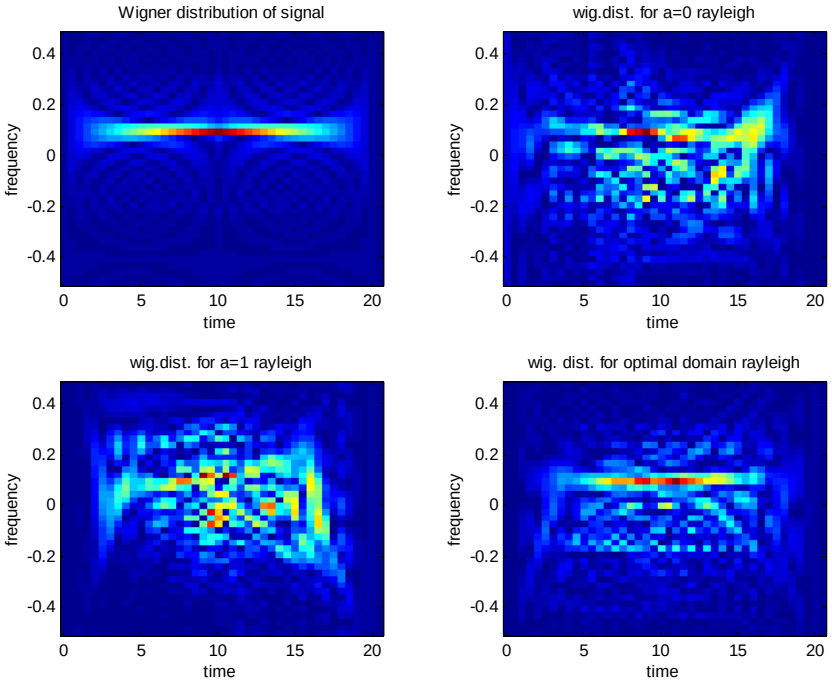

Figure 4.24-(a) Wigner Distribution of signal (b-d) Wigner Distribution of estimated signal in (b)Time domain,(c) Frequency domain and (d)Optimal FrFT domain (Rayleigh faded channel)

Table-4.5: Performance of Optimum FrFT Domain Beamformer compared with Frequency (a=1) and Time Domain (a=0) beamformer in Rayleigh channel for a moving source

S. No	Velocity of Source (m/sec)	Optimum Domain for AWGN channel	Optimum Domain for Rayleigh channel	Beamformer MSE for SNR=20 dB			Reduction in MSE in %	
				Time Domain a=0	Freq. Domain a=1	Optimum Domain $a=a_{opt}$	Optimum Vs. Time Domain	Optimum Vs. Freq. Domain
1	0	-0.2	-0.5	0.9075	3.5613	0.4936	45.6%	86.1%
2	10	-0.3	0.1	0.9244	3.6976	0.5136	44.4%	86.1%
3	20	-0.3	0.2	0.8661	3.5478	0.4809	44.4%	86.4%
4	30	-0.4	0.1	0.8188	3.4705	0.4906	40.0%	85.6%
5	40	0.1	-0.6	0.8373	3.8210	0.4755	43.2%	87.5%
6	50	0	-0.3	0.7418	3.4728	0.4733	36.2%	86.3%
7	60	-0.4	-0.1	0.7999	3.4263	0.4571	42.7%	86.6%
8	70	0.1	0.1	0.8192	3.4921	0.4404	46.2%	87.2%
9	80	0.2	-0.2	0.8308	3.4147	0.4678	43.7%	86.3%
10	90	-0.4	0.4	0.8788	3.1376	0.4766	45.7%	84.8%
11	100	-0.3	0.1	0.8298	3.4756	0.4860	41.4%	86.0%

Table-4.6: MSE of moving and accelerating source for Optimum Domain Beamformer in Rayleigh channel

S. No	Velocity of Source (m/sec)	Acceleration of Source (m/sec^2)	Optimum domain for moving source	Optimum domain for Acc. source	MSE of moving source	MSE of Acc. Source
1	10	2	-0.4	0	1.83	1.61
2	10	6	0.1	-0.1	1.52	1.35
3	20	2	0.1	-0.4	1.35	1.32
4	20	6	-0.3	0.1	2.35	2.31
5	40	2	0.2	-0.4	1.37	1.30
6	40	6	-0.5	0	1.66	1.54
7	60	2	0	-0.5	1.32	1.22
8	60	6	-0.5	-0.2	1.25	1.16
9	80	2	-0.2	-0.3	1.84	1.70
10	80	6	0	-0.1	3.32	3.05
11	100	2	-0.2	0.2	1.74	1.68
12.	100	6	-0.1	-0.4	1.18	1.07

Table-4.7: Performance of Optimum FrFT Domain Beamformer compared with Frequency (a=1) and Time Domain (a=0) beamformer in Rayleigh faded channel for an accelerating source

S. No	Velocity of Source (m/sec)	Acc. of Source (m/sec^2)	Beamformer MSE for SNR=20 dB			Reduction in MSE in %	
			Time Domain a=0	Frequency Domain a=1	Optimum Domain a=aopt	Optimum Vs Time Domain	Optimum Vs Freq. Domain
1	10	2	0.8762	3.6717	0.4739	45.9%	87.7%
2	10	6	0.8333	3.3330	0.4637	44.3%	86.0%
3	20	2	0.8535	3.4614	0.4826	43.4%	86.0%
4	20	6	0.8619	3.7221	0.4761	44.7%	87.2%
5	40	2	0.8207	3.3311	0.4632	43.6%	86.0%
6	40	6	0.7941	3.4332	0.4605	45.6%	86.5%
7	60	2	0.8481	3.4178	0.4616	42.0%	86.5%
8	60	6	0.8661	3.5470	0.4809	44.5%	86.4%
9	80	2	0.8188	3.4705	0.4906	40.0%	85.7%
10	80	6	0.8078	3.4710	0.4820	44.5%	86.5%
11	100	2	0.8373	3.8210	0.4755	43.2%	87.5%
12	100	6	0.8481	3.4178	0.4616	45.6%	86.5%

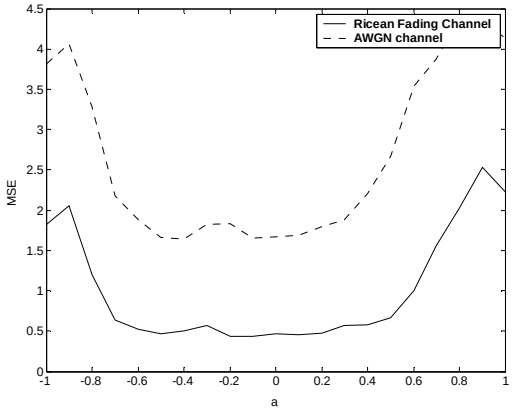

(a) A stationary source

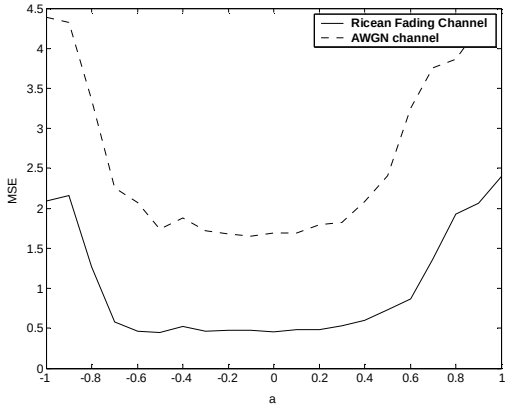

(b) A source with velocity of 20m/sec

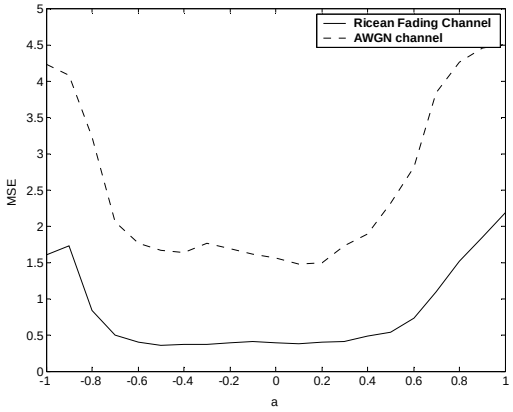

(c) A source with velocity of 40m/sec

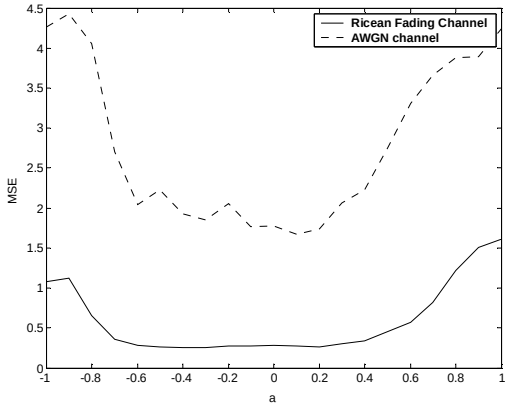

(d) A source with velocity of 60m/sec

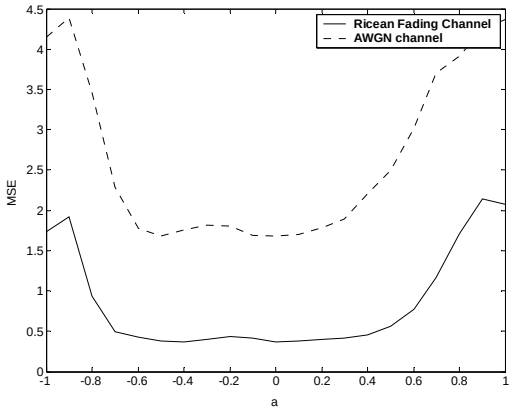

(e) A source with velocity of 80m/sec

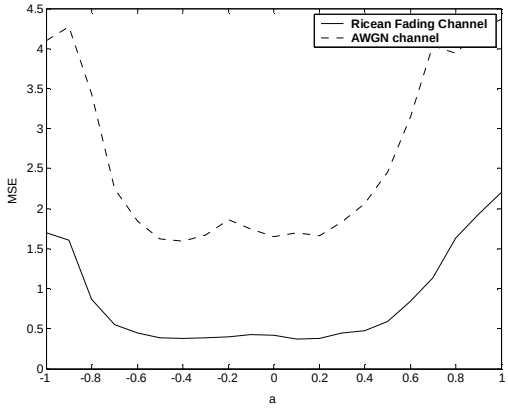

(f) A source with velocity of 100m/sec

Figure 4.25- MSE Vs 'a' of a source moving in Ricean faded channel

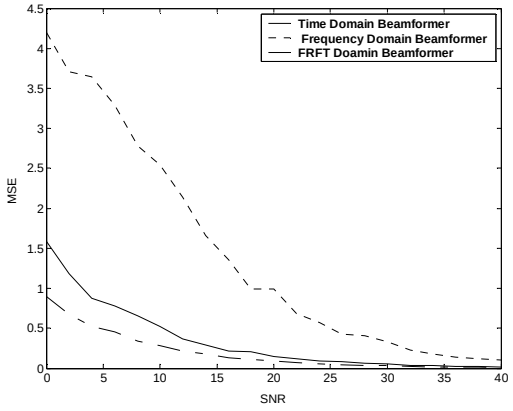

(a) A Stationary Source

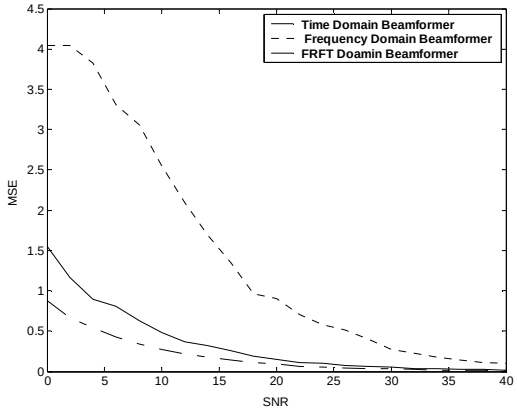

(b) A source with velocity of 20m/sec

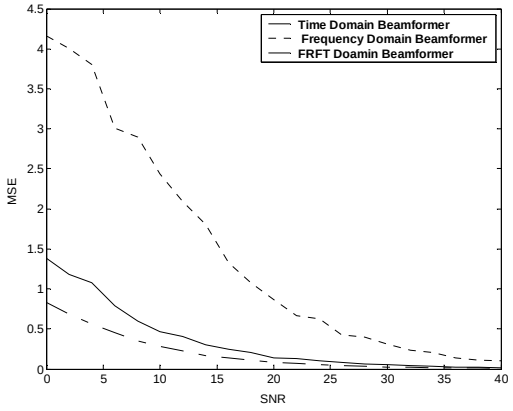

(c) A source with velocity of 40m/sec

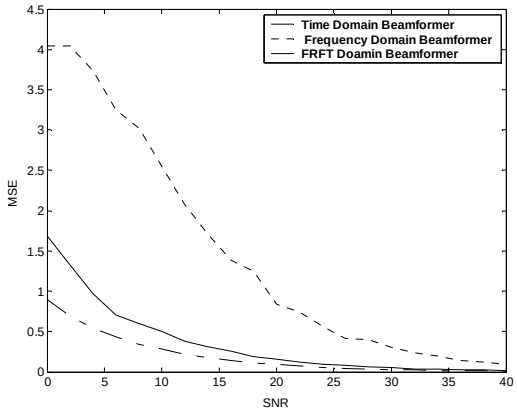

(d) A source with velocity of 60m/sec

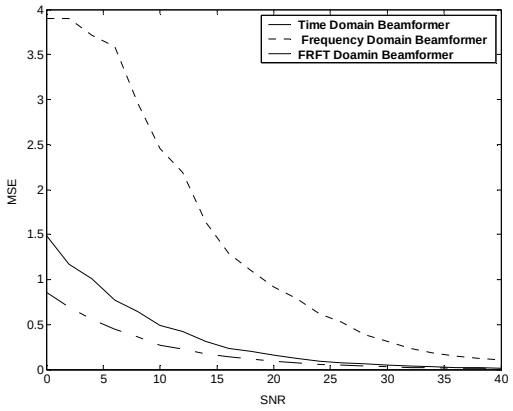

(e) A source with velocity of 80m/sec

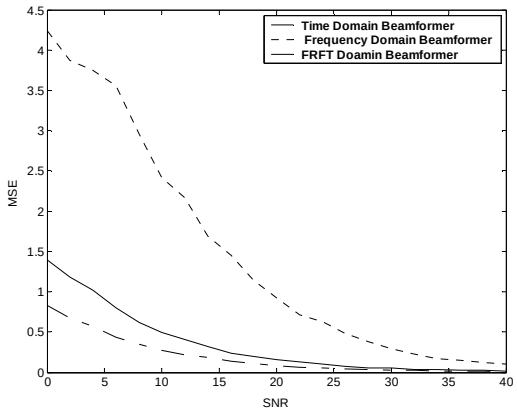

(f) A source with velocity of 100m/sec

Figure 4.26- MSE Vs 'SNR' of a source moving in Ricean faded channel

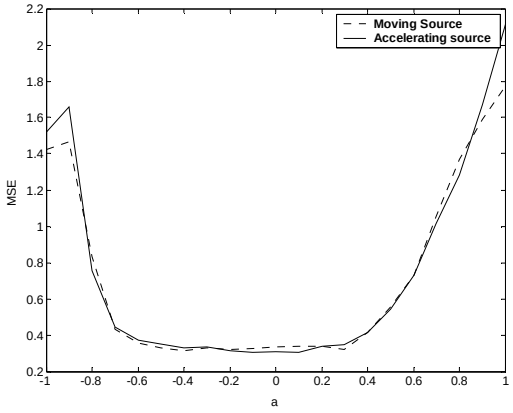

(a) A source with velocity 10m/sec and other source with acceleration 2m/sec^2

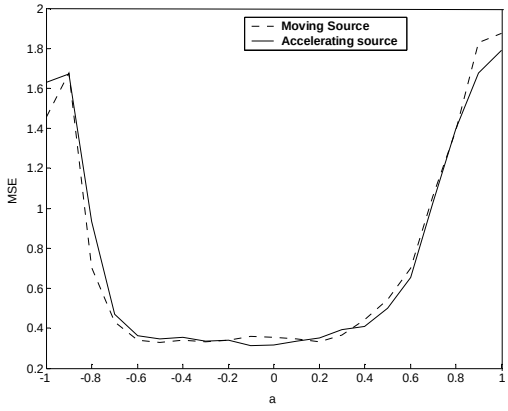

(b) A source with velocity 20m/sec and other source with acceleration 6m/sec^2

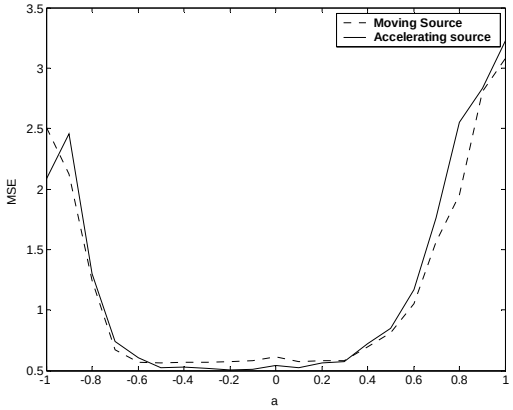

(c) A source with velocity 40m/sec and other source with acceleration 2m/sec^2

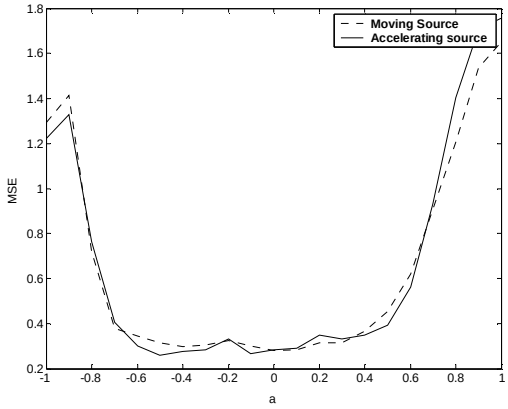

(d) A source with velocity 60m/sec and other source with acceleration 6m/sec^2

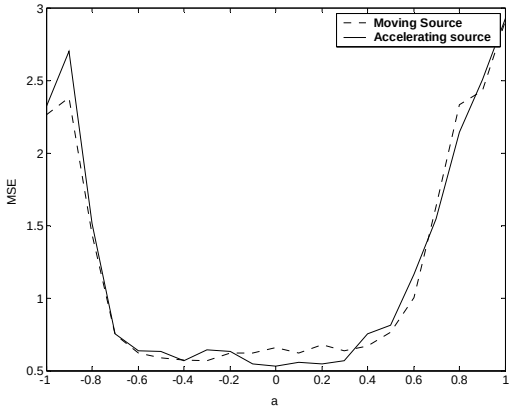

(e) A source with velocity 80m/sec and other source with acceleration 2m/sec^2

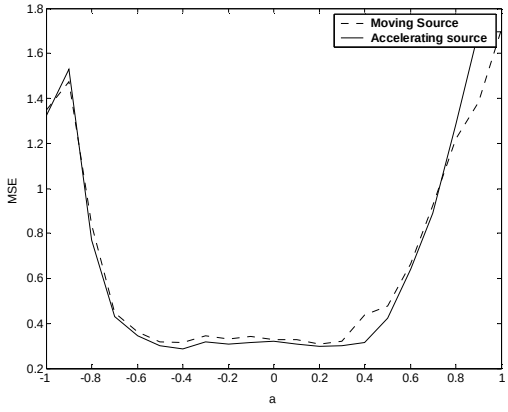

(f) A source with velocity 100m/sec and other source with acceleration 6m/sec^2

Figure 4.27- Comparison of the variation of the MSE with 'a' of two sources, one moving with constant velocity and an other accelerating source moving with zero initial velocity, in Ricean faded channel

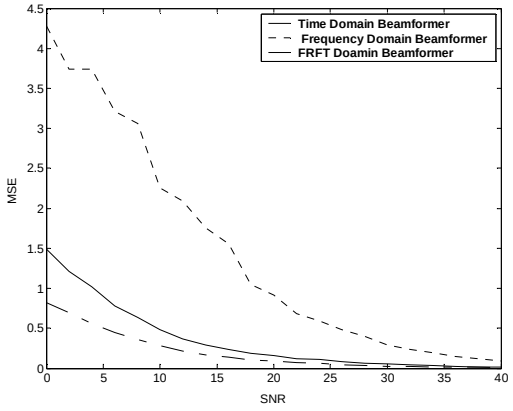

(a) Stationary Source with acceleration 2m/sce^2

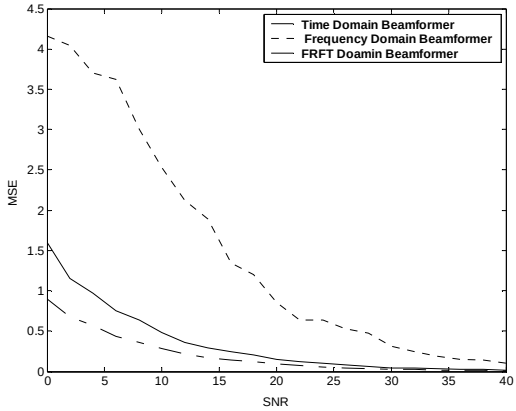

(b) Source with initial velocity 10m/sec and acceleration 2m/sce^2

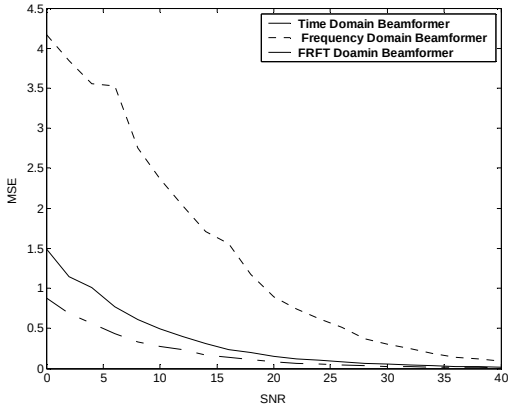

(c) Source with initial velocity 20m/sec and acceleration 6m/sce^2

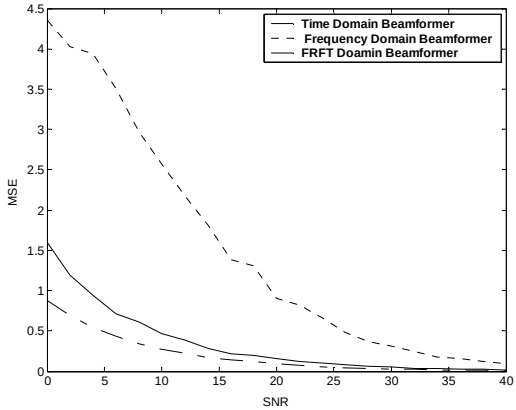

(d) Source with initial velocity 40m/sec and acceleration 2m/sce^2

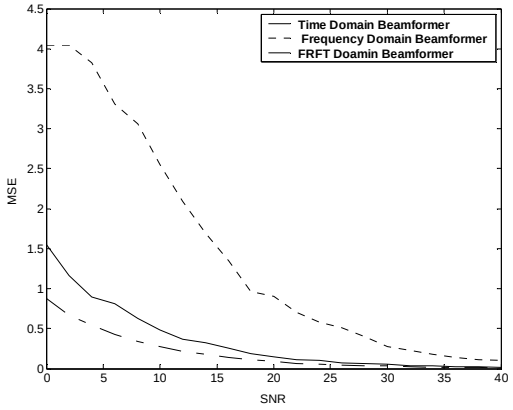

(e) Source with initial velocity 60m/sec and acceleration 6m/sce^2

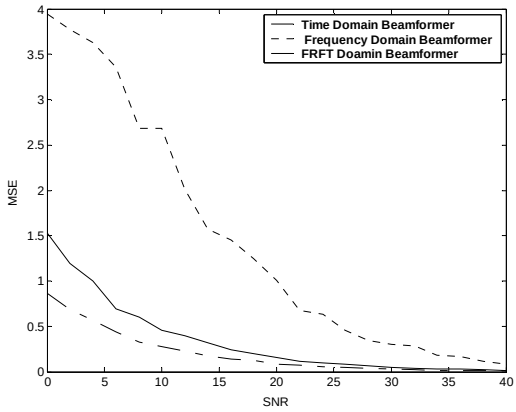

(f) Source with initial velocity 80m/sec and acceleration 2m/sce^2

Figure 4.28- MSE Vs 'SNR' of an accelerating source in Ricean faded channel

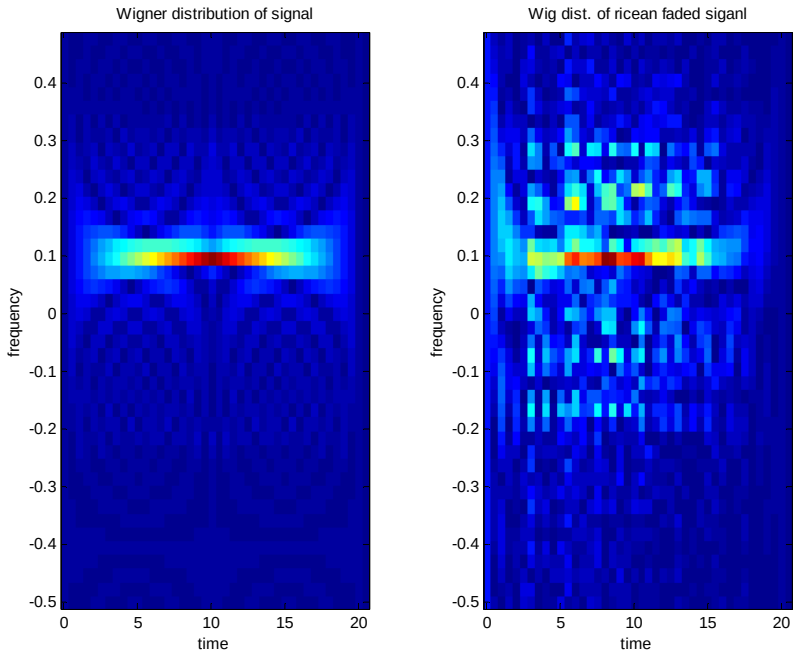

Figure 4.29 – (a) Wigner Distribution of signal (b) Wigner distribution of received Ricean Faded signal (Initial Velocity =10m/sec and acceleration 2m/sec^2)

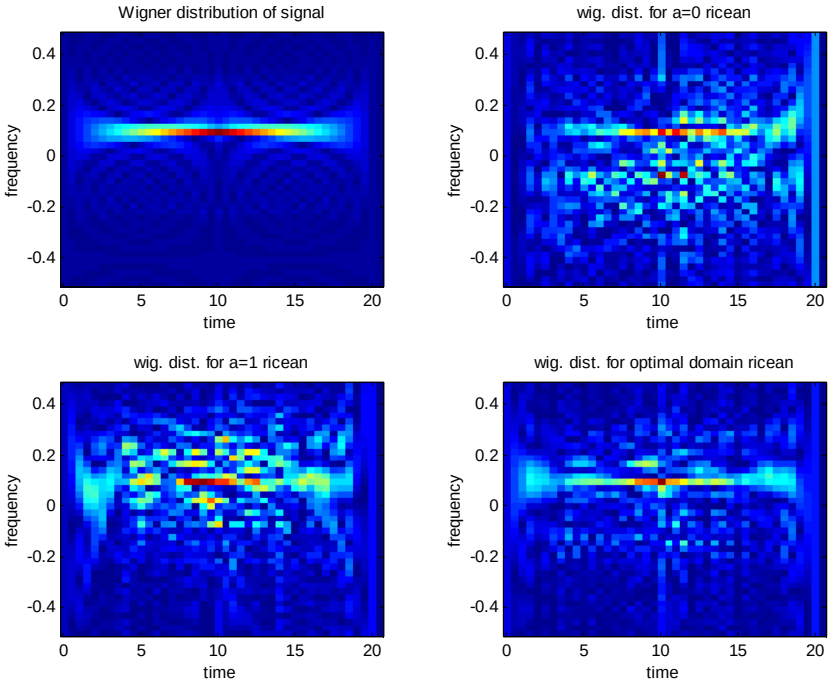

Figure 4.30-(a) Wigner Distribution of signal (b-d) Wigner Distribution of estimated signal in (b) Time domain, (c) Frequency domain and (d) Optimal FrFT domain (Ricean Faded channel)

Table-4.8: Performance of Optimum FrFT Domain Beamformer compared with Frequency (a=1) and Time Domain (a=0) beamformer in Ricean faded channels for a moving source

S. No	Velocity of Source (m/sec)	Optimum Domain for AWGN channel	Optimum Domain for Ricean channel	Beamformer MSE for SNR=20 dB			Reduction in MSE in %	
				Time Domain a=0	Freq. Domain a=1	Optimum Domain $a=a_{opt}$	Optimum Vs. Time Domain	Optimum Vs. Freq. Domain
1	0	-0.4	-0.5	0.1460	0.9105	0.0888	39.0%	91.0%
2	10	-0.1	-0.5	0.1455	0.9380	0.0862	40.7%	90.8%
3	20	-0.4	0.1	0.1460	0.9026	0.0871	40.3%	90.3%
4	30	-0.5	0	0.1566	1.0100	0.0829	47.1%	91.7%
5	40	0.1	-0.5	0.1401	0.8706	0.0817	41.7%	90.6%
6	50	-0.4	-0.4	0.1591	0.8322	0.0878	44.8%	89.4%
7	60	0.1	-0.3	0.1555	0.8355	0.0866	44.4%	89.6%
8	70	0.1	-0.2	0.1590	0.9508	0.0880	44.7%	90.8%
9	80	-0.5	-0.4	0.1603	0.9137	0.0871	45.7%	90.5%
10	90	0	-0.4	0.1480	0.9202	0.0851	42.4%	90.7%
11	100	-0.4	0.1	0.1544	0.9272	0.0842	45.4%	90.9%

Table-4.9: MSE of moving and accelerating source for Optimum Domain Beamformer in Ricean faded channels

S. No	Velocity of Source (m/sec)	Acceleration of Source (m/sec^2)	Optimum domain for moving source	Optimum domain for Acc. source	MSE of moving source	MSE of Acc. Source
1	10	2	-0.4	0.1	0.3149	0.3028
2	10	6	-0.1	-0.5	0.3981	0.3654
3	20	2	0.1	0.1	0.4226	0.3739
4	20	6	-0.5	-0.1	0.3226	0.3131
5	40	2	-0.5	-0.2	0.5577	0.5035
6	40	6	-0.5	0.3	0.4401	0.4346
7	60	2	-0.1	-0.2	0.3250	0.3183
8	60	6	0.0	-0.5	0.2791	0.2609
9	80	2	-0.3	0	0.5662	0.5287
10	80	6	0	-0.4	0.2994	0.2890
11	100	2	-0.1	-0.5	0.2868	0.2824
12.	100	6	0.2	-0.4	0.3081	0.2874

Table-4.10: Performance of Optimum FrFT Domain Beamformer compared with Frequency (a=1) and Time Domain (a=0) beamformer in Ricean faded channel for an accelerating source

S. No	Velocity of Source (m/sec)	Acc. of Source (m/sec^2)	Beamformer MSE for SNR=20 dB			Reduction in MSE in %	
			Time Domain a=0	Frequency Domain a=1	Optimum Domain $a=a_{opt}$	Optimum Vs Time Domain	Optimum Vs Freq. Domain
1	10	2	0.1509	0.8602	0.0870	42.3%	89.9%
2	10	6	0.1531	0.8783	0.0853	44.3%	90.2%
3	20	2	0.1481	0.8659	0.0860	41.2%	90.5%
4	20	6	0.1472	0.8978	0.0834	43.3%	90.7%
5	40	2	0.1571	0.9049	0.0887	43.8%	90.2%
6	40	6	0.1460	0.9905	0.0888	39.2%	91.0%
7	60	2	0.1455	0.9380	0.0862	40.8%	90.5%
8	60	6	0.1460	0.9026	0.0871	40.3%	90.3%
9	80	2	0.1566	1.0100	0.0829	47.0%	91.7%
10	80	6	0.1401	0.8706	0.0817	41.7%	90.6%
11	100	2	0.1591	0.8322	0.0878	44.8%	89.4%
12	100	6	0.1558	0.8355	0.0866	44.4%	89.6%

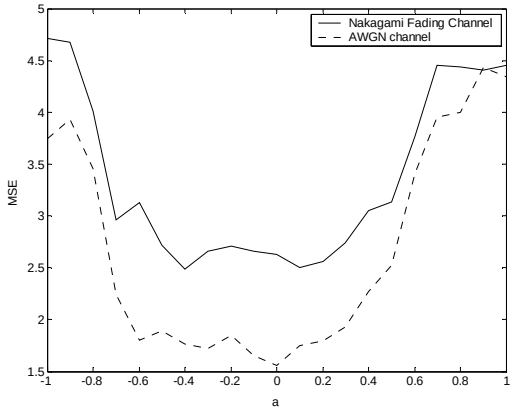

(a) A stationary source

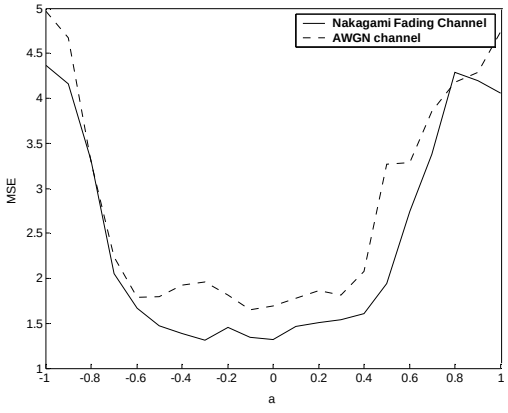

(b) A source with velocity of 20m/sec

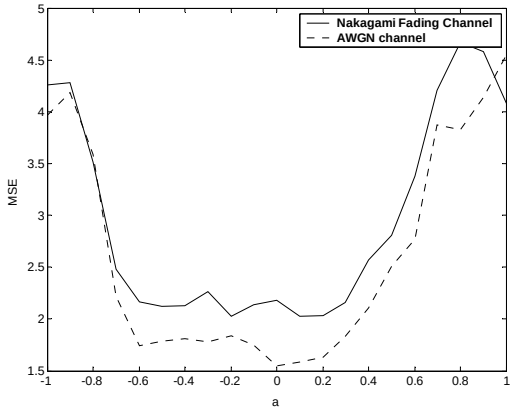

(c) A source with velocity of 40m/sec

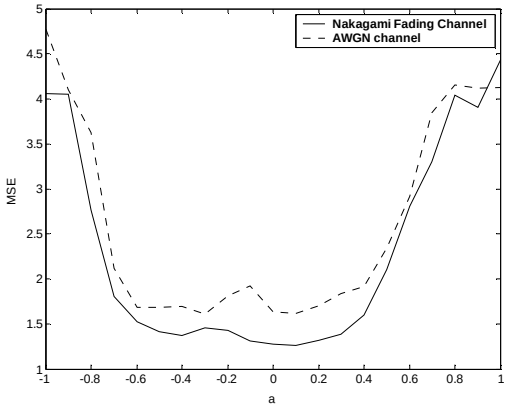

(d) A source with velocity of 60m/sec

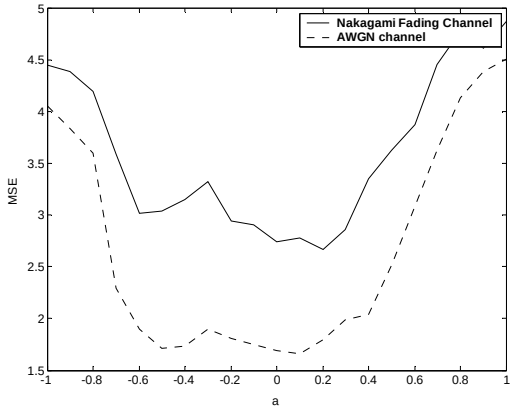

(e) A source with velocity of 80m/sec

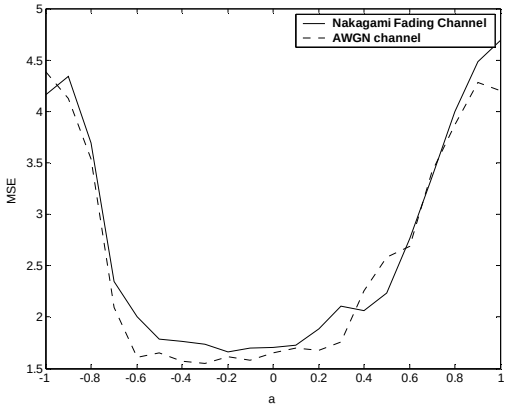

(f) A source with velocity of 100m/sec

Figure 4.31- MSE Vs 'a' of a source moving in Nakagami faded channel

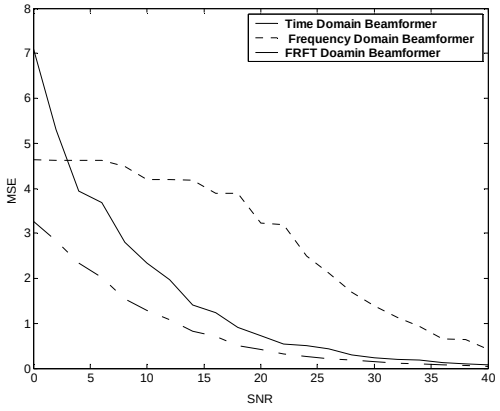

(a) A Stationary Source

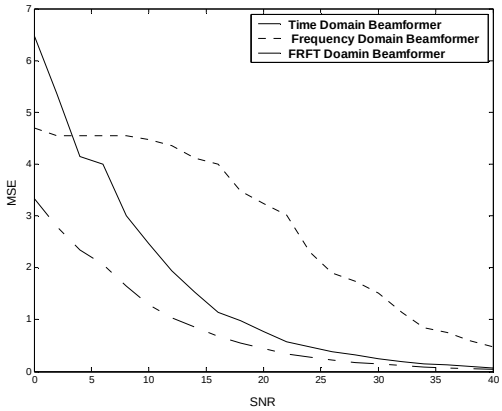

(b) A source with velocity of 20m/sec

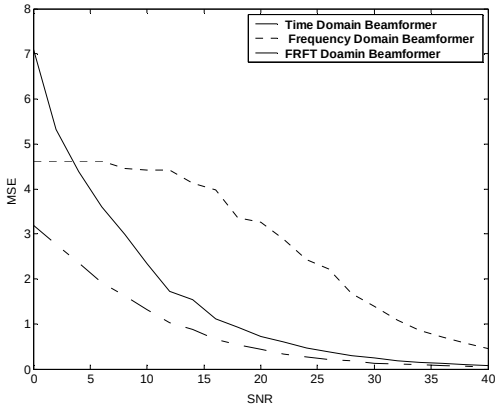

(c) A source with velocity of 40m/sec

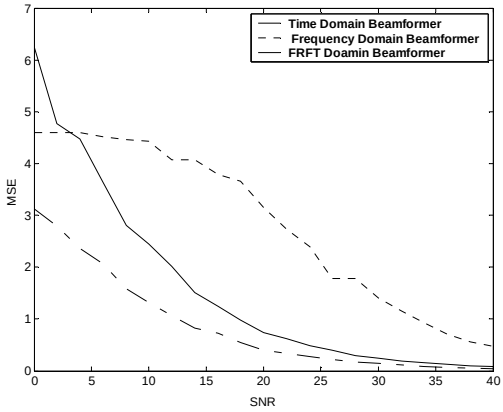

(d) A source with velocity of 60m/sec

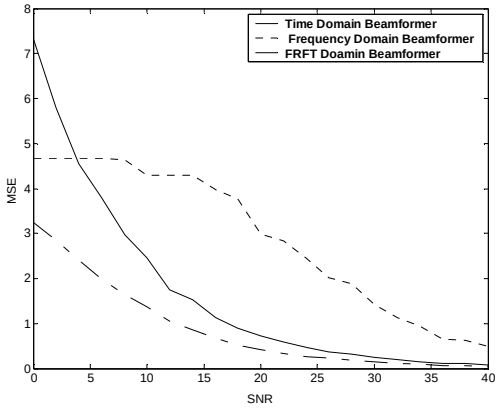

(e) A source with velocity of 80m/sec

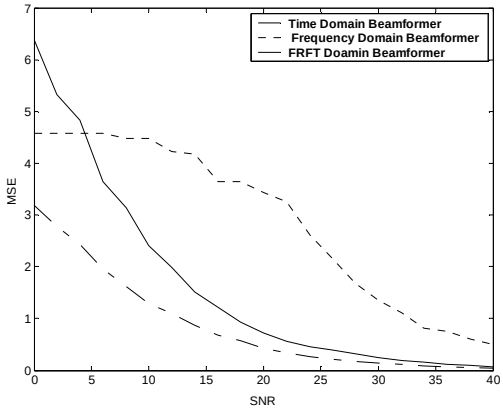

(f) A source with velocity of 100m/sec

Figure 4.32- MSE Vs 'SNR' of a source moving in Nakagami Faded channel

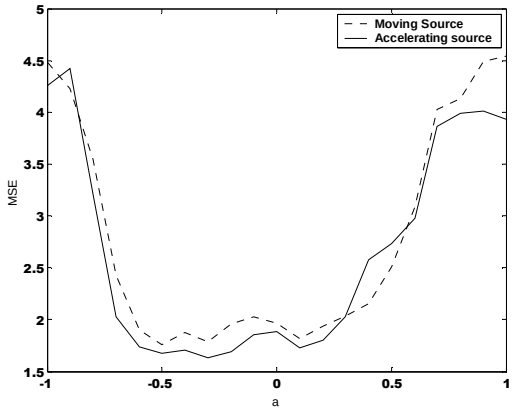

(a) A source with velocity 10m/sec and other source with acceleration 2m/sec^2

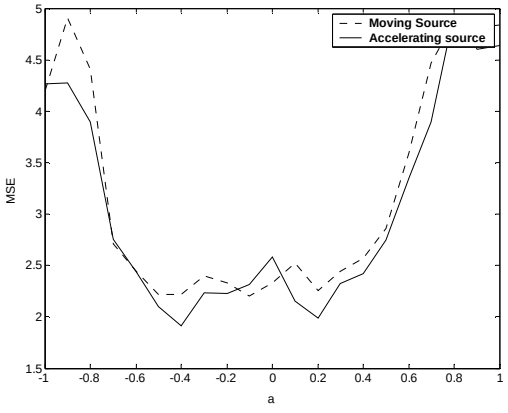

(b) A source with velocity 20m/sec and other source with acceleration 6m/sec^2

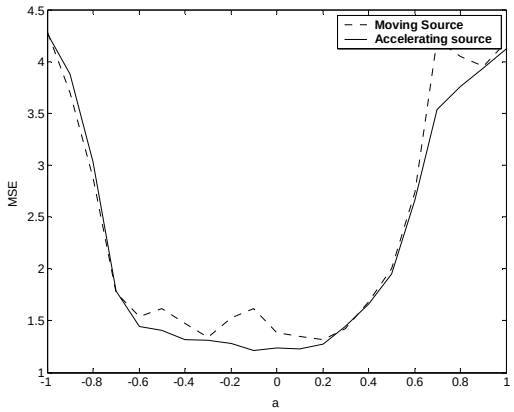

(c) A source with velocity 40m/sec and other source with acceleration 2m/sec^2

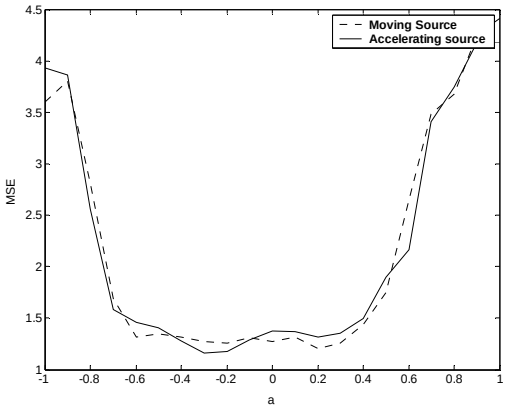

(d) A source with velocity 60m/sec and other source with acceleration 6m/sec^2

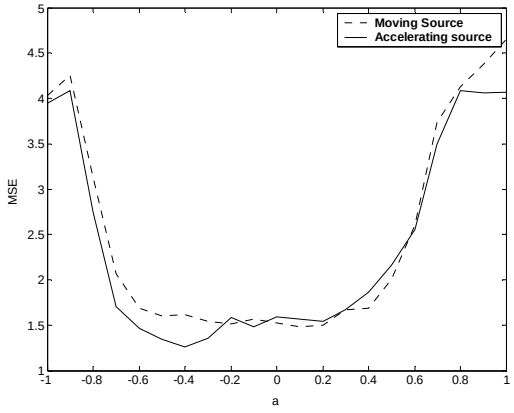

(e) A source with velocity 80m/sec and other source with acceleration 2m/sec^2

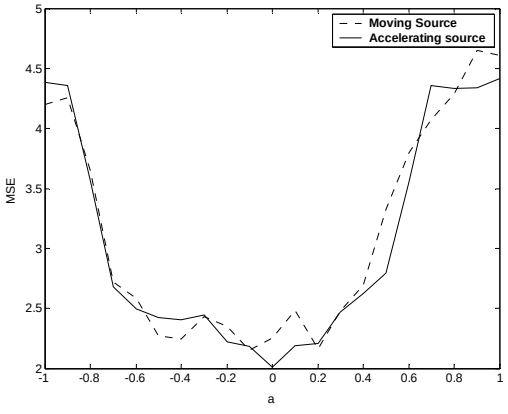

(f) A source with velocity 100m/sec and other source with acceleration 6m/sec^2

Figure 4.33- Comparison of the variation of the MSE with 'a' of two sources, one moving with constant velocity and an other accelerating source moving with zero initial velocity, in Nakagami faded channel

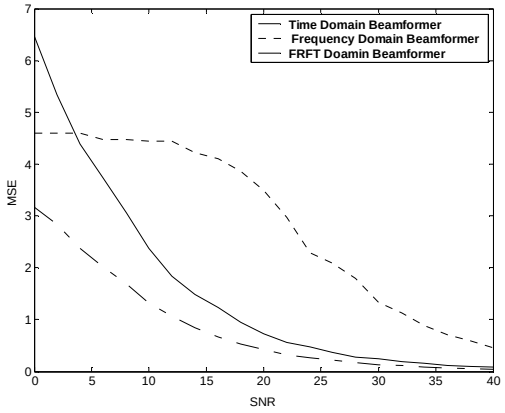

(a) Stationary Source with acceleration 2m/sce^2

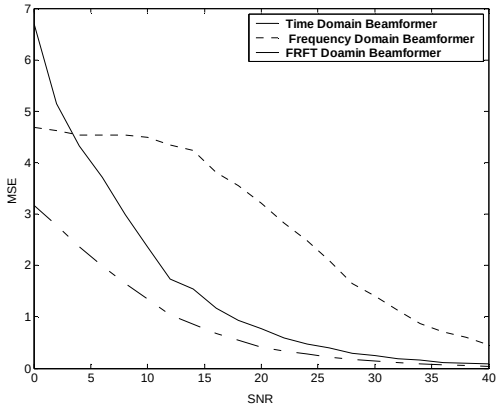

(b) Source with initial velocity 10m/sec and acceleration 2m/sce^2

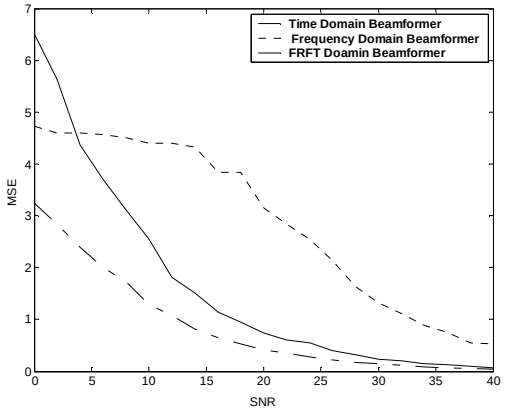

(c) Source with initial velocity 20m/sec and acceleration 6m/sec^2

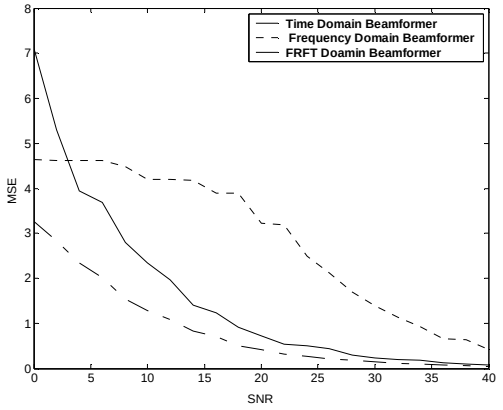

(d) Source with initial velocity 40m/sec and acceleration 2m/sec^2

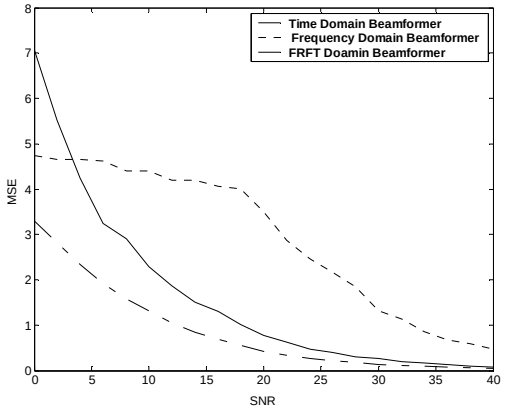

(e) Source with initial velocity 60m/sec and acceleration 6m/sce^2

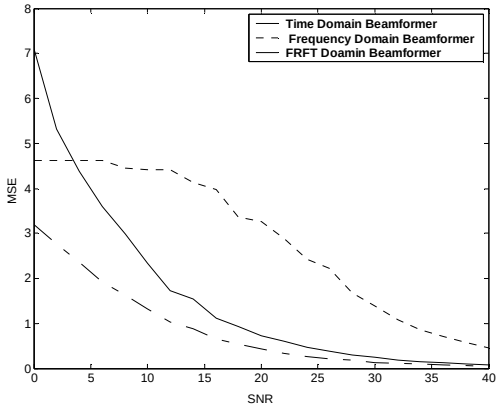

(f) Source with initial velocity 80m/sec and acceleration 2m/sce^2

Figure 4.34-MSE Vs 'SNR' for an accelerating source in Nakagami faded channel

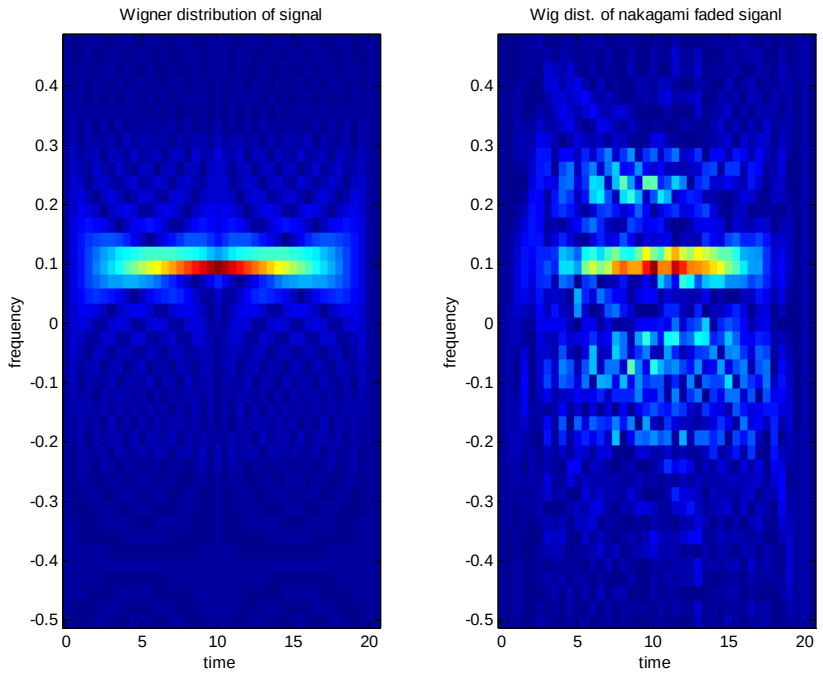

Figure 4.35 - (a) Wigner Distribution of signal (b) Wigner distribution of received Nakagami Faded signal (Initial Velocity =10m/sec and acceleration 2m/sec^2)

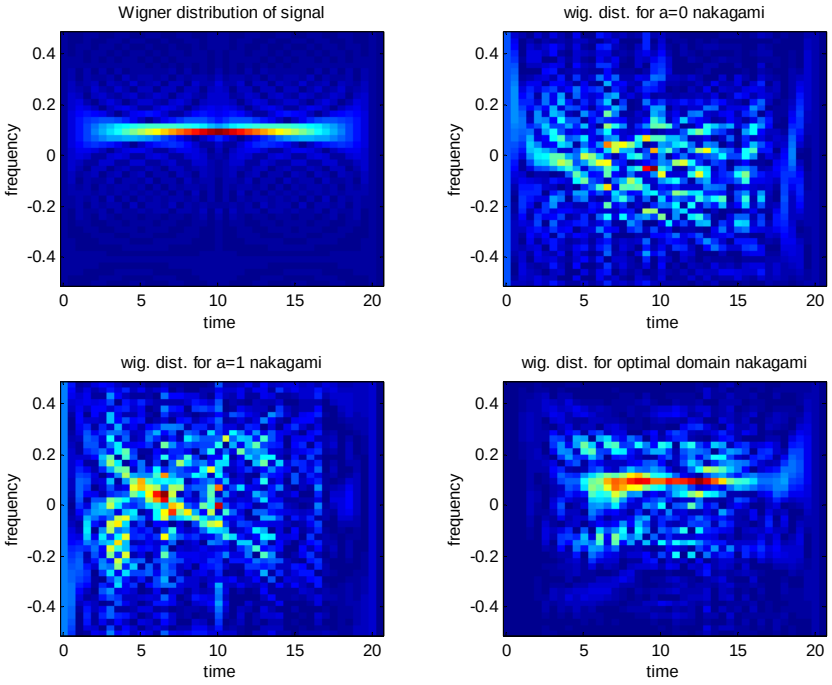

Figure 4.36-(a) Wigner Distribution of signal (b-d) Wigner Distribution of estimated signal in (b) Time domain, (c)Frequency domain and (d)Optimal FrFT domain (Nakagami Faded channel)

Table-4.11: Performance of Optimum FrFT Domain Beamformer compared with Frequency (a=1) and Time Domain (a=0) beamformer in Nakagami faded channel for a moving source

S. No	Velocity of Source (m/sec)	Optimum Domain for AWGN channel	Optimum Domain for Nakagami channel	Beamformer MSE for SNR=20 dB			Reduction in MSE in %	
				Time Domain a=0	Freq. Domain a=1	Optimum Domain $a=a_{opt}$	Optimum Vs. Time Domain	Optimum Vs. Freq. Domain
1	0	0.0	-0.4	0.7187	3.3221	0.4196	41.6%	86.9%
2	10	-0.4	0.0	0.7709	3.3325	0.4275	44.5%	87.2%
3	20	-0.1	-0.3	0.7077	3.2340	0.4423	42.3%	86.3%
4	30	-0.5	-0.2	0.7675	3.4898	0.4234	44.8%	87.9%
5	40	0.0	-0.2	0.7230	3.2531	0.4281	40.8%	86.8%
6	50	-0.2	0.0	0.7720	3.2215	0.4121	46.6%	87.2%
7	60	-0.3	0.1	0.7331	3.1554	0.3948	46.2%	87.5%
8	70	0.1	-0.4	0.7383	3.1333	0.4151	43.8%	86.7%
9	80	0.1	0.2	0.7243	2.9863	0.4135	42.9%	86.1%
10	90	-0.5	-0.5	0.7608	3.5491	0.4357	42.7%	87.7%
11	100	0.3	-0.2	0.7248	3.4397	0.4197	42.0%	87.7%

Table-4.12: MSE of moving and accelerating source for Optimum Domain Beamformer in Nakagami faded channel

S. No	Velocity of Source (m/sec)	Acceleration of Source (m/sec^2)	Optimum domain for moving source	Optimum domain for Acc. source	MSE of moving source	MSE of Acc. Source
1	10	2	-0.5	-0.3	1.75	1.63
2	10	6	-0.5	0.2	2.17	2.02
3	20	2	-0.1	-0.4	1.70	1.49
4	20	6	-0.1	-0.4	2.20	1.91
5	40	2	0.2	-0.1	1.31	1.21
6	40	6	-0.2	-0.3	1.61	1.55
7	60	2	-0.1	-0.4	2.11	1.98
8	60	6	0.2	-0.3	1.20	1.16
9	80	2	0.1	-0.4	1.47	1.25
10	80	6	-0.5	-0.4	1.79	1.63
11	100	2	-0.1	-0.5	1.76	1.67
12.	100	6	-0.1	0	2.14	2.00

Table-4.13: Performance of Optimum FrFT Domain Beamformer compared with Frequency (a=1) and Time Domain (a=0) beamformer in Nakagami faded channel for an accelerating source

S. No	Velocity of Source (m/sec)	Acc. of Source (m/sec^2)	Beamformer MSE for SNR=20 dB			Reduction in MSE in %	
			Time Domain a=0	Frequency Domain a=1	Optimum Domain a=aopt	Optimum Vs Time Domain	Optimum Vs Freq. Domain
1	10	2	0.7634	3.2141	0.4113	46.0%	87.1%
2	10	6	0.7148	3.2124	0.4255	40.5%	86.7%
3	20	2	0.7510	3.3680	0.4184	44.3%	87.5%
4	20	6	0.7358	3.1514	0.4118	44.0%	86.9%
5	40	2	0.7187	3.2232	0.4196	41.6%	86.9%
6	40	6	0.7709	3.3325	0.4275	44.5%	87.1%
7	60	2	0.7677	3.2340	0.4425	42.4%	86.3%
8	60	6	0.7675	3.4898	0.4234	44.8%	87.8%
9	80	2	0.7231	3.2531	0.4281	40.7%	86.8%
10	80	6	0.7720	3.2215	0.4121	46.6%	87.2%
11	100	2	0.7331	3.1554	0.3942	46.2%	87.5%
12	100	6	0.7382	3.1333	0.4151	43.7%	88.7%

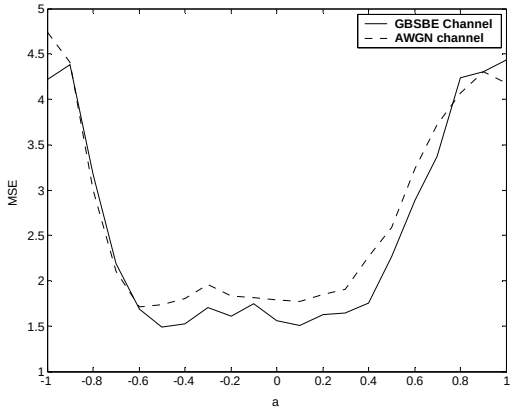

(a) A stationary source

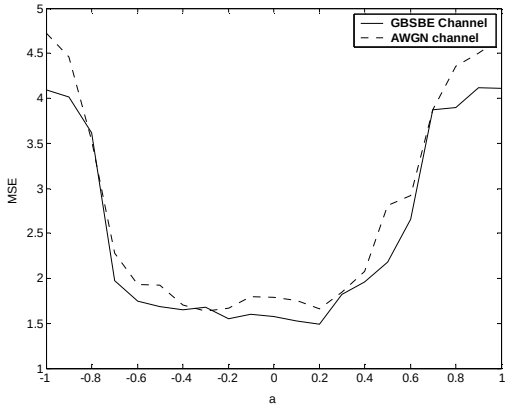

(b) A source with velocity of 20m/sec

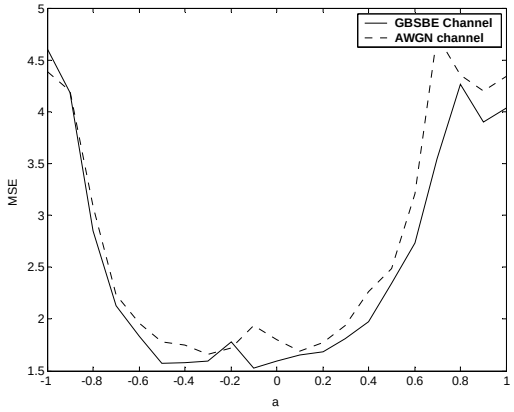

(c) A source with velocity of 40m/sec

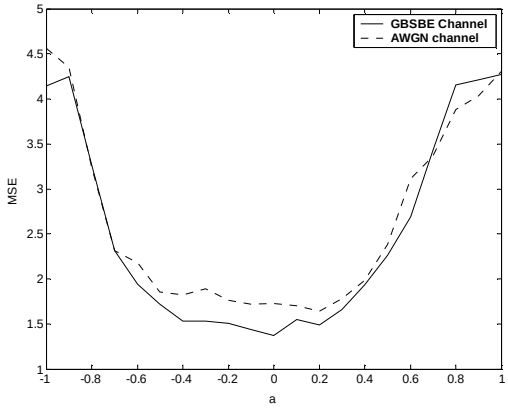

(d) A source with velocity of 60m/sec

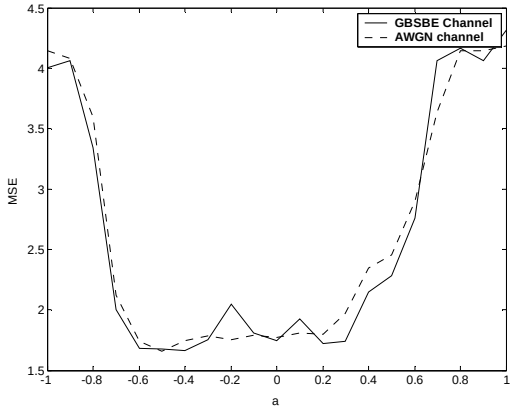

(e) A source with velocity of 80m/sec

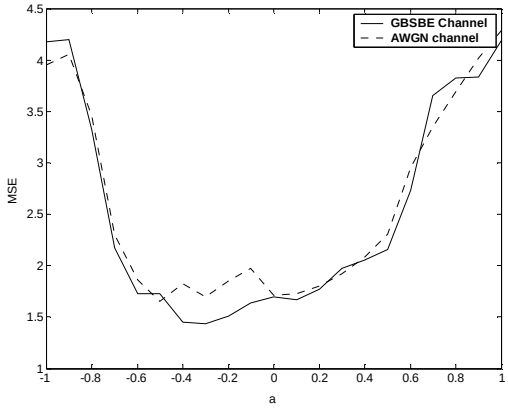

(f) A source with velocity of 100m/sec

Figure 4.37- MSE Vs 'a' of a source moving in GBSBE channel

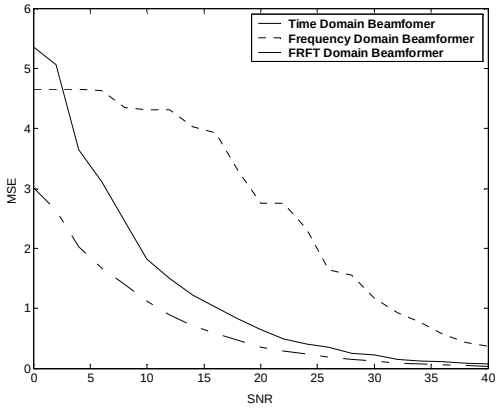

(a) A Stationary Source

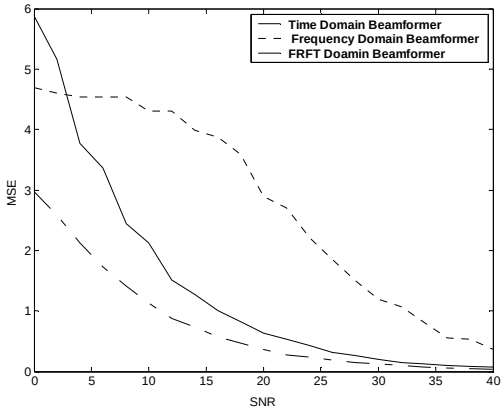

(b) A source with velocity of 20m/sec

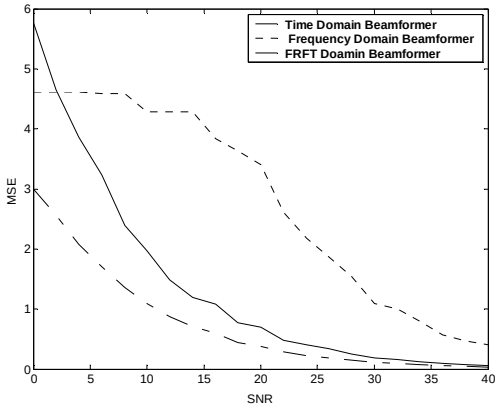

(c) A source with velocity of 40m/sec

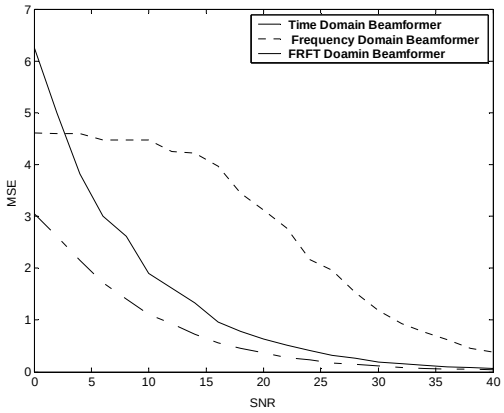

(d) A source with velocity of 60m/sec

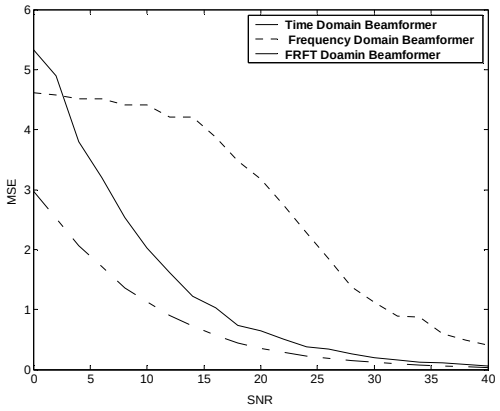

(e) A source with velocity of 80m/sec

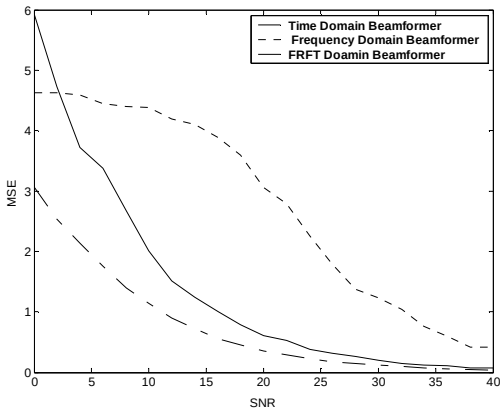

(f) A source with velocity of 100m/sec

Figure 4.38- MSE Vs 'SNR' of a source moving in GBSBE channel

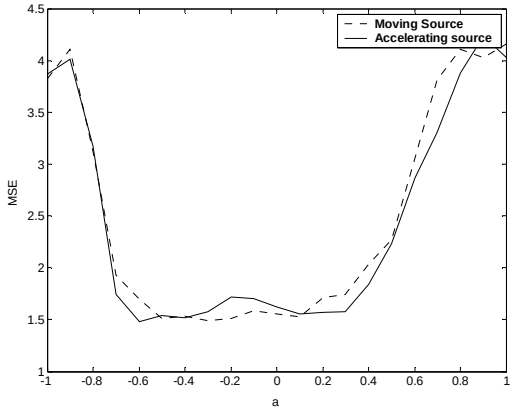

(a) A source with velocity 10m/sec and other source with acceleration 2m/sec^2

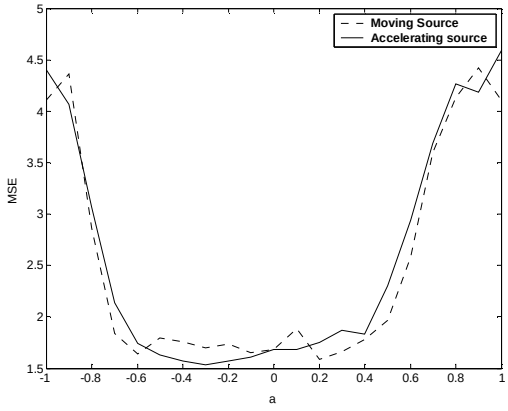

(b) A source with velocity 20m/sec and other source with acceleration 6m/sec^2

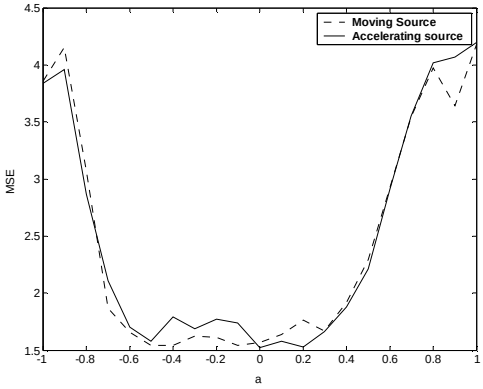

(c) A source with velocity 40m/sec and other source with acceleration 2m/sec^2

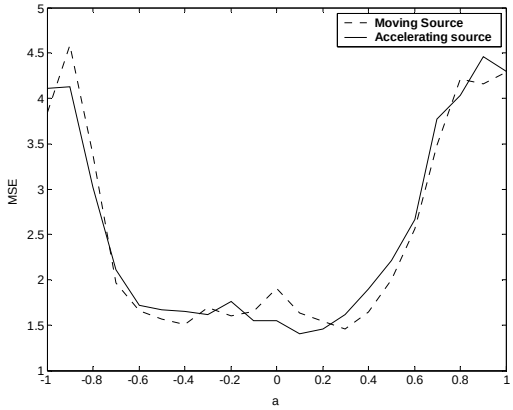

(d) A source with velocity 60m/sec and other source with acceleration 6m/sec^2

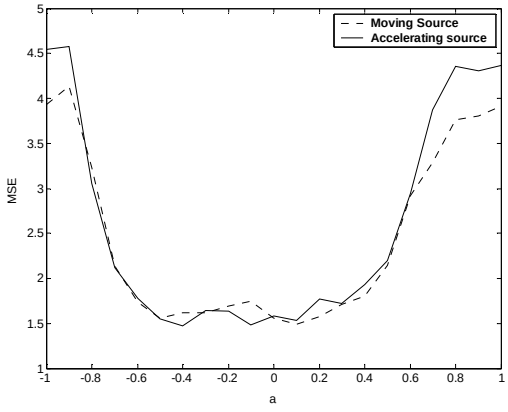

(e) A source with velocity 80m/sec and other source with acceleration 2m/sec^2

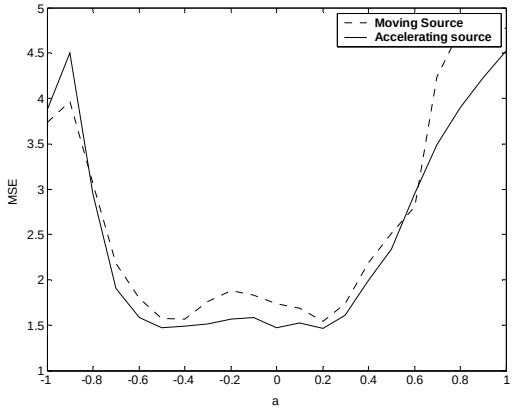

(f) A source with velocity 100m/sec and other source with acceleration 6m/sec^2

Figure 4.39- Comparison of the variation of the MSE with 'a' of two sources, one moving with constant velocity and an other accelerating source moving with zero initial velocity, in GBSBE channel

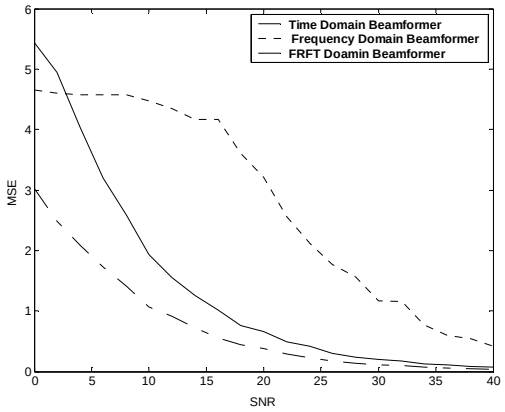

(a) Stationary Source with acceleration 2m/sce^2

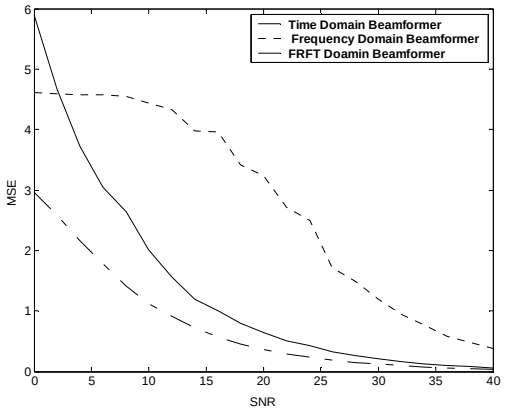

(b) Source with initial velocity 10m/sec and acceleration 2m/sce^2

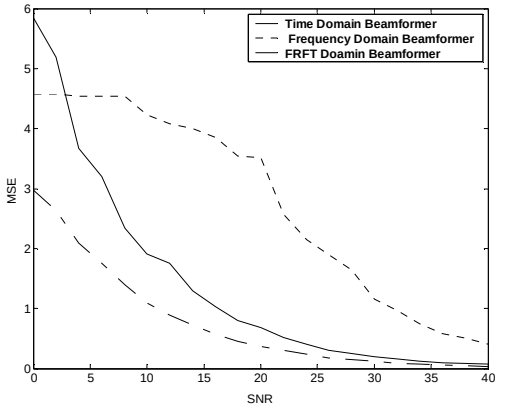

(c) Source with initial velocity 20m/sec and acceleration 6m/sce^2

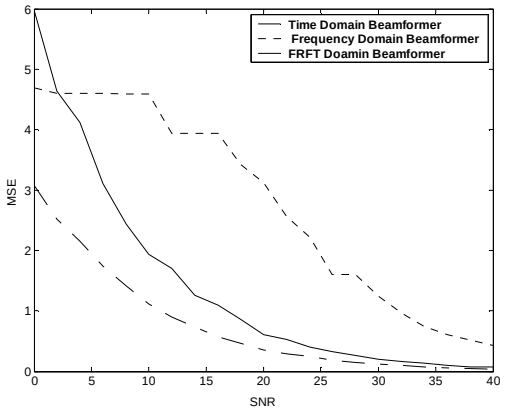

(d) Source with initial velocity 40m/sec and acceleration 2m/sce^2

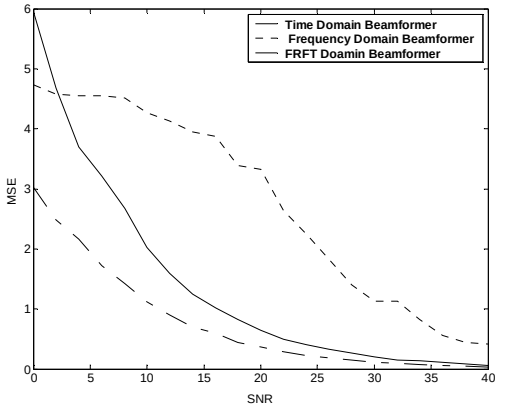

(e) Source with initial velocity 60m/sec and acceleration 6m/sce^2

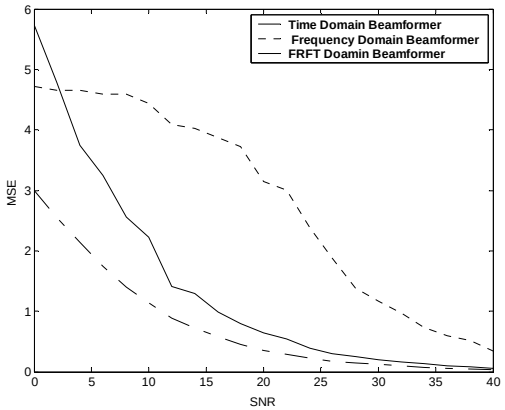

(f) Source with initial velocity 80m/sec and acceleration 2m/sce^2

Figure 4.40- MSE Vs SNR for an accelerating source in GBSBE channel

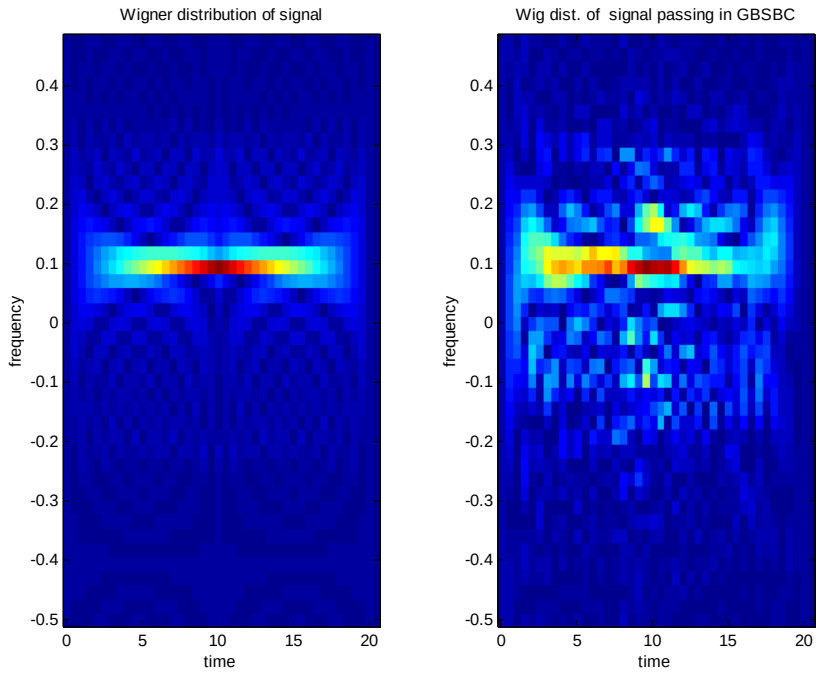

Figure 4.41- (a) Wigner Distribution of signal (b) Wigner distribution of received signal in GBSBE channel (Initial Velocity =10m/sec and acceleration 2m/sec^2)

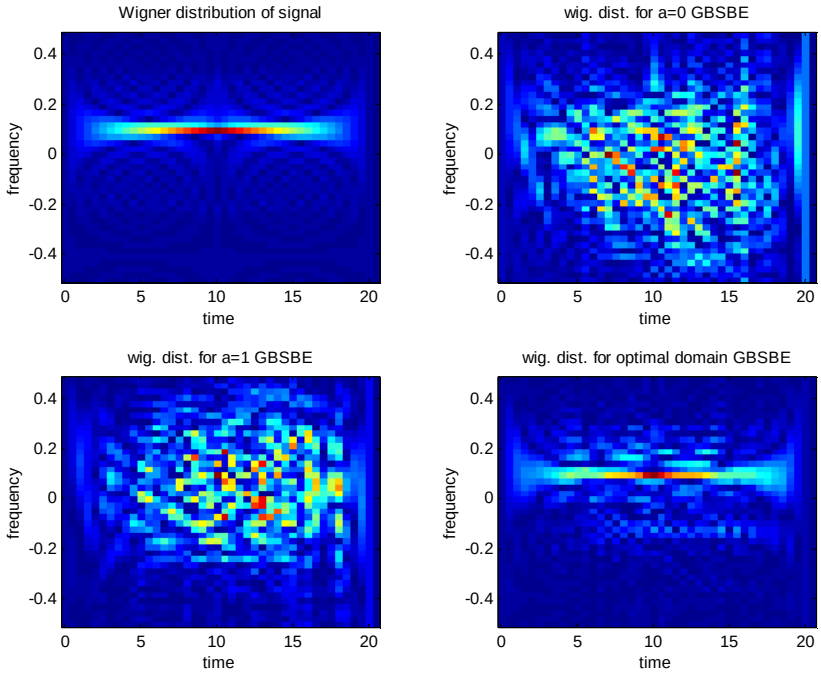

Figure 4.42--(a) Wigner Distribution of signal (b-d) Wigner Distribution of estimated signal in (b) Time domain, (c) Frequency domain and (d) Optimal FrFT domain (GBSBE channel)

Table-4.14: Performance of Optimum FrFT Domain Beamformer compared with Frequency (a=1) and Time Domain (a=0) beamformer in GBSBE channel for a moving source

S. No	Velocity of Source (m/sec)	Optimum Domain for AWGN channel	Optimum Domain for GBSBE channel	Beamformer MSE for SNR=20 dB			Reduction in MSE in %	
				Time Domain a=0	Freq. Domain a=1	Optimum Domain $a=a_{opt}$	Optimum Vs. Time Domain	Optimum Vs. Freq. Domain
1	0	-0.6	-0.5	0.6433	2.7480	0.3567	44.5%	87.0%
2	10	0.2	0.5	0.5684	3.3049	0.3506	38.4%	88.4%
3	20	-0.3	0.2	0.6300	2.8920	0.3576	43.2%	87.6%
4	30	-0.1	-0.4	0.6834	3.0164	0.3778	44.7%	87.4%
5	40	-0.3	-0.1	0.6988	3.4008	0.3427	46.5%	88.9%
6	50	-0.1	-0.4	0.6408	2.9424	0.3603	43.7%	87.7%
7	60	0.2	0	0.6387	3.1263	0.3672	42.5%	88.2%
8	70	0.1	-0.5	0.5981	2.8370	0.3664	38.7%	87.0%
9	80	-0.5	-0.4	0.6421	3.1778	0.3541	44.8%	88.8%
10	90	0.3	0.2	0.6260	3.1788	0.3610	42.3%	88.6%
11	100	-0.5	0.3	0.6126	3.0613	0.3558	41.9%	88.3%

Table-4.15: MSE of moving and accelerating source for Optimum Domain Beamformer in GBSBE channel

S. No	Velocity of Source (m/sec)	Acceleration of Source (m/sec^2)	Optimum domain for moving source	Optimum domain for Acc. source	MSE of moving source	MSE of Acc. Source
1	10	2	0.3	-0.6	1.49	1.48
2	10	6	-0.4	0.3	1.61	1.54
3	20	2	0.2	-0.4	1.53	1.43
4	20	6	0.2	-0.3	1.58	1.53
5	40	2	-0.4	0.0	1.53	1.52
6	40	6	-0.4	-0.1	1.51	1.37
7	60	2	0.2	0.1	1.51	1.48
8	60	6	0.3	0.1	1.45	1.40
9	80	2	0.1	-0.4	1.48	1.46
10	80	6	0.1	-0.2	1.54	1.33
11	100	2	-0.1	-0.4	1.46	1.44
12.	100	6	0.2	0.2	1.54	1.46

Table-4.16: Performance of Optimum FrFT Domain Beamformer compared with Frequency (a=1) and Time Domain (a=0) beamformer in GBSBE channel for an accelerating source

S. No	Velocity of Source (m/sec)	Acc. of Source (m/sec^2)	Beamformer MSE for SNR=20 dB			Reduction in MSE in %	
			Time Domain a=0	Frequency Domain a=1	Optimum Domain $a=a_{opt}$	Optimum Vs Time Domain	Optimum Vs Freq. Domain
1	10	2	0.6477	3.2386	0.3625	44.0%	88.8%
2	10	6	0.6315	2.9977	0.3588	43.1%	88.0%
3	20	2	0.6494	2.8973	0.3516	45.4%	87.6%
4	20	6	0.6777	3.5132	0.3630	46.4%	89.6%
5	40	2	0.6077	3.1258	0.3517	42.1%	88.7%
6	40	6	0.6135	3.2510	0.3608	41.2%	88.9%
7	60	2	0.6411	3.0026	0.3503	45.3%	88.3%
8	60	6	0.6499	3.3256	0.3583	44.7%	89.2%
9	80	2	0.6415	3.1471	0.3521	45.1%	88.8%
10	80	6	0.6513	3.0827	0.3689	43.3%	88.0%
11	100	2	0.6551	3.2131	0.3620	44.9%	88.7%
12	100	6	0.6582	3.0720	0.3638	44.7%	88.1%

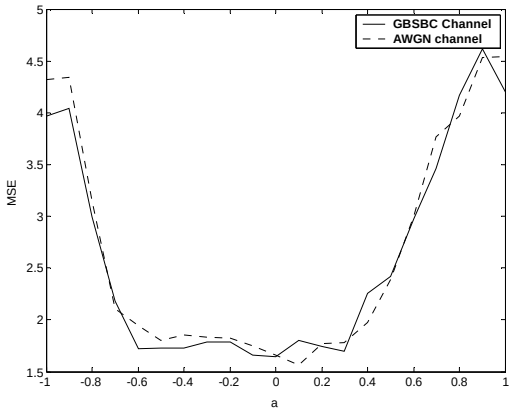

(a) A Stationary Source

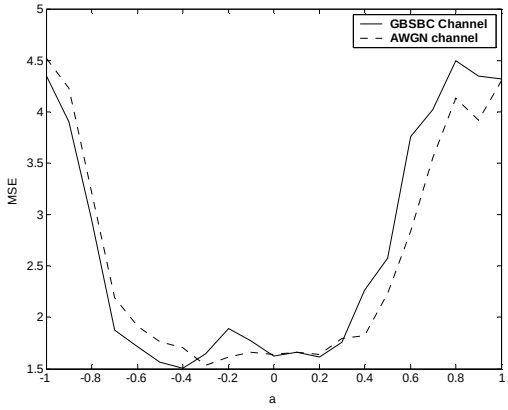

(b) A source with velocity of 20m/sec

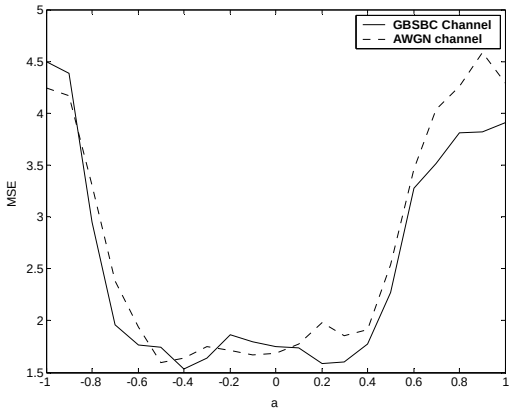

(c) A source with velocity of 40m/sec

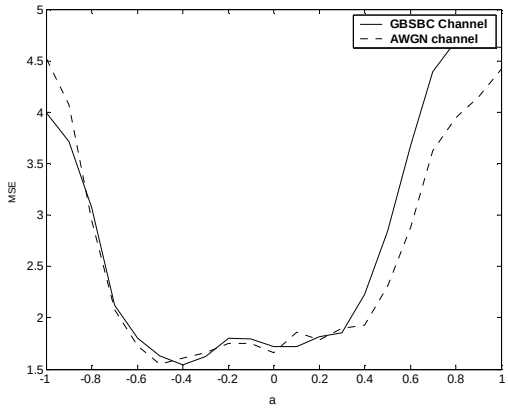

(d) A source with velocity of 60m/sec

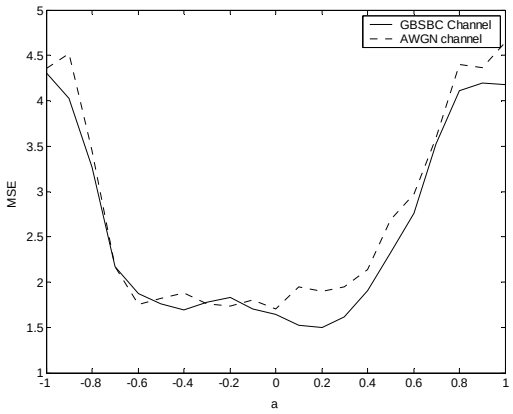

(e) A source with velocity of 80m/sec

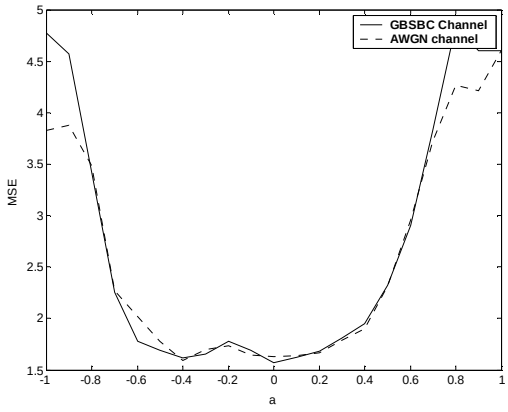

(f) A source with velocity of 100m/sec

Figure 4.43-MSE vs. 'a' for a moving source in GBSBC channel

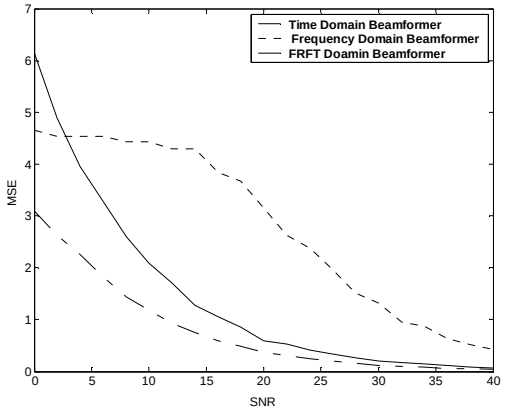

(a) A Stationary Source

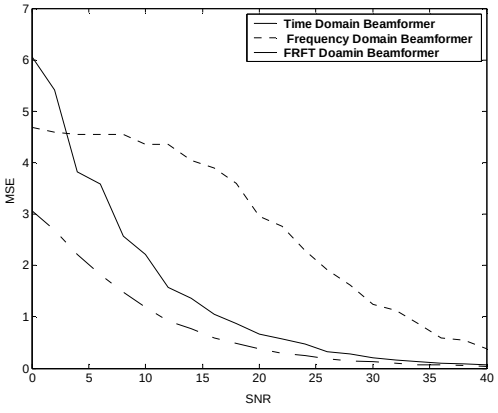

(b) A source with velocity of 20m/sec

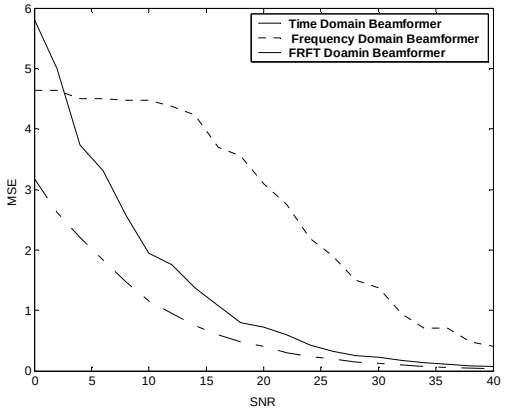

(c) A source with velocity of 40m/sec

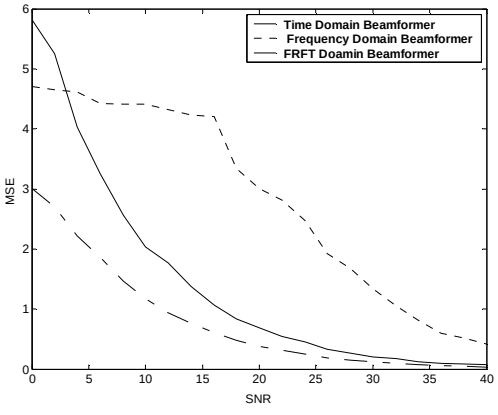

(d) A source with velocity of 60m/sec

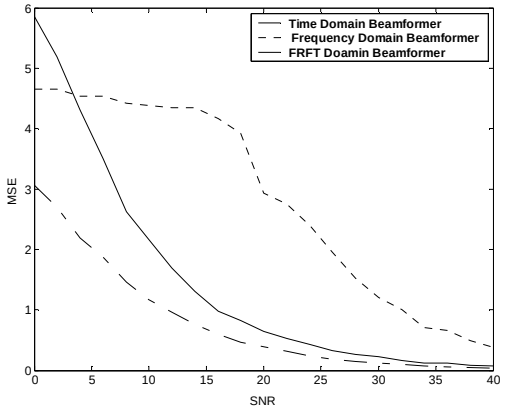

(e) A source with velocity of 80m/sec

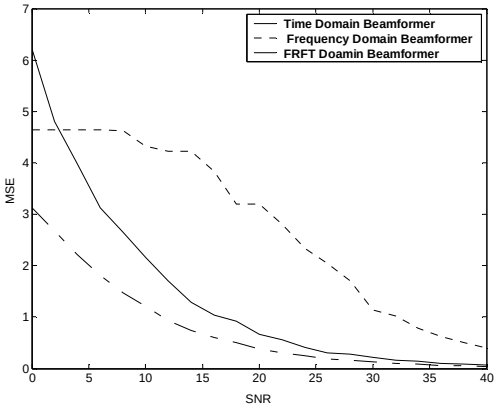

(f) A source with velocity of 100m/sec

Figure 4.44- MSE Vs 'SNR' of a source moving in GBSBC channel

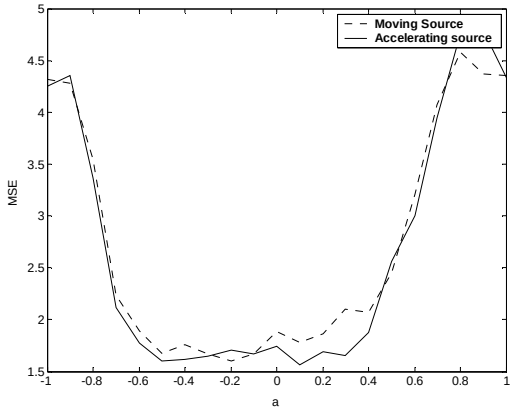

(a) A source with velocity 10m/sec and other source with acceleration 2m/sec^2

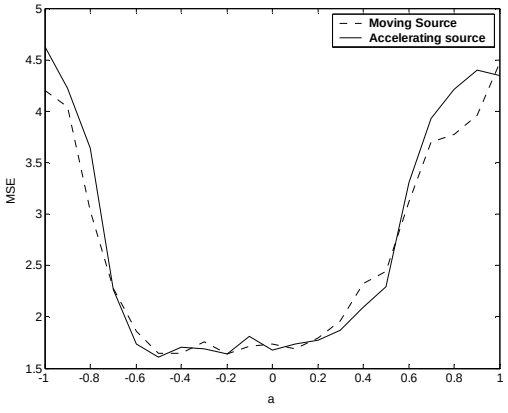

(b) A source with velocity 20m/sec and other source with acceleration 6m/sec^2

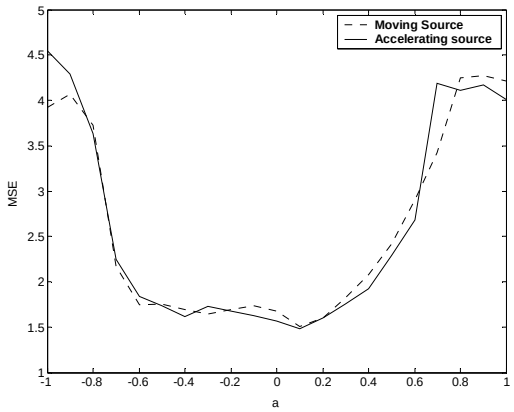

(c) A source with velocity 40m/sec and other source with acceleration 2m/sec^2

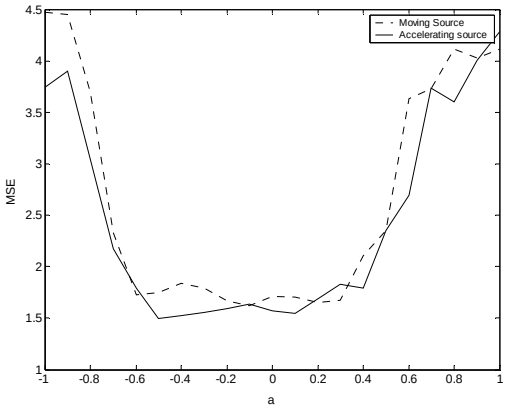

(d) A source with velocity 60m/sec and other source with acceleration 6m/sec^2

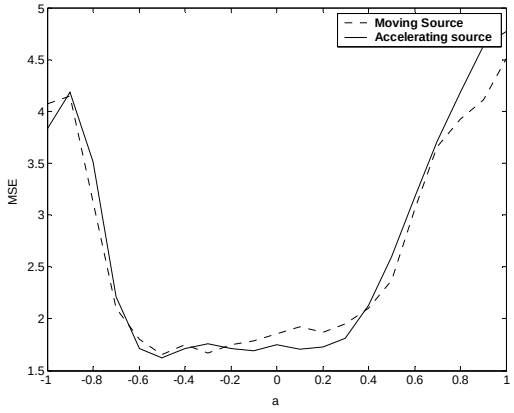

(e) A source with velocity 80m/sec and other source with acceleration 2m/sec^2

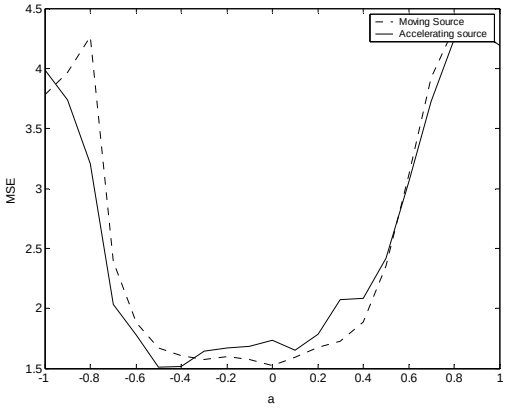

(f) A source with velocity 100m/sec and other source with acceleration 6m/sec^2

Figure 4.45- Comparison of the variation of the MSE with 'a' of two sources, one moving with constant velocity and an other accelerating source moving with zero initial velocity, in GBSBE channel

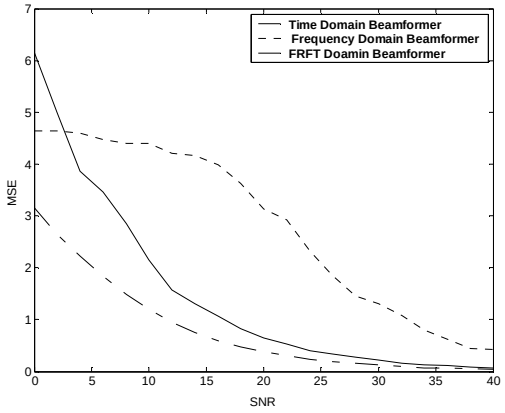

(a) Stationary Source with acceleration 2m/sce^2

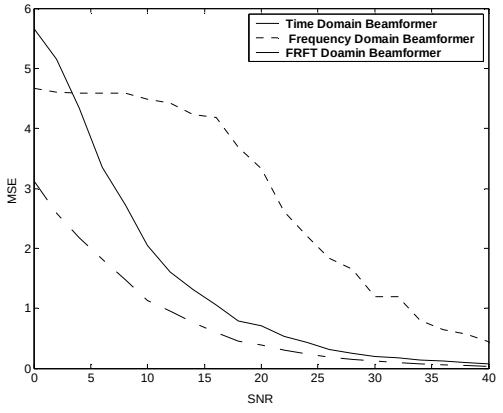

(b) Source with initial velocity 10m/sec and acceleration 2m/sce^2

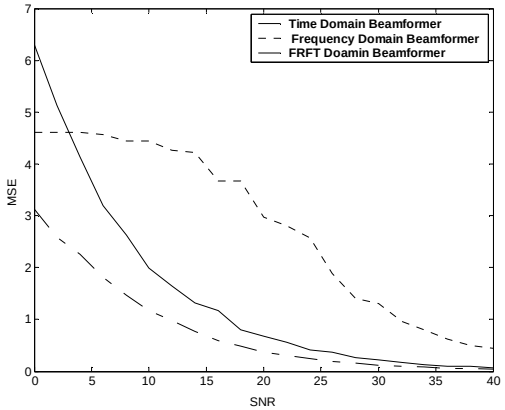

(c) Source with initial velocity 20m/sec and acceleration 6m/sce^2

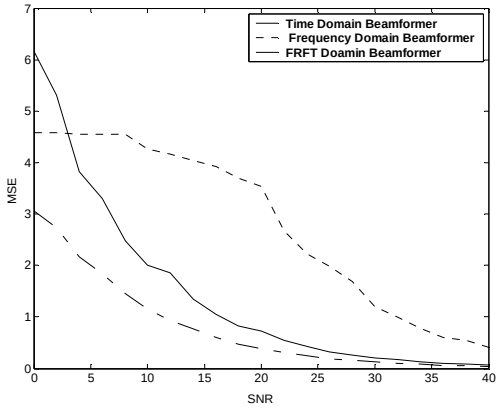

(d) Source with initial velocity 40m/sec and acceleration 2m/sce^2

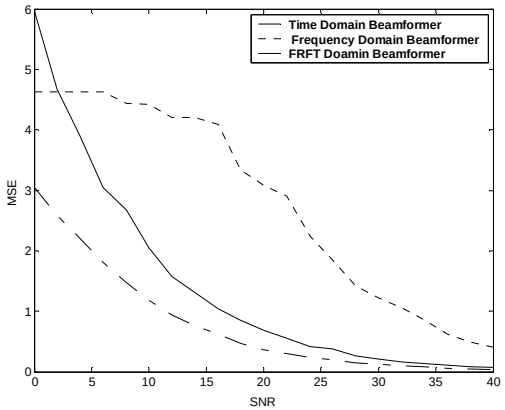

(e) Source with initial velocity 60m/sec and acceleration 6m/sce^2

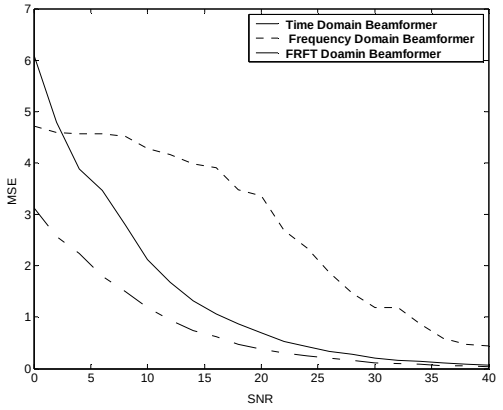

(f) Source with initial velocity 80m/sec and acceleration 2m/sce^2

Figure 4.46- MSE Vs SNR for an accelerating source in GBSBC Channel

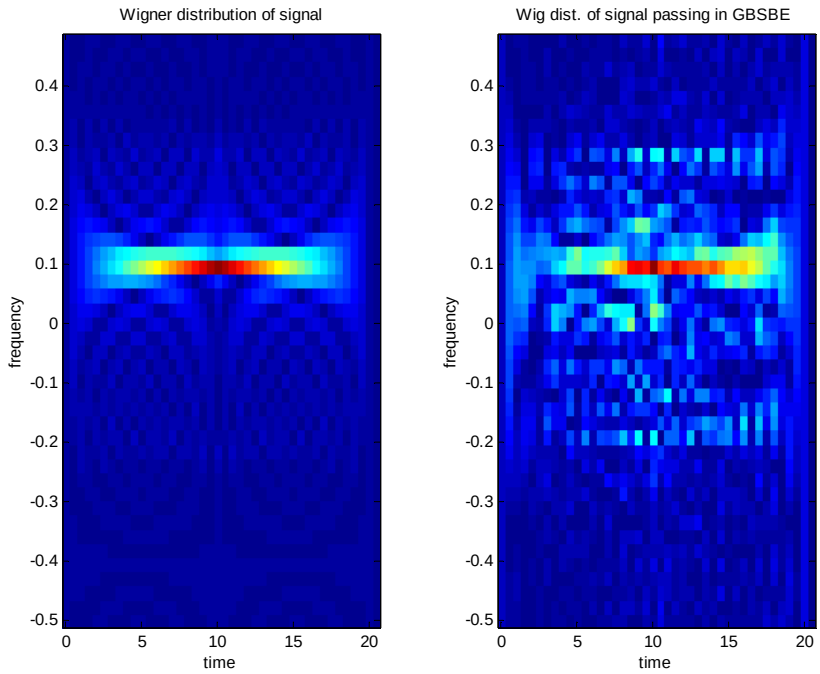

Figure 4.47-(a) Wigner Distribution of signal (b) Wigner distribution of received signal in GBSBC channel (Initial Velocity =10m/sec and acceleration 2m/sec^2)

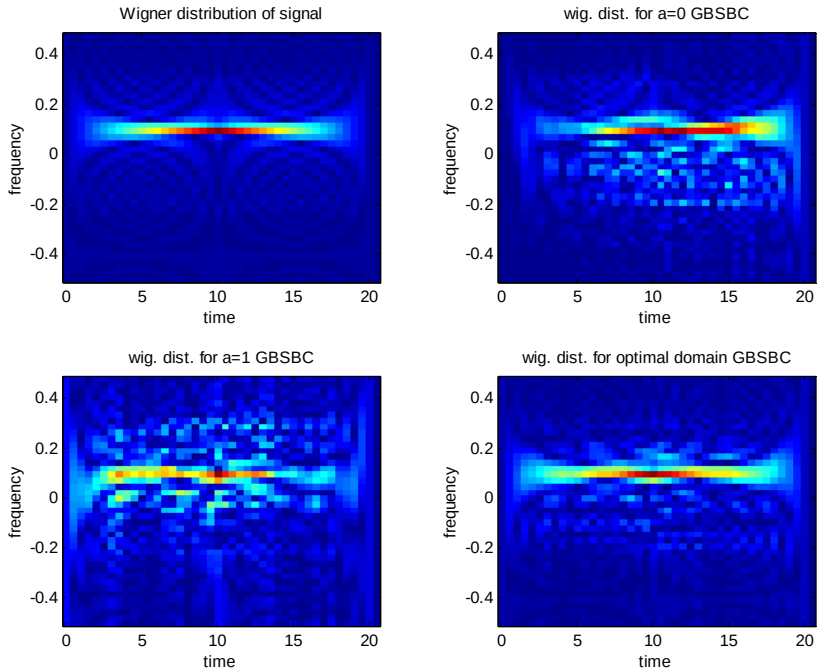

Figure 4.48- (a) Wigner Distribution of signal (b-d) Wigner Distribution of estimated signal in (b) Time domain, (c) Frequency domain and (d) Optimal FrFT domain (GBSBC channel)

Table-4.17: Performance of Optimum FrFT Domain Beamformer compared with Frequency (a=1) and Time Domain (a=0) beamformer in GBSBC channel for a moving source

S. No	Velocity of Source (m/sec)	Optimum Domain for AWGN channel	Optimum Domain for GBSBC channel	Beamformer MSE for SNR=20 dB			Reduction in MSE in %	
				Time Domain a=0	Freq. Domain a=1	Optimum Domain $a=a_{opt}$	Optimum Vs. Time Domain	Optimum Vs. Freq. Domain
1	0	0.1	0.0	0.5943	3.1498	0.3680	38.1%	88.3%
2	10	-0.5	-0.4	0.6658	2.8435	0.3737	43.8%	86.6%
3	20	-0.3	-0.4	0.6557	2.9496	0.3845	43.7%	87.3%
4	30	0.0	-0.1	0.5965	3.1478	0.3684	38.7%	88.1%
5	40	-0.5	-0.4	0.7223	3.9090	0.3990	44.7%	87.1%
6	50	-0.3	-0.4	0.7198	3.6767	0.3944	45.2%	89.3%
7	60	-0.5	-0.4	0.6778	3.0091	0.3784	44.1%	87.4%
8	70	0.1	-0.3	0.6819	3.2299	0.3870	43.2%	88.0%
9	80	0.0	0.2	0.6485	2.9330	0.3846	40.7%	86.9%
10	90	0.1	-0.2	0.6816	3.2376	0.3717	45.4%	88.5%
11	100	-0.4	0.0	0.6554	3.1951	0.3808	41.9%	88.1%

Table-4.18: MSE of moving and accelerating source for Optimum Domain Beamformer in GBSBC channel

S. No	Velocity of Source (m/sec)	Acceleration of Source (m/sec^2)	Optimum domain for moving source	Optimum domain for Acc. source	MSE of moving source	MSE of Acc. Source
1	10	2	-0.2	0.1	1.60	1.56
2	10	6	-0.1	0.1	1.64	1.62
3	20	2	0.2	-0.4	1.55	1.52
4	20	6	-0.2	-0.5	1.63	1.61
5	40	2	0.1	0.1	1.50	1.48
6	40	6	0.2	0.1	1.62	1.46
7	60	2	-0.2	0.1	1.65	1.46
8	60	6	-0.1	-0.5	1.62	1.49
9	80	2	-0.5	-0.5	1.65	1.62
10	80	6	-0.6	-0.5	1.57	1.56
11	100	2	0.2	0.2	1.61	1.58
12.	100	6	0.0	-0.5	1.52	1.51

Table-4.19: Performance of Optimum FrFT Domain Beamformer compared with Frequency (a=1) and Time Domain (a=0) beamformer in GBSBC channel for an accelerating source

S. No	Velocity of Source (m/sec)	Acc. of Source (m/sec^2)	Beamformer MSE for SNR=20 dB			Reduction in MSE in %	
			Time Domain a=0	Frequency Domain a=1	Optimum Domain $a=a_{opt}$	Optimum Vs Time Domain	Optimum Vs Freq. Domain
1	10	2	0.7099	3.3284	0.3937	44.5%	88.1%
2	10	6	0.6901	3.3542	0.3774	45.0%	88.6%
3	20	2	0.6670	3.0842	0.3766	43.5%	87.8%
4	20	6	0.6791	2.9660	0.3698	45.5%	87.5%
5	40	2	0.7268	3.5342	0.3826	47.3%	87.1%
6	40	6	0.6371	3.2174	0.3720	41.6%	88.4%
7	60	2	0.6413	3.3395	0.3785	40.9%	88.7%
8	60	6	0.6788	3.0846	0.3682	45.7%	88.0%
9	80	2	0.6791	3.3528	0.3769	45.9%	88.8%
10	80	6	0.6670	3.2394	0.3703	44.5%	88.6%
11	100	2	0.6728	3.1682	0.3848	42.8%	87.8%
12	100	6	0.6782	3.3380	0.3797	44.0%	88.6%

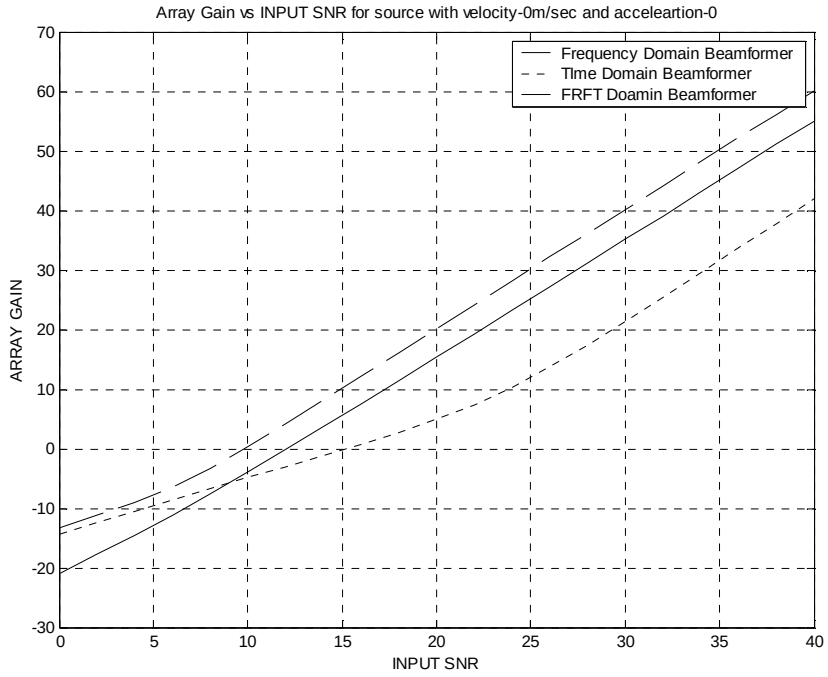

Fig.4.49a Array Gain Vs. Input SNR for a stationary source in AWGN

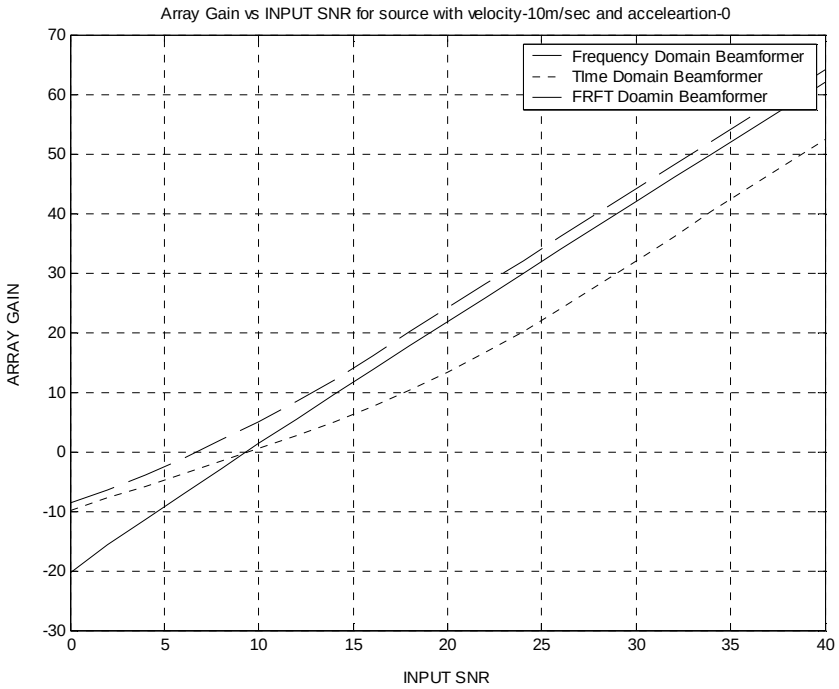

Figure.4.49b: Array Gain Vs. Input SNR for a moving source in AWGN

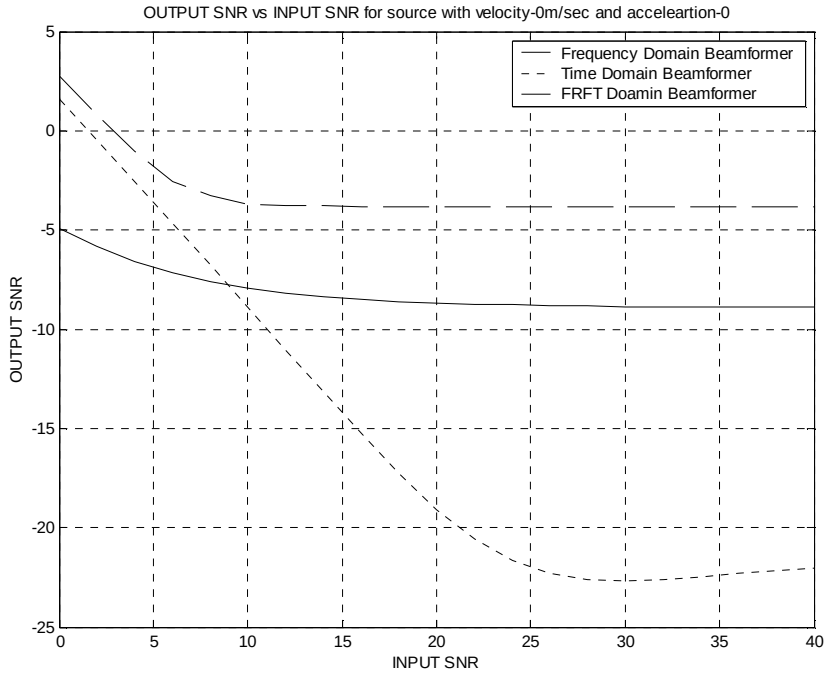

Fig.4.50a Output SNR Vs. Input SNR for a stationary source in AWGN

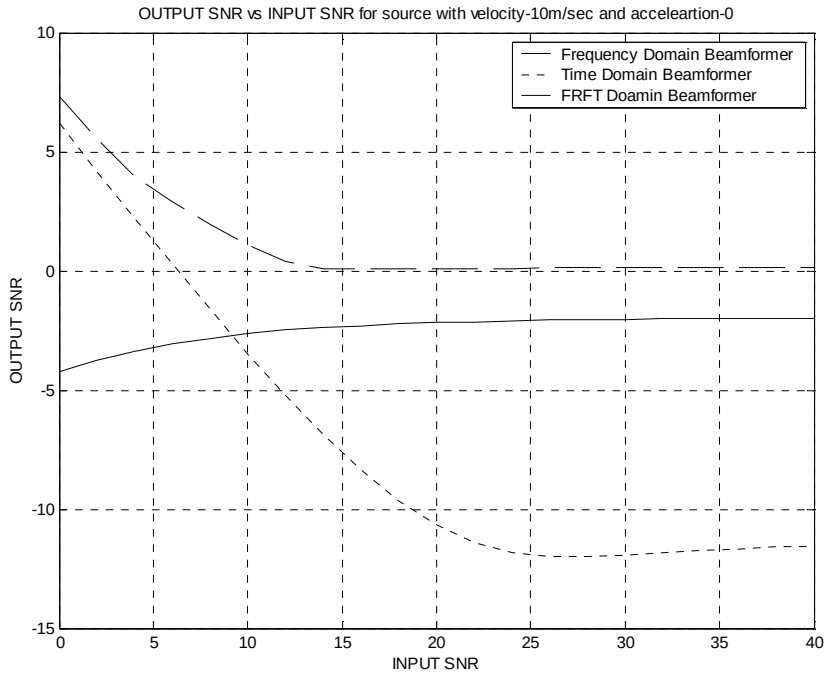

Figure.4.50b: Output SNR Vs. Input SNR for a moving source in AWGN

4.13 RESULTS AND DISCUSSIONS

1. The results of AWGN channels are shown in Fig. 4.13. The source is assumed to be moving with a constant velocity in a direction perpendicular to the direction of array. The results are plotted for different velocities varying from 10m/sec to 100m/sec. The MSE as a function of the FrFT order 'a' with different moving source velocities is given in table 4.2.
2. The third column of table 4.2 clearly shows that there exists a domain in which the MSE is less as compared to any other domain. In this thesis the optimum a^{th} domain is found by calculating MSE for different values of $a \in [-1,1]$ and choosing the value of 'a' that gives minimum MSE. The proposed method reduces to time domain for a=0 and frequency domain for a=1.
3. The variation of MSE as a function of SNR is also plotted in Figs. 4.14. The MSE for optimum FrFT domain filter is always found to be less than for time or frequency domain filter. The improvements in the performance can be easily observed in these plots, especially for low SNR. The performance improvements are tabulated in tables 4.2. In fourth, fifth and sixth columns the MSE are given for time, frequency and optimum domain beamformers for a source moving with different velocities. The MSEs are tabulated for SNR=20 dB. The MSE of the beamformer is found to be less in optimum domain in all cases.
4. Seventh and eighth column give the percentage reduction in MSE in optimum domain as compared to time and frequency domain. In optimum domain the reduction in MSE can be as high as 49% and as low as 39% when compared with time domain beamforming. Similarly the reduction in MSE can vary from 86.8% to 89.0% in optimum domain when compared with frequency domain beamforming. Thus it is demonstrated that the proposed method yields improved results that is smaller MSE, in a moving source scenario, which is common in wireless communication. This is due to the fact that the FrFT is more effective in case, when a moving source produces a frequency shift in signal due to the Doppler Effect. The slight improvements in low SNR for the stationary source is due to the high level of noise, making it possible to extract the signal in some domain rather than a = 0 or a = 1, depending on the realization.
5. The proposed optimum FRFT domain beamformer can be used for yielding small errors in case of accelerating source problems also. The variation of MSE in case of

constant velocity source as well as accelerating source is shown in Fig. 4.15 and the results are tabulated in table 4.3.

6. The MSE of an accelerating source is generally found to be less as compared to source moving with constant velocity. This is due to the fact that FrFT can deal with chirped type degradations much better as compared to Fourier transform because a chirp signal forms a line in the time-frequency plane, and therefore, there exists an order for which such a signal is compact [64]. Chirp signals are not compact in the spatial or time domain. The Wigner distribution of a chirp signal is shown in Fig. 4.51. The effect of the FrFT on the Wigner distribution of a signal is simply a clockwise rotation by an angle α in the time-frequency plane, as illustrated for a chirp signal in Fig. 4.51.

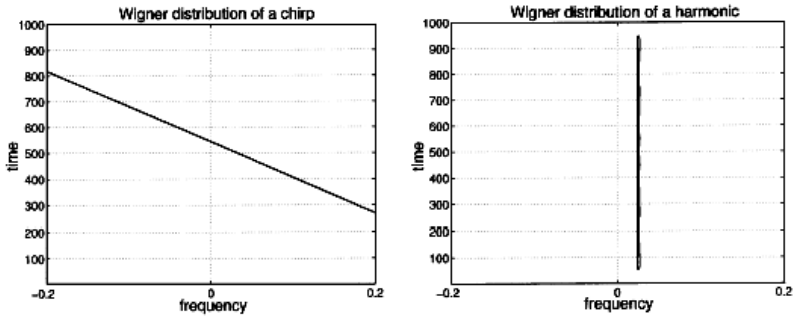

Figure 4.51- Wigner Distribution of a chirp in time frequency plane. A chirp transforms into a vertical line by FrFT into t-f plane which is Wigner distribution of harmonic signal [64]

7. The variation of MSE with SNR for an accelerating source is shown in Fig. 4.16 and results are given in table 4.4. It is again found that FrFT domain beamforming reduces the MSE in case of an accelerating source in AWGN channel as compared to time domain or frequency domain beamforming.
8. The Wigner distribution of the signal and the signal obtained in a=0 domain, a=1 domain and optimal FrFT domain are shown in Figs. 4.17 & 4.18. Fig. 4.17 shows the original as well as received signal with additive noise. In Fig.4.18 (b-d) the Wigner distribution of the estimated signal at the output of beamformer is shown in time (a=0), frequency (a=1) and optimum FrFT domain (a_{opt}).The Wigner distribution is plotted for a single realization.
9. The proposed method of obtaining optimum 'a' is based upon frame by frame basis. To show the superiority of the proposed FrFT beamformer in fading environment

the same results are also plotted for Rayleigh, Nakagami and Ricean faded channels in Figs 4.19 to 4.36[1].

10. The MSE as a function of the FrFT order 'a' of a moving source with varying velocity is plotted in Fig. 4.19 for Rayleigh faded channels. Different optimum domains for moving source in Rayleigh faded channel are given in table 4.5.
11. From the figures in 4.19(a-f) it is clear that there always exist an optimum domain for Rayleigh faded signal, that result in lower MSE as compared to other domains especially a=0(time domain) and a=1(frequency domain). The MSE in case of Rayleigh faded signal can decrease or increase as compared to AWGN channel depending upon constructive or destructive interference.
12. The variation of MSE with SNR for moving source problem is shown in Fig. 4.20 and the results are tabulated in tables 4.5. In optimum domain the reduction in MSE can be as high as 46.2% and as low as 36.2% when compared with time domain beamforming. Similarly the reduction in MSE can vary from 84.8% to 87.5% in optimum domain when compared with frequency domain beamforming.
13. In Fig. 4.21 the variation of MSE with 'a' for moving and accelerating source are plotted. The results are given in table 4.6. In case of Rayleigh faded channels, the MSE for accelerating source is found to be less as compared to moving source clearly showing FrFT as a powerful tool in wireless communication also[1,2].The variation of MSE with SNR for an accelerating source is shown in Fig. 4.22 and results are tabulated in table 4.7. The Wigner distribution for a single realization of Rayleigh case is given in Figs.4.23 & 4.24, which shows that in optimum FrFT domain the energy is more concentrated as compared to time or frequency domain.
14. The results for Ricean channels are plotted in Figs. 4.25 to 4.30 and for Nakagami channels in Figs. 4.31 to 4.36[3]. The results are again compared in tables 4.8-4.13
15. For GBSBE and GBSBC channels the results are shown in Figs. 4.37 to 4.48. The comparison of results is given in tables 4.14-4.19[4].

---

1. [P1] "Fractional Fourier transform based beamforming for next generation of wireless communication systems" Published in ***IETE Journal of Technical Review on Special Issue of Broadband communications***, pp.349-365, September, 2004. (Issue edited by Dr. K. Girdhar of IIT Chennai)
2.[P2] "Optimal Beamforming for Rayleigh faded Time Frequency Varying Channels Using Fractional Fourier Transform", ***J. Indian Inst. Sci., Bangalore***, 85, pp. 27–38, Jan.–Feb. 2005.
3. [P5] "A Novel FrFT beamformer for Rayleigh faded channels" ***accepted for publication in International Journal of Springer on Wireless Personal Communications.***
4. [P6] "Optimal Beamforming for Ricean faded Time Frequency Varying Channels Using Fractional Fourier Transform", submitted after ***revision to International Journal of Numerical Modeling***.
4. [P14] "Fractional Fourier Transform Based Beamforming in Micro-Cellular Environment of Wireless Communication Systems" Proc. of ***IEEE International Conf. of Signal Processing and Communications, IISc, Bangalore***, pp.582-586, Dec. 11-14, 2004.

16. To emphasize further, three different sources, a stationary source, a source moving with a velocity of 10 m/sec and an accelerating source with initial velocity 10 m/sec and acceleration 2 m/sec^2 are taken in the same GBSBE channel. Fig. 4.52 shows the MSE with FrFT order 'a' in above case. The MSE for optimum ($a=a_{opt}$), time (a=0) and frequency domain (a=1) are given in table 4.20. The MSE in case of accelerating source is found to be minimum. Also in all cases the MSE is smaller in optimum FrFT domain ($a=a_{opt}$), as compared to time domain (a=0) and frequency domain (a=1).

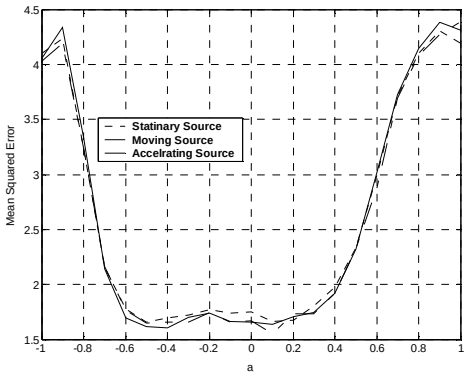

Figure 4.52-MSE in GBSBE channel for stationary, moving and accelerating source

Table-4.20: MSE for optimum ($a=a_{opt}$), time (a=0) and frequency domain (a=1)

Domain	Stationary source	Moving Source	Accelerating source
$a=a_{opt}$	1.552	1.603	1.657
a=0	1.667	1.657	1.751
a=1	4.391	4.373	4.312

17. The fractional Fourier domain filters is a subclass of the class of linear filters [104], but the class of Fractional Fourier domain filters is much broader than the ordinary domain filters, so that in general the optimal filter found in FrFT domain result in much smaller errors as compared to ordinary time or Fourier domain filters. This reduction in error comes at no additional cost because FrFT can be implemented with the same cost as ordinary Fourier transform [27, 59].
18. For time-invariant degradation models and stationary signals and noise, the classical Fourier domain Wiener beamformer, which can be implemented in O (N $\log_2$ N) time, gives the minimum mean-square-error estimate of the original undistorted signal. For time-varying degradations and non-stationary processes, however, the optimal linear estimate requires O (N^2) time for implementation. The beamforming in fractional Fourier domains, which enables significant reduction of

error compared with ordinary Fourier domain beamforming for certain types of degradation and noise (especially of chirped nature), requires only O (N $\log_2$ N) implementation time. Thus, improved performance is achieved at no additional cost [59, 61].

19. The four beamformer performance metrics which depend upon the MSE given in table 3.5 shows that by decreasing the MSE all performance metrics of an array processing architecture in wireless communication shall improve. Thus beamforming in fractional Fourier domain can improve the performance of the beamformer to a large extent, as MSE using FrFT can be reduced up to 91.7%.
20. The FrFT based beamformer provides improved array gain and output SNR in AWGN environment as compared to time and frequency domain beamformer as shown in Figs.4.49 and 4.50. From Fig.4.49(a) and (b) it can be observed that to get an array gain of 20 dB the FrFT beamformer requires 2 dB less input power as compared to frequency domain beamformer and 9 dB less input power as compared to time domain beamformer for a stationary source in AWGN. For a constant velocity source the FrFT beamformer requires 1 dB and 6 dB less input power as compared to frequency and time domain beamformer respectively[5].
21. The FrFT beamformer gives higher output SNR as compared to frequency or time domain beamformer. From Fig.4.50 (a) and (b) it is observed that for input SNR of 20 dB the FrFT beamformer gives 5dB high output power as compared to frequency domain and 11 dB high output power as compared to time domain beamformer for a stationary source in AWGN. For a constant velocity (10m/sec) source in AWGN the FrFT beamformer provides 2 dB and 10.5 dB high output power as compared to frequency and time domain beamformer respectively.
22. It is found that when signal of interest is broadband the beamforming is preferred in frequency domain (i.e. by using Fourier Transform) as compared to time domain [64]. With the introduction of FrFT, having same computational complexity as FT and improved performance (in terms of reduced MSE), the next generation wireless and mobile communications systems shall perform beamforming in Fractional Fourier Domains as compared to frequency domain or time domain. To emphasize this, performance of FrFT is evaluated in terms of BER in mobile environment.

---

5. [P17] "SNR Improvement of Uniform Circular Array Using the Fractional Fourier Transform Beamforming in Radar Environment", ***Proceedings of International Radar Symposium***, ***IRSI-2005, pp.776-781, 19-22 Dec 2005,*** Bangalore, India.

4.14 PERFORMANCE OF FrFT BASED OPTIMUM BEAMFORMER IN INTERFERING MOBILE ENVIRONMENT

The performance of array processing architecture has been studied from MSE point of view in section 4.10. It is shown that the FrFT based beamformer outperforms the frequency domain and time domain beamformer in terms of reducing MSE. Next the symbol error probability (SEP) performance of the FrFT based beamformer is studied in mobile wireless environment. The structure of the beamformer shown in Fig.4.7 also corresponds to that of linear optimum combiner as in SIMO system. With optimum combining (OC), the signals received by several antenna elements are properly weighted and combined to maximize the output signal-to-interference- plus-noise ratio (SINR). In the absence of interference in an additive noise environment, the optimum combiner maximizes the signal-to-noise ratio (SNR) and has the same performance as a maximal ratio combiner (MRC). The SEP for coherent detection of M-ary phase-shift keying using an array of antennas with optimum combining in a Rayleigh fading environment is derived next. Let K is the diversity order and L is the number of interferers. The received signal is given by

$$\boldsymbol{x}(t) = \boldsymbol{g}_s s(t) + \boldsymbol{z}(t), \tag{4.143}$$

where, $\boldsymbol{z}(t)$ is the total interference in the system given by

$$\boldsymbol{z}(t) = \sum_{i=1}^{L} \boldsymbol{g}_i s_i(t) + \boldsymbol{n}(t), \tag{4.144}$$

where, $s_i(t)$ correspond to signal transmitted form the i^{th} user. The desired signal s(t) and interfering users $s_i(t)$ are such that $E[s^2(t)]=E[s^2_i(t)]=1$. The $K \times 1$ noise vector is complex white Gaussian with zero-mean and variance σ_w^2. The channel is modelled as flat Rayleigh fading, and the circularly Gaussian vectors $\mathbf{g}_i$ {i=1,2….L} correspond to the fading coefficients of the i^{th} user. $\mathbf{g}_s$ corresponds to fading vector of desired signal. P_s and P_I correspond to mean power of $\boldsymbol{g}_s$ and $\boldsymbol{g}_I$. The antennas are assumed to be placed distant enough so that the fading at each antenna is independent. The channel is also assumed to be slowly varying, so that the fading coefficients remain unchanged over the frame. The $K \times K$ interference plus noise covariance matrix is given by

$$\boldsymbol{R}_I = \boldsymbol{X}\boldsymbol{X}^H + \sigma_w^2 \boldsymbol{I}, \tag{4.145}$$

where, $\boldsymbol{X}$ is an $K \times L$ matrix with columns given by interfering user's fading coefficient vectors $\mathbf{g}_i$, i.e. X=[$\mathbf{g}_1$…….$\mathbf{g}_L$]. In this analysis, $\boldsymbol{R_I}$ is the interference-plus-noise

covariance matrix. The optimal combining weight vector can be computed from the signal-plus interference-and-noise covariance matrix also. In that case the $\boldsymbol{R_I}$ is replaced by $\boldsymbol{R}$, given by $\boldsymbol{R} = \boldsymbol{g}_s \boldsymbol{g}_s^H + \boldsymbol{R}_I$. As shown in appendix-C the resulting weight vectors provide the same performance as they differ only by a scaling factor.

The signal to interference plus noise ratio (SINR) for this system model is expressed as

$$\text{SINR} = \frac{\left| \boldsymbol{w}_{opt}^a \boldsymbol{g}_s \right|^2}{\boldsymbol{w}_{opt}^a \boldsymbol{R}_I \boldsymbol{w}_{opt}^a}, \tag{4.146}$$

where, $\boldsymbol{w}_{opt}^a$ is the spatially combining weight vector in ath domain. In optimum combining, the antenna weights are derived using the Wiener solution as discussed in section 4.5. The SINR expression corresponding to these weights is

$$\mu = \text{SINR} = \mathbf{g}_s^H \boldsymbol{R_I}^{-1} \mathbf{g}_s. \tag{4.147}$$

The SINR is conditioned on $\mathbf{g}_s$ and $\mathbf{g}_i$ hence it varies at fading rate. Since $\boldsymbol{R_I}$ is a Hermitian matrix it can be diagonalized by a unitary transformation as

$$\boldsymbol{R}_I = \boldsymbol{V} \text{diag}\{\lambda_1, \lambda_2 ..... \lambda_K\} \boldsymbol{V}^T, \tag{4.148}$$

where, $\lambda_1, ... \lambda_K$ are the eigenvalues of $\boldsymbol{R_I}$. Define the vector $\boldsymbol{v} = \boldsymbol{V}\boldsymbol{g}_s = [v_{s1}, v_{s2} \ldots\ldots\ldots v_{sK}]^T$. Since $\boldsymbol{V}$ is unitary, the elements of $\boldsymbol{v}$ retain the properties of the elements $\mathbf{g}_s$. Thus (4.147) can be written as

$$\mu = \sum_{i=1}^{K} \frac{|v_i|^2}{\lambda_i + \sigma_w^2}, \tag{4.149}$$

where, $\boldsymbol{v}^T = [v_1, v_2 \ldots\ldots\ldots v_K]$. Since the elements of $\mathbf{g}_s$ have complex-valued Gaussian distributions, each term $|v_i|^2$ is a chi-square random variable with two degrees of freedom. The joint probability density function (pdf) of $\lambda_1, ... \lambda_K$ can be derived using the theory of multivariate statistics, relating to complex Wishart matrices [114]. The general expression for the joint pdf of the first $N_{min} \underline{\underline{\Delta}} \min\{K, L\}$ unordered eigenvalues $\boldsymbol{\lambda} = (\lambda_1, ... \lambda_K)^T$ of $\boldsymbol{R}_I$, valid for arbitrary K and L is

$$f_{\boldsymbol{\lambda}}(x_1, ... x_{N_{min}}) = \frac{\tilde{K}}{N_{min}!} \left[\prod_{i=1}^{N_{min}} e^{-x_i} x_i^{N_{max} - N_{min}} \right] \prod_{i=1}^{N_{min}-1} \left[\prod_{j=i+1}^{N_{min}} (x_i - x_j)^2 \right], \tag{4.150}$$

where, $N_{max} \underline{\underline{\Delta}} \max\{K, L\}$ and $\tilde{K}$ is the normalizing constant given by

$$\tilde{K} = \frac{\pi^{N_{min}(N_{min}-1)}}{\tilde{\Gamma}_{N_{min}}(N_{max}) \tilde{\Gamma}_{N_{min}}(N_{min})}, \tag{4.151}$$

with $$\tilde{\Gamma}_{N_{min}}(n) = \pi^{N_{min}\frac{(N_{min}-1)}{2}} \prod_{i=1}^{N_{min}} (n-i)! \,. \qquad (4.152)$$

The additional K- N_{min} eigenvalues of $\boldsymbol{R}_I$ are identically equal to zero. The SEP using the chain rule of conditional expectation is given as

$$P_e = E_{\lambda}[P_{e/\lambda}] \qquad \textit{where}$$
$$P_{e/\lambda} = E_{v|\lambda}\left\{ \Pr\left\{ e \mid \mu = \sum_{i=1}^{K} \frac{|v_i|^2}{\lambda_i + \sigma_w^2} \right\} \right\}, \qquad (4.153)$$

where, $\Pr\{e|\mu\}$ is the SEP conditioned on the random variable μ. In deriving (4.153), first perform $E_{v/\lambda}\{.\}$ and average over the channel ensemble of the desired signal to obtain the conditional SEP, conditioned on the random vector $\boldsymbol{\lambda}$, denoted by $P_{e|\lambda}$. Then perform $E_{\lambda}\{.\}$ to average out the channel ensemble of the interfering signals. The conditional SEP, conditioned on $\boldsymbol{\lambda}$, for coherent detection of M-ary PSK in the general case of K antennas and L Gaussian interferers, is given by [114]

$$P_{e|\lambda}(\boldsymbol{\lambda}) = \frac{1}{\pi}\int_0^{\Theta} E_{v|\lambda}\left\{ \exp\left(-\frac{c_{MPSK}}{\sin^2\theta} \sum_{i=1}^{K} \frac{|v_i|^2}{\lambda_i + \sigma_w^2} \right) \right\} d\theta \qquad (4.154)$$

$$= \frac{1}{\pi}\int_0^{\Theta} A(\theta) \prod_{i=1}^{N_{min}} \left[\frac{\sin^2\theta}{\sin^2\theta + c_{MPSK}\dfrac{1}{\lambda_i + \sigma_w^2}} \right] d\theta, \qquad (4.155)$$

where, $c_{MPSK} = \sin^2\left(\frac{\pi}{M}\right)$, $\Theta = \pi\frac{(M-1)}{M}$, and

$$A(\theta) = \left[\frac{\sin^2\theta}{\sin^2\theta + c_{MPSK}\dfrac{1}{\sigma_w^2}} \right]^{K-N_{min}}, \qquad (4.156)$$

and the fact that $\boldsymbol{v}$ is Gaussian with i.i.d. elements is used in deriving (4.155). Using (4.153), the unconditional SEP for OC becomes

$$P_e = \int_0^{\infty} \ldots \int_0^{\infty} \ldots\ldots \int_0^{\infty} P_{e|\lambda}(\boldsymbol{x}) f_{\lambda}(\boldsymbol{x}) dx_1 \ldots dx_{N_{min}}, \qquad (4.157)$$

where, $P_{e|\lambda}(\boldsymbol{x})$ is given in (4.155). (4.157) is exact and valid for arbitrary numbers of antennas and interferers; however, it requires the evaluation of N_{min} fold integrals, which can be cumbersome to evaluate for large N_{min}. This analytical difficulty is

avoided by using the classical theory of orthogonal systems and the properties relating to the Vander-monde matrix. The term $\prod_{i=1}^{N_{min}-1}\left[\prod_{j=i+1}^{N_{min}}(x_i - x_j)\right]$ in (4.150) can also be seen as the determinant of the Vander-monde matrix $\boldsymbol{U}(x_1,.....,x_{N_{min}})$ given by

$$\boldsymbol{U}(x_i,.....,x_{N_{min}}) \underline{\underline{\Delta}} \begin{pmatrix} 1 & 1 & .. & 1 \\ x_1 & x_2 & .. & x_{N_{min}} \\ . & . & . & . \\ . & . & . & . \\ x_1^{N_{min}-1} & x_2^{N_{min}-1} & .. & x_{N_{min}}^{N_{min}-1} \end{pmatrix}. \tag{4.158}$$

Therefore, the pdf can also be written as

$$f_{\lambda}(x_1,.....,x_{N_{min}}) = \frac{\tilde{K}}{N_{min}!}\left|\boldsymbol{U}(x_i,.....,x_{N_{min}})\right|^2 \prod_{i=1}^{N_{min}} e^{-x_i} x_i^{N_{max}-N_{min}} . \tag{4.159}$$

Let
$$\psi(\lambda,\theta) \underline{\underline{\Delta}} \frac{\lambda+\sigma_w^2}{\lambda+\sigma_w^2+\frac{c_{MPSK}}{\sin^2\theta}}, \tag{4.160}$$

and using (4.159) and (4.160) then (4.157) becomes

$$P_e = \frac{\tilde{K}}{N_{min}!}\frac{1}{\pi}\int_0^{\Theta} A(\theta)\int_0^{\infty}....\int_0^{\infty}....\left|\boldsymbol{U}(x_1,.....,x_{N_{min}})\right|^2 \times\left[\prod_{i=1}^{N_{min}} \psi(x_i,\theta) x_i^{N_{max}-N_{min}} e^{-x_i} dx_i\right] d\theta . \tag{4.161}$$

The evaluation of (4.161) is difficult because the integrand does not factor and the number of integral depends on the minimum of the number of antennas and interferers. An efficient method to reduce (4.161) to the SEP expression involving a single integral with finite integration limits is given next based on a classical technique commonly used in mathematical physics involving orthogonal systems. Consider a more general problem of evaluating

$$E_{\lambda}\left\{\prod_{i=1}^{N_{min}} z(\lambda_i,\theta)\right\}, \tag{4.162}$$

where, $z\{x,\theta\}$ is a nonnegative function, and the average is with respect to the distribution of the eigenvalues given by (4.159). This problem can be efficiently solved by using some classical results from orthogonal polynomials, as follows. For each $\theta \in [0,\Theta]$, let $\rho_{\theta}^{N_{min}}$ be the space of all polynomials with degree less than or equal to $N_{min} - 1$ with measure

$$du_{\theta}(x) = z(x,\theta) x^{N_{max}-N_{min}} e^{-x} dx , \tag{4.163}$$

equipped with the inner product and norm defined, respectively, by

$$\langle f.g\rangle(\theta)\underline{\Delta}\underline{\underline{\Delta}}\int_0^\infty f(x)g(x)z(x,\theta)x^{N_{\max}-N_{\min}}e^{-x}dx \tag{4.164}$$

$$\|f\|_\theta^2\underline{\Delta}\underline{\underline{\Delta}}\int_0^\infty f(x)f(x)z(x,\theta)x^{N_{\max}-N_{\min}}e^{-x}dx \tag{4.165}$$

If the nonnegative function $z(x,\theta)$ is such that $u_\theta(x)$ is increasing in at least N_{min} points of x, then the elements $1, x, x^2, ..., x^{N_{min}-1}$ of the Hilbert Space $\rho_\theta^{N_{min}}$ are linearly independent. This implies that there exists an orthogonal system $\{\phi_n(x,\theta)\}_{n=0}^{N_{min}-1}$ with

$$\phi_n(x,\theta)=\phi_{n,0}(\theta)+\phi_{n,1}(\theta)x+.....+\phi_{n,n}(\theta)x^n\ , \tag{4.166}$$

such that $\langle\phi_{n,}\phi_m\rangle(\theta)=\|\phi_n\|_\theta^2\delta_{n,m,}$ where $\delta_{n,m}$ is the Kronecker delta function defined by

$$\delta_{n,m}\underline{\Delta}\underline{\underline{\Delta}}\begin{cases}1, & n=m\\ 0, & n\neq m\end{cases} \tag{4.167}$$

The orthogonal system $\{\phi_n(x,\theta)\}_{n=0}^{N_{min}-1}$ can be obtained by a Gram–Schmidt procedure using the measure $du_\theta(x)$, as shown in Appendix D. Hence, an uncountable number of orthogonal systems can be constructed, each generated by the measure $du_\theta(x)$ indexed by $\theta\in[0,\Theta]$.

Theorem 1:

$$E_\lambda\left\{\prod_{i=1}^{N_{min}}z(\lambda_i,\theta)\right\}=\tilde{K}\prod_{n=0}^{N_{min}-1}\|\phi_n\|_\theta^2\ , \tag{4.168}$$

where, $\tilde{K}$ is given in (4.151) and $\prod_{n=0}^{N_{min}-1}\|\phi_n\|_\theta^2$ is the product norm squares of all the elements in a particular orthogonal system generated by $du_\theta(x)$.

Proof:

$$E_\lambda\left\{\prod_{i=1}^{N_{min}}z(\lambda_i,\theta)\right\}=\frac{\tilde{K}}{N_{min}!}\int_0^\infty....\int_0^\infty....\left|\boldsymbol{U}(x_1,.....,x_{N_{min}})\right|^2\times\prod_{i=1}^{N_{min}}z(x_i,\theta)x_i^{N_{max}-N_{min}}e^{-x_i}dx_i \tag{4.169}$$

For any given $\theta\in[0,\Theta]$, the Vander-monde matrix $\boldsymbol{U}(x_1,...,x_{N_{min}})$ can be transformed, using the orthogonal system generated by $du_\theta(x)$, into $\tilde{\boldsymbol{U}}(x_1,.....,x_{N_{min}};\theta)$ defined by

$$\tilde{\boldsymbol{U}}(x_1,...,x_{N_{min}};\theta)\underline{\Delta}\underline{\underline{\Delta}}\begin{pmatrix}\phi_0(x_1,\theta) & \phi_0(x_2,\theta) & .. & \phi_0(x_{N_{min}},\theta)\\ \phi_0(x_1,\theta) & \phi_0(x_2,\theta) & .. & \phi_1(x_{N_{min}},\theta)\\ . & . & . & .\\ . & . & . & .\\ \phi_{N_{min}-1}(x_1,\theta) & \phi_{N_{min}-1}(x_2,\theta) & .. & \phi_{N_{min}-1}(x_{N_{min}},\theta)\end{pmatrix}, \tag{4.170}$$

by means of elementary row operations. Since the determinant is invariant to such row operations

$$\left|\boldsymbol{U}\left(\mathrm{x}_1,....,\mathrm{x}_{\mathrm{N}_{\min}}\right)\right| = \left|\tilde{\boldsymbol{U}}\left(\mathrm{x}_1,.....,\mathrm{x}_{\mathrm{N}_{\min}};\theta\right)\right| \tag{4.171}$$

Let $S_{N_{\min}}$ be the set of all permutations of integers $\{0,1,.....,\mathrm{N}_{\min}-1\}$ and let $\delta \in \mathrm{S}_{\mathrm{N}_{\min}}$ denote the particular function $\delta:(0,1,.....,\mathrm{N}_{\min}-1)\rightarrow(\delta_1,\delta_2,....,\delta_{\mathrm{N}_{\min}})$ which permutes the integers $\{0,1,.....,\mathrm{N}_{\min}-1\}$. The determinant can be written as

$$\left|\tilde{\boldsymbol{U}}\left(\mathrm{x}_1,.....,\mathrm{x}_{\mathrm{N}_{\min}}\right)\right| = \sum_{\delta\in \mathrm{s}_{\mathrm{N}_{\min}}} \mathrm{sgn}\{\delta\} \prod_{\mathrm{i}=1}^{\mathrm{N}_{\min}} \phi_{\delta_{\mathrm{i}}}\left(\mathrm{x}_{\mathrm{i}},\theta\right) \tag{4.172}$$

where

$$\mathrm{sgn}\{\delta\} = \begin{cases} +1 \textit{ for even permutation} \\ -1 \textit{ for odd permutation} \end{cases} \tag{4.173}$$

Substituting (4.171) and (4.172) into (4.169) gives

$$\mathrm{E}_{\lambda}\left\{\prod_{\mathrm{i}=1}^{\mathrm{N}_{\min}} \mathrm{z}\left(\lambda_{\mathrm{i}},\theta\right)\right\} = \frac{\tilde{\mathrm{K}}}{\mathrm{N}_{\min}!}\int_0^{\infty}...\int_0^{\infty} \sum_{\alpha\in \mathrm{s}_{\mathrm{N}_{\min}}} \sum_{\delta\in \mathrm{s}_{\mathrm{N}_{\min}}} \mathrm{sgn}\{\alpha\}\mathrm{sgn}\{\delta\}$$

$$\times \prod_{\mathrm{i}=1}^{\mathrm{N}_{\min}} \phi_{\alpha_{\mathrm{i}}}\left(\mathrm{x}_{\mathrm{i}},\theta\right)\phi_{\delta_{\mathrm{i}}}\left(\mathrm{x}_{\mathrm{i}},\theta\right)\mathrm{x}_{\mathrm{i}}^{\mathrm{N}_{\max}-\mathrm{N}_{\min}}\mathrm{e}^{-\mathrm{x}_{\mathrm{i}}}\mathrm{dx}_{\mathrm{i}} = \frac{\tilde{\mathrm{K}}}{\mathrm{N}_{\min}!} \sum_{\alpha\in \mathrm{s}_{\mathrm{N}_{\min}}} \sum_{\delta\in \mathrm{s}_{\mathrm{N}_{\min}}} \mathrm{sgn}\{\alpha\}\mathrm{sgn}\{\delta\}$$

$$\times \prod_{\mathrm{i}=1}^{\mathrm{N}_{\min}} \left\langle \phi_{\delta_{\mathrm{i}}}\left(\mathrm{x}_{\mathrm{i}},\theta\right), \phi_{\delta_{\mathrm{i}}}\left(\mathrm{x}_{\mathrm{i}},\theta\right)\right\rangle \tag{4.174}$$

Using the orthogonality property of $\{\phi_n(x,\theta)\}_{n=0}^{N_{\min}-1}$, (4.174) becomes

$$\mathrm{E}_{\lambda}\left\{\prod_{\mathrm{i}=1}^{\mathrm{N}_{\min}} \mathrm{z}\left(\lambda_{\mathrm{i}}\right)\right\} = \frac{\tilde{\mathrm{K}}}{\mathrm{N}_{\min}!} \sum_{\alpha\in \mathrm{s}_{\mathrm{N}_{\min}}} \sum_{\delta\in \mathrm{s}_{\mathrm{N}_{\min}}} \mathrm{sgn}\{\alpha\}\mathrm{sgn}\{\delta\} \times \prod_{\mathrm{i}=1}^{\mathrm{N}_{\min}} \left\|\phi_{\delta_{\mathrm{i}}}\right\|_{\theta}^2 \delta_{\alpha_{\mathrm{i}},\delta_{\mathrm{i}}}$$

$$= \frac{\tilde{\mathrm{K}}}{\mathrm{N}_{\min}!} \sum_{\delta\in \mathrm{s}_{\mathrm{N}_{\min}}} (\mathrm{sgn}\{\delta\})^2 \prod_{\mathrm{i}=1}^{\mathrm{N}_{\min}} \left\|\phi_{\delta_{\mathrm{i}}}\right\|_{\theta}^2 = \tilde{\mathrm{K}} \prod_{\mathrm{n}=0}^{\mathrm{N}_{\min}-1} \left\|\phi_{\mathrm{n}}\right\|_{\theta}^2 ,$$

where, the fact that the cardinality of $S_{N_{\min}}$ is equal to $\mathrm{N}_{\min}!$ in obtaining the last equality is used. This completes the proof of *Theorem 1*.Using *Theorem 1,* define following theorem.

Theorem 2: The SEP for coherent detection of M-ary PSK signals using OC with K - element antenna array in the presence of L uncorrelated equal-power cochannel interferers and thermal noise in Rayleigh fading is given by

$$\mathrm{P}_{\mathrm{e}} = \frac{\tilde{\mathrm{K}}}{\pi}\int_0^{\Theta} \mathrm{A}(\theta)\mathrm{C}(\theta)\mathrm{d}\theta \tag{4.175}$$

where, A(θ) is given by (4.156), and $C(\theta)\underline{\Delta}\prod_{n=0}^{N_{\min}-1}\left\|\phi_n\right\|_{\theta}^2$, with $\mathrm{N}_{\min} = \min\{\mathrm{K},\mathrm{L}\}$ is the product norm squared of all the elements in a particular orthogonal system generated by

of $du_\theta(x)$ of (4.163) using $z(x,\theta)=\psi(x,\theta)$. The integrand is a product of two functions A(θ) and C(θ); the former function A(θ) involves trigonometric functions and is given by (4.156), and the latter function C(θ) can be evaluated easily on the approach illustrated in [105].

4.14.1 BER of Optimum FrFT combiner for single interferer case

The SEP expression (4.175) can be efficiently and rapidly evaluated even for a large number of antennas and/or cochannel interferers. But for the case of single interferer with BPSK simple BER expressions are available in literature. As the simulation study in thesis is based on single interferer with BPSK modulation these BER expressions are reviewed next, which are based on moment generating function. For the case of a single interferer (L=1) for which (4.147) can be rewritten as $\mu=\sum_{i=1}^{K}\frac{|v_i|^2}{\lambda_i}$ and eigenvalues of $\boldsymbol{R_I}$ are given as

$$\lambda_i=\begin{cases}\sum_{i=1}^{K}\left|\boldsymbol{g}_{I,i}\right|^2+\sigma_w^2 & i=1\\ \sigma_w^2 & i=2,3,.....K\end{cases}, \qquad (4.176)$$

where, $\boldsymbol{g}_I^T=[g_{I,1},g_{I,2}.....g_{I,K}]$. Each of the $\left\{\left|\boldsymbol{g}_{I,n}\right|^2\right\}$ is a chi square random variable with two degrees of freedom. Due to the mutual independence of the terms in redefined μ, the Moment generating function (MGF) of μ conditioned on λ_1 is given by

$$\phi_{\mu/\lambda_1}(s)=\frac{1}{(1-s\frac{P_s}{\lambda_1})(1-s\frac{P_s}{\sigma_w^2})^{K-1}}, \qquad (4.177)$$

where, $P_s=E[|\mathbf{g}_{s,n}|^2]$, n=1,2,……K, is the mean signal power per antenna and $\boldsymbol{g}_s^T=[g_{I,1},g_{I,2}.....g_{s,K}]$. Let $\mu_s=\frac{P_s}{\sigma_w^2}$ denote the mean signal to noise ratio (SNR) per antenna (channel). The conditional pdf of μ can be found by applying inverse Laplace transform to (4.177) and is given by

$$f_{\mu/\lambda_1}(\mu)=\frac{\lambda_1\mu^{K-1}e^{-\lambda_1\mu/P_s}\,{}_1F_1(K-1;K;\frac{(\lambda_1-\sigma_w^2)\mu}{P_s}}{\sigma_w^2\Gamma(K)\mu_s{}^K},\ \mu\geq 0,\lambda_1\geq\sigma_w^2;K\geq 1, \qquad (4.178)$$

where, ${}_1F_1(.)$ is the confluent hypergeometric function and Γ(.) is the standard gamma function. Clearly, if the interference is fading, λ_1 is a random variable that assumes new

values at the fading rate. In case the λ_1 is assumed to be constant then λ_1 is replaced by its mean value $E[\lambda_1] = KP_I + \sigma_w^2$ in (4.178) where, $P_I=E[|\mathbf{g}_{I,n}|^2]$, n=1,2,……K. Conditioned on λ_1 the probability of bit error is given by

$$\begin{aligned} P_{e/\lambda_1} &= \int_0^\infty \boldsymbol{Q}(\sqrt{2\mu})\, f_{\mu/\lambda_1}(\mu)\, d\mu \\ &= \frac{1}{2} - \frac{1}{2}\int_0^\infty \mathrm{erf}(\sqrt{\mu})\, f_{\mu/\lambda_1}(\mu)\, d\mu \end{aligned}, \tag{4.179}$$

where, $\boldsymbol{Q}(x) = \frac{1}{2\pi}\int_x^\infty \exp(-\frac{y^2}{2})dy$ is the Gaussian $\boldsymbol{Q}$-function and erf(.) is the error function. The equation can be simplified further by using identity $\mathrm{erf}(\sqrt{\mu}) = \frac{2}{\sqrt{\pi}}\sqrt{\mu}e^{-\mu}\,{}_1F_1(1;3/2;\mu)$

$$P_{e/\lambda_1} = \frac{1}{2} - \frac{\lambda_1\Gamma(K+1/2)P_s^{K+(1/2)}F_2(K+1/2,1,K-1;3/2,K;\frac{P_s}{\lambda_1+P_s},\frac{\lambda_1-\sigma_w^2}{\lambda_1+P_s})}{\sqrt{\pi}\sigma_w^2\Gamma(K)\mu_s{}^K(\lambda_1+P_s)^{K+1/2}}, \tag{4.180}$$

where, $F_2(.)$ is Appell's hypergeometric function. It can be shown that the series in (4.180) converges. Since each of $\left\{\left|\boldsymbol{g}_{I,n}\right|^2\right\}$ has a Chi-Square distribution, $\lambda_1 = \sum_{i=1}^{K}\left|g_{2,i}\right|^2 + \sigma_w^2$ has the pdf

$$f_{\lambda_1}(\lambda_1) = \Gamma^{-1}(K)P_I^{-K}(\lambda_1-\sigma_w^2)^{K-1}e^{-((\lambda_1-\sigma_w^2)/P_I)} \qquad \lambda_1 \geq \sigma_w^2 . \tag{4.181}$$

The bit error probability (BEP) averaged over all values of λ_1 is given by

$$P_e = \int_0^\infty P_{e/\lambda_1} f_{\lambda_1}(\lambda_1)d\lambda_1 . \tag{4.182}$$

Substituting (4.180) and (4.181) in (4.182)

$$\begin{aligned} P_e = \frac{1}{2} - \frac{\Gamma(K+\frac{1}{2})P_s^{K+\frac{1}{2}}}{\sqrt{\pi}\sigma_w^2\Gamma(K)\mu_s{}^K}\frac{1}{\Gamma(K)P_I^K}\int_{\sigma_w^2}^\infty \frac{\lambda_1}{(\lambda_1+P_s)^{K+1/2}}(\lambda_1-\sigma_w^2)^{K-1}e^{-((\lambda_1-\sigma_w^2)/P_I)} \\ \times F_2(K+1/2,1,K-1;3/2,K;\frac{P_s}{\lambda_1+P_s},\frac{\lambda_1-\sigma_w^2}{\lambda_1+P_s})d\lambda_1 \end{aligned} . \tag{4.183}$$

Integral in (4.183) can be evaluated numerically. A simple upper bound on (4.180) is derived using $Q(\sqrt{2\mu}) \leq \frac{1}{2}e^{-\mu}$ and integral tables [58,114] as

$$P_{e/\lambda_1} \leq \frac{1}{2}\frac{\lambda_1}{(\lambda_1+P_s)(1+\mu_s)^{K-1}} . \tag{4.184}$$

The upper bound on average P_e is obtained by averaging (4.184) over density of λ_1 and is given by

$$P_e \le A\left[(K-1)!-(-1)^{K-2}\frac{P_s}{P_I}\eta^{K-1}e^{\eta}Ei(-\eta)+\sum_{i=1}^{K-1}(i-1)(-\eta)^{K-1-i}\right], \quad (4.185)$$

where, Ei(.) is exponential integral , A $=(2(1+\mu_s)^K\Gamma(K))^{-1}$ and $\eta=(P_s+\sigma_w^2)/P_I$ .An exact closed form expression can also be found for single interferer case. Let $x_1=\boldsymbol{g}_1\boldsymbol{g}_1^T$ gives interfering power. Since components of $\mathbf{g}_1$ are complex Gaussian, $\mu_1=\frac{x_1}{\sigma_w^2}$ is a Gamma distributed random variable of order K representing the SNR of the interference at the output of the combiner, and has probability density function (pdf) given by

$$p_{\mu_1}(\mu_1)=\frac{1}{\bar{\mu}_1^K\Gamma(K)}\mu_1^{K-1}\exp(-\frac{\mu_1}{\bar{\mu}_1}), \qquad \mu_1 \ge 0, \quad (4.186)$$

where, $\bar{\mu}_1=\frac{P_I}{\sigma_w^2}$ is the average interference SNR per antenna. Also the pdf of the SNR of the desired signal at the output of the combiner, $\mu_s=\frac{\boldsymbol{g}_s^T\boldsymbol{g}_s}{\sigma_w^2}$ is given by

$$p_{\mu_s}(\mu_s)=\frac{1}{\bar{\mu}_s^K\Gamma(K)}\mu_s^{K-1}\exp(-\frac{\mu_s}{\bar{\mu}_s}), \qquad \mu_s \ge 0, \quad (4.187)$$

where, $\bar{\mu}_s=\frac{P_s}{\sigma_w^2}$, i=1,2,……,K is the average SNR for the desired signal per antenna. Since the interference-to-noise power is a random variable with pdf as in (4.187), the average BER is obtained as [58, 74,114]

$$\begin{aligned}P_e &= \int_0^{\infty} P_{e/\mu_1}(\mu_1)p_{\mu_1}(\mu_1)d\mu_1 \\ &= \frac{1}{2}\left[1-\sqrt{\frac{\bar{\mu}_s}{\bar{\mu}_s+1}}\sum_{k=0}^{K-2}\binom{2k}{k}\left(\frac{1}{4(\bar{\mu}_s+1)}\right)^k\right]- \\ &\quad \frac{1}{2\Gamma(K)(-\bar{\mu}_1)^{K-1}}\left\{\sqrt{\frac{\pi\bar{\mu}_s}{\bar{\mu}_1}}\exp\left(\frac{\bar{\mu}_s+1}{\bar{\mu}_1}\right)\operatorname{erfc}\left(\sqrt{\frac{\bar{\mu}_s+1}{\bar{\mu}_1}}\right)-\sqrt{\frac{\bar{\mu}_s}{\bar{\mu}_s+1}}\sum_{k=0}^{K-2}\frac{(2k)!}{k!}\left(\frac{-\bar{\mu}_1}{4(\bar{\mu}_s+1)}\right)^k\right\},\end{aligned} \quad (4.188)$$

where, $P_{e/\mu_1} = \frac{1}{2}\left\{1-\sqrt{\frac{\bar{\mu}_s}{\bar{\mu}_s+1}}\sum_{k=0}^{K-2}\binom{2k}{k}\left(\frac{1}{4(\bar{\mu}_s+1)}\right)^k - \left[\sqrt{\frac{\bar{\mu}_s}{\bar{\mu}_s+\mu_1+1}}-\sqrt{\frac{\bar{\mu}_s\mu}{\bar{\mu}_s+1}}\sum_{k=0}^{K-2}\binom{2k}{k}\left(\frac{-\bar{\mu}_1}{4(\bar{\mu}_s+1)}\right)^k\right](-\mu_1)^{-(K-1)}\right\}$.

The optimum combiner gives the same system performance as MRC when no interfering signals are present at the receiver. Thus the average BER for MRC may be obtained by substituting $\mu_1=0$ in (4.188) to give

$$P_{e,MRC} = \frac{1}{2}\left[1-\sqrt{\frac{\bar{\mu}_s}{\bar{\mu}_s+1}}\sum_{k=1}^{K-1}\binom{2k}{k}\left(\frac{1}{4(\bar{\mu}_s+1)}\right)^k\right]. \quad (4.189)$$

For Nakagami fading channel given by (4.92) and for integer values of Nakagami parameter m the conditional average probability of error for coherent detection is given by [74]

$$P_{e/\mu_1} = \frac{1}{2\sqrt{\pi}}\left(\frac{m}{m+\bar{\mu}_s}\right)^{m(K-1)}\sqrt{\frac{\bar{\mu}_s}{m+\bar{\mu}_s}}\times$$
$$\left[\left\{\frac{\Gamma(Km-m+\frac{1}{2})}{\Gamma(Km-m+1)}\left(\frac{1+\mu_1}{\frac{\bar{\mu}_s}{m}}\right)^{m-1}\times {}_2F_1\left(1,m(K-1)+1/2;m(K-1)+1;\frac{m}{m+\bar{\mu}_s}\right)\right\} - \sum_{k=0}^{m-1}\frac{\Gamma(k+1)\Gamma(Km-k-\frac{1}{2})}{\Gamma(Km-k)}\times\left(\frac{1+\mu_1}{1+\frac{\bar{\mu}_s}{m}}\right)^{m-1-k}\right]$$
$$\times {}_2F_1\left(m-k,Km-k-\frac{1}{2};Km-k;-\frac{m\mu_1}{m+\bar{\mu}_s}\right), \quad (4.190)$$

where, ${}_2F_1$ is the hyper geometric function. The average BER is obtained as

$$P_e = \int_0^\infty P_{e/\mu_1}(\mu_1)p_{\mu_1}(\mu_1)d\mu_1. \quad (4.191)$$

The mathematical analysis of BPSK with optimum combiner in interference and noise is analyzed above for a single interferer case.

4.14.2 Monte Carlo Simulation of BER

In this section some simulation results are presented to illustrate the effects of FrFT based optimum beamformer on the average BER in an interfering environment. The simulations are presented for the case of single interferer. The focus is to use Monte Carlo simulations to demonstrate the BER performance in three different domains of FrFT in SIMO system. The BER is plotted for different number of antennas

M=3,4,5. The channel is modelled as flat Rayleigh faded and vector **g** is comprised of i.i.d complex Gaussian random variables $\mathcal{CN}(0,1)$.The complex Gaussian distribution with mean m and covariance matrix K is denoted as $\mathcal{CN}(m,K)$. The noise is considered as white. For the BER of BPSK a frame consisting of 100 bits is sent from transmitter with all the bits having random values ±1. The results below have been obtained from 10000 independent runs of such frames. The decision variable at the output of the optimal beamformer is simply $Re\{\boldsymbol{w}_{opt}^{a}\boldsymbol{x}(t)\}$. The decisions are obtained in a=0, a=1 and $a=a_{opt}$ domain by using the weight vector obtained in respective domains. The optimum domain is computed in each frame. The results are plotted in figures 4.53-4.59. The MSE vs. SNR curve in Fig.4.53 shows the sum of all the MSEs obtained in each domain during all runs for M=5 in Rayleigh faded channel. Fig.4.53 again shows the superiority of optimum FrFT domain beamformer as total MSE of the beamformer during all runs is less in optimum FrFT domain as compared to time or frequency domain. The plots of MSE vs. SINR were obtained for other cases also, but are not shown as these plots were similar to Fig.4.53. The average BER versus the average received SINR, defined as $\mu_b = \frac{M\bar{\mu}_s}{1+L\bar{\mu}_1}$, is also plotted for several values of M. A single Rayleigh faded interferer with $\bar{\mu}_I = 0\,\text{dB}$ is considered in all simulations. Figure 4.54 shows the improvement obtained by optimum FrFT beamformer over other optimal beamformers as it requires 1.3 dB less input power as compared to time domain beamformer for a BER of 10^{-2}. In case of M=4 and for a BER of 10^{-2} optimum FrFT Beamformer requires 4 dB and 9 dB less input power as compared to time and frequency domain beamformer as shown in Fig.4.55. Fig.4.56 shows the improvement of 5 dB and 10 dB in optimum FrFT domain as compared to time and frequency domain for M=5. The same results are plotted for Nakagami faded channel also in Figs. 4.57-4.59. The application of optimum FrFT beamformer is considered in chapter 5 in linear receive processing in MIMO systems.

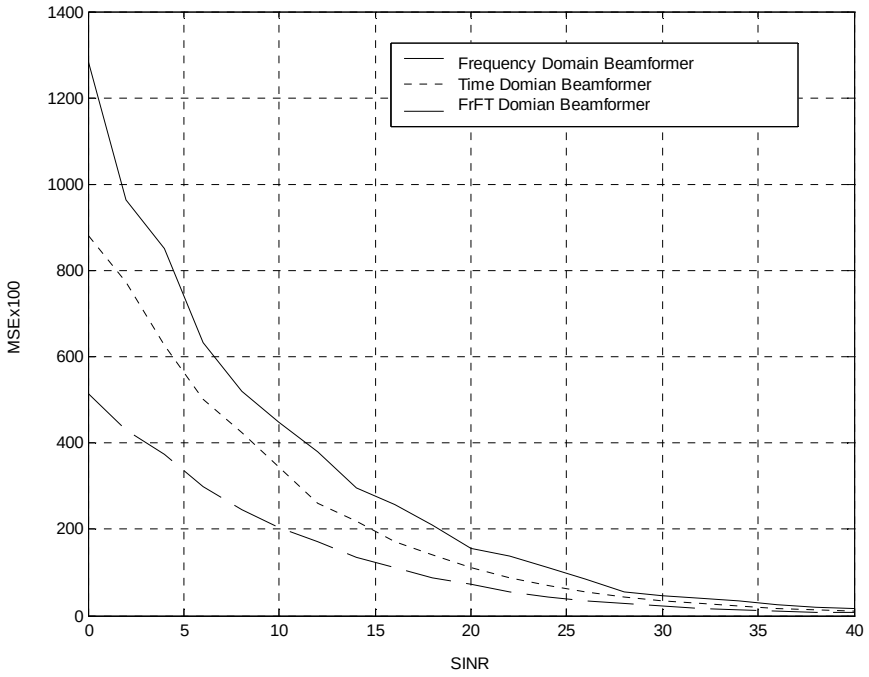

Figure 4.53- Total MSE vs. SINR for beamformer in various domains for Rayleigh faded channel with M=5

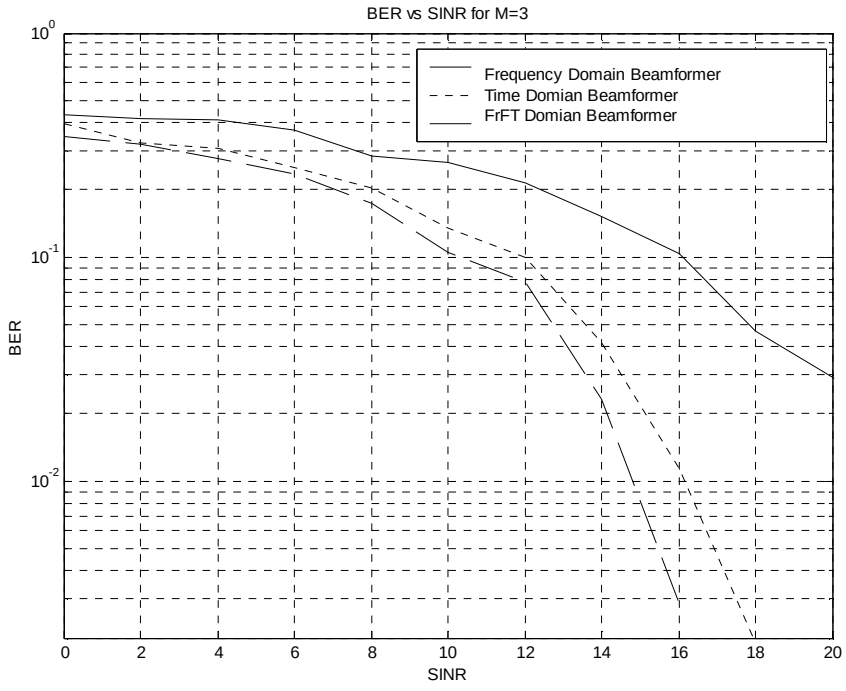

Figure 4.54- BER vs. SINR for BPSK modulation in Rayleigh Faded channel for M=3

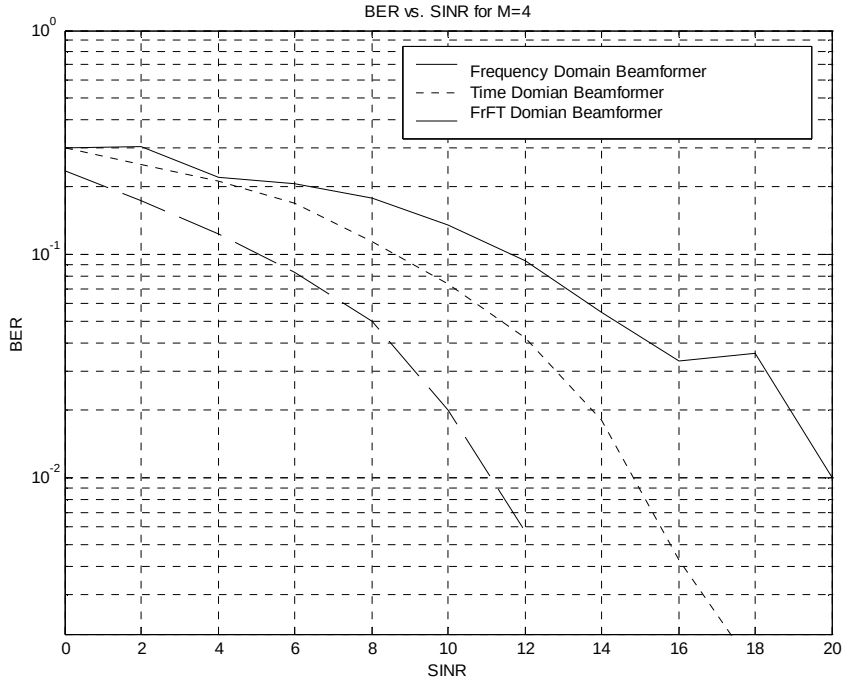

Figure 4.55- BER vs. SINR for BPSK modulation in Rayleigh Faded channel for M=4

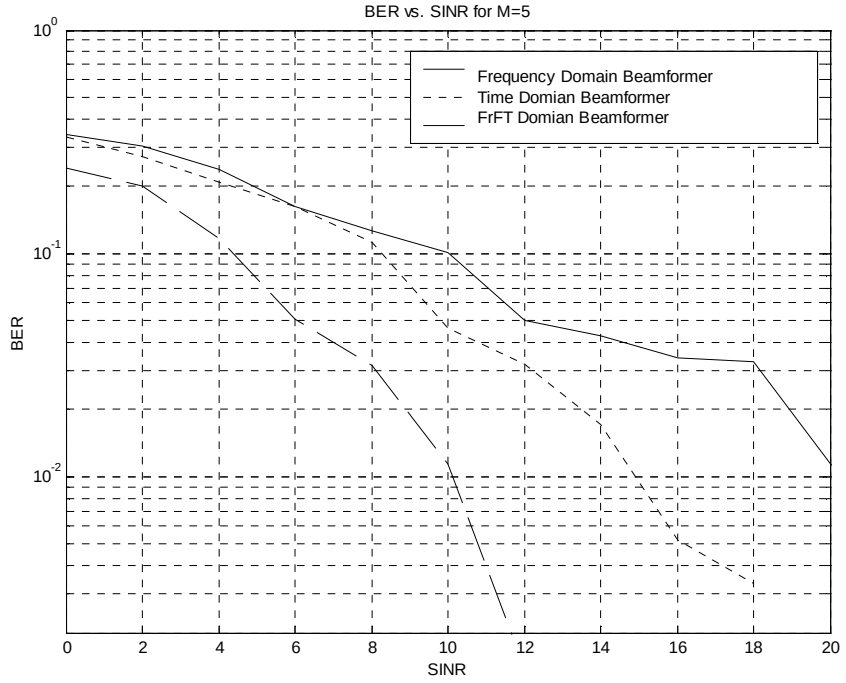

Figure 4.56- BER vs. SINR for BPSK modulation in Rayleigh Faded channel for M=5

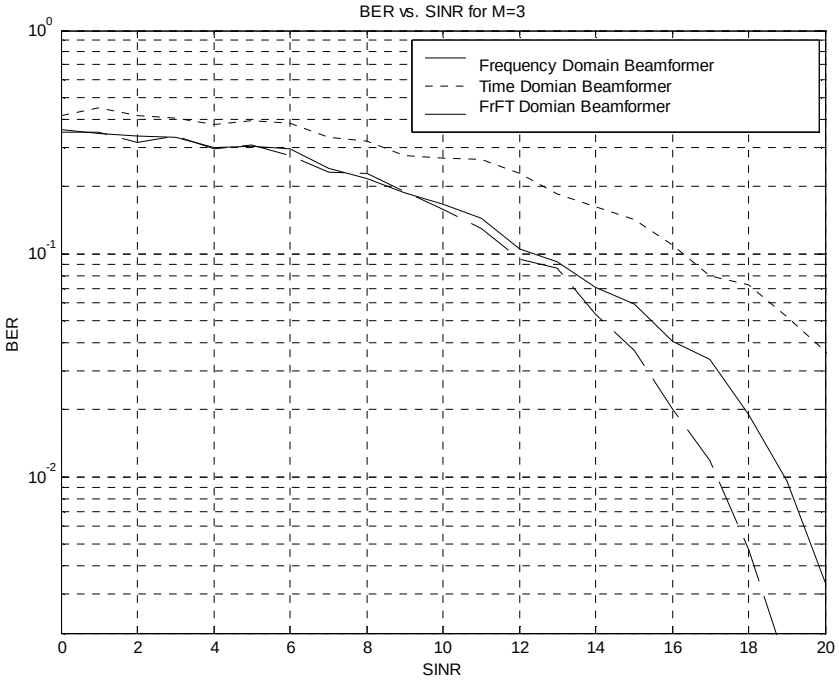

Figure 4.57- BER vs. SINR for BPSK modulation in Nakagami Faded channel for M=3

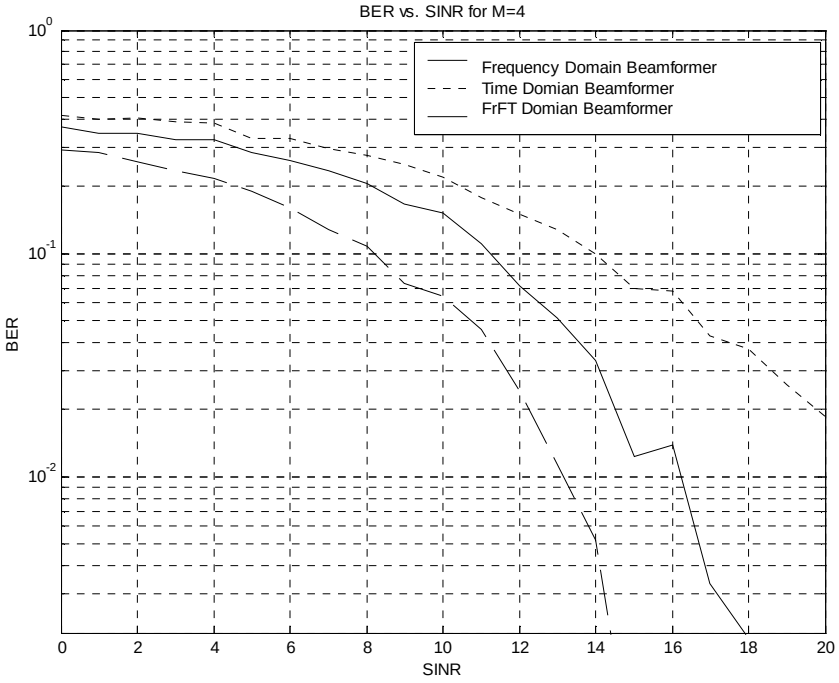

Figure 4.58- BER vs. SINR for BPSK modulation in Nakagami Faded channel for M=4

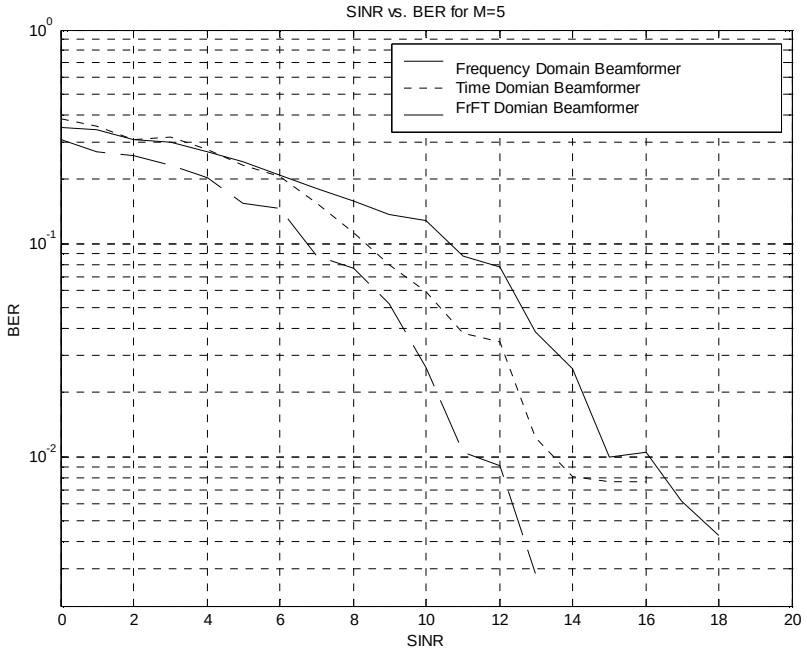

Figure 4.59- BER vs. SINR for BPSK modulation in Nakagami Faded channel for M=5

4.15 SUMMARY OF THE CHAPTER

A method of optimal beamforming for various multipath fading channels in mobile and wireless communication using the Fractional Fourier Transform (FrFT) is considered in this chapter. The method is found to be useful in moving and accelerating source problems. In case the source is moving, the Doppler Effect produces frequency shift. In case of accelerating source a chirped type signal is produced. With both types of degradations present, it is shown that the FrFT improves the performance of beamformer in multipath fading, micro and macro cellular environments with the same complexity as the conventional Fast Fourier Transform (FFT). The BER of optimal FrFT beamformer is less as compared to time or frequency domain optimal beamformers[6]. In next chapter the benefits of FrFT domain beamformer is explored in MIMO systems. In chapter 6 the application of low side lobe and adaptive algorithms is proposed in terms of reducing RF hazards.

---

6. [P25] "BER reduction in SIMO system using FrFT based optimal beamformer" submitted to IEEE Transaction on Vehicular Technology.

Chapter 5

FrFT BASED RECEIVE ARRAYS FOR MIMO SYSTEMS

5.1 INTRODUCTION

A core idea in MIMO system is *space–time* signal processing in which time (the natural dimension of digital communication data) is complemented with the spatial dimension inherent in the use of multiple spatially distributed antennas. As such MIMO systems can be viewed as an extension of the so-called *smart antennas*, a popular technology using antenna arrays for improving wireless transmission dating back several decades. Clearly, in a MIMO link, the benefits of conventional smart antennas are retained since the optimization of the multiantenna signal is carried out in a larger space, thus providing additional degrees of freedom.

MIMO systems have a number of advantages over traditional SISO systems such as the beamforming (or array) gain, the diversity gain and the multiplexing gain. The beamforming and diversity gains are no exclusive of MIMO systems and also exist in SIMO and MISO systems. The multiplexing gain, however, is a unique characteristic of MIMO systems. An overview of the gains of MIMO systems is given in [57]. A brief discussion about these gains and their mutual comparison is given next.

Beamforming or Array gain: Array gain means average increase in the SNR at receiver that occurs due to coherent combining effect of multiple antennas at the transmitter or receiver or both. If the BER of a communication system is plotted with respect to the transmitted power or the received power per antenna (using a logarithmic scale) then the beamforming gain is characterized as a shift of the curve due to the gain in SINR. In case of MIMO and MISO systems array gain exploitation requires channel knowledge at the transmitter [9].

Diversity Gain: Diversity gain is the improvement in link reliability obtained by receiving replicas of the information signal through independently fading links, branches or dimensions. This type of diversity is clearly related to the random nature of

the channel and is closely connected to the specific channel statistics. If the BER of a communication system is plotted with respect to the transmitted power or the received power per antenna (using a logarithmic scale), the diversity gain is easily characterized as the increase of the slope of the curve in the low BER region. The main forms of diversity traditionally exploited in wireless communications systems are temporal diversity, frequency diversity, code diversity, polarization diversity and spatial diversity [57,137]. Diversity can be exploited at the transmitter and/or receiver antenna array. Receive diversity can be used in case of SIMO systems. A wide variety of methods exist for processing the signals received from antenna arrays in SIMO systems. Transmit diversity is applicable to MISO systems and has become an active area of research.

Transmit diversity is more difficult to exploit than receive diversity since it requires special modulation and coding schemes, whereas receive diversity simply needs the multiple receive dimensions to fade independently without requiring any specific modulation or coding scheme. Extracting transmitter diversity in systems is possible with or without channel knowledge at transmitter [9]. In absence of the channel knowledge at transmitter, Space Time diversity coding is transmit coding technique that relies on coding across space (transmit antennas) to extract diversity. There are various other coding techniques also available which can be used in transmit diversity [9,160,161]. If the channels of all the transmit antennas to the receive antennas have independent fades the diversity order of this channel is equal to the number of transmit antennas. Utilization of diversity in MIMO systems requires a combination of receive and transmit diversity described above.

Spatial Multiplexing (SM): SM offers a linear (the number of transmit–receive antenna pairs or min (M_R, M_T)) increase in the transmission rate (capacity) for the same bandwidth and with no additional power expenditure [9]. This increase is obtained through the use of multiple dimensions at both sides of the communication link [57]. While the beamforming and the diversity gains can be obtained when multiple dimensions are present at either transmit or the receive side, multiplexing gain requires multiple dimensions at both ends of the link. Thus SM is possible only in MIMO channels [9]. SM increases transmission rates proportional to the number of transmit-receive antenna pairs. SM also allows the capacity increase in the multi-user format [9].

Interference Reduction: Co-channel interference arises due to frequency reuse in wireless channels. When multiple antennas are used, the differentiation between the spatial signatures of the desired and co channel signals can be exploited to reduce the interference. Interference reduction requires knowledge of the channel of the desired signal. Interference reduction can also be implemented at the transmitter, where the goal is to minimize the interference energy sent towards the co channel users while delivering the signal to the desired one [9]. Interference reduction allows the use of aggressive reuse factors and improves network capacity.

It may not be possible to exploit all the leverages simultaneously due to conflicting demands on the spatial degrees of freedom (or the number of antennas). The degrees to which these conflicts are resolved depend upon the signaling scheme and the receiver design [9].

5.1.1 Tradeoffs between Various Gains in MIMO Systems

Beamforming and Diversity Gains: Beamforming gain is a concept that refers to the combination of multiple copies of the same signal for a specific channel realization regardless of the channel statistics. Diversity gain, however, is directly connected to the statistical behavior of the channel. With multiple receive dimensions, both gains can be simultaneously achieved by a coherent combination of the received signals and there is no tradeoff between them. With multiple transmit dimensions; beamforming gain requires channel knowledge at the transmitter whereas diversity gain can be achieved even when the channel is unknown.

Beamforming and Multiplexing Gains: Maximum beamforming gain in a MIMO system implies that only the maximum singular value of the channel should be used [9]. In terms of multiplexing gain, however, the optimum strategy is to use a subset of the channel singular values according to a water-filling strategy [174]. In other words, maximum beamforming gain requires establishing a single sub stream for communication, whereas maximum multiplexing gain requires, in general, establishing several simultaneous sub streams.

Diversity and Multiplexing Gains: Multiple antennas are used for increasing the amount of diversity or the number of degrees of freedom in wireless communication system. Both diversity and multiplexing gains can be simultaneously obtained for a given multiple antenna channel but there is a tradeoff between how much of each for any coding scheme can get. Since the diversity gain is related to the BER (it is the slope

of the BER curve in the high SNR region) and the multiplexing gain is related to the achieved rate, the diversity-multiplexing tradeoff is essentially the tradeoff between the error probability and the data rate of a system [174]. Next, a brief overview of space time wireless communication systems is given.

5.2 SPACE TIME WIRELESS COMMUNICATION SYSTEMS

A typical space time wireless communication system with M_T transmit antennas and M_R receive antennas is shown in Fig 5.1 [9]. A digital source in the form of a binary data stream is fed to simplified transmitting blocks encompassing the functions of error control coding and mapping to complex modulation symbols. The later produces several separate symbol streams. Each is then mapped onto one of the multiple TX antennas. Mapping may include linear spatial weighting of the antenna elements or linear antenna space–time *precoding*. After upward frequency conversion, filtering and amplification the signals are launched into the wireless channel. At the receiver, the signals are captured by multiple antennas and demodulation and demapping operations are performed to recover the message. The level of intelligence, complexity and *a priori* channel knowledge used in selecting the coding and antenna mapping algorithms can vary a great deal depending on the application. This determines the class and performance of the multiantenna solution that is implemented. A review of space-time processing techniques up to 1997 can be found in [12].

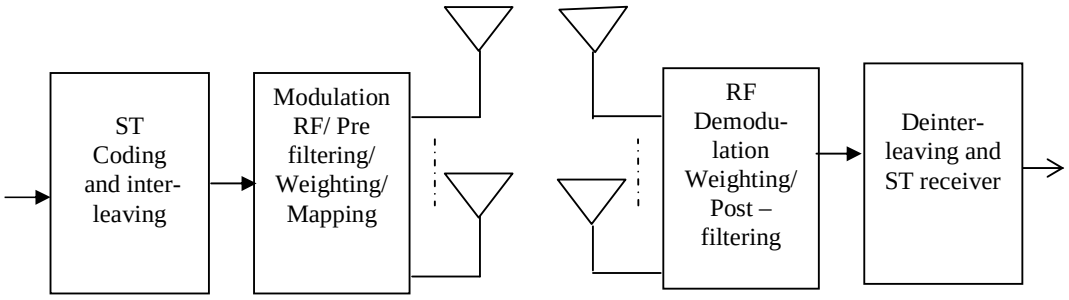

Figure 5.1: Schematic of a ST wireless communication system [9]

5.3 CAPACITY OF MIMO SYSTEMS

Channel capacity is a convenient measure to analyze the potential gain of MIMO systems compared to SISO systems. Information theory provides means to explore the ultimate limits of reliable data transmission.

5.3.1 Capacity of Flat Faded Deterministic Channel

Consider a MIMO system with M_R and M_T number of antenna elements at receiver and transmitter, respectively as shown in Fig.5.1. The channel can be represented by a channel matrix **H** of dimension $M_R \times M_T$. The channel has a bandwidth of 1 Hz and is frequency flat over this band. Let **s** be the vector of transmitted signal with dimension $M_T \times 1$. The vector **y** of dimension $M_R \times 1$ is the corresponding received signal on the receiver array. The input–output relation over a symbol period assuming single-carrier (SC) modulation is given by

$$\mathbf{y} = \sqrt{\frac{E_s}{M_T}}\mathbf{H}\mathbf{s} + \mathbf{n}, \tag{5.1}$$

where, **n** is AWGN with $E[\mathbf{n}\mathbf{n}^H] = \mathbf{N_0}\mathbf{I}_{M_R}$. E_s is the total energy available at the transmitter over a symbol period. The total average transmitted power over a symbol period is constrained by assuming that the covariance matrix of **s**, $\mathbf{R}_{ss}$ satisfies $tr[\mathbf{R}_{ss}]=M_T$, where tr[.] indicates the transpose of the matrix. For a deterministic channel **H**, the capacity (with channel perfectly known at receiver) is given by [9]

$$C_{det} = \max_{tr(\boldsymbol{R}_{ss})=M_T} \log_2 \det(\boldsymbol{I}_{M_R} + \frac{E_s}{M_T N_0}\boldsymbol{H}\boldsymbol{R}_{ss}\boldsymbol{H}^H). \tag{5.2}$$

The capacity is measured in bps/Hz. The capacity C_{det} in (5.2) is referred as the error free spectral efficiency or the data rate per unit bandwidth that can be sustained over MIMO link [9]. Thus given a bandwidth of W Hz the maximum achievable data rate over this bandwidth is WC_{det} bps [9].

5.3.2 Unknown-CSIT Capacity

If the channel state information (CSI) is not known at Transmitter, then vector **s** may be chosen statistically non preferential i.e. $\boldsymbol{R}_{ss} = \boldsymbol{I}_{M_T}$. This implies that the signals transmitted from the individual antennas are independent and equipowered. The capacity of MIMO channels in the absence of channel knowledge is given by

$$\mathbf{C}_{cu} = \log_2 \det(\mathbf{I}_{M_R} + \frac{E_s}{M_T N_0}\mathbf{H}\mathbf{H}^{\mathbf{H}}). \tag{5.3}$$

Let eigen-decomposition of $\mathbf{H}\mathbf{H}^{\mathbf{H}}$ be $\mathbf{Q}\boldsymbol{\Lambda}\mathbf{Q}^{\mathbf{H}}$, where **Q** is an $M_R \times M_R$ matrix satisfying $\mathbf{Q}^{\mathbf{H}}\mathbf{Q}=\mathbf{Q}\mathbf{Q}^{\mathbf{H}} = \mathbf{I}_{M_R}$ and $\boldsymbol{\Lambda}=\text{diag}\{\lambda_1, \lambda_2 \ldots\ldots\ldots \lambda_{M_R}\}$ with $\lambda_i \geq 0$ and $\lambda_i \geq \lambda_{i+1}$. The capacity of MIMO channel can be expressed as [9]

$$\mathbf{C}_{cu} = \sum_{i=1}^{r} log_2 (1 + \frac{E_S}{M_T N_0} \lambda_i), \quad (5.4)$$

where, r is the rank of the channel and λ_i (i=1,2,……r) are the positive eigenvalues of $\mathbf{HH}^H$. It follows from (5.4) that multiple scalar spatial data pipes (also known as spatial modes) open up between transmitter and receiver resulting in significant performance gains over the SISO case. For example, $\mathbf{C}_{cu}$ increases by r b/s/Hz for every 3-dB increase in transmit power (for high transmit power), as opposed to 1 b/s/Hz in conventional SISO channels. The number of these parallel channels equals the rank of **H**, and the gain of the i^{th} equivalent parallel channel is equal to λ_i and the transmit power E_S/M_T [9].

5.3.3 Channel Known at Transmitter

If the CSI is provided at the transmitter, the total available power can be optimally distributed on M_T transmit antennas, a solution that is usually referred to as *water filling* (WF). When the channel is known to both transmitter and receiver, the individual channel modes may be accessed through linear processing at the transmitter and receiver [9, 43]. The capacity of the MIMO channel is the sum of the individual parallel SISO channel capacities and is given by

$$\mathbf{C}_{WF} = \sum_{i=1}^{r} log_2 (1 + \frac{E_S \gamma_i}{M_T N_0} \lambda_i), \quad (5.5)$$

where, $\gamma_i = E\{|s_i|^2\}$,(i=1,2,……r) reflects the transmit energy in the i^{th} sub-channels and satisfies $\sum_{i=1}^{r} \gamma_i = M_T$. The mutual information is maximized if optimal energy γ_i^{opt} is allocated as given by

$$\gamma_i^{opt} = \left(\mu - \frac{M_T N_0}{E_S \lambda_i} \right)^+, \text{ (i=1,2,……r)}, \quad (5.6)$$

where, μ is a constant and is determined so as to satisfy the constraint on total energy transmitted i.e. $\sum_{i=1}^{r} \gamma_i^{opt} = M_T$ and $(x)^+$ implies

$$(x)^+ = \begin{cases} 0 & \text{if} \quad x < 0 \\ x & \text{if} \quad x \geq 0 \end{cases}. \quad (5.7)$$

The optimal energy is found iteratively through the water pouring algorithm [9].

5.3.4 Capacity of Random MIMO Channels

For the case of a randomly time-varying channel, the definition of the capacity depends on the bursts duration (codeword length) T_{code}. Here, the capacity is a random variable whose instant value depends on the corresponding **H** matrix. Let Δ be defined as coherence interval of the channel (without dimension), as the number of symbol periods during which the propagation coefficients are almost constant. If $T_{code} >> \Delta$, channel is said to behave ergodically and an ergodic (statistical average) capacity C_{av} is defined which again means the maximum attainable mutual information [9]. If $T_{code} << \Delta$, the maximum mutual information is not equal to the channel capacity and the Shannon capacity of the channel may be even zero [43]. When the instant capacity is less than the pre assumed value, a channel *outage* is said to be occurred. The outage probability is a useful parameter in studying channel capacity. Here, a tradeoff should be made between the expected throughput and outage [9, 86]. In the literature, the capacity for a given outage probability is sometimes called *outage capacity*. Outage analysis quantifies the level of performance that is guaranteed with a certain level of reliability. q% outage capacity $\mathbf{C}_{out,q}$ is defined as the information rate that is guaranteed for (100-q)% of the channel realizations i.e. Pr.($\mathbf{C}_{cu} \leq \mathbf{C}_{out,q}$)=q% [9], where Pr. means probability.

The performance criterion of wireless systems that is capacity has been described briefly. The other performance criteria are diversity gain, coding gain and array gain. To classify these gains the knowledge of spatial diversity techniques and MIMO signaling rates is required. The MIMO signaling rates are discussed next.

5.4 MIMO SIGNALING RATES

Let us discus code architecture and rate definition to classify various coding schemes. A general coding architecture is shown in Fig. 5.2. The generic coding architecture is applicable equally to all coding schemes. A block of qK bits is input to a block that performs the functions of temporal coding, interleaving and symbol mapping. In the process q(N-K) parity bits are added and N symbols are output. 2^q is the modulation order. The N symbols are input to a Space Time (ST) encoder that adds (M_TT-N) parity symbols and packs the resulting M_TT symbols into an $M_T \times T$ frame of length T. The block/frame is transmitted over T symbol periods and is referred to as ST Codeword [9].

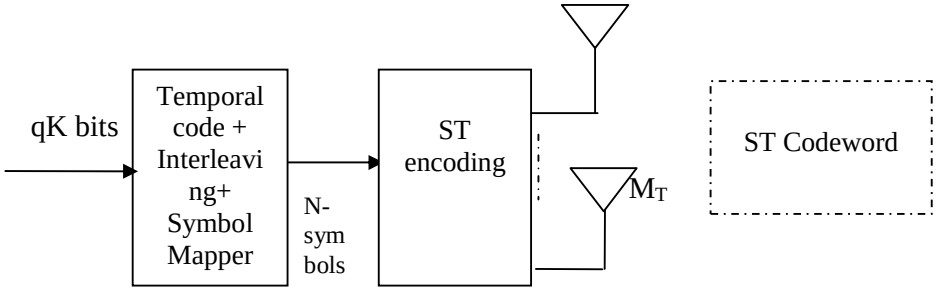

Figure 5.2: Coding architecture [9]

The signaling rate on channel is qK/T bits/transmission and should not exceed channel capacity. The signaling rate is rewritten as

$$\frac{qK}{T} = q\left(\frac{qK}{qN}\right)\left(\frac{N}{T}\right) = q\, r_t\, r_s, \tag{5.8}$$

where, r_t is the temporal code rate of the outer encoder and r_s is the spatial code rate defined as the average number of independent symbols transmitted from M_T antennas over T symbol periods. When all transmit antennas send one symbol per symbol period r_s=1(STD). M_T independent symbol periods per symbol period are sent to get $r_s=M_T$ (SM). Depending upon the choice of encoding a spatial rate varying from 0 to M_T can be achieved. The Alamouti's scheme is a rate 1 design for systems with two transmits antennas [9]. The various form of spatial diversity in MIMO systems is discussed next. Throughout this chapter the focus is on the case where the transmitter does not have channel state information and the receiver knows the channel perfectly.

5.5 SPATIAL DIVERSITY IN MIMO SYSTEMS

The use of diversity is to combine independent faded samples to achieve the desired goal of increasing the SNR and reducing the BER. The decrease in BER by using diversity is discussed next with suitable examples.

5.5.1 Receive Antenna Diversity

In receive diversity one transmit antenna and M_R receive antennas are assumed. This is equivalent to have M_R identical independent Rayleigh fading links between the transmitter and receiver. Let symbol 's' is drawn from scalar constellation with unit average energy. To leverage diversity, the transmitter transmits the same symbol's' across all links. Assuming flat fading conditions, the channel vector **h** for such a system is given by

$$\mathbf{h} = [h_1, h_2 \ldots\ldots\ldots\ldots\ldots h_{M_R}]^T. \tag{5.9}$$

The output of the channel is given by

$$y_i = \sqrt{E_s}\, h_i s + n_i, \quad i=1\ldots\ldots\ldots M_R, \tag{5.10}$$

where, E_S is the symbol energy available to transmitter for each M_R diversity branch. y_i is the received signal corresponding to i^{th} diversity branch, h_i is the channel transfer function corresponding to i^{th} diversity branch, and n_i is Zero Mean Circularly Symmetric Complex Gaussian (ZMCSCG) noise with variance N_0. The noise on each branch is assumed to be uncorrelated. The receiver combines the received signals. To maximize the SNR the receiver performs Maximal ratio combining, i.e., the weight vector $\boldsymbol{w}=\mathbf{h}^H$. The output of the receiver is given by

$$z = \sqrt{E_s}\mathbf{h}^H\mathbf{h}x + \mathbf{h}^H\mathbf{n}, \tag{5.11}$$

where, z is the receiver output and $\boldsymbol{w}=\mathbf{h}$ is the weight vector. The effective channel is thus a scalar channel and scalar detection techniques can be applied. The SNR at the receiver is given by

$$\eta = \sum_{i=1}^{M} |h_i|^2 \rho, \tag{5.12}$$

where, $\rho=E_s/N_0$ is the average SNR at the receive antenna in SISO fading link. Assuming maximum likelihood (ML) detection, the corresponding probability of error is given by [9, 74]

$$P_e \approx \overline{N}_e \mathbf{Q}\left(\sqrt{\frac{\eta d_{min}^2}{2}}\right), \tag{5.13}$$

where, $\overline{N}_e$ and d_{min} are the number of nearest neighbors and the minimum distance of separation of underlying scalar constellation, respectively. **Q**(.) is **Q** function defined as $\boldsymbol{Q}(x) = \frac{1}{\sqrt{2\pi}} \int_x^\infty e^{-\frac{t^2}{2}} dt$. Applying Chernoff bound $\boldsymbol{Q}(x) \le e^{-\frac{x^2}{2}}$ and using (5.12) and (5.13) the P_e is upper bounded as

$$P_e \le \overline{N}_e \exp[-(\sum_{i=1}^{M} |h_i|^2)\frac{\rho d_{min}^2}{4M_R}]. \tag{5.14}$$

(5.14) shows that the receive diversity affects the slope of SER (Symbol Error Rate) vs. SNR curve on log-log scale [9]. The magnitude of slope equals the diversity order M_R. The error probability as a function of SNR for different number of diversity branches M_R for Binary Phase Shift Keying (BPSK) transmission scheme is plotted in Fig.5.3. The noise is taken as ZMCSCG with equal variance. The SNR is varied from 0 to 30 dB. The channel is assumed to be flat Rayleigh faded channel. Increasing M_R decreases

the error probability. Within receive diversity combining there are three common techniques for combining: Selection Combining (SC), Maximal Ratio Combining (MRC) and Equal Gain Combining (EGC). For all three, the goal is to find a set of weights ***w.*** The three techniques differ in how this weight vector is chosen. In all the three cases it is assumed that the receiver has the required knowledge of the channel fading vector **h**. The bit error probability as a function of SNR for various combining techniques is plotted in Fig.5.4. The modulation is again taken as BPSK and the channel as Rayleigh fading channel. In this case one transmitting antenna and two receiving antennas have been assumed. From Fig.5.4 it is observed that the best performance of the system is for the MRC, while the worst is for the SC. The improvement in the case of EGC is comparable to that of maximal ratio combining.

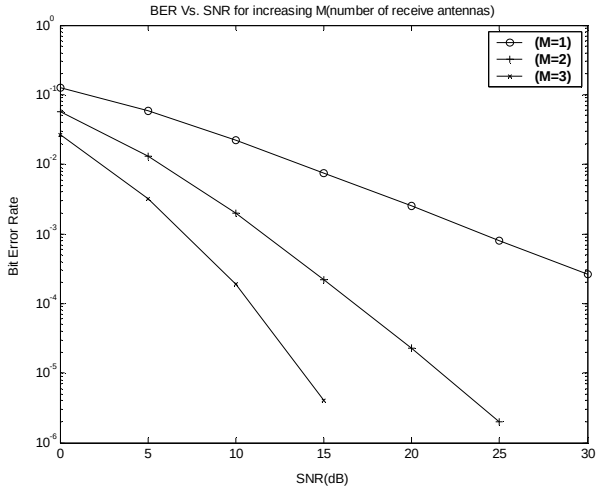

Figure 5.3: Variation of BER with SNR with number of receive antennas

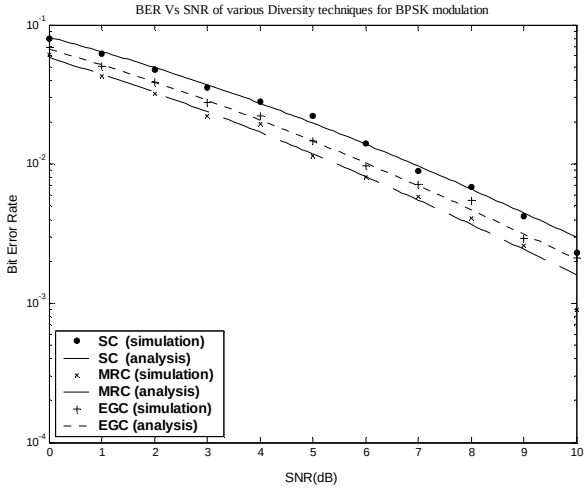

Figure 5.4: Performance of various receive diversity techniques (M_T=1, M_R=2)

Although receive diversity is capable of extracting full diversity gain and array gain. The performance improvement is proportional to the number of receive antennas. However deploying multiple antennas at receiver terminal is often not feasible due to cost and space limitations. Instead use of multiple antenna at the transmitter in combination with transmit antenna diversity technique has become popular [9,143].

5.5.2 Transmit Diversity

In transmit diversity M_T transmit antennas and one or more receive antennas are used. Spatial diversity in systems with multiple antennas at the transmitter requires the signal to be preprocessed or pre-coded prior to transmission [9]. The set of schemes aimed at realizing joint encoding of multiple TX antennas are called STCs. In these schemes, a number of code symbols equal to the number of TX antennas are generated and transmitted simultaneously, with one symbol from each antenna. These symbols are generated by the *space–time encoder* such that by using the appropriate signal processing and decoding procedure at the receiver, the diversity gain and/or the coding gain is maximized.

There has been increased interest in these techniques since 1990s [78,143]. The two space–time coding techniques- space time diversity coding ($r_s \leq 1$) and spatial multiplexing ($r_s = M_T$) are used in MIMO systems. The space-time diversity coding technique is further of mainly two types: space-time trellis coding (STTC) and space-time block coding (STBC). STTC [160] may not be practical or cost-effective due to the high complexity of the ML detector. In an attempt to reduce complexity, orthogonal STBC that can be optimally decoded with a simple linear processing at the receiver was introduced [143]. This first smart antenna simple technique called Space-Time-Transmit-Diversity (STTD) based on a simple code proposed by Alamouti is adopted for 3G WCDMA standard. This simple technique has since been adopted or proposed for a number of different wireless standards also such as 802.16. It is thus important to understand its performance under practical conditions.

5.6 ALAMOUTI'S SIMPLE TRANSMIT DIVERSITY (STD) TECHNIQUE

In this technique Alamouti assumed two antennas at the transmitter and one antenna at the receiver; although this technique is applicable to any number of receive antennas [143]. In STD two different symbols s_1 and s_2 are transmitted simultaneously from antennas 1 and 2 during first symbol period followed by $-s_2^*$ and s_1^* during next

symbol period, where * is the complex conjugate operation. Transmit diversity can be applied both in the presence and absence of channel knowledge at the transmitter. Here this technique in absence of channel knowledge at transmitter is discussed. However the receiver has the perfect channel knowledge. The transmitted signals from the transmitting antennas are equipowered. It is assumed that the channel remains constant over the two symbol periods and is frequency flat. Therefore $\mathbf{h}$= [h_1, h_2] and the signals y_1 and y_2 received over two symbol periods are

$$y_1 = \sqrt{\frac{E_s}{2}} h_1 s_1 + \sqrt{\frac{E_s}{2}} h_2 s_2 + n_1 , \tag{5.15}$$

$$y_2 = -\sqrt{\frac{E_s}{2}} h_1 s_2^* + \sqrt{\frac{E_s}{2}} h_2 s_1^* + n_2 , \tag{5.16}$$

where, n_1 and n_2 are ZMCSCG with $E[|n_1|^2]= E[|n_2|^2]=N_0$ and $E_s/2$ is the average transmit energy per symbol period per antenna. The received signals can be written in vector form as

$$y = \sqrt{\frac{E_s}{2}} \begin{bmatrix} h_1 & h_2 \\ h_2^* & -h_1^* \end{bmatrix} \begin{bmatrix} s_1 \\ s_2 \end{bmatrix} + \begin{bmatrix} n_1 \\ n_2^* \end{bmatrix}, \tag{5.17}$$

$$= \sqrt{\frac{E_s}{2}} \mathbf{H_{eff}} \mathbf{s} + \mathbf{n} , \tag{5.18}$$

where, $\mathbf{s}=[s_1, s_2]^T$ and $\mathbf{n}=[n_1 ,n_2]^T$. The effective channel matrix $\mathbf{H_{eff}}$ is orthogonal. The decision variable $\mathbf{z}=[z_1, z_2]^T$ corresponding to s_1 and s_2 can be expressed as

$$\mathbf{z} = \mathrm{Re}[\mathbf{H_{eff}} \mathbf{y}] . \tag{5.19}$$

Hence the effective channel for the symbol is

$$\begin{bmatrix} z_1 \\ z_2 \end{bmatrix} = \sqrt{\frac{E_s}{2}} \begin{bmatrix} |h_1|^2 + |h_2|^2 & 0 \\ 0 & |h_1|^2 + |h_2|^2 \end{bmatrix} \begin{bmatrix} s_1 \\ s_2 \end{bmatrix} + \mathrm{Re}[\mathbf{H^H n}] . \tag{5.20}$$

(5.20) shows that optimum two fold diversity gain can be achieved compared to the case of single transmission antenna. The received SNR η per symbol becomes

$$\eta = \frac{\|\mathbf{h}\|_F^2 \rho}{2}, \tag{5.21}$$

where, ρ is the average SNR at the input of receive antenna. Alamouti's scheme extracts diversity order of 2 even in the absence of channel knowledge at the transmitter $E\{\|h\|_F^2\} = 2$, therefore the average SNR at the receiver $\eta=\rho$. Hence absence of channel

knowledge at the transmitter does not allow array gain. The performance of Alamouti's scheme for BPSK modulation is shown in Fig.5.5. The theoretical performance of transmit diversity with increasing number of transmit antennas is shown in Fig.5.6.

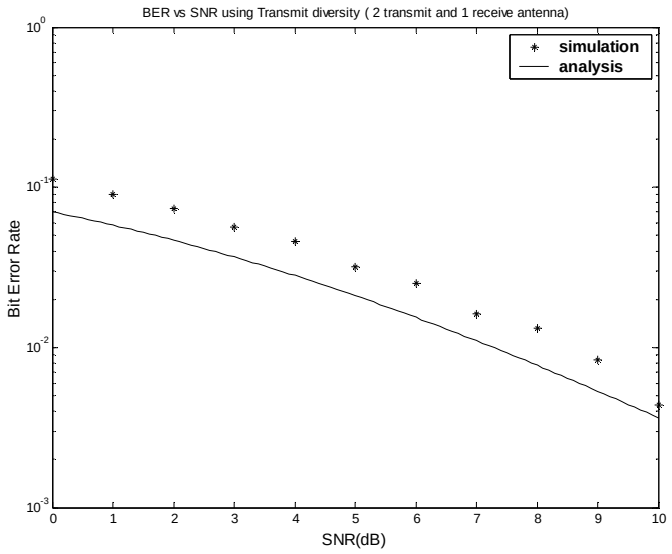

Figure 5.5: Performance of Transmit diversity with 2 TX and 1 RX antenna

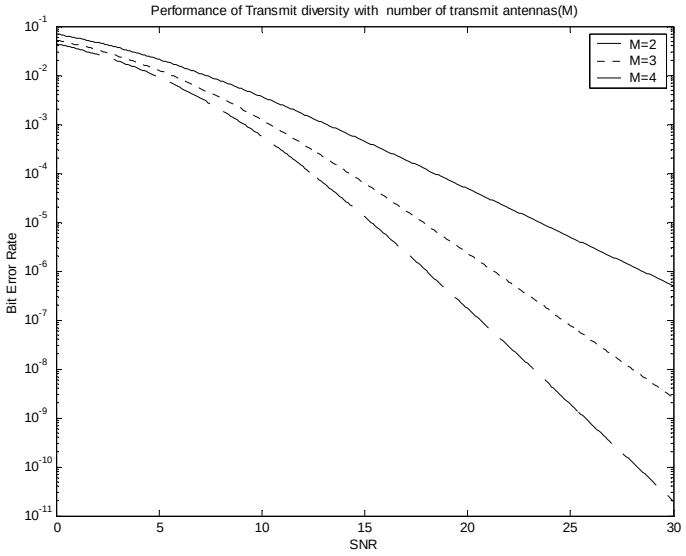

Figure 5.6: Performance of transmit diversity with M TX and 1 RX antenna

The above analysis of transmit diversity assumes perfect knowledge of fading coefficients at the receiver. However the channel estimation is never perfect and noise errors are present in estimation. Next the effect of channel estimation error on the transmit diversity is discussed.

5.6.1 Effect of Imperfect channel estimation on transmit diversity

A number of papers have appeared in the literature discussing the effect of channel estimation error (CER) on the two schemes STD and MRC. Effects of channel estimation errors were first discussed in [161]. Practically, reducing the channel estimation error entails a multitude of techniques. Many of those would require complex processing and a large number of iterations to reduce the channel estimation error. This may become prohibitive for real-time applications such as voice and video in fast-fading situations. The channel estimation error can be reduced by using FrFT filtering as discussed in chapter 4. Before discussing the use of optimum FrFT filtering in reducing CER, the effect of errors on STD and MRC scheme is discussed first.

5.6.2 System Model

A typical STD system with one receive antenna is discussed even though the analysis herein is applicable to an arbitrary number of receive antennas. The transmission is assumed to be BPSK. The channel is assumed to be slow flat faded channel which introduces multiplicative distortion. The transmitting antennas are spaced sufficiently apart so that the received signals are statistically independent. A complex baseband representation of the system as in [143] is used. The data bits to be sent are assumed to be random. As in [143], two signals are simultaneously transmitted from two transmit antennas during two consecutive symbol intervals. Fig.5.7 shows a block diagram of the two-branch Alamouti scheme [143] with one receiver. In first symbol period the signals transmitted from antennas zero and one are denoted by s_0 and s_1, respectively. During the next symbol period, signals $(-s_1^*)$ and s_0^* are transmitted from antennas zero and one, respectively. The multipath channel coefficients between transmit and receive antennas are denoted by h_i (i=0,1). Assuming that the channels remain stationary across at least two consecutive symbols, thus $h_0(t) = h_0(t+T) = \alpha_0 e^{j\theta_0}$ and $h_1(t) = h_1(t+T) = \alpha_1 e^{j\theta_1}$, where T is the duration of a symbol ,α_i (i=1,2) is the magnitude and θ_i (i=1,2) is the phase. Thus multipath channel coefficients change slowly and look like constants to be estimated. The received signals at time t and time t+T at receiving antenna are denoted by r_0 and r_1, respectively and can be expressed as

$$\begin{aligned} r_0 &= h_0 s_0 + h_1 s_1 + n_0 \\ r_1 &= -h_0 s_1^* + h_0 s_0^* + n_1 \end{aligned}, \qquad (5.22)$$

where, n_i (i=0,1) is the AWGN in the i^{th} branch channel with zero mean and variance σ_w^2.

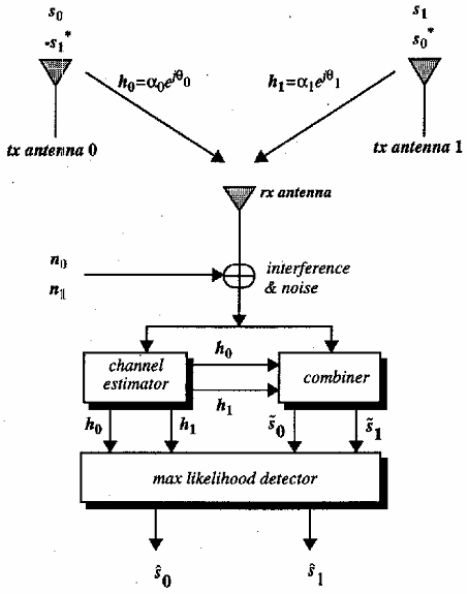

Figure 5.7: Alamouti transmit diversity scheme with one receiver [143]

For BPSK modulation s_i is real and hence $s_i^* = s_i$. Two decision statistics based on the linear combination of the received signals are formed. The decision statistics, denoted by $\tilde{s}_0$ and $\tilde{s}_1$ are given by

$$\begin{aligned} \tilde{s}_0 &= h_0^* r_0 + h_1 r_1^* \\ \tilde{s}_1 &= h_1^* r_0 - h_0 r_1^* \end{aligned} \quad . \tag{5.23}$$

Substituting the values of r_0 and r_1 in above equations

$$\begin{aligned} \tilde{s}_0 &= (\alpha_0^2 + \alpha_1^2)\, s_0 + h_0^* n_0 + h_1 n_1^*, \\ \tilde{s}_1 &= (\alpha_0^2 + \alpha_1^2)\, s_1 - h_0 n_1^* + h_1^* n_0. \end{aligned} \tag{5.24}$$

$\tilde{s}_0$ and $\tilde{s}_1$, the combined signals are sent to the maximum likelihood detector in which for these two signals, decision rules are used to recover the original signal. If $\mathrm{Re}(\tilde{s}_i)>0$, then $s_i=+1$ is chosen otherwise $s_i= -1$ is chosen.

In case of MRC with one transmit and two receive antennas the combined signal is

$$\tilde{s}_{0,\mathrm{MRC}} = h_0^* r_{0,\mathrm{MRC}} + h_1^* r_{1,\mathrm{MRC}} \ , \tag{5.25}$$

where, $r_{i,MRC}=h_i s_0+n_i$, i=0,1. The maximum likelihood decision rule is equivalent to choosing $s_0=1$ if $(\mathrm{Re}(\tilde{s}_{0,\mathrm{MRC}}) > 0)$ and choosing $s_0= -1$ otherwise. The STD scheme yields the same BER as MRC scheme for fixed value of the power radiated per transmit

antenna assuming that the channel gains h_0 and h_1 can be perfectly estimated at the receiver [143].

All the derivations in the above section are under the consideration of perfect channel evaluation, which is composed of channel gain evaluation. But in practice there are many factors that may change the characteristics of channel. Let the channel gains are expressed as

$$\hat{h}_i = h_i + z_i \qquad i = 0,1 \quad , \tag{5.26}$$

where, $z_i = \beta_i e^{j\phi_i}$, represents estimation error. When β_i and ϕ_i are equal to zero at the same time, the channel evaluation becomes perfect and referred to as perfect channel evaluation.

5.6.3 Performance with imperfect channel estimation

The performance of MRC and STD schemes are analyzed by obtaining the BER of these schemes with Gaussian distribution of z. The decision random variable (RV) for the MRC scheme is denoted by $U_{MRC}= \mathrm{Re}(\tilde{s}_{0,MRC})$. For given values of s_0, s_1, h_0, h_1, z_0 and z_1, the combined signal is given by $\tilde{s}_{0,MRC} = (h_0 + z_0)^* r_{0,MRC} + (h_1 + z_1)^* r_{1,MRC}$. The mean and variance of the decision RV can be written as

$$E(U_{MRC}) = [(\alpha_0^2 + \alpha_1^2) + \alpha_0\beta_0 \cos(\theta_0 - \phi_0) + \alpha_1\beta_1 \cos(\theta_1 - \phi_1)]s_0 . \tag{5.27}$$

$$\sigma^2_{U_{MRC}} = [\alpha_0^2 + \beta_0^2 + 2\alpha_0\beta_0 \cos(\theta_0 - \phi_0) + \alpha_1^2 + \beta_1^2 + 2\alpha_1\beta_1 \cos(\theta_1 - \phi_1)]\sigma_w^2 . \tag{5.28}$$

Since U_{MRC} has a Gaussian distribution the BER [74] is

$$P_{e,MRC} = \mathbf{Q}\left(\frac{\xi}{\sigma_{U_{MRC}}}\right), \tag{5.29}$$

where, $$\xi = [(\alpha_0^2 + \alpha_1^2) + \alpha_0\beta_0 \cos(\theta_0 - \phi_0) + \alpha_1\beta_1 \cos(\theta_1 - \phi_1)], \tag{5.30}$$

and $$\boldsymbol{Q}(x) = \frac{1}{\sqrt{2\pi}} \int_x^\infty e^{-\frac{y^2}{2}} dy . \tag{5.31}$$

In STD scheme two bits are transmitted simultaneously. By symmetry the BERs of both the bits are equal, so the BER of only one of the bit say s_0 is considered. The corresponding decision variable is denoted by $U_{STD}= \mathrm{Re}(\tilde{s}_{0,STD})$. For given values of s_0, s_1, h_0, h_1, z_0 and z_1, the combined signal is $\tilde{s}_{0,STD} = (h_0 + z_0)^* r_{0,STD} + (h_1 + z_1)^* r_{1,STD}$. The mean and the variance of the decision RV can be written as

$$E(U_{STD}) = \xi s_0 + b s_1, \tag{5.32}$$

where, $$b = \alpha_1\beta_0 \cos(\theta_1 - \phi_0) - \alpha_0\beta_1 \cos(\theta_0 - \phi_1), \quad (5.33)$$

and ξ is given by (5.30). The variance of U_{STD} is same as the variance $\sigma^2_{U_{MRC}}$ of U_{MRC} as given in (5.28). If the perfect transmission is assumed and the noise is following the Gaussian distribution, then U_{STD} is a linear function of independent Gaussian random variable. As the maximum of E [U_{STD}] and minimum of E [U_{STD}] are considered and selected, the average BER of STD scheme for s_0 can be given as [74]

$$P_{e,STD} = \left[\mathbf{Q}\left(\frac{\xi + b}{\sigma_{U_{STD}}} \right) + \mathbf{Q}\left(\frac{\xi - b}{\sigma_{U_{STD}}} \right) \right]. \quad (5.34)$$

Using the symmetry of **Q**(.) function, $P_{e,STD} > P_{e,MRC}$,i.e STD scheme has a higher BER than MRC scheme if ξ is positive. From (5.32) ξ is positive for $\beta_i < \alpha_i$, i=0, 1. For the present case a Rayleigh fading channel is assumed and channel estimation errors are modelled as samples of complex Gaussian RVs. The variance of real and imaginary components of h_i and z_i are denoted as σ^2_H and σ^2_Z. The signal to noise ratio (SNR) and estimation error to signal ratio (ESR) is defined as $\frac{\sigma^2_H}{\sigma^2_N}$ and $\frac{\sigma^2_Z}{\sigma^2_H}$, respectively. Fig.5.8 shows the BER vs. SNR for ESR=-10dB in case of MRC and STD schemes.Fig.5.8 shows that with channel estimation error the performance of STD is 3 dB poorer than MRC for all values of input power.

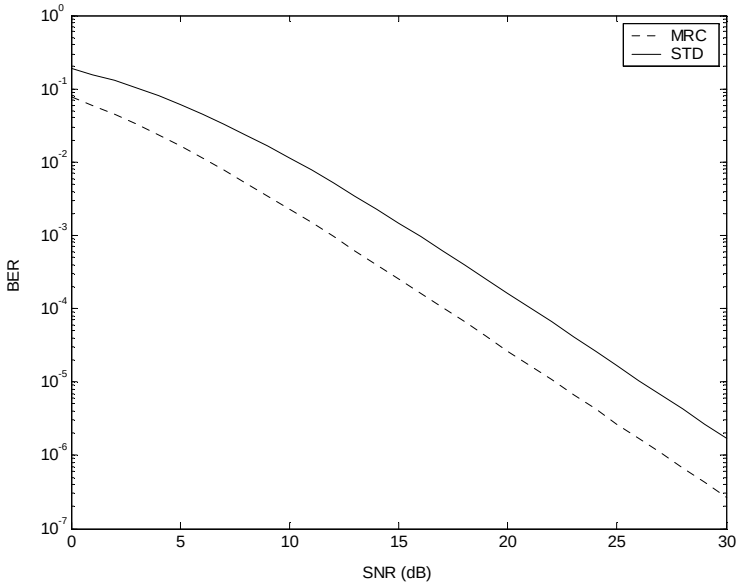

Figure 5.8: BER of MRC and STD scheme against SNR for ESR=-10dB

5.6.4 Reduction in channel estimation error using FrFT based estimation

In this section the reduction of channel estimation error using FrFT is explored. Channel estimation is done using PSAM (Pilot Symbol Assisted Modulation) [83]. Reference [83] provides a detailed description of PSAM method. Specifically the data is formatted into M symbols with first symbol of each frame used for pilot symbol having a known value as shown in Fig.5.9. In this pilot symbols are periodically inserted into the data symbols to estimate the fading. The channel is assumed to be flat fading with AWGN.

P	Data Symbols (M-1) Symbols)	P	Data Symbols (M-1) Symbols)

Figure 5.9: Frame Format, P-Pilot Symbol

The fading channel output is given by

$$r(t)=h(t)\, s(t)+n(t), \tag{5.35}$$

where, n(t) is AWGN with variance $\sigma_w^2 = N_0/2$. h(t) is complex Gaussian multiplicative fading process with variance σ_h^2 and s(t) is the transmitted signal given by

$$s(t) = A \sum_{k=-\infty}^{\infty} b(k)p(t - kT), \tag{5.36}$$

where, T is the symbol duration, b(k) is the k^{th} symbol value for BPSK, A is amplitude factor and p(t) is unit energy pulse. The symbols are formatted into the frames of length M in which pilot symbols at times *i*=kM have a known value $\tilde{b}$. It is better to randomize the pilot values to avoid transmitting tones, but it does not affect the analysis.

No inter-symbol interference is assumed and fading is assumed to be slow enough not to cause appreciable distortion of pulses. After receiving the signal, the first task of the receiver is channel estimation, where the complex fading amplitudes are estimated as prior to de-interleaving and decoding. The classical linear approach to channel estimation is to use a Wiener filter, which minimizes the mean square error (MSE) of the estimates in the presence of noise. The symbol spaced samples r (kT) of the receiver are given by

$$r(k)= h(k)\, b(k)_+ n(k), \quad \text{for } k=0, \ldots, K, \tag{5.37}$$

where, h(k) represents channel fading, b(k) represents data and pilot symbol and n(k) is

AWGN noise sample. K is the total number of nearest pilot symbols. With out loss of generality take b(0) as pilot symbol and consider the detection of b(k), $\lfloor -M/2 \rfloor \le k \lfloor (M-1)/2 \rfloor$. $\lfloor . \rfloor$ means floor symbol. Using K nearest pilot symbols the channel state estimator prepares an estimate of channel gain h(k) given by

$$\hat{h}(k) = \sum_{i=-\lfloor (k-1)/2 \rfloor}^{\lfloor k/2 \rfloor} u^*(i,k) r(iM), \tag{5.38}$$

where, coefficients u(i,k) depend on the position k with in the frame. The optimum estimate that results in coefficient vector **u** is given by

$$\mathbf{u}(k) = \mathbf{R}^{-1}\mathbf{q}(k), \tag{5.39}$$

where, **R** is K×K correlation matrix of vector **r** of the received pilot samples in K nearest pilot symbols. **q** is the K×1 cross correlation vector given by

$$\mathbf{q}(k) = \frac{1}{2} E[h(k)^* \mathbf{r}]. \tag{5.40}$$

The estimated fading coefficient is given by

$$\hat{h}(k) = \mathbf{u}^*(k)\mathbf{r}. \tag{5.41}$$

The mean square estimation error then attains minimum value

$$\sigma_z^2(k) = \sigma_h^2 - \sigma_{\hat{h}}^2. \tag{5.42}$$

The estimation error is uncorrelated with r(iM) and $\hat{h}(k)$. The above analysis shows that the error is introduced by Gaussian noise when obtaining pilot symbols. The estimation error can be reduced by reducing MSE between estimated fading and actual fading coefficients. The MSE can be reduced by estimating the fading coefficients in FrFT domain as discussed in chapter 4. In simulation a known BPSK signal was passed through Rayleigh channel with AWGN. The noise is taken as ZMCSCG with variance one. As discussed in section 3.4 the beamformer of Fig.4.7 is equivalent to an FIR filter also. Hence an FIR filter of order 5 as shown in Fig.3.4 with FrFT processing is used to estimate coefficients in FrFT domain. The MSE was found in optimum FrFT, frequency and time domain. The MSE vs. SNR is shown in Fig.5.10.

As shown in Fig.5.10 the MSE in optimum FrFT domain is found to be less as compared to time or frequency domain estimation. Thus FrFT domain estimation of fading coefficients provides improved estimate of **h**. Fig.5.11 shows the performance of BPSK, in Rayleigh fading channel when estimation error is reduced using FrFT as FrFT can effectively remove the Gaussian noise in a^{th} domain. Reducing estimation error of fading coefficients is equivalent to reducing BER. For a bit error rate of 10^{-2}

the estimation in optimum FrFT domain achieves a gain of 1.2 dB over time domain estimation and about 5.3 dB over frequency domain estimation. The BER vs. SNR for STD scheme for different values of ESR have been plotted in Fig 5.12. It shows that the BER improves quite rapidly with decrease in ESR, which also shows that reduction in estimation error increases the performance of the system. For a BER of 10^{-2} reduction in ESR by 10dB increases the gain of the system by 5.5 dB.

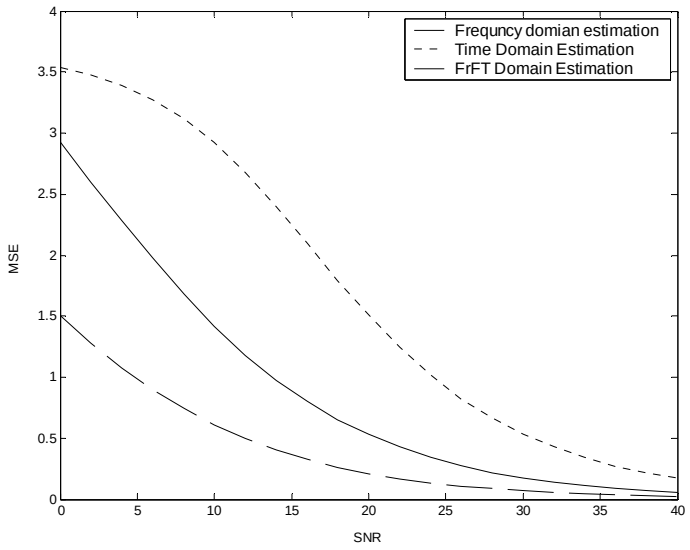

Figure 5.10: MSE vs. SNR for a signal in Rayleigh faded channel

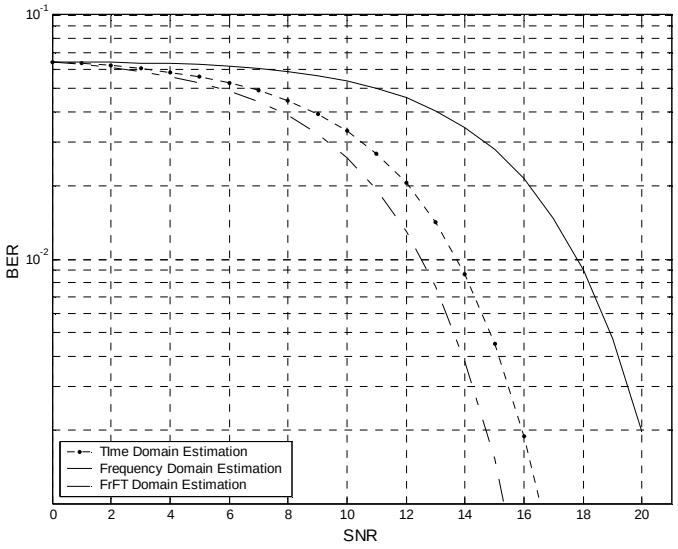

Figure 5.11: Performance of BPSK with different channel estimation techniques

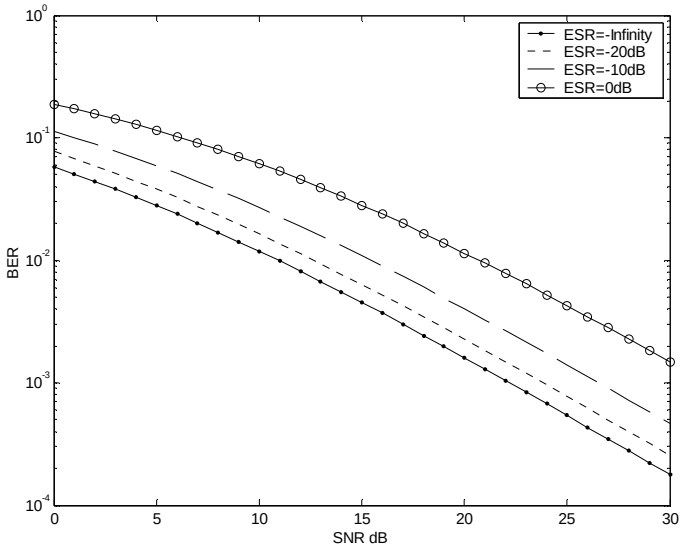

Figure 5.12: BER vs. SNR for STD scheme for different values of ESR

5.7 BEAMFORMING IN MIMO SYSTEMS

In a system with multiple transmit antennas; information can be transmitted by employing various transmission techniques. One way is to transmit a weighted version of the same information symbol from all the antennas. The weights can be adjusted to compensate for the distortion caused by the downlink channel on transmit signals. This method is called *transmit beamforming* and requires the receiver to estimate the downlink channel and feed back this information to the transmitter from time to time [30, 133,137]. However providing a separate feedback link increases the complexity at the receiver. Transmission schemes which do not require downlink channel estimation are usually called as open loop transmit diversity techniques. In these schemes, all antennas transmit simultaneously. As downlink channel information is not available, the total transmit power is distributed equally among all the antennas. Open loop schemes have less complex signaling formats and are easier to implement in practical systems. In this thesis the performance improvement in open loop transmit diversity techniques is considered using receive beamforming. In MIMO systems t*he meaning of the term beamforming, initially used for smart antennas applications, is referred to a* ***linear processing scheme along an arbitrary dimension (not necessarily the spatial dimension)****,* ***becoming then a virtual beamforming*** *[34]*. In this chapter the receive

beamforming at receiver is explored using MMSE criterion. The beamforming in MIMO is of two types single and multiple beamforming discussed next [34].

5.7.1 Single Beamforming (Beam Vector)

Single beamforming for MIMO channels means, a single beam vector at the transmitter and at the receiver is used. The concept of single beamforming is the natural extension of the classical beamforming approach used for smart antennas to the case of MIMO channels. Single beamforming means that a single symbol is transmitted at each transmission through the MIMO channel. Therefore, only one data stream needs to be considered (as opposed to multiple beamforming approach) and coding and transmission can be done in a much easier manner (as in traditional single-antenna systems) [6]. A single beamforming system is shown in Fig.5.13 with M_T transmit and M_R receive antennas.

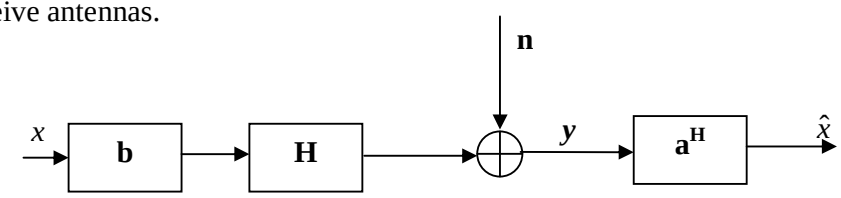

Figure 5.13: Single beamforming

The transmitted vector when using a beamvector **b** of size $M_T \times 1$ at the transmitter is

$$\mathbf{s} = \mathbf{b}x, \tag{5.43}$$

where, x is the scalar data symbol to be transmitted assumed zero-mean and with unit energy E $[|x|^2] = 1$, and the total average transmitted power $P_T = \|\mathbf{b}\|^2$. P_T is power in units of energy per transmission (the power in units of energy per second is $P_s = P_T / T_s$ where T_s is the duration of a transmission). Assuming that the receiver uses a beamvector $\mathbf{a}^H$ of size $1 \times M_R$, the estimated data symbol is

$$\hat{x} = \mathbf{a}^H \mathbf{y} . \tag{5.44}$$

5.7.2 Multiple Beamforming (Beam Matrix)

The concept of single beamforming of (5.43) can be extended to more general case of multiple beamforming at both sides of the link. Multiple beamforming means that $L > 1$ symbols are simultaneously transmitted through the MIMO channel [34]. The multiple beamforming case is shown in Fig.5.14. The transmitted vector **s** uses a transmit linear processing matrix **B** of size $M_T \times L$ and is given by

$$\mathbf{s} = \mathbf{B}x = \sum_{i=1}^{L} \mathbf{b}_i x_i , \tag{5.45}$$

where, $\mathbf{x} = [x_1 \cdots x_L]^T$ is the data vector of size L×1of L data symbols assumed zero-mean, with unit energy, and uncorrelated with $E[\mathbf{x}\mathbf{x}^H] = \mathbf{I}_L$. These data symbols are drawn from a set of constellation is assumed to be $L \le \min(M_T, M_R)$. Vector $\mathbf{b}_i$ is the i^{th} column of matrix **B** and can be regarded as the beamvector associated to the i^{th} data symbol x_i, *i.e.*, multiple beamforming architecture.

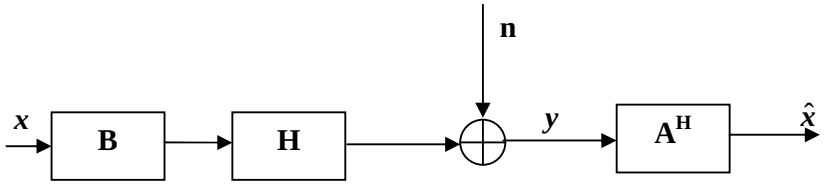

Figure 5.14: Multiple beamforming

The output of the MIMO channel is given by $M_R \times 1$ vector **y** as

$$\mathbf{y}=\mathbf{H}\mathbf{s}+\mathbf{n}\,, \tag{5.46}$$

where, **H** is $M_R \times M_T$ channel matrix. **n** is $M_R \times 1$ ZMCSCG interference-plus-noise vector with covariance matrix $\mathbf{R}_n$. The receiver uses the linear receive processing matrix $\mathbf{A}^H$ of size $L \times M_R$, to estimate the data vector as

$$\hat{\mathbf{x}} = \mathbf{A}^{\mathbf{H}}\mathbf{y}\,. \tag{5.47}$$

The total average transmitted power (in units of energy per transmission) is

$$P_T = E[\|\mathbf{s}\|^2] = \mathrm{tr}[\mathbf{B}\mathbf{B}^H]. \tag{5.48}$$

The single beamforming case can be easily derived from multiple beamforming case. It can be observed that the i^{th} column of **B** and **A**, $\mathbf{b}_i$ and $\mathbf{a}_i$, respectively, can be interpreted as the transmit and receive beam vectors, respectively, associated to the i^{th} transmitted symbol x_i. The estimated symbol at the receiver is given by

$$\hat{x}_i = \mathbf{a}_i^H(\mathbf{H}\mathbf{b}_i x_i + \mathbf{n}_i),\ i=1\ldots\ldots\ldots\ldots L, \tag{5.49}$$

where, $(\mathbf{n}_i = \sum_{j\neq i}\mathbf{H}\mathbf{b}_j x_j + \mathbf{n})$ is the equivalent noise seen by the i^{th} substream, with covariance matrix

$$\mathbf{R}_{ni} = \sum_{j\neq i}\mathbf{H}\mathbf{b}_j\mathbf{b}_j^H\mathbf{H}^H + \mathbf{R}_n\,. \tag{5.50}$$

The optimum receive beam matrix **A** is found using *proposition 1* which is based on derivation of optimal weights using MMSE criterion. Since in this chapter linear processing at receiver is discussed so the optimal beam matrix **A** at receiver is found assuming no processing on transmitter side. This means all transmitted signals from different antennas are equipowered.

5.7.3 Linear processing at receiver only

Proposition 1: Optimum weight matrix using MMSE criterion

To derive the optimal weight matrix consider a MIMO system as shown in Fig.5.15. **s** is the transmitted signal vector of size $M_T \times 1$ with auto-correlation matrix $\mathbf{R}_{ss}$. **H** is a MIMO channel of size $M_R \times M_T$. **y** is the received vector of size $M_R \times 1$ at the input of receiver. **n** is the additive noise vector with autocorrelation matrix $\mathbf{R}_{nn}$. **s** and **n** are statistically independent. **y** is the input to MMSE receiver given by **y**=**Hs**+**n**.

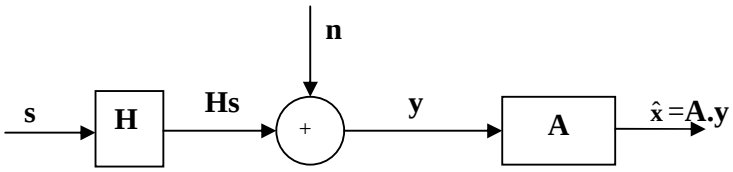

Figure 5.15: MIMO Receiver

The error vector between desired and estimated signal is given by

$$\mathbf{e} = \mathbf{s} - \hat{\mathbf{x}}. \tag{5.51}$$

The mean squared error is given by $$J = E\|\mathbf{e}\|^2 = \mathrm{E}[\mathbf{e}^H\mathbf{e}], \tag{5.52}$$

where, J is called cost function to be minimized.

The optimal weight matrix is given by $\mathbf{A}=\mathbf{R}_{ss}\mathbf{H}^H(\mathbf{H}\mathbf{R}_{ss}\mathbf{H}^H+\mathbf{R}_{nn})^{-1}$. (5.53)

Proof: Let the error autocorrelation matrix is given by

$$\mathbf{R}_{ee}=\mathbf{e}^H\mathbf{e}, \text{ then } I = \text{tr}\,\mathbf{R}_{ee}=\text{tr}\,E[\mathbf{e}^H\mathbf{e}], \tag{5.54}$$

where, tr is trace of error matrix.

$J=\text{tr}E[(\mathbf{s}-\hat{\mathbf{x}})(\mathbf{s}-\hat{\mathbf{x}})^H]=\text{tr}\,E[(\mathbf{s}-\mathbf{A}\mathbf{y})(\mathbf{s}-\mathbf{A}\mathbf{y})^H]=\text{tr}\,E[(\mathbf{s}-\mathbf{A}\mathbf{y})(\mathbf{s}^H-\mathbf{y}^H\mathbf{A}^H)]$,

$=\text{tr}E[\mathbf{s}\mathbf{s}^H-\mathbf{s}\mathbf{y}^H\mathbf{A}^H-\mathbf{A}\mathbf{y}\mathbf{s}^H+\mathbf{A}\mathbf{y}\mathbf{y}^H\mathbf{A}]=\text{tr}(E[\mathbf{s}\mathbf{s}^H]-E[\mathbf{s}\mathbf{y}^H]\mathbf{A}^H-\mathbf{A}E[\mathbf{y}\mathbf{s}^H]+\mathbf{A}E[\mathbf{y}\mathbf{y}^H]\mathbf{A})$. (5.55)

Lemma 1: If Matrix $\mathbf{R}_{yy}$ is Hermitian, positive definite then has Eigen values ≥ 0

Lemma 2: $\text{tr}(\mathbf{C}+\mathbf{D})=\text{tr}\,\mathbf{C}+\text{tr}\,\mathbf{D}$

According to lemma 1, decomposition of $\mathbf{R}_{yy}$ is always possible.Eigenvalue decomposition of $\mathbf{R}_{yy}$ is given by

$$\mathbf{R}_{yy} = \mathbf{U}^H\mathbf{\Lambda}\mathbf{U} = \mathbf{U}^H\mathbf{\Lambda}^{1/2}\mathbf{\Lambda}^{1/2}\mathbf{U} = (\mathbf{\Lambda}^{1/2}\mathbf{U})^H(\mathbf{\Lambda}^{1/2}\mathbf{U}) = \mathbf{U}^H\mathbf{U}. \tag{5.56}$$

U is called square root of $\mathbf{R}_{yy.}$ $\mathbf{\Lambda}=\text{diag}(\lambda_1,\lambda_2,\ldots\ldots\ldots\lambda_{M_R})$, diagonal matrix with eigenvalues of $\mathbf{R}_{yy}$. Substituting the value of Ryy in (5.55).

$$J=\text{tr}(\mathbf{R}_{ss}-\mathbf{R}_{sy}\mathbf{U}^{-1}.\mathbf{U}.\mathbf{A}^H-\mathbf{A}\mathbf{U}^H(\mathbf{U}^H)^{-1}\mathbf{R}_{ys}+\mathbf{A}\mathbf{U}^H\mathbf{U}\mathbf{A}^H), \tag{5.57}$$

$$=\text{tr}(\mathbf{R}_{ss}-\mathbf{R}_{sy}\mathbf{U}^{-1}.(\mathbf{U}^H)^{-1}\mathbf{R}_{ys}+\mathbf{R}_{sy}\mathbf{U}^{-1}.(\mathbf{U}^H)^{-1}\mathbf{R}_{ys}-\mathbf{R}_{sy}\mathbf{U}^{-1}.\mathbf{U}\,\mathbf{A}^H-\mathbf{A}\mathbf{U}^H(\mathbf{U}^H)^{-1}\,\mathbf{R}_{ys}$$
$$+\mathbf{A}\mathbf{U}^H\mathbf{U}\mathbf{A}^H). \tag{5.58}$$

Now $(\mathbf{R}_{sy})^H=\mathbf{R}_{ys}$. Therefore,

$$J=tr(\mathbf{R}_{ss}-\mathbf{R}_{sy}\mathbf{U}^{-1}.(\mathbf{U}^H)^{-1}\mathbf{R}_{ys}+ [\mathbf{A}\mathbf{U}^H-\mathbf{R}_{sy}\mathbf{U}^{-1}][\mathbf{A}\mathbf{U}^H-\mathbf{R}_{sy}\mathbf{U}^{-1}]^H. \quad (5.59)$$

The first two terms of (5.59) are always greater than zero (using lemma 2) and J minimum results when $(tr\ [\mathbf{A}\mathbf{U}^H-\mathbf{R}_{sy}\mathbf{U}^{-1}]) = 0$

$$\mathbf{A}\mathbf{U}^H=\mathbf{R}_{sy}\mathbf{U}^{-1}. \quad (5.60)$$

$$\mathbf{A}=\mathbf{R}_{sy}\mathbf{U}^{-1}(\mathbf{U}^H)^{-1}=\mathbf{R}_{sy}\ (\mathbf{U}^H\mathbf{U})^{-1}\ . \quad (5.61)$$

$$\mathbf{A}= \mathbf{R}_{sy}\mathbf{R}_{yy}^{-1}. \quad (5.62)$$

Now let us find $\mathbf{R}_{yy}$ and $\mathbf{R}_{sy}$:

$$\mathbf{R}_{yy}=E[\mathbf{y}\mathbf{y}^H]=E[(\mathbf{H}\mathbf{s}+\mathbf{n})(\mathbf{H}\mathbf{s}+\mathbf{n})^H] = \mathbf{H}\ E[\mathbf{s}\mathbf{s}^H]\mathbf{H}^H+\mathbf{H}E[\mathbf{s}\mathbf{n}^H]+E[\mathbf{n}\mathbf{s}^H]\mathbf{H}^H+E[\mathbf{n}\mathbf{n}^H]$$

$$= \mathbf{H}\mathbf{R}_{ss}\mathbf{H}^H+\mathbf{H}\mathbf{R}_{sn}+\mathbf{R}_{ns}\mathbf{H}^H+\mathbf{R}_{nn}. \quad (5.63)$$

$$\mathbf{R}_{sn}=E[\mathbf{s}\mathbf{n}^H]. \quad (5.64)$$

$$\mathbf{R}_{sy}=E[\mathbf{s}\mathbf{y}^H]=E[\mathbf{s}(\mathbf{H}\mathbf{s}+\mathbf{n})]=E[\mathbf{s}\mathbf{s}^H]\mathbf{H}^H+E[\mathbf{s}\mathbf{n}^H]= \mathbf{R}_{ss}\mathbf{H}^H+\mathbf{R}_{sn}. \quad (5.65)$$

As **s** and **n** are statistically independent they are uncorrelated and **n** is of zero mean. Thus $\mathbf{R}_{sn}= \mathbf{R}_{ns}=0$. Substituting (5.65) in (5.64) and (5.63)

$$\mathbf{R}_{yy}=\mathbf{H}\mathbf{R}_{ss}\mathbf{H}^H+\mathbf{R}_{nn}. \quad (5.66)$$

$$\mathbf{R}_{sy}=\mathbf{R}_{ss}\mathbf{H}^H. \quad (5.67)$$

Substituting (5.66) and (5.67) in (5.62)

$$\mathbf{A}= \mathbf{R}_{ss}\mathbf{H}^H(\mathbf{H}\mathbf{R}_{ss}\mathbf{H}^H+\mathbf{R}_{nn})^{-1}. \quad (5.68)$$

Knowing **s**, **H** and **n** the optimal weight matrix can be found.

Special case: If $\mathbf{R}_{ss}=E_s\mathbf{I}_M$, and $\mathbf{R}_{nn}=\sigma_w^2\mathbf{I}_N$ then from (5.68)

$$\mathbf{A}= \mathbf{H}^H(\mathbf{H}\mathbf{H}^H+\sigma_w^2\mathbf{I}_N)^{-1}. \quad (5.69)$$

5.7.4 Optimal receive weight vector for joint processing at transmitter and receiver

The error vector using (5.45) and (5.47) is given by $\mathbf{e} = \mathbf{x} - \hat{\mathbf{x}}$.

The MSE is defined as covariance matrix $\mathbf{E}$ of error vector given by $E[\mathbf{e}\mathbf{e}^H]$.

$$\mathbf{E}(\mathbf{A},\mathbf{B}) =\mathbf{R}_{ee}=E[(\mathbf{x}-\hat{\mathbf{x}})(\mathbf{x}-\hat{\mathbf{x}})^H],$$

$$= (\mathbf{A}^H\mathbf{H}\mathbf{B} - \mathbf{I})(\mathbf{B}^H\mathbf{H}^H\mathbf{A} - \mathbf{I})+ \mathbf{A}^H\mathbf{R}_n\mathbf{A},$$

$$=\mathbf{A}^H(\mathbf{H}\mathbf{B}\mathbf{B}^H\mathbf{H}^H + \mathbf{R}_n)\mathbf{A} + \mathbf{I} - \mathbf{A}^H\mathbf{H}\mathbf{B} - \mathbf{B}^H\mathbf{H}^H\mathbf{A}\ .$$

Using proposition 1 the optimum receive beam matrix $\mathbf{A}^*$ *is given by*

$$\boldsymbol{A}^* = (\boldsymbol{H}\boldsymbol{B}\boldsymbol{B}^H\boldsymbol{H}^H + \boldsymbol{R}_n)^{-1}\boldsymbol{H}\boldsymbol{B}, \quad (5.70)$$

$$= \boldsymbol{R}_n^{-1}\boldsymbol{H}\boldsymbol{B}(I + \boldsymbol{B}^H\boldsymbol{H}^H\boldsymbol{R}_n^{-1}\boldsymbol{H}\boldsymbol{B})^{-1}. \quad (5.71)$$

The MSE of the i^{th} substream is given by the i^{th} diagonal element of the covariance error matrix $\mathbf{E}$

$$[\mathbf{E}]_{ii}=\mathbf{a}^H{}_i(\mathbf{H}\mathbf{b}_i\mathbf{b}^H{}_i\mathbf{H}^H + \mathbf{R}_{ni})\mathbf{a}_i + 1-\mathbf{a}^H{}_i\mathbf{H}\mathbf{b}_i - \mathbf{b}^H{}_i\mathbf{H}^H\mathbf{a}_i\,. \tag{5.72}$$

The derivation of the receive beamvectors $\mathbf{a}_i$'s can be independently done for each of the substreams since the choice of the receive beamvector for one substream does not affect the others as can be seen from (5.72). The optimum receive beamvectors are given by

$$\mathbf{a}^*{}_i = (\mathbf{H}\mathbf{b}_i\mathbf{b}^H{}_i\mathbf{H}^H + \mathbf{R}_{ni})^{-1}\,\mathbf{H}\mathbf{b}_i\ . \tag{5.73}$$

Similarly for single beamforming case the optimum beamvector is given by

$$\mathbf{a}^* = (\mathbf{H}\mathbf{b}\mathbf{b}^H\mathbf{H}^H + \mathbf{R}_n)^{-1}\,\mathbf{H}\mathbf{b}. \tag{5.74}$$

The concentrated MSE matrix is obtained by putting (5.71) into (5.72)

$$\begin{aligned}\mathbf{E}(\mathbf{B}) = \mathbf{E}(\mathbf{B},\mathbf{A}^*) &= \mathbf{I} - \mathbf{B}^H\mathbf{H}^H(\mathbf{H}\mathbf{B}\mathbf{B}^H\mathbf{H}^H + \mathbf{R}_n)^{-1}\mathbf{H}\mathbf{B},\\ &= \mathbf{I} - \mathbf{B}^H\mathbf{H}^H\mathbf{R}_n^{-1}\,\mathbf{H}\mathbf{B}(\mathbf{I} + \mathbf{B}^H\mathbf{H}^H\mathbf{R}_n^{-1}\,\mathbf{H}\mathbf{B})^{-1},\\ &= (\mathbf{I} + \mathbf{B}^H\mathbf{H}^H\mathbf{R}_n^{-1}\mathbf{H}\mathbf{B})^{-1}. \end{aligned}\tag{5.75}$$

The matrix inversion lemma has been used to prove the result. The MSE at the i^{th} substream is given by

$$\mathrm{MSE}_i=\frac{1}{1+\mathbf{b}_i^{\mathbf{H}}\mathbf{H}^{\mathbf{H}}\mathbf{R}_{ni}^{-1}\mathbf{H}\mathbf{b}_i}\,. \tag{5.76}$$

Similarly it can be shown that the MSE for the single beamforming case is given by

$$\mathrm{MSE}(\mathbf{b})= \mathrm{MSE}(\mathbf{b}, \mathbf{a}^*)=1/(1 + \mathbf{b}^{\mathrm{H}}\mathbf{H}^{\mathrm{H}}\mathbf{R}_n^{-1}\,\mathbf{H}\mathbf{b}). \tag{5.77}$$

5.7.5 Measure of quality of receive beamforming

The quality of communication system depends upon various measures like SINR, BER and MSE. These measures are defined below for joint beamforming at transmitter and receiver, but they are applicable to receive only beamforming also as discussed in section 3.10.

5.7.5.1 SINR

The SINR of i^{th} established stream or link in case of multiple beamforming is given by

$$\mathrm{SINR}(\mathbf{B},\mathbf{a_i})= \frac{\left|\mathbf{a}_i^{\mathrm{H}}\mathbf{H}\,\mathbf{b}_i\right|^2}{\mathbf{a}_i^{\mathrm{H}}\mathbf{R}_{ni}\mathbf{a}_i} = \frac{\mathbf{a}_i^{\mathrm{H}}(\mathbf{H}\mathbf{b}_i\mathbf{b}_i^{\mathrm{H}}\mathbf{H}^{\mathrm{H}})\mathbf{a}_i}{\mathbf{a}_i^{\mathrm{H}}\mathbf{R}_{ni}\mathbf{a}_i}\,. \tag{5.78}$$

The optimum receive beamvector that maximizes the SINR is given by

$$\mathbf{a}_i^{*} = \alpha_i\ \mathbf{R}_{ni}^{-1}\ \mathbf{H}\mathbf{b}_i. \tag{5.79}$$

where α_i is an arbitrary scaling factor that does not affect the SINR. Alternatively, the SINR in (5.78) can be upper-bounded as

$$\text{SINR}=\frac{\left|\mathbf{a}_i^{\text{H}}\mathbf{H}\,\mathbf{b}_i\right|^2}{\mathbf{a}_i^{\text{H}}\mathbf{R}_{ni}\mathbf{a}_i}\le \mathbf{b}_i^{\text{H}}\mathbf{H}^{\text{H}}\mathbf{R}_{ni}^{-1}\mathbf{H}\mathbf{b}_i\,, \tag{5.80}$$

simply by using Cauchy-Schwarz's inequality with vectors($\mathbf{R}_{ni}^{-1/2}\mathbf{H}\mathbf{b}_i$)and($\mathbf{R}_{ni}^{1/2}\mathbf{a}_i$) :

$$|(\mathbf{a}_i^{H}\mathbf{R}_{ni}^{1/2}\,)\,(\mathbf{R}_{ni}^{-1/2}\mathbf{H}\mathbf{b}_i)|^2\le(\mathbf{a}_i^{H}\mathbf{R}_{ni}\mathbf{a}_i^{H})\,(\mathbf{b}_i^{H}\mathbf{H}^{H}\mathbf{R}_{ni}^{-1}\,\mathbf{H}\mathbf{b}_i). \tag{5.81}$$

The upper bound in (5.80) is achieved when $\mathbf{R}_{ni}^{1/2}\,\mathbf{a}_i \propto \mathbf{R}_{ni}^{1/2}\mathbf{H}\mathbf{b}_i$ or, equivalently, by (5.79). It is important to remark that (5.79) is identical to (5.73) up to a scaling factor, *i.e.*, the Wiener filter is also optimal in terms of maximizing the SINR. Using the optimal receive beamvector (5.79), the SINR in (5.78) reduces to

$$\text{SINR}_i\,(\mathbf{B}) = \text{SINR}_i\,(\mathbf{B},\,\mathbf{a}_i^{*}\,) = \mathbf{b}_i^{\text{H}}\,\mathbf{H}^{H}\mathbf{R}_{ni}^{-1}\,\mathbf{H}\mathbf{b}_i. \tag{5.82}$$

Comparing now (5.82) with (5.76), it is clear that the SINR and the MSE are related by

$$\text{SINR}_i=\frac{1}{\text{MSE}_i}-1. \tag{5.83}$$

Note that the SINR in (5.83) is a convex decreasing function of the MSE (clearly, minimizing the MSE is tantamount to maximizing the SINR).

5.7.5.2 Optimum Receive Beamformer in Terms of BER

The performance of a digital communication system is given in terms of symbol error probability or BER. Assuming that the interference-plus-noise component is Gaussian distributed, the symbol error probability P_e can be analytically expressed as a function of the SINR.

$$\text{P}_\text{e} = \alpha\boldsymbol{Q}(\sqrt{\beta(\text{SINR})}\,, \tag{5.84}$$

where, α and β are constants that depend on the signal constellation and **Q**(.) is the **Q** function defined as

$$\mathbf{Q}(\text{x})=\frac{1}{2\pi}\int_{\text{x}}^{\infty}\text{e}^{-\frac{\lambda^2}{2}}\text{d}\lambda\,. \tag{5.85}$$

To design a system directly in terms of BER, its relationship with SINR and MSE has to be found. Both the exact BER function and the Chernoff upper bound are convex decreasing functions of the SINR as proved in Appendix E. Since the BER is decreasing in the SINR, it follows that the Wiener filter minimizes the BER. Using (5.83) in (5.84), the error probability can be alternatively expressed as a function of the MSE

$$\text{P}_\text{e} = \alpha\boldsymbol{Q}(\sqrt{\beta(\text{MSE}^{-1}-1)}\,. \tag{5.86}$$

Both the exact BER function and the Chernoff upper bound happen to be convex increasing functions of the MSE for sufficiently small values of the argument (for BPSK and QPSK constellations, this is true for any value of the argument) [74]. Since the BER is increasing in the MSE, minimizing the BER is tantamount to minimizing the MSE and it then follows that the Wiener filter minimizes the BER (in the multiple beamforming case, the BER of each substream depends only on its corresponding MSE). The lower the BER the better the system, since it means that less error are made when estimating the transmitted bits. It has been shown in the above that the wiener criteria based beamformer is optimal linear receive beamformer in the sense that each of the MSE's is minimized, each of the SINR's is maximized and each of the BER's is minimized. *Hence, any reasonable system has to be designed to have a low MSE. One such beamformer is FrFT beamformer described in chapter 4.The FrFT beamformer can decrease MSE further in a^{th} order fractional domain, can improve SINR and reduce BER.*

5.7.6 Optimum Receive Beamformer in FrFT Domain [104]

The optimal single beamformer in fractional Fourier domain is derived first. The signal observation model is given by

$$\mathbf{y}=\mathbf{H_d}\,\boldsymbol{x}+\mathbf{n}, \tag{5.87}$$

where, $\mathbf{y}, \boldsymbol{x}, \mathbf{n}$ are column vectors with M_R elements and $\mathbf{H_d}$ is an $M_R \times M_R$ matrix. It is assumed that input and output processes and noise are finite length random processes and that the correlation matrix of the input random process ($\mathbf{R}_{xx}$) and noise ($\mathbf{R}_{nn}$) are known. It is further assumed that the noise $\mathbf{n}$ is independent of the input process $\mathbf{x}$ and is zero mean. If the linear estimate is expressed in the form $\hat{\mathbf{x}} = \mathbf{Hy}$ then the optimal general linear estimator of $\mathbf{H}$ minimizing the mean square error between the actual signal $\mathbf{x}$ and estimated signal $\hat{\mathbf{x}}$ can be shown to satisfy $\mathbf{R}_{yx}=\mathbf{H}\,\mathbf{R}_{yy}$.

$$\sigma_e^2 = \frac{1}{M_R}\mathrm{E}[(x-\hat{x})^{\mathrm{H}}(x-\hat{x})], \tag{5.88}$$

In this chapter a class of linear estimators is considered which correspond to filtering in single fractional Fourier domain and the estimate can be expressed as

$$\hat{\boldsymbol{x}} = \boldsymbol{F}^{-a}\boldsymbol{\Lambda}_{\tilde{h}}\boldsymbol{F}^{a}\boldsymbol{y}, \tag{5.89}$$

where, $\mathbf{F}^{-a}$ and $\mathbf{F}^{a}$ are discrete fractional Fourier transform matrices of order –a and a, respectively, and $\boldsymbol{\Lambda}_{\tilde{h}}$ is a diagonal matrix whose diagonal consists of the elements of

the vector $\tilde{\boldsymbol{h}}$. This estimate corresponds to a multiplicative filter in the a[th] fractional Fourier domain. Since the fractional Fourier transformation is a unitary transformation, the MSE can be defined in a[th] domain also,

$$\sigma_e^2 = \frac{1}{M_R} E[(x_a - \hat{x}_a)^H (x_a - \hat{x}_a)], \tag{5.90}$$

where, $\boldsymbol{x}_a = \mathbf{F}^a \boldsymbol{x}$ and $\hat{\boldsymbol{x}}_a = \boldsymbol{\Lambda}_{\tilde{h}} \boldsymbol{F}^a \boldsymbol{y} = \boldsymbol{\Lambda}_{\tilde{h}} \boldsymbol{y}_a$. Assume 'a' is fixed then problem is to minimize σ_e^2 with respect to complex vector $\tilde{\boldsymbol{h}}$, then the σ_e^2 can be written as

$$\sigma_e^2 = \frac{1}{M_R} E\left[\sum_{l=1}^{N} \left| x_{al} - h_l y_{al} \right|^2\right], \tag{5.91}$$

where, x_{al}, y_{al} and $\tilde{h}_l = \tilde{h}_{lr} + \tilde{h}_{li}$ are the elements of vectors $\mathbf{x}_a$,$\mathbf{y}_a$ and $\tilde{\boldsymbol{h}}$. Equating the partial derivatives of σ_e^2 with respect to $\tilde{h}_{lr}$ *and* $\tilde{h}_{li}$, the optimal filter vector is given by

$$\tilde{h}_{opt,l} = \frac{E[x_{al} y_{al}^*]}{E[|y_{al}|^2]} \qquad l=1,2,\ldots\ldots M_R. \tag{5.92}$$

The numerator is simply the $(l,l)^{th}$ element of $\mathbf{R}_{x_a y_a}$ and the denominator is the $(l,l)^{th}$ element of $\mathbf{R}_{y_a y_a}$, where the correlation matrices $\mathbf{R}_{x_a y_a}$ and $\mathbf{R}_{y_a y_a}$ can be obtained from the input and noise correlation matrices as

$$\boldsymbol{R}_{x_a y_a} = \boldsymbol{F}^a (\boldsymbol{R}_{xx} \boldsymbol{H}^H) \boldsymbol{F}^{-a} \tag{5.93}$$

$$\mathbf{R}_{y_a y_a} = \mathbf{F}^a (\mathbf{H} \mathbf{R}_{xx} \mathbf{H}^H + \mathbf{R}_{nn}) \mathbf{F}^{-a}. \tag{5.94}$$

(5.93) and (5.94) provide the solution to our minimization problem in the discrete time setting and can be compared with (5.73) and (5.74) the solution obtained for optimum receive beamvectors for multiple and single beamforming cases respectively. In multiple beamforming case the MSE of each substream has to be minimized in a[th] order fractional Fourier domain. For a given transmit beam vector, the receive beamvector for the i^{th} stream can be further optimized using FrFT domain receive beamforming. This optimal receive beamformer will further reduce the MSE in the a[th] domain as compared to time or frequency domain. Reducing the MSE is equivalent to increasing SINR and decreasing BER. Thus any properly designed system based on FrFT domain beamformer should attempt to minimize the MSEs, maximize the SINRs and minimize the BERs. One such system proposed is Optimal FrFT based MIMO Receive Beamformer (OFMRB). The proposed OFMRB can be put at the front end of the

MIMO receiver with each receiving antenna as shown in Fig.5.16. The performance of optimal MIMO receive beamformer is studied next using suitable examples.

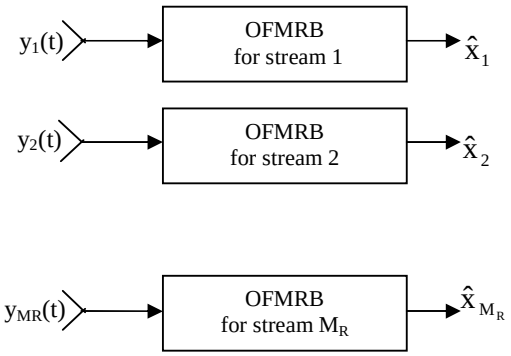

Figure 5.16: Proposed Optimal FrFT based MIMO Receive Beamformer

5.7.7 Numerical Example

In the following example two MIMO systems 2×2 and 4×4 have been simulated with OFMRB. The modulation is assumed to be BPSK. The channel is assumed to be Rayleigh faded. The fading is assumed to be slow such that the value of fading does not change during transmission of during one complete symbol period. The channel is completely known at the receiver. The channel does not have temporal inter-symbol interference. The fading from any transmit antenna to receive antenna is also assumed to be independent. In the proposed scheme instead of feeding the signal directly to matched filter decoder the signal is first fed to OFMRB. Each receiving antenna has an OFMRB at the front end. The receive beamformer estimates the received signal in optimum domain with reduced MSE. The transmitter and proposed OFMRB are shown in Fig.5.17 (a) and Fig.5.17 (b).The transmitted signals from different antennas are equipowered. The signal form the k^{th} antenna can be given as

$$s_k(t) = \sqrt{\frac{2P}{K^2}} b_k(t) \cos(2\pi f_c t) \qquad 1 \le k \le K, \tag{5.95}$$

where, P represent total transmitted power. $b_k(t)$ represent input data bits from k^{th} antenna. f_c is the carrier frequency. The transmitting and receiving antennas are assumed to be linear arrays with spacing d between them so that received and transmitted signals are uncorrelated. The receiver is assumed to be stationary. Each receiving antenna with OFMRB at its front end gives the optimum output with weights ***w*** calculated in FrFT domain.

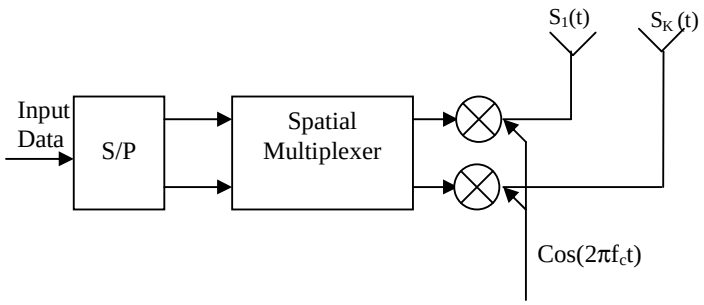

Figure 5.17(a): Transmitter

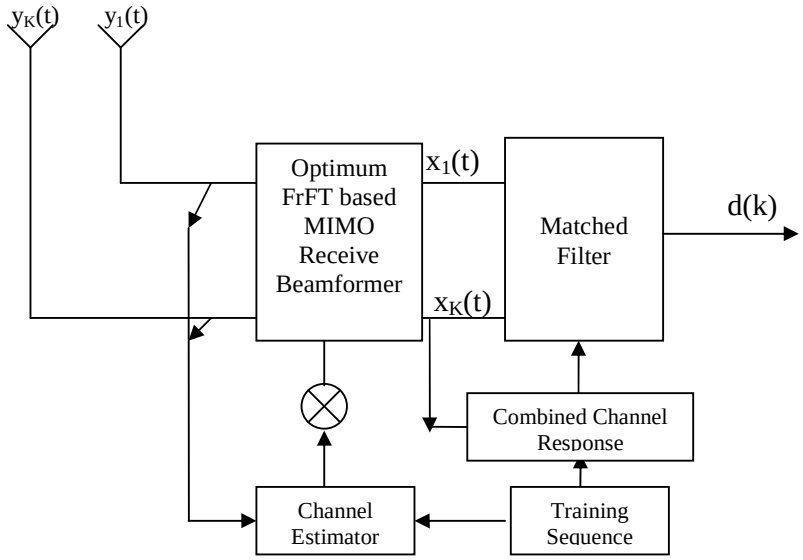

Figure 5.17 (b): Optimal FrFT based MIMO Receive Beamformer

Consider 4 × 4 spatial multiplexed MIMO system. The input to the first OFMRB is

$$y_1(t)=h_{11}s_1(t)+ h_{21}s_2(t)+ h_{31}s_3(t)+ h_{41}s_4(t)+\mathbf{n}, \quad (5.96)$$

where, **n** is ZMCSCG vector with equal variance. The first OFMRB knows the channel response $h_{11.}$ Receiver treats all other signals except $s_1(t)$ as interference. The output signal of OFMRB can be expressed as

$$x_1(t) = \boldsymbol{w}_1^{H}\, \mathbf{y}_1(t), \quad (5.97)$$

where, $\boldsymbol{w}_1$ are the weights obtained in FrFT domain. In general the k^{th} output signal can be expressed as

$$x_k(t) = \boldsymbol{w}_k^{\mathbf{H}}\, \mathbf{y}_k(t), \qquad 1 \le k \le K \quad (5.98)$$

where, $\mathbf{y}_k(t)$ is the k^{th} input vector and $\boldsymbol{w}_k=[w_1,w_2\ldots\ldots\ldots\ldots w_K]$ is the optimum weight vector for the k^{th} OFMRB calculated in optimum FrFT domain. These optimum

weights are calculated in each symbol period. The matched filter recovers the transmitted sequence from the optimum estimated signal with minimized inter-stream interference and noise. The theoretical BER can be calculated using (5.84).

5.7.8 Monte Carlo simulation of spatial multiplexed system

In this work the performance of the proposed OFMRB is evaluated in terms of BER and BLER using Monte Carlo simulations. The channel is modelled as flat Rayleigh faded, and coefficients of channel are modelled as i.i.d (independent identically distributed) ZMCSG RVs with variance 0.5 in each dimension i.e. $h_{i,j} \sim \mathcal{CM}(0,1)$. The modulation is assumed to be BPSK and in case of BPSK, SEP reduces to BER. For the BER of BPSK a block consisting of 100 bits is sent from each transmitter with all the bits having random values ±1. The results below have been obtained from 10000 independent runs of such blocks. The noise is considered as white with zero mean and variance one. The total MSE in all runs vs. SNR curve for OFMRB is shown in Fig.5.18. The performance is shown in Fig.5.19 and 5.20 for 2×2 and 4×4 spatial multiplexed systems.

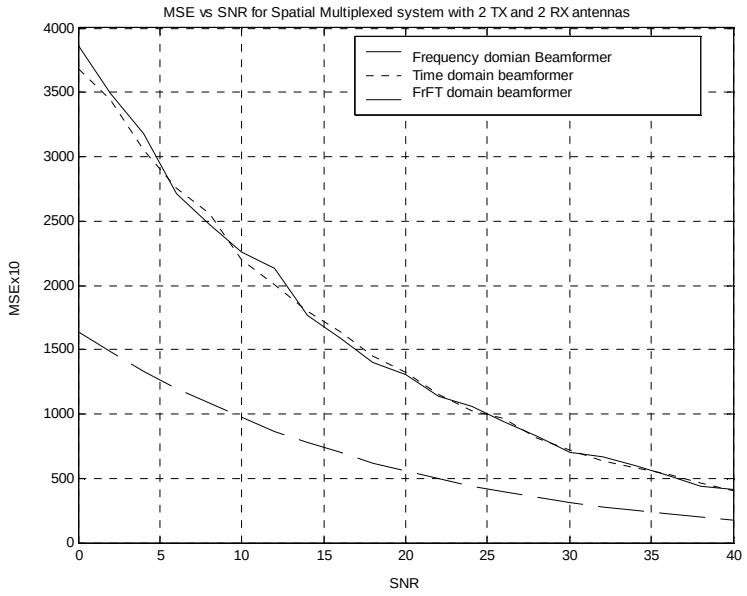

Figure 5.18: MSE Vs. SNR for OFMRB

Fig.5.18 is plotted for a stationary source. It is shown that OFMRB's MSE is less as compared to time or frequency based receive beamformers for all values of SNR, especially at low SNRs. The MSE in three domains is given in table 5.1.

Table-5.1: MSE in case of various receivers in MIMO (SNR=10 dB)

Receiver	SUM of MSEs in all runs
Time based MMSE receiver	22000
Frequency based MMSE receiver	22600
OFMRB	10000

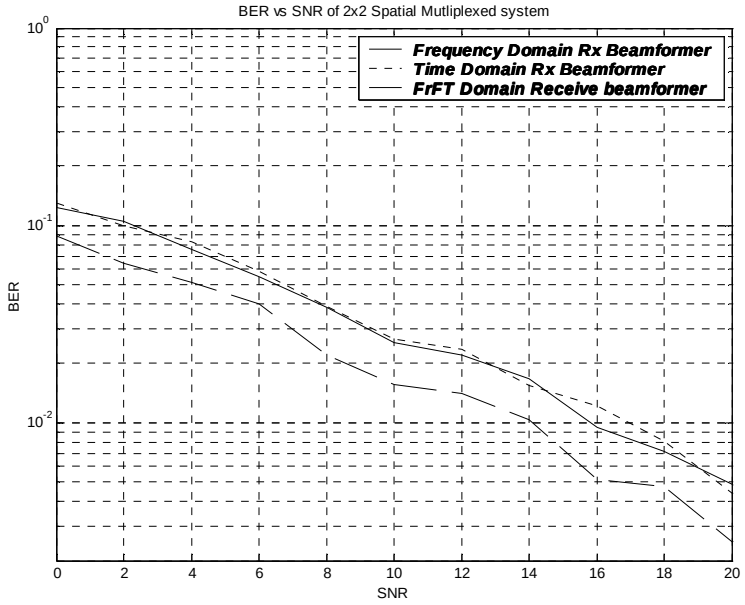

Figure 5.19: Comparison of BER of OFMRB with other MMSE receivers for 2×2 spatial multiplexed MIMO system

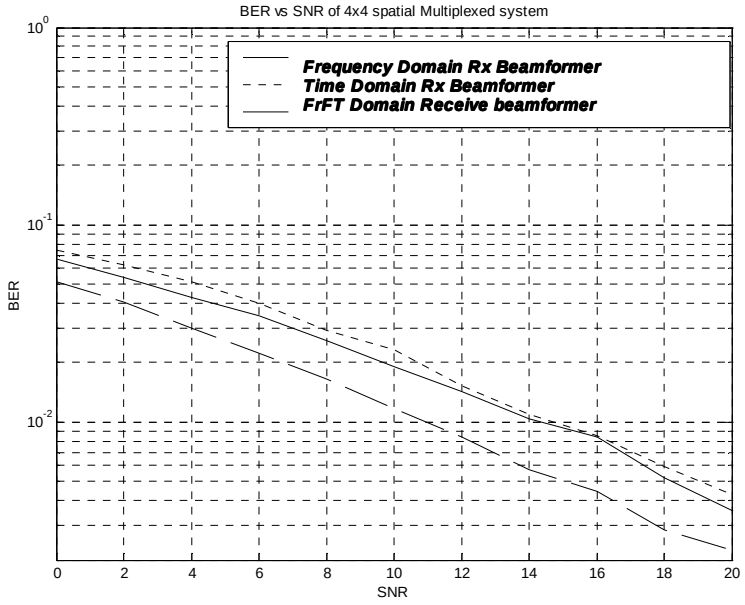

Figure 5.20: Comparison of BER of OFMRB with other MMSE receivers for 4×4 spatial multiplexed MIMO system

It is observed from Fig.5.19 and Fig.5.20 that the proposed OFMRB performs better than a time or frequency domain MMSE receive beamformers. In case of 2×2 MIMO systems for achieving a BER $\leq 10^{-2}$, the proposed OFMRB requires 2.9 dB and 1.7 dB less input signal power as compared to time domain and frequency domain MMSE receive beamformers respectively. Also in the case of 4×4 MIMO system the proposed OFMRB requires 2.7 dB and 2.3 dB less power as compared to time domain and frequency domain receive MMSE beamformers mainly due to effective removal of Gaussian noise and interference. If the transmission is in form of blocks of L_B bits, then the block error rate (BLER) is defined as

$$P_{BLER} = 1 - (1 - BER)^{L_B}, \tag{5.127}$$

where, L_B is block length. The block error rate for 2×2 and 4×4 SM MIMO systems is shown in Figs. 5.21 and 5.22. It can be observed from Fig.5.21 and 5.22 that OFMRB provides a gain of 2.6 dB and 2.9 dB over time and frequency domain MMSE receive beamformers respectively at 10% BLER in 2×2 MIMO system, while it provides a gain of 4.1dB and 3.4 dB over time and frequency domain MMSE receive beamformer respectively at 10% BLER in 4×4 MIMO systems.

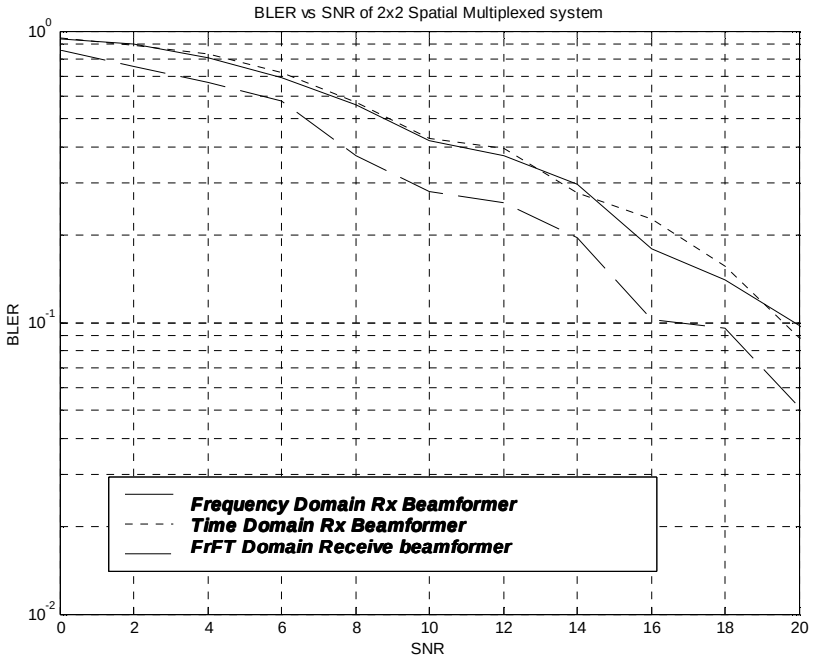

Figure 5.21: Comparison of BLER of OFMRB with simple MMSE receiver for 2×2 spatial multiplexed MIMO system

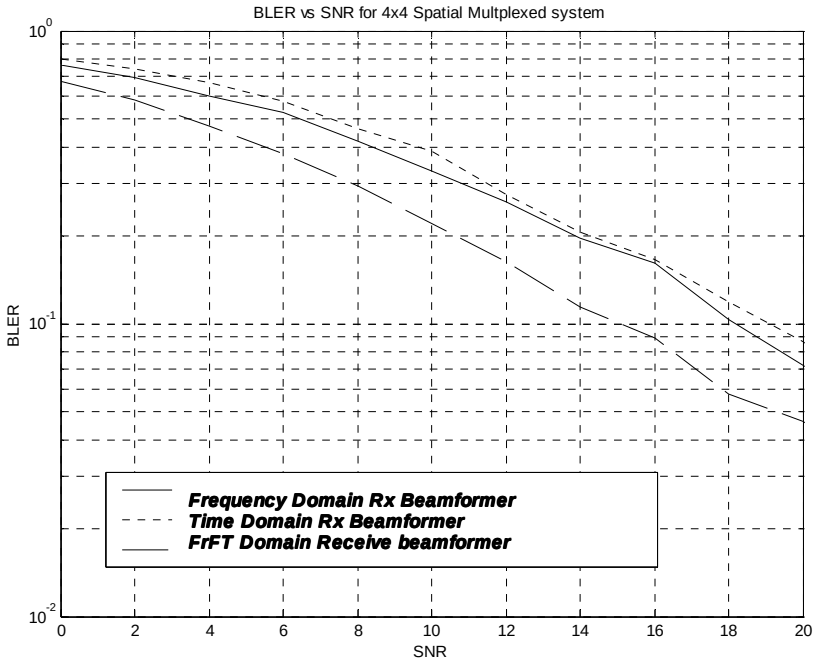

Figure 5.22: Comparison of BLER of OFMRB with simple MMSE receiver for 4×4 spatial multiplexed MIMO system

5.8 Rate One Alamouti's Scheme with OFMRB

In Alamouti's rate one orthogonal space time block coded system (OSTBC), explained in section 5.6 with perfect channel knowledge at the receiver, the scalar detection techniques are used for detecting the transmitted signal. In this thesis it is proposed to use OFMRB with OSTBC Alamouti's scheme also. The OFMRB can be put at the front end of each receiving antenna of OSTBC system as proposed for spatial multiplexed system shown in Fig.5.16. The proposed structure of transmitter and receiver of OSTBC with MMSE receive beamformer is shown in Fig.5.23 and 5.24. The transmitter has only two antennas, while receiver can has one or more antennas.

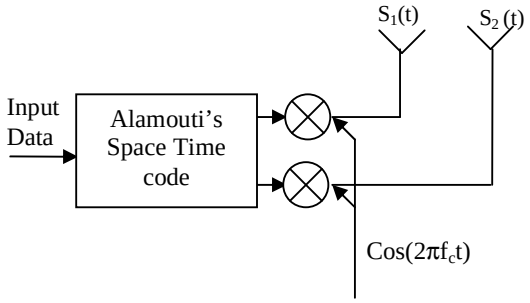

Figure 5.23: Rate 1 Transmission using Alamouti's scheme

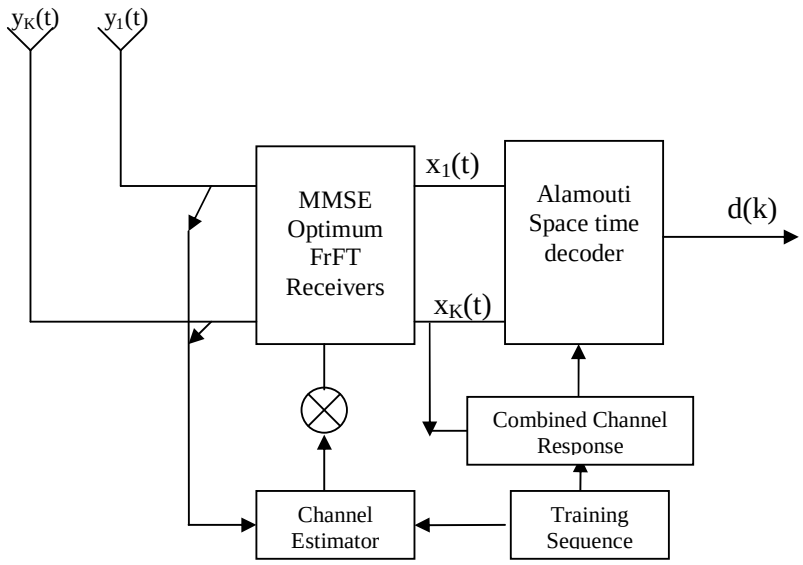

Figure 5.24: Proposed receive beamforming scheme for space time coded system

To emphasize the advantage of using OFMRB with OSTBC, firstly the performance of a simple MMSE receiver is compared with scalar detector used in Alamouti's scheme with the help of a simulation example. In this example BPSK modulation was used. The noise was taken as ZMCSCG with equal variance one. The SNR is varied from 0 to 20 dB. The channel is modelled as flat Rayleigh faded, and coefficients of channel are modelled as independent identically distributed (i.i.d) ZMCSG RVs with variance 0.5 in each dimension i.e. $h_{i,j} \sim \mathcal{CN}(0,1)$. 20000 of symbol pairs were transmitted with rate one scheme and received symbols ware detected with both ML detector and MMSE receiver. The bit error rate of OSTBC system, for both scalar as well as MMSE receiving scheme with different number of receive diversity branches is plotted in Fig.5.25. The performance with QPSK transmission is also shown in Fig.5.26. It can be observed form figures 5.25 and 5.26 that the BER performance of rate one OSTBC system with a simple MMSE receiver is comparable to that of ML receiver. Hence the OFMRB proposed for spatial multiplexed systems can be used with OSTBC system also. Moreover the OFMRB can also be used to cancel co-channel interference in MIMO systems. The MSE vs. SNR performance of OSTBC system with OFRMB is shown in Fig. 5.27. It is again shown in Fig. 5.27 that MSE in optimum FrFT domain is always less as compared to time and frequency domain. The performance of the proposed OFMRB scheme for 2×1 and 2×2 rate 1

OSTBC systems using BPSK modulation is shown in figures 5.28-29 with the same simulation parameters as for SM systems.

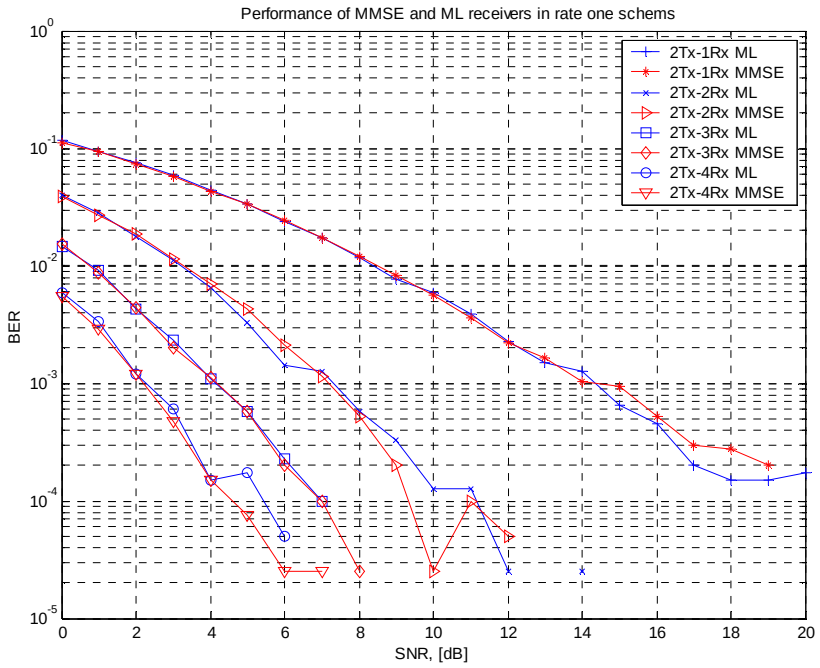

Figure 5.25 Performance of rate one OSTBC scheme with ML and MMSE receivers with BPSK Modulation

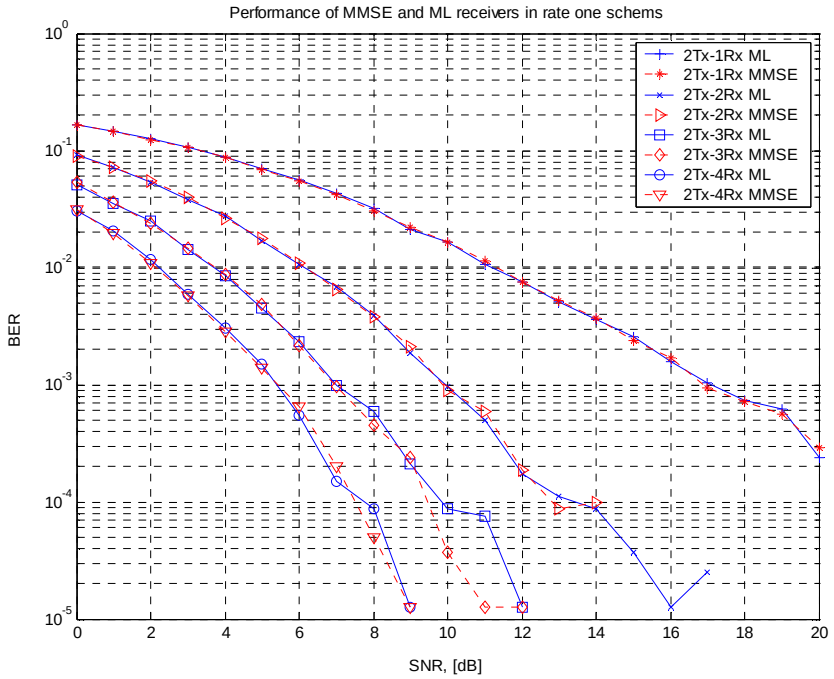

Figure 5.26 Performance of rate one OSTBC scheme with ML and MMSE receivers with QPSK Modulation

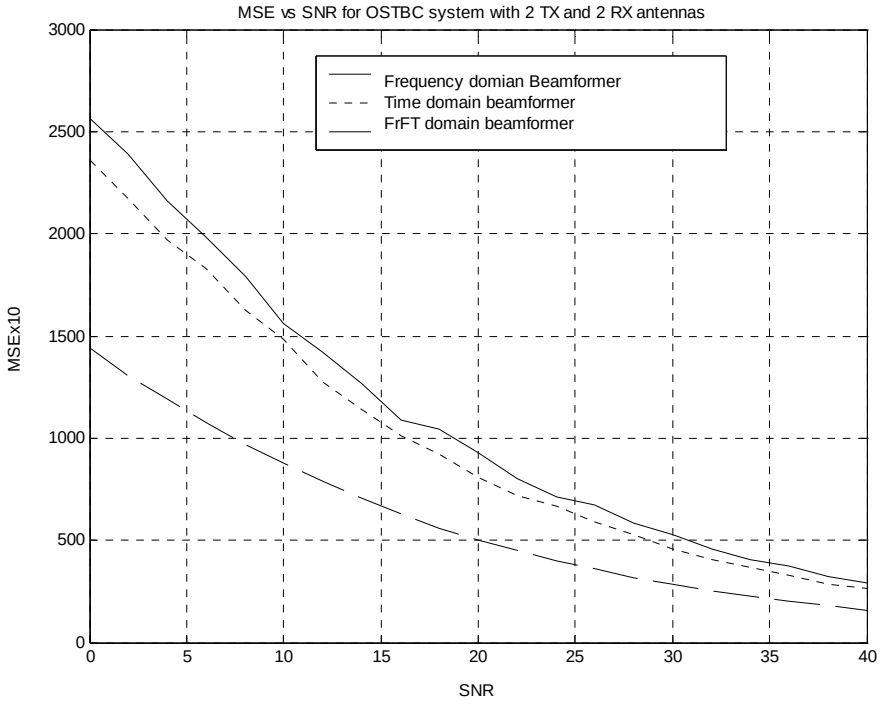

Figure 5.27 MSE vs. SNR for rate one OSTBC system with 2 TX and 2 RX Antennas

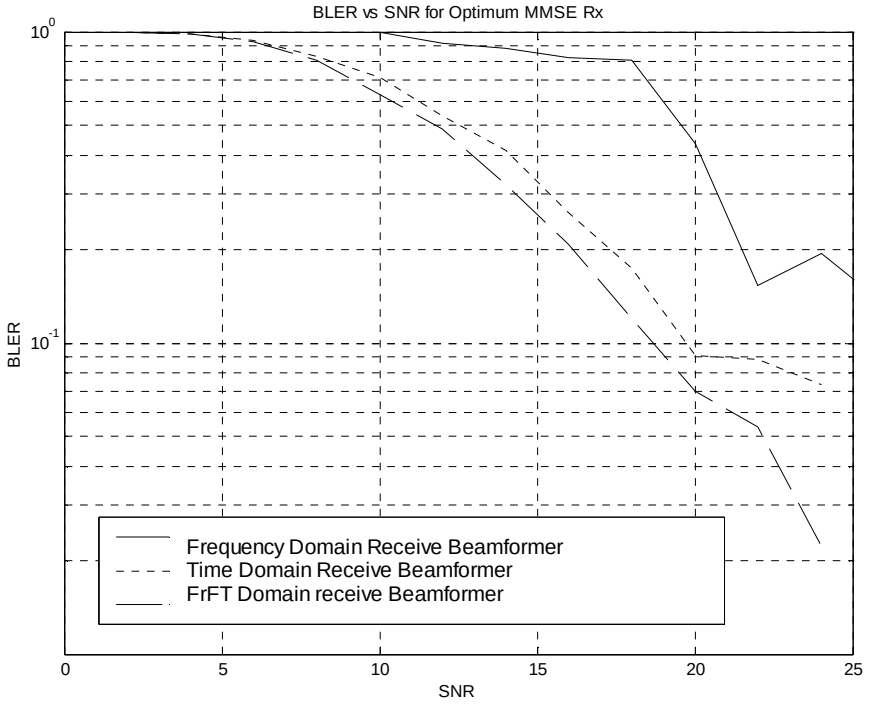

Figure 5.28-Performance of a 2×1 system using OSTBC and BPSK modulation

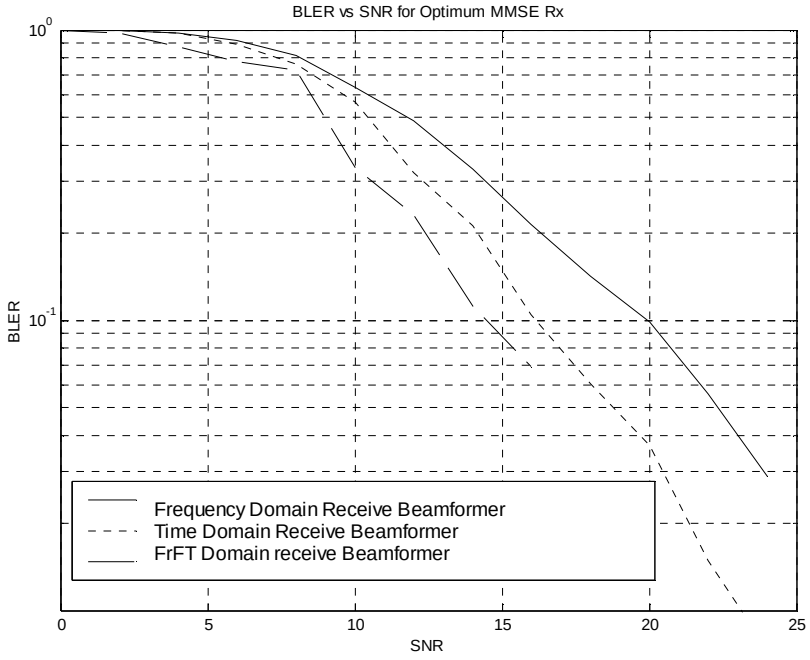

Figure 5.29-Performance of a 2×2 system using OSTBC and BPSK modulation

From Figures 5.28 and 5.29 it is clear that OFMRB outperforms both time domain and frequency domain beamformers in case of virtual receive beamforming. For 2 × 1 OSTBC system the OFMRB provides a gain of 1 dB over time domain beamformer for a BLER ≤10%.In case of 2×2 OSTBC system the gain provided by OFMRB over time and frequency domain beamformer is 1.7 dB and 5.5 dB for a BLER ≤10%.

The MSE with OFMRB is found to be less as compared to time or frequency domain for both spatial multiplexed as well as rate one OSTBC system as shown in Fig.5.18 and 5.27. The BER Vs MSE performance of 2 × 2 spatial multiplexed is shown in Fig. 5.30. It can be observed from Fig. 5.30 that FrFT domain receive beamformer BER is always less than time or frequency domain beamformer for any value of MSE. Thus linear receive processing with OFMRB can be extended to convex optimization theory applied to joint transmitter and receiver design in MIMO channels as proposed in [34]. As stated in [34] most engineering problems are not convex when directly formulated and many of them have hidden convexity to be able to use convex optimization theory. Thus OFMRB helps us to reformulate any original non-convex problem to convex form as it reduces MSE further as compared to time or frequency domain.

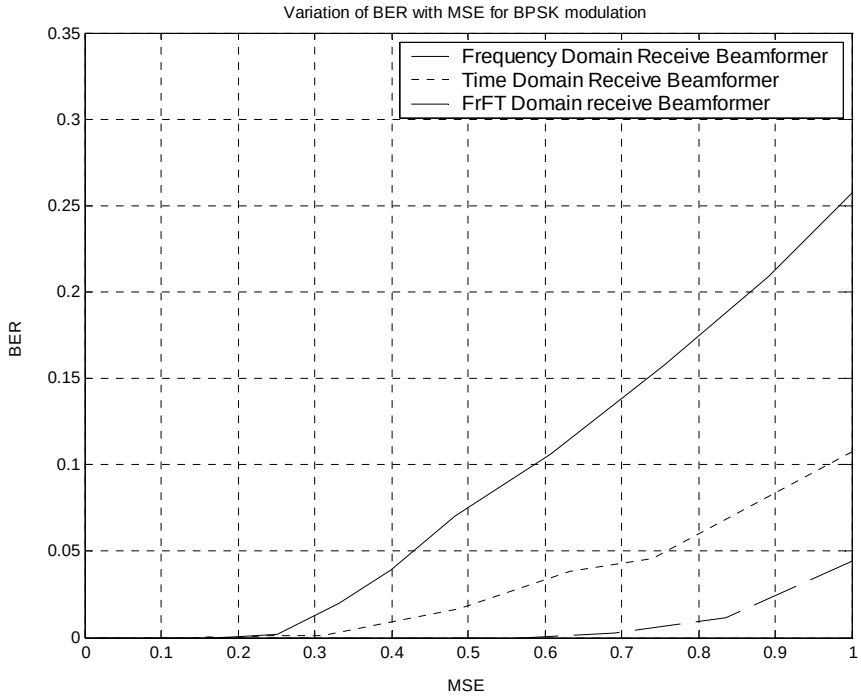

Fig. 5.30 Variation of BER with MSE of 2×2 spatial multiplexed system with different receive beamformers

5.9 SUMMARY OF THE CHAPTER

In this chapter the FrFT based receive array processing is proposed for the improvement of the MIMO systems. Firstly it is proposed that Channel estimation errors can be reduced using FrFT domain channel estimation[1]. It is shown through simulation that by using FrFT based channel estimation the performance of Alamouti's scheme can be improved further. Secondly it is shown that by using optimal FrFT based receive beamformer the BER and BLER of spatial multiplexed system can be reduced further in comparison to time or frequency domain MMSE receive beamformer[2]. The BLER performance of rate one OSTBC system can also be improved with OFMRB. Further it is proposed that OFMRB can also help in optimal FrFT based joint transmitter-receiver design using convex optimization theory.

Following articles have been reported from this chapter for publication:

1. [P24] "Improved channel estimation in transmit diversity scheme using Fractional Fourier Transform" submitted to Electronics Letters
2. [P27] "BER reduction in Spatial Multiplexed systems using FrFT based MIMO receive beamformer" submitted to International Journal of Springer on Wireless Personal Communications.

Chapter 6

SMART ANTENNA AT THE WIRELESS HANDHELD TERMINAL

6.1 INTRODUCTION

With operators and manufacturers preparing and deploying 3G systems, the increasing growth of mobile phone users has created a need for higher capacity in the cellular network [26, 90, 120, 122]. Even as more spectrum is allocated, demand for higher data rate services and steadily increasing numbers of users, will motivate service providers to seek ways of increasing the capacity of their systems. One way of overcoming the capacity problem is by using antenna arrays on the handset [152-153]. Till now the use of antenna arrays at a wireless handheld terminal (WHT) has been viewed unfavorably because of technical difficulties. But the new generation of high-speed, low power digital signal processors and miniaturized radio frequency (RF) components has facilitated computationally complex operations and support of multiple RF chains for array processing at the handheld terminal possible. The research in smart antenna at the WHT going on in various universities and companies, as described in section 2.6, has been in the direction of Diversity, Capacity improvement, Reduction of multi- path fading, Suppression of interference signals, Improvements of call reliability, Mitigation against dead zones, Increased data rates, Spectral efficiency. But no work has been reported so far, in the direction of controlling the radiation hazards by using smart antenna at WHT. The conventional antennas cause coupling with the head, but there can be reduced or no coupling with the head by use of smart antennas. In this chapter the use of smart antenna in controlling radiation hazards is suggested. The smart antenna can form a low or depressed side lobe towards the direction of head as proposed in chapter 3 or it can adaptively track the direction of head and can form a low side lobe in that direction. An exhaustive analysis is presented to find the effectiveness of smart antenna in controlling radiation hazards. The RF radiation hazards are described first.

6.2 WHAT ARE RF HAZARDS?

The RF electromagnetic radiations (EMR) are defined in the range from 300 Hz to 300 GHz [67]. Natural and man made sources generate EMR of different frequencies. The common RF fields are

1. Monitors and video display units (3- 30KHz)
2. AM and FM Radio (30 KHz – 300 MHz)
3. Mobile base stations and handsets, TV Broadcast (0.3 – 3 GHz)
4. Radar Satellite links and microwave communication (3 – 30 GHz)

Radio frequency EMR are considered to be non-ionizing radiations unlike X-Rays and Gamma rays. These radiations are too weak to break bonds that hold molecules in the cell together and therefore produce ionization. This process produces molecular changes that can lead to damage in biological tissue. A biological effect occurs when a change can be measured in a biological system after the introduction of some type of stimuli. However, a biological effect, in and of itself, does not necessarily suggest the existence of a biological hazard. A biological effect only becomes a biological hazard when it causes impairment to the health of the individual or his or her offspring. It has been known for many years that exposure to sufficiently high levels of RF EMR can heat biological tissues and potentially cause tissue damage. This is because the human body is unable to cope with the excessive heat generated during exposure to high RF levels. The effects resulting from RF exposure are usually described in one of three ways [75]:

- **Thermal effects**

These effects from RF fields are defined as those effects resulting from a measurable temperature increase. That is, the effect(s) occurs in the exposed biological material (tissue, cell, etc.) as a result of the material being heated by the RF fields.

- **Nonthermal effects**

These effects occur in an exposed material when the RF energy deposited into the biological material results in a temperature increase less than the normal temperature fluctuation of the material.

- **Athermal effects**

These effects occur when the RF field deposits sufficient heat energy into a biological material to cause an increase in temperature, but no temperature rise is observed.

The electric and magnetic fields produced in the body by a nearby electromagnetic source may cause both thermal and non-thermal biological effects [66]. It is proved that any biological effect from mobile phones is much more likely to result from electric rather than from magnetic fields [67]. The force produced by an electric field on charged objects, such as the mobile ions present in the body, causes them to move resulting in electric currents, and the electrical resistance of the tissue in which the currents are flowing, results in heating. This heat input causes the temperature to rise and it continues to do so until the heat input is balanced by the rate at which it is removed, mostly by blood flowing to and from other parts of the body. It is estimated that it takes several minutes; from the moment RF exposure occurs, for the irradiated parts of the body to reach their final equilibrium temperatures.

It has also been observed that most adverse effects of RF fields occur in the frequency range 1 MHz to 10 GHz [19]. Cellular telephones and wireless communication systems are introduced in the society at a very rapid rate and are using frequencies in the above-mentioned range. For a mobile phone to work it must radiate and it is also unavoidable that part of the radiated power be absorbed in the human head. There are various methods suggested for reducing radiation hazards like pasting a sticker called 'NO WAVE' on mobile phone, which protects mobile phone user from dangerous EMR. But there is a serious doubt about the protection power of this sticker. Minimizing the hazardous biological effects should be through the control of transmitted power at the handset. With the advent of smart antennas it is possible to shape handset antenna beam in such a way that there is 'cone of null' or low side lobe in a direction, in which user head is located. In this chapter the use of smart antennas in transmit mode has been analyzed for lowering the power absorbed by various tissues. This activity is motivated by two factors [67]:

(a) A need to evaluate the rise in temperature of biological tissues due to RF exposure.

(b) A need to evaluate performance of smart antenna at the handset.

6.3 MITIGATION OF BIOLOGICAL EFFECT OF HANDSET ANTENNA

The first step necessary for an assessment of potential risks is to analyze and quantify the electromagnetic fields induced in the various tissues of human head caused by the use of a WHT. To analyze the possible range of the induced field strength in the

various tissues requires an extensive effort, since the local field strength depends upon a number of parameters, such as [125]

1. Operational frequency of the antenna and the input power.
2. Position of device w.r.t. head.
3. Design of the device.
4. The outer shape of the head.
5. Distribution of the various tissues in the head.
6. Electrical properties of the tissues.

The last three factors are different for different individuals and can even change with time. The electrical parameters of human head vary with the level of physical and metabolic activity, health and age. The variations of all these properties make the study of absorption of RF energy complex. Simplifications are therefore required. In this study following simplifications have been made,

(1) The human head is initially reduced to a homogenous, semi-infinite, planar multilayered model of different tissues.

(2) The RF energy incident on tissue is assumed to be plane wave.

6.3.1 Electrical Properties of Tissues

The electrical properties of tissues [84] vary depending upon their water contents. The tissues span the range of water contents normally found in soft non-fatty tissues which is roughly 60-90% by weight, but much lower in fatty tissues. The interaction of RF fields with tissue is determined by electrical properties electrical permittivity ε, the magnetic permeability μ_p , electrical conductivity σ of the tissue and frequency of incident wave [19]. For all nonmagnetic media like tissue μ_p may be taken equal to the magnetic permeability of free space μ_0. For time varying fields the losses in the tissue may be taken into account by regarding electrical permittivity to be complex and given by

$$\varepsilon = \varepsilon_0\left(\varepsilon' - i\varepsilon''\right) = \varepsilon_0\left(\varepsilon' - i\frac{\sigma}{\omega\varepsilon_0}\right), \tag{6.1}$$

where, $$\varepsilon' = \mathrm{Re}\left[\frac{\varepsilon}{\varepsilon_0}\right] \text{ is called dielectric constant} \tag{6.2}$$

and $$\mathrm{Tan}[\delta] = \frac{\varepsilon''}{\varepsilon'} = \frac{\sigma}{\omega\varepsilon_0} \text{ is called loss tangent.} \tag{6.3}$$

Loss tangent accounts for loss in tissue. As stated earlier the ε' and σ of a tissue are frequency dependent. The following relations give the frequency dependence over the range 10MHz to 17GHz at 37°C [84].

$$\varepsilon' = 1.71 f^{-1.3} + (\varepsilon_s^m - 4) / [1 + (f/25)^2], \tag{6.4}$$

$$\sigma = 1.35 \cdot f^{0.13} \sigma_{0.1} + \frac{[0.0222(\varepsilon_s^m - 4) f^2]}{[1 + (f/25)^2]}, \tag{6.5}$$

where, f is frequency in GHz, σ is conductivity in mS/cm, $\sigma_{0.1}$ is electrical conductivity at 0.1 GHz and ε_s^m =Extrapolated microwave permittivity. The values of $\sigma_{0.1}$ and ε_s^m are given in the literature [84] and are tabulated in table 6.1

Table-6.1: Electrical properties of tissues of head [84]

Tissue of body	(1-P) Volume Fraction of water	ε_s^m Extrapolated Permittivity	$\sigma_{0.1}$ conductivity at 0.1 GHz	σ_s^m Extrapolated conductivity
Brain (Grey Matter)	0.84	44	7.0	11.3
Brain(White Matter)	0.74	34	4.8	7.5
Muscle	0.795	47	7.0	24
Liver	0.09	10	0.5	1
Fat	0.795	43	6.7	23
Spleen	0.79	46	No data available	19

The dielectric measurements mentioned above were all made at normal body temperature of 37°C. The permittivity and conductivity of tissues change less than 2% per degree centigrade, which is small for all practical purposes. The permittivity, conductivity and loss tangent of various tissues of head are shown in Figs.6.1-6.3.

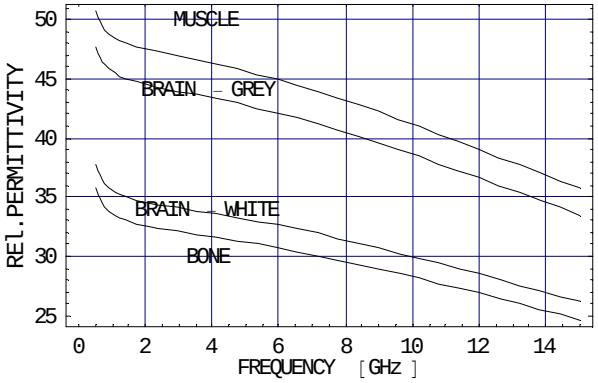

Figure 6.1-Variation of relative permittivity with frequency (GHz)

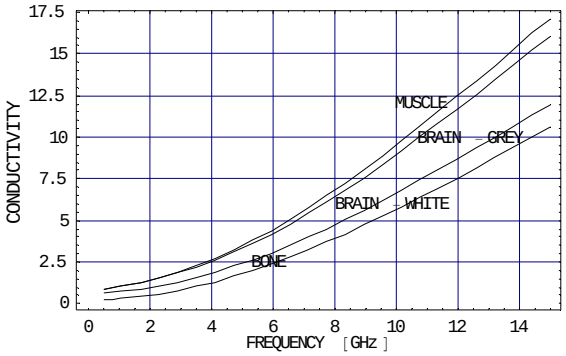

Figure 6.2-Variation of conductivity in (mS/cm) with frequency (GHz)

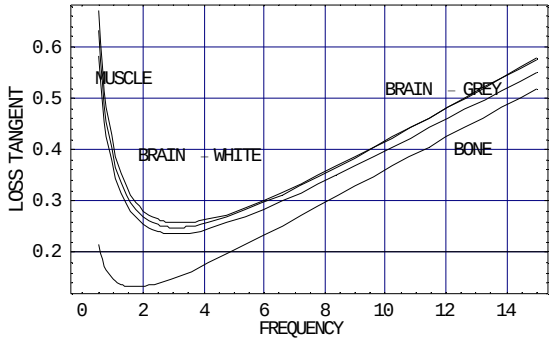

Figure 6.3-Variation of loss tangent with frequency (GHz)

The variation of ε' and σ are explained as follows, depending upon the time period of charging of cell membranes the ε' varies. In case the time period of the electromagnetic field is larger than the time period of charging, the tissue behaves as a good capacitor with large ε'. At higher frequencies the period of the field may be smaller than the charging time period of the tissue resulting in the low value of ε'. But at frequencies in excess of 100MHz the capacitive reactance of the tissue is so small that it may be assumed to be short-circuited. At frequencies in excess of 1GHz the dipolar relaxation of the tissue water determines the variation in dielectric properties with frequency. The rapid increase in σ at frequencies above 1 GHz arises from the polar properties of the water molecules present in the tissue.

6.4 PROPAGATION OF RF ENERGY THROUGH HUMAN HEAD

The propagation of electromagnetic wave in tissue was studied mathematically by solving the Maxwell's field equations under appropriate boundary conditions [40,125]. In the tissue each layer is assumed to be source free, isotropic and

homogeneous medium. The electric and magnetic fields in tissue are obtained by solving the wave equations

$$(\nabla^2 + k^2)\, E = 0, \tag{6.6}$$

$$(\nabla^2 + k^2)\, H = 0, \tag{6.7}$$

where, $$k = \alpha + i\,\beta\,, \tag{6.8}$$

α is attenuation constant and β is phase constant.

Also $$k^2 = \omega^2\mu_p\varepsilon - i\omega\mu_p\sigma = \omega^2 / c^2\,(\varepsilon' - i\,\varepsilon''), \tag{6.9}$$

where, c is the velocity of light.

$$\varepsilon'' = \sigma/(\omega\varepsilon_0) = \text{imaginary part of permittivity}, \tag{6.10}$$

$$\alpha = \frac{\omega\sqrt{\mu_p\varepsilon}}{\sqrt{2}}\frac{\varepsilon''}{\varepsilon'} \qquad \text{and} \tag{6.11}$$

$$\beta = \omega\sqrt{\mu_p\varepsilon}[1 + 0.125\,(\frac{\varepsilon''}{\varepsilon'})^2]\,. \tag{6.12}$$

Intrinsic wave impedance= $$\eta = \sqrt{\frac{\mu_p}{\varepsilon}}\left[1 - 0.378\left(\frac{\varepsilon''}{\varepsilon'}\right)^2 + i0.5\,\frac{\varepsilon''}{\varepsilon'}\right]. \tag{6.13}$$

For a linearly polarized incident uniform plane wave along z direction

$$E = E_i e^{-\alpha z} e^{i(\varpi t - \alpha z)}\,, \tag{6.14}$$

$$H = H_i e^{-\alpha z} e^{i(\varpi t - \alpha z)}\,. \tag{6.15}$$

Power density in tissue P_i=E x H= $$P_i = \frac{|E_i^2|}{2\eta}\,. \tag{6.16}$$

6.4.1 Depth of Penetration

From (6.14) it is seen that the wave is attenuated as it travels through the tissue. At a distance of $z=1/\alpha$ the magnitude of E and H fields are reduced to 36% of their initial value. Similarly, it is seen that power density is reduced to 13.5% of its initial value at $z=1/\alpha$. This distance is called depth of penetration (DOP).

$$\text{DOP} = \frac{1}{\alpha} = \frac{\sqrt{2}}{\varpi\sqrt{\mu_p\varepsilon}}\frac{\varepsilon''}{\varepsilon'}\,. \tag{6.17}$$

It is clear from (6.17) that depth of penetration depends upon electrical properties of tissue. Fig.6.4 shows that as frequency increases DOP decreases and the properties of muscle and brain grey matter is almost same.

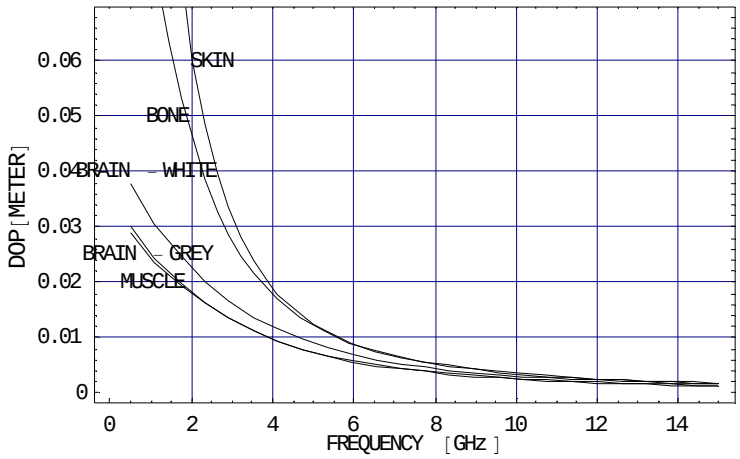

Figure 6.4-Variation of DOP (meters) with frequency (GHz)

6.5 POWER INCIDENT ON VARIOUS TISSUES OF HEAD

The modeling of human head is essential in order to find the power incident on various tissues in human head. As the wavelength of operation is very small compared to the dimensions of human body, the human body is considered as a planar multiplayer model. The head is composed of seven tissues. The location of various tissues has been determined from magnetic resonance image as well as the cross sectional anatomy. The head consists of skin, which is normally less than 0.4mm thick. Just below skin lies a layer, 1.25cm thick, of bone and fat, both of which are low water content medium and hence low loss medium. Beneath the bone lies muscle, which has high water content medium hence constitute high loss medium. After muscle lies brain tissues, whose electrical properties are similar to that of muscle tissues. In general, the head is modelled as stratified lossy medium of M isotropic and homogenous layers of planar geometry characterized by ε_n, σ_n, μ_{pn}, h_{tn}, n =1,2…….. M where h_{tn} denotes the thickness of n^{th} layer. The M^{th} layer is assumed to be semi infinite. All the layers are assumed to be infinite in x-y directions as shown in Fig.6.5

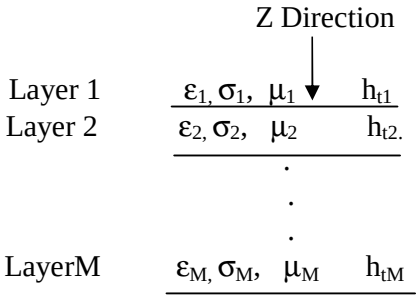

Figure 6.5-Model of head with various tissue layers

When a uniform plane wave is incident on the surface of tissue, a part of this is reflected and remaining is transmitted through body [40,163]. As the wave propagates through tissue it gets attenuated. The reflection and transmission properties of various tissues are function of electromagnetic properties of layers, frequency of operation, angle of incidence and type of polarization and thickness of layer. This case is for oblique incidence but for the case of WHT the wavelength of operation is small and antennas are held very close to the body, therefore it may be possible to consider that waves are normally incident at the surface of human body. For normal incidence there is no distinction between parallel and perpendicular polarization. The case of parallel polarization is considered here. To simplify the calculations consider the case of 3 layers as shown in Fig. 6.6. The same theory can be extended to any number of layers.

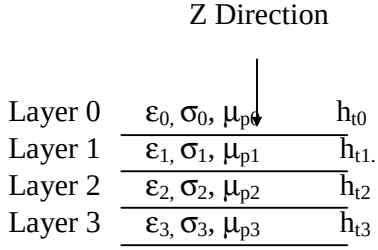

Figure 6.6-Model of 3 Layers considered for analysis

Let the uniform plane wave be traveling along z direction and incident normally on a boundary that is parallel to z=0 plane. A part of energy is transmitted and part of this is reflected back. Let E_i, E_r, E_t be the field strength of incident, reflected and transmitted wave. The continuity of tangential components of E and H requires

$$E_i + E_r = E_t \,, \tag{6.18}$$

$$H_i + H_r = H_t. \tag{6.19}$$

The following convention for reflection coefficients are considered throughout this chapter;

- R_{xy}*:* Reflection Coefficient of layer *'y'*
- Left hand subscript *'x'* indicates the medium form which wave is incident
- Right hand subscript *'y'* indicates the medium on which wave is incident
- For example R_{01} indicates the reflection coefficient of layer1 and wave is incident from layer 0, which is free space. The same notation will apply to Transmission coefficient also.

- For reflected and transmitted field one more subscript ‘r’ or ‘t’ is added to indicate transmitted or reflected field. For example *Erxy* indicates electric field reflected in layer *‘y’*. Subscript *‘x’* indicates the medium form which wave is incident. Subscript *‘y’* indicates the medium on which wave is incident.

For the first layer these conditions give reflected and transmitted fields are

$$E_{r01} = \frac{\eta_1 - \eta_0}{\eta_1 + \eta_0} E_i = R_{01} E_i , \tag{6.20}$$

$$E_{t01} = \frac{2\eta_1}{\eta_1 + \eta_0} E_i = T_{01} E_i , \tag{6.21}$$

where, T_{01} and R_{01} are transmission and reflection coefficients of layer 1.

E_{12} = Transmitted field in layer 1 reaching boundary (2, 1) of layer 2 and layer 1

$$= E_{t01}\, e^{-\alpha_1 h_1}. \tag{6.22}$$

A part of this field is reflected back and again reaches boundary (1, 0) given by

$$E_{r12} = \frac{\eta_2 - \eta_1}{\eta_1 + \eta_2} E_{21} = R_{12} E_{12} = R_{12} E_{t01} e^{-\alpha_1 h_1} . \tag{6.23}$$

E_{10} = Field reaching (1, 0) boundary $= E_{r12}\, e^{-\alpha_1 h_1} = R_{12} E_{t01}\, e^{-2\alpha_1 h_1}$. (6.24)

At (1,0) surface a part of this is transmitted and a part is reflected back, again the reflected field is $E'_{r10} = \frac{\eta_1 - \eta_0}{\eta_1 + \eta_0} E_{10} = R_{10} R_{12} E_{t01} e^{-2\alpha_1 h_1}$. (6.25)

Since $R_{01}=R_{10}$, therefore R_{10} can be replaced with R_{01} in (6.25)

$$E'_{r10} = \frac{\eta_1 - \eta_0}{\eta_1 + \eta_0} E_{10} = R_{01} R_{12} E_{t01} e^{-2\alpha_1 h_1} . \tag{6.26}$$

This reflected field again reaches interface (2,1) and field reaching (2,1) interface after 1st reflection $E'_{12} = E'_{r10} e^{-\alpha_1 h_1} = R_{01} R_{12} E_{t01} e^{-3\alpha_1 h_1}$. (6.27)

On reaching (1,2) interface a part of field is reflected back again, hence the net field reaching (1 2) interface after multiple reflections is E_{12} given by

$$E_{12} = E_{t01} e^{-\alpha_1 h_1} + R_{01} R_{12} E_{0t1} e^{-3\alpha_1 h_1} + \left(R_{01} R_{21}\right)^2 E_{t01} e^{-5\alpha_1 h_1} + \ldots\ldots\ldots\ldots , \tag{6.28}$$

$$= E_{t01} e^{-\alpha_1 h_1} \left[\frac{1}{1 - R_{01} R_{12} e^{-2\alpha_1 h_1}} \right] = \frac{2\eta_1}{\eta_1 + \eta_2} \left[\frac{1}{1 - R_{01} R_{12} e^{-2\alpha_1 h_1}} \right] e^{-\alpha_1 h_1} E_i . \tag{6.29}$$

The field reaching (1,2) interface becomes the incident field on layer 2 and above theory can be extended to find fields reaching other layers. For example the field reaching (2,3) interface is given by (6.30)

$$E_{23} = \frac{2\eta_1}{\eta_1 + \eta_0}\left[\frac{1}{1 - R_{01}R_{12}e^{-2\alpha_1 h_1}}\right]e^{-\alpha_1 h_1}\frac{2\eta_2}{\eta_1 + \eta_2}\left[\frac{1}{1 - R_{12}R_{23}e^{-2\alpha_2 h_2}}\right]e^{-\alpha_2 h_2}E_i \,. \tag{6.30}$$

Now the total field reaching interface (1,2) is the sum of the field reflected back from the layer (2,3) and field reaching (1,2) after multiple reflections in layer 1. The effects of fields reaching interface (1,2) after reflection back from subsequent layers is negligible and is therefore neglected. The field reaching back layer (1,2) after reflection from layer (2,3) is

$$E_{12}^{"} = R_{32}E_{23}e^{-\alpha_2 h_2} \,. \tag{6.31}$$

The total field incident on layer (1, 2) is sum of (6.29) and (6.31)

$$E_{12}^{T} = E_{12} + E_{12}^{"} \,. \tag{6.32}$$

Knowing the total field incident the power flow is calculated using Poynting theorem

$$\mathrm{P_i} = \text{Average power flow/area in incident field} = \frac{|E_i|^2}{2}\mathrm{Re}\left[\frac{1}{\eta_i}\right]. \tag{6.33}$$

$$\mathrm{P_r} = \text{Power flow /area in reflected field} = \frac{|E_i|^2}{2}\mathrm{Re}\left[\frac{1}{\eta_i}\right]|R_c| \,. \tag{6.34}$$

$$\mathrm{Pt} = \text{Power flow/area in transmitted field} = \frac{|E_i|^2}{2}\mathrm{Re}\left[\frac{1}{\eta_i}\right]|T_c| \,. \tag{6.35}$$

where, R_C is reflection coefficient of tissue and T_C is transmission coefficient of tissue. Power absorbed at z=0 using principle of conservation of energy is given by

$$\mathrm{P_a}(0) = \mathrm{P_i} - \mathrm{P_r} - \mathrm{P_t} \,. \tag{6.36}$$

Power absorbed at any point z in the first layer is given by

$$P_a(z) = \frac{2}{DOP}P_a(0)e^{-2\alpha_1 h_1} \,. \tag{6.37}$$

6.6 RESULTS AND DISCUSSION FOR POWER DEPOSITION

Based on above analysis above, a study of the effects of thickness of skin, bone, muscle and brain on the power-transferred ratio (PTR) has been carried out. The thickness of skin, bone and muscle are assumed to be 0.4mm, 1.25cm and 1cm respectively. In this work the three frequencies considered are 900 MHz (GSM), 1850 MHz (WCDMA) and the frequency of 6 GHz, considering the satellite mobile phones (although power requirement by such phones is high as compared to GSM and

WCDMA handsets). The results of power absorbed by various tissues are shown in the Figs.6.7-6.13.

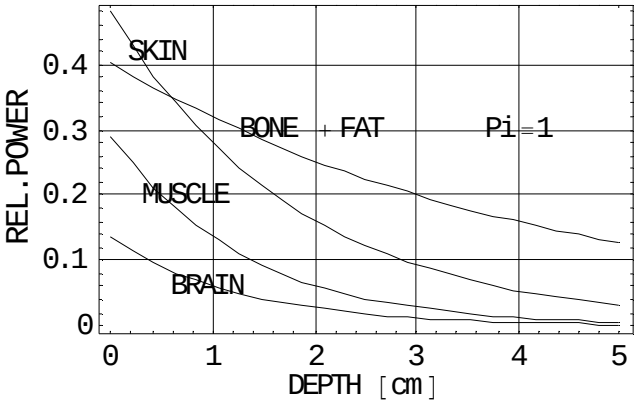

Figure 6.7-Relative power absorbed in various tissues of head at 900MHz

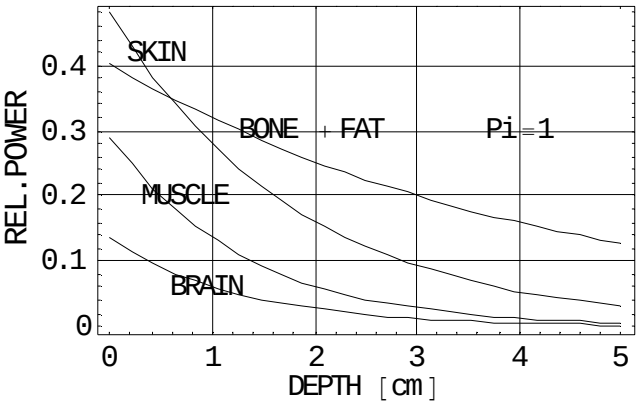

Figure 6.8- Relative power absorbed in various tissues of head at 1850MHz

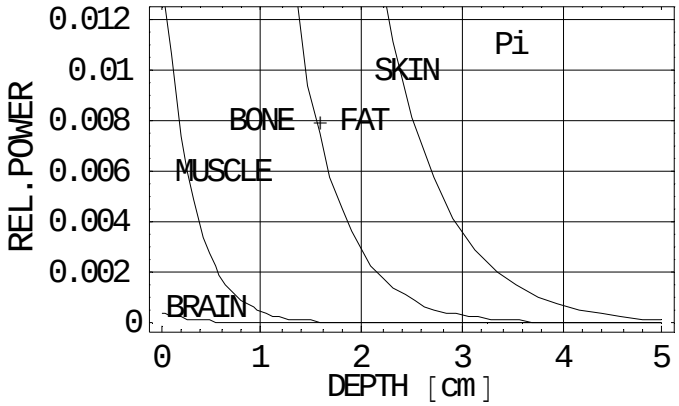

Figure 6.9- Relative power absorbed in various tissues of head at 6 GHz

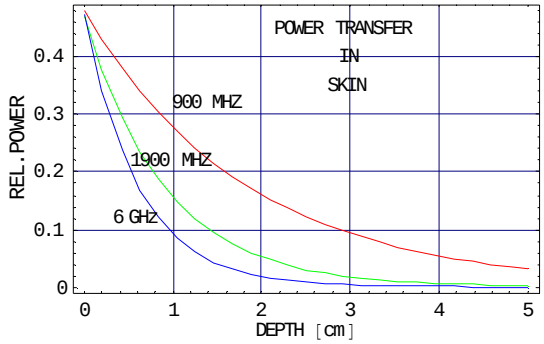

Figure 6.10-Relative power transmitted in skin at 900 Mhz, 1850Mhz & 6Ghz

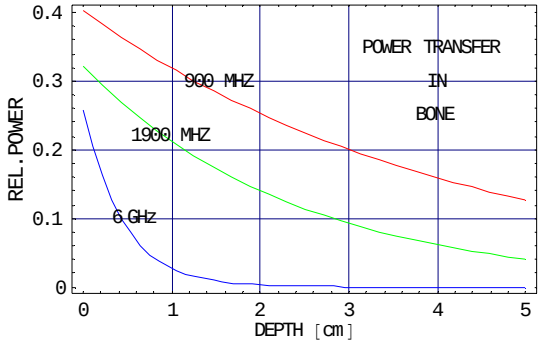

Figure 6.11-Relative power transmitted in bone at 900 Mhz, 1850Mhz & 6Ghz

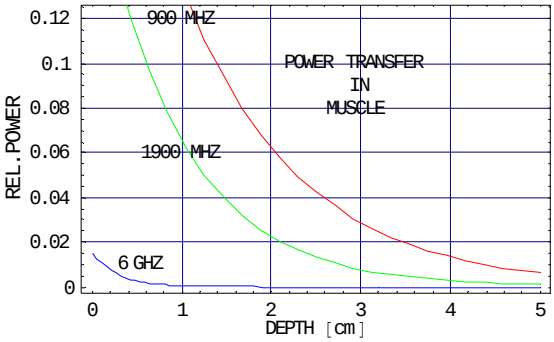

Figure 6.12-Relative power transmitted in muscle at 900 Mhz, 1850Mhz & 6Ghz

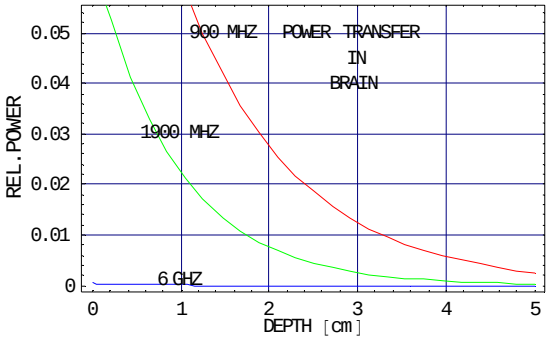

Figure 6.13-Relative power transmitted in brain at 900 Mhz, 1850Mhz & 6Ghz

Table-6.2: Relative power absorbed in various tissues at 900MHz, 1850MHz and 6GHz

Frequency	Skin	Bone	Muscle	Brain
900 MHz	0.48 Pi	0.39 Pi	0.30 Pi	0.13 Pi
1850 MHz	0.47 Pi	0.32 Pi	0.21 Pi	0.08 Pi
6 GHz	0.47 Pi	0.25 Pi	0.015 Pi	0.0004 Pi
Pi=Incident Power Density				

Finally, based on the above analysis and results, the following points can be considered

1. At 900MHz head absorbs 48% of incident power and 47% of incident power is absorbed at 1850MHz and 6GHz.
2. At all frequencies the power decay at skin, muscle and brain is fast while power at bone decays slowly due to poor conductivity of the bone tissues.
3. The use of higher frequency band is suitable for cellular mobile communication, as it is seen from the table 6.2 that 0.04% & 8% of incident power is reaching brain at 1850MHz & 6GHz respectively as compared to 13% at 900MHz.

4. The power absorbed by head at all frequencies is of the order of 47% of incident power. Shaping the radiation pattern such that less power is directed towards head can decrease it. An attempt can be made to create a cone of null or depressed side lobe in the direction of head in beam pattern.
5. Using adaptive antennas at the mobile handset can decrease the power incident on the human head. The adaptive antenna shall form a cone of null or low side lobe towards the human head in its radiation pattern. As seen from the table 6.2 that at all frequencies about half the power is reflected back towards the antenna, after reflection from the human head and it can be considered as interference at the same frequency. Knowing the DOA of this a low or depressed side lobe can be formed towards this interference.

It may be pointed out that the assumption that the incident wave is a plane wave is simplistic and may not be a realistic one in view of near field situation.

6.7 THERMAL PROFILES OF HUMAN HEAD

The one-dimensional bio-heat transfer equation has been solved to find the thermal profiles of human head for semi-infinite plane of tissues irradiated by microwave power. When tissue is exposed to microwave radiation it absorbs some of the electromagnetic energy that is converted into heat. Without cooling effect of blood flow and heat loss from the tissue surface, the calculated tissue temperature rises without limit and no steady state solution is obtained [91].

6.7.1 Development of Bio-Heat Transfer Equation

6.7.1.1 Heat energy generated

As discussed earlier let P_i be the power incident on the surface of tissue. Then power density of wave at a distance z inside tissue whose attenuation constant is α

$$P_z(z) = P_i.e^{-\alpha z} \tag{6.38}$$

Power lost by the wave while traveling in the tissue

$$-dP_z(z) = -\frac{dP_z(z)}{dz}dz = \alpha P_z(z).dz = \frac{P_z(z)}{LP_i}.P_i.dz\,, \tag{6.39}$$

where, $z = 1/\alpha$ = Depth of penetration $= \frac{\chi P_i}{L}.dz\,,$ (6.40)

and χ = Fraction of energy transmitted in the tissue.

Equivalent heat energy deposited by incident wave in time dt in the volume of tissue of cross-section A and depth dz = $Q_p Adzdt = \frac{\tau.P_i}{J.L}.A.dt.dz$, (6.41)

where, J= Mechanical equivalent of heat.

In a small time *dt* the element of volume receives energy through source Q_pAdzdt, therefore its temperature rises though say ΔT, hence its internal energy rises by

= mass x Specific Heat x Temperature Rise.

$$(\gamma_t.\text{Adz}).c_t.\Delta T = \gamma_t.c_t.\frac{\partial T}{\partial t}.\text{Adzdt}, \quad (6.42)$$

where, c_t = Specific heat of tissue Cal/gm-^{0}C and γ_t= Density of tissue in gm/cm^3

6.7.1.2 Heat Energy Lost

The heat loss is due to following reasons

(a) Thermal Conduction

Conduction is the process in which heat transfer takes place by molecular diffusion. The amount of heat energy flowing per second per unit area of the cross-section is proportional to temperature gradient ∇T. The amount of energy lost by volume Adz in interval dt is

$$Q_c = -\varsigma\frac{\partial^2 T}{\partial z^2}\text{A.dz.dt}, \quad (6.43)$$

where, ς is a constant.

(b) Blood circulation

The thermo regulation process of the body tries to maintain the temperature of the human body. If the temperature of the body rises, the vascular system tries to bring down the temperature by an increased blood flow through the volume. If T_0 is the temperature at which the arterial blood enters the volume under consideration and T is the temperature at which it leaves the body.

Q_b = Heat loss in time dt = $w_b.c_b.\Delta T.A.dz.dt$, (6.44)

where, w_b(= γ_bm) is mass flow rate of blood through unit volume in gm/cm^3,c_b is specific heat of blood in cal/gm-^{0}C, γ_b is the density of blood in gm/cm^3, m is volumetric flow rate of blood per unit of the mass of tissue in cm^3/(gm-sec) and ΔT=T-T_0 is temperature rise in degree centigrade. From (6.41-6.44) using the principle of conservation of energy

$$Q_p A dz dt = \gamma_t c_t \frac{\partial T}{\partial t} A dz dt - \varsigma \frac{\partial^2 T}{\partial z^2} A dz dt + w_b c_b \Delta T A dz dt \ . \quad (6.45)$$

Solving the above equation

$$\gamma_t c_t \frac{\partial T}{\partial t} = \varsigma \frac{\partial^2 T}{\partial z^2} - w_b c_b \Delta T + Q_p . \quad (6.46)$$

$$\zeta \frac{\partial T'}{\partial t} = \frac{\partial^2 T'}{\partial z^2} - \lambda T' + q , \quad (6.47)$$

where T' =T-T_0 = Differential temperature increase and

$$\zeta = \frac{\gamma_t c_t}{\varsigma}, \quad \lambda = \frac{w_b c_b}{\varsigma}, \quad q = \frac{Q_p}{\varsigma} . \quad (6.48)$$

6.8 SOLUTION OF BIO HEAT TRANSFER EQUATION

Before proceeding to solve the bio heat transfer equation mathematically, requires knowledge of the physical and thermal properties of tissue, which are strongly dependent on structures and composition of tissue. For ready reference, some of the properties of various types of tissue of human head are tabulated in table 6.3.

Table-6.3: Various Properties of Tissues of human head [79, 91, 108]

Tissue	Density gm/cm^3	Sp. Heat Cal/gm-^{0}C	Thermal ConductivityCal/cm-^{0}C-s	Avg. Blood Flow ml/100gm-min
Skin	1.2	0.83	0.00105	12.8
Bone	1.25	0.73	0.00344	-
Muscle	1.07	0.81	0.00153	2.7
Brain (Grey)	1.05	0.81	0.00114	6.4
Brain (white)	1.21	0.74	0.00314	2.4
Blood	1.06	0.93	0.00545	-

In studying the temperature profiles, there are two major processes that determine the temperature profile in tissue. The first one is the heating effect of the microwaves incident on the tissue. The heating effect is maximum at the surface and it decreases exponentially, with the depth in tissue. The second one is surface cooling produced by radiation from the surface by convection and evaporation of sweat. The cooling effect also decreases with depth. Therefore, the temperature increase is the net result of these two effects that oppose each other. Hence it is expected that temperature profile would have a peak at some depth as shown in Fig.6.14.

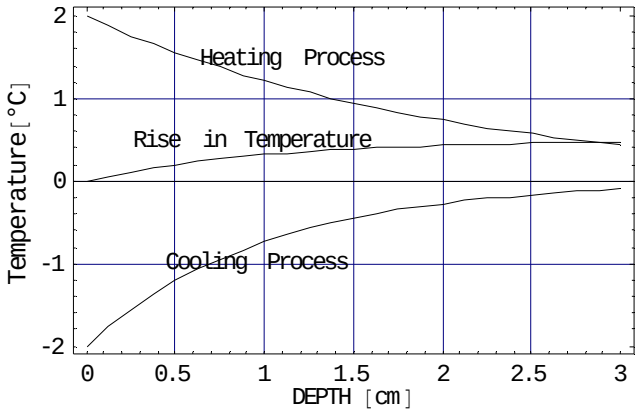

Figure 6.14-Rise in Temperature of Tissue

6.8.1 Boundary Conditions for Solution of Bio-Heat Transfer Equation

As discussed above under the action of incident power, surface cooling caused by blood profusion and other effects, a temperature distribution along z direction gets built up in the tissue [91]. Initially the temperature profile changes simultaneously with time but as $t \to \infty$, the temperature profile stabilizes and becomes steady with respect to time. In the steady state

$$T'(\infty, t) = 0 \ . \tag{6.49}$$

The heat flow is proportional to arterial blood temperature T_0 and surface cooling temperature T_c where heat transfer takes place by convection, radiation or combination of the two. The surface cooling gives the boundary condition

$$\frac{\partial T'}{\partial z}(z=0,t) = h'(T' + T_0 - T_c), \tag{6.50}$$

where, T_c = Temperature outside tissue plane. Value of h′ varies with environmental conditions. The value of h′ is 0.25/cm for a nude man at 30^0C with a wind speed of 0.6 m/sec [91]. If skin is wet the h increases by a factor of 5 or so. In general case $T_0 \neq T_c$, so there exist an initial temperature gradient near tissue surface given by steady state solution of 6.47

$$T'(z,0) = \frac{h'(T_c - T_0)}{h' + \sqrt{\lambda}}.\mathrm{Exp}\left(-z\sqrt{\lambda}\right). \tag{6.51}$$

6.8.2 Steady State Solution

In steady state $\frac{\partial T}{\partial t} = 0$ and equation becomes

$$\frac{d^2 t}{dz^2} = \lambda T - q \, . \tag{6.52}$$

The solution of (6.52) subject to boundary conditions (6.49-6.50) is

$$T(z,\infty) = \frac{q}{\lambda - \frac{1}{L^2}}\left[\mathrm{Exp}\left(-\frac{z}{L}\right) - \frac{h' + \frac{1}{L}}{\sqrt{\lambda + h'}}\mathrm{Exp}\left[-z\sqrt{\lambda}\right] + T_i \right]. \qquad (6.53)$$

Where T_i is the initial temperature given by the (6.54) when no microwave power is applied

$$T_i = \frac{h'(T_c - T_0)}{h' + \sqrt{\lambda}}.\mathrm{Exp}\left(-z\sqrt{\lambda}\right). \qquad (6.54)$$

The location of peak temperature within tissue Z_{Peak} is obtained by equating the first derivative of (6.53) to zero and yeilds

$$Z_{peak} = \frac{1}{\sqrt{\lambda - \frac{1}{L}}}\left[Ln\left(L\sqrt{\lambda}\right) + Ln\left[1 + \frac{\lambda - \frac{1}{L^2}}{q}\left(T_c - T_0\right) \right] \right]. \qquad (6.55)$$

6.9 EXPERIMENTAL DETAILS

The steady temperature distribution or the temperature profiles in the skin, bone and fat, muscle and brain irradiated by microwave power at three cellular frequencies 900 MHz, 1850MHz and 6GHz are plotted. The steady state temperature of head tissues as a function of depth has been calculated for the following cases.

1. Low surface cooling (LSC) $h' = 0$
2. Normal Surface cooling (NSC) $h' = 0.25$
3. Extra Surface Cooling (ESC) $h' = 1.5$

Before finding the temperature profiles, it is important to know the distribution of penetrating power density (in mw/cm^2) penetrating the surface of head. It has been found, in case of dipole, the microwave power density varies along the axis of antenna. When antenna is held about 0.35 inch from the head, the maximum power density is 60mw/cm^2 at the center of antenna and it falls off rapidly along the axis of antenna as shown in Fig. 6.16.

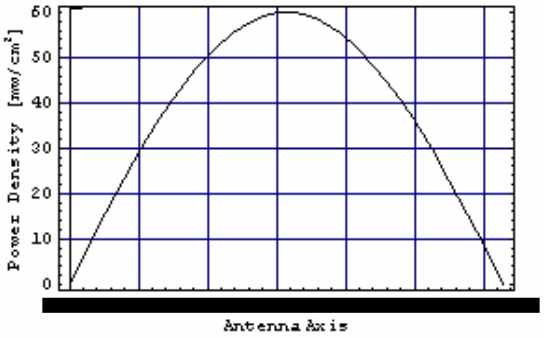

Figure 6.15-Variation of power density along antenna axis

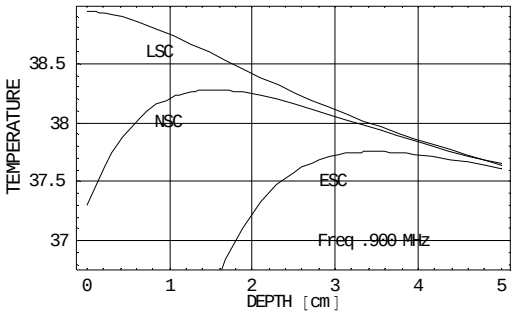

(a) Variation of Skin Temperature

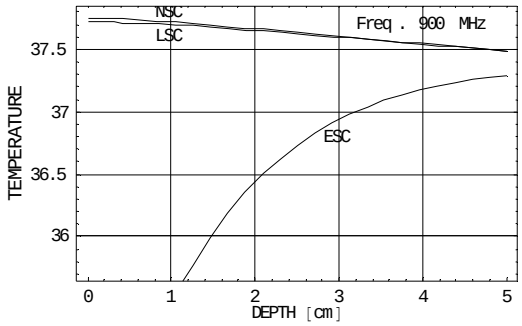

(b) Variation of Bone Temperature

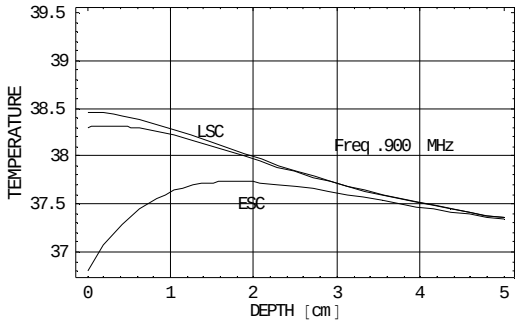

(c) Variation of Muscle Temperature

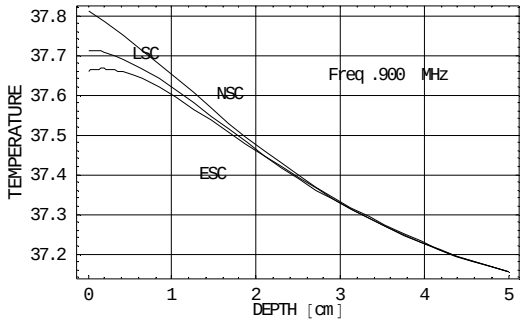

(d) Variation of Brain Temperature

Figure 6.16-Variation of temperature of various tissues in ^{0}C with 100mw/cm^2 incident power density under different surface cooling conditions at 900 MHz.

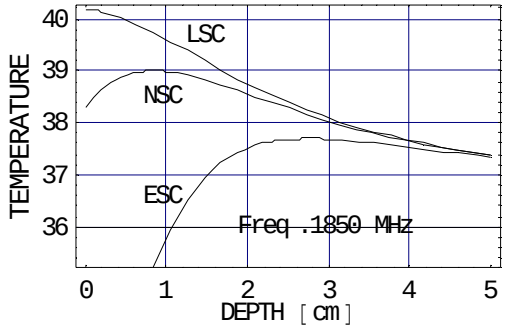

(a) Variation of Skin Temperature

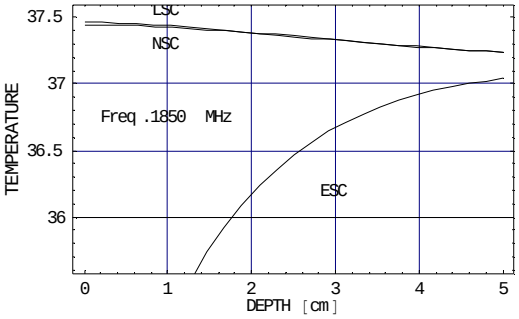

(b)Variation of Bone Temperature

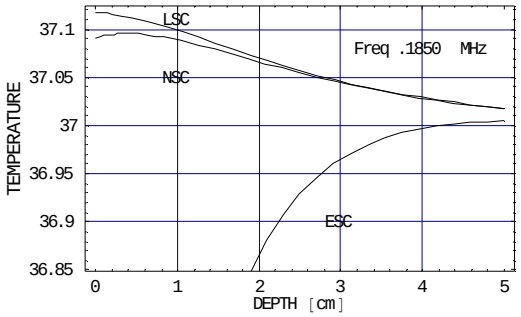

(c) Variation of Muscle Temperature

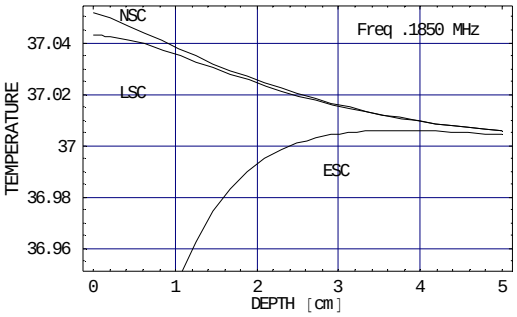

(d) Variation of Brain Temperature

Figure 6.17-Variation of temperature of various tissues in ^{0}C with 100mw/cm2 incident power density under different surface cooling conditions at 1850 MHz.

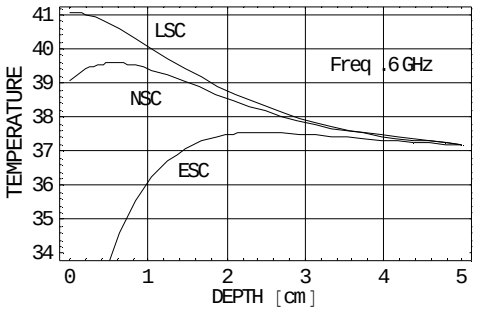

(a)Variation of Skin Temperature

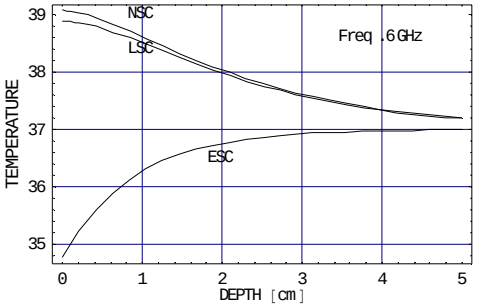

(b)Variation of Bone Temperature

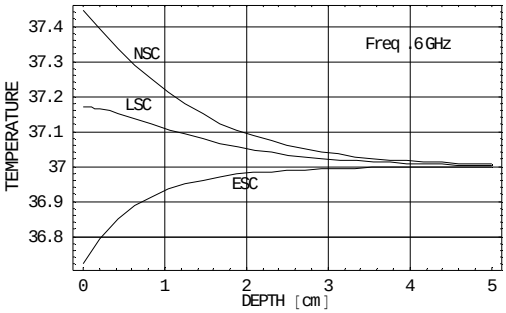

(c)Variation of Muscle Temperature

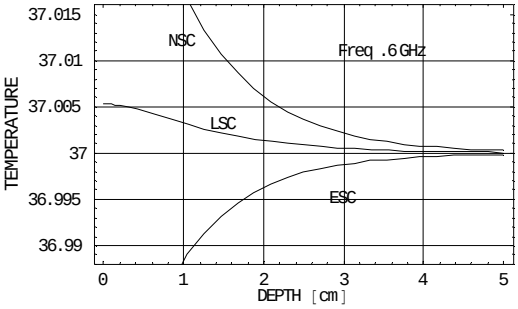

(d)Variation of Brain Temperature

Figure 6.18-Variation of temperature of various tissues in ^{0}C with 100mw/cm^2 incident power density under different surface cooling conditions at 6 GHz.

6.9.1 Results and Discussions

Based on the above discussion, the temperature profiles have been found for the case of power density 100mw/cm^2 taking it to be omni directional power density and the following points may be observed.

1. The temperature profiles for all tissues of head viz. skin, bone, muscle and brain are shown in Figs.6.16 to 6.18, for various incident power densities, when each of the cooling mechanisms is sequentially turned off and when extra cooling is added to all mechanism. In the absence of surface cooling, the tissue temperature is an exponentially decreasing function of distance from the surface, which also gets heated up.
2. The higher frequencies produce peak temperature nearer to the surface and produce high surface heating. Qualitatively it is expected because as frequency increases the depth of penetration of fields in the tissue decreases.
3. The lower frequency produces lower peak temperatures but is located deep inside the tissues.
4. Varying of incident microwave power density changes the magnitude of peak temperature and its location. As incident microwave power density is increased the peak temperature increases and move towards the surface.
5. From the plots it can be seen that flow of blood does has a significant effect on temperature profiles. Therefore, irradiation of actual muscles and of artificial models with same characteristics results in different thermal profiles of the two.
6. The analysis presented above helps in obtaining steady state temperatures only.
7. The above analysis also suggests that temperature rise can be controlled by radiating less power towards the human head.

In the profiles shown below, only for the skin tissue the value of h′ varies, for all other tissues after skin, have less variation of temperature due to thermoregulation process and for them value of h′ is zero. But profiles have been plotted for other values of h′ also.

6.10 ADAPTIVE ANTENNAS AT HANDSET

Smart antennas are designed to maximize effective transmission signal strength, maximize receive sensitivity and cope with-or even positively exploit multipath. As described earlier the adaptive antennas can be used at the handset to reduce power absorbed in the human head. To find the use of adaptive antennas in controlling RF

hazards consider a two-element uniform linear array at the handset as shown in Fig. 6.19

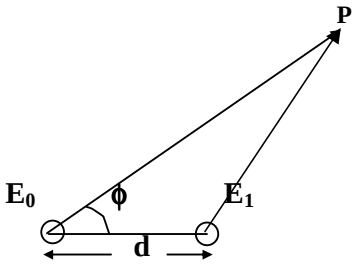

Figure 6.19-Two element ULA at handset

Let these two elements be identical and be fed with phase difference of α. Let E_0, E_1be the field produced at point P by the antenna 1 & 2. The total field at point P is

$$E_T = E_0(1+e^{j\Psi}) \quad = 2E_0 Cos(\frac{\Psi}{2}), \tag{6.56}$$

where $$\Psi = \frac{2\pi d}{\lambda}\cos\phi + \alpha. \tag{6.57}$$

By setting $d=\lambda/4$ and $\alpha=-45^0$. The radiation pattern obtained is shown in Fig. 6.20

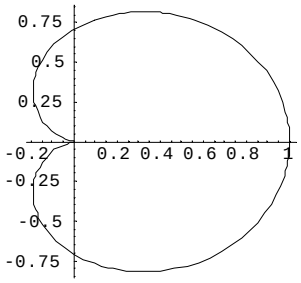

Figure 6.20-Polar Plot of two element ULA with d=λ/4 and α=-45^0

By using a simple two-element ULA at the handset it is possible to create a cone of null towards user head as shown in Fig.6.21.

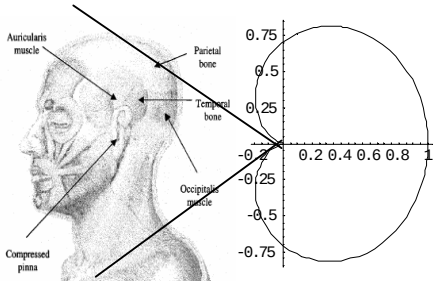

Figure 6.21-A cone of null created towards user head by using two-element ULA

The above arrangement, however, suffers one drawback that as the user changes the position of the handset, the null position will also change and it may happen that the

user head may be immersed in higher power as compared to cone of null. But this gives an idea that it is possible to control the power radiated towards the user's head and adaptive antennas can play a vital role in controlling power radiated.

Consider a two-element array at the mobile handset where the spacing between the elements is $\lambda/2$. Considering the desired signal S (t) arriving from direction θ_s and interference signal I(t) arriving at θ_I (assumed to be reflected signal from head). Both the signals have same frequency f. The signal from each element is multiplied by a complex variable weight and the weighted signals are then summed to form the array output. The two-element array is shown in Fig.6.22.

The output is given as $$Y(t)= Ae^{j2\pi ft}(w_1+w_2), \quad (6.58)$$

where, w_1 and w_2 are complex weights. For Y(t) to be equal to S(t) it is necessary that

$$\mathrm{Re}(w_1)+\mathrm{Re}(w_2)=1 \quad \&$$
$$\mathrm{Im}(w_1)+\mathrm{Im}(w_2)=0. \quad (6.59)$$

where, Re and Im are the real and imaginary values of the weights. The incident interference signal arrives at element 2 with a phase lead of $\pi/2$ w.r.t. element 1.

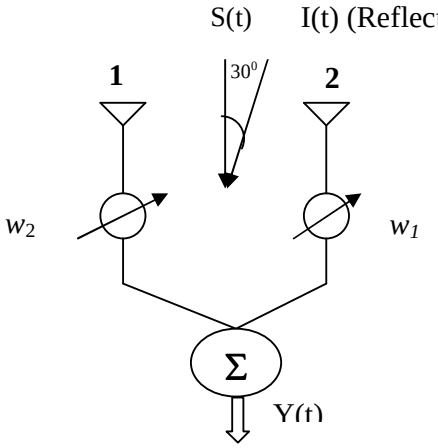

Figure 6.22-Two element array for reduced radiation towards human head

Consequently the array output due to the interference is

$$Y_i(t)=Ne^{j2(\pi)ft}w_1+Ne^{j(2(\pi)ft+\pi/2)}w_2. \quad (6.60)$$

For array output interference response to be zero it is necessary that

$$\mathrm{Re}(w_1)+\mathrm{Re}(w_2)=0 \quad \text{and}$$
$$\mathrm{Im}(w_1)+\mathrm{Im}(w_2)=0. \quad (6.61)$$

Simultaneous solution of above equations yields

$$w_1 = \frac{1}{2} - j\frac{1}{2} \quad \text{and} \qquad w_2 = \frac{1}{2} + j\frac{1}{2}. \tag{6.62}$$

With these weights the array will accept the desired signals while simultaneously rejecting the interference signals. This means the array will form a null towards the direction of the interference i.e. reflected signal.

Therefore an array processor essentially forms a null or depressed side lobe towards the direction of the user's head while maximizing signals from the other directions. The adaptive antennas utilize the signal processing algorithms to continuously distinguish between desired and interfering signals. The adaptive antennas continuously update its beam pattern based on changes in both the desired and interfering reflected signal locations. Hence these adaptive antennas provide each user with a beam which makes possible to transmit and receive signals in a directional area and null or depressed side lobe towards the user head thereby reducing the radiation hazard. A comparison of an omni directional antenna and adaptive antenna at various operating frequencies is given in Figs.6.23-6.26. The power absorbed by various tissues of head at 900 MHz, 1850 MHz and 6 GHz by use of omni as well as adaptive antenna is shown in tables 6.4 to 6.6.

Adaptive antennas can control the rise in temperatures of the various tissues of the human head by controlling the power incident on head adaptively. The omni directional antenna is assumed to have incident power density of 100mw/cm^2, while that of adaptive antenna is taken to be 75mw/cm^2, 50mw/cm^2 and 25mw/cm^2. The rise in temperature of various tissues of head is shown in Figs. 6.26 to 6.31. The temperature rise in various tissues is also shown in tables 6.7-6.10.

It is again emphasized that the model consider here is simplistic it can only serve as guide to find temperature profiles, practically the results may differ. The advantage of this model is that it considers the flow of blood and outside temperature which is not considered in any of the model described in literature for finding temperature profiles. The blood flow acts as a coolant in the body and controls the temperature rise, whenever it occurs. Hence it is proposed that future wireless and mobile communication systems employing antenna arrays at handset can use these arrays for controlling radiation hazards also.

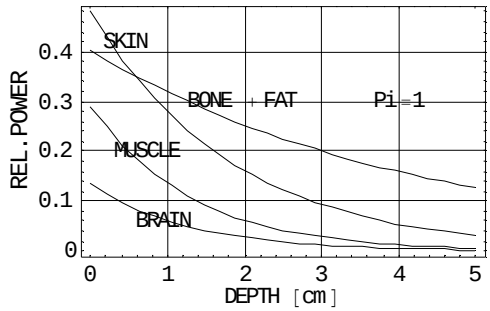

(a) Incident power density P_i

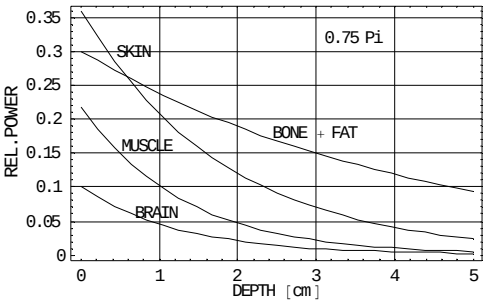

(b) Incident power density 0.75 P_i

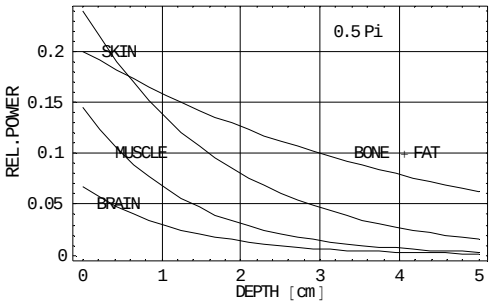

(c) Incident power density 0.50 P_i

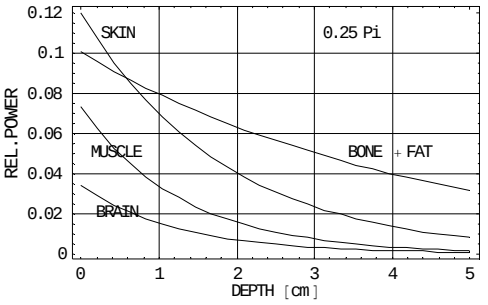

(d) Incident power density 0.25 P_i

Figure 6.23-Comparison of power absorbed in various tissues of head with Omni directional and smart antenna (with lesser incident power towards user's head) at 900 MHz

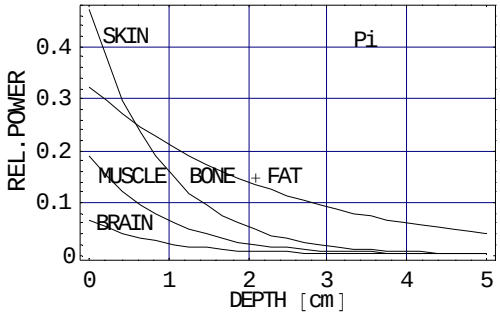

(a)Incident power density P_i

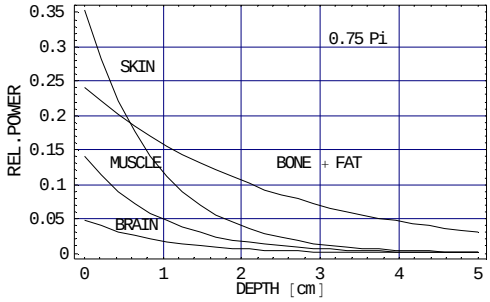

(b)Incident power density 0.75 P_i

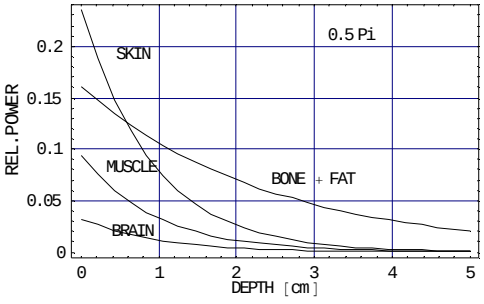

(c) Incident power density0.50 P_i

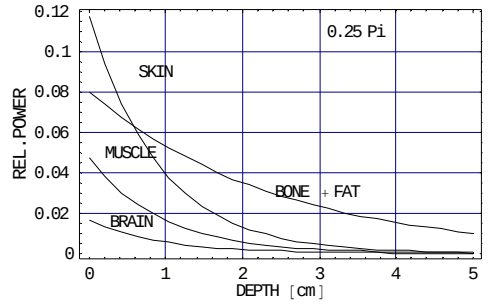

(d) Incident power density 0.25 P_i

Figure 6.24-Comparison of power absorbed in various tissues head with Omni directional and smart antenna (with lesser incident power towards user's head) at 1850 MHz

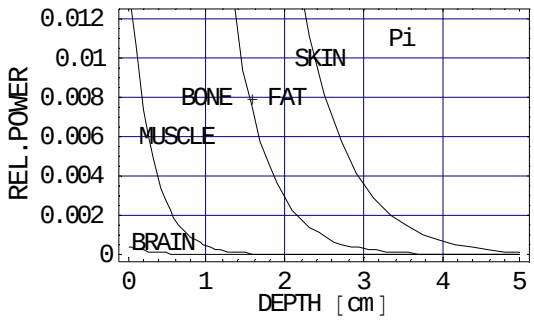

(a)Incident power density P_i

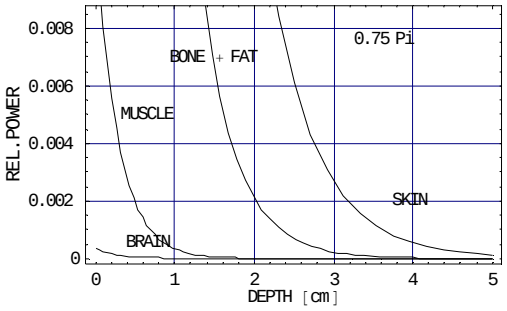

(b)Incident power density 0.75 P_i

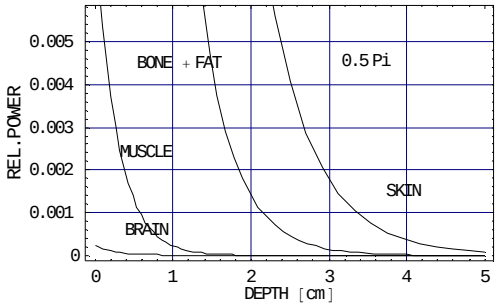

(c)Incident power density 0.50 P_i

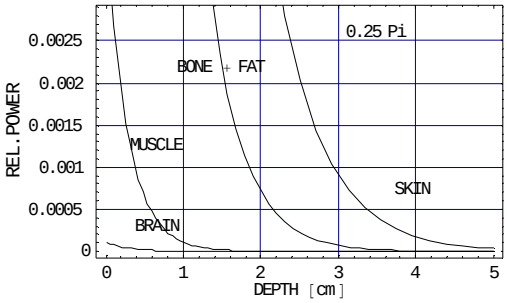

(d)Incident power density 0.25 P_i

Figure 6.25-Comparison of power absorbed in various tissues head with Omni directional and smart antenna (with lesser incident power towards user's head) at 6 GHz.

Table-6.4: Comparison of power absorbed in various tissues by adaptive and omni antenna at a frequency of 900MHz.

POWER ABSORBED IN VARIOUS TISSUES	OMNI DIRECTIONAL ANTENNA POWER (P_i)	ADAPTIVE ANTENNA (WITH REDUCED POWER TOWARDS HEAD)		
		0.25 P_i	0.50 P_i	0.75 P_i
SKIN	48	12	24	36
BONE	39	9.7	19.5	29.2
MUSCLE	30	7.5	15	22.5
BRAIN	13	3.2	6.5	9.75

Table-6.5: Comparison of power absorbed in various tissues by adaptive and omni antenna at a frequency of 1850MHz.

POWER ABSORBED IN VARIOUS TISSUES	OMNI DIRECTIONAL ANTENNA POWER (P_i)	ADAPTIVE ANTENNA (WITH REDUCED POWER TOWARDS HEAD)		
		0.25 P_i	0.50 P_i	0.75 P_i
SKIN	47	11.75	23.5	36.25
BONE	32	8.0	16.0	24.0
MUSCLE	21	6.25	10.5	16.75
BRAIN	8	2.0	4.0	6.0

Table-6.6: Comparison of power absorbed in various tissues by adaptive and omni antenna at a frequency of 6GHz.

POWER ABSORBED IN VARIOUS TISSUES	OMNI ANTENNA POWER (Pi)	ADAPTIVE ANTENNA (WITH REDUCED POWER TOWARDS HEAD)		
		0.25 P_i	**0.50 P_i**	**0.75 P_i**
SKIN	47	11.75	23.5	36.25
BONE	25	6.25	12.5	18.75
MUSCLE	1.5	0.375	0.75	1.125
BRAIN	0.04	0.01	0.02	0.03

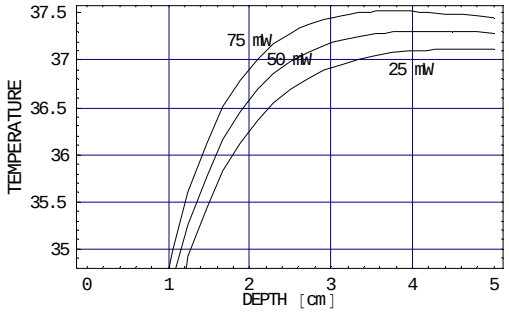

(a) Skin temperature variation with Extra surface cooling

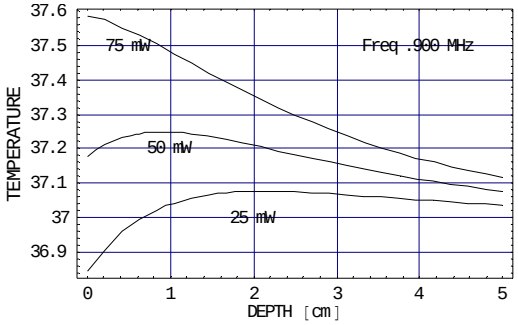

(b) Bone temperature variation with Extra surface cooling

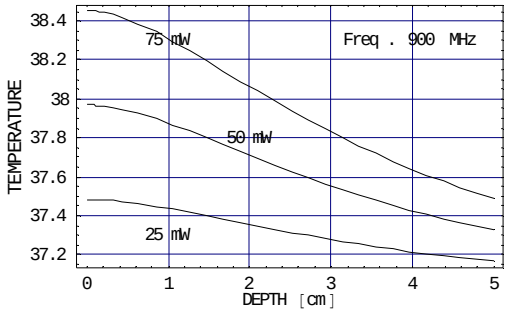

(c)Skin temperature variation with Low surface cooling

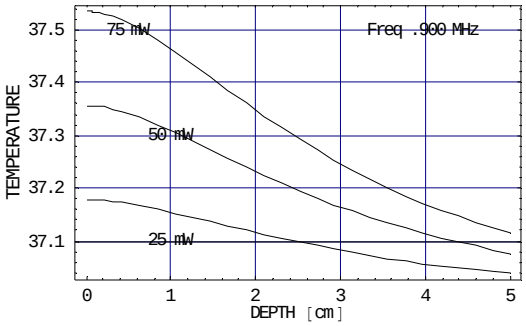

(d) Bone temperature variation with Low surface cooling

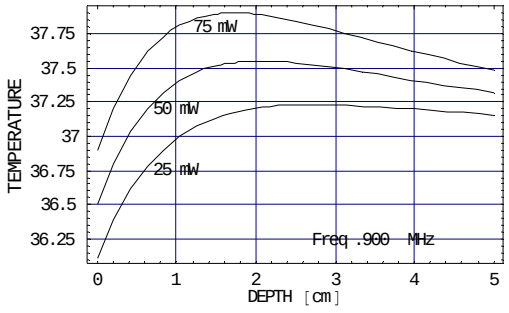

(e) Skin temperature variation with Normal surface cooling

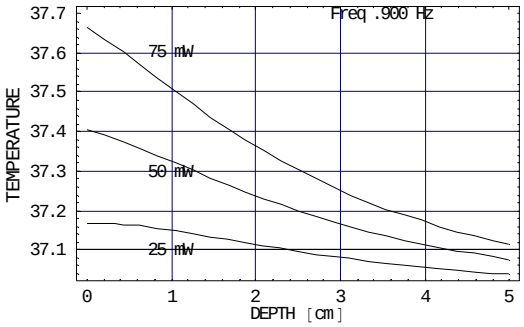

(f) Bone temperature variation with Normal surface cooling

Figure 6.26-Skin and Bone temperature variations with depth under different surface cooling conditions with Smart antenna at 900MHz

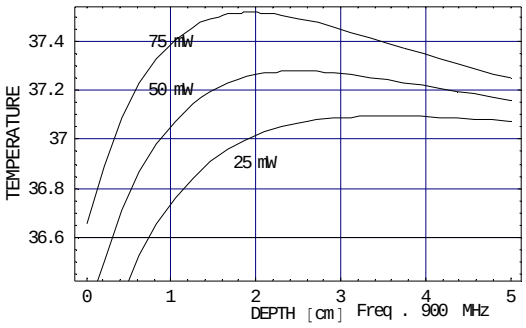

(a) Muscle temperature variation with Extra surface cooling

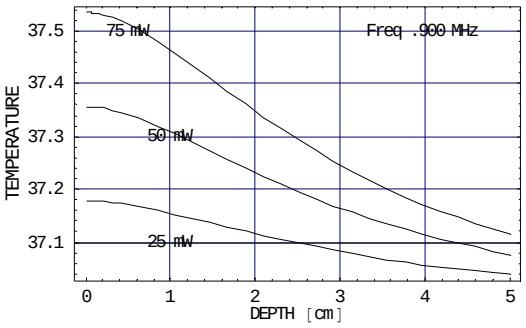

(b) Brain temperature variation with Extra surface cooling

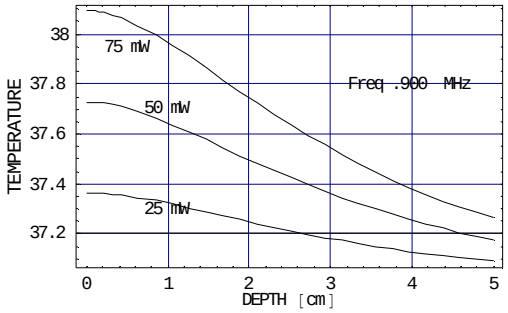

(c) Muscle temperature variation with Low surface cooling

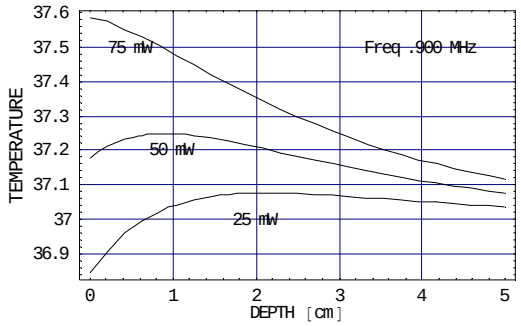

(d) Brain temperature variation with Low surface cooling

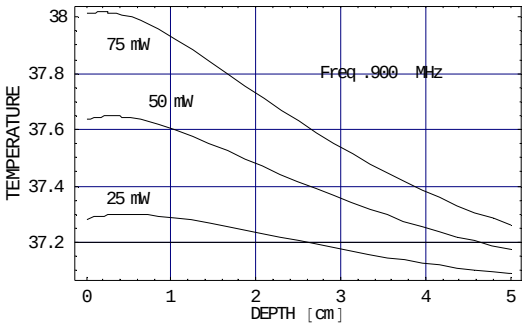

(e) Muscle temperature variation with Normal surface cooling

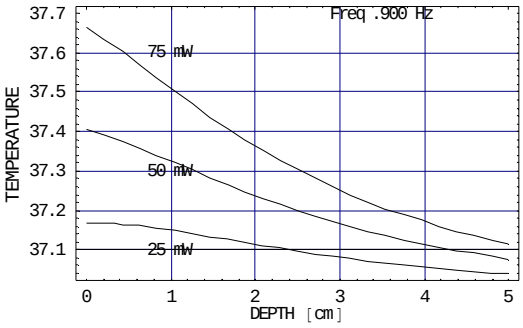

(f) Brain temperature variation with Normal surface cooling

Figure 6.27-Muscle and Brain temperature variations with depth for different surface cooling with Smart antenna at 900Hz.

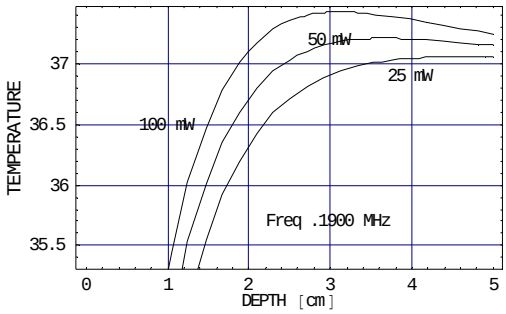

(a) Skin temperature variation with Extra surface cooling

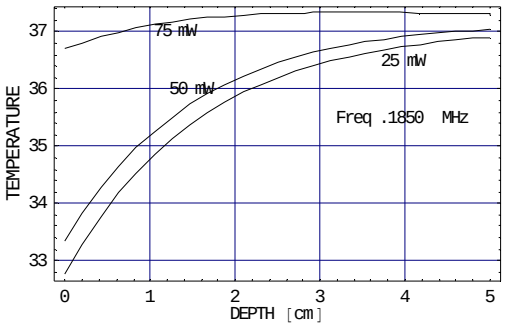

(b) Bone temperature variation with Extra surface cooling

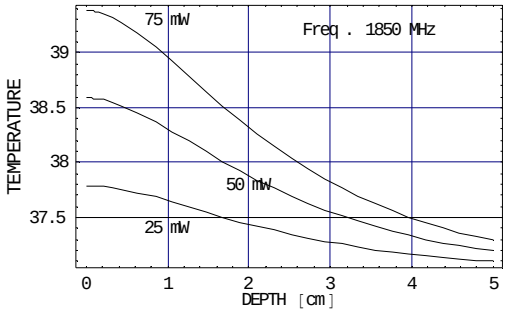

(c)Skin temperature variation with Low surface cooling

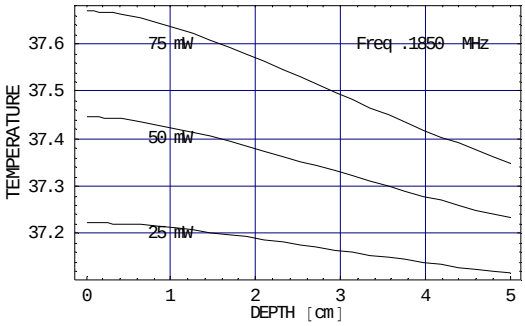

(d) Bone temperature variation with Low surface cooling

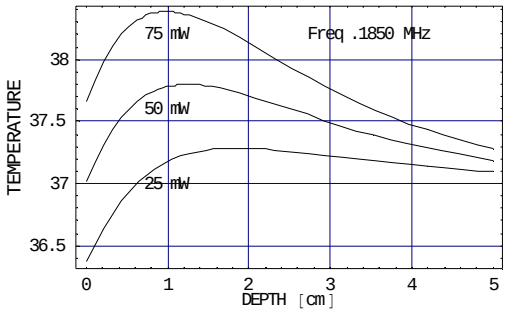

(e) Skin temperature variation with Normal surface cooling

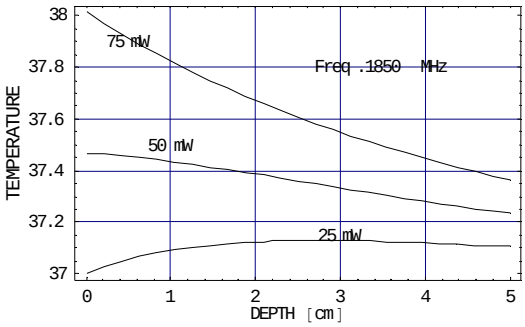

(f) Bone temperature variation with Normal surface cooling

Figure 6.28-Skin and Bone temperature variations with depth under different surface cooling conditions with Smart antenna at 1850MHz.

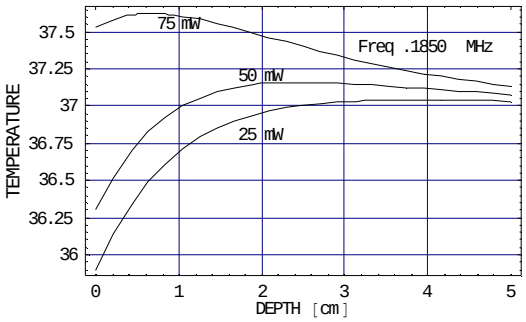

(a) Muscle temperature variation with Extra surface cooling

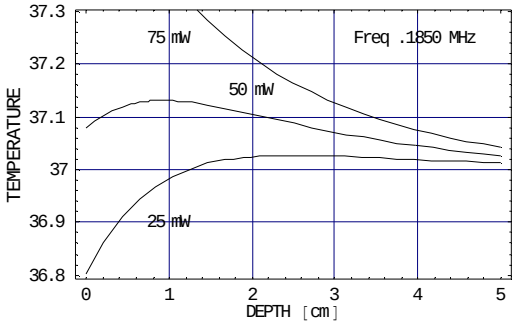

(b) Brain temperature variation with Extra surface cooling

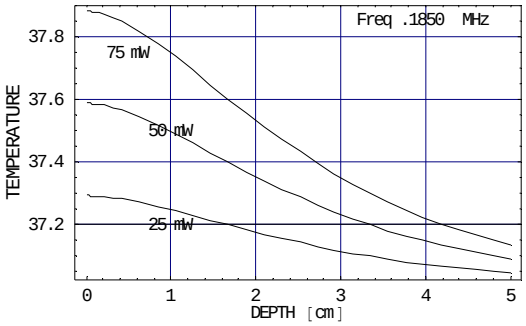

(c) Muscle temperature variation with Low surface cooling

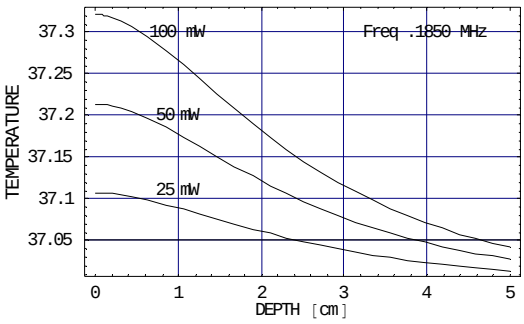

(d) Brain temperature variation with Low surface cooling

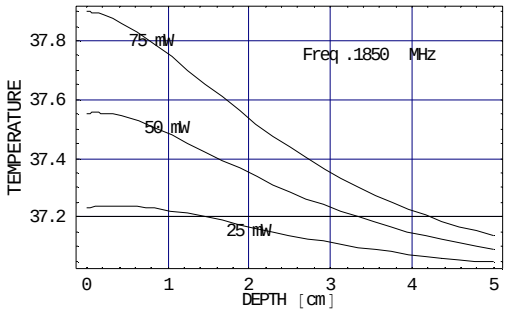

(e) Muscle temperature variation with Normal surface cooling

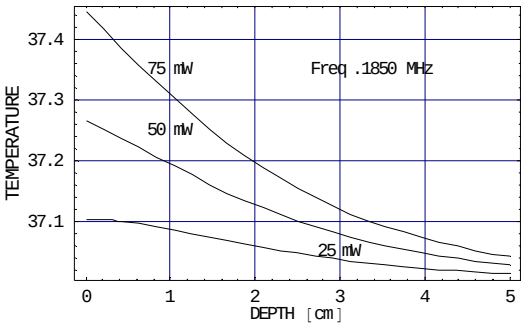

(f) Brain temperature variation with Normal surface cooling

Figure 6.29-Muscle and Brain temperature variations with depth for different surface cooling with Smart antenna at 1850MHz.

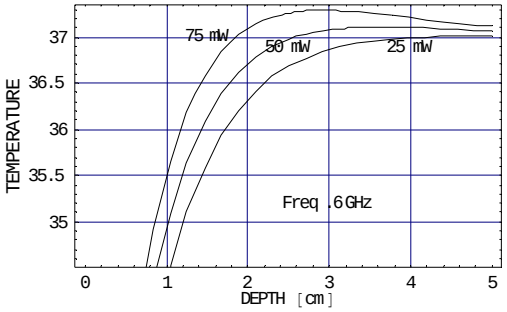

(a) Skin temperature variation with Extra surface cooling

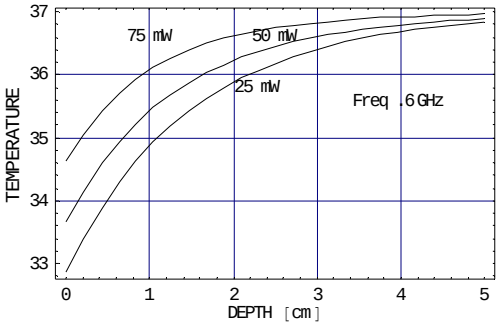

(b) Bone temperature variation with Extra surface cooling

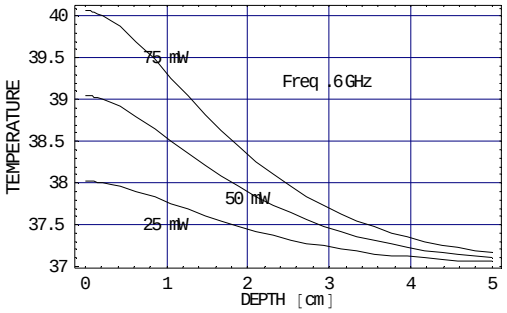

(c)Skin temperature variation with Low surface cooling

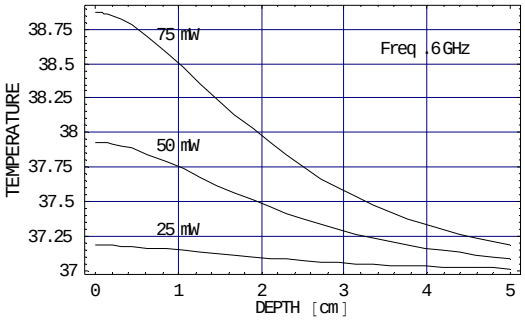

(d) Bone temperature variation with Low surface cooling

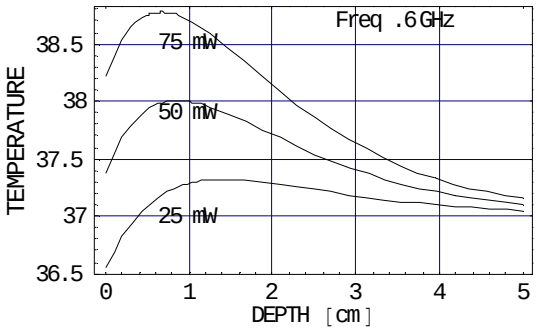

(e) Skin temperature variation with Normal surface cooling

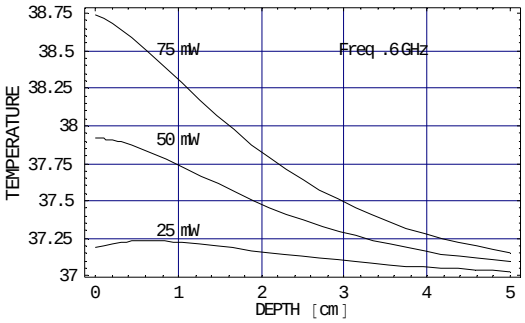

(f) Bone temperature variation with Normal surface cooling

Figure 6.30-Skin and Bone temperature variations with depth under different surface cooling conditions with Smart antenna at 6GHz.

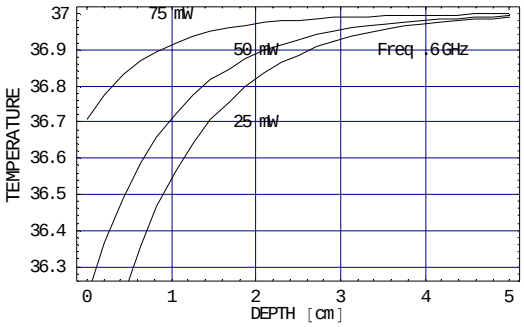

(a) Muscle temperature variation with Extra surface cooling

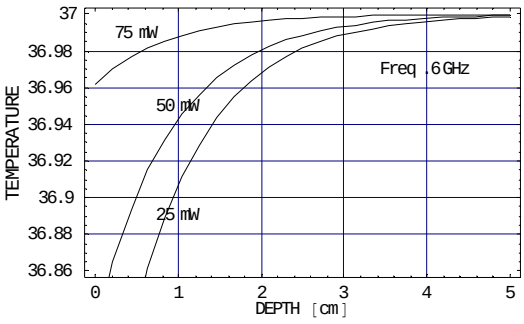

(b) Brain temperature variation with Extra surface cooling

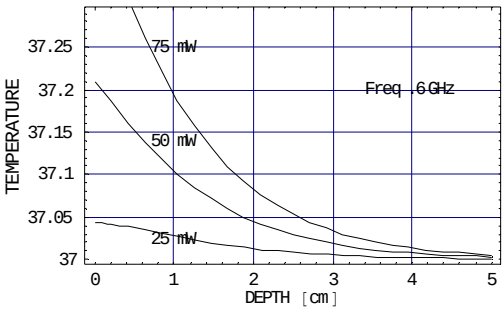

(c) Muscle temperature variation with Low surface cooling

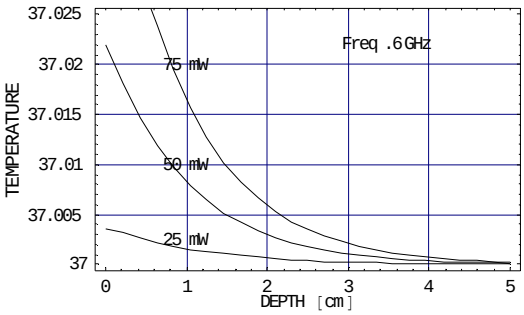

(d) Brain temperature variation with Low surface cooling

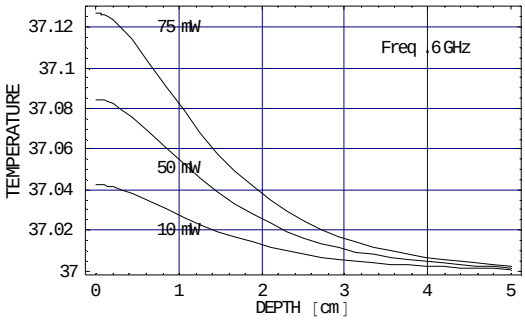

(e) Muscle temperature variation with Normal surface cooling

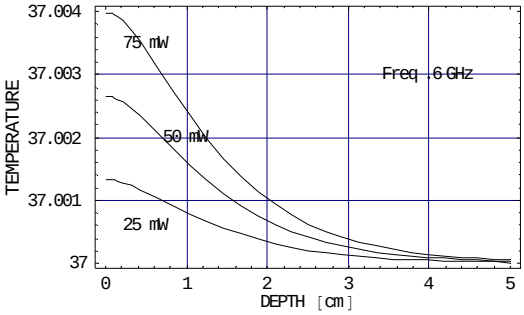

(f) Brain temperature variation with Normal surface cooling

Figure 6.31-Muscle and Brain temperature variations with depth under different surface cooling conditions with Smart antenna at 6GHz

Table-6.7: Peak temperatures in ^{0}C attained by the skin for the case of normal surface cooling

Frequency	Incident power density (mw/cm^2)			
	100	75	50	25
	Omni Antenna	*Adaptive Antenna*	*Adaptive Antenna*	*Adaptive Antenna*
900MHz	38.31	37.9	37.6	37.1
1850MHz	39.01	38.4	37.8	37.1
6GHz	39.55	38.8	38.1	37.1

Table-6.8: Peak temperatures in ^{0}C attained by the bone for the case of normal surface cooling

Frequency	Incident power density (mw/cm^2)			
	100	75	50	25
	Omni Antenna	*Adaptive Antenna*	*Adaptive Antenna*	*Adaptive Antenna*
900MHz	37.8	37.6	37.29	37.10
1850MHz	38.21	37.99	37.51	37.1
6GHz	39.1	38.8	37.92	37.25

Table-6.9: Peak temperatures in ^{0}C attained by the muscle for the case of normal surface cooling

Frequency	Incident power density (mw/cm^2)			
	100	75	50	25
	Omni Antenna	*Adaptive Antenna*	*Adaptive Antenna*	*Adaptive Antenna*
900MHz	38.22	38.0	37.7	37.31
1850MHz	38.10	37.9	37.58	37.20
6GHz	37.21	37.5	37.20	37.10

Table-6.10: Peak temperatures in ^{0}C attained by the brain for the case of normal surface cooling

Frequency	Incident power density (mw/cm^2)			
	100	75	50	25
	Omni Antenna	*Adaptive Antenna*	*Adaptive Antenna*	*Adaptive Antenna*
900MHz	37.8	37.7	37.4	37.12
1850MHz	37. 5	37.4	37.26	37.10
6GHz	37.03	37.025	37.022	37.004

6.11 RESULTS AND DISCUSSIONS

From the above analysis it is shown that by having smart antenna at the mobile handset, the most adverse effects of the RF fields can be reduced. For example at 900

MHz, the temperature rise of brain tissue can be reduced from 37.80^0 to 37.12^0 by the use of smart antenna at the handset, which can form a low or depressed side lobe towards the human head. It is found that frequency range from 1 MHz to 10 GHz is responsible for induced heating, resulting in the rise of tissues temperature more than 1^0. Induced heating in body may provoke various physiological and thermoregulatory responses including a decreased ability to perform mental or physical tasks as body temperature increases. Similar effects have been reported in people subjected to heat stress e.g. people working in hot environments and suffering from prolonged fever. Besides the thermal effects the EMR can induce non-thermal effects also into the body. There are some other reported Symptoms and diseases attributed to RF Fields [66, 73, 100, 102, 147].

International guidelines have also been established for limiting exposure to radio frequency non-ionizing radiation [66]. There is a maximum power the phone can use for communication, and it is called Telephone Communication Power (TCP). This is to ensure that the phones radiate sufficient power to work properly. The TCP is the figure of merit of a mobile phone, when it is transmitting. The higher the TCP, the better the phone will work in transmit mode. On the other hand, the possible radiation hazards are characterized in terms of a Specific Absorption Rate (SAR) distribution that should be as low as possible or at least below some standard limits. Both the TCP and the SAR are proportional to the maximum power that can be radiated by the phone. Therefore a high quality phone must provide a good compromise between high TCP and low SAR. This is possible by directing the radiation from the phone away from the head. The less absorption in the head, the lower is the SAR. So the best compromise between the high TCP and low SAR is to make the antenna radiate less power towards head [165] and adaptive handset at antenna will provide an optimum solution to the problem of high TCP and low SAR.

6.12 SUMMARY OF CHAPTER

The WHT devices include (but not limited to): handset in cellular systems, wireless local area networks access points and user terminals, PDA, Bluetooth access points and terminals and indoor wireless fixed point to point systems. Smart antenna on the handset can offer many benefits like increased coverage, data rates, reduced interference and increase in spectrum efficiency etc. But there is no work suggesting the control of radiation hazards using smart antenna. In this chapter by means of simple

mathematical calculations the power absorbed and their thermal profiles of head have been found. The use of smart antennas in reducing radiation hazards is proposed. The power absorbed and rise in temperature of various tissues of head is compared for omni directional as well as smart antenna. These results can serve as a guide for any antenna designer. The interaction of the handset antenna with the human head has been studied by modeling head as a homogeneous, semi-infinite and planar multilayered model of different tissues. In determining the temperature rise the effect of blood flow and transfer of heat from tissue into space is taken into account[1-5].

---

1. [P9]"Adaptive Antennas at the Cellular Mobile Handset for reduced deposition of power in Human Head", Proceedings of ***Workshop on Advances in Smart Antennas for Software Radios held in conjunction with 13th Annual Virginia Tech/MPRG Group Symposium on Wireless Personal Communications***, Virginia,pp.82-90, June 4-6 2003
2. [P10]"Use of adaptive Antenna at the cellular mobile handset for reduced radiation hazards" accepted at ***IEEE 9th Asia Pacific Conference on Communications, APCC2003*** *at* George town, Pena nag, Malaysia, September 21-24,2003
3. [P11]"Adaptive antennas at the mobile handset for reduced radiation hazards: An analysis" ***Proceedings of IEEE Vehicular Technology Conference, Fall 2003, Orlando, USA, pp.3154-3158, October 6-9, 2003***.**(Invited Paper)**
4. [P12]"Adaptive Antennas at the Cellular Mobile Handset for reduced SAR in Human Head" ***Proceedings of IEEE 6th International Symposium on Antennas, Propagation and EM theory, Beijing, China,*** pp.360-368, October 28-Nov 1, 2003.
5. [P7] "Adaptive Antenna at Wireless Communication Handheld Terminal For Reducing Power Deposition In Human Head" ***revised and submitted to Radio Science Journal, USA***

Chapter 7

CONCLUSIONS AND FUTURE SCOPE OF WORK

7.1 CONCLUSIONS

This thesis is an outcome of the studies performed towards developing beamforming algorithms for array processing architectures of *mobile and wireless communication* systems. The results presented in this thesis constituted four targets. First, new side lobe control beamforming algorithms suitable for array processing architectures of CDMA based systems are developed for interference reduction. These algorithms are analyzed and the advantages of these algorithms to array processing architectures are quantified. The second target of this thesis is the development and application of advanced array signal processing techniques to mobile and wireless communication systems that have a practical implementation complexity and achieve high performance levels. This work is prompted by the current thrust in mobile and wireless technology, to look for new approaches and technologies, to improve the performance of array processing architectures. The second target is achieved by development of FrFT based beamforming algorithm in non stationary environments, towards improving the performance of array processing architectures of adaptive antenna, from the point of view of reducing MSE and BER. The third target is the application of FrFT based arrays in MIMO systems. The reduction in channel estimation errors caused by Gaussian noise using FrFT based estimation is suggested. A new FrFT based receive beamformer is proposed which can be extended to design of joint transmit-receive beamforming. Lastly, the effectiveness of smart antenna in controlling radiation hazards at the handset is explored, in the light of establishing the advantages of smart antenna over a single antenna system at the handset. From the results of these extensive investigations the following algorithmic and quantitative conclusions are drawn which will enhance the current state of art in mobile and wireless communication technology. The contributions listed below are in the same order as they were presented in this thesis. However the detailed results and discussions

are presented in each chapter.

To begin with, it is shown that conventional arrays based on nulling procedure are unlikely to be applicable in practical CDMA based wireless communication systems even if their beamforming procedure is valid for coherent interferers. *In CDMA systems it is proposed that smart antenna will control interference by forming main lobe towards desired user and low/depressed side lobe towards the undesired users or interferers.* Hence narrow beam low side-lobe algorithms, which can taper array weights of any beamformer with suitable taper function, are considered appropriate for CDMA systems ***[P20]***. ***A new procedure for tapering in fractional Fourier domain is outlined. The resultant taper obtained is called FrFT Taper.*** *The FrFT taper is based upon the concept of multiplying two taper functions in some a^{th} domain and then forming the beam with weights obtained by taking inverse FrFT of the resultant of multiplication in some q^{th} domain.* ***The weights obtained by the FrFT taper are found to be practically realizable in all domains.*** **The FrFT taper can be used at the *front end of an antenna array system before adaptive array processing architecture in mobile and wireless communications [P8, P13, P18, P19]***. This idea of tapering gives more flexibility to antenna designer as FrFT taper is found to be more versatile (now only one parameter 'a' is to be varied to get a new taper with new radiation pattern) than fixed tapers. *Information capacity improvement offered by employing a tapered beamformer in wireless communication system is addressed in this research. A relationship between the information capacity with respect to a desired user's signal and the sensor array beam pattern is established. The capacity function is found to be having a one-to-one relationship with the beam pattern of the array and its salient features are directly related to those in the beam pattern. This function is used to analyze capacity in an interfering environment of wireless networks. This function provides a bound for the improvements in information capacity possible via the use of spatial filtering in CDMA based wireless communication systems. It is concluded, that for minimum drop in capacity as the angles of arrival of any interfering users move through the sidelobes, the maximum sidelobe level must be as low as possible*. ***A relationship between number of interferers and side lobe level of the beamformer is derived which can be used by antenna designer as a guideline for choosing side lobe level.*** It is established that any array processing algorithm which can decrease the maximum side lobe level equivalent to Chebyshev will definitely improve the capacity of CDMA based wireless communication system, where number of interferes are quite

large. ***A new method of synthesizing Chebyshev-like low side-lobe beam patterns with adjustable beamwidth and steering invariance is also proposed. The proposed matrix based algorithm called MBC (Multi Beam Constraint) is computationally efficient and is applicable where DOA of interferers could not be identified due to antenna array resolution [P16].*** *The MBC converges remarkably fast with in few iterations and provides a low side lobe level to all interferers in case they are uniformly distributed in the side lobe region. I*f the interferers are concentrated over a broad angle, the algorithm places a low side level in the direction of these interferes. *It is known that in case of large angular spread of interference a sharp null can not provide efficient interference suppression. But the MBC can form a broad low side lobe towards the direction of this largely spread interference.* It is also established through Monte Carlo simulations, that the array processing architecture based on proposed algorithm outperforms the other two, Chebyshev and adaptive beamformers in an interfering environment where a large number of interferers surround the array. *It is proposed from this study that the MBC algorithm which can decrease the maximum side lobe level equivalent to Chebyshev will definitely improve the performance of CDMA based wireless communication system, where the number of interferes is quite large.* It is shown that for number of interferers equal to 65, the proposed algorithm provides 2dB more array gain as compared to SMI algorithm [**P5**, **P15, P21, P22, P26**].

Another important aspect of beamforming algorithm and environment has been studied from a signal processing perspective. This interdisciplinary character is a major theme of this target that has resulted in the development of advanced array processing algorithm in non stationary mobile and wireless environments. Thus the key result is the derivation of the optimum FrFT based beamformer for multipath signals over AWGN channels. The proposed FrFT based optimum beamforming algorithm is developed with many important advantages; main among them is improved MSE performance relative to the time and frequency domain beamforming algorithms. The performance of FrFT beamformer is evaluated based on SNR of input signal and MSE. The proposed algorithm is shown to be capable of handling moving (producing Doppler shift in mobile wireless) and accelerating sources (producing chirped signal in wireless communication) effectively as compared to other frequency or time domain algorithms. In order to analyze the proposed new array signal processing algorithm statistical models for fading channels based on the characterization of different fading properties are considered The optimum FrFT beamformer is also evaluated in microcellular and

macro-cellular environments using GBSBE and GBSBC channel models. ***Simulation results have established that FrFT based beamformer performs better than the time domain or frequency domain beamformer under all channel impairments. It is concluded that there exists a domain in which the MSE is less as compared to any other frequency or time domain even for multipath fading signals over AWGN channel [P1-P2, P4, P6, P14]. Performance analysis results of the FrFT beamformer showed improved performance especially for low SNR*** [**P1-P2**, **P4**]. It is demonstrated that the proposed method yields improved results that are smaller MSE at all SNR, in a moving source scenario, which is common in mobile wireless communication. The percentage reduction in MSE for a moving source in FrFT domain as compared to frequency and time domain in various fading channels is shown in table 7.1. As shown in table 7.2 the proposed optimum FrFT domain beamformer can be used for yielding small errors in case of accelerating source problems which is common in wireless communication.

Table-7.1: Comparison of reduction in MSE of FrFT domain beamformer with frequency and time domain beamformer for a moving source

S.No	Type of Channel	FrFT beamformer Vs. Time domain beamformer		FrFT beamformer Vs. Frequency domain beamformer	
		Min	Max	Min	Max
1	AWGN	39.5%	46.4%	86.8%	89.0%
2.	Rayleigh	36.6%	46.2%	84.8%	87.5%
3.	Ricean	39.0%	47.1%	89.4%	91.7%
4.	Nakagami	40.8%	46.6%	86.1%	87.9%
5.	GBSBE	38.4%	46.5%	87.0%	88.9%
6.	GBSBC	38.1%	45.4%	86.6%	89.3%

Table-7.2: Comparison of reduction in MSE of FrFT domain beamformer with frequency and time domain beamforming for an accelerating source

S.No	Type of Channel	FrFT beamformer Vs. Time domain beamformer		FrFT beamformer Vs. Frequency domain beamformer	
		Min	Max	Min	Max
1	AWGN	37.2%	47.7%	86.6%	88.6%
2.	Rayleigh	40.0%	45.9%	85.7%	87.7%
3.	Ricean	39.2%	47.0%	89.4%	91.7%
4.	Nakagami	40.5%	46.6%	86.3%	88.7%
5.	GBSBE	41.2%	46.4%	87.6%	89.6%
6.	GBSBC	40.9%	45.9%	87.1%	88.8%

Simulation results for different fading channels demonstrate the merits of the algorithm. The existing beamforming algorithms are not very effective in rapidly time-varying channels, while the FrFT based algorithm maintains superiority over the existing algorithms in time varying channels in terms of MSE. In this entire work it is assumed that velocity and acceleration of the source is known at the array processor.

The FrFT beamformer also provides increased output SNR and array gain as compared to frequency domain and time domain beamformer in AWGN environment [**P17**]. ***The BER performance of FrFT beamformer is also studied in an interfering environment for one transmitting and large number of receiving antennas as in SIMO system. The BER of FrFT beamformer is found to be less than time domain or frequency domain beamformer in case of Rayleigh and Nakagami faded channels.*** The improvement obtained by optimum FrFT beamformer over other optimal beamformers is demonstrated through Monte Carlo simulations. It is shown that FrFT beamformer requires 1.3 dB less input power as compared to time domain beamformer for a BER of 10^{-2} with 3 receive diversity branches. In case of four diversity branches and for a BER of 10^{-2} optimum FrFT Beamformer requires 4 dB and 9 dB less input power as compared to time and frequency domain beamformer. The improvement is 5 dB and 10 dB in optimum FrFT domain as compared to time and frequency domain for five receiving antennas. The same results are obtained for Nakagami faded channel also. ***It is shown that FrFT beamformer requires less input power as compared to time and frequency domain beamformer. Based on simulation results obtained it is concluded that FrFT beamformer shall become an integral part of next generation mobile and wireless communication systems as it can decrease BER further as compared to time or frequency domain beamformer[P25].***

A brief overview of MIMO systems is given with help of simulations. STD is considered to be an efficient signaling strategy for MIMO systems without channel state information at transmitter [**P23**]. With STD a large diversity gain and a high transmission rate can be achieved but it requires perfect CSIR. The performance of STD falls by 3 dB as compared to MRC due to imperfect channel estimation. ***A new FrFT based channel estimation technique using PSAM is proposed. The FrFT based channel estimation provides a gain of 1.2 dB over time domain estimation and about 5.3 dB over frequency domain estimation. The estimation error to signal ratio can be decreased effectively by use of FrFT based estimation [P24].***

A new FrFT based receive beamformer is proposed for spatial multiplexed and rate one Orthogonal Space Time Block Coded MIMO systems. The proposed optimal FrFT based receive beamformer can be put at the front end of the MIMO receiver in these systems. Each receiving antenna has an OFMRB at its front end which gives the optimum output with weights $\boldsymbol{w}$ calculated in FrFT domain. The performance of the receive beamformer is studied for 2×2 and 4×4 spatial multiplexed systems. The proposed OFMRB outperforms the simple MMSE receiver in terms of BER and BLER. The performance improvement in terms of BER is summarized in table 7.3. Similarly the performance improvement in terms of BLER is given in table 7.4.

Table.7.3: Improvement achieved by proposed beamformer in terms of BER

Type of MIMO system	Gain of OFMRB over (Target BER $\leq 10^{-2}$)	
	Time Domain RX beamformer	Freq. Domain RX beamformer
2×2 SM system	2.9dB	1.7dB
4×4 SM system	2.7dB	2.3dB

Table.7.4: Improvement achieved by proposed beamformer in terms of BLER

Type of MIMO system	Gain of OFMRB over (Target BLER ≤ 10%)	
	Time Domain RX beamformer	Freq. Domain RX beamformer
2×2 SM system	2.6dB	2.9dB
4×4 SM system	4.1dB	3.4dB

It is proposed that OFMRB shall replace the time and frequency domain MMSE receive beamformer in spatial multiplexed systems as it provides less BER and BLER as compared to both MMSE based time and frequency domain receive beamformers [P26].

The Alamouti's scheme with MMSE receiver is proposed. It is shown through simulation that the performance of OSTBC system remains same, whether we use ML receiver or MMSE receiver. The performance of rate one OSTBC system is also studied with OFMRB. It is again shown that OFMRB outperforms both time and frequency domain beamformers in terms of BLER. The OFMRB offers a gain of 1 dB and 1.5 dB over time domain beamformer for both rate one 2×1 and 2×2 OSTBC systems.

A novel concept of reducing RF hazards using adaptive antenna at handset is proposed. The basic idea is that through the use of adaptive beamforming techniques, a handheld radio with an antenna array can receive a desired signal while rejecting interfering signal, which is considered as reflection from head. It is shown that at all frequencies the head reflects back approximately 50% of the incident power. This reflected signal can be considered as the interference at the same frequency. Using a

planar multilayer model for human head and with normally incident plane wave it is observed that about 48% of the incident power is absorbed by human head at all frequencies. The 13% & 8% of the incident power reaches brain at 900 MHz and 1850 MHz respectively, where as 0.04% of the incident power reaches brain at 6 GHz. *It is shown that higher frequency band is suitable for mobile communications from point of view of reducing RF hazards.* ***It is established that by use of adaptive antennas at the handset the power absorbed by various tissues can be decreased.***

The thermal profiles of the head tissues have been found for steady state condition using bio-heat transfer equation. The temperature rise of the various tissues due to incident power density has been found taking into account the effect of blood flow and surface cooling. ***It is found that higher frequencies produce peak temperatures nearer to the surface and produce high surface heating. The lower frequencies produce lower peak temperatures but are located deep inside the tissues. As incident microwave power density is increased the peak temperature increases and move towards surface. Shaping the radiation pattern such that less power is directed towards head can decrease the magnitude of peak temperatures and its location. It is established that the flow of blood does have significant effect on temperature profiles. Therefore, irradiation of actual muscles and of artificial models with same characteristics results in different thermal profiles of two.***

With the use of adaptive antennas at handset the power absorbed by brain reduces to 3.2% of the incident power at 900 MHz as compared to 13% in case of omni-directional antenna. The adaptive antenna here reduces the power incident on head to one- fourth of the power radiated by omni directional antenna. *It is established that by using an adaptive antenna at handset with reduced incident power density the temperature rise can be effectively controlled.* The peak temperature attained by the brain tissues are given below in table 7.5. It is established that future mobile handset employing adaptive antenna could also reduce the RF hazards [**P7, P9, P10, P11, P12**].

Table- 7.5: Peak temperature attained by brain tissue with conventional and adaptive antenna

Freq. of operation	**Peak brain tissue temperature by use of**			
	Omni Antenna with incident power density 100mw/cm^2	***Adaptive Antenna with incident power density 75mw/cm^2***	***Adaptive Antenna with incident power density 50mw/cm^2***	***Adaptive Antenna with incident power density 100mw/cm^2***
900MHz	37.8^{0}C	37.7^{0}C	37.4^{0}C	37.12^{0}C
1850MHz	37. 5^{0}C	37.4^{0}C	37.26^{0}C	37.10^{0}C
6GHz	37.03^{0}C	37.025^{0}C	37.022^{0}C	37.004^{0}C

7.2 FUTURE SCOPE OF WORK

Although this thesis has answered several questions related to the development of algorithms & signal processing techniques for array processing architecture of mobile wireless systems, several topics that can be explored in future are listed below:

The validation of various low side-lobe design techniques suggested is the next logical step. The array processing architecture will lend itself well to this segment of research. Using the array, the data can be collected and the proposed technique can be validated. The simulated results of the performance metrics about the array processing architectures can be compared to the actual measurements.

The optimum FrFT based beamformer for multipath signals over AWGN channels is based on the parameter ‘a’. The proposed method of obtaining optimum 'a' is based upon frame by frame basis on the basis of calculating the MSE for sufficiently closely spaced discrete values of ‘a’ (for example, by step size of 0.1). In practice the optimum 'a' that gives minimum MSE requires an efficient on-line procedure for its efficient computation which can be taken up as a research problem for further study.

All analyses in this thesis are primarily based on outdoor propagation environments. Future research may apply the techniques developed in this thesis to different environments in order to further test these techniques. The BER of BPSK in SIMO system using FrFT based beamformer is found in slow flat faded channel but the technique can be extended for BPSK and other modulation techniques in frequency selective channels also to find SER. The practical implementation of FrFT based optimal beamformer can be taken up as a research problem.

In this thesis FrFT based receive beamformer is proposed. The joint optimal FrFT based transmit receive processing can be taken up as a research issue by which one can design optimal precoder in FrFT domain. Beamforming gain domain in a MIMO system using maximum singular value of channel in optimum FrFT can be explored further.

In this thesis the head has been modeled as planar multilayer model. For more accurate results the head can be modeled as sphere and power reaching various tissues and thermal profiles can be found. The thermal profiles presented in this study correspond to steady state condition; the transient analysis of these thermal profiles can be taken up as further research issue.

Appendix-A

Noise Corruption Leads to Partial Correlation of Signals

Assume $s_1(t)$ and $s_2(t)$ are correlated signals with variances σ_1 and σ_2. The normalized correlation coefficient of $s_1(t)$ and $s_2(t)$ is given by

$$r_{s_1 s_2}(t_1, t_2) = \frac{E[s_1(t_1) s_2(t_2)]}{\sqrt{\sigma_1 \sigma_2}} \quad . \tag{A.1}$$

Now assume noise is added to these signals. Noise is assumed to be uncorrelated with the signals. So we have now

$$y_1(t) = s_1(t) + n_1(t), \quad \text{and} \quad y_2(t) = s_2(t) + n_2(t). \tag{A.2}$$

Let noise n_1 and n_2 is zero mean and with variances σ_{n_1} and σ_{n_2} respectively. The cross correlation of $y_1(t)$ and $y_2(t)$ is given by

$$R_{y_1,y_2}(t_1, t_2) = E[y_1(t) y_2(t)],$$

$$= E[s_1(t) s_2(t)] + E[s_1(t) n_2(t)] + E[s_2(t) n_1(t)] + E[n_1(t) n_2(t)],$$

$$R_{y_1,y_2}(t_1, t_2) = R_{s_1 s_2}(t_1, t_2) + R_{s_1 n_2}(t_1, t_2) + R_{s_2 n_1}(t_1, t_2) + R_{n_1 n_2}(t_1, t_2). \tag{A.3}$$

In equation second and third term are zero since signal and noise are uncorrelated. Fourth term is also zero, since noise of one sensor is assumed to be uncorrelated to noise of other sensor. Therefore

$$R_{y_1,y_2}(t_1, t_2) = R_{s_1 s_2}(t_1, t_2). \tag{A.4}$$

Now variance of $y_1(t)$

$$E[y_1^2(t)] = E[s_1(t) + n_1(t)]^2 = E[s_1^2(t)] + E[n_1^2(t)] + 2E[s_1(t) n_1(t)],$$

$$\sigma_{y_1} = \sigma_1 + \sigma_{n_1} \quad . \tag{A.5}$$

Similarly for $y_2(t)$ $\qquad \sigma_{y_2} = E[y_2^2(t)] = \sigma_2 + \sigma_{n_2}$. (A.6)

Therefore, normalized cross correlation is given by

$$r_{y_1,y_2}(t_1, t_2) = \frac{R_{y_1,y_2}(t_1, t_2)}{\sqrt{\sigma_{y_1} \sigma_{y_2}}}. \tag{A.7}$$

Using equation (A.4) in (A.7) $\qquad r_{y_1,y_2}(t_1, t_2) = \frac{R_{s_1 s_2}(t_1, t_2)}{\sqrt{(\sigma_1 + \sigma_{n_1})(\sigma_2 + \sigma_{n_2})}}$. (A.8)

Comparing (A.1) and (A.8) we can see that numerator remains same but denominator in (A.8) is larger as compared to (A.1). Hence correlation is reduced.

Appendix-B

Choice of K in a wideband beamformer:

Consider a N tap causal FIR filter with x(n) as input and y(n) as output. The transfer function of FIR causal filter having N taps is given by

$$H(z) = \sum_{n=0}^{N-1} h(n) z^{-n} , \tag{B.1}$$

where, h(n) is the impulse response of filter.

The output of filter is given by

$$y(iT) = \sum_{n=0}^{N-1} h(n) x(iT - nT) . \tag{B.2}$$

(B.1) can be written as

$$H(e^{j\omega T}) = \sum_{n=0}^{N-1} h(n) e^{-j\omega nT} . \tag{B.3}$$

$$M(\omega) = \left| H(e^{j\omega T}) \right| = \left| H e^{-j\omega T} \right| \theta(\omega) = -\theta(-\omega) .$$

$$\text{Phase delay} = \tau_p = -\frac{\theta(\omega)}{\omega} , \qquad \text{Group delay} = \tau_g = -\frac{d\theta(\omega)}{d\omega} . \tag{B.4}$$

Group delay is the delayed response of the filter as a function of ω to a signal. Filters for which τ_p and τ_g are constant, are called constant time delay or linear phase filters. Therefore for phase to linear

$$\theta(\omega) = -\tau\omega \qquad\qquad -\pi \langle \omega \langle \pi , \tag{B.5}$$

where, τ = constant phase delay of samples. From (B.3)

$$H(e^{j\omega}) = \sum_{n=0}^{N-1} h(n) e^{-j\omega n} = \pm \left| H(e^{j\omega}) \right| e^{-jz\omega} . \tag{B.6}$$

$$\theta(\omega) = -\tau\omega = \tan^{-1} = -\frac{\sum_{n=0}^{N-1} h(n) \sin \omega nT}{\sum_{n=0}^{N-1} h(n) \cos \omega nT} . \tag{B.7}$$

$$\sum_{n=0}^{N-1} h(n)(\cos \omega nT \sin \omega\tau - \sin \omega nT \cos \omega\tau) = 0 . \tag{B.8}$$

Finally we get $$\sum_{n=0}^{N-1} h(n) \sin(\omega\tau - \omega nT) = 0 . \tag{B.9}$$

Solution of (B.9) is given by $\tau = \frac{(N-1)T}{2}$, (B.10)

and $h(n) = h(N-1-n)$ for $0 < n < N-1$. (B.11)

Thus the number of taps is equal to the length of the channel divided by the symbol rate. The tapped delay allows each element to have a phase response that varies with frequency, compensating for the fact that lower frequency signal components have less phase shift for a given propagation distance where as higher frequency signal components have greater phase shift as they travel the same length. This makes the response of array the same across different frequencies.

For a linearly constrained wideband beamformer the K is defined as follows:

A processor having *M* sensors and *K* taps per sensor has MK weights and requires ***K*** constraints to determine its look direction frequency response. The remaining MK- *K* degrees of freedom in choosing the weights may be used to minimize the total power in the array output. Since the look-direction frequency response is fixed by the *K* constraints, minimization of the total output power is equivalent tom minimizing the non look- direction noise power, so long as the set of signal voltages at the taps is uncorrelated with the set of noise voltages at these taps.

[Otis Lamont Frost, "An Algorithm for Linearly Constrained Adaptive Array Processing", Proceedings of the IEEE, Vol. 60, No. 8, August 1972]

Appendix-C

The MVDR Beamformer minimizes total output power

$$P = E\left[\left|\boldsymbol{w}^H \boldsymbol{x}(n)\right|^2\right] = \boldsymbol{w}^H \boldsymbol{R}_x \boldsymbol{w}, \quad \text{(C.1)}$$

subject to constraint $\boldsymbol{w}^H \boldsymbol{v}(\theta_s) = 1$.

$$\hat{\boldsymbol{w}}_0 = \frac{\boldsymbol{R}_x^{-1}\boldsymbol{v}(\theta_s)}{\boldsymbol{v}^H(\theta_s)\boldsymbol{R}_x^{-1}\boldsymbol{v}(\theta_s)} \quad . \quad \text{(C.2)}$$

In case the estimate of $\boldsymbol{R}_{i+n}$ is available then the optimum weight vector is given by

$$\boldsymbol{w}_0 = \frac{\boldsymbol{R}_{i+n}^{-1}\boldsymbol{v}(\theta_s)}{\boldsymbol{v}^H(\theta_s)\boldsymbol{R}_{i+n}^{-1}\boldsymbol{v}(\theta_s)} \quad . \quad \text{(C.3)}$$

Theoretically both weight vectors are identical $\boldsymbol{w}_0 = \hat{\boldsymbol{w}}_0$. (C.4)

Proof:

Let the received signal be given by $x(t) = s(t) + n(t) + i(t)$, (C.5)

where, s(t), n(t) and i(t) are desired, noise and interference signals respectively. Then received correlation matrix is given by

$$\boldsymbol{R}_x = \boldsymbol{s}\boldsymbol{s}^H + \sigma_n^2 \boldsymbol{I} + \boldsymbol{R}_I = \boldsymbol{s}\boldsymbol{s}^H + \boldsymbol{R}_{i+n}, \quad \text{(C.6)}$$

where, $\boldsymbol{s}$ is received signal vector and $\boldsymbol{R}_{i+n}$ is noise plus interference correlation matrix. The proof of the statement $\boldsymbol{w}_0 = \hat{\boldsymbol{w}}_0$ is given using matrix inversion lemma.

Matrix Inversion Lemma:

Lemma: Let $\boldsymbol{A}$ be an N x N invertible matrix and let $\boldsymbol{x}$ and $\boldsymbol{y}$ be two N x 1 vectors s.t $(\boldsymbol{A} + \boldsymbol{x}\boldsymbol{y}^H)$ is invertible then

$$(\boldsymbol{A} + \boldsymbol{x}\boldsymbol{y})^{-1} = \boldsymbol{A}^{-1} - \frac{\boldsymbol{A}^{-1}\boldsymbol{x}\boldsymbol{y}^H\boldsymbol{A}^{-1}}{1 + \boldsymbol{y}^H\boldsymbol{A}^{-1}\boldsymbol{x}}. \quad \text{(C.7)}$$

Proof: $\boldsymbol{A} + \boldsymbol{x}\boldsymbol{y}^H = \boldsymbol{A}(\boldsymbol{I} + \boldsymbol{A}^{-1}\boldsymbol{x}\boldsymbol{y}^H)$.

$$(\boldsymbol{A} + \boldsymbol{x}\boldsymbol{y}^H)^{-1} = (\boldsymbol{I} + \boldsymbol{A}^{-1}\boldsymbol{x}\boldsymbol{y}^H)^{-1}\boldsymbol{A}^{-1}. \quad \text{(C.8)}$$

If matrix $(\boldsymbol{I} + \boldsymbol{A})$ is invertible then $(\boldsymbol{I} + \boldsymbol{A})^{-1} = \boldsymbol{I} - \boldsymbol{A} + \boldsymbol{A}^2 - \boldsymbol{A}^3 + \ldots\ldots\ldots$,

Therefore, $(\boldsymbol{I} + \boldsymbol{A}^{-1}\boldsymbol{x}\boldsymbol{y}^H)^{-1} = \boldsymbol{I} - \boldsymbol{A}^{-1}\boldsymbol{x}\boldsymbol{y}^H + (\boldsymbol{A}^{-1}\boldsymbol{x}\boldsymbol{y}^H)^2 - (\boldsymbol{A}^{-1}\boldsymbol{x}\boldsymbol{y}^H)^3 + \ldots\ldots\ldots$,

Since $(\boldsymbol{I} + \boldsymbol{A}^{-1}\boldsymbol{x}\boldsymbol{y}^H)$ is invertible. Therefore, substituting in (C.2)

$$(\boldsymbol{A} + \boldsymbol{x}\boldsymbol{y}^H)^{-1} = \boldsymbol{A}^{-1} - \boldsymbol{A}^{-1}\boldsymbol{x}\boldsymbol{y}^H\boldsymbol{A}^{-1} + \boldsymbol{A}^{-1}\boldsymbol{x}(\boldsymbol{y}^H\boldsymbol{A}^{-1}\boldsymbol{x})\boldsymbol{y}^H\boldsymbol{A}^{-1} - \ldots\ldots\ldots,$$

$$= \boldsymbol{A}^{-1} - \boldsymbol{A}^{-1}\boldsymbol{x}\boldsymbol{y}^{\mathrm{H}}\boldsymbol{A}^{-1}\left[1 - \boldsymbol{y}^{\mathrm{H}}\boldsymbol{A}^{-1}\boldsymbol{x} + (\boldsymbol{y}^{\mathrm{H}}\boldsymbol{A}^{-1}\boldsymbol{x})^{2} - .....\right],$$

$$= \boldsymbol{A}^{-1} - \frac{\boldsymbol{A}^{-1}\boldsymbol{x}\boldsymbol{y}^{\mathrm{H}}\boldsymbol{A}^{-1}}{1 + \boldsymbol{y}^{\mathrm{H}}\boldsymbol{A}^{-1}\boldsymbol{x}}. \qquad \text{(C.9)}$$

Since the scalar $\boldsymbol{y}^{\mathrm{H}}\boldsymbol{A}^{-1}\boldsymbol{x} \neq 1$, due to invertibility of $(\boldsymbol{I} + \boldsymbol{A}^{-1}\boldsymbol{x}\boldsymbol{y}^{\mathrm{H}})$. Therefore,

$$(\boldsymbol{A} + \boldsymbol{x}\boldsymbol{y}^{\mathrm{H}}) = \boldsymbol{A}^{-1} - \frac{(\boldsymbol{A}^{-1}\boldsymbol{x}\boldsymbol{y}^{\mathrm{H}}\boldsymbol{A}^{-1})}{1 + \boldsymbol{y}^{\mathrm{H}}\boldsymbol{A}^{-1}\boldsymbol{x}}. \qquad \text{(Proved)}$$

From (C.6), $\boldsymbol{R}_{\mathrm{x}} = \boldsymbol{s}\boldsymbol{s}^{\boldsymbol{H}} + \boldsymbol{R}_{\mathrm{i+n}}$ using Matrix Inversion Lemma**,** We have

$$\boldsymbol{R}_{\mathrm{x}}^{-1} = \boldsymbol{R}_{\mathrm{i+n}}^{-1} - \frac{\boldsymbol{R}_{\mathrm{i+n}}^{-1}\boldsymbol{s}\boldsymbol{s}^{\mathrm{H}}\boldsymbol{R}_{\mathrm{i+n}}^{-1}}{1 + \boldsymbol{s}^{\mathrm{H}}\boldsymbol{R}_{\mathrm{i+n}}^{-1}\boldsymbol{s}}. \qquad \text{(C.10)}$$

$$\boldsymbol{s}^{\mathrm{H}}\boldsymbol{R}_{\mathrm{x}}^{-1}\boldsymbol{s} = \boldsymbol{s}^{\mathrm{H}}\boldsymbol{R}_{\mathrm{i+n}}^{-1}\boldsymbol{s} - \frac{(\boldsymbol{s}^{\mathrm{H}}\boldsymbol{R}_{\mathrm{i+n}}^{-1}\boldsymbol{s})^{2}}{1 + \boldsymbol{s}^{\mathrm{H}}\boldsymbol{R}_{\mathrm{i+n}}^{-1}\boldsymbol{s}},$$

$$\boldsymbol{s}^{\mathrm{H}}\boldsymbol{R}_{\mathrm{x}}^{-1}\boldsymbol{s} = \frac{\boldsymbol{s}^{\mathrm{H}}\boldsymbol{R}_{\mathrm{i+n}}^{-1}\boldsymbol{s}}{1 + \boldsymbol{s}^{\mathrm{H}}\boldsymbol{R}_{\mathrm{i+n}}^{-1}\boldsymbol{s}}. \qquad \text{(C.11)}$$

Similarly

$$\boldsymbol{R}_{\mathrm{x}}^{-1}\boldsymbol{s} = \boldsymbol{R}_{\mathrm{i+n}}^{-1}\boldsymbol{s} - \frac{\boldsymbol{R}_{\mathrm{i+n}}^{-1}\boldsymbol{s}\boldsymbol{s}^{\mathrm{H}}\boldsymbol{R}_{\mathrm{i+n}}}{1 + \mathrm{s}^{\mathrm{H}}\mathrm{R}_{\mathrm{i+n}}^{-1}\mathrm{s}},$$

$$= \frac{\boldsymbol{R}_{\mathrm{i+n}}^{-1}\boldsymbol{s} + \boldsymbol{s}^{\mathrm{H}}(\boldsymbol{R}_{\mathrm{i+n}}^{-1}\boldsymbol{s})^{2} - \boldsymbol{s}^{\mathrm{H}}(\boldsymbol{R}_{\mathrm{i+n}}^{-1}\boldsymbol{s})^{2}}{1 + \boldsymbol{s}^{\mathrm{H}}\boldsymbol{R}_{\mathrm{i+n}}^{-1}\boldsymbol{s}} = \frac{\boldsymbol{R}_{\mathrm{i+n}}^{-1}\boldsymbol{s}}{1 + \boldsymbol{s}^{\mathrm{H}}\boldsymbol{R}_{\mathrm{i+n}}^{-1}\boldsymbol{s}}. \qquad \text{(C.12)}$$

Therefore

$$\frac{\boldsymbol{R}_{\mathrm{x}}^{-1}\boldsymbol{s}}{\boldsymbol{s}^{\mathrm{H}}\boldsymbol{R}_{\mathrm{x}}^{-1}\boldsymbol{s}} = \frac{\boldsymbol{R}_{\mathrm{i+n}}^{-1}\boldsymbol{s}}{\boldsymbol{s}^{\mathrm{H}}\boldsymbol{R}_{\mathrm{i+n}}^{-1}\boldsymbol{s}} \qquad \text{(C.13)}$$

Hence optimal weights by two methods are equivalent.

APPENDIX-D

Derivation of the Orthogonal System

As pointed out in (4.166), the polynomials $1, x, x^2, ..., x^{N_{\min}} - 1$ in the Hilbert Space $\rho_\theta^{N_{\min}}$, with inner product and norm given by (4.174) and (4.175), respectively, are linearly independent. Therefore, we can apply the Gram–Schmidt procedure to obtain the orthogonal systems as follows. First, polynomial 1 gives the function as follows:

$$1 \to \phi_0(x,\theta) = 1. \tag{D.1}$$

The polynomial produces the second function by

$$x \to \phi_0(x,\theta) = x - \frac{\langle x, \phi_0(x,\theta)\rangle}{\|\phi_0\|_\theta^2}\phi_0(x,\theta). \tag{D.2}$$

In general, the polynomial $x^n \quad for \quad n = 0,..., N_{\min} - 1$ for transforms into

$$x^n \to \phi_n(x,\theta) = x^n - \sum_{j=0}^{n-1} \frac{\langle x^n, \phi_j(x,\theta)\rangle}{\|\phi_j\|_\theta^2}\phi_j(x,\theta). \tag{D.3}$$

Now, adopting the following notation for polynomials:

$$\phi_n(x,\theta) = \phi_{n,0}(\theta) + \phi_{n,1}(\theta)x + \cdots + \phi_{n,n}(\theta)x^n. \tag{D.4}$$

The norm square of $\phi_n(x,\theta)$ can be expressed as

$$\|\phi_n\|_\theta^2 = \sum_{l=0}^{n}\sum_{m=0}^{n}\phi_{n,1}(\theta)\phi_{n,m}(\theta)\langle x^1, x^m\rangle. \tag{D.5}$$

Using the inner product (D.2) with $z(x,\theta) = \psi(x,\theta)$, $\|\phi_n\|_\theta^2$, becomes

$$\|\phi_n\|_\theta^2 = \sum_{l=0}^{n}\sum_{m=0}^{n}\phi_{n,1}(\theta)\phi_{n,m}(\theta)G_{l+m}(\theta), \tag{D.6}$$

where

$$G_k(\theta) \underline{\Delta}\int_0^\infty x^{k+N_{\max}-N_{\min}} e^{-x}\psi(x,\theta)dx. \tag{D.7}$$

A closed-form expression for $G_k(\theta)$ can be derived starting from the integrals

$$\int_0^\infty x^k e^{-x}\frac{x+a}{x+a+b}dx = k! - b\left[(-1)^{k-1}(a+b)^k \times e^{a+b}Ei(-a-b) + \sum_{m=1}^{k}(m-1)!(-a-b)^{k-m}\right], \tag{D.8}$$

where $E_i(.)$ is the exponential integral function. Using (D.8) in (D.7) and the relations between the exponential integral function and the incomplete Gamma function $\Gamma(a,z)$, we finally have

$$G_{k-N_{max}+N_{max}}(\theta) = \varsigma(\theta)^{k_e\varsigma(\theta)}\, k!\left[\varsigma(\theta)(1+k)\times\Gamma(-1-k,\varsigma(\theta)+\sigma_w^2(-k,\varsigma(\theta)\right], \qquad \text{(D.9)}$$

where, $\varsigma(\theta) = c_{MPSK}\dfrac{1}{(\sin^2\theta)}$. The coefficients $\phi_{n,m}(\theta)$ can be calculated iteratively using the following formula, which we derive as follows. Substituting (D.4) into (D.3) gives

$$\phi_n(x,\theta) = x^n - \sum_{j=0}^{n-1}\frac{1}{\left\|\phi_j\right\|_\theta^2}\left\langle x^n, \sum_{k=0}^{j}\phi_{j,k}(\theta)x^k\right\rangle\times\sum_{m=0}^{j}\phi_{j,m}(\theta)x^m,$$

$$= x^n - \sum_{j=0}^{n-1}\frac{1}{\left\|\phi_j\right\|_\theta^2}\sum_{k=0}^{j}\phi_{j,k}(\theta)\left\langle x^n, x^k\right\rangle\times\sum_{m=0}^{j}\phi_{j,m}(\theta)x^m .$$

Once again, using the inner product (4.164) with $z(x,\theta) = \psi(x,\theta)$, we have

$$\phi_n(x,\theta) = x^n - \sum_{m=0}^{n-1}\left[\sum_{j=m}^{n-1}\frac{1}{\left\|\phi_j\right\|_\theta^2}\phi_{j,m}(\theta)\times\sum_{j=0}^{j}\phi_{j,k}(\theta)G_{n+k}(\theta)\right]x^m . \qquad \text{(D.10)}$$

Comparing (D.4) and (D.10), we obtain the m^{th} coefficient of the nth polynomial as

$$\phi_{n,m}(\theta) = -\sum_{j=m}^{n-1}\frac{1}{\left\|\phi_j\right\|_\theta^2}\phi_{j,m}(\theta)\sum_{k=0}^{j}\phi_{j,k}(\theta)G_{n+k}(\theta) \text{ for } m = 0,\cdots,n-1, \qquad \text{(D.11)}$$

with $\phi_{n,n}(\theta) = 1$.

Appendix-E

Analysis of the Error Probability Function

In this appendix, the proof that the BER function and the corresponding Chernoff upper bound are convex decreasing functions of the SINR and convex increasing functions of the MSE (for sufficiently small values of the MSE) is given.

The symbol error probability can be analytically expressed as a function of the SINR as

$$P_e = \alpha Q(\sqrt{\beta(SINR)}\,. \tag{E.1}$$

As an example, for M-ary PAM, M-ary QAM,and M-ary PSK constellations this relation is specifically given by

$$P_e^{PAM} \cong 2(1-\frac{1}{M})Q\left(\sqrt{\frac{3}{M^2-1}SINR}\right), \tag{E.2}$$

$$P_e^{QAM} \cong 4(1-\frac{1}{\sqrt{M}})Q\left(\sqrt{\frac{3}{M-1}SINR}\right) \text{ and} \tag{E.3}$$

$$P_e^{PSK} \cong 2Q\left(\sqrt{2\sin^2(\frac{\pi}{M})SINR}\right) \text{ for } M\geq 4. \tag{E.4}$$

Note that $\alpha \geq 1$ and $\beta \leq 1$. See Table.E for specific values of the parameters (recall that M is the constellation size and $k = \log_2 M$ the number of bits per symbol).

BER as a function of the SINR

To prove that the BER function is convex decreasing in the SINR, it suffices to show that the first and second derivatives of $Q(\sqrt{\beta x})$ are negative and positive, respectively (A positive scaling factor preserves monotonicity and convexity):

$$\frac{\partial Q(\sqrt{\beta x})}{\partial x} = -\sqrt{\frac{\beta}{8\pi}}e^{-\beta x/2}x^{-1/2} < 0 \qquad 0 < x < \infty\,. \tag{E.5}$$

$$\frac{\partial^2 Q(\sqrt{\beta x})}{\partial x^2} = \frac{1}{2}\sqrt{\frac{\beta}{8\pi}}e^{-\beta x/2}x^{-1/2}(\frac{1}{x}+\beta) > 0 \qquad 0 < x < \infty\,. \tag{E.6}$$

The same can be done for the Chernoff upper bound $e^{-\beta x/2}$:

$$\frac{\partial e^{-\beta x/2}}{\partial x} = -\frac{\beta}{2}e^{-\beta x/2} < 0 \qquad 0 < x < \infty\,. \tag{E.7}$$

$$\frac{\partial^2 e^{-\beta x/2}}{\partial x^2} = \frac{\beta^2}{4}e^{-\beta x/2} > 0 \qquad 0 < x < \infty\,. \tag{E.8}$$

BER as a function of the MSE

To prove that the BER function is convex increasing in the MSE (assuming a MMSE receiver), it suffices to show that the first and second derivatives of $Q(\sqrt{\beta(x^{-1}-1)})$ are both positive.

$$\frac{\partial Q(\sqrt{\beta(x^{-1}-1)})}{\partial x} = -\sqrt{\frac{\beta}{8\pi}} e^{-\beta(x^{-1}-1)/2}(x^3 - x^4)^{-1/2} \geq 0 \qquad 0 < x < 1. \tag{E.9}$$

$$\frac{\partial^2 Q(\sqrt{\beta(x^{-1}-1)})}{\partial x^2} = \frac{1}{2}\sqrt{\frac{\beta}{8\pi}} e^{-\beta(x^{-1}-1)/2}(x^3 - x^4)^{-1/2}\left(\frac{\beta}{x^2} - \frac{3-4x}{x-x^2}\right) \geq 0 \qquad 0 < x \leq x_{z_1} \quad x_{z_2} \leq x \leq 1 \tag{E.10}$$

where the zeros are $x_{z_1} = \frac{(\beta+3) - \sqrt{\beta^2 - 10\beta + 9}}{8}$ and $x_{z_2} = \frac{(\beta+3) + \sqrt{\beta^2 - 10\beta + 9}}{8}$ (it has been tacitly assumed that $\beta \leq 1$). It is remarkable that for $\beta = 1$ both zeros coincide, which means that the BER function is convex for the whole range of MSE values. To be more specific, BPSK and QPSK constellations satisfy this condition and, consequently, their corresponding BER function is always convex in the MSE. Consider now the Chernoff upper bound $e^{-\beta(x^{-1}-1)/2}$

$$\frac{\partial e^{-\beta(x^{-1}-1)/2}}{\partial x} = \frac{\beta}{2} e^{-\beta(x^{-1}-1)/2} x^{-2} > 0 \qquad 0 < x < \infty. \tag{E.11}$$

$$\frac{\partial^2 e^{-\beta(x^{-1}-1)/2}}{\partial x^2} = \frac{\beta}{2} e^{-\beta(x^{-1}-1)/2} x^{-4}\left(\frac{\beta}{2} - x\right) \geq 0 \qquad 0 < x < \frac{\beta}{4}. \tag{E.12}$$

The Chernoff upper bound is then convex increasing in the MSE for MSE $\leq \beta/4$ (see Table for specific values). Concluding, as a rule-of-thumb, both the exact BER function and the Chernoff upper bound are convex increasing functions of the MSE for a BER $\leq 2 \times 10^{-2}$ (see Table E). The MSE vs. BER for various modulation schemes is shown in Figure-E.

Table E- Parameters and convexity region of the BER for well-known constellations [74].

Constellation	M	k	α	$\beta\ (\simeq)$	$x_{z_1}\ (\simeq)$	Convexity region of BER(MSE)
BPSK	2	1	1	1	0.5	$\text{BER} \leq 1.587 \times 10^{-1}$
4-PAM	4	2	1.5	0.2	6.834×10^{-2}	$\text{BER} \leq 3.701 \times 10^{-2}$
16-PAM	16	4	1.875	0.0118	3.927×10^{-3}	$\text{BER} \leq 1.971 \times 10^{-2}$
QPSK	4	2	2	1	0.5	$\text{BER} \leq 1.587 \times 10^{-1}$
16-QAM	16	4	3	0.2	6.834×10^{-2}	$\text{BER} \leq 3.701 \times 10^{-2}$
64-QAM	64	6	3.5	0.0476	1.596×10^{-2}	$\text{BER} \leq 2.526 \times 10^{-2}$
8-PSK	8	3	2	0.2929	10.15×10^{-2}	$\text{BER} \leq 3.576 \times 10^{-2}$
16-PSK	16	4	2	0.0761	2.559×10^{-2}	$\text{BER} \leq 2.218 \times 10^{-2}$
32-PSK	32	5	2	0.0192	6.414×10^{-3}	$\text{BER} \leq 1.692 \times 10^{-2}$

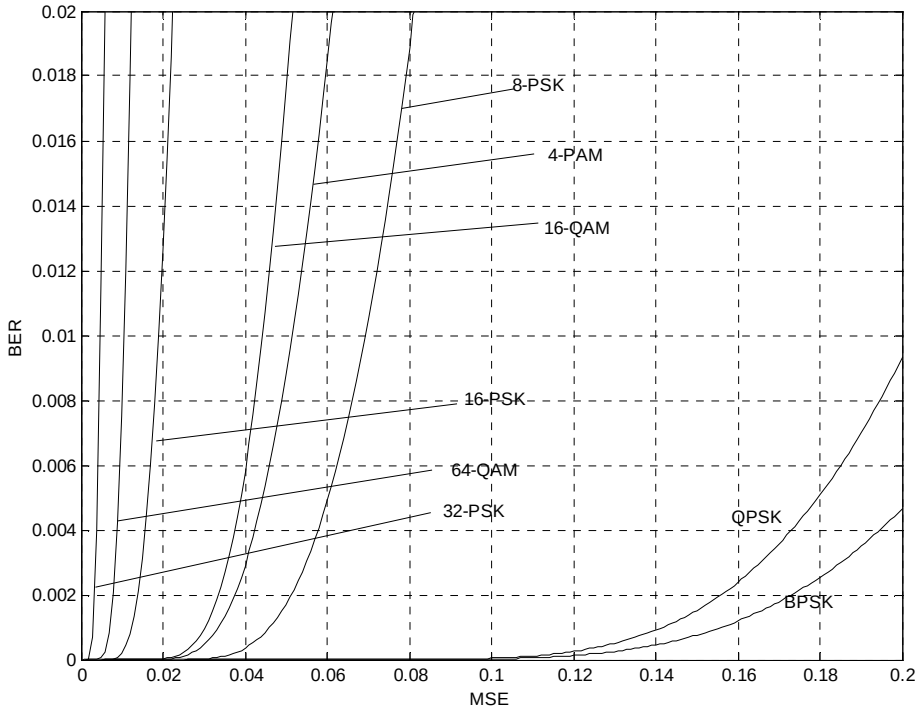

Figure E: Plot showing variation BER with MSE for various modulation techniques

Appendix-F

Expressions for Various Taper Functions:

S. No	Taper Function	Expression of the taper function
1.	Uniform	$w(n)=1, \quad 0 \le \lvert n \rvert \le N/2$ $w(n)=0, \quad$ otherwise
2.	Taylor Kaiser	$w(n)=\frac{I_0[\pi\beta\sqrt{1-(2n/N)^2}]}{I_0[\pi\beta]}$, $0 \le \lvert n \rvert \le N/2$ $0 \le \beta \le 10$ $I_0(x)$ is zero-order modified Bessel function of first kind. β is ripple control parameter.
3.	Dolph Chebyshev	$W(n)=(-1)^n \frac{\cos[N\cos^{-1}\{\beta\cos(\pi n/N)\}]}{\cosh[N\cosh^{-1}(\beta)]}$, $0 \le \lvert n \rvert \le N-1$, where, $\beta=\cosh[1/N\cosh^{-1}(10^{\alpha})]$, α is main lobe to side lobe ratio. (Inverse DFT is required to compute data window)
4.	Binomial	$w(n)=\frac{(N-1)!}{n!(N-1-n)!}$, $\quad 0 \le n \le N-1$,

Appendix-G

Expressions for Discrete version of FrFT (DFrFT) [59]

The samples of fractional Fourier transform $f_a(u)$ of a function can be computed in terms of the samples of f(u). For a function f(u) equation (3.65) can be written as

$$f_a(u) = A_\alpha e^{i\pi \cot\alpha\, u^2} \int e^{-j2\pi \csc\alpha\, uu'} [e^{j\pi \cot\alpha\, u'^2} f(u')] du'. \qquad \text{(G.1)}$$

It is assumed that the representation $f_a(u_a)$ of the signal f in all fractional Fourier domains are confined to the interval [-Δu/2, Δu/2]. As per the reference [59], the samples (k= -N to N-1) of $f_a(u)$ are obtained by following equation

$$f_a\left(\frac{k}{2\Delta u}\right) = \frac{A_\alpha}{2\Delta u} \sum_{l=-N}^{N-1} e^{i\pi[\cot\alpha(k/2\Delta u)^2 - 2\csc\alpha\, k\, l/(2\Delta u)^2 + \cot\alpha(l/2\Delta u)^2]} f\left(\frac{l}{2\Delta u}\right). \qquad \text{(G.2)}$$

Direct computation of (G.2) requires $O(N^2)$ operations. A fast O(N log N) algorithm can be obtained by putting (G.2) in the form

$$f_a\left(\frac{k}{2\Delta u}\right) = \frac{A_\alpha}{2\Delta u} e^{i\pi(\cot\alpha - \csc\alpha)(k/2\Delta u)^2} \times \sum_{l=-N}^{N-1} e^{i\pi \csc\alpha((k-l)/2\Delta u)^2} e^{i\pi(\cot\alpha - \csc\alpha)/(l/2\Delta u)^2} f\left(\frac{l}{2\Delta u}\right). \qquad \text{(G.3)}$$

The finite summation in (G.2) is recognized as convolution in (G.3). The convolution can be computed in O(N log N) time by using fast Fourier transform(FFT). The final samples are obtained by a final chirp modulation.

The above algorithm of DFrFT is limited to the range $0.5 \le |a| \le 1.5$. Using index addititvity property of the fractional Fourier transform this range can be extended to all values of a easily. For example for the range $-0.5 \le a \le 0.5$, we observe that

$$F^a = F^{a+1-1} = F^{a+1}F^{-1}. \qquad \text{(G.4)}$$

Equations (G.2) and (G.3) represent the discrete versions of FrFT.

List of Publications

Refereed Journals Pub

1. "Fractional Fourier transform based beamforming for next generation of wireless communication systems" Published in *IETE Journal of Technical Review on Special Issue of Broadband communications*, pp.349-365, September, 2004. *(Issue edited by Electrical Engineering Department of IIT Chennai).*
2. "Optimal Beamforming for Rayleigh faded Time Frequency Varying Channels Using Fractional Fourier Transform", *J. Indian Inst. Sci.*, Bangalore, **85**, pp. 27–38, Jan.–Feb. 2005.
3. "3G Evolution towards Broadband", Telecommunications: The Indian Journal of Telecommunications, (Special issue on broadband services) pp.41-47, May-June 2005.
4. "A Novel FrFT beamformer for Rayleigh Faded Channels" accepted for publication in International Journal of Springer on Wireless Personal Communications.
5. "Output SNR Improvement in Array Processing Architectures of WCDMA Systems by Low Side Lobe Beamforming" accepted for publication in International Journal of Springer on Wireless Personal Communications.
6. "Optimal Beamforming for Ricean faded Time Frequency Varying Channels Using Fractional Fourier Transform", submitted after revision *to International Journal of Numerical Modeling*.
7. "Adaptive Antenna at Wireless Communication Handheld Terminal for Reducing Power Deposition in Human Head" revised and resubmitted to Radio Science Journal, USA.

Refereed International Conferences

8. "Analysis of rectangular and Bartlett windows in fractional Fourier domain using Mathematica 4.1", accepted at *5th International Mathematica Symposium* held at Imperial college London from 7-11, July 2003.

9. “Adaptive Antennas at the Cellular Mobile Handset for reduced deposition of power in Human Head”, Proceedings of *Workshop on Advances in Smart Antennas for Software Radios held in conjunction with 13th Annual Virginia Tech/MPRG Group Symposium on Wireless Personal Communications,* Virginia,pp.82-90, June 4-6 2003.
10. “Use of adaptive Antenna at the cellular mobile handset for reduced radiation hazards” accepted at *IEEE 9th Asia Pacific Conference on Communications, APCC2003 at* George town, Pena nag, Malaysia, September 21-24,2003.
11. "Adaptive antennas at the mobile handset for reduced radiation hazards: An analysis" Proceedings of *IEEE Vehicular Technology Conference*, Fall 2003, Orlando, USA, pp.3154-3158, October 6-9, 2003.***(INVITED PAPER)***.
12. "Adaptive Antennas at the Cellular Mobile Handset for reduced SAR in Human Head" Proceedings of *IEEE 6th International Symposium on Antennas, Propagation and EM theory,* Beijing, China, pp.360-368, October 28-Nov 1, 2003.
13. "Rectangular and Triangular line source Amplitude distribution in Fractional Fourier Domain" Proceedings of International Radar Symposium, IRSI-2003, Bangalore, India, pp.308-314, Dec. 03-05, 2003.
14. “Fractional Fourier Transform Based Beamforming in Micro-Cellular Environment of Wireless Communication Systems” Proceedings of IEEE International Conference of Signal Processing and Communications, Indian Institute of Sciences, Bangalore, pp.582-586, Dec. 11-14, 2004.
15. “Performance Improvement in Array Processing Architectures of WCDMA Systems by Low Side Lobe Beamforming”, Proceedings of IEEE 9th International conference on Personal Wireless Communications,pp.324-328, 24-26th January, 2005, N.Delhi
16. “Independent Angular steering of each zero of a directional pattern of a linear array” International Conference on challenges in Networking and Future Comm.(CNFE-05),APIIT, Panipat, India,pp.91-95,April 9-10,2005.
17. “SNR Improvement of Uniform Circular Array Using the Fractional Fourier Transform Beamforming in Radar Environment”, Proceedings of International Radar Symposium, IRSI-2005, pp.776-781, 19-22 Dec 2005, Bangalore, India.

National Conferences

18. "Smart Antennas for Wireless Communication Systems", Proceedings of IE(E) on Challenges ahead with IT, SLIET, Longowal,pp.130-134, Jan 19-20, 2002.
19. "Rectangular & Bartlett windows in Fractional Fourier domain", Proceedings of National Conference of Mathematical & Computer Applications in *Science and Engineering* ,TIET, Patiala, Jan-2003.
20. "Fractional Fourier domain analysis of Generalized Cosine windows", Proceedings of IETE and CSI on Services through IT enabled systems, SITES-2003, Gwalior, pp.144-151, 19-20 April, 2003.
21. "Interference rejection in WCDMA systems using tapered beamformers", Proceedings of IE(E) on CDMA Technology: Advanced wireless services for today and tomorrow, N.Delhi,pp.85-90, April 2-3, 2004.
22. "Output SNR Improvement in Array Processing Architectures of WCDMA Systems by Low Side Lobe Beamforming", Proceedings of National Conference of Communications ***(NCC-2005)*** IIT, Kharagpur pp167-171, 28-29th January, 2005.
23. ***Invited Talk*** *on "Transmit Diversity Schemes-A Review"* in Conference on Information and Communication Technologies, JMIT Radur, 9-11 February, 2006.

Communicated

24. "Improved channel estimation in transmit diversity scheme using Fractional Fourier Transform" submitted to IEE Electronics Letters
25. "BER reduction in SIMO system using FrFT based optimal beamformer" submitted to IEEE Transaction on Vehicular Technology.
26. "Performance improvements in various performance metrics of array processing architectures of CDMA based systems by use of low side lobe beamforming" Communicated to IETE Journal of research.
27. "BER reduction in Spatial Multiplexed systems using FrFT based MIMO receive beamformer" submitted to International Journal of Springer on Wireless Personal Communications

References

[1]. 3GPP Available: http://www.3g.co.uk/PR/Jan2003/4667.htm.

[2]. 3GPP Third Generation Partnership Project, TS 25.102-105, version June2001. Available: http//: www.3gpp.org/ftp/Specs/

[3]. A. A. M. Saleh, and R. A. Valenzuela, "A Statistical model for Indoor Multipath Propagation", IEEE J. Select. Areas Commun. Vol.-5, No.2, pp. 128-137, Feb. 1987.

[4]. A. F. Naguib, "Adaptive antennas for CDMA wireless networks," Ph.D. dissertation, Stanford University, Aug. 1996.

[5]. A. J.Viterbi, "Principles of Spread Spectrum Multiple Access Communications", Ist ed., Addison-Wesley Wireless communication series, June 1995.

[6]. A. Narula, M. J. Lopez, M. D. Trott, and G. W. Wornell, "Efficient use of side information in multiple-antenna data transmission over fading channels," *IEEE Journal on Sel. Areas in communications*, vol. 16, no. 8, pp. 1423–1435, Oct. 1998.

[7]. A. J. Paulraj and C. B. Papadias, "Space-time processing for wireless communications", IEEE Transaction on Vehicular Technology, vol. 43, pp.691-697, Aug. 1994.

[8]. A. J. Paulraj, R. Roy, and T. Kailath, "Estimation of Signal Parameters by Rotational Invariance Techniques (ESPRIT)", Proc. of 19th Asilomar Conference on Circuits, Systems and Comp., 1985.

[9]. A. J. Paulraj, Rohit Nabar and Dhananj Gore, "Introduction to Space time Wireless Communications", Cambridge University Press, 2003.

[10]. A. J. Paulraj, Dhananjay A. Gore,Rohit U. Nabar, And Helmut Bölcskei, "An Overview of MIMO Communications—A Key to Gigabit Wireless" Proceedings of the IEEE, vol. 92, no. 2,pp. 198-218, February 2004

[11]. A. J. Paulraj and T. Kailath, "Increasing capacity in wireless broadcast systems using distributed transmission/directional reception," Patent 5 345 599, 1994.

[12]. A. J. Paulraj and C. B. Papadias, "Space-time processing for wireless communications,"*IEEE Signal Processing Magazine*, vol. 14, no. 6, pp. 49–83, Nov. 1997.

[13]. A. Salmasi and K.S.Gilhousen, “On the system design aspects of Code Division Multiple Access applied to Digital Cellular and Personal Communication Networks”, Proceedings of IEEE vehicular Technology Conference,ST.Louis,pp.57-62, 1991.

[14]. A.Rao, “Adaptive algorithms for spatial adaptive interference rejection”, IEEE ICPWC conference, pp.326-329, May 2002

[15]. Adolf W. Lohmann, “Image Rotation. Wigner Rotation and the Fractional Fourier Transform”, J. Opt. Soc. of Am.-A:10, pp. 2181-2186, 1993.

[16]. A. J. Paulraj, D. Gesbert, C. Papadias , “Smart Antennas for Mobile Communications”, Encyclopedia For Electrical Engineering, John Wiley Publishing Co., 2000

[17]. Ana Perez Neira, Xavier Mestre and Javier Rodriquez, “Smart antenna in software Base radio station”, IEEE Comm. Magazine, pp.166-173, February 2001.

[18]. Antenova, “New Generation Technology”, Oct, 2002. Available at: http://www.antenova.com/

[19]. Antonios Drossos, Veli Santomaa, and Niels Kuster, “The Dependence of Electromagnetic Energy Absorption Upon Human Head Tissue Composition in the Frequency Range of 300–3000 MHz”, IEEE Trans. on Microwave Theory and Techniques, vol. 48, no. 11,pp 1988-1995, November 2000.

[20]. B. Agee, A. V. Shell, and W. A. Gardner, “Spectral Self-Coherence Restoral: A New Approach to Blind Adaptive Signal Extraction Using Antenna Arrays”, Proc. IEEE, vol. 78, pp. 753–767, April 1990.

[21]. B. D. Van Veen and K. M. Buckley, “Beamforming: A versatile approach to spatial filtering”, IEEE ASSP Magazine, pp. 4-24, April 1988.

[22]. B. Ottersten and M. Viberg, “Analysis of Subspace Fitting Based Methods for Sensor Array Processing”, in Proc. ICASSP‘89, vol. IV, (Glasgow, Scotland), pp. 2807– 2810, 1989.

[23]. B. Widrow and S. D. Stearns, “Adaptive Signal Processing”, Prentice-Hall, Upper Saddle River, NJ, 1985.

[24]. B.D Carlson and D.Willna, “Antenna pattern synthesis using weighted least squares”, IEE Proceedings-H, vol.139, no.1, pp.11-16, Feburary1992.

[25]. C Braun, M Nilsson and R D Murch, “ Measurements of Interference rejection capability of smart antenna on mobile telephones”, IEEE 49th Vehicular

technology conference, Houston, Texas, USA, Vol.2 , pp 1068-1078, May 1999.

[26]. C Hasan and W. Lu Willie, “Guest editorial: 3G wireless and beyond”, Elsevier Journal of Computer Communications no.26 pp. 1905–06, 2003.

[27]. C. Candan, M.A. Kutay, H.M. Ozaktas, “The discrete fractional Fourier transform”, IEEE Trans. Signal Proc., vol. 48, no.5, pp. 1329–1337, May 2000.

[28]. C. L. Dolph, “A current distribution for broadside arrays which optimizes the relationship between beam width and side-lobe level”, Proc. IRE pp.335–348, 1946.

[29]. C.Christodoulou and N.Herscovici “Smart Antennas in Wireless Communications: Base-Station Diversity and Handset Beamforming”, IEEE Antennas and Propagation Magazine Vol.3, no.5, pp.142-151, May 2000.

[30]. D. Gerlach, A.J. Paulraj, “Adaptive transmitting antenna arrays with feedback” ,*IEEE Signal Processing Letters*, vol.1, pp.150-152, October 1994.

[31]. D. C. Ricks, P. G. Cifuentes, and J. S. Goldstein, “What is optimal processing for nonstationary data?”, Proc. 34th Asilomar Conf. Signals, Syst. Comput., Paci_c Grove, CA, November 2000.

[32]. D. G. Manolakis, V. K. Ingle, and S. M. Kogon “Statistical and Adaptive Signal Processing”, McGraw-Hill, Boston, 2000.

[33]. D. Karaminas & A. Manikas, “Super resolution broad null beamforming for cochannel interference cancellation in mobile radio networks”, IEEE transaction of Vehicular Technology, vol.43, no.3, pp689-697, May2000.

[34]. Daniel P. Palomar, “Unified Design of Linear Transceivers for MIMO Channels,” in Smart Antennas – State-of-the-Art, Vol. 3, Chapter 18, EURASIP Hindawi Book Series on SP&C, T. Kaiser, A. Bourdoux, H. Boche, J. R. Fonollosa, J. B. Andersen, and W. Utschick, Editors, September, 2005 (The references listed in this chapter are also referred)

[35]. David Gesbert, Mansoor Shafi, Da-shan Shiu, Peter J. Smith, and Ayman Naguib, “From Theory to Practice: An Overview of MIMO Space–Time Coded Wireless Systems”, IEEE Journal on selected areas in communications, vol. 21, no. 3,pp.281-302, April 2003

[36]. D. Gu and C. Leung, ”Performance analysis of transmit diversity scheme with imperfect channel estimation,” Electronics letters, 2003,39 (4) pp. 402-403.

[37]. D. Tse, P. Viswanath, “Fundamentals of Wireless Communication”, Cambridge University Press, May 2005

[38]. E. Buracchini et al, “Performance analysis of a mobile system based on combined SDMA/CDMA access technique”, IEEE ISSTA’96, Mainz, Germany, pp.370-374, September 1996

[39]. E. Kreyszig, “Advanced Engineering Mathematics”, New York: John Wiley, 1983.

[40]. E.C.Jordan and K.G.Balmin “Electromagnetic waves and radiating systems”, London, Prentice Hall International, 1995

[41]. Erik Dahlman, Bjorn Gudmundson, Matts Nilsson, and Johan Skold, “UMTS/IMT-2000 Based on Wideband CDMA”, IEEE Communications Magazine, vol. 36, pp. 70-80, September 1998.

[42]. Erik Dahlman, Per Beming, Jens Knutsson, Fredrik Ovesjo, Magnus Persson, and Christiaan Roobol, "WCDMA- The Radio Interface for Future Mobile Multimedia Communications”, IEEE Transactions on Vehicular Technology, vol. 47, No. 4, pp. 1105-1118, November 1998.

[43]. E. Telater, “Capacity of Multi-Antenna Gaussian Channel”, AT&T Bell Labs, Tech. Memo., June 1995.

[44]. F J Harris, “On the use of Window Functions for Harmonic Analysis with Discrete Fourier Transform”, Proceedings of IEEE, vol.66,pp 51-83, Jan 1978.

[45]. F.Adachi, M. Sawahasi and H.Suda, “Wideband DS-CDMA for next generation mobile communications systems”, IEEE communications Magazine, vol.163, pp.56-69, 1998.

[46]. Faisal Shad, Terence D.Todd, Vytas Kezys and John Litva, “Dynamic slot allocation (DSA) in indoor SDMA/TDMA using smart antenna base station”, IEEE/ACM transactions on networking, vol.9, no.1, pp. 69-81, Feb.2002.

[47]. Feng. X., and C.Leung.: ‘Performance sensitivity comparison of two diversity schemes’, Electronics letters., 2000, 36, (9), pp. 838-839.

[48]. G. Dolmans and L. Leyton, “Performance study of an adaptive dual antenna handset for indoor communications”, IEE proceedings Microwave, Antennas and Propagation, Vol.146, No 2, pp 138-144, April 1999.

[49]. G. K. Chan, “Effects of sectorization on the spectrum efficiency of cellular radio systems”, IEEE Trans. Vehicular Tech., vol. 41, no. 3, pp.217–225,March,1992.

[50]. G. Foschini, “Layered space time architecture for wireless communication in a fading environment when using multiple antennas “, Bell Labs Tech J., pp. 41–59, 1996.

[51]. G. Foschini and M. Gans, “On limits of wireless communications in a fading environment when using multiple antennas,” *Wireless Personal Communications*, vol. 6, pp. 311–335, 1998.

[52]. G. J. Foschini, G. D. Golden, R. A. Valenzuela, and P. W. Wolniansky, “Detection algorithm and initial laboratory results using the V-BLAST space–time communication architecture,” Electron. Lett., vol. 35, no. 1, pp. 14–15, 1999.

[53]. G. J. Foschini, G. D. Golden, P. W. Wolniansky, and R. A. Valenzuela, “Simplified processing for wireless communication at high spectral efficiency,” *IEEE J. Select. Areas Commun.—Wireless Commun. Series*, vol. 17, pp. 1841–1852, 1999.

[54]. G. Ginis and J. Cioffi, “Vectored transmission for digital subscriber line systems,” *IEEE Journal on Selected Areas in Communications (special issue on Twisted Pair Transmission)*, vol. 20, no. 5, pp. 1085–1104, June 2002.

[55]. G. B. Giannakis, A. Scaglione, P. Stoica, S. Barbarossa, and H. Sampath, “Optimal designs for space-time linear precoders and decoders,” *IEEE Trans. on Signal Processing*, vol. 50, no. 5, pp. 1051–1064, May 2002.

[56]. G. Turin, “Introduction to Spread-Spectrum Anti multipath Techniques and their Application to Urban Digital Radio”, Proc. of IEEE, vol. 68, pp. 328–353, March 1980.

[57]. H. B¨olcskei and A. J. Paulraj, “Multiple-input multiple-output (MIMO) wireless systems,” in *The Communications Handbook*, J. Gibson, Ed., pp. 90.1–90.14. CRC Press, 2nd edition, 2002.

[58]. H. Exton, *Handbook of Hypergeometric Integrals: Theory, Applications,Tables, Computer Programs*. New York: Wiley, 1978.

[59]. H.M. Ozaktas, O. Arikan, M.A. Kutay, G. Bozdagi, “Digital computation of the fractional Fourier transform”, IEEE Trans. Signal Proc. vol.44, no.9, pp.2141–2149, Septemeber,1996.

[60]. H.M. Ozaktas, Z. Zalevsky, M.A. Kutay, “The Fractional Fourier Transform with Applications in Optics and Signal Processing”, Wiley, New York, 2001.

[61]. H.M.Ozaktas, Billur Barshan, D.Mendlovic , L.Onural. Convolution, "Filtering and Multiplexing in Fractional Domains and Their Relation to Chirp and Wavelet Transforms", J. Opt. Soc. of Am.-A.; 11, pp.547-559, 1994.

[62]. H Singh et. al ",Wavelet transforms for computing the probability of detection", Infrared imaging Systems; Design, Analysis, Modeling and Testing, Vol.2743, pp.302-310, April, 1996.

[63]. I. S. Reed, J. D. Mallett, and L. E. Brennan, "Rapid convergence rate in adaptive arrays", IEEE Trans. Aerospace Electron. System, AES-10(6): pp.853-863, November 1974.

[64]. I.S.Yetik and A. Nehorai. "Beamforming Using Fractional Fourier Transform", IEEE Trans. Signal processing.; vol.5, no.6, pp.1663-1668, June2003

[65]. I.S.Yetik, M.A.Kutay, H. Ozaktas , H.M.Ozaktas, "Continuous and Discrete Fractional Fourier Domain Decomposition", Proc. IEEE Int. Conf. Accoust. Speech, Signal Process, pp.93-96, 2000.

[66]. ICNIRP, "Guidelines for limiting exposure to time-varying electric, magnetic and electromagnetic fields (up to 300 GHz) ", Health Physics, vol. 74, no.4, pp. 494, April 1998.

[67]. IEEE Trans. On Microwave Theory and Techniques, "Special Issue on biological effects of microwaves" vol.44, no.10, October 1996.

[68]. ITU Rec M. 1036, "Spectrum considerations for implementation in the bands 1885-2025MHz and 2110-2200 MHz", Geneva Switzerland.

[69]. ITU, "ITU approves the key characteristics for the radio interfaces of third generation mobile systems", ITU Press Release, March 1999.

[70]. ITU, "Wideband cdma-One (TIA cdma2000) Radio Transmission Technology Proposal", International Telecommunication Union, Radio communication Study Groups, June 1998. Available at: http://www.cdg.org/frame_3giis.html

[71]. I. E. Telatar, "Capacity of multi-antenna Gaussian channels," *European Trans. On Telecommunications (ETT)*, vol. 10, no. 6, pp. 585–595, Nov.-Dec. 1999.

[72]. J. Bach Andersen, P.E.Mogensen, G.Frølund Pedersen, "Exposure Aspects of W-CDMA- Report to The GSM Association", Center for Personkommunikation Aalborg University, Denmark, Dec 2001

[73]. J. E. Moulder, L. S. Erdreich, R. S. Malyapa, J. Merritt, W. F. Pickarde and Vijayalaxmi, “Cell Phones and Cancer: What Is the Evidence for a Connection?”, Radiation Research, vol. 151, 513–531 ,1999

[74]. J. G. Proakis, “Digital Communications”, second ed., McGraw-Hill, 1989.

[75]. J. H. Bernhardt, R. Matthes and M. H. Repacholi, “Non-Thermal Effects of RF Electromagnetic Fields”, International Commission on Non-Ionizing Radiation, Oberschleissheim, 1997.

[76]. J. H.Winters, “On the Capacity of Radio Communication Systems with Diversity in a Rayleigh Fading Environment”, IEEE J. Select. Areas Communication, vol.-5, no.5, pp. 871–878, June 1987.

[77]. J. H.Winters, “Signal Acquisition and Tracking with Adaptive Arrays in Digital Mobile Radio System IS-54 with Flat Fading”, IEEE Trans. Vehicular Tech., vol.-42, no.4, pp. 377–384, July 1993.

[78]. J. H. Winters, “The diversity gain of transmit diversity in wireless systems with rayleigh fading,” *IEEE Trans. on Vehicular Technology*, vol. 47, no. 1, pp. 119–123, Feb. 1998.

[79]. J.B.Leonard, K.R.Foster and T.W.Athey, “Thermal properties of tissue equivalent phantom model”, IEEE Trans. on BME, Vol.31, No.7, pp 553, May1984.

[80]. J.C.Liberti and T.S.Rappaport, “Smart antennas for wireless communications: IS95 and Third Generation CDMA applications”, Prentice Hall, 1998.

[81]. J.Choi & Gi.Hun Lee, “A single beamformer for antenna array CDMA systems”, Elsevier Journal of Signal Processing, vol.81,pp.321-334,2001.

[82]. J.H.Winters and Micahl J Gans, “The range increase of adaptive versus phased arrays in mobile radio system”, IEEE Trans. on Vehicular Technology, vol.48, no.2, pp.353-362, March 1998.

[83]. J. K. Cavers, “An analysis of pilot symbol assisted modulation for Rayleigh fading channels,” *IEEE Trans. Veh. Technol.*, vol. 40, no. 4, pp. 1389–1399, Nov. 1991.

[84]. J.L.Schepps and K.R.Foster “The UHF and microwave dielectric properties of normal and tumor tissues: variation in dielectric properties with water contents” Phy. Med. Biol., Vol.25, no.6, pp 1149-1159.

[85]. Jay E Padgett, Christoph G. Gunther and Takeshi Hattori, “Overview of Wireless Personal Communications”, IEEE Communications Magazine, vol. 33, no. 1, pp. 28-41, January 1995.

[86]. J. B. Andersen, “Array gain and capacity for known random channels with multiple element arrays at both ends,” *IEEE Journal on Selected Areas in Communications*, vol. 18, no. 11, pp. 2172–2178, Nov. 2000.

[87]. John Litva and Titus Kwok-Yeung Lo, “Digital beam forming in wireless Communications”, Artech House, Boston, London, 1996.

[88]. Jonathan S Blogh, Peter J Cherriman and Lajos hanzo, “ Adaptive array assisted dynamic channel allocation techniques”, IEEE JSAC, vol.19, no.2, pp.305-311, February 2001.

[89]. Josef Johannes Blanz, Apostolos papathanassiou, Martin Haardt and Ignasi Furio, “Smart antennas for combined DOA and joint channel estimation in time slotted CDMA mobile radio systems with joint detection”, IEEE Trans. on Vehicular Technology, vol.49, no.2, pp.293-306, March 2000.

[90]. Justin Chuang and Nelson Sollenberger, “Beyond 3G: Wideband wireless data access based on OFDM and dynamic packet assignment”, IEEE Communications Magazine, pp. 78-87, July 2000

[91]. K.R.Foster,H.N.Kritikos and H.P.Schwan, “ Effect of surface cooling and blood flow on the microwave heating of tissues”, IEEE Trans. On BME Vol.25, no.5, pp.494, May 1978

[92]. Kumar R, “System level improvements in Down Link of TD-CDMA Mobile Communications”, PhD Thesis, Indian Institute of Science, Bangalore,2001

[93]. Kai Kit Wing, Roger S.K.Cheng, Khalid Ben Lataief and Ross D Murch, “Adaptive antennas at the mobile and base station in an OFDM/TDMA systems”, IEEE Trans. on Communications, vol.49, no.1, pp.195-205, January. 2001.

[94]. L. B. Milstein, “Wideband Code Division Multiple Access”, IEEE Journal of Selected Areas in Communications, Vol. 18, no. 8, pp. 1344-1354, August 2000.

[95]. L. J. Griffiths and C. W. Jim, “An alternative approach to linearly constrained adaptive beamforming”, IEEE Trans. Antennas Propagation, vol.30, no.1, pp.27-34, January

[96]. L.B. Almeida, “The fractional Fourier transform and time–frequency representations”, IEEE Trans. Signal Proc. vol.42, no.11, pp.3084–3093, November 1994.

[97]. Lu Xiaode, Gao Benquing and Lui Ruixiang, “Application of Monte Carlo algorithm in beamforming for smart antenna”, IEEE PIMRC, pp.203-206,2003

[98]. M. Bengtsson and B. Ottersten, “Optimal and suboptimal transmit beamforming,” in *Handbook of Antennas in Wireless Communications*, Ed. CRC Press, 2001.

[99]. M . Marcus and S. Das, “The potential use of Adaptive antenna to increase land mobile frequency reuse”, IEE 2nd International conference Radio Spectrum Conversation Techniques, Birmingham, U.K, pp.113-117, Sept.1983.

[100]. M. A. Stuchly, “Biological concerns in wireless communications”, Crit.Rev. Biomed. Eng., vol.26, pp.117–151, 1998.

[101]. M. Flament, F. Gessler, F. Lagergren, O.Queseth, R. Stridh, M. Unbehaun, J. Wu, J. Zander, “Telecom Scenarios 2010 - a wireless infrastructure perspective", 2002.
Available at:http://www.s3.kth.se/radio/4GW/public/Papers/ScenarioReport.pdf

[102]. M. H. Repacholi, A. Basten, V. Gebski, D. Noonan, J. Finnie and A. W. Harris, “Lymphomas in Em-Pim1 transgenic mice exposed to pulsed 900 MHz electromagnetic fields”, Radiation. Res., vol. 147, pp. 631–640, 1997.

[103]. M. Tadashi et al., “Beam selection performance analysis of a switched multi-beam antenna system in mobile communication environments”, IEEE Trans. on vehicular technology, vol.46, no.1, pp.10-19, Feb.1997.

[104]. M.A. Kutay, H.M. Ozaktas, O. Arikan, L. Onural, “Optimal filtering in fractional Fourier domains”, IEEE Trans. Signal Proc. vol.45, no.5, pp.1129–1143, May 1997.

[105]. Marco Chiani, Senior Member, IEEE, Moe Z. Win, Senior Member, IEEE, and Alberto Zanella, Member, IEEE, “Error Probability for Optimum Combining of M-ary PSK Signals in the Presence of Interference and Noise”, IEEE Transactions On Communications, vol. 51, no. 11, pp.1949-1957, Nov. 2003

[106]. M.B Knudsen, M. Jenner and G.F Pedersen, “Front end for Smart Antenna System for Interference Reduction in a GSM/GPRS/EDGE/UMTS Handset”, 2002.
Available at:http://tele.auc.dk/semesterinfo/s9rfde2000/projprops/RF_Phased4

[107]. M.Chryssomallis, “Smart Antennas”, IEEE Antennas and Propagation Magazine, vol.42, No.3, June2000.

[108]. M.Krudesen and Jens Overgaard “Identification of thermal models for human tissues”, IEEE transaction on BME, Vol.33, No.5, pp477, May 1986.

[109]. M.Mouly and M.B.Pautet, “The GSM system for mobile communications”, published by auhors, 1992.

[110]. Martin Haardt & Quentin Spencer, “Smart antennas for wireless communications beyond the third generation”, Elsevier Journal of Computer Communications no.26 pp. 41–45, 2003.

[111]. Massimiliano (Max) Martone, “A Multicarrier System Based on the Fractional Fourier Transform for Time–Frequency-Selective Channels”, IEEE transactions on communications, vol. 49, no. 6, pp.1011-1020,June 2001.

[112]. Maxime Flament, Fredrik Gessler, Fredrik Lagergren,Olav Queseth, Rickard Stridh, atthias Unbehaun, Jiang Wu, Jens Zander, “ An approach to 4th generation wireless infrastructures –Scenarios and key research issues”, 4th generation working group report.

[113]. Ming Jo Ho et al., “Performance of switched beam antenna for cellular radio systems”, IEEE Trans. on Vehicular Technology, vol.47, no.1, pp.11-19, February 1998.

[114]. P.R. Dighe, R.K. Mallik, S.S. Jamuar, ”Analysis of transmit-receive diversity in Rayleigh fading, *IEEE Trans. on Communications*, vol. 51,n. 4, pp. 694-703, Apr. 2003.

[115]. P. Balaban and J. Salz, “Optimum Diversity Combining and Equalization in Data Transmission with Application to Cellular Mobile Radio - Part I: Theoretical Considerations, Part II: Numerical results”, IEEE Trans. Commun., vol. 40, no.5, pp. 885–907, May 1992.

[116]. P. Petrus, J. H. Reed, and T. S. Rappaport, “Geometrically based statistical channel model for macro cellular mobile environments”, Proc., IEEE Veh. Tech. Conf., pp. 844-848, Apr. 1996.

[117]. Paul petrus, Richard B Ertel and Jeffrey H Reed, “Capacity enhancement using adaptive arrays in an AMPS system”, IEEE Trans. on Vehicular Technology, vol.47, no.3, pp.717-727, August 1998.

[118]. Q. Spencer, M. Rice, B. Jeffs, and M. Jensen, “A statistical model for angle of arrival in indoor multipath propagation”, in Proc., IEEE Veh. Tech. Conf., 1997.

[119]. QCTEST, “1xEV-DO Trial phone product from Qualcomm, 2001”, Available at: http://www.qualcomm.com/qctest/products/qtp5500.html

[120]. Qi.Bi, George I.Zysman and Hank Menkas, “Wireless mobile communications at the start of the 21st century”, IEEE Communication magazine, pp.110-116, January 2001.

[121]. Qualcomm Inc., “Wideband Spread Spectrum Digital Cellular System”,April 1992. Proposed EIA/TIA Interim Standard.

[122]. R. Becher, M. Dillinger, M. Haardt, W. Mohr, “Broadband wireless access and future communication networks”, Proceedings of the IEEE vol. 89,no.1,pp 58–75,2001

[123]. R. G. Vaughn, “On Optimum Combining at the Mobile”, IEEE Transactions on Vehicular Technology, vol. 37, no. 4, pp. 181-188, November 1988.

[124]. R. Gooch and J. Lundell, “The CMA Array: An Adaptive Beamformer for Constant Modulus Signals”, Proc. ICASSP‘86, (Tokyo), pp. 2523–2526, April 1986.

[125]. R. Khanna, “A compact broadband antenna for cellular phones with reduced radiation hazards”, ME thesis, IISc, Bangalore.

[126]. R. Kohno et al., “Combination of an adaptive array antenna and a canceller of Interference for Direct Sequence Spread spectrum multiple access system”, IEEE JSAC, vol.8, no.4, pp.675-682, May 1990.

[127]. R. Mostafa, K. Dietze, R. C. Palat , W. L. Stutzman and J.H. Reed , “Demonstration of real time wideband diversity at the handset in Indoor wireless channel”, IEEE 54th Vehicular Technology conference, Atlantic city, NJ,USA, Vol.4, pp2072-2076 Oct. 2001

[128]. R. Prasad and T. Ojanpera, “An Overview of CDMA Evolution toward Wideband CDMA”, IEEE Communications Surveys, Vol.1, No. 1, pp. 2-29, Fourth Quarter 1998.

[129]. R. Prasad, W.Mohr, W.Konhauser, “Third generation mobile communication systems”, Artech House, Boston, 2000.

[130]. R. S. Kennedy, “Fading Dispersive Communication Channels”, New York, John Wiley and Sons, 1969.

[131]. R.T.Compton, “An adaptive antenna in spread spectrum communication system”, Proc of the IEEE, vol. 66, no.3, pp. 289-298, March 1978.

[132]. Rajanish kumar et. al,” A deterministic propagation model for the microcellular environment using multiple two dimensional planes”, International Journal of Electronics, volume 88, no.12,pp.1205-1224, 2000.

[133]. R.W. Heath Jr., S. Sandhu, A. J. Paulraj, “Antenna selection for spatial multiplexing systems with linear receivers”, *IEEE Communications Letters*, vol.5, pp.142-144, April 2001.

[134]. R. Negi, A. M. Tehrani, and J. Cioffi, “Adaptive antennas for space-time coding over block-time invariant multi-path fading channels,” in Proc. 49th IEEE Vehicular Technology Conference (VTC’99), pp. 70–74, Houston, Texas, May 16-20, 1999.

[135]. Richard B.Ertel and Paulo Cardieri, K.W.Sowerby, T.S.Rappaport & J.H.Reed, “Overview of spatial channel models for antenna array communication systems”, IEEE Personal Communications systems, pp. 10-21, Feb 1998.

[136]. Rodney Vaughan, “Spaced directive antennas for mobile communications by Fourier transform method”, IEEE Trans. on Antenna Propagation, vol.48, no.7, pp. 1025-1032, July 2000.

[137]. R.S. Blum, J.W. Winters, “On optimum MIMO with antenna selection”, *IEEE International Conference on Communications*, vol.1, pp.386-390, May 2002.

[138]. S. Andersson, B.Carlqvist, B. Hagerman and R.Lagerholm “Enhancing cellular network capacity with adaptive antennas”, Ericsson Review No. 3, 1999.

[139]. S. C. Swales et al, “The performance enhancement of multi beam adaptive base-station antennas for cellular land mobile radio systems”, IEEE Trans. Vehic. Tech. 39, no. 1, pp.56–67, Jan 1990.

[140]. S. Choi & D.Shim, “A novel adaptive beamforming algorithm for a smart antenna in a CDMA Mobile communication environment”, IEEE transaction on Vehicular Technology, vol.49, no.5, pp.1793-1806, September 2001.

[141]. S.Choi and D.Yun, “Design of adaptive array for tracking the source of maximum power and its application to CDMA mobile communications”, IEEE Trans. on Antenna Propagation, vol. 45, no.9, pp.1393-1404, September 1997

[142]. S. Haykin, “Adaptive Filter Theory”, Prentice-Hall, 3rd ed., Upper Saddle River, NJ, 1996.

[143]. S. M. Alamouti, “A simple transmit diversity technique for wireless communications,” *IEEE Journal on Selected Areas in Communications*, vol. 16, no. 8, pp. 1451–1458, Oct. 1998.

[144]. S. M. Leach, A. A. Agius, S. Stavrou, S. R. Saunders, “Diversity performance of intelligent Quadrifilar Helix antenna in mobile satellite systems”, IEE proceedings Microwave, Antennas and Propagation, Vol.147, No 3,pp 305-310, August 2000

[145]. S. Sandhu, R. Heath, A. J. Paulraj, “Space-Time block codes versus space-time trellis codes”, *IEEE International conference on communications*, vol.4, pp. 1132-1136, 2001.

[146]. S. Mayrargue, “Spatial Equalization of a Radio-Mobile Channel without Beamforming Using Constant Modulus Algorithm (CMA)”, Proc. of ICASSP‘93, vol. III, pp. 344–347, 1993.

[147]. S. Milham, “Increased mortality in amateur radio operators due to lymphatic and hematopoietic malignancies”, Am. J. Epidemiol. 127, pp.50–54, 1988.

[148]. S.C. Pei, M.H. Yeh, “The discrete fractional cosine and sine transforms”, IEEE Trans. Signal Proc., vol. 49, no.6, 1198–1207, June 2001.

[149]. S.Choi , D.Shim and T.K.Sarkar, “ A comparison of tracking beam arrays and switching beam arrays operating in a CDMA mobile communication channel”, IEEE antennas and propagation magazine, vol.41, no.6, pp.10-22, December 1999.

[150]. S.Choi and D.Yun, “Design of adaptive array for tracking the source of maximum power and its application to CDMA mobile communications”, IEEE Trans. on Antenna Propagation, vol. 45, no.9, pp.1393-1404, September 1997

[151]. S.Durrani & M.E.Bailkowski , “Simulation of the performance of smart antenna in the reverse link of CDMA system”, IEEE MTT-S Digest, pp. 575-578,2003.

[152]. S.W. Kim, D.S.Ha and D.H.Kim , “Performance gain of smart antennas with diversity combining at handsets for 3GPP WCDMA systems”, 13th International conference on Wireless Communications (Wireless 2001), Calgary, Alberta, Canada, pp 235-242, July 2001.

[153]. S.W. Kim, D.S.Ha and D.H.Kim , “Performance of Smart Antennas with Adaptive Combining at handsets for the cdma2000 system”, IEEE 54th Vehicular Technology conference, Atlantic city, NJ, USA, Vol.4, pp2048-2052 Oct. 2001

[154]. Shinya Tanaka, Atsushi Harada, Taisuke Ihara, Mamoru Sawahashi and Fumiyuki Adachi, " Combined effect of coherent adaptive antenna array diversity and SINR based fast transmit power control in WCDMA reverse link", IEICE Trans of Communications, Vol. E84-B, no.3 ,pp.425-433, March2001

[155]. T. Ohgane, T. Shimura, N. Matsuzawa, and H. Sasaoka, "An Implementation of a CMA Adaptive Array for High Speed GMSK Transmission in Mobile Communications", IEEE Trans. Veh. Technol., vol.42, no3, pp.282–288, August 1993.

[156]. T.S.Rappaport, "Wireless Communications; Principles and Practice", NJ; Prentice Hall PTR,1996.

[157]. Tero Ojanpera and Ramjee Prasad, "An Overview of Air Interface Multiple Access for IMT-2000/UMTS", IEEE Communications Magazine, vol. 36, pp. 88-95, September 1998.

[158]. V.K.Garg, "IS95 CDMA and cdma 2000- Cellular/PCS systems Implementation", Pearson Education Asia, 2002.

[159]. V.M.Bogachev and I.G.Keselev, "Optimum combining of signals in space diversity reception", Telecom Radio Engg, vol. 34/35, pp.83-85, October1980.

[160]. V. Tarokh, N. Seshadri, and A. R. Calderbank, "Space-time codes for high data rate wireless communications: Performance criterion and code construction," *IEEE Trans. on Information Theory*, vol. 44, no. 2, pp. 744–765, March 1998.

[161]. V. Tarokh, N. Seshadri,,A.Naguib and A. R. Calderbank, "Space-time codes for high data rate wireless communications: Performance criteria in the presence of channel estimation errors," *IEEE Trans. on Communications*, vol. 47, no. 2, pp. 199-207, Feb,1999.

[162]. W C Jakes, "Microwave Mobile communication", Wiley, New York, 1974

[163]. W. L. Stutzman and G. A. Thiele, "Antenna Theory and Design", John Wiley & Sons, New York, 1981.

[164]. W. R. Braun and U. Dersch, "A Physical Mobile Radio Channel Model", IEEE Trans. Veh. Tech., vol.40, no.2, pp. 472–482, May 1991.

[165]. W. Stewart, "Independent Expert Group on Mobile Phones", Mobile Phones and Health, NRPB, UK, May 2000. Available at:www.iegmp.org.uk

[166]. W. Sweldens and B. M. Hochwald, "Differential unitary space-time modulation," IEEE Trans. on Communications, vol. 48, no. 12, pp. 2041–2052, Dec. 2000.

[167]. W.C.Y.Lee, “Mobile Cellular Telecommunications systems”, McGraw Hill, 1989.

[168]. Wireless World Research Forum (WWRF), “The book of visions 2001—visions of the wireless world”, version 1.0, December 2001.Available at: www.wirelessworld- reserach.org.

[169]. Y. Li et al, “Performance evaluation of a cellular base station multi beam antenna”, IEEE Transaction. Vehicular Technology, vol. 46, no. 1, pp. 1–9,1997

[170]. Y.Ogawa, M.Ohmiya and K.Itoh, “An LMS adaptive array for multipath fading reduction”, IEEE Transaction on Aerospace and Electron Systems, vol.23, no.1, pp.17-23, January 1987.

[171]. Y.S.Yeh and D.O.Reudink, “Efficient spectrum utilization for mobile radio systems using space diversity”, IEEE trans. on Communication, vol. COM-30, no.3, pp. 447-455, March 1982.

[172]. Yueh Karen Lee, R.chandershekhran and John J. Shynk, “Separation of cochannel GSM signals using an adaptive array”, IEEE transaction signal processing, vol.47, no.7, pp.1977-1989, July 1999.

[173]. Zoran Zvonar, Bjorn A Bjerke and John G Proakis,” Antenna diversity combining schemes for WCDMA systems in fading multipath channels”, IEEE transactions on wireless communications, vol. 3, no. 1, pp.97-106, Jan.2004.

[174]. Zheng.L and D. N. C. Tse, “Diversity and multiplexing: A fundamental tradeoff in multiple antenna channels,” *IEEE Trans. on Information Theory*, vol. 49, no. 5, pp. 1073–1096, May 2003.

Vita

Rajesh Khanna was born on ***13th September, 1965*** at Ambala. He received his B.Sc(Engg.) degree in Electronics & Communication in ***1988*** from ***Regional Engineering College, Kurukshetra*** *with honors*. He then joined ***Hartron R&D*** center and developed many projects for industry and Defence. In 1993, he joined ***Ministry of Information & Broadcasting*** as Assistant Station Engineer after clearing the exam of ***Indian Engineering Services(IES)*** in 1990 and was posted at All India Radio, Jallandhar. There, he looked after operation and maintenance of 300KW, Jallandhar transmitter and 100 KW, Urdu Service transmitter. He ***installed dynamic carrier controller, new 2x100 KW transmitter and new Antenna Tuning Unit (ATU) at AIR, Jallandhar***. In 1996 he joined ***Indian Institute of Sciences, Bangalore*** for higher studies. He obtained M.E degree in Electrical Communication Engineering *with distinction* in 1998 from *IISc, Bangalore*. Presently he is working as Assistant Professor in the Department of Electronics and Communication at Thapar Institute of Engg. & Technology, Patiala.